SYSTEM RESPONSE OF LIQUEFIABLE DEPOSITS:

Insights from advanced analyses of case-histories from the 2010–2011 Canterbury earthquakes

A Thesis Submitted in Partial Fulfilment of the Requirements
for the Degree of Doctor of Philosophy in

Earthquake Engineering

By

Nikolaos Ntritsos

February, 2021

Department of Civil and Natural Resources Engineering
University of Canterbury

ABSTRACT

Advanced seismic effective-stress analysis is used to scrutinize the liquefaction performance of 55 well-documented case-history sites from Christchurch. The performance of these sites during the 2010-2011 Canterbury earthquake sequence varied significantly, from no liquefaction manifestation at the ground surface (in any of the major events) to severe liquefaction manifestation in multiple events. For the majority of the 55 sites, the simplified liquefaction evaluation procedures, which are conventionally used in engineering practice, could not explain these dramatic differences in the manifestation.

Detailed geotechnical characterization and subsequent examination of the soil profile characteristics of the 55 sites identified some similarities but also important differences between sites that manifested liquefaction in the two major events of the sequence (YY-sites) and sites that did not manifest liquefaction in either event (NN-sites). In particular, while the YY-sites and NN-sites are shown to have practically identical critical layer characteristics, they have significant differences with regard to their deposit characteristics including the thickness and vertical continuity of their critical zones and liquefiable materials.

A CPT-based effective stress analysis procedure is developed and implemented for the analyses of the 55 case history sites. Key features of this procedure are that, on the one hand, it can be fully automated in a programming environment and, on the other hand, it is directly equivalent (in the definition of cyclic resistance and required input data) to the CPT-based simplified liquefaction evaluation procedures. These features facilitate significantly the application of effective-stress analysis for simple 1D free-field soil-column problems and also provide a basis for rigorous comparisons of the outcomes of effective-stress analyses and simplified procedures.

Input motions for the analyses are derived using selected (reference) recordings from the two major events of the 2010-2011 Canterbury earthquake sequence. A step-by-step procedure for the selection of representative reference motions for each site and their subsequent treatment (i.e. deconvolution and scaling) is presented. The focus of the proposed procedure is to address key aspects of spatial variability of ground motion in the near-source region of an earthquake including extended-source effects, path effects, and variation in the deeper regional geology.

The ability of the adopted analysis procedure to simulate key aspects of ground response in liquefiable deposits including the observed ground motions at several strong motion station sites of Christchurch is first demonstrated. Effective stress analyses of the 55 case history sites are then used to identify key mechanisms of system response of liquefiable deposits and quantify their effects on the development and evolution of liquefaction throughout the deposit including its surface manifestation. The vertical continuity of critical zones and liquefiable soils is identified as a key factor in system-response mechanisms that intensify liquefaction manifestation (e.g. YY-sites). Conversely, the lack of vertical continuity in the case of interbedded deposits of liquefiable and non-liquefiable soils (e.g. NN-sites), is identified as a key factor in system-response mechanisms that mitigate liquefaction manifestation. The scrutiny of the effective-stress analyses results highlights the important effects of system response of liquefiable deposits and demonstrates the potential for significant improvements in liquefaction damage assessment when such effects are appropriately considered.

Overall, this study sets a paradigm for rigorous forensic assessments of ground response including comparative analyses and consistent treatment, from model calibration and definition of input motions to evaluation and interpretation of results, of a large number of (case-history) sites. It also demonstrates how such a comprehensive approach can provide valuable insights into various aspects of ground response and seismic performance that enable us to inform and advance current engineering practices.

Keywords: case history; earthquake; effective stress analysis; liquefaction; system response

ACKNOWLEDGEMENTS

First and foremost, I would like to express my sincere gratitude to my supervisor Professor Misko Cubrinovski for his continuous support, guidance, and encouragement throughout the course of this project. I greatly appreciate his always wise advice, kindness, and understanding. I am also very grateful for his careful review of the draft of this dissertation.

I would also like to thank Professor Brendon Bradley for his invaluable advice and support, and for thoroughly reviewing parts of this dissertation.

I wish to thank Professor Steven Kramer and Professor Jonathan Stewart for taking their valuable time to thoroughly review the thesis and provide constructive comments.

Insightful comments and suggestions by Professor Jonathan Bray at the early stage of this research are also greatly appreciated.

Thanks to Dr. Sjoerd van Ballegooy, Dr. Christopher McGann, Dr. Robin Lee, Dr. Hoby Razafindrakoto, Dr. Karim Tarbali, and Christopher de la Torre for kindly providing valuable data that have contributed greatly to the quality of this research.

I would like to extend my gratitude to all members of the geotechnical engineering research group of the University of Canterbury and especially Aimee Rhodes, Dr. Maxim Millen, Dr. Claudio Cappellaro, and Ribu Dhakal. Aimee studied first the system response of liquefying deposits of Christchurch and has assisted in scrutinizing the in-situ data used in the present study. Fruitful discussions with Maxim, Claudio, and Ribu have inspired parts of this research.

Special thanks to my officemates: Claudio Cappellaro, Jian Cui, Ribu Dhakal, Ashu Kedia, and Jono MacIntyre, and to all past and current postgraduate students of the Civil and Natural Resources Engineering department, for the many great moments we have shared together in and out of the office. I also wish to thank the admin staff of the department and the QuakeCoRE admin team for their continuous support and efficiency in managing administrative issues.

Although not directly related to the present research, it would be impossible not to mention my gratitude to my former supervisors including Professor George Gazetas, Professor Ioannis Anastasopoulos, and Professor Carlo Lai. Their inspiring enthusiasm for research and strong encouragement to continue further my studies have been crucial to my decision to pursue a doctorate degree.

The funding for this research has been provided jointly by the QuakeCoRE New Zealand Centre for Earthquake Resilience and the New Zealand Earthquake Commission (EQC). Their support is gratefully acknowledged.

Last but not least, I would like to thank all those people who have supported and influenced me throughout the course of this research: my parents and my brother, my lifelong friends from Greece, the many new friends I made in New Zealand and while travelling overseas over the last four years.

TABLE OF CONTENTS

LIST OF FIGURES

Page

LIST OF TABLES

Page

1 INTRODUCTION

1.1 Overview

Liquefaction assessment including triggering and consequences of liquefaction is routinely carried out by geotechnical engineers using semi-empirical *simplified procedures* which are largely based on observations from case histories (e.g. Seed et al. 1985, Robertson and Wride 1998, Youd et al. 2001, Moss et al. 2006, Idriss and Boulanger 2008, Boulanger and Idriss 2014). Such liquefaction case histories essentially reflect the overall response of soil deposits and associated severity of liquefaction manifestation for a specific earthquake excitation. However, despite the intent to capture the overall performance of the deposit at a given site, in the simplified procedures each layer is considered in isolation, and a factor of safety against liquefaction triggering, maximum shear and volumetric strains are estimated separately for each layer, and independently from the response of other layers in the deposit. In other words, interactions between different layers in the deposit in the dynamic response, and through the excess pore water pressure redistribution and water flow are ignored. Hence, principal mechanisms of cross-interactions between layers or *system-response* effects of liquefying deposits that potentially contribute to the severity of liquefaction manifestation and associated damage are not accounted for in the simplified procedures. Liquefaction damage indices, such as *LSN* (van Ballegooy et al. 2014) and *LPI* (Iwasaki et al. 1978), use specific weight functions to quantify the damage potential of liquefying layers depending on their proximity to the ground surface, but still, when calculating the cumulative damage index for a given site, a simple superposition of independent effects from each layer is used, while cross-interactions between layers during the development of liquefaction and post-liquefaction triggering are simply ignored.

In the 2010-2011 Canterbury Earthquake Sequence, widespread and damaging liquefaction affected nearly half of the urban area of Christchurch including 60,000 residential buildings and properties (van Ballegooy et al. 2014, Cubrinovski et al. 2019). Particularly severe liquefaction occurred in the eastern suburbs of Christchurch along the Avon River where lateral spreading also occurred (Cubrinovski and Robinson 2016). After the 2010-2011 earthquakes, several studies were carried out to scrutinize the accuracy of simplified liquefaction evaluation procedures in predicting liquefaction triggering (manifestation) and associated damage. Green et al. (2014) found that the CPT-based procedures of Idriss and

Boulanger (2008), Robertson and Wride (1998), and Moss et al. (2006) accurately predicted the liquefaction manifestation for the majority of 25 well-documented case history sites from Christchurch and Kaiapoi. van Ballegooy et al. (2014) and Maurer et al. (2014) used the large CPT database in Christchurch to find that liquefaction damage indices, such as LSN and LPI, were capable of depicting the general trends in liquefaction damage, and provided an improved definition and guidance for use of such damage indices. However, these studies also found that, in a significant number of cases, predictions from the simplified methods were inconsistent with field observations. In particular, systematic over-predictions of liquefaction occurrence were observed in specific areas and for certain types of soils and stratification of deposits including silts, silty sands with non-plastic or low-plasticity fines, and interbedded deposits composed of liquefiable and non-liquefiable soils.

The reasons for these mis-predictions by the simplified methods can be many including, on the one hand, the relatively poor (as compared to clean sands) quality of the material and behavioural characterization of silty soils at the element level (*element-level response*), and on the other hand, the neglect in the evaluation of various cross-interactions between layers within the deposit (*system response*). Findings from high-quality laboratory studies (e.g. Beyzaei et al. 2018) on the element-level response and associated cyclic resistance of Christchurch silty soils are generally consistent with the respective estimates from simplified liquefaction triggering procedures. Yet, other studies (Cox et al. 2017, Boulanger et al. 2018, Yost et al. 2019) have suggested that the combined effect of: (1) under-prediction of fines content, which is a key parameter used in the simplified methods to estimate (adjust) the cyclic resistance of fines-containing soils; (2) thin-layer and transition zone effects on the measured cone penetration resistance; and (3) a false assumption of fully saturated soils below the groundwater table, can lead to a severe under-prediction of the actual in-situ liquefaction resistance of silty soils. Although, clearly, addressing some of the above limitations of the default practices and assumptions in the application of the simplified method can improve predictions, the associated corrections to the element-level response (cyclic resistance of individual layers) do not seem to fully explain the large discrepancies (in number of cases and significance of mis-prediction) between the predictions of the simplified method and the actual observations of liquefaction manifestation from the 2010-2011 Canterbury earthquakes.

In this context, the present dissertation explores effects of the system response of Christchurch deposits based on rigorous back-analyses of 55 well-documented case histories of level ground free-field sites that showed vastly different performance during the earthquakes, from no liquefaction manifestation to extreme severity of liquefaction. The study builds upon previous work by Rhodes (2017) and Cubrinovski et al. (2019) who used seismic effective stress analyses to identify key system response mechanisms of representative soil profiles from Christchurch and demonstrated that such mechanisms can profoundly impact the occurrence and severity of liquefaction manifestation at the ground surface. The aim of the present study is twofold:

(1) To develop a robust methodology for forensic effective stress analysis of sites in the near-source region which: (a) can be consistently applied across all 55 sites of interest; (b) can

accurately simulate the seismic demand induced by the considered earthquakes and the associated response of liquefiable soils and deposits; and, (c) will allow for rigorous comparisons with the predictions of simplified procedures for liquefaction assessment.

(2) Using the results from the analyses, to scrutinize the complex system response of liquefiable deposits, identify key interaction mechanisms and quantify their effects, and examine their combined influence on the development of liquefaction throughout the deposit and its severity of manifestation at the ground surface.

1.2 Thesis Organization

The present thesis is organized in the following chapters.

This chapter lays out the motivation for the study and briefly describes the main objectives and thesis outline.

Chapter 2 provides a brief but essential background required to better appreciate the key research questions and contributions from this study. Key features of the 2010-2011 Canterbury earthquakes, fundamental aspects of sandy soil behaviour, limitations and challenges of liquefaction assessment methods, and past developments in aspects of the system response of liquefiable deposits are reviewed.

Chapter 3 presents a detailed geotechnical characterization and analysis of the 55 investigated sites. The near-surface geology and geomorphology of Christchurch and the performed investigations at the 55 sites are discussed first. Then, key soil profile characteristics of the 55 sites are comparatively examined in relation to their associated performance (liquefaction manifestation) during the Canterbury earthquakes. Supplementary material to this chapter including soil profiles and results from liquefaction triggering analysis for all 55 sites is provided in Appendix A.

Chapter 4 describes the seismic effective stress analysis procedure used to assess the performance of the 55 sites. The proposed procedure includes the following main steps: (a) determination of a simplified soil profile; (b) determination of characteristic soil behaviour and associated constitutive model parameters for each layer of the simplified profile; (c) definition of input ground motion; and, (d) definition of numerical model (mesh, initial and boundary conditions) and analysis parameters. The procedure is designed with the objective to facilitate its practical application by, essentially, using the same input data and the same definition of liquefaction resistance as the simplified CPT-based liquefaction evaluation procedures. These features also provide a basis for rigorous comparisons of the outcomes of effective-stress analyses and simplified procedures.

Chapter 5 discusses key steps and challenges in defining representative input ground motions for the forensic analyses of the 55 near-source sites. Within-event recorded surface ground

motions at selected strong motion station sites of Christchurch are used as reference motions to derive the respective input ground motions for each site of interest and for each considered earthquake. The selection and treatment (i.e. deconvolution and amplitude scaling) of reference within-event ground motions are discussed with emphasis on the key factors of (near-source) spatial ground motion variability that need to be considered in these processes. A novel 'amplitude-duration' scaling approach which targets both the amplitude and duration of ground motion is introduced. Supplementary material to this chapter is provided in Appendix B.

Chapter 6 evaluates the performance of alternative input motions and associated simulations of ground response using the developed effective-stress analysis procedure at 13 strong motion station sites of Christchurch. The performance of each simulation is evaluated by comparing recorded surface motions to those predicted by the effective-stress analyses. The comprehensive evaluation of the simulated responses of the strong motion station sites serves as validation for the adopted input motions and effective-stress analysis procedure and indicates important factors to consider in the analyses of the 55 Christchurch sites. Supplementary results from the analyses of the strong motion station sites are provided in Appendix C.

Chapter 7 presents a comprehensive scrutiny and system-level interpretation of the effective-stress analyses of the 55 sites. Important effects of system response of liquefiable deposits are first illustrated through example responses of selected sites associated with different severity of liquefaction manifestation. Based on a systematic analysis and quantification of the computed responses of the 55 sites, five principal types of system responses are identified and discussed. Limitations of simplified procedures are examined in the context of the identified types of system responses, and a new system-response based framework for assessment of liquefaction manifestation is introduced. The comprehensive scrutiny of the analyses results highlights the important effects of system response of liquefiable deposits and demonstrates the potential for significant improvements in liquefaction damage assessment when such effects are appropriately incorporated. Characteristic results from the effective-stress analyses for all 55 sites are provided in Appendix D.

Chapter 8 summarizes key findings and contributions from this dissertation and discusses future research needs.

2 BACKGROUND

2.1 Introduction

While the ultimate goal of this research is to elucidate the system response of liquefiable deposits and provide a framework for quantification of the relevant mechanisms and effects, a variety of requisite tasks, which do not strictly pertain to the main research goal, have been addressed. Rather than thoroughly reviewing here the literature relevant to these topics, the scope of this chapter is to provide the reader with the essential context needed to understand better the key research questions and appreciate the pertinent contributions. Further background information and previous work on specific topics is provided in the relevant chapters.

Observations from the 2010-2011 Canterbury Earthquake Sequence (CES) were the key motivation for this research, and the evaluation of selected case-histories from these earthquakes is at the core of the adopted research methodology. Hence, key aspects of the 2010-2011 Canterbury earthquakes are discussed first in this chapter. Next, some fundamental aspects of the shear response of sandy soils are briefly reviewed. Then, an overview of the current state-of-practice and state-of-the-art methods for liquefaction assessment with emphasis on the advantages and limitations of each method is presented. Finally, previous research findings and current understanding on aspects of the system response of liquefiable deposits are discussed.

2.2 The 2010-2011 Canterbury Earthquake Sequence

In the period between September 2010 and December 2011, Christchurch, New Zealand was hit by a series of strong earthquakes, known as the Canterbury Earthquake Sequence (CES) (e.g. Elwood et al. 2014). The sequence included four events with moment magnitude $M_w \geq 5.9$ and other five earthquakes with M_w 5.0–5.8. The causative faults of these earthquakes were either in the proximity to or within the city boundaries. Surface ground motions from the 2010-2011 CES were recorded across Christchurch and its environs by a dense network of strong motion stations (e.g. Bradley and Cubrinovski 2011, Bradley 2012, Bradley 2015). Particularly severe ground motions were recorded during the 22 February 2011 M_w6.2

Christchurch earthquake. With spectral accelerations at several locations exceeding the regional seismic design spectra at the time, the February 2011 earthquake was devastating, causing 185 fatalities, collapse of two multi-storey reinforced concrete buildings, and collapse or partial collapse of many unreinforced masonry structures. In total, the 2010-2011 CES caused tremendous damage to buildings and infrastructure, and total economic loss of approximately 30 billion NZ dollars (or about 15% of New Zealand's GDP) (Cubrinovski and Robinson 2016).

The geotechnical aspects of the 2010-2011 Canterbury earthquakes were exceptional, both in terms of extent and severity of damage. In particular, widespread and damaging liquefaction affected nearly half of the urban area of Christchurch including 60,000 residential buildings and properties. Liquefaction and lateral spreading also caused heavy damage to several multi-storey buildings in the Central Business District (CBD), as well as damage to roads, bridges, and buried pipe networks of potable and wastewater systems (e.g. Cubrinovski et al. 2010, 2011, 2012, 2014, Bray et al. 2014, O'Rourke et al. 2014, van Ballegooy et al. 2014). Fig. 2.1 illustrates the distribution and severity of liquefaction-induced land damage across the urban area of Christchurch in the four major events of the sequence (Russell and van Ballegooy 2015). The documentation of the severity of liquefaction in these maps is based on observations of the surface manifestation of liquefaction in the form of soil ejecta and differential ground surface settlement (subsidence). The former was documented in detailed field inspections on a property-by-property basis. Contours of the estimated peak ground accelerations for each earthquake are also shown in this figure. It can be seen that extensive and repeated liquefaction was triggered in specific areas of the city, particularly in the eastern suburbs along the Avon River, whereas many other areas to the south and west of CBD did not manifest liquefaction even when subjected to the severe ground shaking induced by the 22 February 2011 earthquake. Investigating these differences in the performance among various Christchurch sites through interpretation of their system response is the main subject of this thesis.

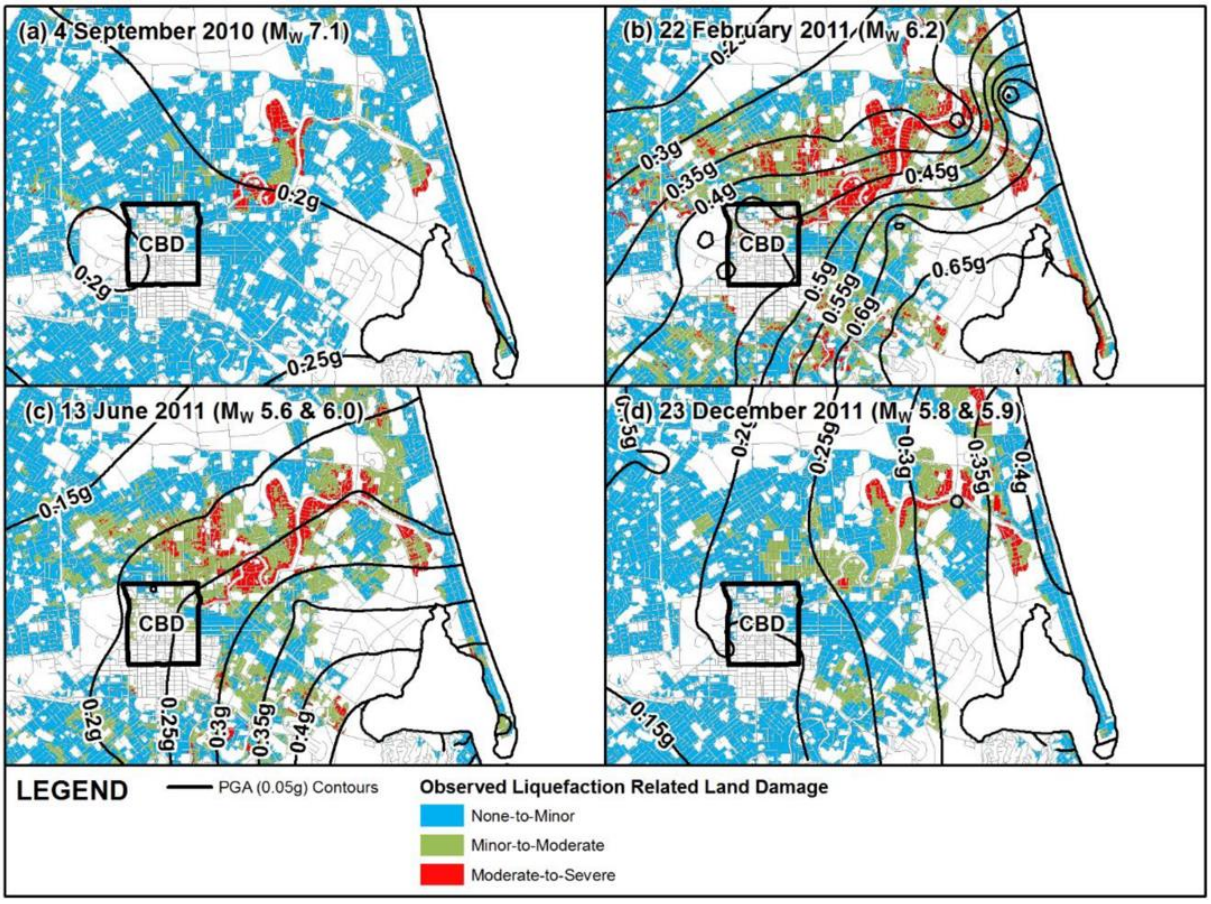

Fig. 2.1 Christchurch maps showing the inferred levels of earthquake shaking (PGA) and the observed land damage for urban residential properties after the four major events in the sequence: (a) 4 September 2010; (b) 22 February 201; (c) 13 June 2011; (d) 23 December 2011 earthquakes (Russell and van Ballegooy 2015); *the illustrated median estimates of PGA were obtained on the basis of the prediction from empirical ground motion prediction equations, the observations of ground motion intensity at nearby strong motion stations, and the within-event spatial correlation of ground motion intensity (Bradley 2014).*

2.3 **Shear Response of Sandy Soils**

2.3.1 Liquefaction resistance

When granular materials are subjected to monotonic or cyclic shear loads (i.e. primary type of loading during earthquake shaking), they exhibit a tendency for volume change due to rearrangement of their particles, a phenomenon known as dilatancy in granular materials (Reynolds 1885). Under undrained conditions and for soil materials fully saturated with water, volume change cannot be realized because of the low compressibility of water; instead, it is compensated by an equivalent change in the pore water pressure and, which in turn results into a change in the effective stress (i.e. change in the contact forces between soil particles).

Fig. 2.2 illustrates a typical response of a medium-dense saturated sand to undrained cyclic simple shear of constant stress amplitude, under constant total vertical stress (Seed et al. 2003). In this figure, the bottom left plot (Fig. 2.2c) illustrates the evolution of the excess pore water pressure ratio (r_u), defined as the ratio of the excess pore water pressure (u_e) to the initial vertical effective stress (σ'_{vo}; σ'_c in the figure); the bottom right plot (Fig. 2.2d) shows the development of cyclic shear strains (γ) with the number of loading cycles; the top right plot (Fig. 2.2b) shows the normalized shear stress versus shear strain response ($\tau/\sigma'_{vo} - \gamma$); and the top left plot (Fig.2.2a) shows the effective stress path ($\tau/\sigma'_{vo} - \sigma'_v/\sigma'_{vo}$). It can be seen from these test records that the pore water pressure builds up steadily throughout cyclic loading and eventually approaches a value nearly equal to the initial vertical effective stress ($r_u \approx 1.0$). These changes in the pore water pressure are accompanied by a progressive net reduction in the vertical effective stress and a progressive softening of the soil as manifested in the shear stress–shear strain response. The cyclic shear strains are relatively small for the first 25–27 cycles until significant excess pore water pressures have been generated, after which the strains start increasing significantly with each additional cycle. Liquefaction triggering is said to have occurred in such tests when the excess pore water pressure ratio r_u or, more commonly, the shear strain (single amplitude (SA) or double amplitude (DA) strain) exceeds a certain threshold (e.g. SA strain > 3% or DA strain > 5-7.5%).

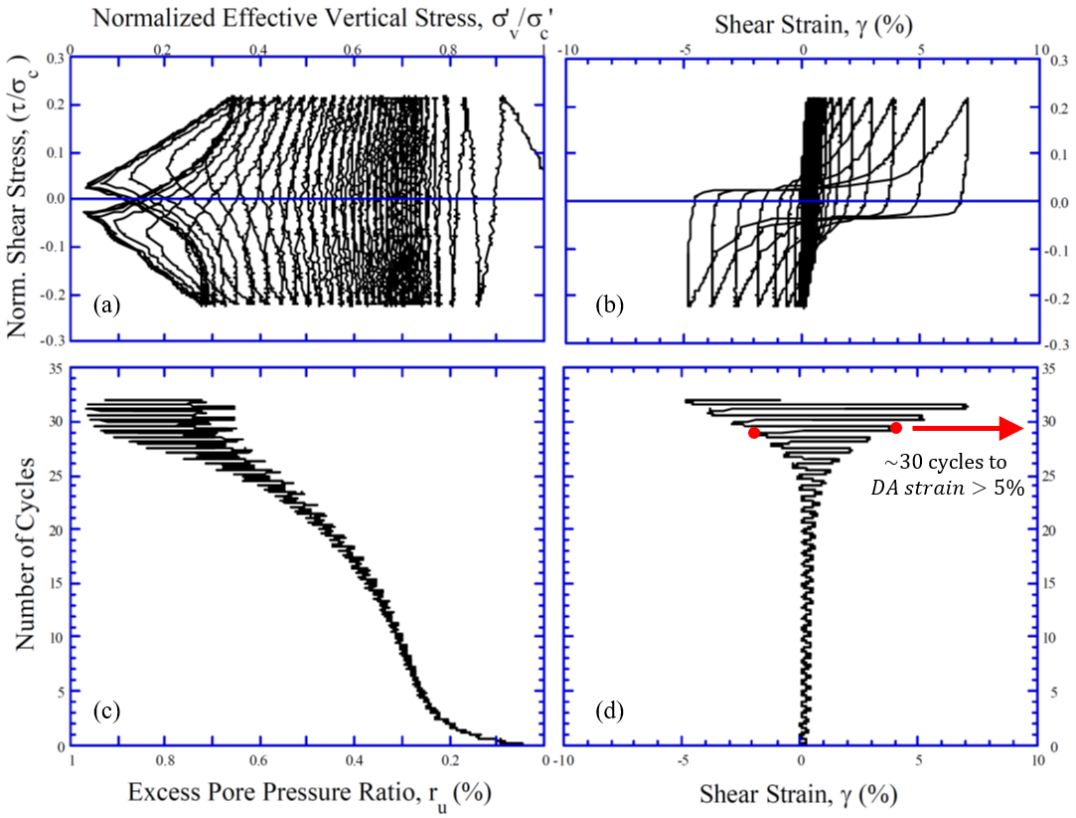

Fig. 2.2 Characteristic response of medium-dense ($D_r = 50\%$) Monterey #30/0 sand (with initial vertical effective stress $\sigma'_{vo} = 85$ kPa) to undrained cyclic simple shear: (a) stress path, (b) stress-strain curve, (c) development of excess pore water pressure with number of loading cycles, (d) development of shear strain with number of loading cycles. Liquefaction triggering (DA strain in excess of 5%) for the given stress amplitude occurs after about 30 loading cycles (modified after Seed et al. 2003).

Liquefaction can be triggered by different combinations of applied shear stress amplitude and number of loading cycles. In the above example, about 30 cycles of uniform stress amplitude $CSR = \tau/\sigma'_{vo} = 0.20$ are required to trigger DA strains (peak-to-peak strains in one cycle) in excess of 5%, which is herein adopted as the liquefaction triggering threshold. The combination of shear stress amplitude (CSR) and number of cycles (N_c) required to cause triggering of liquefaction, or a certain level of strain in the soil, are typically represented with $CSR - N_c$ relationship referred to as a liquefaction resistance curves (LRC), as shown in Fig. 2.3a.

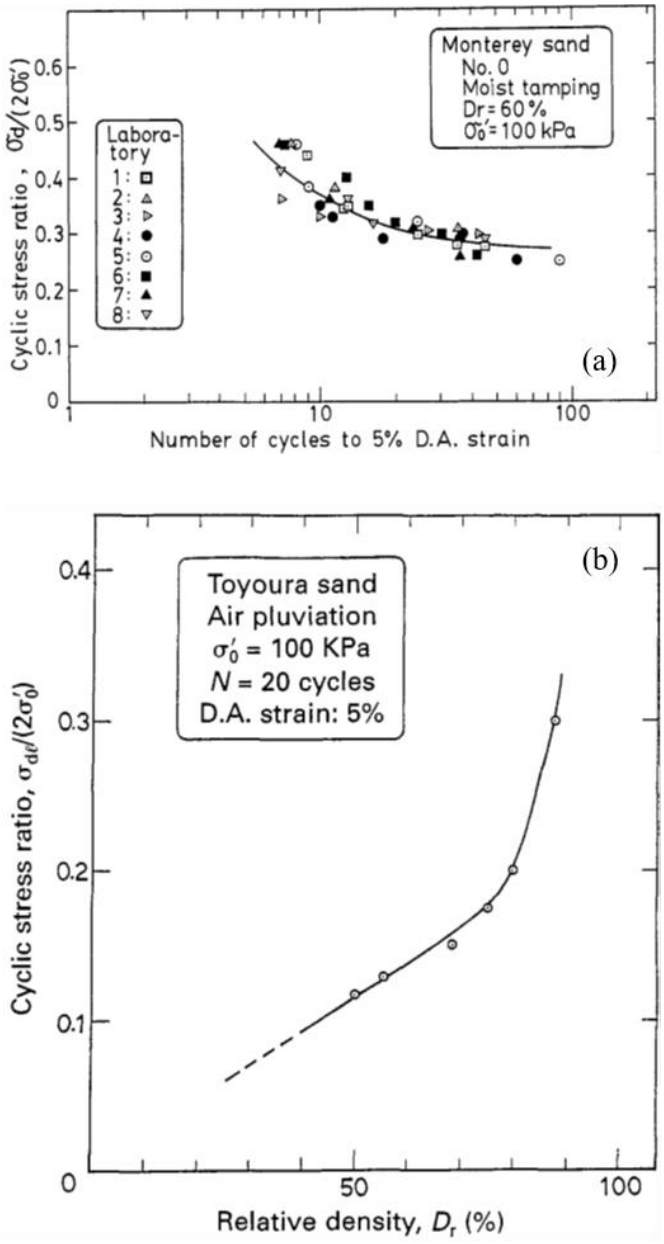

Fig. 2.3 Cyclic stress ratio (CSR) required to cause triggering of liquefaction (DA strain 5%): (a) CSR versus number of loading cycles for a given initial state (relative density, confining stress, fabric), (b) CSR versus relative density for a given number of loading cycles, confining stress, and soil fabric (Ishihara 1995).

Another format of representing the resistance of a soil to liquefaction triggering is to plot the shear stress amplitude required to trigger liquefaction at a given number of cycles against the initial relative density of the soil, as shown in Fig. 2.3b. As can be seen from this figure, the stress amplitude required to trigger liquefaction in 20 cycles increases with an increasing rate as the relative density of the sand increases. The relative density has long been recognized as a dominant factor influencing the cyclic liquefaction resistance of sands.

2.3.2 State concept interpretation of sand behaviour

The stress-strain behaviour of sand and its resistance against liquefaction triggering depends upon several factors including the relative density, confining stress, fabric, fines content, initial static shear, age, mineralogy, and others. A convenient way for characterizing the influence of some of these factors, and particularly the relative density and confining stress, on sand behaviour is through the use of the critical state soil mechanics (e.g. Schofield and Wroth 1968) and state concept interpretation (Roscoe and Poorooshasb 1963, Been and Jefferies 1985). The critical state, or the nearly synonymous steady state of deformation, refers to the conditions that exist in sand when it is being sheared continuously under monotonic loading with no changes in volume or stress occurring, and it defines the critical state line (CSL) (or steady state line (SSL)), which represents all possible combinations of void ratio (e) and confining effective stress (p') at the critical state (Fig. 2.4). The critical state line of a given soil is uniquely defined in the $e - p'$ plane. In other words, irrespective of the initial state, each monotonic shear test of a given sand ends up at its critical state line.

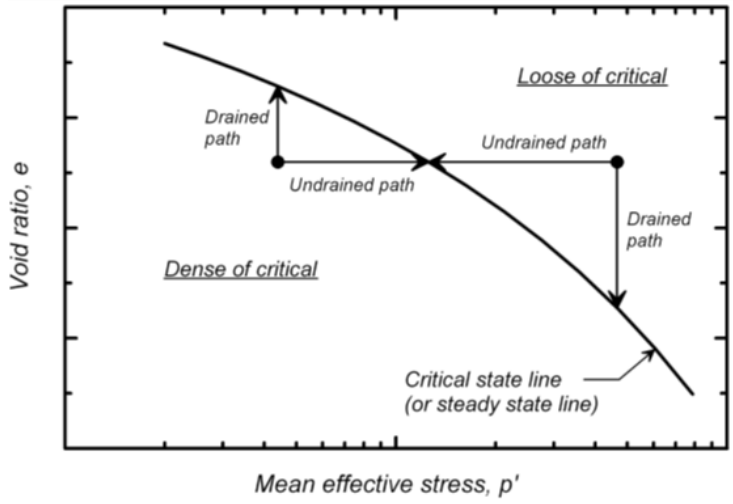

Fig. 2.4 Critical (or steady) state line and stress paths for monotonic drained loading with constant mean effective stress (p') and undrained loading (constant volume shearing) of saturated loose-of-critical and dense-of-critical sands (Idriss and Boulanger 2008).

The position of the initial state of a given sand in the $e - p'$ plane relative to its critical state line defines the $e - p'$ path and stress–strain response, for a given loading and drainage conditions. All initial $e - p'$ states that are 'loose of critical' (i.e. above the CSL) will show contractive behaviour upon monotonic shearing (i.e. decrease in volume in drained shear or decrease in effective stress in undrained shear). On the other hand, all initial $e - p'$ states that are 'dense of critical' (i.e. below the CSL) will show dilative behaviour (increase in volume in drained shear or increase in effective stress in undrained shear). Moreover, the further the initial state is from the critical state line, the more contractive or more dilative the sand behaviour is. Stress paths for monotonic drained loading with constant p' and undrained loading (constant volume shearing) of saturated loose-of-critical and dense-of-critical sands are schematically illustrated in Fig. 2.4.

The state concept can also be used to characterize the behaviour of sand in cyclic shear. In this case, dense-of-critical sands can also experience contraction of their soil skeleton in drained conditions (i.e. net volume decrease at the end of each half-cycle), or increase in pore water pressure and reduction in effective stress in undrained conditions. In both loose and dense sands, pore water pressures can build up in the course of undrained cyclic loading and eventually reach a state in which a peak pore water pressure equal or nearly equal to the initial effective confining stress is attained ('initial liquefaction'). For loose sands, this condition is accompanied by a rapid increase in cyclic shear strains upon further continuation of loading. For dense sands, a state of $r_u \approx 1.0$ does not produce such large changes in the deformability of the soil, instead, the shear strain increases steadily and gradually with progression of the loading cycles. This type of behaviour observed in dense-of-critical sands is known as 'cyclic mobility' (Castro 1975). Fig. 2.5 shows characteristic stress paths and stress-strain curves for loose sand and dense sand obtained from cyclic torsional shear tests (Ishihara 1985).

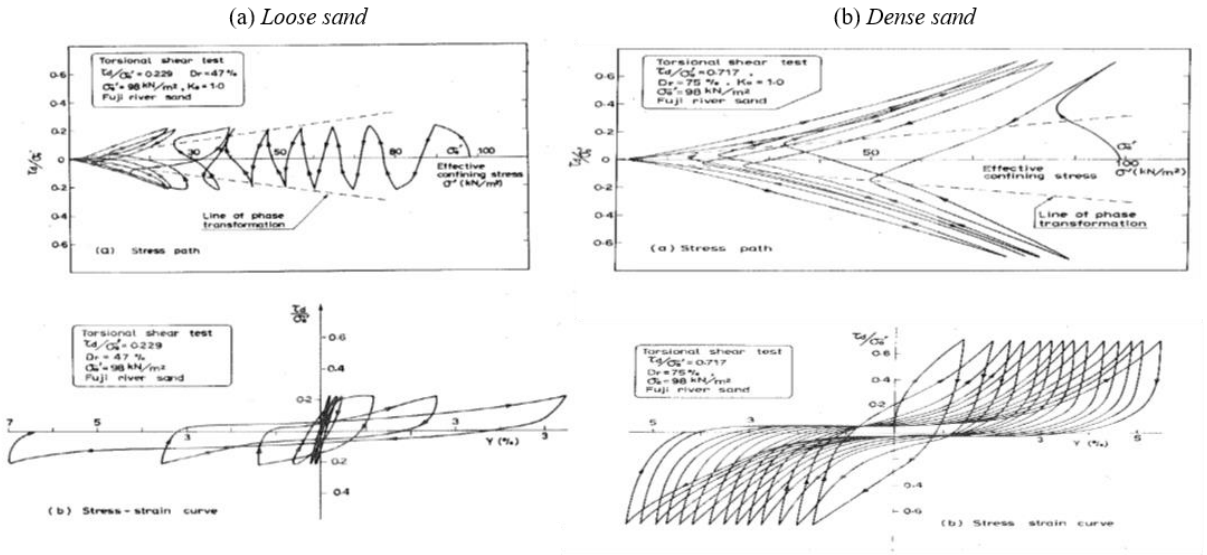

Fig. 2.5 Characteristic stress paths (top row) and stress-strain curves (bottom row) for (a) loose sand and (b) dense sand, obtained from cyclic torsional shear tests on Fuji river sand (Ishihara 1985).

As it can be seen from Fig. 2.5, both loose and dense sands can develop excess pore water pressures and large cyclic shear strains associated with liquefaction triggering, when sheared with sufficiently high level of loading for each case, but their response and consequences of liquefaction are dramatically different. Loose sands show highly contractive behaviour and can produce extremely large deformations following initial liquefaction. On the other hand, liquefaction triggering of dense sands results in large but limited strains (cyclic mobility), because the sand exhibits dilative behaviour and can mobilize significant shear resistance with increasing strains.

2.3.3 Effects of partial saturation and partial drainage

So far in this section, it has been assumed that the soil is fully saturated with water and that shear loading occurs under fully undrained conditions. However, field conditions may actually involve partially saturated soils and water flow into and out of soil elements both during and after the earthquake shaking. Partial saturation (i.e. part of voids filled with air) is typically encountered in soils above the groundwater table but it may be present also below the groundwater table due to groundwater table fluctuations and other natural processes. Partial drainage of soil elements (i.e. inflow or outflow of water and change in soil volume) can take place both during and after the earthquake shaking as a result of pore water pressure redistribution and seepage of water towards the ground surface, as discussed later in this chapter.

Numerous laboratory studies (cyclic triaxial tests) have examined the influence of partial saturation on the cyclic (liquefaction) resistance (e.g. Sherif et al. 1977, Yoshimi et al. 1989, Grozic et al. 2000, Tsukamoto et al. 2002, Yang et al. 2004, Nakazawa et al. 2004, Okamura et al. 2006, Okamura and Soga 2006, Kamata et al. 2009, Tsukamoto et al. 2014). In these studies, the increase in liquefaction resistance is typically expressed in $K_s - V_p$ relationships, where K_s is the ratio of the cyclic resistance of the partially saturated soil to the cyclic resistance of the same soil in fully saturated conditions, and V_p is used as an indicator of the degree of saturation of the soil. The association of K_s with V_p is typically adopted for practical convenience because, in contrast with the degree of saturation or B-value, V_p can be relatively easily measured in the field. Fig. 2.6a shows a $K_s - V_p$ relationship derived from cyclic triaxial tests on Toyoura sand at varying degrees of saturation (Tsukamoto et al. 2002). It can be seen from this figure that a substantial increase in liquefaction resistance is possible under partially saturated conditions ($V_p < 1500$ m/s).

Several laboratory studies have also focused on the shear behaviour of fully saturated sands using controlled volumetric strain paths (water injection/volume expansion or water extraction/volume contraction) to simulate partial drainage conditions (e.g. Boulanger and Truman 1996, Vaid and Eliadorani 1998, Tokimatsu et al. 2001, Sento et al. 2004, Yoshimine et al. 2006). Fig. 2.6b illustrates the monotonic stress-strain response of a medium-dense Toyoura sand subjected to varying levels of water injection, after initially sheared cyclically under undrained conditions until a DA strain of 0.5% is reached (Tokimatsu et al. 2001). The

parameter a in this plot is proportional to the ratio between volumetric and shear strains and increases with increasing volume of water injection. Under undrained conditions ($a = 0$) the specimen shows a strain-hardening behaviour, but with increasing a (increasing water injection) the behaviour becomes more contractive until, eventually, with a sufficient amount of water injection ($a = 1$), the specimen completely loses its shear resistance and undergoes flow liquefaction. The experimental evidence suggests that even strongly dilative dense-of-critical sands can exhibit highly contractive behaviour and flow liquefaction if a sufficient amount of pore water is absorbed, but the tendency for reduction in the shear resistance of the soil seems to be more pronounced as the soil density decreases and as the maximum cyclic shear strain during the undrained loading increases.

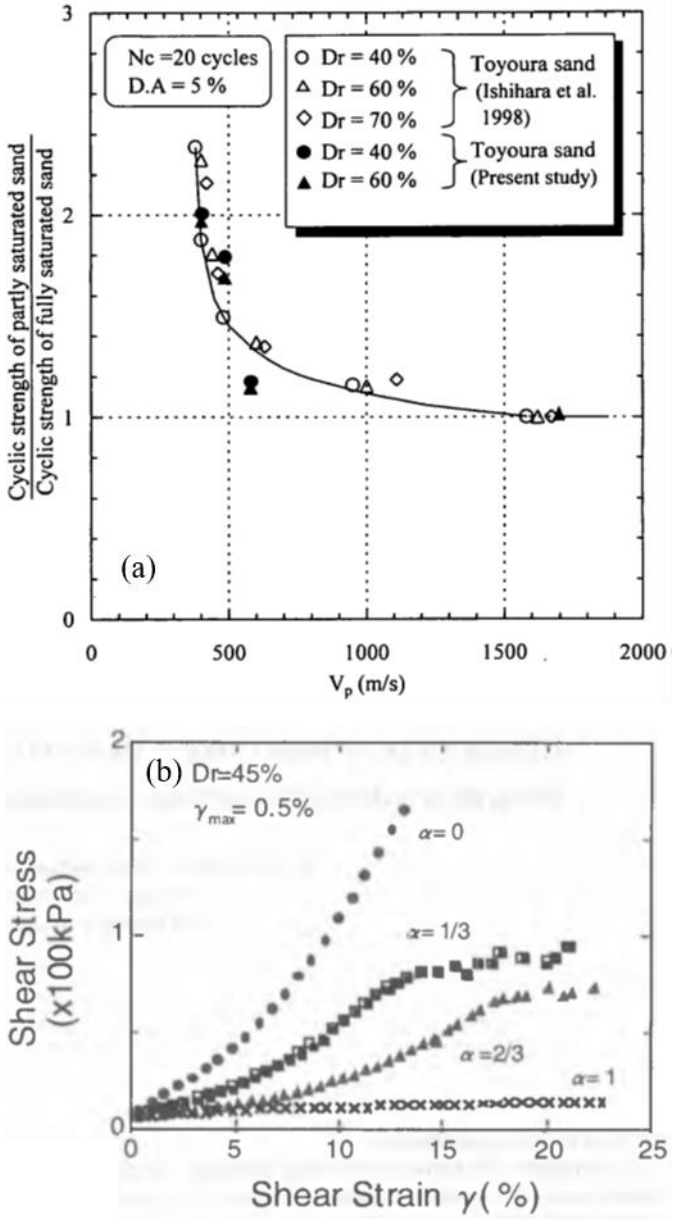

Fig. 2.6 (a) Effect of partial saturation ($V_p < 1500$ m/s) on cyclic resistance (Tsukamoto et al. 2002); (b) Monotonic shear stress – shear strain response of medium-dense saturated sand with water injection ($a > 0$) following undrained cyclic shear to 0.5% DA strain (Tokimatsu et al. 2001).

Effects of partial saturation and partial drainage are most often ignored in the liquefaction assessment employed in engineering practice. However, it is clear from the above that both can have a significant impact on soil response and overall performance evaluation of liquefiable deposits.

2.4 Liquefaction Assessment

Liquefaction assessment including triggering and consequences of liquefaction can be carried out using either semi-empirical methods (simplified procedures) (e.g. Robertson and Wride 1998, Youd et al. 2001, Idriss and Boulanger 2008, Boulanger and Idriss 2014) or advanced numerical methods, such as the seismic effective stress analysis. Only the most relevant aspects, advantages and limitations of the two approaches are discussed in this section. Further discussion on the limitations of the simplified procedures and details of the effective stress analysis method are provided in subsequent chapters.

2.4.1 Simplified procedures

The current state-of-practice in liquefaction assessment is still largely based on the procedures developed by the late Professor Seed and his co-workers in the 1970's (e.g. Seed and Idriss 1971, Seed 1979). In these stress-based procedures, earthquake-induced cyclic shear stresses (CSR) are compared with the cyclic (liquefaction) resistance (CRR) of the soil. Liquefaction triggering is predicted at those depths in the deposit where the induced shear stresses exceed the cyclic resistance or the factor of safety against liquefaction triggering is less than 1.0 ($FS_L = CRR/CSR \leq 1.0$).

The cyclic (liquefaction) resistance CRR is typically estimated through correlations with some in-situ test index, such as the normalized overburden-corrected cone tip resistance q_{c1N} (in the case of the CPT-based procedures) or the overburden and energy ratio corrected SPT blow-count $(N_1)_{60}$ (in the case of the SPT-based procedures). q_{c1N} (or $(N_1)_{60}$) is used as a proxy for the effects of the relative density on CRR (Fig. 2.3b), but it also reflects other important factors (e.g. fabric, stress history, age) that affect liquefaction resistance. Correlations between CRR and q_{c1N} (in the case of the CPT-based procedures) have been developed based on case histories of liquefaction manifestation in which $CSR - q_{c1N}$ pairs were identified for each case history (site). The $CSR - q_{c1N}$ pairs at each site represent the values of the seismic demand (load) and penetration resistance for the critical layer that was considered responsible for the liquefaction manifestation at the site. The liquefaction resistance (CRR) as a function of q_{c1N} is defined from the (approximate) triggering curve in the $CSR - q_{c1N}$ plane that separates case histories in which liquefaction was manifested at the ground surface from case histories in which such manifestation was not evident, as illustrated in Fig. 2.7. Note, however, that the absence of evidence of liquefaction at the ground surface does not

necessarily mean absence of liquefaction in the deposit; in fact, liquefaction may have been triggered at depth and not manifested at the ground surface.

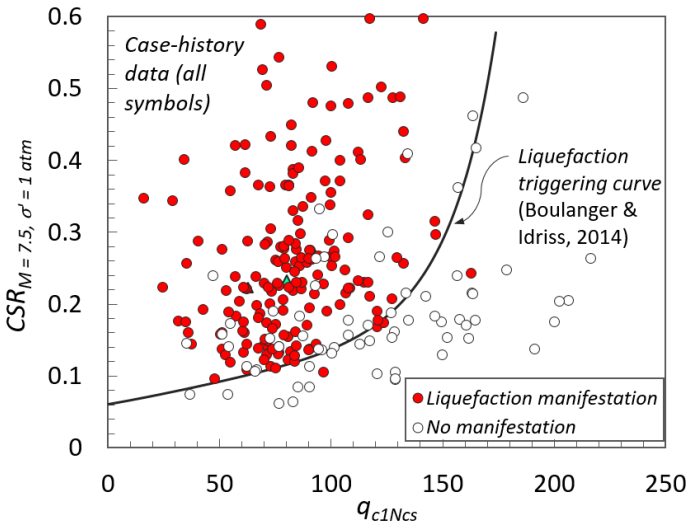

Fig. 2.7 CPT-based liquefaction triggering correlation of Boulanger and Idriss (2014), for $M_w = 7.5$ and $\sigma'_{vo} = 1$ atm.

Note that as Fig. 2.3b refers to the mobilized CRR at a constant number of loading cycles and constant confining stress, so does Fig. 2.7 refers to the CRR corresponding to a reference condition of earthquake magnitude $M_w = 7.5$ (used as a proxy for the number of loading cycles) and effective overburden stress $\sigma'_{vo} = 1$ atm. To represent all case-history data of varying M_w and σ'_{vo} values onto the same graph of the reference condition, appropriate (magnitude scaling MSF and overburden stress K_σ) correction factors have been applied to the estimated CSR (Eq. 2-1) for each case-history. The inverse correction factors are used in forward applications to estimate CRR for conditions different than the reference condition. In addition, the penetration resistance q_{c1N} is also adjusted to account for the effects of fines content (FC) on penetration resistance (e.g. Cubrinovski 2019), thus yielding the reference 'equivalent clean sand' penetration resistance (q_{c1Ncs}) plotted in Fig. 2.7.

The earthquake-induced CSR (for either a case-history or forward site liquefaction assessment) can be estimated at any depth (z) in the deposit either using ground response analysis or, alternatively, approximated as (Seed and Idriss 1971):

$$CSR = 0.65 \frac{\sigma_{vo}}{\sigma'_{vo}} \frac{a_{max}}{g} r_d(M_w, z) \tag{2-1}$$

where σ_{vo} and σ'_{vo} are the initial total and effective vertical stress at depth z, a_{max} is the maximum ground surface acceleration in g, and r_d is the shear stress reduction coefficient which can be expressed as a function of M_w and z. In this relationship, it is assumed that a_{max} and CSR are not affected by the development of excess pore water pressures during earthquake shaking. This means that the CSR value calculated from Eq. 2-1 (or through an

equivalent linear or total-stress nonlinear ground response analysis) is realistic only for cases in which $CSR < CRR$, i.e. for points below the triggering curve in Fig. 2.7 which do not experience enough pore pressure build-up to affect the shear stress-strain response of the soil. In cases where $CSR \gg CRR$, the actual CSR value in the field can be substantially less that the value calculated from Eq. 2-1, both within and above the liquefied layer, as a result of significant excess pore water pressure build-up and loss in effective stress. In such cases ($CSR \gg CRR$), CSR is still used as an index for the seismic demand in the simplified procedures but has no physical reality (Dobry and Abdoun 2015). Liquefaction effects on seismic demand are further discussed in section 2.5.

Consequences of liquefaction without considering interactions between layers

The case histories used in the development of liquefaction triggering correlations essentially reflect the overall response of soil deposits and associated severity of liquefaction manifestation for a specific earthquake excitation. However, despite the intent to capture the overall performance of the deposit at a given site, in the simplified procedures each layer is considered in isolation, separately from any other layers in the deposit. Consider, for instance, the six-layer soil profile depicted in Fig. 2.8, in which layers 3 and 5 are susceptible to liquefaction, whereas layers 1, 2, 4 and 6 are non-liquefiable. In the simplified procedure, the estimates of CRR (Fig. 2.7) and CSR (Eq. 2-1) for each layer are independent of the response of the other layers. In other words, potential effects of excess pore water pressures and liquefaction of a layer on the seismic demand and shear resistance of other layers in the deposit are not considered. A factor of safety against liquefaction triggering (FS_L) is defined as the ratio between CRR and CSR for each layer, and it is subsequently used in empirical charts (e.g. Ishihara and Yoshimine 1992) to estimate maximum shear strains (γ_{max}) and post-liquefaction reconsolidation volumetric strains ($\varepsilon_{v,max}$), again separately for each layer. In the final step of the assessment (for free-field level ground sites), liquefaction damage indices, such as LSN (van Ballegooy et al. 2014) and LPI (Iwasaki et al. 1978), are calculated using specific weighting functions to quantify the damage potential of liquefying layers depending on their proximity to the ground surface. But still, as illustrated in Fig. 2.8, when calculating the cumulative damage indices a simple superposition of independent effects from each layer is used, while cross-interactions between layers through the dynamic response, excess pore water pressures, and water flow are simply ignored. Hence, principal mechanisms of interaction or system-response effects of liquefying deposits that potentially contribute to the severity of liquefaction manifestation are not accounted for in the simplified procedures.

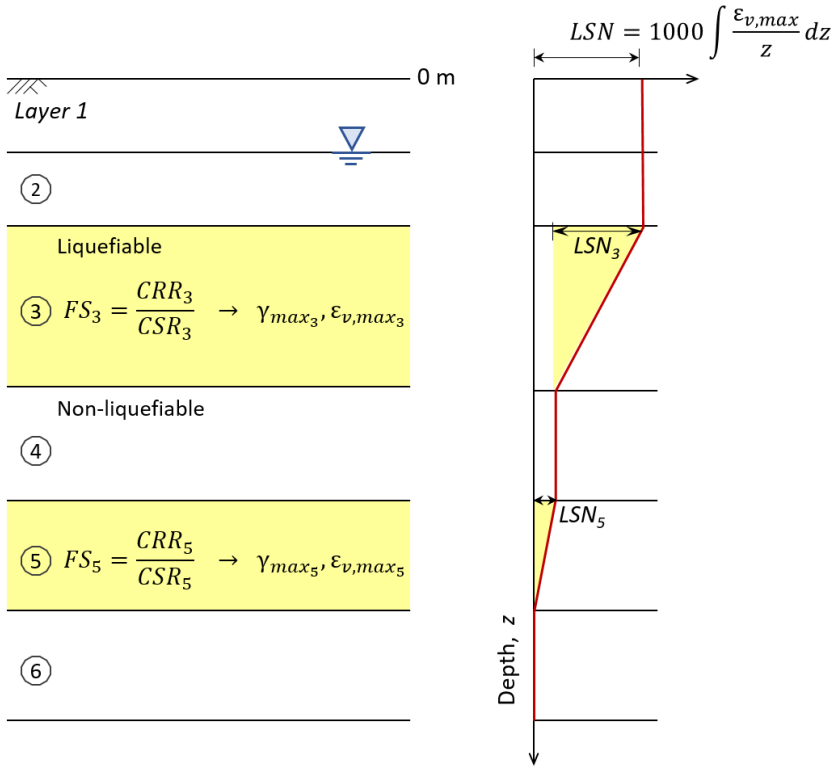

Fig. 2.8 Schematic illustration of liquefaction assessment using simplified approach: (a) factor of safety against liquefaction triggering, maximum shear strain, and post-liquefaction volumetric strain are calculated independently for each layer, (b) cumulative damage index is calculated for the deposit by superposition of individual effects from each layer (modified after Cubrinovski 2019).

2.4.2 Seismic effective stress analysis

The seismic effective stress analysis is one of the most advanced numerical methods used in geotechnical engineering. It allows to simulate many important aspects of the complex dynamic behaviour of soils during earthquakes, including pore pressure development, reduction in the effective stress and resulting deformations, and their effects on foundations and supported structures. Importantly, such analysis considers the response of the deposit as a whole allowing for interactions between layers in the dynamic response (e.g. liquefaction effects on ground motion) and through pore water pressure redistribution and water flow (e.g. partial drainage and seepage-induced liquefaction). On the downside, effective stress analysis can be challenging in the application due to the specialized data and skills required, commonly including high-quality sampling and laboratory testing of soils, use of appropriate input ground motions, complex calibration procedures for sophisticated constitutive models, and also in-depth understanding by the user of the phenomena considered, constitutive relationships used, and numerical solutions adopted in the analysis. These drawbacks have limited the application of the effective stress analysis to critical lifelines and structures where the cost and effort to perform the analysis can be generally justified. An objective of this thesis is to address some of the above limitations and provide guidance on the application of

seismic effective stress analysis for both forensic (historic) and forward (future) site liquefaction assessment.

2.5 On the System Response of Liquefiable Deposits

The importance of system response effects on the seismic response of liquefiable deposits has long been recognized in the pertinent literature. For instance, in a review of historic cases of earthquake-induced liquefaction, Ambraseys and Sarma (1969) noted that *'... as soon as deeper strata liquefied they ceased to transmit the earthquake vibrations to the overlying deposits'*. In the same paper, the authors also stated that *'... an initially stable layer of small compressibility may liquefy as a result of the liquefaction of an underlying loose deposit'*. With these two statements, Ambraseys and Sarma pointed at two important system-response and cross-layer interaction mechanisms of liquefiable deposits, namely, (a) liquefaction-induced 'seismic isolation' or, more generally, modification of seismic waves (demand) due to ground softening, and (b) liquefaction-induced seepage and associated phenomena. In the following, an overview of the current understanding of these phenomena based on previous research is presented first, and then, key findings from a previous work on the system response of representative soil profiles from Christchurch are discussed.

2.5.1 Liquefaction effects on seismic demand

The development of excess pore water pressure in the soil is accompanied by a reduction in the effective stress and subsequent softening of the soil (Fig. 2.2). The progressive softening of the soil as excess pore water pressure builds up during the seismic loading changes the dynamic characteristics of the site (i.e. overall flexibility and damping). In particular, the ability of the soil to transmit high frequency waves is generally decreased, whereas its ability to transmit low frequency waves is increased. This change in transmission characteristics generally occurs relatively gradually as excess pore water pressure builds up, but becomes more clearly evident at a time near the initiation of liquefaction, when the excess pore water pressure approaches the initial confining stress and the effective stress drops to nearly zero. In loose sands, this state is accompanied by a rapid softening of the soil which is manifested with an abrupt change in the frequency content of the surface ground motion (Kramer et al. 2016). Denser sands also exhibit softening and gradual change in the transmission characteristics, but the tendency for dilation in these soils and regain of soil stiffness with amplitude often result in the manifestation of sharp high-frequency spikes on the surface acceleration which are superimposed upon the long-period response of the softened soil (Iai et al. 1995, Bonilla et al. 2005, Kramer et al. 2011). A characteristic surface horizontal acceleration record from the 22 February 2011 M_w6.2 Christchurch earthquake with such 'cyclic mobility spikes' following initial liquefaction and associated soil softening is illustrated in Fig. 2.9.

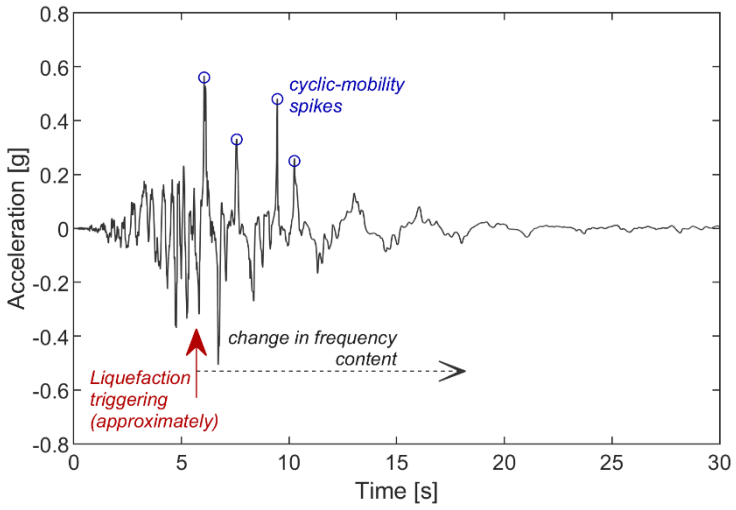

Fig. 2.9 Horizontal component ground motion recorded at the Christchurch Botanical Gardens (CBGS station) during the 22 February 2011 earthquake showing characteristic effects of liquefaction on the surface ground motion.

With reference to the ground motion that would have occurred at a site in the absence of excess pore water pressures (i.e. no liquefaction), liquefaction and associated soil softening generally tend to reduce the short-period amplitudes of motion ($T < 1.0$ s) and increase the long-period ones ($T > 1.0$ s) (Youd and Carter 2005, Kramer et al. 2011). Liquefaction triggering of dense sands that exhibit cyclic mobility type of behaviour may cause amplification also in short periods ($T < 0.05$ s) and increase in the peak ground acceleration due to the high-frequency spikes described previously (Gingery et al. 2015). Key factors influencing the magnitude of liquefaction-induced ground motion amplification or de-amplification are the time of liquefaction triggering, or, in simplified-method terms, the factor of safety against liquefaction triggering (Youd and Carter 2005, Kramer et al. 2011), the thickness of the liquefied soil (Kokusho 2014, Bouckovalas et al. 2016), and the relative density (e.g. Dashti et al. 2010, Kokusho 2014). Stronger wave attenuation is observed when liquefaction of thick and loose soil layers occurs relatively early in the ground motion (or when FS_L is low).

Needless to say, the aforementioned liquefaction-induced changes in the ground motion also affect the cyclic shear stresses (demand) in the soils overlying the liquefied layer, as noted by Ambraseys and Sarma (1969). This effect has not yet been quantified and is currently ignored by the simplified methods for liquefaction assessment.

2.5.2 Effects of liquefaction-induced seepage

Consider the layered soil profile in Fig. 2.10a, in which a liquefiable layer of loose sand is overlain by a finer-grained crust, which can be either non-liquefiable by composition (e.g. clay or plastic silt) or liquefiable soil at a denser initial state (e.g. dense silty sand or non-plastic silt). Earthquake shaking induces high excess pore water pressures and eventually

triggers liquefaction throughout the loose sand layer, but no significant excess pore water pressures have been generated in the crust during the strong shaking. In the loose sand layer, the excess pore water pressures are now equal to the initial vertical effective stresses, and they increase with depth as the initial vertical effective stress also increases with depth (Fig. 2.10b). The resulting distribution of excess pore water pressures throughout the soil profile is associated with upward hydraulic gradients which result in upward flow of water through the soil profile and towards the ground surface (Fig. 2.10c).

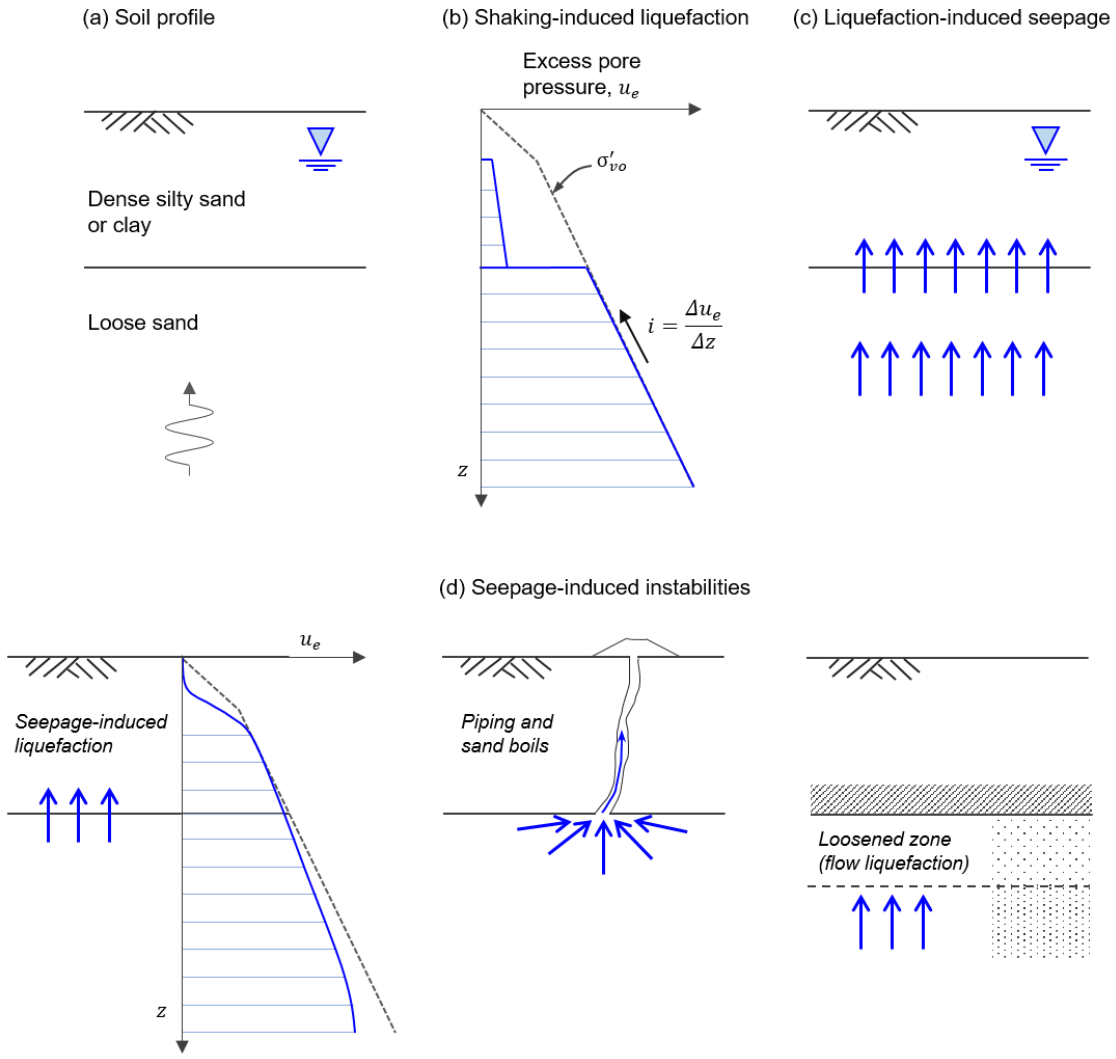

Fig. 2.10 Liquefaction-induced seepage in layered deposit and associated phenomena.

Fig. 2.10d schematically illustrates three severe complications that may arise from the upward seepage of pore water both during and after the earthquake shaking:

(1) If the overlying finer-grained crust layer is liquefiable, then the upward flow of pore water can cause high enough hydraulic gradients in the crust (increase in the excess pore water pressures) to buoy up its soil particles and liquefy the initially stable crust soil. Early

theoretical work on the mechanism of seepage-induced liquefaction of initially stable surficial soils has been presented by Housner (1958), Ambraseys and Sarma (1969), and Yoshimi and Kuwabara (1973).

(2) Another possibility for the seeping pore water is to cause hydraulic fracturing and break through at concentrated cracks or piping channels within the crust layer. These may form at locations where the crust is thinner that it is in the surroundings or where there are pre-existing weaknesses in the crust which are further exacerbated under the pressure of the seeping water eventually forming tubes or pipes that extend up to the ground surface. The water flowing through these pipes may carry suspended soil particles from the liquefied layer and/or soil particles from the upper layer which are deposited at the ground surface in the form of sand boils. Sand boils is amongst the most commonly observed types of liquefaction manifestation in the field and has also been replicated in several experimental simulations of liquefaction (e.g. Scott and Zuckerman 1973, Liu and Qiao 1984, Elgamal et al. 1989, Fiegel and Kutter 1994).

(3) If the seeping water from the liquefied layer cannot easily dissipate through the pores or cracks of the surficial crust (i.e. when the crust is sufficiently less permeable than the liquefied lower layer and relatively homogeneous without any weaknesses), it will start accumulating in the upper part of the liquefied layer beneath the interface with the less permeable crust. Contraction of the soil skeleton with outflow of pore water will take place in the lower parts of the liquefied layer (reconsolidation; decrease in void ratio), and expansion (dilation) with net inflow of pore water will occur in the upper parts of the liquefied layer (loosening; increase in void ratio). This process has been described as void redistribution (Whitman 1985), and it can progress with time to even develop a water film (interlayer) with zero shear strength immediately beneath the less pervious crust (e.g. Seed 1987). The consequences of void redistribution can be disastrous in the presence of static shear stresses acting along the dilation (loosened) zone of the liquefied soil, but void redistribution may adversely affect the resisting capacity of soils also during the earthquake shaking. The mechanism of void redistribution has been studied extensively using primarily physical model tests (e.g. Dobry and Liu 1992, Arulanandan et al. 1993, Fiegel and Kutter 1994, Balakrishnan and Kutter 1999, Kokusho 1999, 2000, Kokusho and Kojima 2002, Kulasingam et al. 2004, Malvick et al. 2008) and also numerical simulations (e.g. Yang and Elgamal 2002, Seid-Karbasi and Byrne 2007, Boulanger et al. 2013).

It is important to recognize that the above effects do not exclude one another but may occur in parallel or in sequence. In any case, all three effects are indicators of severely loosened soil near the ground surface and consequent large kinematic demands to engineering structures. Features of the liquefied lower layer that can enhance the manifestation of such phenomena are a large compressibility and thickness (which increase the total volume of water expelled by the liquefied soil), and high hydraulic conductivity (which makes the water available fast) (Dobry 1989). On the other hand, a strong coherence, integrity, and large thickness of the crust layer can effectively prevent liquefaction manifestation at the ground surface (e.g. Scott and Zuckerman 1973, Ishihara 1985), without, however, excluding the possibility of void

redistribution related failures. In conclusion, it is clear from the above discussion that liquefaction manifestation reflects the response of the entire system in which, apart from the initial state of the critical layer for liquefaction manifestation, deposit characteristics such as the soil stratigraphy (layer thicknesses and sequence), and permeability and compressibility contrasts within the deposit may play a very significant role.

2.5.3 System response of representative Christchurch soil profiles

Rhodes (2017) performed a series of seismic effective stress analyses to investigate the seismic response of representative soil profiles from Christchurch. The simplified stratification and q_{c1Ncs} values for two out of the four representative soil profiles analyzed in this study are illustrated in Fig. 2.11. The YY-profile represents the characteristics of sites that manifested moderate-to-severe liquefaction in both the two major events of the 2010-2011 CES, namely the 4 September 2010 M_w7.1 Darfield earthquake and the 22 February 2011 M_w6.2 Christchurch earthquake (Fig. 2.1). Key features of this soil profile are the presence of a critical zone with relatively low penetration resistance at shallow depth immediately below the groundwater table, the gradual increase in q_{c1Ncs} with depth, and the fact that all top 10 m of the deposit, which are the most relevant for liquefaction manifestation at the ground surface, are composed of liquefiable soils including the nominal crust above the water table and the soils below the critical zone. The NN-profile represents the characteristics of sites that did not manifest liquefaction in any event of the CES. In this case, a relatively thin critical layer of low resistance is identified again at shallow depth, but low tip resistance liquefiable layers are present also at greater depths, and, importantly, there is no vertical continuity of liquefiable layers as in the YY-profile, rather the critical layer is sandwiched between non-liquefiable soils.

Key system response mechanisms identified by the effective stress analyses of the YY- and NN-profiles were summarized by Cubrinovski et al. (2019), and are schematically illustrated in Fig. 2.11.

In the YY-deposit (Fig. 2.11a), (1) liquefaction first develops in the loose, shallow, and thick critical zone only after a few seconds of shaking. (2) The already liquefied soil in the critical zone is then subjected to substantial additional disturbance due to seepage action and upward flow of water from the underlying layers into the critical zone. The underlying layers have higher resistance and do not liquefy, but develop excess pore pressures higher (in absolute numbers) than the excess pore water pressures in the overlying critical zone, hence eventuating upward flow toward the critical zone. This water inflow under high pressures exacerbates the fluidization and instability of the soil structure in the liquefied critical zone. (3) Finally, the soil above the water table at shallow depths below the ground surface, also liquefies and loses its effective stress due to an upward water flow from the critical zone towards the ground surface (seepage-induced liquefaction). This effectively creates a liquefied zone from the ground surface to 6 m depth that receives an additional influx of water from the

deeper part of the deposit. Arguably, in the system response of the YY-profile the whole deposit contributes to the severity of liquefaction manifestation at the ground surface.

In the NN-deposit (Fig. 2.11b), (1) liquefaction triggering first occurs in the deeper liquefiable layer of low penetration resistance. (2) The liquefaction of the deep layer results in a substantial reduction of accelerations and seismic demand for all layers above its depth. (3) The reduction in the seismic demand in conjunction with beneficial effects of partial saturation on the liquefaction resistance of the shallow critical layer prevent occurrence of liquefaction in this layer. This effectively results in a non-liquefied crust from the ground surface to 8.5 m depth, and therefore, the liquefaction at depth below 8.5 m would be unlikely to manifest at the ground surface for the seismic demands imposed by the 2010-2011 Canterbury earthquakes.

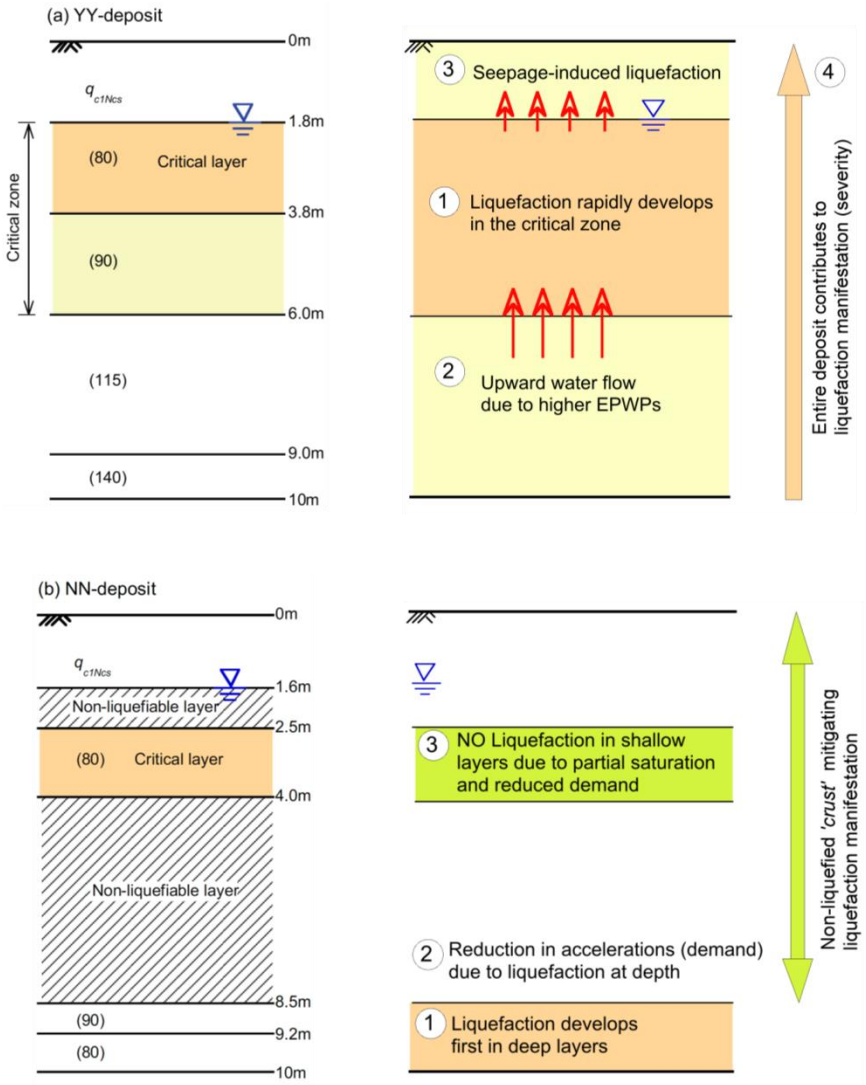

Fig. 2.11 Characteristic Christchurch soil profiles and associated system response mechanisms: (a) YY-deposit representing sites that manifested liquefaction in both the 4 September 2010 and 22 February 2011 earthquakes, (b) NN-deposit representing sites that did not manifest liquefaction in either event (modified after Cubrinovski et al. 2019).

These initial studies on the response of representative Christchurch soil profiles indicate that system response had a governing influence on liquefaction manifestation during the 2010-2011 CES, sometimes by increasing the severity and consequences of liquefaction through the processes described in Fig. 2.11a, and others by contributing to the reduction in the likelihood for development of liquefaction and its manifestation at the ground surface through the processes of Fig. 2.11b. The present research aims to further elucidate and quantify these mechanisms through a comprehensive assessment of the responses of the 55 investigated sites.

2.6 **Summary**

Key takeaway points from the background presented in this chapter are outlined in the following.

(1) In the 2010-2011 CES, evidence of severe and repeated liquefaction was observed in specific areas of Christchurch, whereas many sites in other areas did not manifest liquefaction in any of the events.

(2) Under undrained cyclic shear, liquefaction triggering can occur over a wide range of relative densities, but the consequences of liquefaction are vastly different between loose and dense sands. The state concept provides a robust and rigorous way to characterize the effects of density and confining stress on the stress-strain response and liquefaction resistance of soils.

(3) Soils in the field may be partially saturated even when located below the groundwater table. Partial saturation can result in substantial increase of the cyclic resistance of liquefiable soils.

(4) Partial drainage of soil elements (i.e. inflow or outflow of water and change in volume) can take place both during and after the earthquake shaking as a result of pore water pressure redistribution and seepage of water towards the ground surface. Experimental evidence and field observations suggest that partial drainage with net inflow of water can result in significant reduction (and even complete loss) of the shear resistance compared to that a given soil would mobilize under fully undrained conditions. The tendency for reduction in shear resistance appears to be more pronounced as the soil density decreases and as the maximum cyclic shear strain during the undrained loading phase increases.

(5) Simplified methods for liquefaction assessment consider each layer in isolation and separately from any other layer in the deposit. In other words, cross-interactions between layers in the dynamic response and through pore water pressure redistribution and water flow are ignored in the simplified methods.

(6) The seismic effective stress analysis method considers the response of the deposit as a whole allowing for interactions between layers both during and after the earthquake shaking.

This method allows for consideration of key elements in the soil response and field deposits, such as build-up of excess pore water pressures, flow of water and realistic modelling of stress-strain behaviour of soils under complex earthquake loading. Despite these advantages, effective stress analysis can be challenging in the application due to the specialized data and skills required, including high-quality sampling and laboratory testing of soils, complex calibration procedures for sophisticated constitutive models, and careful selection of appropriate input motions for the analysis.

(7) Soil liquefaction and associated ground softening modify the seismic waves propagating through the liquefied layer by generally de-amplifying high-frequency waves and amplifying low-frequency waves. Key factors influencing the magnitude of liquefaction-induced ground motion amplification or de-amplification include the time of liquefaction triggering (whether it occurs early or late in the ground motion), the thickness of the liquefied soil, and its relative density.

(8) Seepage of pore water following liquefaction can cause severe instabilities which may include seepage-induced liquefaction of the surficial crust, loss of crust integrity and formation of sand boils at the ground surface, and severely loosened zones of liquefied soil beneath interfaces with less pervious soils. Permeability and compressibility contrasts and layer thicknesses play a key role in the manifestation and severity of these phenomena.

(9) Initial effective stress analyses of representative Christchurch soil profiles have identified important system response mechanisms of liquefiable deposits. The system response of sites that manifested moderate-to-severe liquefaction in both major events of the CES (YY-sites) involve: (i) rapid liquefaction of a shallow critical layer; (ii) additional disturbance of the liquefied critical layer due to seepage action and inflow of water from the underlying soils; and (iii) vertically unconstrained water flow, and seepage-induced liquefaction in shallow soils above the water table. This sequence of mechanisms increases the severity and consequences of liquefaction for the YY-sites. The system response of sites that did not manifest liquefaction in any of the CES events (NN-sites) involves: (i) first occurrence of liquefaction in a deep layer of low resistance; (ii) isolation or vertical confinement of the liquefied layer by capping non-liquefiable layers and reduction of the seismic demand for the overlying layers; (iii) increased cyclic resistance of the critical layer at shallow depth due to partial saturation. This combination of mechanisms effectively mitigates liquefaction manifestation for the NN-sites.

3 INVESTIGATED CHRISTCHURCH SITES

3.1 Introduction

In the period between September 2010 and December 2011, a series of strong earthquakes occurred in the Canterbury region of New Zealand. Four of these earthquakes caused a significant seismic demand and liquefaction-induced damage in the urban area of Christchurch. The first in the sequence was the 4 September 2010 M_w7.1 Darfield (04Sep10) earthquake, which caused peak ground accelerations of about 0.20 g in most of Christchurch, and severe liquefaction and lateral spreading along the Avon River (Cubrinovski et al. 2010). Fig. 3.1a shows areas of liquefaction-induced land damage in the 04Sep10 earthquake, where solid symbols indicate the locations of the 55 sites, which are subject of this thesis. An equivalent liquefaction-induced land damage map for the most destructive 22 February 2011 M_w6.2 Christchurch (22Feb11) earthquake is shown in Fig. 3.1b. As the source of this event was practically within the city boundaries (along the southeast perimeter of the city), it generated more severe ground motions and triggered more extensive liquefaction in the eastern suburbs of Christchurch. In this event, the peak ground accelerations were generally in the range from 0.35 g to 0.55 g in the areas affected by widespread liquefaction. Again, the most severe liquefaction and lateral spreading were manifested along the Avon River (Cubrinovski et al. 2011, Cubrinovski and Robinson 2016).

At each of the 55 sites, detailed assessment of land damage was conducted by Tonkin&Taylor engineers using field inspections, observations from aerial photography, and estimates of settlement (subsidence) based on pre- and post-earthquake LiDAR surveys. The severity of liquefaction manifestation at the 55 sites during the 04Sep10 and 22Feb11 earthquakes varied from no liquefaction manifestation at the ground surface to very severe liquefaction, in which case a large area of the site was covered by thick soil ejecta.

Bases on the observed liquefaction manifestation, the 55 sites were herein classified into three groups for the purpose of an initial screening analysis: (i) sites that manifested liquefaction (soil ejecta) in both the 04Sep10 and 22Feb11 earthquakes (YY-cases, shown with red symbols in Fig. 3.1); (ii) sites that did not manifest liquefaction in the 04Sep10 earthquake but manifested liquefaction in the 22Feb11 earthquake (NY-cases; black symbols in Fig. 3.1); and, (iii) sites that did not manifest liquefaction in either event (NN-cases; green symbols in

Fig. 3.1). Details of the liquefaction manifestation characteristics for the 55 sites are provided in Tables 3.1 and 3.2.

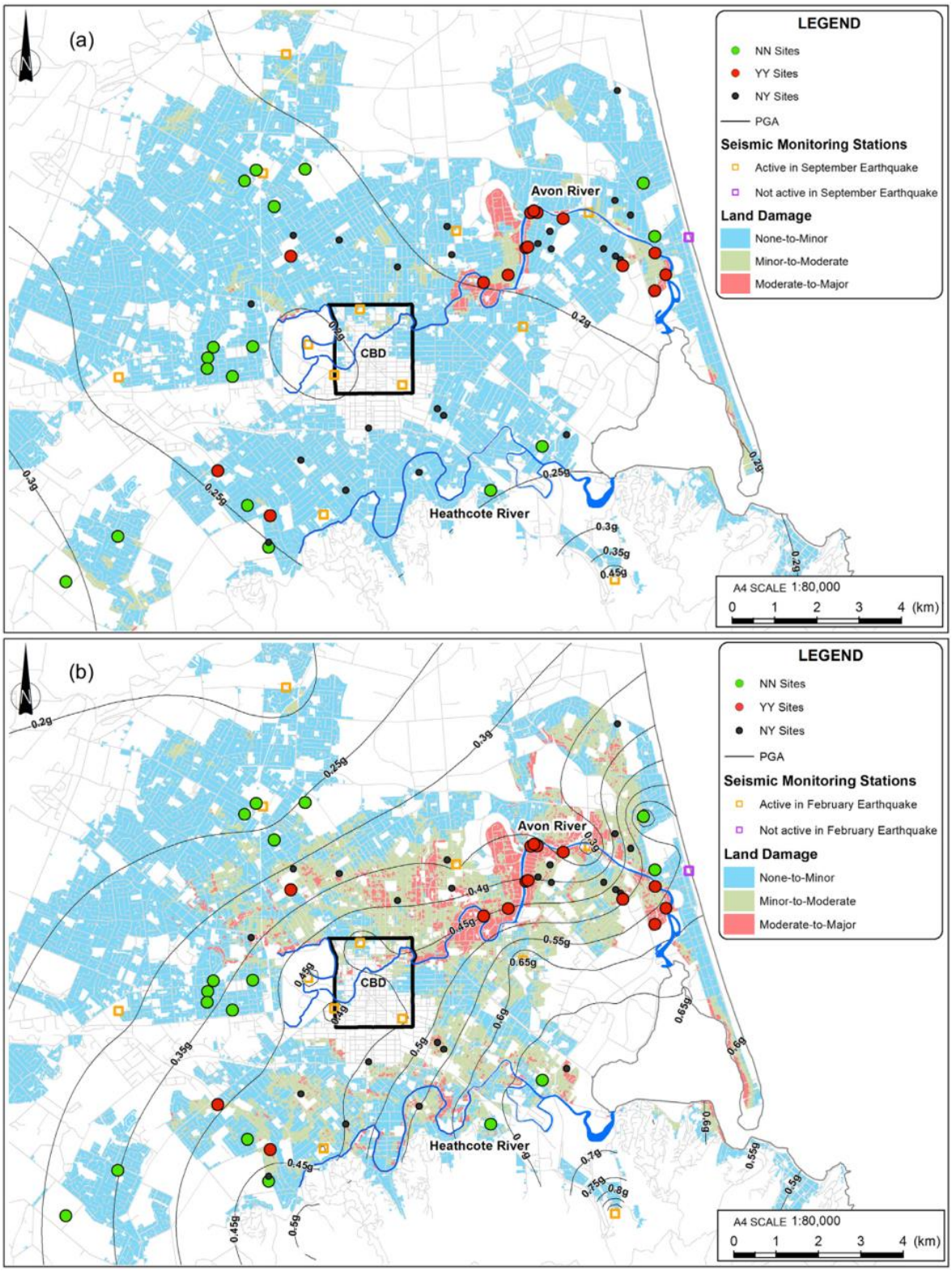

Fig. 3.1 Locations of 55 investigated sites (circular symbols) and land damage caused by soil liquefaction (background colors) in (a) 04Sep10 earthquake; (b) 22Feb11 earthquake (after Cubrinovski et al. 2019)

Table 3.1 Geographic coordinates and liquefaction manifestation characteristics for the investigated 55 sites.

				Liquefaction manifestation		
NZGD ID[a]	Suburb	Latitude	Longitude	04Sep10	22Feb11	Classification
21508	Avonside	-43.5163	172.6713	Severe	Severe	YY
44439	Avondale	-43.5148	172.6785	Severe	Severe	YY
21509	Avondale	-43.5090	172.6837	Moderate	Severe	YY
34460	Avondale	-43.5088	172.6843	Severe	Severe	YY
57354	Avondale	-43.5081	172.6872	None	Severe	NY
38758	Avondale	-43.5093	172.6911	None	Moderate	NY
57342	Avondale	-43.5055	172.6908	None	Severe	NY
29035	Avondale	-43.5015	172.6851	Severe	Severe	YY
36414	Avondale	-43.5011	172.6861	Moderate	Severe	YY
34454	Avondale	-43.5015	172.6871	Moderate	Severe	YY
45	Avondale	-43.5028	172.6946	Minor	Severe	YY
21506	Bexley	-43.5102	172.7215	Minor	Severe	YY
158	Bexley	-43.5149	172.7247	Minor	Minor	YY
175	Bexley	-43.5183	172.7213	Severe	Severe	YY
57349	Aranui	-43.5093	172.7065	Moderate	Moderate	YY
57347	Aranui	-43.5108	172.7099	None	Minor	NY
57348	Aranui	-43.5116	172.7114	None	Moderate	NY
38797	Aranui	-43.5128	172.7120	Minor	Severe	YY
57343	North New Brighton	-43.5067	172.7214	None	None	NN
38742	North New Brighton	-43.5021	172.7144	None	Moderate	NY
34431	North New Brighton	-43.4990	172.7098	None	Severe	NY
57350	North New Brighton	-43.4952	172.7181	None	None	NN
38752	Parklands	-43.4755	172.7107	None	Moderate	NY
57366	Shirley	-43.5104	172.6620	None	Severe	NY
57346	Shirley	-43.5043	172.6607	None	Minor	NY
57362	Shirley	-43.5130	172.6461	None	Minor	NY

[a] CPT identification code in New Zealand Geotechnical Database (NZGD 2020).

Table 3.1 Geographic coordinates and liquefaction manifestation characteristics for the investigated 55 sites (Continued).

				Liquefaction manifestation		
NZGD ID	Suburb	Latitude	Longitude	04Sep10	22Feb11	Classification
57341	Woolston	-43.5488	172.6954	None	Severe	NY
57360	Woolston	-43.5513	172.6882	None	Moderate	NY
57365	Hillsborough	-43.5606	172.6731	None	None	NN
57357	Waltham	-43.5446	172.6595	None	Severe	NY
57356	Waltham	-43.5432	172.6576	None	Severe	NY
57355	Sydenham	-43.5472	172.6375	None	Minor	NY
57353	St Martins	-43.5568	172.6522	None	Severe	NY
638	Somerfield	-43.5605	172.6307	None	Minor	NY
37818	Spreydon	-43.5540	172.6175	None	Minor	NY
57344	Hoon Hay	-43.5658	172.6085	Minor	Severe	YY
57340	Hoon Hay	-43.5715	172.6080	None	Minor	NY
36417	Hoon Hay	-43.5636	172.6019	None	None	NN
36421	Hoon Hay	-43.5726	172.6081	None	None	NN
57364	Hoon Hay	-43.5562	172.5933	None	Moderate	NY
57352	Halswell	-43.5701	172.5639	None	None	NN
36419	Halswell	-43.5797	172.5487	None	None	NN
57319	Riccarton	-43.5361	172.5976	None	None	NN
57337	Riccarton	-43.5344	172.5903	None	None	NN
36418	Riccarton	-43.5321	172.5905	None	None	NN
57345	Riccarton	-43.5299	172.5921	None	None	NN
36420	Riccarton	-43.5298	172.6037	None	None	NN
5567	Fendalton	-43.5207	172.6033	None	None	NN
57358	St Albans	-43.5072	172.6291	None	Minor	NY
57359	Papanui	-43.5106	172.6149	Moderate	Severe	YY
57363	Merivale	-43.5061	172.6157	None	Moderate	NY
57361	Papanui	-43.5000	172.6101	None	None	NN
57339	Papanui	-43.4921	172.6193	None	None	NN
57351	Papanui	-43.4945	172.6015	None	None	NN
57338	Papanui	-43.4922	172.6049	None	None	NN

Most of the sites (32 of 38 sites) that liquefied in the 22Feb11 earthquake manifest liquefaction in the subsequent 13 June 2011 M_w6.0 earthquake, and some of these sites also re-liquefied during the last in the sequence 23 December 2011 M_w5.9 earthquake. To eliminate some of the complexities associated with re-liquefaction, this research focuses on the performance of the sites during the first two events. It is worth emphasizing that the 17 NN-sites did not manifest liquefaction in any event during the CES (2010–2011 earthquakes).

Table 3.2 Summary of liquefaction manifestation at the 55 sites during the 04Sep10 and 22Feb11 Canterbury earthquakes.

Earthquake	Liquefaction manifestation		
	YY (15 sites)	NY (23 sites)	NN (17 sites)
04Sep10	Yes	No	No
22Feb11	Yes	Yes	No

In this chapter, similarities and differences between soil deposits that exhibited liquefaction in both earthquakes (YY-cases) and those deposits where no liquefaction manifestation was observed in either event (NN-cases) are examined. To avoid additional complexities in the interpretation, the intermediate NY-cases have been left out from the initial screening analysis of this chapter. Characteristics of the near-surface geology and geomorphology of Christchurch are discussed first, followed by a description of the performed geotechnical investigations at the 55 sites, and, finally, a comprehensive scrutiny of the soil profile characteristics of the YY-sites and NN-sites.

3.2 **Near-surface Geology and Geomorphology**

Christchurch is primarily situated upon a low relief, alluvial landscape, on the east coast of New Zealand's South Island. Its subsurface is characterized by a complex interbedded structure of Quaternary formations, resulting from fluvial deposition of rivers flowing eastward from the foothills of the Southern Alps (i.e. the mountain range of the South Island), and marine sediments deposited in times of marine transgression (Brown and Weeber 1992). Near-surface soils consist of alluvial sands, silts, and drained peat swamps (Springston formation), interlayered with beach, estuarine, lagoonal, dune, and coastal swamp deposits comprising gravel, sand, clay, shell, and peat (Christchurch formation). The spatial variation of these near-surface soils is illustrated in the geological map of Fig. 3.2. A schematic east-west shallow geological cross-section is presented in Fig. 3.3.

Considering their composition, age, and depositional environment, the near-surface Christchurch soils are considered highly susceptible to liquefaction, and in some cases (when deposited in a loose state) they may exhibit very low liquefaction resistance (Cubrinovski and McCahon 2011). As illustrated in Fig. 3.3, these soft surface deposits have a thickness that vary across the city, between about 10 and 40 m, and overlie the denser Riccarton Gravel. The latter is the uppermost gravel of a thick sequence (~ 500 m thickness in CBD) of interlayered formations of gravels and fine-grained soils of an older age. The water table throughout most of urban Christchurch is shallow, from about 1 to 3 m depth from the ground surface, meaning, mostly, high degrees of saturation in the liquefiable soils below these depths.

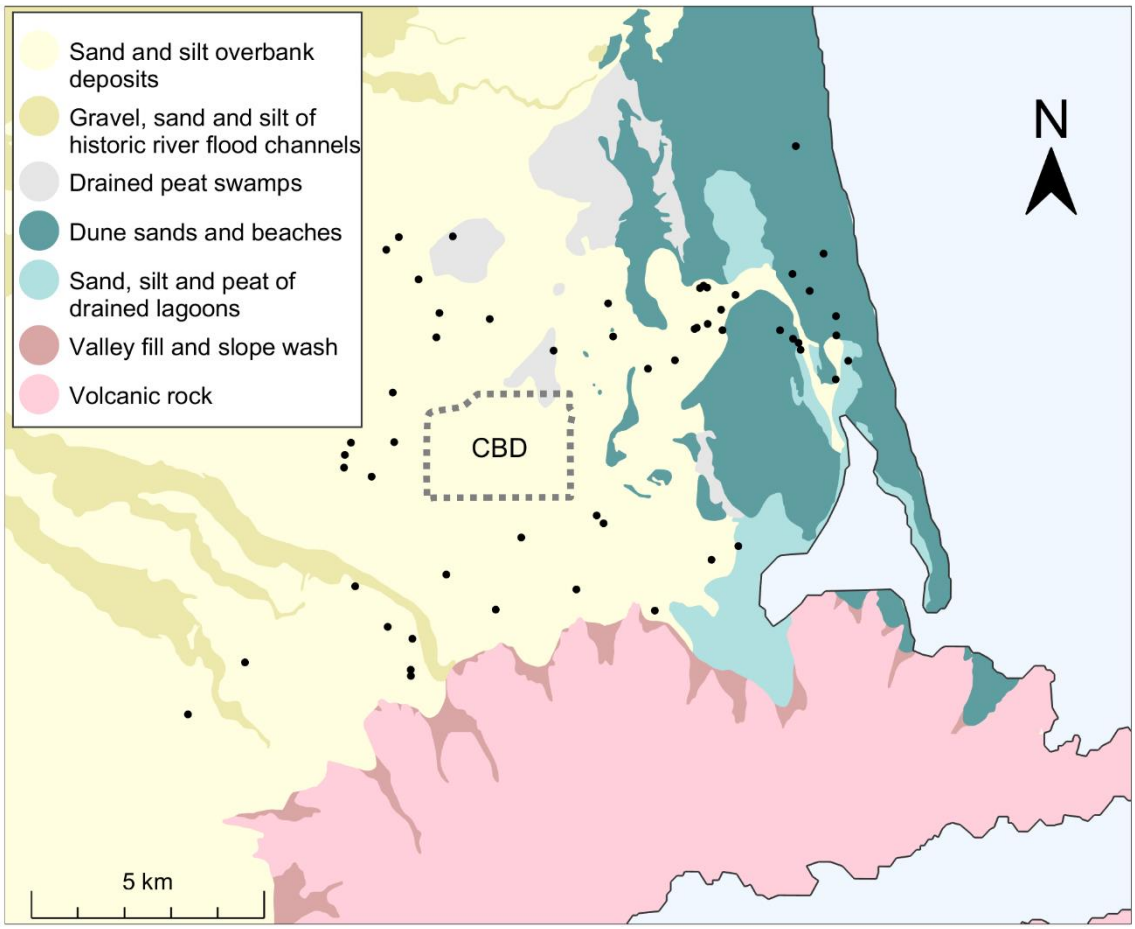

Fig. 3.2 Geological map of Christhurch (modified after Brown and Weeber 1992). *Black dots indicate the locations of the 55 investigated sites*.

3.3 **Geotechnical Characterization**

At the time of the 2010–2011 Canterbury earthquakes, little was known about the details and spatial characteristics of the soil stratigraphy, besides the general geological features described in the previous section. In the succeeding years, extensive geotechnical

investigations were undertaken including a vast number of CPTs (van Ballegooy et al. 2014, NZGD 2020) and exploratory soil borings, and also numerous geophysical surveys, piezometer measurements, and laboratory tests on retrieved soil samples (Stringer et al. 2015, Taylor 2015, Beyzaei et al. 2018, Markham et al. 2018). The '55 sites' is a subset of high-quality field investigation data including CPTs and high-resolution (at 200 mm intervals) compression wave and shear wave velocity (V_p and V_s respectively) measurements obtained using the direct-push cross-hole technique (Cox et al. 2018). A large number of disturbed samples were recovered from target soils/layers of selected sites for index testing in the laboratory to determine the grain-size distribution, fines content, and plasticity of fines. At each of the 55 sites, borehole data are also available, at a close but non-intrusive distance from the locations of CPT and cross-hole testing. The above site investigation data for the 55 sites can be openly accessed on the New Zealand Geotechnical Database (NZGD 2020) using the CPT ID numbers and coordinates provided in Table 3.1. CPT and V_p data for the top 11 m of the subsurface profiles of the 55 sites are also provided in Appendices A & D of this dissertation.

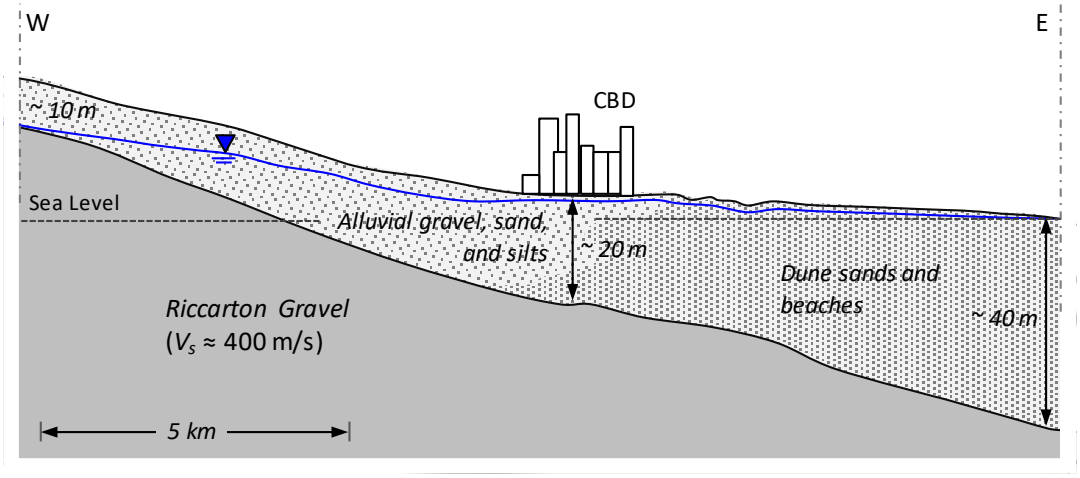

Fig. 3.3 Schematic east-west geological cross section of Christchurch, indicating the thickness of surface soils (depth to Riccarton Gravel) and depth to groundwater table (modified after Cubrinovski et al. 2010).

3.4 **Simplified Soil Profiles**

Simplified soil profiles were determined for each of the 55 sites primarily based on the CPT data (Appendix A). Two principal advantages of CPT over other in-situ tests are that it provides a practically continuous record of the penetration resistance throughout depth, and that it allows to infer the soil profile from empirical correlations between soil (behaviour) types and the various CPT measurements. In this study, simplified soil profiles were determined by first identifying depth intervals over which the normalized overburden corrected cone tip resistance (q_{c1N}) and the soil behaviour type index (I_c) can be

approximated by constant values, as illustrated in Figs. 3.4b and 3.4c for a site in Papanui (northwest Christchurch). On this basis, distinct soil layers with representative q_{c1N} and I_c values were defined. The layers were then classified based on the I_c value into soil behaviour type associated with: coarse sands and gravelly soils ($I_c \leq 1.3$), sandy silts and non-plastic silts ($1.3 < I_c \leq 1.8$), sands with small amount of fines ($1.8 < I_c \leq 2.1$), sandy silts and non-plastic silts ($2.1 < I_c \leq 2.6$), and non-liquefiable silt/clayey/peat soils ($I_c > 2.6$). By and large, the soil behaviour types inferred from the CPT data, using the above (approximate) I_c boundaries separating soil behaviour type, were consistent with the respective borehole data, as indicated in Figs. 3.4a and 3.4b for the example Papanui site. The average V_s and V_p values within each layer of the simplified profiles were also noted. The V_p profiles were used as a principal indicator for the level of saturation throughout the depth of the deposits in conjunction with a detailed groundwater table model for Christchurch (van Ballegooy et al. 2014). As indicated in Fig. 3.4e, partially saturated soils with V_p values substantially lower than 1500 m/s were often encountered at large depths, up to 5-6 m below the groundwater table, particularly at highly stratified sites with interbedded liquefiable and non-liquefiable soil layers (Fig. 3.4b).

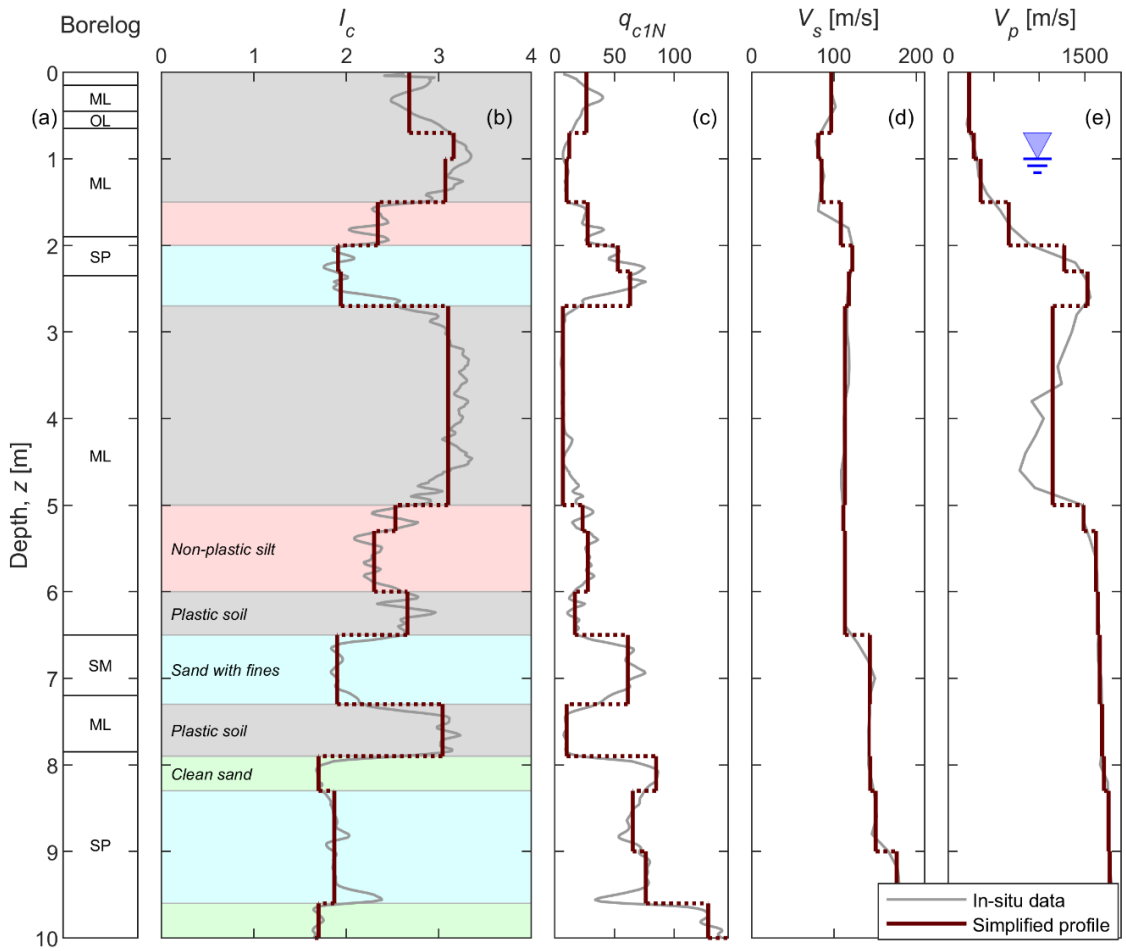

Fig. 3.4 Determination of a simplified soil profile for a Papanui site: (a) visual (USCS) soil classification based on borehole data; (b) I_c values and I_c-based classification of soil behaviour type; (c) q_{c1N} values; (d) V_s values; and, (e) V_p values.

Careful inspection of the CPT data and thereafter determination of a simplified soil profile, as above, allow for rigorous soil profile scrutiny and interpretation in various aspects of liquefaction assessment, including identification and characterization of critical layers in the deposit, identification of potential system-response effects, and also consideration of different levels of uncertainties in the estimates of the cyclic resistance associated with varying quality of material and behavioural characterization of different soil types (Cubrinovski 2019). The importance of this latter point can be elucidated if one considers, for example, the fact that in the simplified procedures, a significant adjustment of the measured penetration resistance (and consequently, cyclic resistance) is prescribed for soils other than clean sands, based solely on the highly uncertain fines content of these soils.

3.5 Critical Layers and Evaluation of Damage Indices

Current semi-empirical liquefaction triggering procedures have been developed based on case histories of liquefaction manifestation in which $CSR - q_c$ pairs (in the case of CPT-based procedures) were identified for each case history (site). The $CSR - q_c$ pairs at each site represent the values of the seismic demand (load) and penetration resistance for the critical layer that was considered responsible for the liquefaction manifestation at the site. In effect, the critical layer can be seen as the layer that is most likely to trigger and manifest liquefaction at the ground surface of a given site.

With this background in mind, triggering analyses were performed for the 04Sep10 and 22Feb11 earthquakes using the Boulanger and Idriss (2014) liquefaction triggering procedure to identify the critical layers for each of the 55 sites. In the analyses, equivalent clean sand penetration resistances (q_{c1Ncs}) were derived using the respective adjustments for fines content specified in Boulanger and Idriss (2014), with the fines content (FC) inferred from the default correlation between I_c and FC provided therein. Estimates of the conditional PGA at each site were made using the methodology outlined in Bradley (2014) (see Fig. 3.1 for estimated median PGA contours across Christchurch). Factors of safety against liquefaction triggering (FS_L) were computed throughout depth, for the top 10 m of the deposits. Subsequently, maximum shear strains, post-liquefaction volumetric strains, and liquefaction damage indices, LPI and LSN, were estimated for each site and each earthquake. Typical results of such analyses are shown for the Papanui site and the 22Feb11 earthquake in Fig. 3.5. There are several layers at which liquefaction triggering is predicted at this site. The shallowest layer from 1.5 to 2.7 m depth appears to be the most likely critical layer from a liquefaction manifestation viewpoint, because it is 1.2 m thick, with low factor of safety, and very close to the ground surface (1.5 m depth). The second candidate layer is at depth from 5 to 6 m, it has slightly lower factor of safety, but it is much deeper and it is also overlaid by a thick non-liquefiable soil layer, and therefore its manifestation at the ground surface in the absence of liquefaction in the shallow layer is unlikely for the CES events. For the same reason, the deeper layers are also eliminated as potential critical layers as they are unlikely to

manifest at the ground surface ahead of the shallower critical layers. Hence, in this case, the shallowest layer was identified as the critical layer, and the second layer at 5 m depth was considered as a possible alternative (contributing) critical layer. The above illustrates that the identification of critical layer(s) is not always straightforward, and that in addition to the lowest liquefaction resistance, the position of the layer within the soil profile and its thickness should be considered in the assessment. In that regard, liquefaction damage indices that combine these three features can provide guidance in the selection. As indicated in Figs. 3.5e and 3.5f, the largest increments in LPI and LSN occur within the identified critical layer(s). Clearly, shallow critical layers immediately below or close to the ground surface can most easily manifest liquefaction at the ground surface.

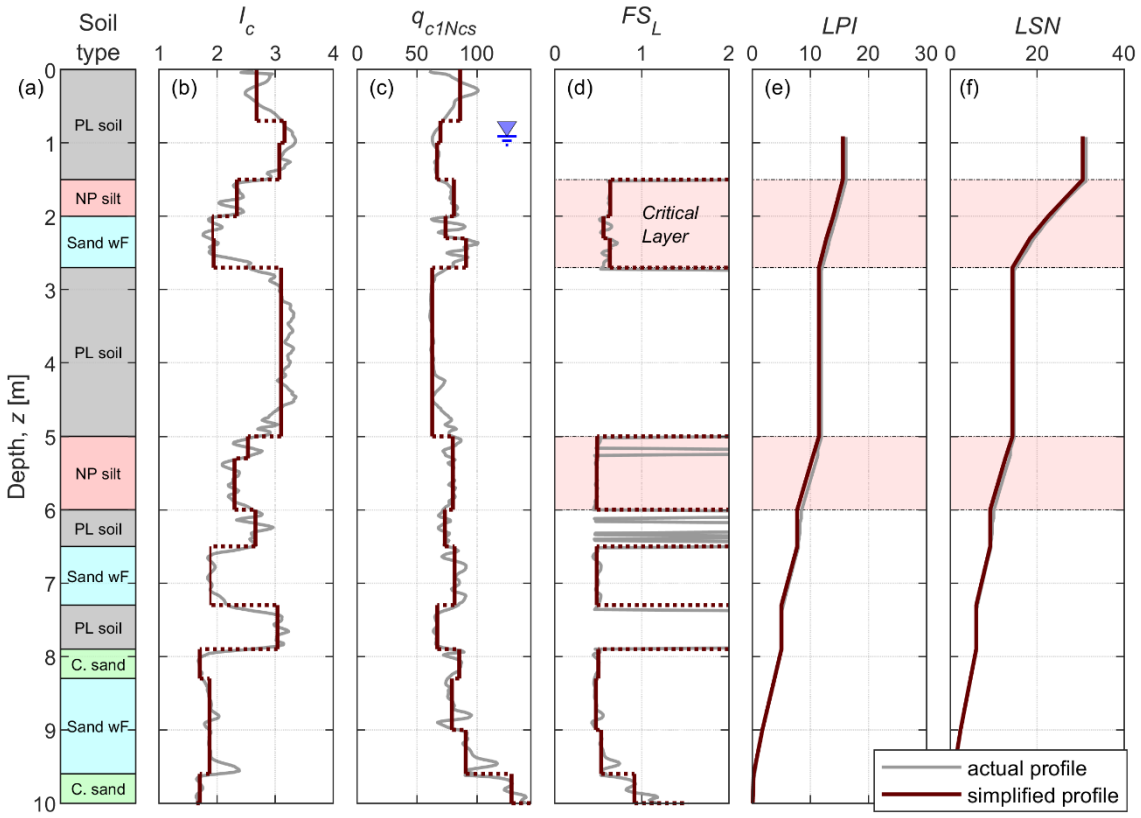

Fig. 3.5 Determination of critical layer(s) for a simplified profile of a Papanui site: (a) characteristic soil behaviour type units; (b) I_c values; (c) q_{c1N} values; (d) FS_L values for the 22Feb11 earthquake; and damage indices: (e) LPI; and, (f) LSN; *potential critical layers are marked with the shading*.

Following the above reasoning, critical layers from a liquefaction manifestation viewpoint were identified for all 55 sites. For several sites, in addition to the shallowest critical layer, one or two additional (alternative) critical layers were also identified, which were at a greater depth in the deposit, but showed either similar or slightly lower liquefaction resistance than the principal (shallower) critical layer.

Fig. 3.6 comparatively shows characteristics of the critical layers for the YY-sites (which manifested liquefaction in both earthquakes) and NN-sites (which did not manifest

liquefaction in either event), with box-and-whisker plots. These are weighted-average values for the critical layer for which the thickness of sublayers within the critical layer was used as a weighting factor. It is apparent that, in terms of median values there is essentially no difference between the critical layers of YY-sites and NN-sites. In fact, the YY-sites and NN-sites have identical median values of their critical layers for the normalized clean-sand equivalent tip resistance ($q_{c1Ncs} = 86$), soil behaviour type ($I_c = 2.15$), and depth to top of the critical layer ($z_{CL} = 2.1$ m). Hence, the dramatic difference in liquefaction manifestation between the YY-sites and NN-sites cannot be explained through differences in the characteristics of their critical layers. In both cases, the critical layer is shallow, just two meters below the ground surface, and has low penetration resistance ($q_{c1Ncs} \approx 86$). In view of the governing role of the critical layer in determining the outcomes of the prediction by the simplified procedures, this implies that current simplified liquefaction assessment procedures would not be able to discriminate between the extreme difference in liquefaction manifestation observed at the YY-sites and NN-sites.

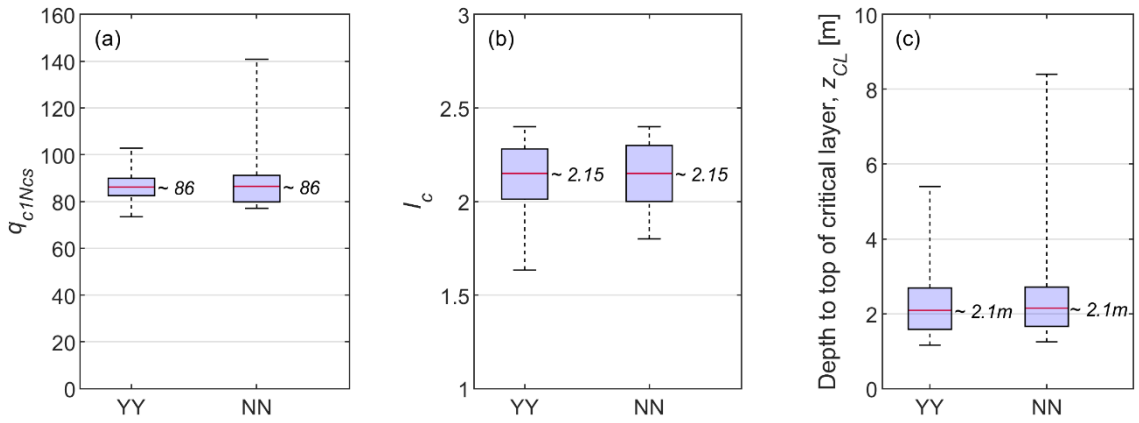

Fig. 3.6 Comparative illustration of critical layer characteristics for YY-sites and NN-sites using box and whisker plots: (a) clean sand equivalent cone tip resistance (q_{c1Ncs}) of the critical layer; (b) soil behaviour type index (I_c) of the critical layer; (c) depth to top of the critical layer (z_{CL}).

Fig. 3.7 summarizes the computed LSN values in terms of box-and-whisker plots. It is evident from this figure that out of the 34 cases for the NN-sites (17 sites for two events), no occurrence or minor liquefaction is predicted for only 3 cases (9% of the cases), whereas for 31 cases (91% of the cases) liquefaction manifestation was heavily overestimated. For most of the no-liquefaction manifestation sites (NN-cases) major to severe liquefaction was predicted. On the other hand, for the YY-sites, the simplified analyses mis-predicted the observed liquefaction manifestation in 47% of the cases (14 out of 30 predictions). A summary of the simplified analyses predictions is given in Table 3.3.

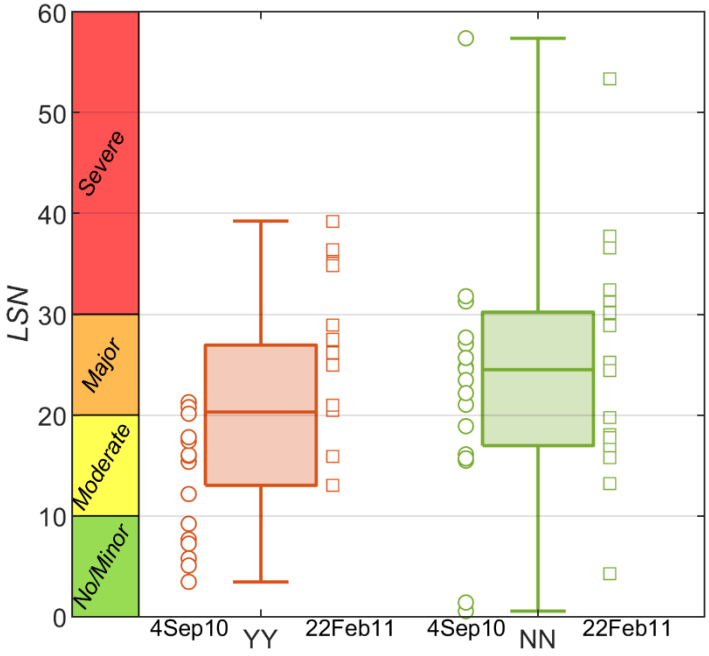

Fig. 3.7 Box and whisker plots summarizing results from simplified analyses in terms of estimated liquefaction damage index *LSN* for YY-sites (red symbols) and NN-sites (green symbols), for the 04Sep10 and 22Feb11 earthquakes.

Detailed results from the simplified liquefaction triggering analysis and damage index evaluation for all 55 sites are provided in Appendix A.

Table 3.3 Summary of results from simplified analysis (*LSN* predictions).

LSN-based prediction[a]	YY (15 sites)	NN (17 sites)
Good agreement	53%	9%
Under-estimation	27%	–
Over-estimation	20%	91%

[a] Agreement between predictions and observations.

3.6 Critical Zone and Vertical Continuity of Liquefiable Soils

One of the key motivations behind this research was to investigate the effects of system response of liquefiable deposits including interactions between layers at different depths through the dynamic response, pore water pressure dissipation and seepage action due to water flow. In this context, the critical layer represents only one, albeit a significant component in the assessment of liquefiable deposits.

To examine further the characteristics of YY- and NN-deposits in relation to their potential for liquefaction manifestation at the ground surface, a 'critical zone' was also defined for each site. The critical zone includes the critical layer but also other layers of low resistance, which are vertically continuous (connected) and in contact with the critical layer(s). Fig. 3.8d illustrates the definition of the critical zone for a site in Avondale (eastern Christchurch). In this site, two critical layers have been identified (Fig. 3.8c); a shallow and thick layer from 2.6 to 4 m, and an alternative layer at 6.1 m depth from the ground surface, which has lower factor of safety but it is much deeper and much thinner (only 0.4 m thick) than the shallowest layer. Apart from these two layers, there are several other layers with relatively low liquefaction resistance and factor of safety less than one for the 22Feb11 earthquake. In fact, a continuous critical zone of relatively low liquefaction resistance is encountered from 2.1 to 6.9 m depth, practically connecting the shallow and deep critical layers. It is anticipated that the critical zone will strongly interact and essentially work as a unit (connected zone) during the development of liquefaction and post-liquefaction through water flow and pore water pressure redistribution. The development of such relatively thick and vertically connected liquefied zone will create conditions for severe liquefaction manifestation through high, continuous and vertically unconstrained excess pore water pressures, with strong upward flow of water towards the ground surface, and consequent soil ejecta.

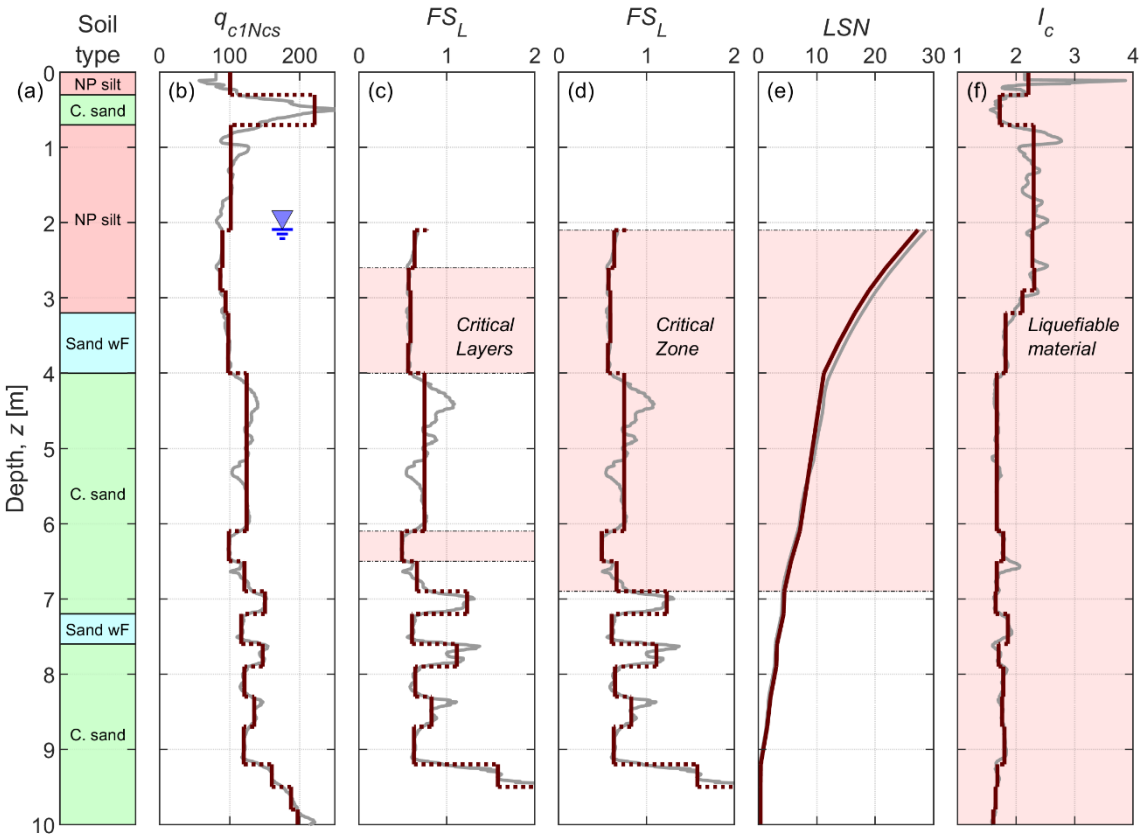

Fig. 3.8 Determination of critical zone and zone of liquefiable soils (by composition) for a simplified profile in Avondale: (a) characteristic soil behaviour type units; (b) q_{c1Ncs} values; (c) FS_L profile for the 22Feb11 earthquake and critical layers; (d) FS_L profile for the 22Feb11 earthquake and critical zone; (e) LSN values; (f) I_c profile and zone of liquefiable material.

One may further develop this concept by considering not only a critical zone in the deposit that is anticipated to liquefy during the shaking, but also by considering the thickness and continuity of potentially liquefiable soils throughout the depth of the deposit. This zone of liquefiable materials will encompass the critical zone, but also soils above and below the critical zone that are liquefiable by composition. Such soils are expected to develop excess pore water pressures either due to cyclic shear stresses induced by the earthquake (e.g. sandy soils below the critical zone) or due to water flow inducing seepage-induced liquefaction in the shallow soils above the water table. Such zone of liquefiable soils is illustrated in Fig. 3.8f for the Avondale profile, where nearly all soils in the top ten meters are potentially liquefiable ($I_c < 2.6$). One may anticipate that liquefiable and pore pressure generating soils above and below the critical zone could further exacerbate liquefaction effects and make liquefaction manifestation at the ground surface even more severe.

Figs. 3.9a, 3.9b, and 3.9c comparatively show the thickness of the critical zone, cumulative thickness of sand layers with $I_c \leq 1.8$, and cumulative thickness of liquefiable soils ($I_c < 2.6$), respectively, for the YY-sites and NN-sites. Unlike the identical characteristics of their critical layers, there are clear differences between the YY-sites and NN-sites with regard to these overall deposit characteristics. While the median value for the thickness of the critical zone of the YY-sites is only slightly larger than the respective thickness of the NN-sites, about 40% of the YY-sites have nearly double thickness of the critical zone. Moreover, the majority of the sites that liquefied in both earthquakes (YY-sites) have a vertically continuous zone of liquefiable materials in the top 10 m of the deposit, of which about 6 m (on average) consists of clean sands. The respective thickness of the liquefiable materials for NN-sites is 50% smaller with a median value of approximately 5 m cumulative thickness of liquefiable soils, and cumulative clean sand thickness of only 1.2 m in the top 10 m of the deposit. Importantly, at the NN-sites the liquefiable layers are vertically discontinuous, interrupted by (sandwiched between) non-liquefiable soils, and capped by a non-liquefiable crust.

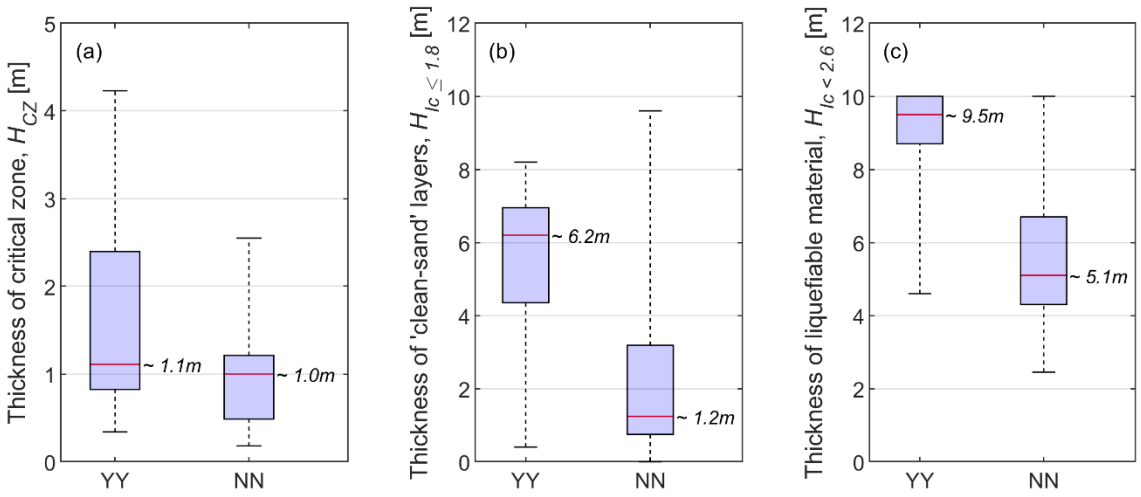

Fig. 3.9 Comparison of deposit characteristics of YY- and NN-sites: (a) thickness of a continuous critical zone (H_{CZ}); (b) cumulative thickness of sand layers with $I_c \leq 1.8$ ($H_{I_c \leq 1.8}$); (c) cumulative thickness of liquefiable materials ($H_{I_c < 2.6}$).

3.7 **Partially saturated soils**

The V_p measurements from the high-resolution cross-hole testing provide important observations with regard to the degree of saturation of soils and deposits (Appendix D). Fig. 3.10 comparatively shows the distribution of the compressional velocities of the critical layers for the YY-sites and NN-sites in terms of box-and-whisker plots. It can be seen that a considerable portion of the critical layers, more than 25%, for both the YY-sites and the NN-sites have compressional velocities associated with partial saturation (substantially lower than 1500 m/s). No significant differences can be observed between the YY-sites and the NN-sites, with respect to the saturation conditions of their critical layers. Fig. 3.11 illustrates plots of V_p versus depth from the groundwater table for layers from all 55 sites, classified based on their soil behaviour type. The moving median, 25th and 75th percentile V_p's with a sliding (across depth) window of 2 m are also shown in this figure. There is a clear distinction in the saturation conditions among the various soil types: (i) non-liquefiable soils show compressional velocities consistent with partial saturation up to depths of 6 m below the groundwater table; (ii) silty soils also show large propensity for partial saturation, with a substantial portion of such soils showing partial saturation at depths within 3-5 m from the water table; (iii) sands predominantly show full saturation, except for a shallow portion of about 1 m immediately below the water table. The above imply that NN-deposits, which are largely composed of non-liquefiable soils and non-plastic or low-plasticity silts (Fig. 3.9), could actually be partially saturated over a substantial depth below the water table. Fig. 3.12 comparatively shows the variation of V_p with depth from the groundwater table for the liquefiable soil layers ($I_c \leq 2.6$) of the YY- and NN-sites. As expected, a considerable portion of the liquefiable soils of the NN-deposits is partially saturated, with V_p less than 1000 m/s up to a depth of about 4 m below the groundwater table. At the YY-sites, partial saturation is largely confined within the first meter from the water table.

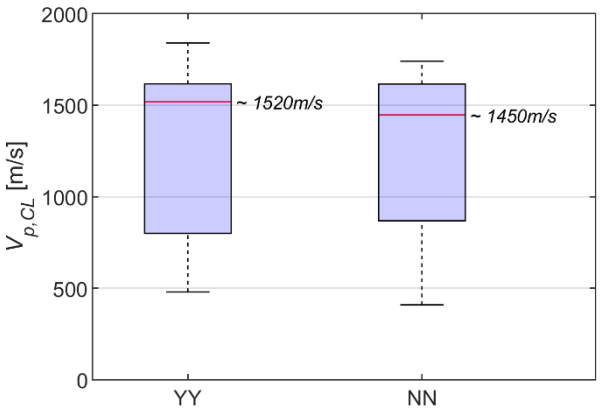

Fig. 3.10 Comparison of the compressional wave velocities of the critical layer ($V_{p,CL}$) for YY-sites and NN-sites using box and whisker plots.

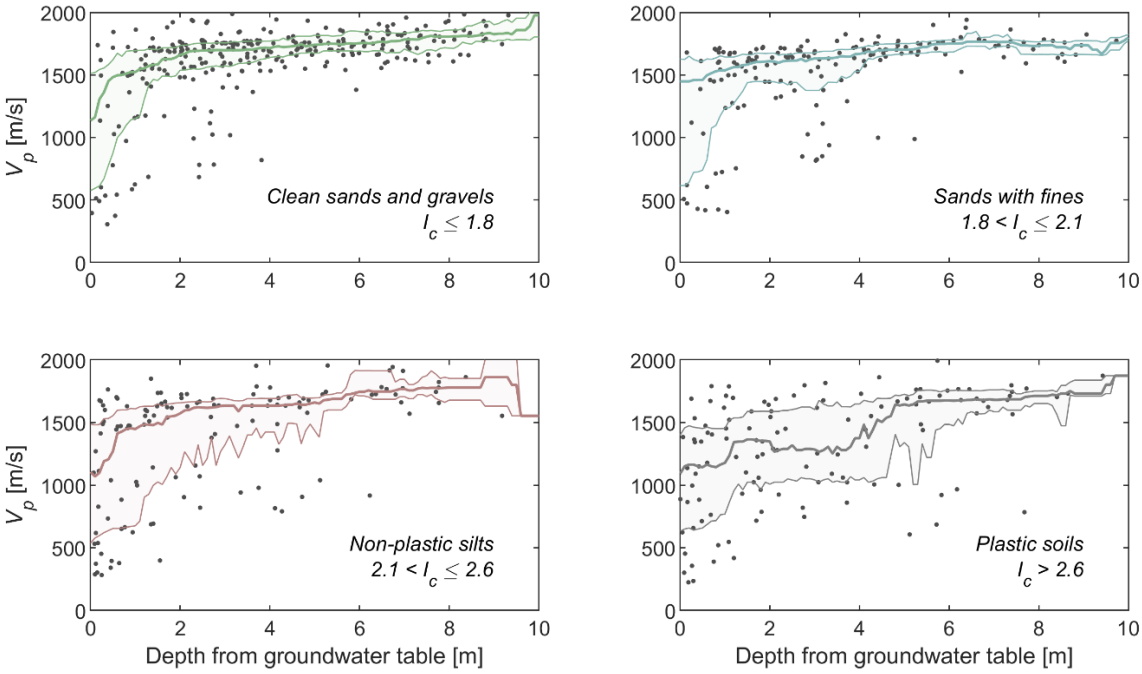

Fig. 3.11 V_p versus depth below groundwater table for the layers of the simplified profiles of the 55 sites, classified by their corresponding soil behaviour type. *The thick continuous lines and the shaded areas represent the moving median and interquartile range of the data across depth, respectively*.

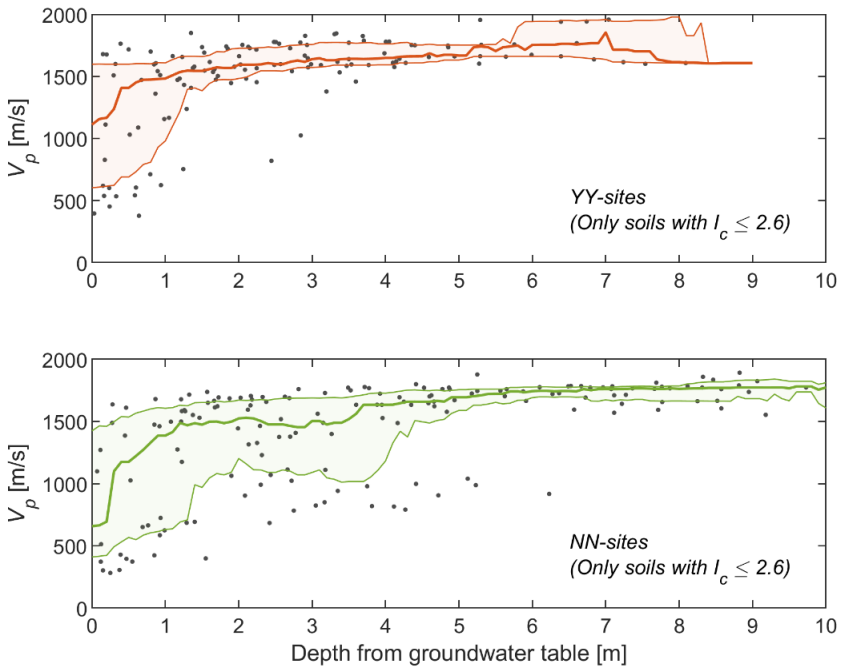

Fig. 3.12 Comparative illustration of V_p versus depth below groundwater table for the layers of the simplified profiles of the YY-sites and NN-sites. *The thick continuous lines and the shaded areas represent the moving median and interquartile range of the data across depth, respectively*.

Partial saturation is known to increase the liquefaction resistance due to an increased compressibility of the soil skeleton and consequent reduction in pore pressure generation during cyclic loading (e.g. Tsukamoto et al. 2002). Laboratory testing of Christchurch soils has indicated that a substantial increase in the cyclic resistance of partially saturated silty soils can, in fact, be achieved at higher compressional velocities than those required to reach the same levels of increase in clean sands (Baki et al. 2020). Therefore, not only the NN-deposits are often partially saturated over relatively large depths from the water table, but the beneficial effects of partial saturation on the cyclic resistance of the (predominant) silty soils in such deposits can be very significant.

3.8 **Summary**

There are essentially no differences in the characteristics of the critical layers between the sites that manifested liquefaction in both earthquakes (YY-sites) and the sites that did not manifest liquefaction in either event (NN-sites). For both YY- and NN-sites, the critical layer has low tip resistance ($q_{c1Ncs} \approx 85$) and is located at shallow depth of approximately 2 m below the ground surface. Therefore, simplified triggering analyses and evaluation of damage indices were not able to discriminate between the vast difference in the (liquefaction) performance of the YY-sites and NN-sites.

The YY-sites and NN-sites have important differences with regard to their deposit characteristics.

The YY-sites are generally characterized by vertically continuous liquefiable soils in the top 10 m and shallow water table at about 2 m depth. These deposits are typically composed of a shallow silty sand or sandy silt layer in the top 2 – 3 m, overlying a vertically continuous 7 – 8 m thick sand or fine sand layer up to 10 m depth. Partial saturation, when present at soils below the groundwater table, is typically confined within the top 1 m from the water table. The vertical continuity of liquefiable sands, absence of non-liquefiable layers, including absence of a non-liquefiable crust, are key features of the YY-sites, which manifested liquefaction in both earthquakes. A characteristic soil profile for a YY-site is shown in Fig. 13a.

The NN-sites, on the other hand, are highly stratified deposits consisting of interbedded liquefiable and non-liquefiable soils. A crust of non-liquefiable soil, shallow water table at about 1 to 2 m depth, partial saturation of plastic and non-plastic silt layers up to a depth of about 4 m below the groundwater table, horizontal ‘grid’ of non-liquefiable layers and vertical discontinuity of liquefiable soils are key features of the NN-sites, which did not manifest liquefaction in either earthquake. Fig. 13b shows a typical soil profile for an NN-site.

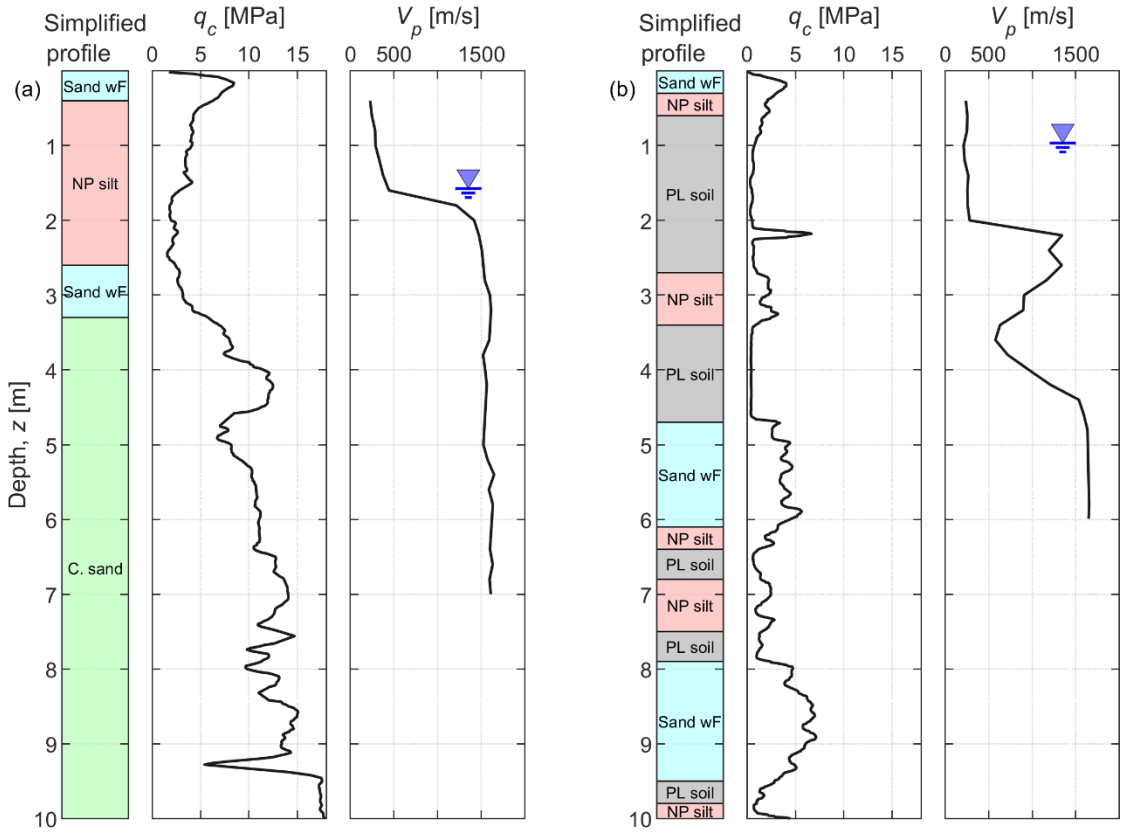

Fig. 3.13 General characteristics of the top 10 m of the YY- and NN-deposits: (a) characteristic soil units, q_c and V_p values for a typical YY-profile (manifested liquefaction in both major earthquakes); and (b) characteristic soil units, q_c and V_p values for a typical NN-profile (did not manifest liquefaction in either event).

The intermediate NY-sites (not discussed in this chapter) have highly varying soil profile characteristics, somewhere between those of the NN- and YY-deposits, and their response is highly demand-dependent. Characteristic features of the NY-deposits and their effects on the system response and liquefaction manifestation are rigorously examined in Chapter 7 using the results of seismic effective stress analyses.

4 EFFECTIVE STRESS ANALYSIS PROCEDURE

4.1 Introduction

As part of this research, a CPT-based effective stress analysis procedure was developed for analyzing the responses of the 55 Christchurch sites in a consistent and practical manner that would also allow for rigorous comparisons with the predictions by the simplified procedures. Besides serving the specific objectives of this study, the developed analysis procedure can be seen as a generalized CPT-based 1D effective stress analysis procedure for the liquefaction assessment of free-field level ground. One of the key objectives in mind when developing the proposed procedure was to facilitate the application of advanced seismic effective stress analysis allowing for easy calibration and minimizing the required input and modelling decisions from the user. In that regard, a key characteristic of the proposed procedure is that it has been automated in a way that it requires the same input data and uses the same definition of liquefaction resistance as the simplified CPT-based liquefaction assessment procedures. These features of the proposed procedure significantly facilitate its application into practice, and also provide a basis for rigorous comparisons of the outcomes of effective-stress analyses and simplified procedures.

The following key steps of the proposed effective-stress analysis procedure are described in this chapter.

(1) Determination of a simplified soil profile from CPT data,

(2) Determination of characteristic soil behaviour and associated constitutive model parameters for liquefiable soil layers,

(3) Determination of constitutive model parameters for non-liquefiable soil layers,

(4) Definition of input ground motion(s), and

(5) Definition of numerical model and analysis parameters.

In the first step, the nearly continuous CPT profile is discretized into a number of distinct layers or depth intervals over which the CPT data can be approximated by constant values. As illustrated in the previous chapter, this soil profile ‘simplification’ assists in the identification of characteristic layers in the deposit, and allows for more rigorous engineering scrutiny and interpretation. Steps 2 and 3 involve the definition of a target soil behaviour and the

subsequent determination of constitutive model parameters that can simulate this target behaviour. For liquefiable soils, the main objective is to accurately simulate the cyclic (liquefaction) resistance for a range of soil densities, confining stresses and number of loading cycles of interest. The target liquefaction resistance is determined using the simplified procedure for liquefaction triggering based on empirical CPT charts (e.g. Fig. 2.7). For non-liquefiable soils, the target cyclic stress-strain relationship is defined using strain-dependent modulus reduction and damping ratio curves, commonly employed in ground response analyses. In the fourth step, the input ground motion is defined. For forward applications, an automated ground motion selection algorithm is recommended for selecting ground motions representative of the seismic hazard and earthquake scenarios of interest. For back-analyses of case-history sites (forensic analyses), a comprehensive discussion on the selection and modification of within-event recorded ground motions is provided in the next chapter. In the final step of the procedure, the numerical model is defined by selecting appropriate model dimensions, mesh (element) size, boundary conditions, and initial stress state of the soil. Also, analysis parameters such as computational time increment, integration scheme and numerical damping are adopted, and the dynamic effective-stress analysis is then executed. Fig. 4.1 summarizes the key steps in the proposed CPT-based effective-stress analysis procedure.

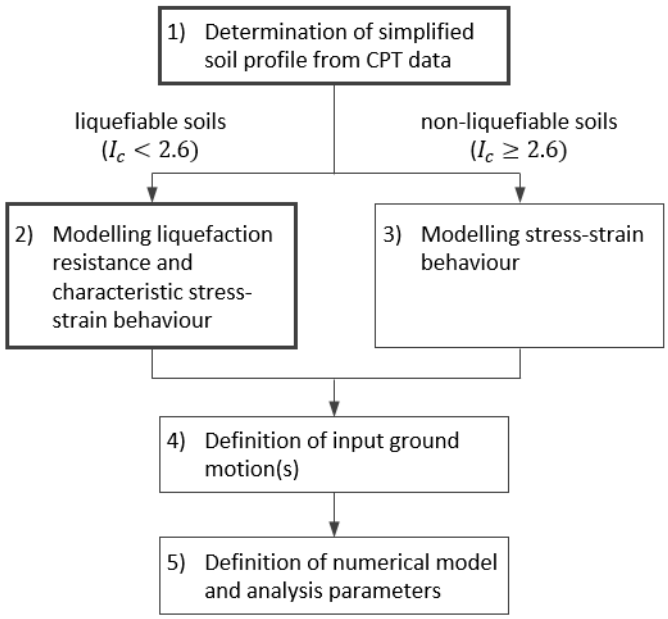

Fig. 4.1 Key steps in the proposed CPT-based effective stress analysis procedure.

4.2 **Determination of Simplified Soil Profile (Step 1)**

The determination of a simplified soil profile from the CPT data was thoroughly discussed in the previous chapter. The soil profile simplification allowed for rigorous analyses of the soil profile characteristics of the 55 sites, which led to important findings regarding the

differences in the deposit characteristics between sites that manifested liquefaction in both the two major earthquakes of the 2010-2011 CES (YY-sites), and sites that did not manifest liquefaction in any of the events (NN-sites). Clearly, this process can substantially enhance the engineering interpretation of the overall site characteristics and facilitate the identification of potential system-response mechanisms. Furthermore, the determination of a simplified soil profile is essential for the numerical model, where the problem domain, the soil deposit in this case, needs to be discretized into an assemblage of finite elements with specific model properties and constitutive behaviour.

Determining a simplified profile from the original CPT traces can, however, be quite tedious, particularly when a large number of CPT profiles has to be processed. Several approaches for automating this process have been proposed in the literature (e.g. Wang et al. 2013, Ching et al. 2015). For the purposes of this study, a more practical, yet efficient algorithm for automating the determination of simplified CPT profiles was developed and is discussed in the following.

4.2.1 CPT profile discretization algorithm

Key requirements in the layering definition for liquefaction assessment are that the discretization is fine enough to allow detection of thin seams of liquefiable soils and that the I_c and q_{c1Ncs} values (which determine the soil behaviour type and liquefaction resistance, respectively) of the simplified profile are as close as possible to the actual CPT traces. These were the two key considerations in the development of the algorithm described in the flow chart and side notes of Fig. 4.2.

More specifically, the main goal of the developed algorithm is to identify a simplified profile with I_c and q_{c1Ncs} step-functions of depth (i.e. piecewise constant), denoted as $\bar{I}_c$ and $\bar{q}_{c1Ncs}$, respectively, that minimize the dispersion of the actual I_c and q_{c1Ncs} data around them. Apart from the actual I_c and q_{c1Ncs} traces of the CPT, the algorithm requires four input parameters: the maximum tolerable coefficients of variation for I_c and q_{c1Ncs} within each layer, denoted as CV_{I_c} and $CV_{q_{c1Ncs}}$, respectively, and the minimum (T_{min}) and maximum layer thicknesses (T_{max}) for the simplified profile. Indicative values for the input parameters are given in the flow chart of Fig. 4.2. After inspection of the output of the algorithm (i.e. generated simplified profile), these parameters can be adjusted accordingly if a finer or coarser layering is desired for the analysis.

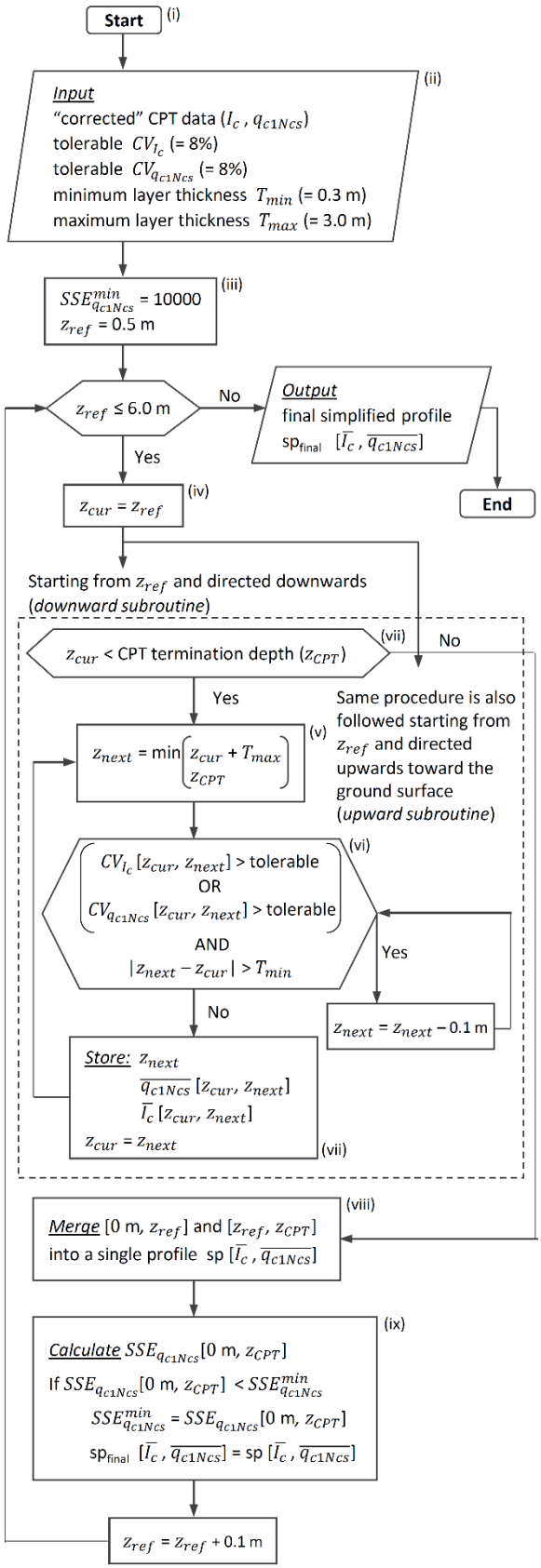

Sidenotes

i. The algorithm is identifying I_c and q_{c1Ncs} step-functions of depth (i.e. piecewise constant) that minimize the dispersion around the actual I_c and q_{c1Ncs}.

ii. Required input: (a) I_c and q_{c1Ncs} profiles from CPT data; (b) maximum tolerable coefficients of variation for I_c and q_{c1Ncs} within each layer of the simplified profile (CV_{I_c} and $CV_{q_{c1Ncs}}$ dictate the degree of refinement in the discretization); (c) minimum (T_{min}) and maximum layer thicknesses (T_{max}) for the simplified profile. The adopted values are indicative only.

iii. The algorithm starts from a particular depth in the deposit, z_{ref}, and executes two subroutines, i.e. "*upward*" and "*downward*" subroutines, one after the other, to determine the locations of layer boundaries above and below z_{ref}, respectively. All z_{ref} depths from 0.5 to 6.0 m with a step of 0.1 m are considered.

iv. In each subroutine, z_{ref} is assigned to a local variable, z_{cur}.

v. Each subroutine initially assumes the next layer boundary, z_{next}, is located at a distance T_{max} from z_{cur}. If this assumption places the next layer boundary (z_{next}) above the ground surface ($z_{next} < 0$ m) in the upward subroutine or below the termination depth of the CPT ($z_{next} > z_{CPT}$) in the downward subroutine, then $z_{next} = 0$ m or $z_{next} = z_{CPT}$ is adopted accordingly.

vi. For the assumed z_{next}, the median $\overline{I_c}$ $[z_{cur}, z_{next}]$, $\overline{q_{c1Ncs}}$ $[z_{cur}, z_{next}]$ and coefficients of variation CV_{I_c} $[z_{cur}, z_{next}]$, $CV_{q_{c1Ncs}}$ $[z_{cur}, z_{next}]$ are computed. If either CV_{I_c} or $CV_{q_{c1Ncs}}$ are greater than the respective maximum tolerable coefficients of variation, the layer thickness is decreased by 0.1 m. This process of gradually decreasing the layer thickness is repeated either until both CV_{I_c} and $CV_{q_{c1Ncs}}$ are within tolerance or the layer thickness reaches T_{min}. In either case the subroutine exits the loop and stores z_{next}, $\overline{I_c}$ and $\overline{q_{c1Ncs}}$.

vii. Then, z_{next} replaces z_{cur} and steps v-vi are repeated to find the next layer boundary. The subroutine is terminated when $z_{next} = z_{CPT}$ (in the downward subroutine) or $z_{next} = 0$ m (in the upward subroutine).

viii. After execution of the two subroutines, the stored z_{next}, $\overline{I_c}$ and $\overline{q_{c1Ncs}}$ are merged to define a single discretized $\overline{I_c}$ – $\overline{q_{c1Ncs}}$ profile (sp [$\overline{I_c}$, $\overline{q_{c1Ncs}}$]) from the ground surface to the termination depth of the CPT.

ix. The total sum of the squared residuals $SSE_{q_{c1Ncs}}$ between the actual q_{c1Ncs} and the median $\overline{q_{c1Ncs}}$ profile is calculated. A new starting depth is assigned to z_{ref} and steps iii-ix are repeated. In general, different z_{ref} starting points yield slightly different $\overline{I_c}$ and $\overline{q_{c1Ncs}}$ profiles and different $SSE_{q_{c1Ncs}}$. The soil profile sp [$\overline{I_c}$, $\overline{q_{c1Ncs}}$] with the minimum $SSE_{q_{c1Ncs}}$ is adopted as the final simplified profile.

Fig. 4.2 Flow chart and sidenotes describing the main steps and details of the algorithm for determination of simplified soil profiles from CPT data.

To assess its effectiveness in determining simplified soil profiles for actual soil deposits, the algorithm described in Fig. 4.2 was applied to the 55 Christchurch sites. After a positive visual inspection of the obtained simplified profiles for each site, triggering analyses and evaluation of liquefaction damage indices (LSN and LPI) were performed using both the simplified ($\bar{I}_c$ and $\bar{q}_{c1Ncs}$) and the actual (I_c and q_{c1Ncs}) profiles, for the 04Sep10 and 22Feb11 earthquakes (i.e. two different combinations of peak ground surface acceleration and earthquake magnitude for each site). Results from all analyses for the simplified and actual profiles are comparatively shown in Fig. 4.3, in terms of LPI (Fig. 4.3a) and LSN (Fig. 4.3b). The vast majority of the computed damage indices in these plots fall on or close to the 1:1 line indicating that the estimated liquefaction performance from the analyses using the simplified profiles is consistent with the results of the analyses with the original profiles. This validates the use of the proposed algorithm for determination of a representative simplified CPT soil profile for liquefaction analysis. That being said, it is important to emphasize that the proposed algorithm is intended to assist users and not replace their engineering judgement in determining a simplified profile. In particular, prediction of fictitious layers at layer interfaces is not uncommon in these automated procedures, and so the user must always review the output and make adjustments when deemed necessary. The use of automated procedures for correcting CPT data for thin-layer and transition zone effects (e.g. Boulanger and DeJong 2018) prior to the application of the algorithm can significantly help to avoid such issues.

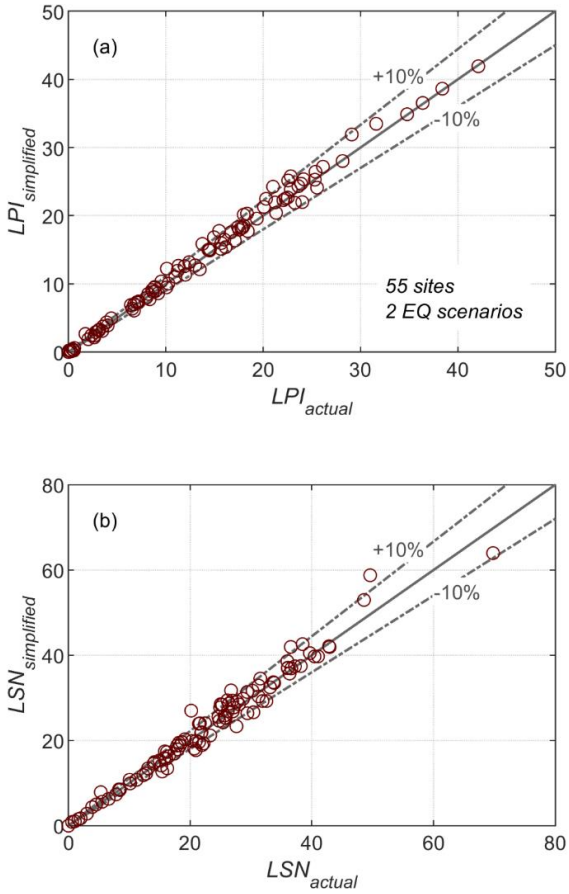

Fig. 4.3 Comparison between damage index predictions using the actual and simplified profiles for the 55 Christchurch sites: (a) LPI values, (b) LSN values.

The automated algorithm for the discretization of CPT profiles was used in the development of simplified soil profiles for the 55 Christchurch sites, in conjunction with an interface (transition zone) detection and correction algorithm, as per Boulanger and DeJong (2018). Adjustments were made when necessary. The adopted simplified profiles for all 55 sites are illustrated in Appendix A.

4.3 Modelling of Liquefiable Soils (Step 2)

4.3.1 Stress-Density Model

An elastic-plastic constitutive model, called the Stress-Density Model (S-D Model) (Cubrinovski and Ishihara 1998a, 1998b) which was specifically tailored for analysis of liquefaction problems, is employed in the effective-stress analysis. Key assumptions in the elastic-plastic formulation of the S-D Model are: (i) continuous yielding or vanishing elastic region, (ii) combined isotropic and kinematic hardening plasticity, (iii) dependence of the plastic strain increment direction on the stress increment direction (hypoplasticity), (iv) modified hyperbolic stress-strain relationship, and (v) an energy based stress-dilatancy relationship. In terms of soil behaviour, this translates into a capability of the model to accurately simulate highly nonlinear stress-strain behaviour both under monotonic loading (from small strains to large strains or steady state of deformation) and irregular cyclic loading.

Another major feature of the S-D Model is that it utilizes the state-concept approach for modelling the combined effects of density and confining stress on stress-strain behaviour of sand. In this context, there are two key elements in the model.

First, the state index (I_s) proposed by Ishihara (1993) and Verdugo (1992) is used as a key variable in the model controlling the stress-strain behaviour of sand as a function of the density and confining stress state of the soil. The definition of I_s for a sand at an initial void ratio e and mean normal stress p' is schematically illustrated in Fig. 4.4. Two characteristic states of sand are employed in its definition, i.e. the quasi steady state (QSS-line) and an upper reference state (UR-line). The quasi steady state represents a particular case of phase transformation, and occurs following a temporary drop in the shear stress upon undrained shearing of loose sands. An advantage of using the QSS-line in the definition of I_s is that it incorporates the effects of fabric of packing, however, because the quasi steady state if often difficult to attain in practice, the fabric-independent steady state line (SS-line) is commonly used, instead of the QSS-line, to define I_s in the S-D Model. The UR-line is associated either with the threshold void ratio e_0 above which the initial states lead to a zero strength at the steady state upon undrained shearing, or with the isotropic consolidation line for the loosest state. By definition, I_s takes values of 1.0 for initial $e - p'$ states on the QSS-line (or SS-line) and 0 for initial $e - p'$ states on the UR-line.

Second, the state index is employed in the model as a current variable rather than an initial state parameter. In other words, the stiffness and peak strength of the sand (and, consequently, the stress-strain curve) are dependent on the current value of I_s (i.e. current density and normal stress level, at each loading step). This feature of the S-D Model permits modelling of strain-softening (or strain-hardening) behaviour for loose (or dense) sands and provides an elegant mechanism for modelling complex post-liquefaction phenomena including significant change in density/volume such as void redistribution. Importantly, the behaviour of a given sand at any density and confining stress can be simulated using the same set of material parameters.

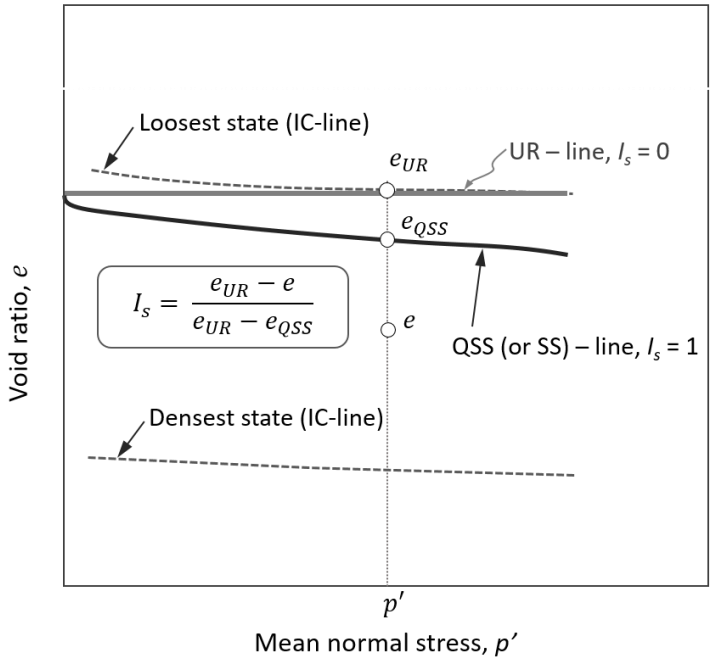

Fig. 4.4 Definition of state index I_s for a current state of mean normal stress p' and void ratio e.

The S-D Model has been extensively verified through rigorous simulations of down-hole array records at liquefaction sites, seismic centrifuge tests, large-scale shake table tests and numerous case histories (e.g. Cubrinovski et al. 2008). The model has been implemented in the finite element code DIANA-J and also in an in-house design code of Taisei Corporation (Japan), and is currently at the final stage of its verification in FLAC2D and OpenSees.

4.3.2 Liquefaction resistance

For liquefaction problems, the key requirement from the constitutive model is to accurately simulate the development of excess pore water pressures under irregular cyclic loading (earthquake excitation). This ability needs to be demonstrated through a simulation of target liquefaction resistance curves in element test simulations.

Liquefaction resistance curves (LRCs) represent the combination of shear stress amplitude (CSR) and number of cycles (N_c) required to cause liquefaction or a certain level of strain in the soil, e.g. 3%, 5% or 7.5% double amplitude strain. They are typically expressed as $CSR - N_c$ relationships and are used as a key soil property in the calibration of constitutive models for effective-stress analysis. LRCs are commonly derived from a series of liquefaction tests on soil samples in the laboratory in which samples of 'identical' (or similar) density are subjected to cyclic shear stresses of uniform amplitude under undrained conditions. Each sample is tested at a different cyclic stress ratio in order to establish the LRC across various $CSRs$ or over a range of approximately $N_c = 1 - 30$ cycles, which is the most relevant number of cycles for earthquake loading. In this way, multiple sets of LRCs can be derived using target soil samples for all different soil types (i.e. soils with different grain-size distribution, fines content, grain shape, mineralogy, etc.) present at the site of interest by testing each soil at different densities and confining stresses.

In the absence of experimental data and for generic applications, LRCs can be alternatively derived by directly following conventional procedures for liquefaction evaluation based on empirical liquefaction triggering charts. This alternative approach treats each different soil type as an equivalent clean sand, using a single set of LRCs for the relevant range of densities and confining stresses of interest. In the present study, the Boulanger and Idriss (2014) CPT-based liquefaction triggering procedure was used to determine a set of representative LRCs through the following steps:

1) For a given q_{c1Ncs} value, the cyclic resistance ratio CRR corresponding to earthquake magnitude $M_w = 7.5$ and effective overburden stress of $\sigma'_{vo} = 100$ kPa is estimated using Eq. 4-1:

$$CRR_{M=7.5,\sigma'_{vo}=1} = \exp\left[\frac{q_{c1Ncs}}{113} + \left(\frac{q_{c1Ncs}}{1000}\right)^2 - \left(\frac{q_{c1Ncs}}{140}\right)^3 + \left(\frac{q_{c1Ncs}}{137}\right)^4 - 2.80\right] \quad (4\text{-}1)$$

2) The maximum value of the magnitude scaling factor (MSF_{max}) is estimated using Eq. 4-2:

$$MSF_{max} = 1.09 + \left(\frac{q_{c1Ncs}}{180}\right)^3 \leq 2.2 \quad (4\text{-}2)$$

3) The b value describing the slope of the LRC in the $CSR - N_c$ space is computed from MSF_{max} using Eq. 4-3:

$$b = c_0 + c_1(MSF_{max}) + c_2(MSF_{max})^2 + c_3(MSF_{max})^3 + c_4(MSF_{max})^4 \quad (4\text{-}3)$$

where $c_0 = -3.0176$, $c_1 = 7.0217$, $c_2 = -5.7685$, $c_3 = 2.152$ and $c_4 = -0.3$.

Eq. 4-3 provides an approximate expression of the $MSF_{max} - b$ relationship presented in Fig. A.16 of Boulanger and Idriss (2014).

4) The number of equivalent cycles corresponding to earthquake magnitude $M_w = 7.5$ ($N_{M=7.5}$) is then estimated using Eqs. 4-4 and 4-5:

$$N_{M=7.5} = N_{min} \cdot (MSF_{max})^{\frac{1}{b}} \tag{4-4}$$

where

$$N_{min} = \left(\frac{1.0}{0.65}\right)^{\frac{1}{b}} \left(\frac{3}{4}\right) \tag{4-5}$$

5) Next, for a given effective overburden stress σ'_{vo}, the overburden stress correction factor K_σ is estimated using Eqs. 4-6 and 4-7:

$$K_\sigma = 1 - C_\sigma \ln\left(\frac{\sigma'_{vo}}{P_a}\right) \tag{4-6}$$

where P_a is the atmospheric pressure, and

$$C_\sigma = \frac{1}{37.3 - 8.27(q_{c1Ncs})^{0.264}} \leq 0.3 \tag{4-7}$$

6) For a given number of equivalent loading cycles N_c, the magnitude scaling factor MSF is estimated using Eq. 4-8:

$$MSF = \left(\frac{N_{M=7.5}}{N_c}\right)^b \tag{4-8}$$

7) Finally, the cyclic resistance for the given combination of q_{c1Ncs} and σ'_{vo} at N_c cycles is estimated using Eq. 4-9:

$$CRR = CRR_{M=7.5,\sigma'_{vo}=1} \cdot MSF \cdot K_\sigma \tag{4-9}$$

Repeating steps 6 and 7 for different N_c values, over the range of cycles of interest, yields the LRC for the soil with penetration resistance q_{c1Ncs} and effective overburden stress σ'_{vo}, under zero static shear stress (level ground conditions). In the same way, empirical LRCs can be derived for any given $q_{c1Ncs} - \sigma'_{vo}$ combination which is within the range of applicability of the corresponding simplified procedures.

The above procedure effectively reduces simplified liquefaction triggering procedures to a set of LRCs. Such LRCs derived from the Boulanger and Idriss (2014) liquefaction triggering procedure following the above steps 1-7, for various q_{c1Ncs} values and an effective overburden stress of $\sigma'_{vo} = 100$ kPa, are shown with solid lines in Fig. 4.5.

Apart from bypassing the need for laboratory tests of target soil samples, another advantage of the above empirical approach for establishing the target LRCs is the fact that it allows for fair comparisons of the outcomes of effective-stress analyses and simplified procedures, as the same definition of liquefaction resistance is used in both methods. On the other hand, this same feature could be seen as a limitation of the procedure because the large uncertainty associated with the characterization of liquefaction resistance of soils other than clean sands (e.g. silty sands with non-plastic, low-plasticity or plastic fines) in the simplified procedures

(e.g. Cubrinovski et al. 2019) is carried over to the effective-stress analysis. This is considered an acceptable limitation for the purpose of the present study which focuses on explaining discrepancies between (liquefaction manifestation) observations and predictions by the simplified procedures on the basis of system response rather than through limitations in the characterization of the element-level behaviour. Nonetheless, the poor characterization of the behaviour of silty soils, relative to that of clean sands, is recognized as a potentially important factor contributing to discrepancies between field observations and predictions by simplified liquefaction evaluation procedures.

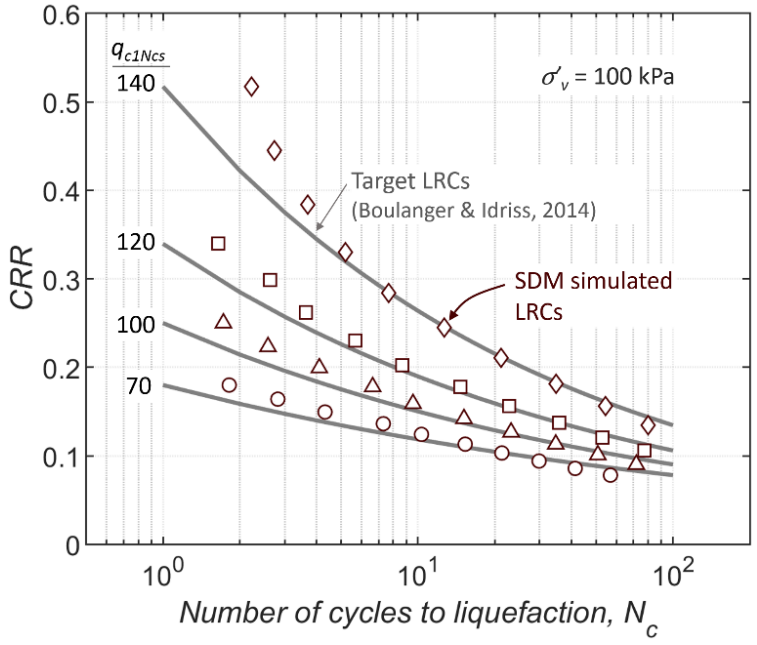

Fig. 4.5 Target LRCs (solid lines) obtained using the Boulanger and Idriss (2014) liquefaction triggering procedure, and S-D Model (SDM) simulated LRCs (open symbols) for different q_{c1Ncs} values (i.e. different void ratios in S-D Model) and $\sigma'_{vo} = 100$ kPa.

4.3.3 S-D Model calibration for liquefiable soils

The goal is now to determine S-D Model parameters that can reproduce the target LRCs (defined as above) in element test simulations. The S-D Model has four groups of input parameters: elastic parameters, reference states, stress-strain parameters and dilatancy parameters. Cubrinovski and Ishihara (1998b) have established a set of S-D Model parameter values for dry-pluviated Toyoura sand, after a series of laboratory tests, including drained and undrained, monotonic and cyclic (liquefaction) tests. As Toyoura sand is often used as a representative clean sand for liquefaction studies, these values were used as a basis for the determination of a set of new S-D Model parameters that can simulate the target (empirical) liquefaction resistance curves. In this process, the stress-strain parameters were kept the same

as for Toyoura sand, whereas other parameters of the model were varied in a trial-and-error process to identify the best-fit values providing the most accurate simulation for the whole set of the target LRCs. The new S-D Model parameter values resulted from the above calibration process are listed in Table 4.1. For reference, the original S-D Model parameters for dry-pluviated Toyoura sand are also shown in this table. It is important to note that changes in elastic, dilatancy, and reference line parameters were relatively small and definitely within an acceptable range of variation.

Table 4.1 Stress-Density Model parameters.

Material parameter	Toyoura sand[a]	Generic sand[b]
Elastic parameters		
Shear constant, A	250	310
Poisson's ration, v	0.20	0.25
Exponent, n	0.60	0.80
Reference lines		
UR-line (Void ratios and normal stresses in kPa), (e_U, p_U)	(0.895, ≤ 400)	(0.895, ≤ 400)
QSS-line (Void ratios and normal stresses in kPa), (e_Q, p_Q)	(0.877, 1)	(0.875, 1)
	(0.877, 10)	(0.874, 10)
	(0.873, 30)	(0.873, 30)
	(0.870, 50)	(0.872, 50)
	(0.860, 100)	(0.871, 100)
	(0.850, 200)	(0.868, 200)
	(0.833, 400)	(0.860, 400)
Stress-strain parameters		
Peak stress ratio coefficients, a_1, b_1	0.592, 0.021	0.592, 0.021
Max. shear modulus coefficients, a_2, b_2	291, 55	291, 55
Min. shear modulus coefficients, a_3, b_3	98, 13	98, 13
Degradation constant, f	4	4
Dilatancy parameters		
Dilatancy coef. (small strains), μ_0	0.22	0.22
Dilatancy coef. (cyclic loading), μ_{cyc}	0.00	-0.02
Critical state stress ratio, M	0.607	0.620
Dilatancy strain, S_c	0.0055	0.0040

[a] Model parameters from Cubrinovski and Ishihara (1998b).

[b] Compatible with Boulanger and Idriss (2014).

Fig. 4.5 shows with open symbols the LRCs obtained using simulations with the new set of S-D Model parameters. These S-D Model simulated LRCs are established through a series of element test simulations in which a soil element, at an initial stress-density state, is subjected to a given amplitude of uniform stress cycles. Liquefaction triggering is assumed to occur in the simulation cycle at which the double amplitude (DA) shear strain exceeds 5%. The number of cycles required to cause liquefaction and develop 5% DA strain is then used

together with the applied level of cyclic stress to define the soil resistance (i.e. one symbol in Fig. 4.5) at the given stress-density state.

The simulation of the target LRCs shown in Fig. 4.5 is considered sufficiently accurate for liquefaction analysis. Small discrepancies do occur at higher stress ratios, but overall, simulated and target curves show a reasonably good agreement across $N_c = 1 - 50$ cycles. In addition, the adopted S-D Model parameter values provide a reasonably accurate simulation of the tail of the target LRCs, at low cyclic stress amplitudes, which defines the threshold CSR separating between liquefaction and no-liquefaction. This detail is particularly important, as underestimation of the liquefaction resistance for low shear stresses can lead to substantial overprediction of pore water pressures in the seismic effective stress analysis.

It is important to note that, a single set of values for the S-D Model parameters was used to simulate the target LRCs across different q_{c1Ncs} values (i.e. soil densities), by only adjusting the initial void ratio e in the S-D Model to achieve a good fit. The use of a single set of parameter values across various densities is a distinctive feature of the S-D Model which comes as a result of the incorporation of the state-concept characterization of soil behavior into the model. To facilitate the application of the S-D Model over a range of different q_{c1Ncs} values that may result from the profile simplification process, an expression for estimating the void ratio e that provides the best fit of the LRC for a given q_{c1Ncs} value was developed as follows:

$$e = -0.315[1 + \exp(-0.128 q_{c1Ncs} + 18.8)]^{-0.142} + 0.931 \quad (4\text{-}10)$$

For a target LRC associated with a specific q_{c1Ncs} value, this expression was used to derive the respective e value for the S-D Model in the element test simulations shown in Fig. 4.5. Using the minimum and maximum void ratios for the reference Toyoura sand, $e_{min} = 0.616$ and $e_{max} = 0.988$, respectively, Eq. 4-10 can be rewritten in terms of relative density D_r as:

$$D_r = 0.847[1 + \exp(-0.128 q_{c1Ncs} + 18.8)]^{-0.142} + 0.153 \quad (4\text{-}11)$$

Fig. 4.6 shows the relationship of Eq. 4-11 together with three common empirical $D_r - q_{c1Ncs}$ expressions for clean sands (Tatsuoka et al. 1990, Idriss and Boulanger 2008, Robertson and Cabal 2012). It can be seen that Eq. 4-11 slightly underestimates D_r for q_{c1Ncs} between 60 and 100 compared to the empirical estimates, whereas it overestimates D_r for q_{c1Ncs} greater than 130. Nevertheless, given the large uncertainty in these empirical expressions, expected differences between laboratory-based and field-based LRCs, and the success of Eqs. 4-10 and 4-11 in simulating the target LRCs across a wide range of q_{c1Ncs} values, while using the same set of values for the S-D Model parameters, which was the primary goal in this calibration exercise, these small deviations of Eq. 4-11 from the range of empirical $D_r - q_{c1Ncs}$ correlations are considered acceptable.

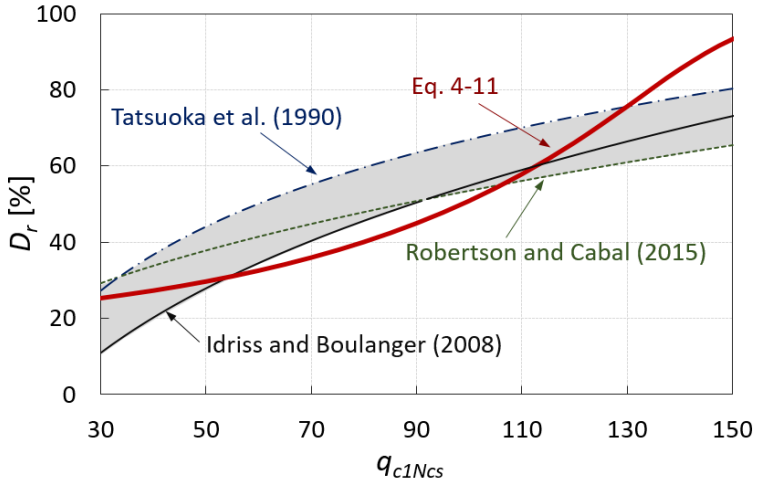

Fig. 4.6 Comparison between empirical $D_r - q_{c1Ncs}$ relationships and Eq. 4-11 used in the calibration of the S-D Model.

Another benefit from the embodiment of the state-concept modelling to the S-D Model is that it accounts for the combined effects of density and confining stress on the liquefaction resistance and cyclic stress-strain behaviour of sand. In the simplified methods, the effect of confining stress on liquefaction resistance is addressed through the use of the K_σ factor (Eqs. 4-6 and 4-7), defined as:

$$K_\sigma = \frac{CRR_{\sigma'_{vo}}}{CRR_{\sigma'_{vo}=1}} \tag{4-12}$$

where $CRR_{\sigma'_{vo}}$ is the CRR of a soil under a specific value of σ'_{vo}, and $CRR_{\sigma'_{vo}=1}$ is the CRR of the same soil for a reference value of $\sigma'_{vo} = 1$ atm. Fig. 4.7 shows (with solid lines) a set of $K_\sigma - \sigma'_{vo}$ curves obtained using the Boulanger and Idriss (2014) expressions (Eqs. 4-6 and 4-7), and the corresponding S-D Model simulated relationships (dashed lines with open symbols) using the generic parameters from Table 4.1, for q_{c1Ncs} values of 70, 100 and 140, and σ'_{vo} from 20 to 400 kPa. The two sets of curves (target and S-D Model simulated) show a reasonably good agreement, with the S-D Model simulated curves manifesting a slightly stronger effect of confining stress on liquefaction resistance, particularly near the boundary values of the q_{c1Ncs} principal range of interest (i.e. $q_{c1Ncs} \approx 50 - 150$) where the largest discrepancies occur. However, it is important to note that the trends with respect to the influence of q_{c1Ncs} on $K_\sigma - \sigma'_{vo}$ are well captured in these simulations.

In summary, the above calibration of the S-D Model provides a reasonably accurate modelling of target liquefaction resistance curves over the relevant range of cyclic shear stresses for earthquake engineering ($N_c = 1 - 30$ cycles), including the threshold CSR separating between liquefaction and no-liquefaction, and across all densities or penetration resistances ($q_{c1Ncs} \approx 50 - 150$) and confining stresses of interest ($\sigma'_{vo} \approx 20 - 400$ kPa). The above are considered key requirements for the calibration of any constitutive model for

dynamic analysis targeting liquefaction problems. Finally, note that q_{c1Ncs} and σ'_{vo} are the only input parameters required by the model.

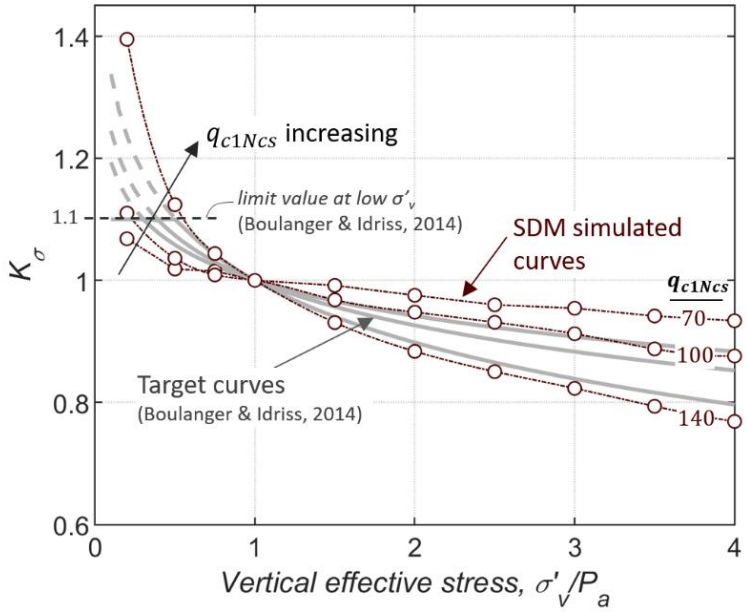

Fig. 4.7 Comparison between Boulanger and Idriss (2014) (solid lines) and S-D Model (SDM) simulated (dashed lines with open symbols) $K_\sigma - \sigma'_{vo}$ relationships for various q_{c1Ncs} values.

4.3.4 Modelling of partial saturation effects on cyclic (liquefaction) resistance

The effects of partial saturation on the cyclic resistance of liquefiable soils can also be incorporated in the proposed calibration of the S-D Model by modifying key model parameters affecting the cyclic resistance. In this case, a lab-based model for the increase in liquefaction resistance due to partial saturation, proposed by Hossain et al. (2013), is adopted as the target model. In this model, the ratio of the CRR of the partially saturated soil ($CRR_{ps,N=20}$) to the respective CRR of the same soil in fully saturated conditions ($CRR_{fs,N=20}$), for a reference number of $N_c = 20$ loading cycles, is given as a sole function of V_p, as indicated in Fig. 4.8. An appropriate correction factor is then used to account for the effects of density and number of loading cycles on the reference ratio $\left(CRR_{ps}/CRR_{ps}\right)_{N=20}$. Modifying the dilatancy strain parameter (S_c) of the S-D Model with V_p, while keeping all other S-D Model parameters unchanged, as in Table 4.1, was shown to provide reasonably good simulations of the corresponding CRR increase, in accordance with the Hossain et al. (2013) model, for various initial stress and density states, and number of loading cycles. Eq. 4-13 is suggested for calibration of the S_c parameter of the S-D Model based on the assigned V_p value of the corresponding soil layer:

$$S_c = 0.03 \cdot 1.005^{-V_p} + 0.0040 \tag{4-13}$$

where V_p is in units of m/s. Note that for large values of V_p ($V_p \geq 1400$ m/s), Eq. 4-13 yields $S_c \approx 0.0040$, which is equal to the suggested parameter value for fully saturated conditions (Table 4.1). The performance of Eq. 4-13 in element test simulations of the liquefaction resistance of partial saturated soils against the predictions of the target Hossain et al. (2013) model, for various initial densities of soil (i.e. q_{c1Ncs}), is illustrated in Fig. 4.8. For all practical purposes, the calibration of the S_c parameter in accordance with Eq. 4-13 yields liquefaction resistances for partially saturated soils that are in reasonable agreement with those predicted by the target model. With the above extension of the proposed methodology to allow for incorporation of partial saturation effects on LRC, three input parameters, namely σ'_{vo}, q_{c1Ncs}, and V_p, are required for the semi-empirical modelling of liquefiable soils using the S-D Model.

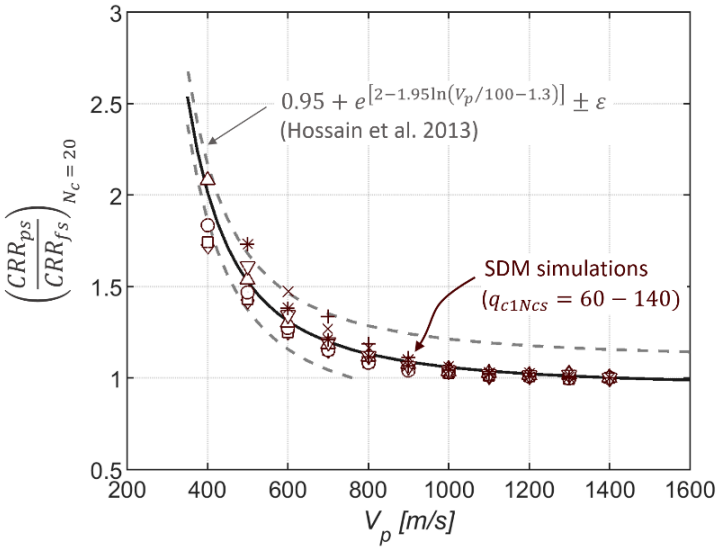

Fig. 4.8 Modelling of partial saturation effects on CRR based on V_p: S-D Model (SDM) simulations (symbols) using Eq. 4-13 compared with the target regression model of Hossain et al. (2013).

4.4 Modelling of Non-Liquefiable Soils (Step 3)

4.4.1 Identification of non-liquefiable soil layers

Natural soil deposits generally have soil layers that are, by composition, susceptible to liquefaction and others that are not. Ideally, index and cyclic testing of retrieved soil samples in the laboratory should be used to distinguish between liquefiable and non-liquefiable soils (e.g. Bray and Sancio 2006). In the absence of soil sample data, the soil behaviour type index I_c or the modified soil behaviour type index I_B (Robertson 2016) obtained from CPT measurements may be used for classification of soil behavior type. As a general rule, in the CPT-based effective-stress analysis approach presented herein, soil layers with $I_c < 2.6$ are

considered liquefiable and they are modelled as described in the previous section; all other soil layers are regarded as non-liquefiable, and their modelling is discussed in this section. Exceptions to this rule apply for liquefiable soils ($I_c < 2.6$) that are not expected to respond in a strongly non-linear manner and develop large excess pore water pressures ($\gamma_{max} \lesssim 0.1 - 0.2\%$). These might be liquefiable (by composition) soils with high q_{c1Ncs} (e.g. $q_{c1Ncs} > 170$) or soils at large depths where the seismic demand is relatively low. Modelling of such soils and conditions must be targeting soil behaviour for strains $\gamma \lesssim 0.1 - 0.2\%$, rather than their liquefaction resistance. Taking this into consideration, in the analyses presented in the following chapters, liquefiable (by composition) soils with $q_{c1Ncs} > 170$ have been modelled as 'non-liquefiable'. Note, however, that vertical flow of water is allowed through such layers.

4.4.2 Target stress-strain behaviour

The nonlinear shear stress–shear strain ($\tau - \gamma$) response of non-liquefiable soils at a constant effective-stress can be approximated by the small strain shear modulus (G_{max}), the peak shear stress (τ_{max}) at large strains, and a strain-dependent model that describes the transition (change in stiffness) from small strains to large strains. Under cyclic loading, a measure for the energy dissipated in each loading cycle is also required. It is common in ground response analysis to represent the strain-dependent variation in stiffness and energy dissipation via modulus reduction (G/G_{max}), and damping ratio (ξ) curves, such as those depicted in Fig. 4.9. In this study, the modulus reduction and damping ratio models proposed by Darendeli (2001) were initially adopted as target curves. Key parameters required for the definition of $G/G_{max} - \gamma$ and $\xi - \gamma$ curves in Darendeli's model are the mean effective confining stress ($\sigma'_{mo} = [(2K_o + 1)/3]\sigma'_{vo}$, where K_o is the earth pressure coefficient at rest), the overconsolidation ratio (OCR), and the soil plasticity index (PI). More often than not, some adjustment of the original Darendeli $G/G_{max} - \gamma$ model is necessary to make the backbone stress-strain curve asymptotically approach the target shear strength (τ_{max}) of the soil at large strains (e.g. Yee et al. 2013). In summary, the complete stress-strain (target) model for non-liquefiable soils can be defined if G_{max}, τ_{max}, K_o, OCR and PI are known. For the purposes of this study, G_{max} values for the layers of the simplified profiles were calculated from the measured V_s values assuming a wet soil density of $\rho_s = 1.89$ Mg/m^3, or, at depths where V_s data from the cross-hole tests were not available, they were estimated from the respective CPT data using the Christchurch-specific empirical correlation proposed by McGann et al. (2015). K_o was assumed equal to 0.5, whereas τ_{max} and OCR were estimated from empirical correlations with the CPT data provided in Robertson and Cabal (2015). PI was assumed equal to 20% for soil layers with $I_c \geq 2.6$, and 0% for all other layers.

4.4.3 Constitutive modelling

Once the target stress-strain model has been defined, a calibration procedure is required in which constitutive model parameters that provide reasonably accurate simulation of the target stress-strain behavior are determined. Any non-linear constitutive model that can concurrently model both the target $G/G_{max} - \gamma$ and the target $\xi - \gamma$ curves could be used. In fact, this is

often difficult to achieve because the Masing rules (1926) that most constitutive models adopt for modelling the hysteretic behaviour of soils during cyclic loading does not necessarily match the corresponding behaviour observed in the lab. Recognizing this limitation, a compromise approach often needs to be taken, where both the target damping and modulus curves are reasonably fitted over the expected range of strains. Fig. 4.9 shows an example of modulus reduction and damping ratio curves simulated using the S-D Model. It can be seen that the S-D Model simulation slightly overpredicts shear stiffness in a range of shear strains from 0.001% to 1%, whereas it significantly overpredicts the damping ratio for shear strains greater than about 0.5%. Provided that the maximum shear strains in the numerical simulations do not exceed (about) 0.5%, such compromise modelling is considered acceptable, as the model is expected to be used only over the range of strains where it shows good performance. Note that, in addition to the damping provided by the hysteretic response of the S-D Model, a small amount of (frequency-dependent) Rayleigh damping is also used in the analysis for numerical stability and to provide damping at small strains where hysteretic damping is nearly zero (Fig 4.9).

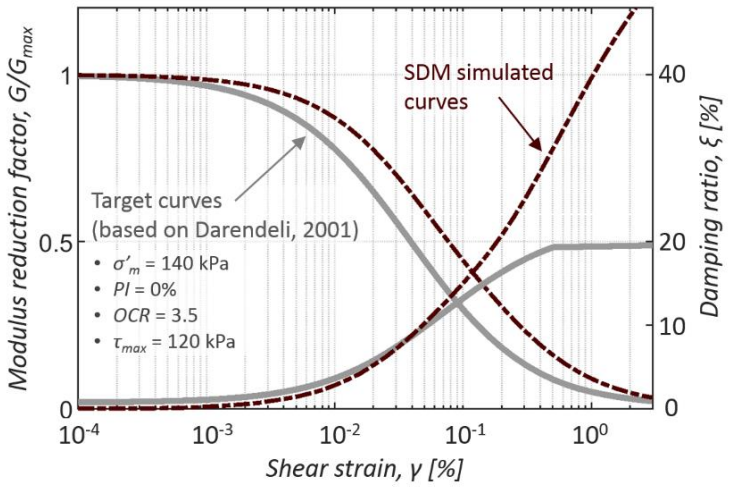

Fig. 4.9 Example target shear modulus degradation and damping ratio curves (solid lines), together with fitted curves from S-D Model (SDM) simulations (dashed lines).

To verify the above approach for modelling non-liquefiable soils, a series of total stress analyses of selected Christchurch sites was performed and the results were compared with analogous simulations using the 1-D nonlinear ground response analysis program DEEPSOIL (Hashash et al. 2016). DEEPSOIL was chosen because it provides a more rigorous modelling option (MRDF) for hysteretic stress-strain response, with a nearly perfect fit for both $G/G_{max} - \gamma$ and $\xi - \gamma$ target curves even at large strains. A comparison between the ground motion and shear strain predictions from total stress analyses with the S-D Model in DIANA-J (DJ-SDM) and GQ/H model with MRDF in DEEPSOIL (DS-GQ/H+MRDF), at different depths of an example site, is presented in Fig. 4.10. It can be seen that the two analyses predict almost identical ground motions, but the DJ-SDM analysis, as expected due to the

overprediction of shear modulus and damping, predicts slightly smaller strains than DS-GQ/H+MRDF. Nevertheless, the S-D Model performance in total stress analysis is, clearly, sufficiently good for the purpose of this study.

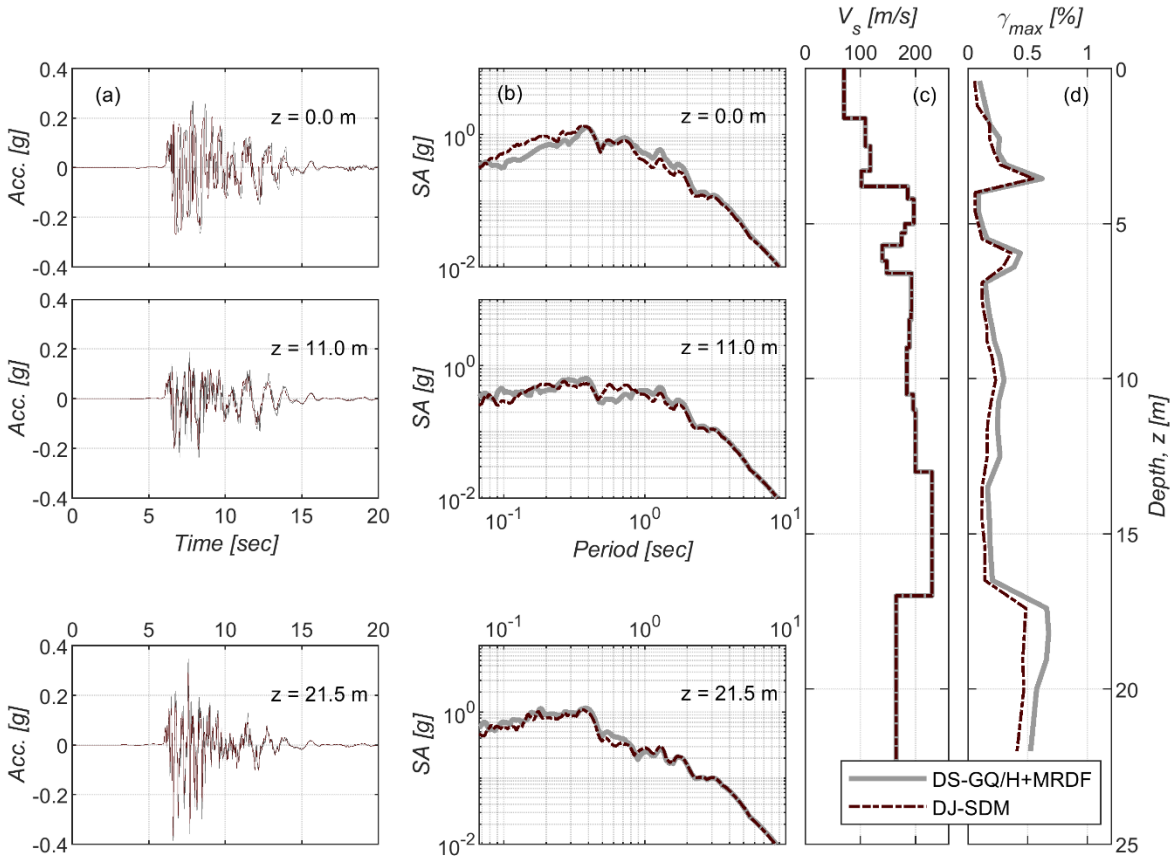

Fig. 4.10 Comparison between total-stress ground response analysis results using the S-D Model in DIANA-J (DJ-SDM, dashed lines) and the GQ/H model with MRDF in DEEPSOIL (DS-GQ/H+MRDF, solid lines): (a) acceleration time series; (b) response spectral accelerations at various depths; (c) V_s profile; (d) maximum shear strains throughout depth.

4.5 Definition of Input Ground Motion(s) (Step 4)

The problem of deriving input ground motions for forensic dynamic analyses of ground and structures is addressed in the following chapter. In this section, for the completeness of the proposed effective-stress analysis procedure, a brief discussion on the selection of input ground motions for forward applications of the method is provided.

Several methods for ground motion selection have been proposed in the literature over the last decades (e.g. Katsanos et al. 2010, Tarbali et al. 2018). Among them, the generalized conditional intensity measure (GCIM) approach (Bradley 2010, Bradley 2011), and other similar methods in concept, allow to rigorously consider multiple intensity measures (IMs) in

the selection. Thus, in the selection of ground motions for liquefaction analyses, the GCIM approach allows for concurrent consideration of amplitude-, duration-, and energy-related IMs which may be equally important.

The GCIM approach for ground motion selection can be broken down into three main steps. The first step entails dis-aggregation of the seismic hazard curve to obtain the contribution from different sources and earthquake events at a given IM level, referred to as the 'conditioning IM' (and denoted as IM_j). The second step involves derivation of the marginal conditional distributions of each (single) considered IM (IM_i) taking into account the contribution of all scenario ruptures to the seismic hazard at the conditioning IM level (IM_j). The obtained marginal IM_i distributions are used to generate realizations of the multivariate $\boldsymbol{IM}$ distribution considering the correlation between the considered IMs, which are then used to assess the appropriateness of the candidate ground motions. In the final step, a database of prospective ground motions is searched to find ground motions that fit best the generated realizations of the $\boldsymbol{IM}$ distribution. A weight vector (w_i) is used to prescribe the relative importance of the considered IM_i and calculate the misfit of each prospective ground motion with respect to the target distribution. Bounds on causal parameters (e.g. magnitude, source-to-site distance, site condition) of prospective ground motions may also be considered prior to conducting IM-based ground motion selection (Tarbali and Bradley 2016). The main steps described above refer to the case in which the seismic hazard is defined in terms of a seismic hazard curve resulting from a probabilistic seismic hazard analysis (PSHA). An analogous process for ground motion selection can be followed in the case of scenario earthquake ruptures (Tarbali and Bradley 2015).

The GCIM approach (including random realizations of the $\boldsymbol{IM}$ distribution) has been implemented in the open-source software for seismic hazard analysis OpenSHA (Bradley 2012, Field et al. 2003). Alternatively, a set of Matlab codes that can be used for computing the GCIM distributions and, subsequently, selecting appropriate ground motions is available from Bradley (2020).

4.6 Numerical Model and Analysis Parameters (Step 5)

In the proposed numerical procedure, fully coupled nonlinear effective-stress analyses are performed using 1-D soil column models (i.e. 1-D vertical wave propagation with 2-D quadratic elements constrained to deform in simple shear) to simulate the free-field response at level ground sites. The soil-column models are developed based on the simplified soil profile and constitutive model parameters defined in steps 1 to 3. In the following, salient features of the numerical model and analysis are discussed.

4.6.1 Mesh geometry

A sketch of the adopted mesh geometry is illustrated in Fig. 4.11. The sizing of the mesh elements is a trade-off between model accuracy and computational efficiency. The minimum element thickness (ΔY) is taken equal to the minimum layer thickness adopted for the simplified profile (i.e. $\Delta Y^{min} = T_{min} = 0.3$ m). The maximum ΔY is taken as the smallest of ΔY_1, ΔY_2 and ΔY_3, which are defined as (see also Fig. 4.11):

$$\Delta Y_1 = \frac{1}{8}\lambda_{min} = \frac{\beta V_s}{8 f_{max}} \tag{4-14}$$

$$\Delta Y_2 = 3\Delta Y_{adj} \tag{4-15}$$

$$\Delta Y_3 = 2.0 \text{ m} \tag{4-16}$$

where V_s is the shear wave velocity of the considered layer (appropriately reduced to account for stiffness degradation at large strains via a reduction factor β), λ_{min} is the wavelength associated with the highest frequency that is considered in the analysis (f_{max}), and ΔY_{adj} is the larger thickness of the two adjacent elements. The condition $\Delta Y \leq \Delta Y_1$ (Eq. 4-14) ensures accurate transmission of waves with frequency up to f_{max} (Kuhlemeyer and Lysmer 1973), whereas the condition $\Delta Y \leq \Delta Y_2$ (Eq. 4-15) is adopted to avoid disproportionate changes in the thickness of adjacent elements. For liquefiable soil elements, to avoid impractically small ΔY_1 values due to a potential large degradation in V_s, a maximum element thickness of 0.6 m is adopted, irrespective of βV_s. The above element size constraints dictate the sizing and number of elements required in the discretization of each layer of the simplified profile.

4.6.2 Initial stress conditions, boundary conditions, and load application

Prior to the dynamic analysis, the initial stress state in the model has to be established. This can be done either by simply calculating the static stresses in each element and imposing them 'externally' as an initial condition onto the model, or by conducting a self-weight gravity analysis for the soil-column. In this analysis, the displacements of the nodes at the base of the column are fixed in both the x- and y-directions, whereas the remaining soil nodes are fixed in the x-direction only. In the subsequent dynamic analysis, nodes at the same elevation are free in the x-direction, but they are tied to share same displacement, thereby enforcing a simple shear mode of deformation. A Lysmer and Kuhlemeyer (1969) dashpot element with dashpot coefficient c is employed at the base of the soil-column to simulate the compliance of the underlying half-space, as schematically illustrated in Fig. 4.11. The soil-column is excited at the base by a horizontal force time history f which is proportional to the known velocity time history of the input ground motion ($\dot{u}$).

Theoretically, the soil-column must be extended deep enough to include an elastic bedrock layer at the bottom. Because the exact soil conditions down to bedrock depth may often not be known, and also because the 1D wave propagation assumption can be increasingly inaccurate

with increasing depth from the ground surface, it is practically sufficient and often advisable to place the base of the soil column at a shallower layer, which is stiff compared to the near-surface soils and is expected to respond with nearly elastic deformations. In the application of the proposed procedure for the analyses of Christchurch sites, the base of the soil column models was assumed at the interface of the strong impedance contrast with the Riccarton Gravel layer which lies at a depth from about 10 to 40 m from the ground surface and has V_s of about 400 m/s (Fig. 3.3). Note that, in such cases, the ground motion selection process should assume soil conditions representative for the underlying half-space (reference layer).

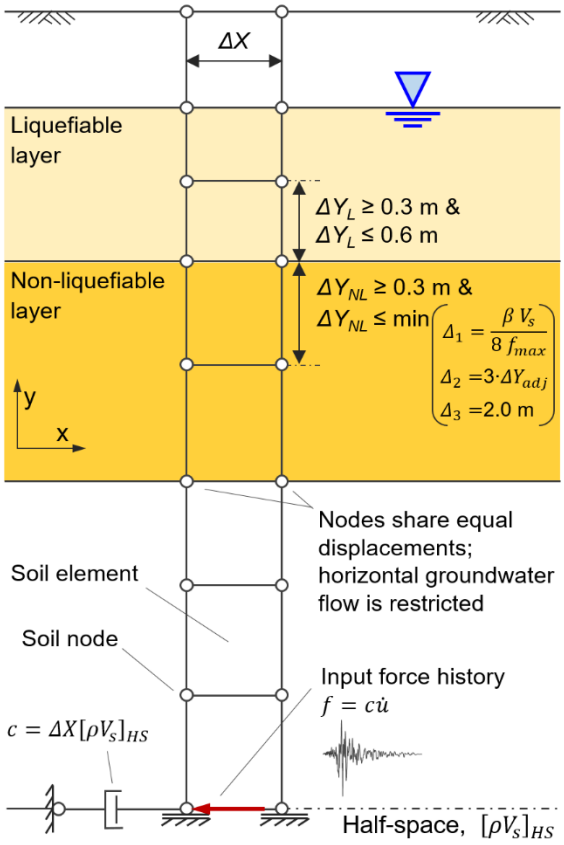

Fig. 4.11 Schematic illustration of the soil-column model used for numerical analyses.

4.6.3 Drainage conditions and permeability values

In the effective-stress analyses, the soil is treated as a two-phase medium based on Biot's equations for dynamic behaviour of saturated porous media (Biot 1956). The analyses are performed assuming drained conditions allowing for pore water redistribution and vertical water flow through and between layers. Horizontal water flow is restricted in the 1-D soil-column analysis. Permeability values (k) for each distinct soil layer can be approximated from the I_c values of the simplified profile using Eq. 4-17 (Robertson and Cabal 2015):

$$k = \begin{cases} 10^{(0.952-3.04I_c)}, & 1.0 < I_c \leq 3.27 \\ 10^{(-4.52-1.37I_c)}, & 3.27 < I_c < 4.0 \end{cases} \quad (\mathrm{m/s}) \qquad (4\text{-}17)$$

It should be noted that in the proposed 1-D simulation of ground response based on the continuum approach, it is assumed that both liquefiable and non-liquefiable (low-permeability) layers are laterally continuous and the overall permeability remains unchanged during the analysis. Disruptions of the lateral continuity of low-permeability layers, due to either pre-existing discontinuities or seepage-induced hydraulic fracturing, as well as changes in hydraulic conductivity that occur within the liquefied soils in the process of and post their liquefaction are not considered in the analysis. It is important that the above limitations of the analysis are recognized and appropriate measures or indicators of the potential for such liquefaction phenomena and their effects on the response and liquefaction manifestation are considered in assessing the seismic (liquefaction) performance at the site of interest, as discussed in Chapter 7.

4.6.4 Analysis parameters and output

In the final step of the procedure, considering the adopted element sizing and anticipated behaviour, analysis parameters such as computational time increment, integration scheme and numerical damping are adopted, and the dynamic effective stress analysis is then executed. In the analyses presented in the following chapters, an implicit Newmark method ($\beta = 0.25$ and $\gamma = 0.5$) was used for time integration with a computational time step of $\Delta t = 0.005\ s$, and Rayleigh damping with proportionality constants $\alpha = 0.114$ and $\beta = 0.002$ applied to the mass and stiffness terms, respectively. These parameters were shown to provide valid results for all analyzed soil-column models.

The output from the effective-stress analysis can be extracted in terms of time-histories of acceleration, velocity, and displacement at any soil node including at the ground surface, as well as stresses, strains, and pore pressures determined for soil elements. Note that post-liquefaction reconsolidation volumetric strains ($\varepsilon_{vc,max}$), associated free-field settlements, and strain-based liquefaction damage indices can be estimated in a post-processing phase by utilizing the computed maximum shear strains γ_{max} from the dynamic effective-stress analysis as input in empirical $\varepsilon_{vc,max} - \gamma_{max}$ relationships (e.g. Ishihara and Yoshimine 1992, Yoshimine et al. 2006). In essence, all key measures of ground response determined from a simplified liquefaction analysis can be easily obtained from the results of the proposed numerical procedure, but the latter would also provide temporal and spatial evolution of the response, while accounting for important dynamic interactions in the response of the soil deposit.

4.7 Summary

A CPT-based effective-stress analysis procedure for liquefaction assessment has been presented in this chapter. Key elements in the proposed procedure can be summarized as follows:

(1) As a first step, a simplified, discretized soil profile is determined from the nearly continuous CPT data. A practical algorithm that automates this process has been presented. Apart from the obvious necessity of a discretized soil profile for the numerical analysis, this profile 'simplification' allows for rigorous scrutiny of the overall site characteristics and identification of critical layers in the deposit. Based on their inferred behaviour characteristics, the soil layers resulting from this process are classified as either liquefiable or non-liquefiable.

(2) Modelling of the liquefiable soil layers focuses on the simulation of their (cyclic) liquefaction resistance, while using representative values for elastic and plastic stress-strain parameters for sand. A set of liquefaction resistance curves (LRCs) were derived over relevant $q_{c1Ncs} - \sigma'_v$ conditions by directly following the simplified liquefaction triggering procedure of Boulanger and Idriss (2014). These target curves were then used to calibrate a constitutive model capable of reproducing the target behaviour over all densities and confining stresses of interest, with a single set of values for model parameters. The calibration methodology was extended to allow for incorporation of partial saturation effects on LRC, using the V_p values measured in the field.

(3) Modelling of the non-liquefiable soil layers targets their cyclic stress-strain response, typically defined in terms of modulus reduction and damping ratio curves. Reasonably accurate and concurrent modelling of target modulus reduction and damping ratio curves over the expected range of shear strains is the key requirement in this case.

(4) With respect to the seismic input for forward applications of the method, it is recommended to select an ensemble of ground motions for the earthquake scenario of interest using the generalized conditional intensity measure (GCIM) approach (Bradley 2010, 2012), or similar method, considering a suitable set of intensity measures (IMs) relevant to liquefaction problems, including not only amplitude-related IMs, but also duration- and energy-related measures, as they are also critical for liquefaction problems.

(5) In the final step, numerical model (i.e. element size, boundary conditions, initial stress state of the soil) and analysis parameters (i.e. computational time increment, integration scheme, numerical damping) are defined. Here, basic rules of a good numerical analysis are followed, always taking into consideration the characteristics of the given soil profile and its anticipated behaviour.

Two important features of the proposed procedure are that it can be fully automated in a programming environment, and that it is directly equivalent (in the definition of cyclic

resistance and required input data) to the CPT-based simplified procedures for liquefaction analysis. These features allow advanced effective-stress analysis to be routinely applied in practice, in parallel with simplified analysis and inform one another.

The proposed effective-stress analysis procedure was implemented for the analyses of the 55 Christchurch sites, as well as for the analyses of 13 strong motion station sites of urban Christchurch. The latter were mainly used for validation purposes as described in the following chapters. A set of Matlab programs were developed to process and interpret the in-situ data, prepare the required input for the effective-stress analysis code, call the code to perform the numerical simulations, and post-process the analysis output. In the numerical simulations, the finite element code DIANA-J (Taisei Corporation 1997) and the S-D Model were employed. It is important to note, however, that the proposed procedure is generally applicable to any finite element or finite difference code and liquefaction-oriented constitutive model provided that these can capture the key aspects of the cyclic soil behaviour in a fully coupled (soil-water) dynamic analysis, as discussed in this chapter.

5 DERIVATION OF INPUT GROUND MOTIONS

5.1 Introduction

To reliably interpret and quantify the influence of system response effects on liquefaction manifestation by means of effective-stress analyses, it is important that the input motions used in the analyses are representative of the shaking intensity induced by the considered earthquake. In defining the input ground motion for forensic analysis at a given site of interest (*target site*), one has the following options: (1) select a suite of representative ground motions from available strong motion databases, relevant to the considered earthquake scenario and predicted distribution of some relevant ground motion intensity measure (IM) at the target site, using standard selection procedures (e.g. Katsanos et al. 2010, Tarbali and Bradley 2015); (2) use synthetic motions obtained from numerical ground motion simulations (deterministic, stochastic or hybrid) for the event of interest (e.g. Boore 2003a, Motazedian and Atkinson 2005, Graves and Pitarka 2010); or (3) use representative *within-event* recorded ground motions, obtained at nearby strong motion station (SMS) sites (*reference sites*) during the specific event of interest, with appropriately modified IMs for the target site. While uncertainty in the determination of the target-site input motion is inevitable in all three methods, methods (2) and (3) allow to reduce this uncertainty by considering event-, region-, and site-specific conditions in the estimation. Numerical simulations (method 2) have the inherent advantage that they can provide ground motions at any geographic location and depth corresponding to a grid-point in the simulation domain, but they are limited by uncertainties in the parameters and modelling approaches describing the fault rupture and wave propagation, among other factors (e.g. Bradley 2019). These limitations restrain the wider acceptance of numerically simulated motions by engineers, who still presently view the use of within-event recorded ground motions as the best-available option, particularly for forensic assessments in densely instrumented regions.

When the choice is made to use within-event recorded ground motions in forensic analysis at a non-instrumented site, potential effects of spatial variation of ground motion must be considered (potential differences in the ground motion between the reference recording site and the target site). I herein specifically refer to effects of spatial variation resulting from physical processes that are generally understood and can be modelled on a physical basis. This is to distinguish from spatial variation of high-frequency ground motion observed at

dense instrument arrays which is largely stochastic in nature (e.g. Zerva 2009). With the above in mind, in a typical 'source-path-site' convolutional interpretation of the physical process, spatial variation may be seen as a result of spatial differences in any of the three components of the convolution. Variation due to differences in the near-surface geology and site response can be addressed by incorporating a correction for the relative site-response between the reference (SMS) site and the target site (e.g. Boore et al. 2003, Maugeri et al. 2011, Bray and Luque 2017). On the other hand, source and path effects reflecting, for instance, possible azimuthal variation in the radiated seismic energy and path attenuation, can be considered in the selection of the reference site (motion) and subsequent scaling of the reference motion to the estimated intensity at the target site (e.g. Pradel et al. 2005, Markham et al. 2016, Tsaparli et al. 2019). Note that source and path effects can contribute significantly to the spatial variability of ground motion in the near-source region of an earthquake.

This chapter discusses key steps and challenges in deriving representative input motions for forensic seismic analysis in the near-source region. The discussion is mainly focused on aspects of the problem relevant to the 04Sep10 and 22Feb11 earthquakes (with more emphasis on the second), but the practical implications for the selection and subsequent treatment of within-event recorded ground motions are generally applicable to any forensic assessment in the near-source region.

5.2 **Strong Motion Station Sites**

The 2010-2011 Canterbury earthquakes were recorded by a high-density network of strong motion instruments across the Canterbury region. The exact locations of SMS sites in urban Christchurch and its environs are indicated in the map of Fig. 5.1 together with the surface projections of the causative fault planes (Beavan et al. 2012) of the 22Feb11 (Fig. 5.1a) and 04Sep10 (Fig. 5.1b) earthquakes. Also shown in this figure are: the locations of available deep (+500 m) shear wave velocity (V_s) profiles (Teague et al. 2018) that are utilized in subsequent sections, approximate contours of the depth to Riccarton Gravel (RG) layer (Fig. 5.1a) and depth to the Banks Peninsula volcanic (BPV) rock (Fig. 5.1b), which underlies the Quaternary sediments of Christchurch and outcrops on the southeast edge of the city (Port Hills), and, finally, the locations of the 55 sites which are subject of this study.

Table 5.1 provides key information for the 13 SMS sites of urban Christchurch, including site class according to the New Zealand earthquake loading standards NZS1170.5:2004 (Standards New Zealand 2004), V_{s30} values, depth to RG, IDs of nearby CPT sites, and source-to-site distances (R_{rup}), recorded geometric mean peak ground accelerations (PGA), and severity of surface liquefaction manifestation for the two considered earthquakes. Further details regarding soil profiles, characteristics of the recorded ground motions, and liquefaction manifestations can be found in relevant publications (e.g. Bradley and Cubrinovski 2011, Tasiopoulou et al. 2011, Bradley 2012, Wotherspoon et al. 2015a).

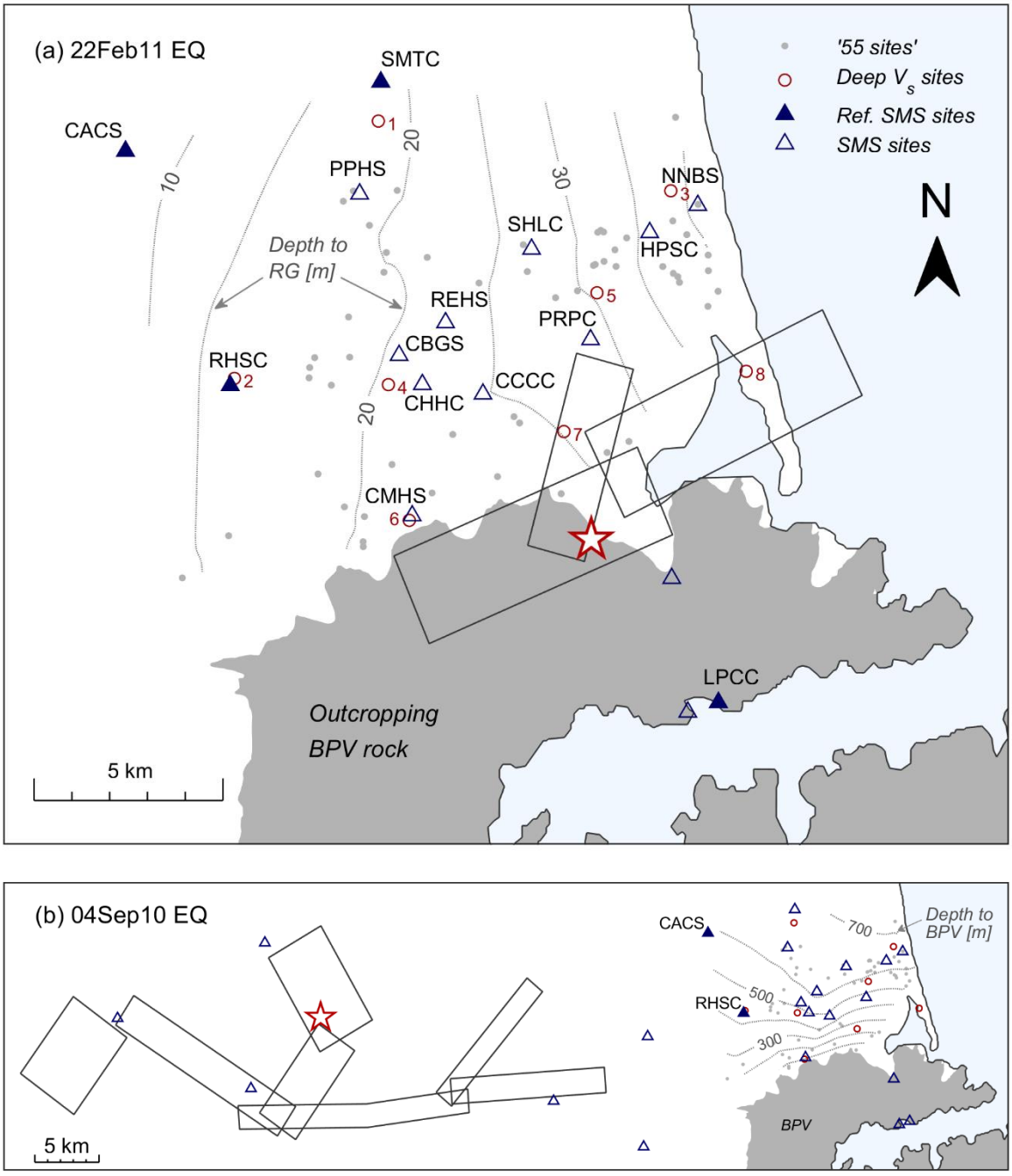

Fig. 5.1 Map of the Christchurch area showing the locations of SMS sites, the locations of selected sites with deep V_s measurements (Teague et al. 2018), the locations of the 55 sites of interest, approximate contours of the depth to the RG and depth to BPV rock (Lee et al. 2017b), and the the surface projections of the causative fault planes (Beavan et al. 2012) of the two considered earthquakes: (a) 22Feb11; and (b) 04Sep10.

Table 5.1 Summary of site characteristics, observed ground motions, and surface liquefaction manifestations for the 13 SMS sites of urban Christchurch.

					2010 M_w7.1 Darfield			2011 M_w6.2 Christchurch		
Station	Site Class[i]	V_{s30}[ii] [m/s]	Depth to RG [m]	Nearby CPTs[iii]	R_{rup}[v] [km]	PGA [g]	SLM[vi]	R_{rup}[v] [km]	PGA[vii] [g]	SLM[vi]
CACS[viii]	D	435	7	--	11.7	0.20	None	12.8	0.21	None
CBGS	D	197	21	CPT1[iv]	14.4	0.16	None	4.7	0.50 (0.32)	None
CCCC	D	182	25	CPT_484	16.2	0.22	None	2.8	0.43 (0.35)	Minor
CHHC	D	196	22	CPT_12257	14.7	0.17	None	3.8	0.37	Moderate
CMHS	D	213	24	CPT_72541	14.0	0.24	None	1.4	0.37	Severe
HPSC	E	150	36	CPT_89	21.7	0.15	Severe	3.9	0.22	Severe
NNBS	D	204	41	CPT_33695	23.1	0.21	None	3.8	0.67 (0.32)	None
PPHS	E	180	19	CPT_1497	15.3	0.22	None	8.6	0.21	None
PRPC	E	196	28	CPT_1396	19.3	0.21	None	2.5	0.63	Minor
REHS	E	155	20	CPT_40480	15.8	0.25	None	4.7	0.52 (0.36)	None
RHSC[viii]	D	286	18	--	10.0	0.21	None	6.5	0.28	None
SHLC	D	201	27	CPT_626	18.6	0.18	None	5.1	0.33	Moderate
SMTC[viii]	D	219	18	--	17.5	0.18	None	10.8	0.16	None

[i] As defined by NZS1170.5 (Standards New Zealand, 2004), i.e. D = deep or soft soil; E = very soft soil.
[ii] Data from https://www.geonet.org.nz/
[iii] Data from the NZGD (2020) unless stated otherwise.
[iv] Data from Wotherspoon et al. (2015a).
[v] R_{rup} = closest distance to the rupture.
[vi] SLM = severity of surface liquefaction manifestation based on the interpretation of Wotherspoon et al. (2015b).
[vii] Values in brackets indicate the PGA prior to the onset of liquefaction (Wotherspoon et al. 2015b), i.e. neglecting post-liquefaction high-frequency acceleration spikes associated with cyclic mobility behaviour.
[viii] Reference station

5.3 **Spatial Variability of Ground-Motion**

Spatial variation of ground motion characteristics was observed in both the two considered earthquakes, but it was much more pronounced in the case of the 22Feb11 earthquake as a result of the proximity of the earthquake source to the studied area. Some of the potential factors contributing to the observed ground-motion variability are considered to be:

(a) The variability in site-response due to differences in the composition and stratification of near-surface soils.

(b) The variation in the deeper geological structure below the SMS sites (e.g. basin effects)

(c) Differences between hanging-wall and footwall motion.

(d) Effects from the finiteness and complexity of the rupture process (source effects).

(e) Path effects related to the attenuation of amplitudes and general increase of duration with distance from the source.

These aspects need to be considered in the selection of reference SMS sites and the subsequent modification of their recorded ground motions for use in forensic analysis at a target site of interest.

5.4 Derivation of Input Motions for Forensic Analysis

The proposed procedure for deriving representative input motions for forensic analysis at a target site involves the following steps:

(1) *Selection of reference SMS site(s) and reference recorded motion(s)*

(2) *Deconvolution of reference motion(s)* by the local site-response at the reference site(s)

(3) *Scaling of deconvolved motion(s)* for source-to-site distance effects

The three key steps involved in the proposed procedure are elaborated in the following sections, in the context of the examined case studies.

5.5 Step 1: Selection of Reference Sites

In the selection of the most representative reference site (motion) for a given target site consideration must be given to: (a) the appropriateness of the candidate reference site for deconvolution analysis; (b) the deeper geological structure below the candidate reference site and the target site and their locations relative to the causative fault; and, (c) source effects on the spatial variation of the characteristics of the radiated seismic energy and generated ground motions.

5.5.1 Site Appropriateness for Deconvolution

Seismic effective-stress analysis, and ground response analysis in general, examines the response of a soil deposit to the motion specified at the underlying (engineering) bedrock (input motion). To derive this input motion for ground response analysis, the recorded (surface) motion of the reference site (i.e. reference motion) needs first to be deconvolved to the depth of the engineering bedrock or, more specifically, to a *reference layer* (*depth*) at which the upward propagating motion would exhibit compatible (similar) ground motion characteristics to those at the corresponding layer of the target site, had the two sites been at similar geographical locations.

In Christchurch, the requirement for the reference site to be appropriate for deconvolution analysis is a major constraint on the selection of reference sites. Deconvolution analysis can be performed formally only within the context of one-dimensional (1D) linear (L) or equivalent linear (EQL) approximations to the complex three-dimensional wave propagation and nonlinear (NL) soil response. The underlying deep basin structure of Christchurch, formed by the outcropping hard BPV rock dipping northwards beneath the surface Quaternary deposits (Fig. 5.1), generates complex 2D and 3D wave propagation phenomena that cannot be explicitly incorporated in such 1D models. Also, the widespread and severe liquefaction documented in Christchurch is associated with highly nonlinear response which cannot be well approximated by linear or equivalent-linear soil models.

Consistent with previous studies (e.g. Markham et al. 2016, Tsaparli et al. 2020), the approach taken here was to assume the base of the numerical models (for the deconvolution and the subsequent effective-stress analysis) at the depth of the first strong impedance contrast below the soft surficial deposits, which is encountered at the interface with the denser Riccarton Gravel (RG) layer ($V_s \approx 400$ m/s) at depths of about 10–40 m from the ground surface. The use of this shallow reference layer is critical for the validity of the 1D wave-propagation assumption, and also for reducing errors due to uncertainties in the geotechnical properties of the soil profile and numerical errors in the deconvolution (e.g. Roesset et al. 1995). It must be recognized, however, that the use of this reference layer (depth), as a single measure for the convolution compatibility between sites, neglects potential differences in ground motion arising from variation in the deeper geological structure below the sites. Hence, the deeper geology needs to be considered as an additional criterion for further optimization of the selection process, as discussed in the following subsection.

As indicated in Table 5.1, in the 22Feb11 earthquake, 9 out of the 13 SMS sites of urban Christchurch had signs of soil liquefaction, either as surface manifestation in the form of soil ejecta, or characteristic spikes in the recorded accelerograms associated with strain hardening behaviour during cyclic mobility. Therefore, these sites cannot be used for deconvolution analysis as their response cannot be well approximated by an EQL soil model. Three out of the remaining sites, namely the Canterbury Aero Club (CACS), Riccarton High School (RHSC), and Styx Mill Transfer Station (SMTC), were considered as reference sites for deconvolution of the respective surface motions recorded during the 22Feb11 earthquake. In

addition to these urban Christchurch sites, the Lyttelton Port (LPCC), which is practically an outcropping rock site located southeast, on the hanging wall of the causative fault (Fig. 5.1a), was also included in the list of reference sites for the 22Feb11 earthquake. Fig. 5.2 shows the shallow V_s profiles of the four selected reference sites. All reference sites but SMTC are comprised of relatively stiff soils ensuring low levels of nonlinear response in the deconvolution analysis. Also, all four sites have relatively shallow depth to RG (or BPV in the case of LPCC), from 6 to 18 m from the ground surface.

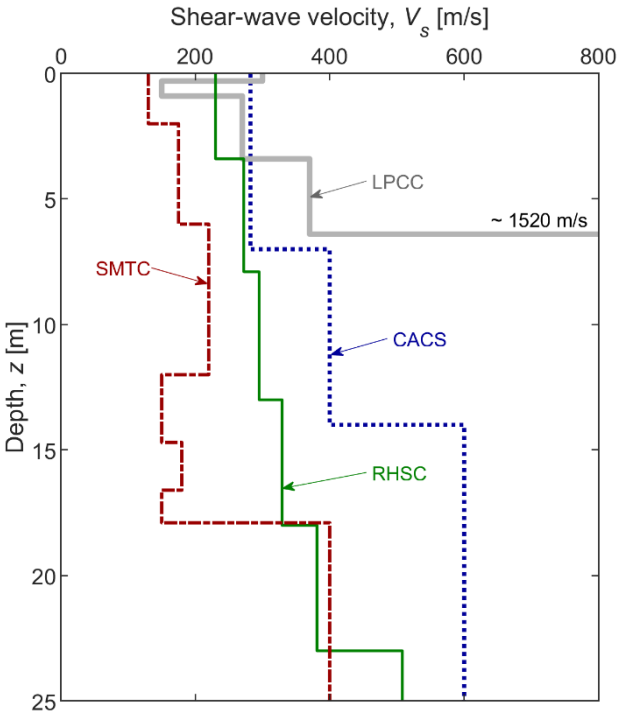

Fig. 5.2 Median shear-wave velocity profiles of the selected reference sites derived from surface-wave testing results reported in Wood et al. (2011), Wotherspoon et al. (2015a), and Teague et al. (2018).

In the case of the 04Sep10 earthquake, while liquefaction might not have occurred in many of the SMS sites, large strains and strongly nonlinear response are still likely. A sufficiently high stiffness of surface soils and shallow depth to RG are again key requirements in the selection of reference sites. With this in mind, the CACS and RHSC sites were selected as reference sites for the 04Sep10 earthquake. In this case, given that Christchurch is outside the immediate near-source region of the 04Sep10 earthquake, it was not deemed necessary to include in the selection additional reference sites.

5.5.2 Deep Geology and Site Location Relative to Fault

As previously alluded to, it is important in the selection of reference sites to also consider the deeper geological structure of the region in order to account for effects which cannot be incorporated in the deconvolution analysis. With respect to the deep geology of the region and their locations relative to the 22Feb11 fault rupture, the SMS sites of Fig. 5.1a can be broadly

grouped into sites located north or northwest of the rupture plane on the deep sedimentary basin ('Christchurch sites'), and sites located south of the fault on the outcropping BPV rock ('Lyttelton sites'). Fig. 5.3 presents a schematic illustration of the deep geology of the region with the main lithological units encountered along a Northwest-Southwest cross section. Approximate values of the shear wave velocity (V_S) are indicated in the figure along with example ray paths of seismic waves from the 22Feb11 rupture. As explained in Bradley and Cubrinovski (2011), the large post-critical angle with which seismic waves from the 22Feb11 earthquake may enter the sedimentary basin of Christchurch through its thickening edge on the southeast end of the city can cause reflection and refractions that lead to a waveguide effect in which surface waves propagate across the basin resulting in enhanced long-period ground motion amplitudes and shaking duration for the Christchurch sites. The absence of such basin-edge and waveguide effects in conjunction with potential differences due to hanging wall effects on the Lyttelton side of the volcanic rock formation, southeast of the rupture, may have resulted in significantly different motions for the Lyttelton sites. These potentially important differences in ground motions question the suitability of the LPCC records for use as reference motions for Christchurch, despite the advantageous features associated with (nearly) outcropping rock characteristics at this site (i.e. negligible soft soil effects).

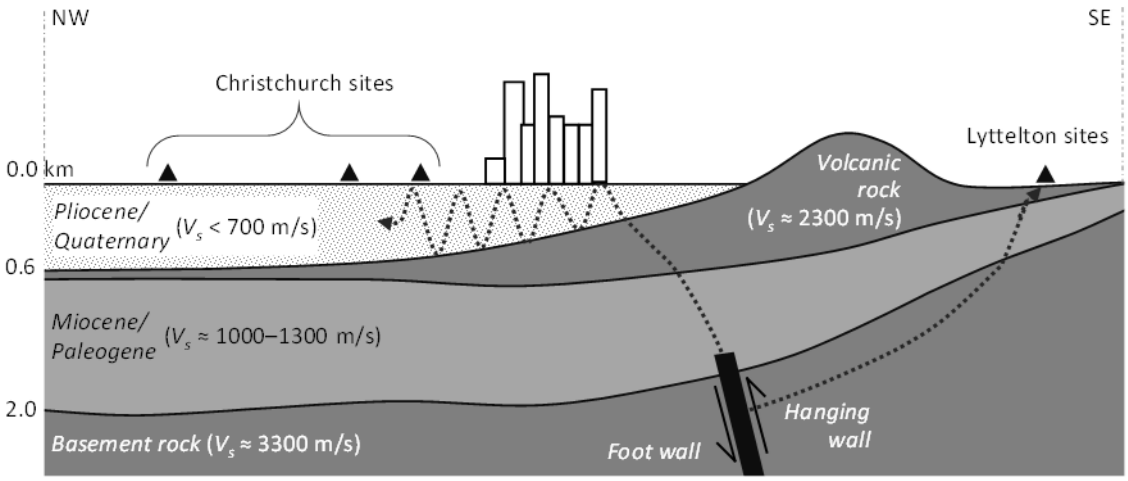

Fig. 5.3 Schematic Northwest-Southwest cross section of the geological structure of Christchurch illustrating how waveguide effects occurring in the sedimentary basin underlying Christchurch affect the recorded ground motions from the 22Feb11 earthquake (modified after Bradley and Cubrinovski 2011; roughly based on the 3D regional velocity model by Lee et al. 2017).

Needless to say, spatial variation of ground motion is expected also among the Christchurch sites as a result of variation in the bedrock topography and varying contributions of different ray paths. Indicatively, for the sites considered in this study, the depth to the strong impedance contrast with the BPV rock (i.e. basin depth) varies from about 100 m in the southern part of the city to nearly 700 m towards the north (Fig. 5.1). These large differences

in the deeper geology are expected to contribute to the ground motion variability across the sedimentary basin.

It is important in forensic seismic assessments to account for this variation in the deeper geological structure of the region and, on this basis, refine the selection of reference sites (motions) so that they are compatible with the target site (e.g. have similar basin depth).

5.5.3 Source Effects

Source effects refer to the spatial variation of both amplitude and phase of ground motion as a result of the rupture process characteristics of a given earthquake (e.g. Mai 2009). While rigorous quantification of source effects requires detailed modelling of the spatiotemporal characteristics of the rupture process and wave transmission to the site of interest, in the following paragraphs it is attempted to explain and illustrate source effects on ground motion variability in a simplified manner, solely on the basis of the fault geometry, relative hypocentre location, and cumulative slip distribution (Fig. 5.4).

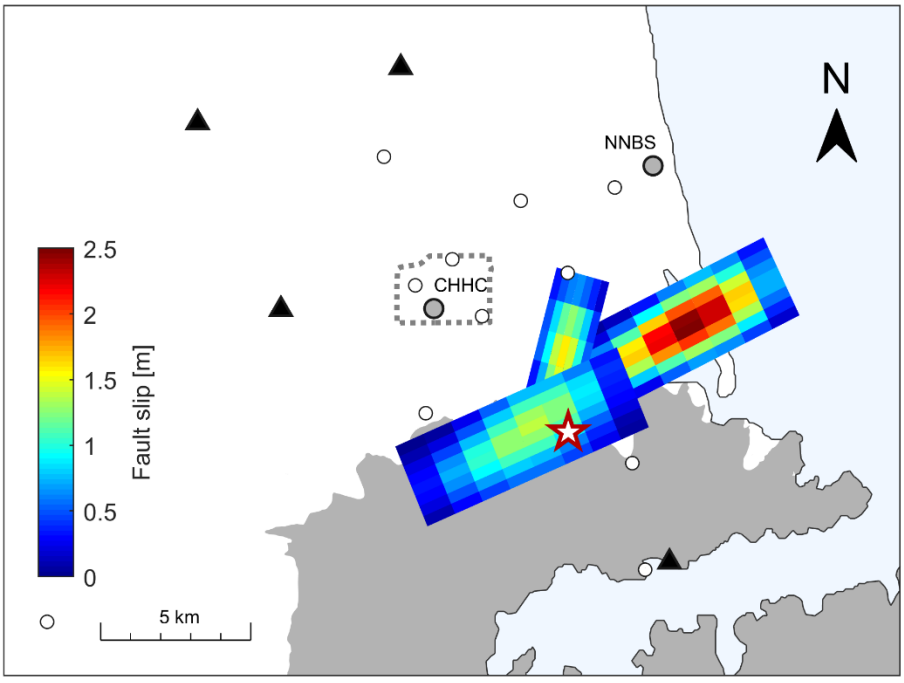

Fig. 5.4 Slip model for the 22Feb11 M_w6.2 Christchurch earthquake (Beavan et al. 2012).

To this end, the focus is placed on two stations with the same source-to-site distance (R_{rup} = 3.8 km) for the 22Feb11 earthquake but at different geographic location (i.e. different source-to-site azimuth), i.e. one (CHHS) located closer to the southwestern segment of the fault and northwest from the earthquake epicenter, and the other (NNBS) northeast from the epicenter and closer to the northeastern fault segment where the maximum slip occurred (Fig. 5.1a). The close proximity of the two sites to the fault and the relatively large asymmetric spatial

extent of the fault, with respect to each of the sites, means that seismic waves emitted by the most distant points on the fault (i.e. points on the northeastern fault segment for CHHC and points on the southwestern fault segment for NNBS) travel longer distances to reach each site and, therefore, will be attenuated more than the seismic waves generated by the closest portions of the rupture (i.e. southwestern fault segment for CHHC and northeastern fault segment for NNBS).

It is common practice in ground motion simulation to model ground motions from large earthquakes (extended-sources) as a summation of signals generated with a proper time delay from smaller earthquakes on the fault or *subfaults*, where each subfault is represented by a point-source at its centre. The amplitude of the Fourier spectrum of each point source is typically taken proportional to the slip (s_{sf}) of the respective subfault (e.g. Boore 2003, Motazedian and Atkinson 2005), hence the radiated energy from each subfault is assumed proportional to the squared subfault slip (s_{sf}^2). Given a geometrical spreading function $G(R_{sf})$ describing the attenuation of Fourier amplitudes with distance from the source (R_{sf}), the contribution of energy from each subfault, normalized by the total incident energy at a site, can be derived as:

$$\hat{E}_{sf} = \frac{{s_{sf}}^2 \left[G(R_{sf})\right]^2}{\sum_{sf} {s_{sf}}^2 \left[G(R_{sf})\right]^2} \tag{5-1}$$

where all subfaults are taken to have identical rupture area, and energy loss due to material damping and wave scattering is considered negligible, a reasonable assumption for the near-source region where geometrical spreading largely dominates the attenuation.

In theory, assuming spherical spreading of body waves in a homogeneous space, wave amplitudes attenuate with distance at a rate proportional to R^{-1}. However, for typical layered earth models higher attenuation rates have been suggested in the literature (e.g. Burger et al. 1987, Ou and Herrmann 1990, Yenier and Atkinson 2014). Using an equivalent point-source simulation model for the 04Sep10 and 22Feb11 earthquakes, Yenier and Atkinson (2014) found that an attenuation rate proportional to $R^{-1.2}$ provides a better fit of the observed ground motions. Using this assumption, Eq. 5-1 can be expressed as:

$$\hat{E}_{sf} \approx \frac{{s_{sf}}^2 {R_{sf}}^{-2.4}}{\sum_{sf} {s_{sf}}^2 {R_{sf}}^{-2.4}} \tag{5-2}$$

Note that Eq. 5-2 can be considered approximately valid only within the range of source-to-site distances in which body-waves are expected to dominate the ground motion ($R < 40$ km, approximately). At larger distances, slower attenuation rates due to a transition from body-wave to surface-wave spreading should be considered.

For a given model of fault slip distribution (Fig. 5.4), Eq. 5-2 can be used to estimate the energy contributed from different portions of the fault to the total energy reaching a site. Such an estimation is shown for the CHHC and NNBS sites in Fig. 5.5 in which a different color-

code has been assigned to each 'patch' on the fault according to the relative contribution of the patch to the total S-wave energy reaching the respective site. It can be seen from the representation of Fig. 5.5 that the high-slip zone on the northeastern fault segment provides most of the incident energy at NNBS (i.e. 75% of the total energy) but its contribution is considerably smaller at the more distant CHHC site for which nearly equal energy participation of all main asperities has been estimated. Also, from the location of the hypocentre it can be inferred that the northeastern asperity with the maximum slip breaks later in time than the southwestern fault segment, and since the seismic waves radiating from the northeastern rupture need to travel longer distances to reach CHHC, they are less likely to constructively interfere with the waves emitted earlier from the closer fault segments. Taking the above into consideration, one can expect longer duration and lower amplitude motion at CHHC, relative to NNBS, due to larger attenuation of seismic waves emitted from the maximum slip zone and temporal spreading (less interference) of wave arrivals originating from different portions of the fault. Conversely, relatively short durations and high amplitudes should be expected at NNBS which is largely dominated by the close-by high-slip zone of the northeastern fault segment. As shown in Fig. 5.5, the recorded vertical ground motions (used here as a proxy for the 'site effects–free' motion) at CHHC and NNBS confirm the above reasoning. Indicatively, the CHHC record has $PGA_{\mathrm{CHHC}} = 0.62$ g, and significant durations $D_{5-75\%} = 3.5$ s, $D_{5-95\%} = 5.7$ s, whereas the NNBS record has $PGA_{\mathrm{NNBS}} = 0.80$ g, and significant durations $D_{5-75\%} = 1.6$ s, $D_{5-95\%} = 3.0$ s.

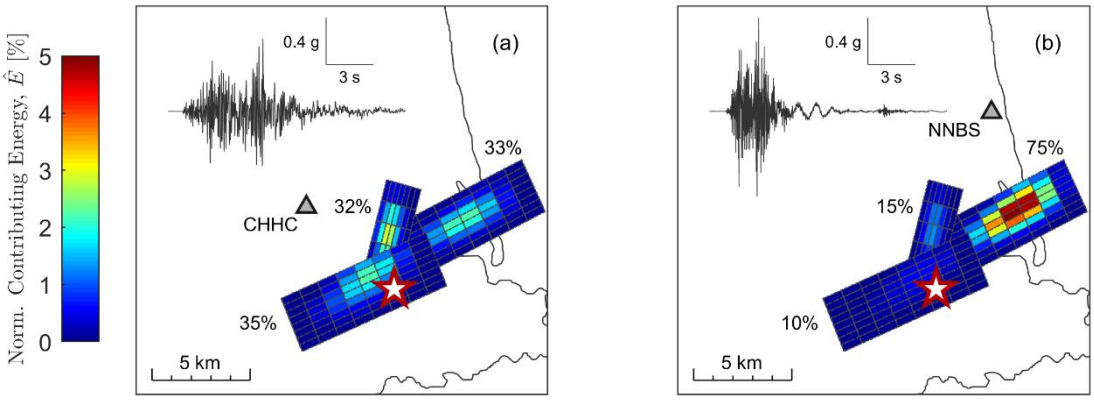

Fig. 5.5 Comparison of vertical ground motion and color-coded distribution of the normalized site-specific S-wave energy from the source (warmer colors indicate the portions of the fault that contribute larger amounts of energy to each site), for two stations with the same source-to-site distance ($R_{rup} = 3.8$ km) but different source-to-site azimuth: (a) CHHC located closer to the southwestern segment of the fault and northwest from the earthquake epicenter (five-pointed star); (b) NNBS located northeast from the epicentre and closer to the northeastern fault segment; values in percent indicate the cumulative normalized energy contributed from each fault segment.

It should be noted that the above interpretation of the observed ground motion variability between CHCH and NNBS based solely on the fault geometry, relative hypocentre location, and cumulative slip distribution is rather simplified as other important source factors, such as rupture velocity, rise time, small-scale slip heterogeneity, etc., as well as path-to-path

variability, which also contribute to the observed variability of ground motions, have been omitted. Nevertheless, the above discussion clearly indicates how the finiteness and spatiotemporal heterogeneity of the fault rupture can greatly contribute to the spatial variability of ground motion in the near-source region. In general, source effects on ground-motion variability are considered to be particularly significant in the region of less than one or two fault lengths distance (Ripperger et al. 2008).

The above discussion emphasizes the need to consider in the selection of reference sites (motions) the various source and wave propagation effects that contribute to near-source ground-motion variability. In other words, the selected reference site should be not only appropriate for deconvolution (to remove the local site effects) but also compatible with the target site, in terms of source and path effects.

5.6 Step 2: Deconvolution Analyses

Deconvolution analyses were performed at each considered reference site (CACS, LPCC, RHSC, and SMTC for 22Feb11; and, CACS and RHSC for 04Sep10) using the 1D ground response analysis program Strata (Kottke and Rathje 2009). This type of analysis takes as input the recorded motion at the surface and produces an 'equivalent-outcrop' motion at a user-specified depth deconvolved by the response of the overlying soils. The nonlinearity in the soil response was approximated by the equivalent linear approach using generic modulus reduction and damping ratio curves for non-plastic soils ($PI = 0$) recommended by Darendeli (2001). In the modelling of the SMTC soil profile, the respective curves for $PI = 20\%$ were adopted at depths where the adjacent borelog indicated the presence of plastic silt or peats. Only one component of motion was considered in the deconvolution analyses at the reference sites and the subsequent effective-stress analyses at the target sites. In particular, the as-recorded orthogonal horizontal components of the reference motions were used to identify the orientation of the maximum Arias Intensity (Arias 1970) axis, and then the maximum horizontal component in the identified direction was used for each reference motion. This was driven by the appreciation that soil nonlinearity and development of excess pore water pressures in liquefiable soils should largely be controlled by the maximum shaking intensity direction (e.g. Cubrinovski et al. 1996). The obtained motions in the maximum Arias intensity direction were low-pass filtered at 15 Hz to prevent unrealistic increase of high-frequency content with depth during deconvolution (Roesset et al. 1995). The filtering process had negligible effect on the recorded ground motions. Deconvolution analyses at the maximum Arias Intensity (AI) direction for the CACS, LPCC, and RHSC sites resulted in maximum shear strains that were generally below 0.1%. Initial deconvolution analyses at the SMTC site, on the other hand, resulted in excessive shear straining and unrealistically large high-frequency amplitudes at the base. A number of modifications to the original analysis were attempted for the SMTC site, including adopting alternative modulus reduction and damping curves and scaling down the input (surface) motion as recommended by Silva (1988), but instabilities in the deconvolution could not be eliminated.

Following the unsuccessful initial attempts, an alternative approach for deconvolving the surface SMTC motion was tested. In this approach, the deconvolved motion is obtained using surface-to-bedrock transfer functions derived from conventional 1D convolution ground response analysis, hence no direct deconvolution analysis is required. In this indirect approach, first the nearby-recorded CACS motion was deconvolved to the respective depth of RG at the SMTC site and scaled in amplitude, using a scaling factor of 1.18, to approximately represent the expected intensity of the RG motion at the SMTC site for the 22Feb11 earthquake; the basis for the derivation of the scaling factor is described in the following subsection. Next, the scaled CACS-based motion was used as a base excitation in an EQL convolution analysis at SMTC. The surface-to-bedrock transfer function obtained from this convolution analysis was then applied to the recorded surface motion at SMTC to derive an equivalent outcrop SMTC motion at the RG level. For verification purposes, the motion obtained based on the indirect approach, as above, was then used as a base input in 1D EQL analysis of the SMTC site. Fig. 5.6 compares the computed surface acceleration response spectrum from this analysis to that of the observed surface ground motion at SMTC. Besides the slight overprediction of PGA and short-period motion ($T \lesssim 0.05$ s), the fit is generally considered satisfactory confirming the efficacy of the indirect deconvolution approach employed at SMTC. Similar convolution analyses to evaluate the respective deconvolved motions were also executed for CACS, LPCC, and RHSC. In all cases, the predicted surface motions were identical to the respective recorded motions.

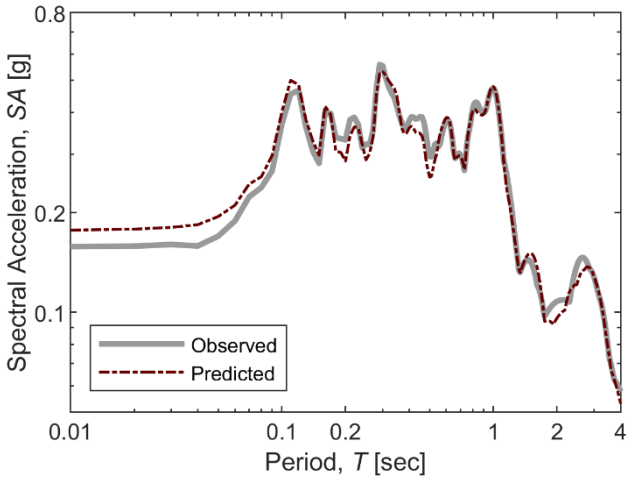

Fig. 5.6 Comparison of the acceleration response spectrum of the observed ground motion at SMTC (22Feb11 earthquake) to that computed from 1D ground response analysis using base input from the indirect deconvolution approach.

A final issue that needs to be addressed here is the conversion of the deconvolved BPV motion at LPCC to an equivalent RG motion for use in the subsequent effective-stress analyses of Christchurch sites. To this end, several deeper V_s profiles, with their locations indicated in Fig. 5.1, were utilized. The process included: first, deconvolution of the recorded LPCC motion to the various depths corresponding to the BPV depth at the locations of the

deep V_S sites (Fig. 5.1a); then, scaling of the deconvolved BPV motions to account for differences in the site-to-source distance between the LPCC site and the respective V_S sites, as described in the next subsection; and, finally, 1D convolution ground response analyses of the deep V_S profiles to identify the equivalent outcrop motions for the RG layer, at each of these sites. Multiple LPCC-based RG motions were derived from this process, one at each deep V_S location, each intended to be used as reference RG motion for the nearby target sites. Note that the above approach for deriving LPCC-based RG motions neglects 2D and 3D wave-propagation effects in the sedimentary basin of Christchurch, and this limitation may far outweigh any advantage of the LPCC-based motions for analysis of Christchurch sites.

Given the results from the 1D deep ground response analyses for the 22Feb11 earthquake, it is interesting to examine the degree of variability in the response of deeper soils, between RG and BPV. Such potential variability and its influence on the RG motion is largely neglected in the CACS-, RHSC-, and SMTC-based motions, as previously alluded to. Fig. 5.7 shows ratio of spectral accelerations of the computed (equivalent-outcrop) RG motion to the respective base BPV motion for eight deep V_S sites. It can be seen that, although the resonance periods are more or less consistent among the examined sites, there are significant differences in the amplification ratios, particularly for vibration periods longer than 1 sec. This suggests that the CACS-, RHSC-, and SMTC-based RG motions should be used with caution in areas where the deeper site-response may be significantly different from that at the respective reference sites. That being said, it should also be mentioned that (at least) certain aspects of the response of the near-surface deposits, and liquefaction triggering in particular, are not expected to be considerably affected by such variations in the low-amplitude long-period ground motion.

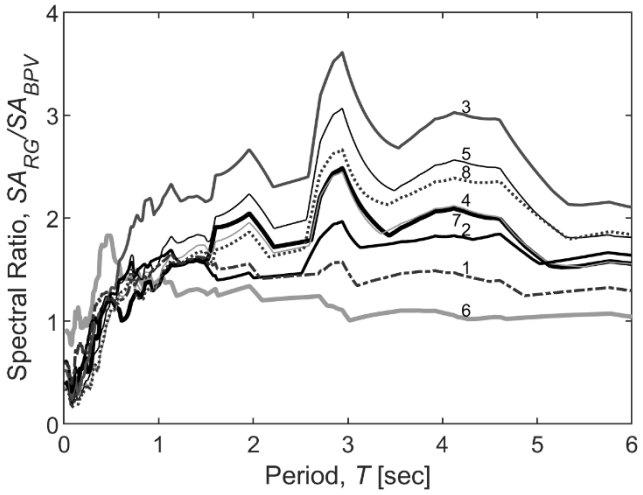

Fig. 5.7 Response spectral ratio of RG to BPV motion (22Feb11 earthquake) as a function of vibration period for various deep V_S profiles with their locations indicated in Fig. 5.1a.

5.7 Step 3: Scaling of Deconvolved Motions

The scaling of the deconvolved motions aims to account for path effects resulting from differences in the source-to-site distance (i.e. closest distance to the fault or rupture distance) between the target site and the reference site. From an engineering perspective, the most important effects of the path are the amplitude attenuation and the general increase of duration with distance. Traditionally, effects on amplitude are considered by scaling the amplitudes of the reference motion to the expected intensity level of a ground motion metric at the target site of interest, via a constant scaling factor. Scaling in time to account for changes in duration has also been considered in past studies but, because of its influence on the frequency content, is generally not recommended (e.g. Bommer and Acevedo 2004). Alternative methods based on response spectral matching are also common in (forward) design applications, they allow for changes in the spectral shape but do not provide direct control over the duration of ground motion.

In the following subsections, the basis for the derivation of amplitude scaling factors is described first and the predictions of different distance-scaling models for the 04Sep10 and 22Feb11 earthquakes are comparatively examined. Then, changes in duration and issues arising from the use of overly high or overly low amplitude scaling factors are discussed. Finally, a novel frequency-domain 'amplitude-duration' scaling method is introduced and further described in Appendix B.

5.7.1 Determination of Amplitude Scaling Factor

Determination of the amplitude scaling factor requires an estimation of the intensity of the input ground motion at the target site of interest. This can be estimated in the form of a probability distribution for a selected ground motion intensity measure (IM) using an appropriate for the region empirical ground motion model (GMM). The amplitude scaling factor can be determined as:

$$SF_{IM} = \exp\left(\overline{\ln IM_t} - \ln IM_r + \delta B + \delta W_t\right) \tag{5-3}$$

where $\overline{\ln IM_t}$ represents the median of IM for a lognormal distribution as predicted by the GMM using appropriate model parameter values for the given earthquake and target site (i.e. earthquake magnitude, source-to-site distance, classification of the reference layer condition, etc.), IM_r represents the (known) intensity of the deconvolved ground motion at the selected reference site, δB is the 'between-event' residual with zero mean and variance σ_B^2, and δW_t is the 'within-event' residual for the target site with zero mean and variance σ_W^2.

Provided a sufficiently large number of strong-motion recordings of the earthquake are available for various geographic locations, it is possible to improve the estimation of the ground motion intensity at the target site by adjusting the GMM using a fixed value for the between-event residual δB that removes the overall bias of the median ground motion prediction, i.e. corrects for average under- or over-estimation of the observed motions, and

reduces uncertainty (i.e. eliminates σ_B^2). Further improvements of the ground motion estimate can be made if one considers, in addition to replacing the event term (δB), the spatial correlation of the within-event residuals (δW) among nearby locations, thereby constraining the estimate at the target site based on nearby observations. Several methods for such a conditional estimation of the level of shaking at a non-instrumented site can be found in the literature (e.g. Douglas 2007, Bommer and Stafford 2012, Bradley 2014, Kwak et al. 2016, Worden et al. 2018). Implementation of these methods for the problem examined herein, where an estimate of the target-site ground-motion IM is required for the reference (layer) condition, can be complicated by the need for, and uncertainty associated with, the conversion of the observed surface ground motions to estimated ground motions for the reference condition at depth.

A simpler approach that is often implicitly adopted in practice (e.g. Pradel et al. 2005, Bray and Luque 2017) is to assume perfect spatial correlation between the reference station and the target site for the considered ground motion IM, which can be, to some degree, justified by the selection of 'target-compatible' recording stations in Step 1. Under this assumption, the scaling factor SF_{IM} can be taken simply as:

$$SF_{IM} = \exp\left(\overline{\ln IM_t} - \overline{\ln IM_r}\right) \tag{5-4}$$

where $\overline{\ln IM_t}$ and $\overline{\ln IM_r}$ are the median estimates of the IM predicted by the chosen GMM for the target site and the reference station, respectively.

5.7.2 Scaling Factors for the 04Sep10 and 22Feb11 Earthquakes

For the purposes of the present study, amplitude scaling factors were determined based on two different distance-scaling models of ground motion: (1) A New Zealand-specific empirical model for the attenuation of pseudospectral acceleration amplitudes (Bradley 2013) referred to as B13; and (2) An equivalent point-source model for the attenuation of Fourier amplitudes (Yenier and Atkinson 2014), referred to as YA14, which has been specifically calibrated against observations from the 04Sep10 and 22Feb11 earthquakes. Both models describe the scaling or attenuation of ground motion amplitudes with distance using the following functional form as a basis:

$$\overline{\ln(IM)} \propto \ln\left(f_P\left(R_{rup}\right)\right) = b \times \ln\left[\left(R_{rup}^n + h^n\right)^{1/n}\right] + \gamma \times R_{rup} \tag{5-5}$$

where f_P denotes the path attenuation function, R_{rup} is the closest distance to the fault rupture plane or simply 'rupture distance', b defines the rate of attenuation due to geometric spreading, h is a magnitude-dependent term that accounts for near-source saturation, n is a constant, and γ defines the rate of anelastic attenuation. The contribution from the anelastic attenuation is generally small for the range of rupture distances of interest to this study, and hence the geometric spreading largely dominates the attenuation. For a given reference site

and target site pair with respective rupture distances $R_{rup,r}$ and $R_{rup,t}$, scaling factors were determined using Eq. 5-4:

$$SF = \exp\left[\ln\left(f_P\left(R_{rup,t}\right)\right) - \ln\left(f_P\left(R_{rup,r}\right)\right)\right] \tag{5-6}$$

For reference-site distances ($R_{rup,r}$) that correspond to the locations of CACS and RHSC (Table 5.1), Fig. 5.8 shows the respective variation of scaling factor as a function of $R_{rup,t}$, for the two considered earthquakes, using the aforementioned distance-scaling models in Eq. 5-6. Scaling factors were estimated for periods that vary from 0.1 to 10 s, and the resulting range of SF values is indicated in the figure. In the case of the 04Sep10 earthquake, for reasons that will be explained in the following, the YA14 model was implemented using two alternative values for the saturation term h, the default $h = 20.6$ km used by the developers for the 04Sep10 earthquake, and an increased value of $h = 33.3$ km. Finally, note that in Fig. 5.8 a linear scaling-factor axis is used for the 22Feb11 earthquake (Fig. 5.8a), but a logarithmic scaling-factor axis is used for the 04Sep10 earthquake (Fig. 5.8b). This is to focus on the respective areas of interest for each earthquake as, generally, $R_{rup,t} < R_{rup,r}$ for the 22Feb11 earthquake, and $R_{rup,t} > R_{rup,r}$ for the 04Sep10 earthquake (see Fig. 5.1 and Table 5.1).

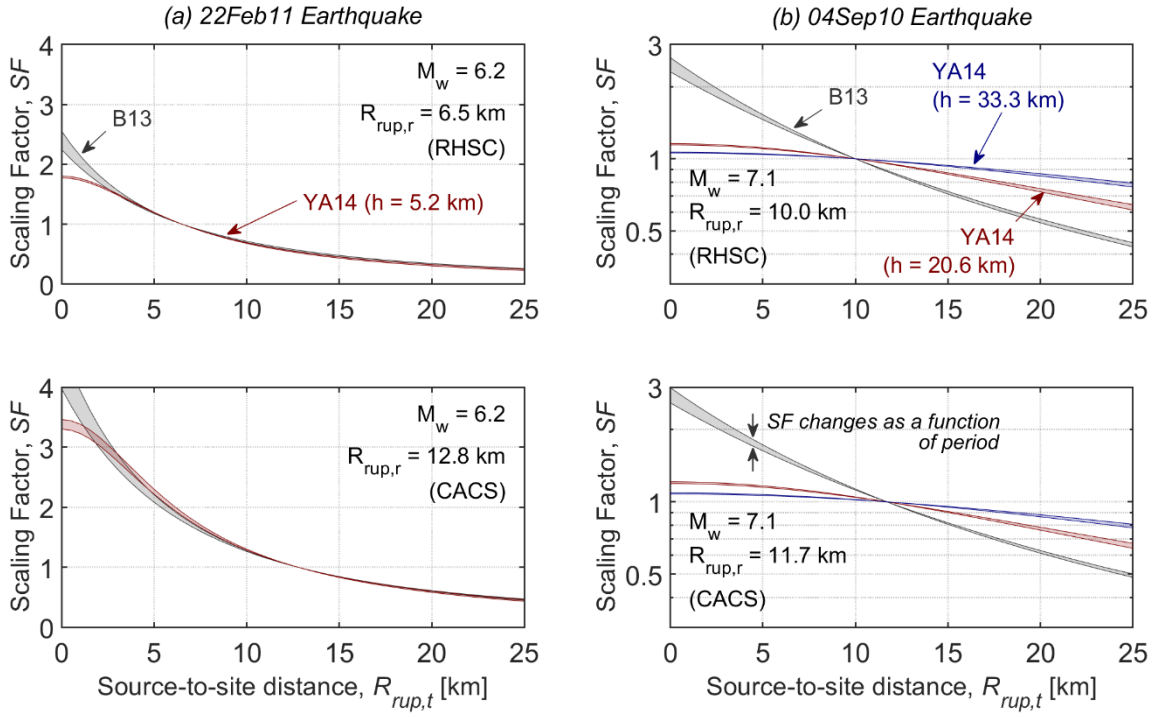

Fig. 5.8 Scaling factors (Eq. 5-6) as a function of source-to-target site distance ($R_{rup,t}$), based on the B13 and YA14 models for the distance-scaling of ground motion, and for reference-site distances ($R_{rup,r}$) that correspond to the locations of RHSC (top row) and CACS (bottom row): (a) 22Feb11 earthquake; and (b) 04Sep10 earthquake; *scaling factors (SF) were computed for periods that vary from 0.1 to 10 s, but only the total (envelope) ranges of SF values are shown in the plots*.

In the case of the 22Feb11 earthquake (Fig. 5.8a), the two ground motion scaling models result in similar scaling factors, with the exception of the very close distances to the rupture ($R_{rup,t} \lesssim 2$ km) where, in contrast to YA14, the B13 model predicts increasingly large scaling factors. A degree of saturation in the scaling factor at these close distances to the fault, as indicated by the YA14 model, seems in fact more reasonable.

In the case of the 04Sep10 earthquake (Fig. 5.8b), significant differences are observed between the two models. The B13 model predicts a strong scaling of the ground motion with distance with scaling factors as low as 0.6 at $R_{rup,t} = 20$ km. On the other hand, the 04Sep10 earthquake-specific YA14 ($h = 20.6$ km) model exhibits a much smoother scaling. This, in fact, is in better agreement with the small variation of surface motions recorded across the city as can be inferred from the PGA values reported in Table 5.1. The observed discrepancy could, at least partly, be attributed to a potentially strong azimuthal variation of the near-source saturation effect for the 04Sep10 earthquake, as explained in the following. In Eq. 5-5, the saturation term h, also often referred to as 'pseudo-depth' (e.g. Yenier and Atkinson 2014) or 'finite fault factor' (e.g. Boore and Thompson 2015), is used to modify the rupture distance R_{rup} to an 'effective distance' $\left(R_{rup}^n + h^n\right)^{1/n}$ which can be thought of as an 'average distance' from all points on the fault or the distance from an equivalent point-source. Given the general geometry of the 04Sep10 earthquake rupture (Fig. 5.1b) and its shallow depth (Beavan et al. 2012), it can be appreciated that sites to the east of the rupture and across the city have larger 'average distances' than the respective distances of sites to the north or south of the epicenter with the same rupture distance R_{rup}. In other words, the actual h varies azimuthally and is larger for sites to the east of the rupture. Regression of the observed ground motions from the 04Sep10 earthquake may have therefore resulted in the YA14 model having an increased estimate of h and smoother apparent scaling of ground motion due to bias towards the extended saturation zone east of the causative faults where the observations are denser. This can effectively explain the observed discrepancy between the generic B13 model and the 04Sep10 earthquake-specific YA14 model in Fig. 5.8b.

The above hypothesis regarding the apparent scaling of ground motion from the 04Sep10 earthquake implies that the actual distance-scaling of ground motion in urban Christchurch, which is the area of concern to this study, may be, not only smoother than that predicted by the B13 model, but also smoother than that of the default YA14 ($h = 20.6$ km) model. While the near-source scaling in the 04Sep10 earthquake-specific YA14 model is primarily influenced by the observations from urban Christchurch, it is not defined exclusively by them. To account for the possibility of extended saturation towards urban Christchurch, an increased value of $h = 33.3$ km (Fig. 5.8b), which corresponds to the 84th percentile of the generic magnitude-dependent model for h proposed in Yenier and Atkinson (2014), was also considered.

In the following, the YA14 ($h = 33.3$ km) model and the default YA14 model with $h = 5.2$ km are adopted as default models for scaling the RG motions for the 04Sep10 and

22Feb11 earthquakes, respectively. For completeness, selected results from effective-stress analyses using the alternative scaling-factor models are presented in Appendix C.

5.7.3 Importance of Duration Changes

Temporal spreading of wave arrivals due to differences in propagation velocities and scattering effects results in an increase of ground motion duration with distance. Empirical models of ground motion duration (e.g. Bommer et al. 2009, Boore and Thompson 2014, Afshari and Stewart 2016) agree that the rate of this increase is greater in the near-source region, while some degree of saturation may be present at the very close distances from the source and for large earthquakes (Bommer et al. 2009).

By and large, the distance-scaling of (significant) duration observed in the recordings of the 04Sep10 and 22Feb11 earthquakes is in good agreement with the trends of the empirical models. In particular, in accordance with the observations, the empirical models predict considerable variation in the median significant duration for the range of source-to-site distances relevant to the 22Feb11 earthquake. To illustrate such effects, Fig. 5.9 compares the 5-75% significant duration ($D_{s,5-75\%}$) of the ground motions recorded at PPHS (R_{rup} = 8.6 km) and CMHS (R_{rup} = 1.4 km) during the 22Feb11 earthquake. While some differences in the observed ground motion duration at the two sites may be due to source and site effects, a great deal of this difference is considered to be due the aforementioned path effects on duration. Amplitude-only scaling does not account for these potentially large changes in duration with distance.

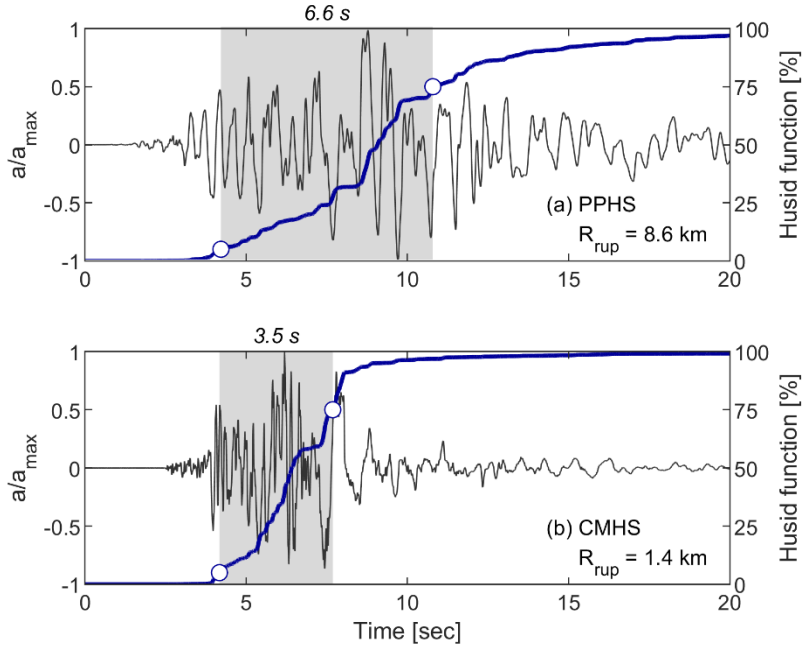

Fig. 5.9 Temporal accumulation of Arias Intensity (Husid function) and $D_{s,5-75\%}$ significant duration (grey shaded time-window) of the fault-normal component of the observed ground motions during the 22Feb11 earthquake at: (a) PPHS (R_{rup} = 8.6 km); and (b) CMHS (R_{rup} = 1.4 km).

5.7.4 Energy Bias

In the case of large difference in the source-to-site distance between the reference site and the target site (relative to their average source-to-site distance), which can often be the case in the near-source region, the use of overly high or overly low scaling factors without accounting for changes in ground motion duration can result in a significantly erroneous energy input in the dynamic analysis, and, consequently, biased estimates of the response of non-linear systems (e.g. Luco and Bazzurro 2007). In the following, this error in the simulated energy content of ground motion is quantified by taking advantage of existing conditional models for the prediction of Arias Intensity (AI).

Several researchers (e.g. Abrahamson et al. 2016, Liu et al. 2016, Macedo et al. 2019) have developed empirical GMMs for AI conditioned on the peak ground acceleration (PGA), some including also the spectral acceleration at 1.0 s period (SA_1). The general functional form of these conditional models is given by:

$$\ln AI = c_1 + c_2 \ln V_{s,30} + c_3 M_w + c_4 \ln PGA + c_5 \ln SA_1 \tag{5-7}$$

in which $V_{s,30}$ is the average shear-wave velocity in the top 30 m of the deposit (in $\mathrm{m/s}$), and c_i are regression coefficients.

Let PGA_r and $SA_{1,r}$ be the peak ground acceleration and 1 s–period spectral acceleration, respectively, at the reference site, and PGA_t and $SA_{1,t}$ be the respective intensity measures at the target site of interest. Then, writing Eq. 5-7 for both sites and taking their difference yields:

$$AI_t = AI_r \cdot (PGA_t/PGA_r)^{c_4} \cdot \left(SA_{1,t}/SA_{1,r}\right)^{c_5} \tag{5-8}$$

where AI_t and AI_r are the Arias Intensities at the target site and the reference site, respectively. It is important to recall that, at this stage, the scaling of ground motions at the 'engineering bedrock' level is examined, and hence, site effects are ignored or assumed identical for the two sites. In the amplitude-only scaling method discussed previously, it is implicitly assumed that spectral accelerations of ground motion exhibit identical scaling with distance irrespective of the vibration period, and such scaling is expressed via the scaling factor SF_{IM} (Eq. 5-4). Using this period-independent scaling assumption in Eq. 5-8 yields:

$$AI_t \approx AI_r \cdot (SF_{SA}\ )^{c_4+c_5} \tag{5-9}$$

Eq.5-9 provides the expected scaling of Arias Intensity with distance for ground motions whose distance-scaling of spectral accelerations can be described via SF_{SA}. At the same time, by definition, the Arias Intensity of a ground motion scaled using a constant factor SF_{SA} is simply ${SF_{SA}}^2$ times greater (or smaller) than the Arias Intensity of the unscaled (reference) motion. Unless the sum of the regression coefficients c_4 and c_5 equals 2, the above implies a discrepancy between an appropriate scaling of energy with distance (as that observed in real

ground motion records) and an erroneous scaling of energy resulting from the amplitude-only scaling approach. To quantify this discrepancy and examine its dependence on the scaling factor, an AI – prediction error is herein defined as:

$$Error_{AI} = \frac{AI_r \cdot (SF_{SA})^2 - AI_t}{AI_t} \cdot 100\% = \left[(SF_{SA})^{2-(c_4+c_5)} - 1\right] \cdot 100\% \qquad (5\text{-}10)$$

in which positive errors indicate overprediction of the Arias Intensity and negative errors indicate underprediction of the Arias Intensity. According to two recent conditional $AI-$ GMMs for active shallow crustal earthquakes (Abrahamson et al. 2016, Liu et al. 2016), the sum $(c_4 + c_5)$ can vary from 1.639 to 1.739, with standard errors included in the estimation of this range. Using these values in Eq. 5-10, the range of errors in the prediction of AI can be estimated as a function of the scaling factor, as depicted in Fig. 5.10.

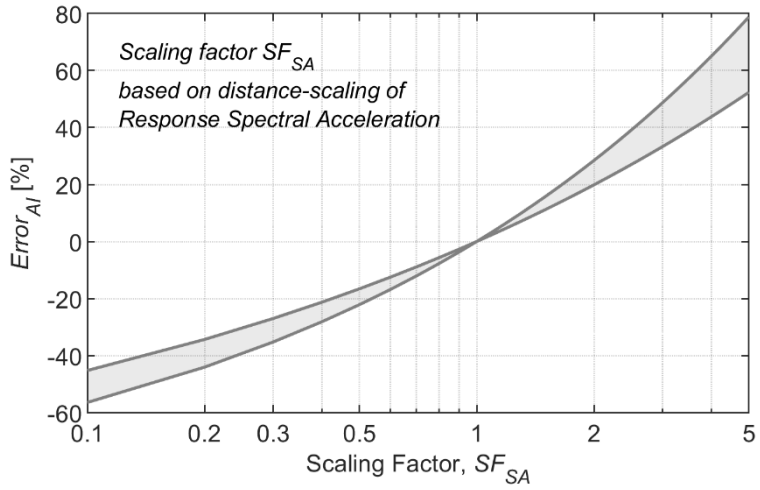

Fig. 5.10 Range of errors in the prediction of Arias Intensity as a function of scaling factor.

It can be seen from this figure that amplitude scaling factors outside a range from, say, 0.5 to 2, while presumably capturing changes in PGA and spectral accelerations from the reference station to the target site as intended, may be associated either with significant under-prediction or over-prediction of the actual AI at the target site, with errors in excess of 20%. This error in the energy content of the input ground motion can lead to biased estimates of the response of nonlinear systems, including liquefiable soil deposits. This is an additional important point that needs to be considered in the selection and scaling of reference motions and in the subsequent interpretation of the analysis results at the target sites.

5.7.5 Amplitude-Duration Scaling

The reason behind the energy bias of the amplitude-only scaling approach lies in the fact that, in this method, potentially large changes in the response spectral amplitudes of ground motion can occur without analogous changes in its duration, as observed in actual earthquake ground motions. As part of this study, an alternative method for scaling ground motions intended to

provide a consistent scaling of amplitude, duration, and energy content with distance was developed. In this method, the scaling is performed in the frequency domain, with amplitude changes applied to the Fourier amplitude spectra, and duration handled by modifications of the Fourier phase spectra. Further details on this method and an example application for effective-stress analysis at a target site are provided in Appendix B.

5.8 **Final Input Motions**

Fig. 5.11 shows (equivalent-outcrop) input acceleration and velocity time-series at PPHS obtained from deconvolution and (amplitude-only) scaling of the four selected reference motions for the 22Feb11 earthquake. The grey-shaded areas in this figure indicate the 5-95% significant duration ($D_{s,5-95\%}$) of each motion. The corresponding pseudo-acceleration response spectra (SA) of the input motions are presented in Fig. 5.12.

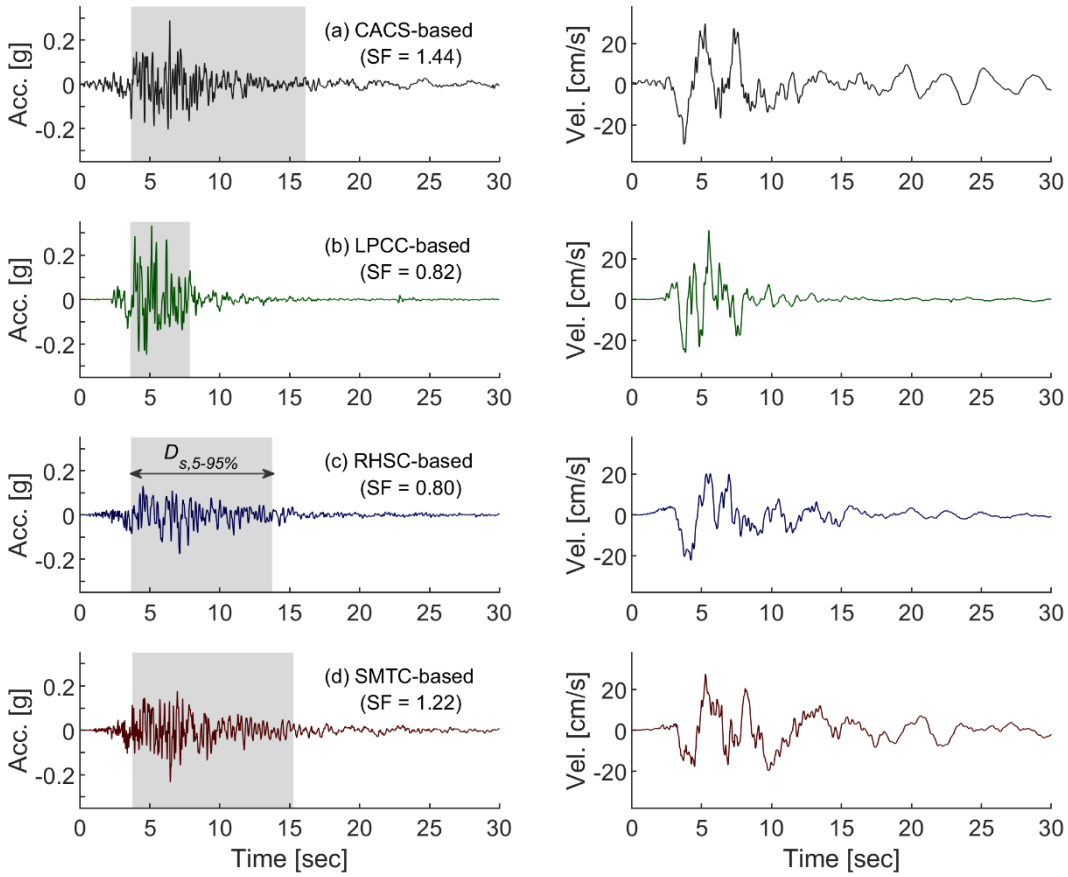

Fig. 5.11 Acceleration and velocity time-series of equivalent-outcrop input motions at PPHS (22Feb11 earthquake) obtained from: (a) CACS; (b) LPCC, (c) RHSC; and, (d) SMTC; *the deconvolved motions from these sites were scaled in amplitude with the scaling factors indicated in the parentheses; the grey-shaded time-windows in the acceleration time-series correspond to the 5-95% significant duration ($D_{s,5-95\%}$) of each input motion.*

Significant differences among the various input motions at PPHS can be observed in Figs. 5.11 and 5.12. In particular, the LPCC-based motion is characterized by a significantly higher intensity of short-to-intermediate period spectral amplitudes ($T \lesssim 1.7$ s), multiple high-frequency spikes in the acceleration time-series, and a rapid drop in the spectral amplitudes of longer periods. It is also interesting to note the remarkably shorter significant duration of this motion and the absence of strong velocity cycles after approximately 8 s in Fig. 5.11. In contrast, relatively long durations, higher long-period amplitudes ($T > 2.0$ s), and strong late velocity cycles are observed in the remaining three motions, and particularly in the CACS- and SMTC-based motions. The observed differences in long-period motion, velocity waveforms, and significant durations, can be explained by the aforementioned differences in surface-wave propagation and the relatively stronger contribution of surface-wave motion with increasing source-to-site distance.

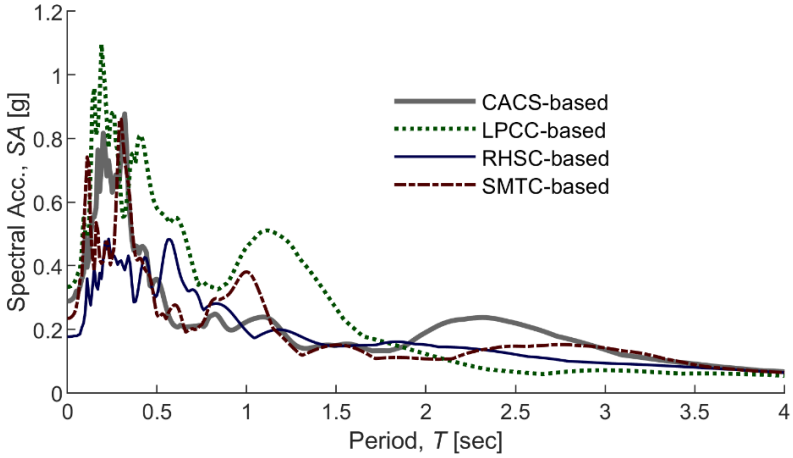

Fig. 5.12 Pseudo-acceleration response spectra for the various input motions at PPHS (22Feb11 earthquake).

The respective waveforms and acceleration response spectra of the input motions at PPHS for the 04Sep10 earthquake are illustrated in Figs. 5.13 and 5.14. In this case, important differences between the input motions from the two considered reference sites are seen at intermediate and long period amplitudes. The effects of these differences on the effective-stress analysis simulations and the predicted ground motions at the surface will be explored in the next chapter.

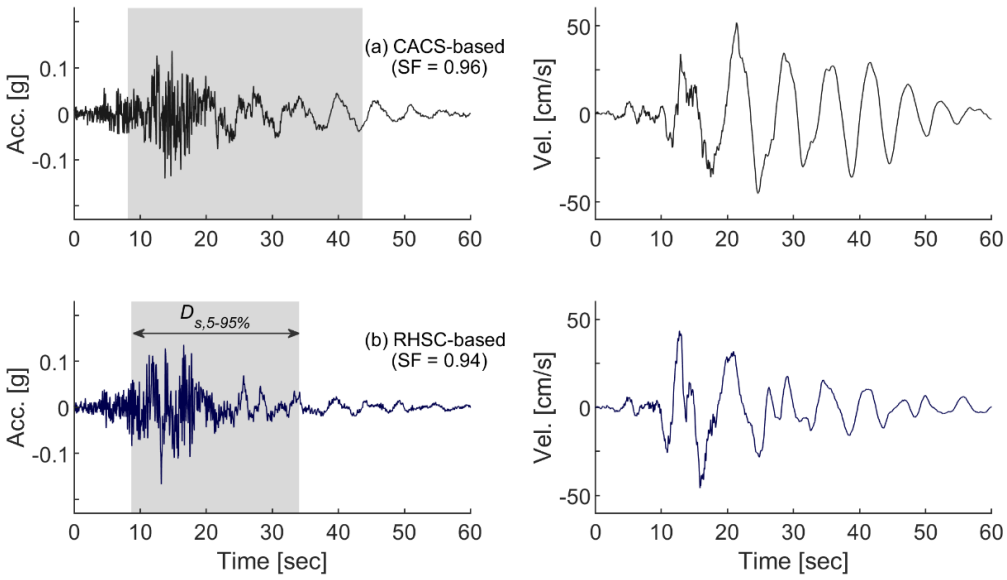

Fig. 5.13 Acceleration and velocity time-series of equivalent outcrop input motions at PPHS (04Sep10 earthquake) obtained from: (a) CACS; and, (b) RHSC; *the deconvolved motions from these sites were scaled in amplitude with the scaling factors indicated in the parentheses; the grey-shaded time windows in the acceleration time-series correspond to the 5-95% significant duration ($D_{s,5-95\%}$) of each input motion.*

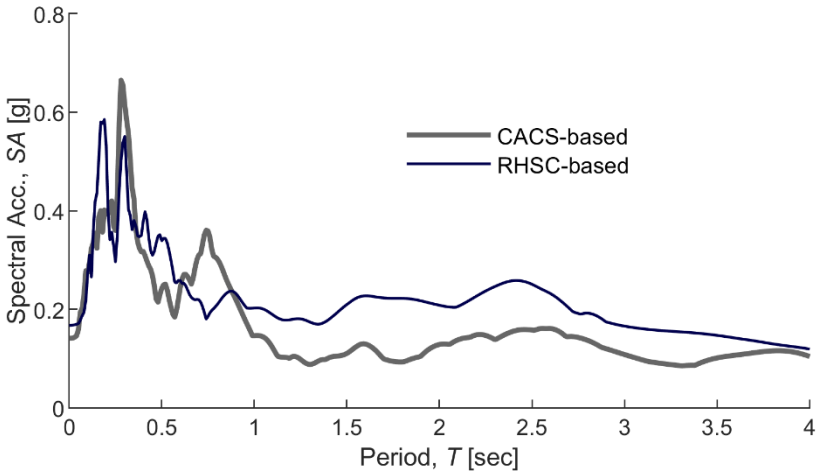

Fig. 5.14 Pseudo-acceleration response spectra for the two input motions at PPHS (04Sep10 earthquake).

5.9 **Summary**

Fig. 5.15 summarizes the key steps and considerations in the derivation of site-specific input ground motions involving:

(1) The selection of a reference site and reference recorded motion with consideration of: (a) the appropriateness of the candidate reference site for deconvolution (i.e. negligible

nonlinearity in the response and shallow thickness of soft soil deposits); (b) potential differences between hanging-wall and footwall motion, in case the considered sites (reference site and target site) are located on opposite sides of the fault; (c) the deeper geological structure below the reference site and the target site (e.g. basin depth); (d) extended-source effects and their impact on the azimuthal variation in radiated seismic energy; and, (e) the proximity of the reference site to the target site, which generally increases the likelihood of similarities in the above characteristics and reduced bias introduced by the subsequent scaling.

(2) The deconvolution of the selected reference motion by the local site-response at the reference site using EQL analysis. Key requirement from this analysis is that the maximum shear strains throughout the soil profile do not exceed a threshold strain (e.g. $\gamma_{max} \approx 0.5\% - 1\%$) beyond which the EQL approximation of the nonlinear soil behaviour is no longer credible.

(3) The scaling of the deconvolved motion to account for path effects arising from differences in the source-to-site distance between the reference site and the target site. Amplitude scaling factors can be derived using Eqs. 5-3 or 5-4. The use of scaling factors that significantly deviate from unity should generally be avoided as significant bias in the energy content of ground motion can be introduced in such cases (Fig. 5.10). To overcome this issue, an alternative 'amplitude-duration' scaling method that provides consistent distance-scaling of amplitude, energy content, and duration was developed as part of this study. This method is described in Appendix B.

(4) Once the input motion is derived, ground response analysis (using either equivalent linear or fully nonlinear models) can be performed at the target site to evaluate its performance and estimate the surface ground motion.

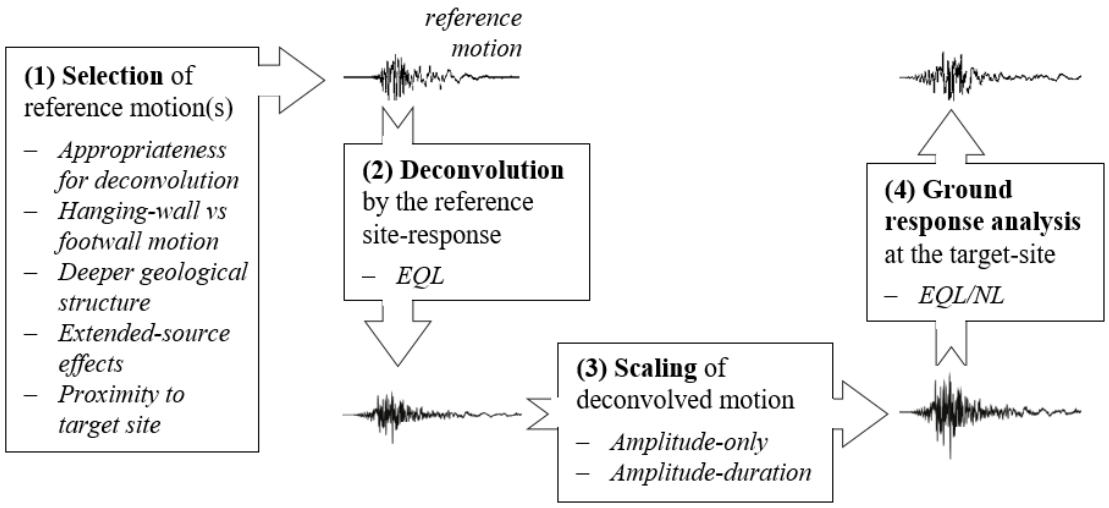

Fig. 5.15 Key steps and considerations in the derivation of input motions for forensic analysis at a target site.

An important conclusion from this chapter is that there is no a unique reference motion that can be considered representative for all sites in the near-source region of an earthquake. Instead, each recorded motion represents the characteristics of the ground motion over a limited geographic area where the various factors contributing to the spatial variability of ground-motion have a similar effect. The adopted ground-motion treatment processes (i.e. deconvolution and scaling) are used to account for some of these factors but they simplify significantly the physical processes that generate the spatial variability of ground motion. The following chapter will evaluate the accuracy with which the input motions derived from these processes can be used to simulate the ground response and observed ground motions at the SMS sites in Christchurch.

6 ANALYSES OF THE STRONG MOTION STATION SITES

6.1 Introduction

The present chapter evaluates the ability of the developed effective-stress analysis procedure to simulate the ground response of liquefying deposits throughout Christchurch, with a specific emphasis on the comparative evaluation of the performance of the various reference motions used for the 04Sep10 and 22Feb11 earthquakes. The performance of each reference motion and associated simulation of ground response are evaluated by comparing recorded surface motions to those predicted by 1D effective-stress analyses at the 13 SMS sites of urban Christchurch (Table 5.1). The implicit assumption in this verification approach is that if the surface ground motion is well-predicted, then both the induced seismic demand and consequent response of the shallow part of the deposit, which is the most relevant for liquefaction manifestation at the ground surface, are well-represented in the analyses. Findings from this study, regarding the quality of the predictions at the studied SMS sites, are used to inform the definition of input motions and indicate important factors to consider in the subsequent effective-stress analyses of the 55 case-history sites.

6.2 Numerical Modelling and Analysis Cases

Input motions derived from the various reference motions, as described in the previous chapter, were used as base excitations of 1D soil-column models to simulate the free-field shallow ground response at the 13 SMS sites of urban Christchurch (Table 5.1).

Effective-stress analyses for the 04Sep10 earthquake were performed using input motions obtained from all three scaling models, illustrated in Fig. 5.8b, for scaling ground motions with distance. The YA14 model with the increased saturation factor ($h = 33.3$ km) yielded the best performance in the simulations and has been adopted as the default model for the analyses presented in this chapter. For completeness, results from the 04Sep10 earthquake simulations using the B13 model and the YA14 ($h = 33.3$ km) model are provided in Figs. C1–C4 of Appendix C. The default YA14 model with $h = 5.2$ km (Fig. 5.8a) has been adopted in scaling the reference motions for the 22Feb11 earthquake simulations.

The soil-column models for the effective-stress analyses were calibrated in accordance with the framework described in Chapter 4, by, first, defining a simplified soil profile from the available in-situ test data, and then, determining appropriate constitutive model parameters for the identified behavioural characteristics of each layer of the simplified profile. An example of adopted simplified soil profile along with values for key layer properties used in the calibration of the constitutive model is illustrated in Fig. 6.1 for the Christchurch Hospital (CHHC) SMS site.

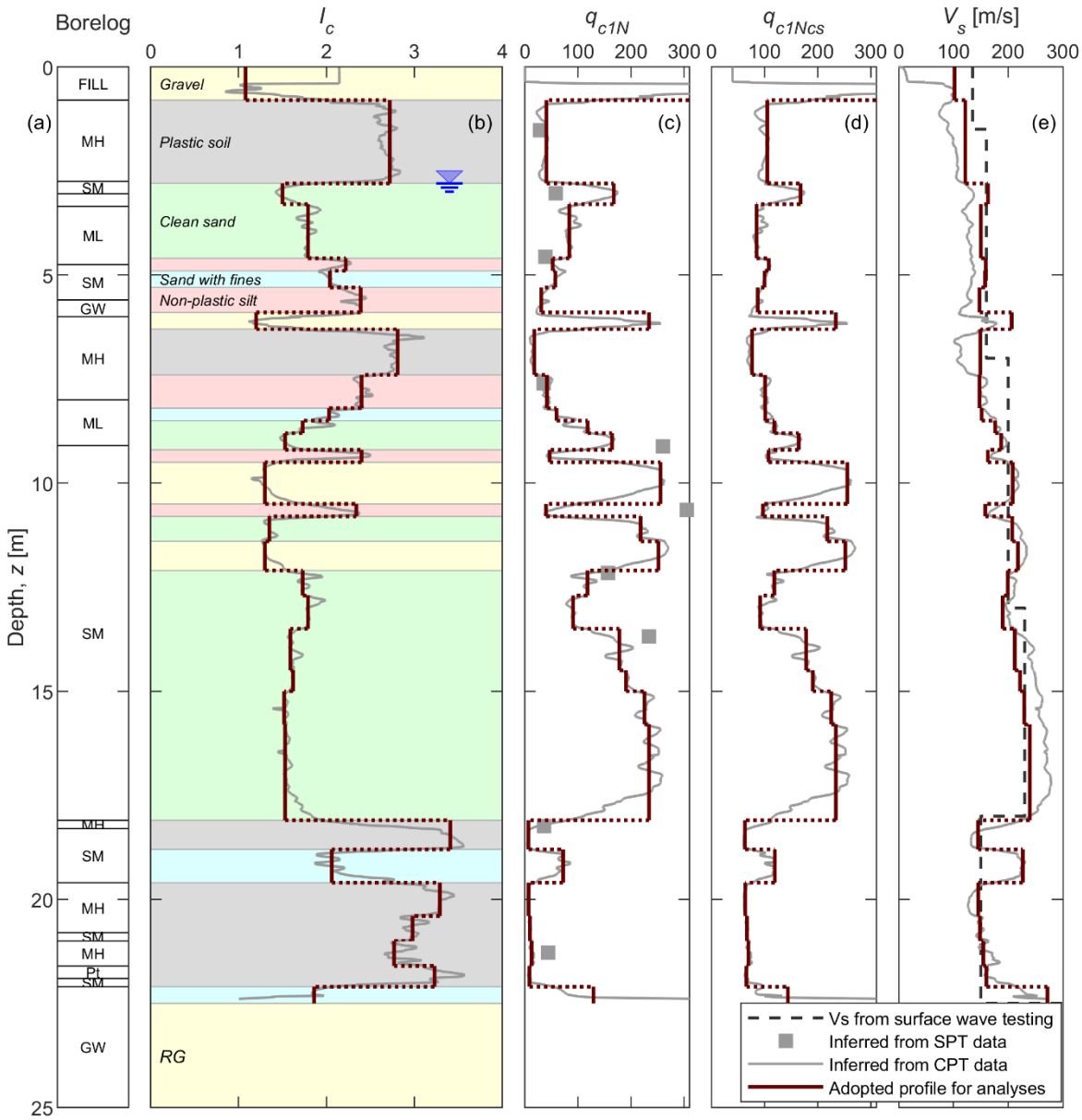

Fig. 6.1 Determination of a simplified soil profile with values key layer properties for the Christchurch Hospital (CHHC) site: (a) visual (USCS) soil classification based on borehole data; (b) I_c values and I_c-based classification of soil behaviour type; (c) q_{c1N} values, including q_{c1N} values converted from the measured SPT blow counts (square symbols) according to Robertson and Cabal (2015); (d) q_{c1Ncs} values; and (e) V_s values.

A series of additional sensitivity analyses were carried out at each SMS site to examine the influence of several factors that may affect the cyclic resistance and overall dynamic characteristics of the deposit including: the I_c threshold separating liquefiable from non-liquefiable soils; the $FC - I_c$ correlation used in estimating q_{c1Ncs} for liquefiable soils; the choice of the CPT used in model calibration among the several CPTs that could be available in close proximity to the considered SMS site; the adopted V_s profile; and the influence of partial saturation on the cyclic resistance of near-surface soils. By and large, the sensitivity of the computed surface ground motion to changes related to the above factors was minor compared to that resulting from the consideration of alternative reference motions or uncertainties in the scaling factor.

In the following, results from 26 seismic effective-stress analyses for the 04Sep10 earthquake (13 SMS sites × 2 reference motions) and 52 analyses for the 22Feb11 earthquake (13 SMS sites × 4 reference motions) are scrutinized.

6.3 Evaluation Approach

The scrutiny of the effective stress analysis simulations is realized by comparing observed and predicted surface ground motions at the 13 SMS sites. Multiple ground motion intensity measures (IMs) are considered in the comparison, and prediction residuals y_{IM} for each IM are calculated in natural logarithmic space as:

$$y_{IM} = \ln\left(IM_{pred}\right) - \ln(IM_{obs}) \tag{6-1}$$

where IM_{obs} is the observed IM obtained from the recorded motion at the ground surface of a given SMS site, and IM_{pred} is the corresponding predicted IM obtained from the effective-stress analysis. Positive y_{IM} residuals indicate overprediction of the observed ground motion, whereas negative y_{IM} residuals indicate underprediction.

A list of the IMs considered and their definition is summarized in Table 6.1. Besides the traditional amplitude-based IMs used in earthquake engineering practice (i.e. PGA, PGV and SA), several energy-based measures of the ground motion intensity, expressing either the cumulative spectral intensity over a range of vibration periods (i.e. SI) or the cumulative intensity of the motion over time (i.e. $PGA_{M7.5}$, AI, CAV, CAV_5), are also considered. The selected energy-based measures have been shown in several past studies (e.g. Kayen and Mitchell 1997, Kramer and Mitchell 2006, Bradley et al. 2009, Kramer et al. 2016, Dashti and Karimi 2017, Karimi and Dashti 2017) to correlate well with either the triggering of liquefaction or its consequences on affected structures and, hence, are the key measures used in evaluating the quality of the predictions. For completeness, representative IMs that characterize the strong motion duration (i.e. D_s) and frequency content of ground motion (i.e. T_m) are also included in the comparisons.

Table 6.1 Ground motion intensity measures considered in the evaluation of the analyses predictions.

Intensity Measure	Notation	Definition	Reference
Peak ground acceleration	PGA	$\max[\lvert a(t)\rvert]$ (1)	--
Peak ground velocity	PGV	$\max[\lvert v(t)\rvert]$ (2)	--
Pseudo-spectral acceleration	$SA(T)$	$\max_t[\lvert a_{str}(T, \xi = 0.05, t)\rvert]$ (3)	--
Spectrum intensity	SI	$\int_{0.1}^{2.5} SV(T, \xi = 0.05)dT$ (4)	Housner (1952)
Magnitude-corrected peak ground acceleration	$PGA_{M7.5}$	PGA/MSF (5)	Kramer et al. (2016)
Arias intensity	AI	$\pi/2g \int_0^\infty [a(t)]^2 dt$	Arias (1970)
Cumulative absolute velocity	CAV	$\int_0^\infty \lvert a(t)\rvert dt$	Benjamin and Associates (1988)
Modified cumulative absolute velocity	CAV_5	$\int_0^\infty \langle\chi\rangle \lvert a(t)\rvert dt$ (6)	Kramer and Mitchell (2006)
Significant duration	D_s	The interval of time over which a portion (percentage) of the total AI is accumulated (7)	Trifunac and Brady (1975)
Mean period	T_m	$\sum(A_i^2/f_i)/\sum A_i^2$ (8)	Rathje et al. (1998)

(1) $a(t)$: acceleration time-series,
(2) $v(t)$: velocity time-series,
(3) a_{str}: oscillator's acceleration time-series, ξ: oscillator's damping,
(4) SV: pseudo-spectral velocity,
(5) $MSF = \left(15/N_{eq}\right)^b$, N_{eq}: number of equivalent loading cycles estimated from $a(t)$ using a peak counting method excluding non-zero crossing peaks, b: slope of LRC taken as 0.34.
(6) $\langle\chi\rangle = 1$, for $\lvert a(t)\rvert > 5\ \mathrm{cm/s^2}$; 0, otherwise,
(7) 20-80% and 5-75% AI thresholds are used for the 04Sep10 and 22Feb11 earthquake simulations, respectively, as these intervals were shown to best describe the respective durations of the main S-wave motion
(8) A_i: Fourier amplitudes, f_i: discrete Fourier transform frequencies between 0.25 and 20 Hz.

6.4 **Characteristic Results from an Individual Analysis**

Before discussing the summarized results from all analyzed SMS sites, it is useful to first examine in more detail key characteristics of the simulated response at an individual site and evaluate the associated liquefaction effects on the surface ground motion (e.g. Kramer et al.

2011, Youd and Carter 2005, Bouckovalas et al. 2016). Fig. 6.2 shows characteristic results from the effective-stress analysis carried out at the Cashmere High School (CMHS) site using an LPCC-based input excitation for the 22Feb11 earthquake. The left column of the figure presents comparisons between the observed and predicted surface ground motions, in terms of acceleration time-series (Figs. 6.2a and 6.2b), temporal evolution of AI (Fig. 6.2c), and spectral acceleration residuals y_{SA} as a function of vibration period T (Fig. 6.2d). Note that, because of the low-pass filtering of the reference motions at 15 Hz (for the purpose of the deconvolution analysis), only the residuals for spectral periods greater than 0.08 s are shown in Fig. 6.2d, as well as in the remaining $y_{SA} - T$ plots of this chapter. The equivalent predictions from a total-stress analysis at the site using the same LPCC-based input excitation are also shown for reference. The right set of columns in Fig. 6.2 is used to show snapshots of the excess pore water pressure ratio r_u profile at characteristic time sections (Fig. 6.2g), for the top 14 m of the deposit, with reference to the soil type (Fig. 6.2e) and penetration resistance (Fig. 6.2f) of each layer.

While some differences between the observed and predicted ground motions are evident in this figure, key characteristics of the observed ground motion, such as the weakening of the ground acceleration following the 2-3 strong acceleration cycles between 3 and 6 s of the time axis in Fig. 6.2a, are well captured by the effective-stress analysis (Fig. 6.2b). This reasonably good agreement in the temporal evolution of the intensity is also reflected in the cumulative AI versus time shown in Fig. 6.2c for the effective-stress analysis. In contrast, the surface ground motion predicted by the total stress analysis does not exhibit the same weakening of the shaking intensity, instead strong acceleration cycles in excess of 0.2 g amplitude continue up until about 8 s, with moderate amplitude cycles following thereafter (Fig. 6.2b). Consequently, AI (Fig. 6.2c) and spectral accelerations at vibration periods from 0.2 to about 0.7 s (Fig. 6.2d) are significantly overpredicted by the total-stress analysis. Discrepancies between the effective-stress and total-stress analyses predictions are particularly notable in spectral accelerations at short periods ($T \lesssim 1.0$ s) (Fig. 6.2d), while they start becoming prominent in the time series at about 4.5 s (Fig. 6.2b), when r_u approaches 1.0 within the deeper weak layers of the deposit, at about 10 and 12.5 m depth from the ground surface (Figs. 6.2f and 6.2g). The loading cycle that follows triggers liquefaction ($r_u \approx 1.0$) at three different depths in the deposit, including in the shallow critical layer near the ground surface, and after that time ($\sim$5 s) differences between the effective-stress analysis and the total-stress analysis become increasingly large (Figs. 6.2b and 6.2c).

Excess pore water pressure build-up and liquefaction of loose soil layers result in softening of the soil deposit with consequent large deformations and increased soil damping, which in turn may significantly reduce the short-period amplitudes of the ground motion after the onset of liquefaction. These liquefaction effects on the ground motion due to a substantial reduction in effective stresses cannot be captured by the total-stress analysis which ignores the generation of excess pore water pressures and their effects on the stress-strain behaviour of the soil.

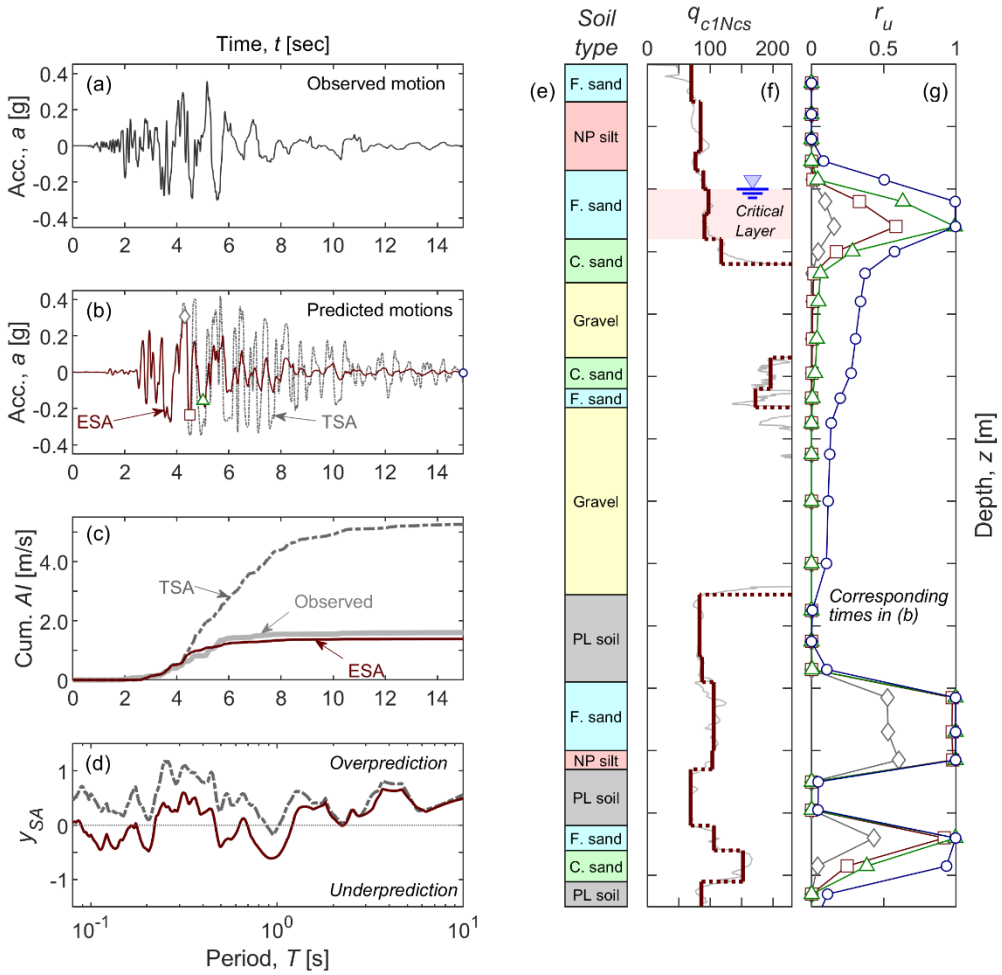

Fig. 6.2 Characteristic results from effective-stress analysis (ESA) and total-stress analysis (TSA) at the CMHS site using an LPCC-based input excitation, and comparisons with the surface ground motion observed at this site during the 22Feb11 earthquake: (a) acceleration time-series of the observed motion; (b) acceleration time-series of the predicted surface motions; (c) temporal evolution of AI; (d) y_{SA} residuals as a function of vibration period; (e) stratification of simplified soil profile; (f) q_{c1Ncs} profile; and (g) computed r_u profiles at characteristic time sections, for the top 14 m of the deposit.

6.5 **Summary Results for the 04Sep10 Simulations**

Summarized results for the 04Sep10 earthquake simulations are illustrated in Fig. 6.3 with box-and-whisker plots representing the distribution of the prediction residuals y_{IM} for the considered IMs across all 11 analyzed (non-reference) SMS sites and for each reference motion (i.e. CACS and RHSC) separately. Analogous plots representing the median spectral acceleration residuals y_{SA}, and the interquartile and total (minimum to maximum of all residuals) ranges of y_{SA} as a function of vibration period are shown in Fig. 6.4. Prediction residuals for selected IMs on a site-by-site basis are provided in Fig. C.5 of Appendix C.

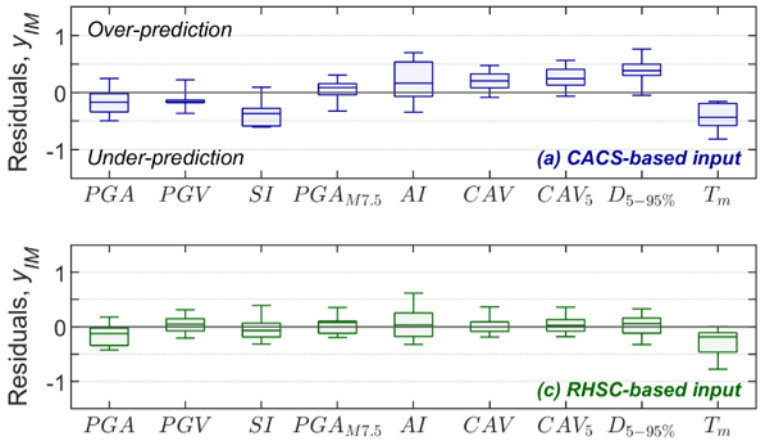

Fig. 6.3 Box-and-whisker plots illustrating the distribution of the considered *IM* residuals for the 04Sep10 earthquake simulations using: (a) CACS-based input motions; and (b) RHSC-based input motions.

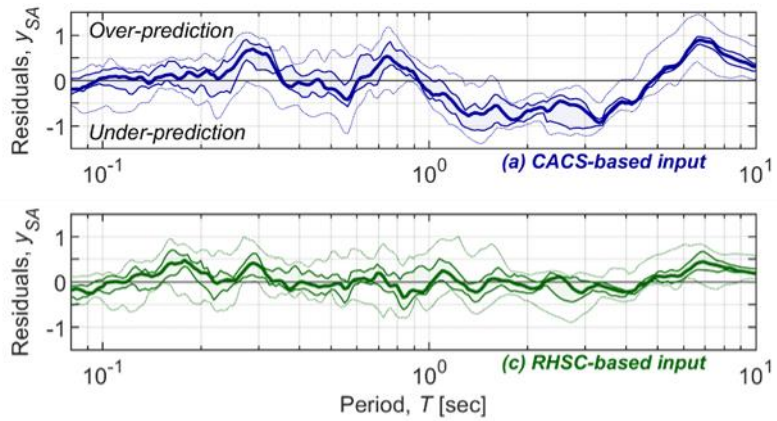

Fig. 6.4 Distribution of the spectral acceleration residuals for the 04Sep10 earthquake simulations as a function of vibration period using: (a) CACS-based input motions; and (b) RHSC-based input motions; *thick lines represent the median of the distribution, shaded regions indicate the interquartile range, and dotted lines show the total (minimum to maximum of all residuals) range.*

The distribution of the residuals in Figs. 6.3 and 6.4 shows some clear differences between the CACS- and RHSC-based simulations. The CACS-based simulations display clear anomalies with significant bias for many of the considered IMs including the spectral amplitudes, particularly at periods longer than 1 s. The RHSC-based simulations show a much better performance with relatively small dispersion and symmetric distribution of the residuals around the zero bias axis for all considered IMs except for PGA and T_m, both of which are generally underpredicted by the simulations. The above observations generally apply also to the spectral amplitudes, though the quality of the prediction somewhat varies as a function of the vibration period. The better performance of the RHSC-based simulations can be explained by the fact that, compared to the CACS site, the RHSC site has more similar orientation relative to the source of the 04Sep10 earthquake (source-to-site azimuth) to that of the

analyzed SMS sites (Fig. 5.1b) and hence more compatible source and wave propagation effects.

Key energy-based ground motion metrics, such as CAV and CAV_5, are exceptionally well predicted by the RHSC-based simulations. Indicatively, the lower and upper quartiles of the residuals for these IMs are about -0.10 and 0.05, respectively, implying ratios of CAV_{pred}/CAV_{obs} from 0.90 to 1.05. The minimum and maximum residuals are -0.17 and 0.29, respectively, corresponding to CAV_{pred}/CAV_{obs} ratios of 0.84 and 1.34. Kramer and Mitchell (2006) showed that the CAV_5 at the bedrock level relates very well with the excess pore water pressure generation in overlying liquefiable soils, while more recent studies (Bray and Macedo 2017, Bullock et al. 2019) have used CAV or modified versions of it (at the free-field ground surface or the bedrock level) as the key ground motion IM in evaluation of liquefaction-induced building settlements. As noted by Kramer and Mitchell (2006), the values of an IM at bedrock and the ground surface are correlated, so the computed low dispersion from the effective-stress analyses at the ground surface corresponds to low dispersion at the bedrock level as well.

It can be concluded that the RHSC-based input motions, in conjunction with the adopted modelling approach for the ground response, seem to provide a reasonably good prediction of the seismic demand induced by the 04Sep10 earthquake. The observed ground motion at CACS appears to have some specific features which are carried over the deconvolution and subsequent ground-response analyses, but they are not apparent in the observed ground motions at other SMS sites in Christchurch.

6.6 Summary Results for the 22Feb11 simulations

A similar format is used in this section to illustrate the results from the 22Feb11 earthquake simulations. In this case, results from simulations at 10 SMS sites, excluding the simulations at the 3 reference sites of urban Christchurch (i.e. CACS, RHSC, and SMTC), are used to define the distributions of the residuals for each considered reference motion. Fig. 6.5 provides plots of the spectral acceleration residuals versus period of vibration for each reference motion.

Strong biases and large dispersion of the residuals are seen for all reference motions in Fig. 6.5. These observations reflect the significant spatial variability of ground motion in the near-source region of the 22Feb11 earthquake. Clearly, in this case, there is no a unique reference motion that can be considered representative across all areas (sites) in the near-source region of the earthquake. In other words, the degree of representativeness of each reference motion varies significantly across the region, and it depends on the compatibility (similarity) of wave-propagation and source effects between the reference site (used in the determination of the input motion) and the target site (used in the subsequent effective stress analysis).

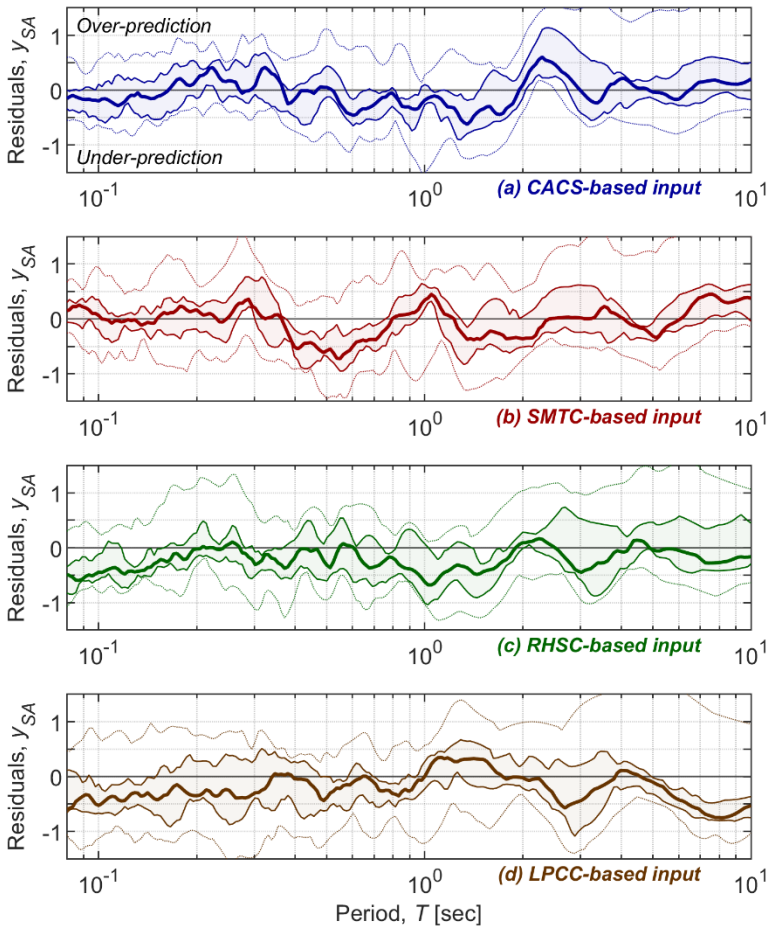

Fig. 6.5 Distribution of the spectral acceleration residuals for the 22Feb11 earthquake simulations as a function of vibration period using: (a) CACS-based input motions; (b) LPCC-based input motions; (c) RHSC-based input motions; (d) SMTC-based input motions; *thick lines represent the median of the distribution, shaded regions indicate the interquartile range, and dotted lines show the total (minimum to maximum of all residuals) range.*

Taking the above into consideration, a separate set of prediction residuals using the simulation with the most representative or 'optimal' input (reference) motion for each site was compiled. The source-to-site distance, source-to-site azimuth, and basin depth were the key factors considered in the selection of the optimal reference motion for each site. The simulation performances of the various reference input motions were also comparatively evaluated at each target SMS site to confirm or revise the initial selection based on these three principal factors. The spectral acceleration residuals for the optimal-input simulations are presented in Fig. 6.6. The respective box-and-whisker plots for the remaining IMs is shown in Fig. 6.7, together with the prediction residuals separately for each reference input motion. The selected optimal reference motions for each target SMS site are reported in Fig. 6.8.

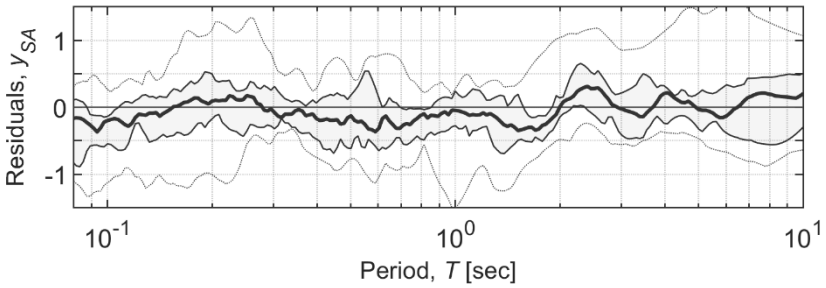

Fig. 6.6 Distribution of the spectral acceleration residuals for the 22Feb11 earthquake simulations as a function of vibration period using as input the optimal reference motion for each analysed site; *thick lines represent the median of the distribution, shaded regions indicate the interquartile range, and dotted lines show the total (minimum to maximum of all residuals) range.*

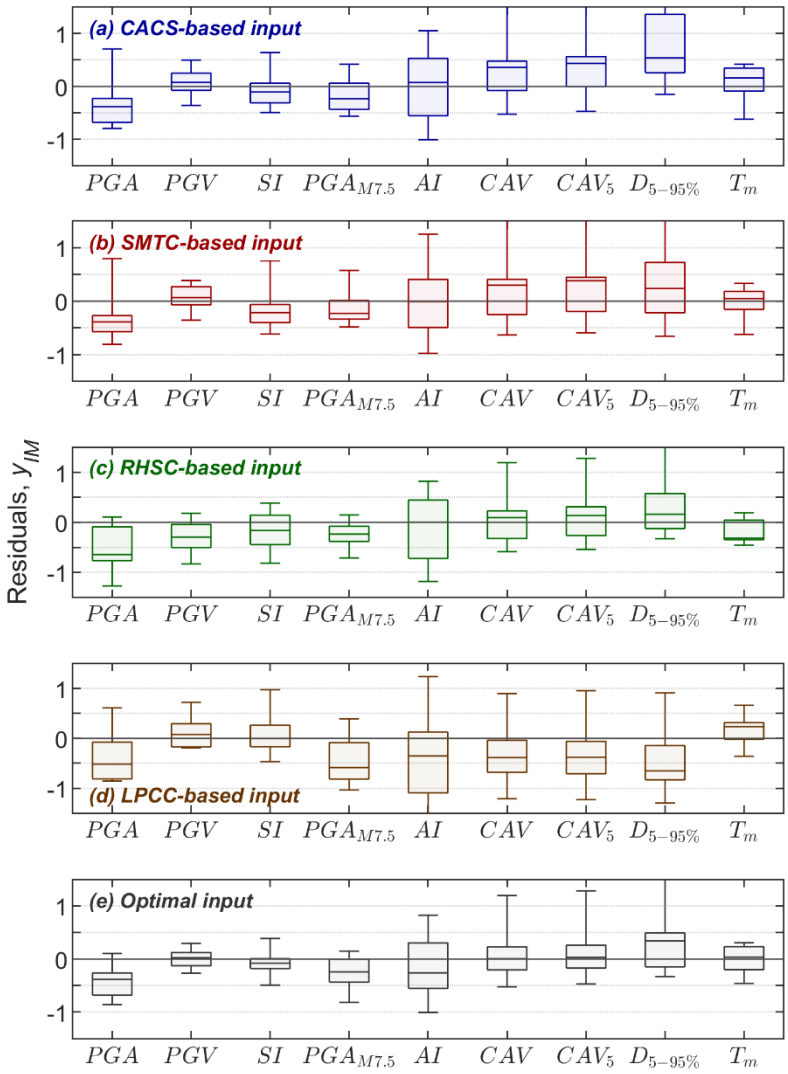

Fig. 6.7 Box-and-whisker plots illustrating the distribution of the considered *IM* residuals for the 22Feb11 earthquake simulations using: (a) CACS-based input motions; (b) LPCC-based input motions; (c) RHSC-based input motions; (d) SMTC-based input motions; and (e) the optimal input motion for each analysed site.

The following key observations and associated explanatory hypotheses can be made with respect to Figs. 6.5–6.7.

First, there is a tendency for underprediction of short-period spectral amplitudes ($T < 0.2$ s) by the CACS-, RHSC-, and LPCC-based simulations and underprediction of PGA and $PGA_{M7.5}$ for all reference motions. Kaklamanos and Bradley (2018) observed a similar effect of underprediction of high-frequency motion in total-stress simulations of numerous vertical array records from Japan, and they attributed it to a potential breakdown in the 1D site-response assumptions and/or the poor resolution of the shear-wave velocity profiles. In addition to the above effects, discrepancies in the high-frequency components of motion are to be expected as a result of the different analysis methods employed in the deconvolution (at the reference site) and convolution (at the target site), and particularly of the different damping formulation schemes used in these methods. Equivalent-linear analysis uses time-invariant and frequency-independent damping, which is known to often result in overprediction of high-frequencies with depth during deconvolution (e.g. Roesset et al. 1995). On the other hand, in the nonlinear convolution analysis damping is provided by the hysteretic response of the S-D model, and it varies with time as the severity of shaking changes. A small amount of Rayleigh damping is also used in the nonlinear analysis for numerical stability and to provide damping at small strains where hysteretic damping is near zero. High-frequency motion is sensitive to the above differences in the modelling of soil damping between the equivalent-linear and nonlinear analyses. Rayleigh damping and excessive hysteretic damping of non-liquefiable layers at large strains – a result of Masing unload/reload rules in S-D model – in nonlinear analysis are suspected to contribute to the observed loss in high-frequency content in the computed motions from the present study.

Second, the CACS-, SMTC- and RHSC-based simulations tend to overpredict the significant duration $D_{5-75\%}$, whereas the LPCC-based analyses display a severe underprediction bias. The latter is related to 2D and 3D basin effects which are absent from the LPCC reference motion, as previously discussed. On the other hand, the tendency for overprediction of $D_{5-75\%}$ by CACS-, SMTC- and RHSC-based simulations is likely a manifestation of strong path effects on duration which are neglected in the adopted amplitude-only scaling approach. As a result, the use of reference motions, such as CACS and SMTC, which are recorded at large distances from the rupture compared to the analyzed near-source sites (Table 5.1), produces significant overpredictions of $D_{5-75\%}$. These biases in strong motion duration also affect the predictions of other IMs. For instance, it can be seen that the CAV and CAV_5 residuals are generally consistent with the residuals of $D_{5-75\%}$. With regards to AI, the opposing effects of overprediction of duration and underprediction of high-frequency motion seem to have a balancing effect on the median AI for the relevant simulations, but they contribute to the large dispersion of the residuals as the two effects alternately dominate one another depending on the separation distance between the reference and target sites.

Third, the consideration of site-specific optimal reference motions reduces both the overall bias in the predictions and the dispersion of the residuals for nearly all examined IMs (Fig. 6.7e). By considering the optimal input motion for each target site, the use of inadequate

reference motions at locations with significantly different source-to-site geometry and deeper geological conditions from the reference site has been prevented to some extent. Yet, not all target sites have a suitable nearby reference site, and, hence, considerable dispersion of the residuals for many *IM*s still persists (Figs. 6.6 and 6.7e).

To get a better understanding of the source of this persisting variation in the residuals of the optimal-input simulations, and also to evaluate their performance at the various urban areas of interest, in Fig. 6.8 the residuals of key *IM*s are examined on a site-by-site basis. Some clear spatial trends in the residuals of the optimal-input simulations can be observed in this figure. These include a general underpediction of ground motion at the CBD sites (i.e. CBGS, CHHC, REHS, and CCCC) and an overprediction of ground motion at sites northeast of CBD (HPSC and NNBS). A parallel scrutiny of the site-by-site residuals from the 04Sep10 earthquake simulations (Fig. C5) exposes some systematic trends at specific sites, such as REHS and HPSC. The former is a soft peat soil site which has been previously identified (e.g. Bradley 2015) as a site of exceptionally large site amplification, whereas the latter site suffered severe liquefaction and lateral spreading in both events (Table 5.1). The 1D ground-response analyses alone using the available reference motions cannot sufficiently explain the ground motions observed at these sites. A greatly improved performance of the simulations is evident at sites south (i.e. CMHS), west (i.e. RHSC), and north of CBD (i.e. PPHS and SHLC), which generally show only minor residuals. For completeness, the site-by-site residuals for the same *IM*s but including all simulations, rather than only the optimal ones, are provided in Fig. C6 of Appendix C

In summary, the results from the 22Feb11 earthquake simulations show that careful site-specific selection of reference ground motions, with consideration of the key factors of spatial ground motion variability discussed in chapter 5, is essential to achieve a good simulation of the ground response in this earthquake. Based on the findings from the 22Feb11 earthquake simulations, a pair of reference motions has been selected for the analyses of each of the 55 sites (Fig. 3.1). The RHSC motion has been selected for use across all sites, as it corresponds to relatively moderate source-to-site distance and basin depth (Fig. 5.1). In addition to RHSC, the LPCC, CACS, LPCC and SMTC motions have been selected, as the second reference motion, for use at the sites located south, west, east, and north of CBD (Fig. 5.1) respectively. The use of two reference motions per site serves to account for the uncertainty in the input motion, while still using the most representative reference motions for each urban area based on the findings from the analyses of the SMS sites.

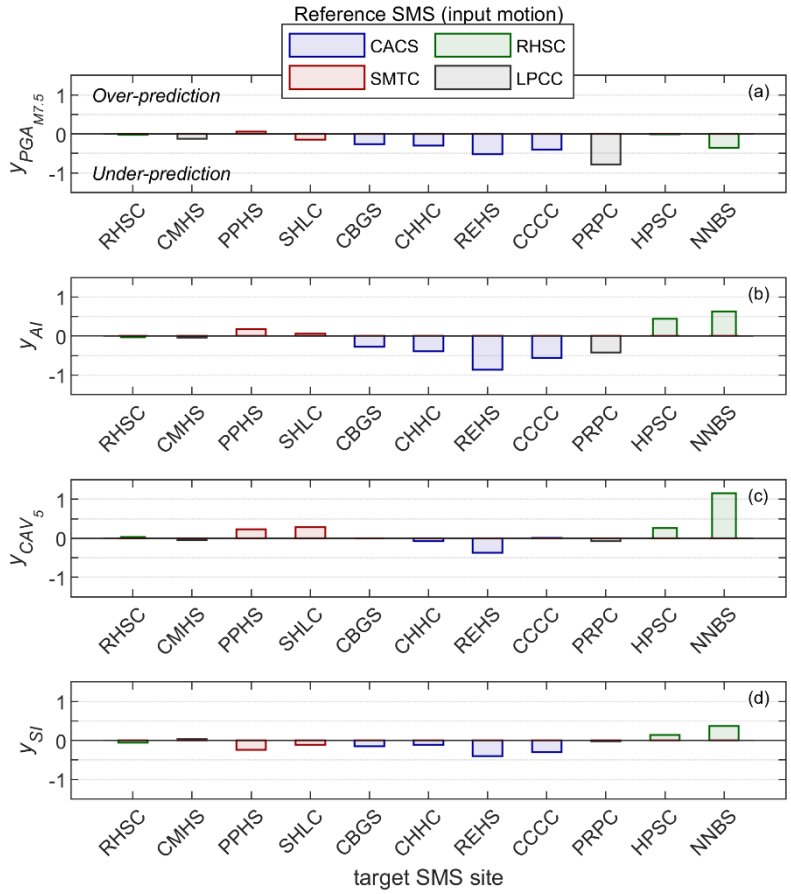

Fig. 6.8 Prediction residuals of the optimal-input simulations on a site-by-site basis for: (a) $PGA_{M7.5}$; (b) AI; (c) CAV_5; and (d) SI.

6.7 **Summary**

The purpose of this chapter was to evaluate the performance of the derived input motions for effective-stress analysis of sites throughout Christchurch and scrutinize the quality of the analysis predictions through rigorous comparisons with available seismic recordings. To this end, 1D effective-stress analyses were carried out at 13 target SMS sites of urban Christchurch using several reference motions for the two considered earthquakes. Importantly, the same approach was used consistently in deriving the input motions, calibrating the effective-stress analysis procedure, and evaluating the quality of the predictions for all analyzed SMS sites and for both considered earthquakes. Results from the effective-stress analyses demonstrated the ability of the adopted analysis procedure to capture key aspects of the ground response in liquefying deposits, but they also highlighted the sensitivity of the predicted surface motion to the input excitation at the base.

In the 04Sep10 earthquake simulations, the reference motion from the Riccarton High School (RHSC) station showed the best performance, with practically no bias in the aggregate and

small dispersion of the prediction residuals for nearly all examined IMs. In contrast to other reference sites, the RHSC site has similar source-to-site azimuth to that for the majority of the target sites and hence more compatible (with the target sites) wave propagation and ground motion characteristics. A key factor for the unbiased prediction of the surface ground motions was the use of scaling factors that correspond to a much smoother distance-scaling of ground motion than that indicated by a New Zealand-specific empirical ground motion model (Bradley 2013) for the relevant range of source-to-site distances (Fig. 5.9b). This weaker attenuation of ground motion with distance was attributed to a spatially extended near-source saturation of ground motion as a result of the orientation of the studied sites relative to the earthquake rupture (Fig. 5.1b).

In the 22Feb11 earthquake simulations, all reference input motions resulted in significant biases and large dispersion of the prediction residuals in the aggregate. This was attributed to a strong spatial variation of ground motion at the engineering bedrock level, as a result of the proximity of the studied sites to the causative fault rupture, and associated extended-source effects and strongly varying path effects. In other words, signature ground motion characteristics rapidly change over short distances in the near-source region of the 22Feb11 earthquake and are significantly affected by the orientation of the sites relative to the source. In this case, instead of seeking for the individual reference motion that can provide the best performance across all sites, one should rather select site-specific (area-specific) optimal reference motions based on similarities in key source-to-site path characteristics (i.e. distance, azimuth, and basin depth) between the reference and target sites. Simulations using such site-specific optimal reference motions based on the above criteria resulted in reduction of both the overall prediction bias and the dispersion of the residuals for nearly all examined IMs. Despite these efforts, considerable bias persisted for sites in CBD and eastern Christchurch. The predictive capacity of the simulations in these regions is constrained by the absence of representative reference motions, among other factors.

The lack of representative enough (i.e. compatible with the target site) reference motions, and the subsequent scaling of deconvolved motions for source-to-site distance effects are considered as the primary sources of errors in the estimation of input motion and prediction of surface ground motion at a target site. Yet, discrepancies between observed and predicted ground motions are also due to bias in the evaluation of site response, in both the deconvolution at the reference sites and the convolution at the target sites. It is important to note that, because of the different methods employed in these processes (i.e. equivalent-linear analysis in deconvolution; nonlinear effective-stress analysis in convolution), some discrepancies, at least in high-frequency motion, should be expected even when the target (convolution) site coincides with the reference (deconvolution) site.

The comprehensive study on the ground response of the SMS sites serves as validation for the adopted effective-stress analysis procedure and has indicated important factors to consider in the analysis of the 55 case-history sites.

7 55 SITES: ANALYSES RESULTS AND SYSTEM-RESPONSE INTERPRETATION

7.1 Introduction

In this chapter, results from the effective-stress analyses of the 55 sites are scrutinized. The analyses were carried out following the proposed effective-stress analysis procedure in Chapter 4 and using the appropriate input motions for each site and for each considered earthquake based on the considerations and findings discussed in Chapters 5 and 6. In total, 165 effective-stress analyses were performed using one input motion for each site for the 04Sep10 earthquake and two input motions per site for the 22Feb11 earthquake.

Despite the good performance of the 04Sep10 earthquake simulations in terms of predicted surface ground motions at the SMS sites (Figs. 6.3 & 6.4), the effective-stress analyses results at some of the 55 sites were clearly problematic for this earthquake. In particular, for a significant number of sites that manifested liquefaction in the 04Sep10 earthquake, triggering of liquefaction was not predicted at any depth in the deposit by the effective-stress analyses. It is worth noting that for most of these sites the simplified analyses also under-estimate liquefaction manifestation, and the factors of safety against liquefaction triggering at the critical layers for liquefaction manifestation are only marginally lower or even higher than 1. The underestimation of the liquefaction response by the effective-stress analysis may be related to the slight underprediction of the high-frequency motion (demand), as observed in Figs. 6.3 & 6.4, and/or inaccuracies in modelling details of the stress-strain soil behaviour and liquefaction resistance (capacity). It needs to be appreciated that the 04Sep10 earthquake corresponds to a threshold demand for liquefaction triggering of the critical layers in Christchurch and, given the relatively low density (liquefaction resistance) of these critical layers which is associated with sudden increase in excess pore water pressure and liquefaction triggering, small differences in the above details can relatively easily alter the predictions of the effective-stress analysis with respect to liquefaction triggering. This is not the case for the 22Feb11 earthquake in which the seismic demand is high enough to cause liquefaction triggering early in the ground motion, for the vast majority of the investigated sites. Future work will attempt to resolve the above issue for the 04Sep10 earthquake simulations.

Given the above limitation, the system-response interpretation presented in this chapter is solely based on, and informed by, the effective-stress analyses results for the 22Feb11 earthquake. Characteristic results from the effective-stress analyses for the 22Feb11 are provided in Appendix D, for all 55 sites. The principal aim of the interpretation of these results discussed in the present chapter is to break down the complex system response of liquefiable deposits, identify and then quantify relevant interaction mechanisms and their effects, and examine their influence on the development of liquefaction throughout the deposit and its severity of manifestation at the ground surface. In this context, deposit characteristics, such as the vertical continuity of liquefiable soils and the thickness of critical zone, which were previously identified as key differentiators between the YY-sites (sites that manifested liquefaction in both 04Sep10 and 22Feb11 earthquakes) and the NN-sites (sites that did not manifest liquefaction in either event), are herein linked to certain system response effects that either intensify or mitigate liquefaction manifestation.

The chapter is organized as follows. First, the various terminologies and notations used are introduced. Then, effective-stress analyses results from selected sites are discussed in detail to illustrate characteristic examples of responses associated with different performances (severity of liquefaction manifestation). Following this initial scrutiny, a procedure for consistent analysis of the system response of liquefiable deposits and quantification of the relevant mechanisms and effects is presented. On this basis, five principal types of system responses are identified and discussed. Limitations of simplified procedures and existing frameworks for liquefaction damage evaluation are examined in the context of the identified types of system responses, and a preliminary system-response based framework for assessment of liquefaction manifestation is introduced. The scrutiny presented in this chapter highlights the important effects of system response of liquefiable deposits and demonstrates the potential for significant improvements in liquefaction damage assessment when such effects are appropriately incorporated.

7.2 Terminology and Notation

This section introduces some standard symbols and terminology that are used throughout this chapter.

The following terms are used to describe key layers and zones of interest in the deposit.

- The term *critical layer* (CL) refers to the layer of the simplified soil profile that, based on CPT profile characteristics and simplified triggering analysis, is the most likely to trigger and contribute to liquefaction manifestation at the ground surface. The critical layer has a low factor of safety, relatively low penetration resistance ($q_{c1Ncs} \approx 75 - 85$) and is typically located at shallow depth from the ground surface ($\lesssim 4$ m).
- The term *critical zone* (CZ) refers to a zone that includes the critical layer but also other layers of low liquefaction resistance (only slightly above that of the critical layer) which

are in contact with the critical layer, and hence create a vertically continuous (connected) zone of weak layers that is expected to work as a unit during the development of liquefaction and post-liquefaction through water flow and pore water pressure redistribution. If there are no low-resistance layers in contact with the critical layer, then the term critical zone (when used in such cases) simply refers to the critical layer.

- The term *triggering layer* (TL) refers to a layer of the simplified profile that is not part of the critical zone and is predicted to liquefy by the effective-stress analysis, i.e. it develops relatively large maximum shear strains ($\gamma_{max} > 1\%$).
- The term *triggering zone* (TZ) refers to a zone of interconnected triggering layers, that is, a vertically continuous zone of liquefied soil outside the critical zone. Multiple triggering zones may exist in a deposit.
- The term *nominal crust* (NC) refers to the top part of the deposit from the ground surface to the top of the shallowest liquefiable layer ($I_c < 2.6$) below the groundwater table. Thus, if the soil immediately below the groundwater table is liquefiable, the bottom of the nominal crust coincides with the groundwater table.

There are two general types of deposits identified in this study:

- Deposits with vertically continuous liquefiable soils below the water table and in the top 10 m, often simply refer to as '*Continuous*' *deposits* in this chapter, and
- *Interbedded deposits* comprising liquefiable and non-liquefiable soils in a relatively fine sequencing that does not allow the formation of thick (vertically continuous) critical zones in the top 5 to 6 m from the ground surface.

Several parameters are used to describe various layer, zone, and deposit characteristics and quantify their responses.

- A subscript of the layer/zone code in parentheses is used to indicate the layer/zone each parameter refers to. For instance, the parameters $q_{c1Ncs(TL)}$, $\gamma_{max(TZ)}$, $r_{u,max(CZ)}$, and $h_{(NC)}$ denote the corrected penetration resistance of a triggering layer, maximum shear strain computed in the triggering zone(s), maximum excess pore water pressure ratio in the critical zone, and thickness of the nominal crust, respectively.
- The subscript $(CZ - TZ)$ refers to the part of the deposit between the critical zone and the shallowest triggering zone below the critical zone. For instance, $H_{NL(CZ-TZ)}$ refers to the cumulative thickness of non-liquefiable (NL) soil between the critical zone and the shallowest triggering zone below the critical zone.
- Similarly, the subscript $(0 - z)$ refers to the part of the deposit from the ground surface to depth z below the ground surface.
- A subscript γ is used to refer to the soil portions of a zone that were predicted to liquefy in the effective-stress analysis and develop large maximum shear strains ($\gamma_{max} > 1\%$). While the triggering zone is by definition a zone of liquefied soil, the critical zone may not necessarily (and completely) liquefy in the effective stress analysis. Hence, the parameters $h_{\gamma(CZ)}$, $z_{\gamma(CZ)}$, and $I_{c\gamma(CZ)}$ with the characteristic subscript γ denote the

thickness of the liquefied part of the critical zone, the depth to the top of the liquefied part of the critical zone, and the average soil behaviour type of the liquefied part of the critical zone, respectively.

- Similarly, a subscript r_u is used to refer to soils in the deposit that develop large excess pore water pressures associated with soil liquefaction ($r_u \approx 1$). Note that soils with $r_u \approx 1$ may not have necessarily develop large maximum shear strains in the analysis (shaking-induced liquefaction). For example, the parameter $h_{r_u(CZ)}$ denotes the thickness of a vertically continuous zone of soil with $r_u \approx 1$ that includes part of the critical zone but it may also extend beyond it to include layers which did not liquefy during shaking ($\gamma_{max} < 1\%$) but liquefy due to seepage action reaching $r_u \approx 1$.
- A lowercase h denotes the thickness of a continuous soil zone with certain characteristics, whereas an uppercase H denotes the cumulative thickness of zones and layers with certain characteristics which are not necessarily connected. For instance, the parameter $H_{\gamma(TZ)}$ denotes the cumulative thickness of the various triggering zones in the deposit, whereas the parameter $h_{\gamma(TZ),max}$ refers to the maximum thickness of a connected triggering zone (with $\gamma_{max} > 1\%$).

Some additional parameters are used to characterize the timing of liquefaction, effects of liquefaction on the seismic demand, and dissipation effects in the deposit.

- The Husid function of the input motion at the base of the soil-column ($\mathcal{H}_b(t)$), defined as the cumulative Arias Intensity at a given time t normalized by the total Arias Intensity accumulated throughout the duration of shaking (e.g. Fig. 5.9), is used to express the timing of liquefaction in a reference layer/zone (e.g. CZ or TZ) relative to the temporal evolution of the intensity of the input excitation. Thus, the symbol $\mathcal{H}_{b,tr(TZ)}$ is used to denote the value of the Husid function at the base of the soil column at the time of first liquefaction triggering outside the critical zone (in the triggering zone that liquefies first). Values of $\mathcal{H}_{b,tr(TZ)}$ closer to 0 indicate early triggering of liquefaction (at an early stage of loading) in the triggering zone, whereas values of $\mathcal{H}_{b,tr(TZ)}$ approaching 1 correspond to late triggering of liquefaction (closer to the end of shaking). Similarly, $\mathcal{H}_{b,tr(CZ)}$ denotes the value of the base Husid function at the time of first liquefaction triggering in the critical zone.
- The effects of pore water pressure generation and liquefaction on the seismic demand are characterized by an Arias Intensity Ratio (AIR) defined as the ratio of the Arias Intensity demand at a given depth or layer (typically the critical layer) predicted by the effective-stress analysis to the Arias Intensity predicted at the same depth or layer by an equivalent total-stress analysis in which pore water pressure development was suppressed (while all else being equal, as the same constitutive model was used for both the effective-stress and total-stress analyses).
- Among other parameters, two depth parameters are used to describe and quantify effects from the dissipation of excess pore water pressures in the deposit. $z_{max@u_e \geq \sigma'_{vo(CZ)}}$ or simply z_{max} denotes the maximum depth in the deposit where the excess pore water

pressure has reached values equal to or greater than the initial vertical effective stress at the top of the critical zone. $z_{min@r_u \geq 0.7}$ or simply z_{min} denotes the minimum depth in the deposit where the excess pore water pressure ratio has, at some point of the analysis including during dissipation, reached or exceeded 0.7.

The various terms and notations introduced above will become clearer in the following sections once they are discussed and illustrated in the context of specific responses of deposits. The reader is advised to refer back to this section for clarifications, when deemed necessary.

7.3 Detailed Analyses Results for Selected Sites

7.3.1 Example response for a YY-site in Avondale

Figs. 7.1a and 7.1b show the simplified CPT profile (q_{c1Ncs} values and characteristic soil units based on q_c and I_c) and V_p profile, respectively, for an example site in Avondale (northeast Christchurch; CPT_29035) which manifested severe liquefaction effects (large volumes of ejected material) including lateral spreading in both 04Sep10 and 22Feb11 earthquakes (YY-site). The deposit of this site is comprised of fully saturated ($V_p > 1500$ m/s) and vertically continuous liquefiable soils below the shallow water table and includes several low resistance layers in the top 6 m. Results from simplified triggering analyses using the Boulanger and Idriss (2014) procedure, as discussed in section 3.5, are presented in Figs. 7.1c and 7.1d for both earthquakes and indicate the presence of a shallow, thick, and continuous critical zone (CZ) connecting the low resistance layers at various depths from 1.9 m to 6 m from the ground surface. The factor of safety (FS_L) in the weakest layers of the critical zone is only slightly lower than 1 in the case of the 04Sep10 earthquake but significantly lower for the 22Feb11 earthquake. Layers with similarly low or only slightly greater FS_L value than the lowest FS_L obtained for the shallow critical zone, are also present at larger depth of about 8 m. The results obtained from the simplified triggering analyses were used in the evaluation of liquefaction damage indices, LPI and LSN, with the respective predictions shown in Figs. 7.1e and 7.1f. Both indices suggest severe liquefaction effects and surface manifestation for the 22Feb11 earthquake ($LPI > 15$ and $LSN > 30$), in agreement with the observed liquefaction manifestation at this site, but they show diverging estimations of the severity of manifestation for the 04Sep10 earthquake, from none-to-minor ($LPI < 5$) to moderate-to-major ($LSN \approx 20$) manifestation.

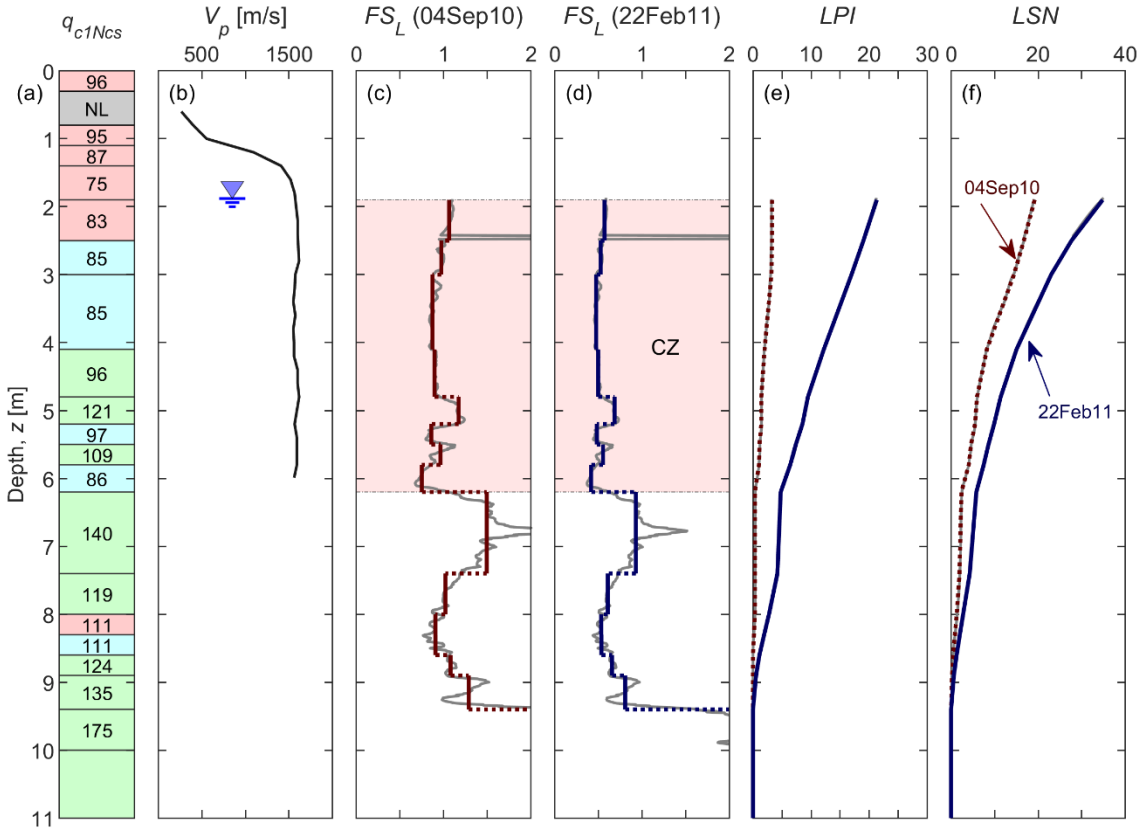

Fig. 7.1 Soil profile characteristics and simplified analysis results for the Avondale YY-site (CPT_29035): (a) q_{c1Ncs} values and characteristic soil units illustrated with different colours based on I_c (*for interpretation of the references to colour refer to section 3.4*); (b) V_p profile; (c) FS_L values for the 04Sep10 earthquake; (d) FS_L values for the 22Feb11 earthquake and identified critical zone (CZ); (e) LPI; (f) LSN, for the top 11 m of the deposit.

Results from effective-stress analysis of the Avondale site for the 22Feb11 earthquake are illustrated in Fig. 7.2 in terms of acceleration and excess pore water pressure (u_e) time histories at selected depths. Excess pore water pressures develop rapidly in the critical zone ($z = 3.8$ m) and also in the deeper weak soil layers ($z = 8.2$ m), below the critical zone. Liquefaction is triggered ($u_e \approx \sigma'_{vo}$) within the first two strong acceleration cycles from approximately 5.5 to 8 s (of the computational time) first in the critical zone, but also almost concurrently in the deeper soils below the critical zone. Effects of liquefaction are evident in the acceleration time-series at the ground surface with the abrupt change in the frequency content and reduction of acceleration amplitudes following initial liquefaction. Pore water pressure redistribution through upward flow of water can be clearly seen in the u_e time-histories following the end of strong shaking after about $t = 20$ s. Migration of pore water from areas of higher hydraulic head (higher excess pore water pressure) towards areas with lower hydraulic head (lower excess pore water pressure) is manifested in the gradual reduction of excess pore water pressure in the deeper triggering zone which developed the highest excess pore water pressure in the deposit ($u_e \approx 90$ at $z = 8.2$ m), the prolonged state of liquefaction ($u_e \approx \sigma'_{vo}$) in the critical zone ($z = 3.8$ m) as it is subjected to a continuous

supply of water from deeper soils of higher hydraulic head, and the gradual increase of excess pore water pressure above the critical zone ($z = 2.3$ m) due to upward flow of water from the liquefied critical zone towards the ground surface.

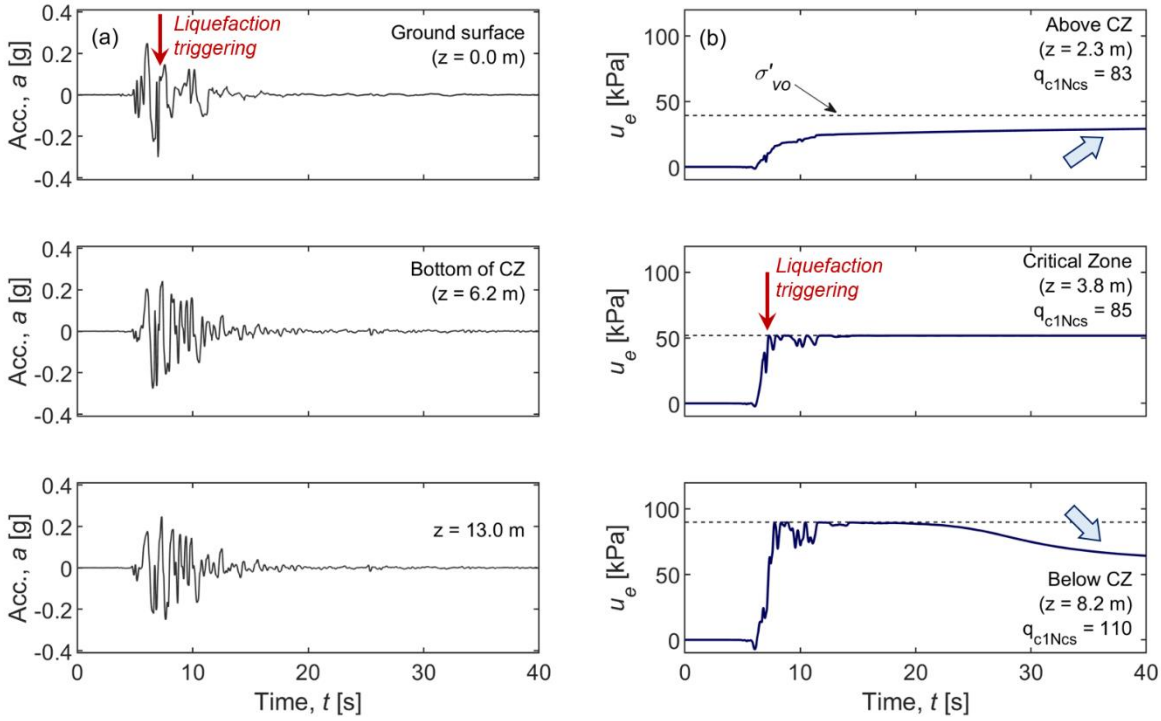

Fig. 7.2 Effective-stress analysis results at selected depths for the Avondale YY-site: (a) acceleration time histories; (b) excess pore water pressure time histories.

Fig. 7.3 illustrates excess pore water pressures at specific time sections and computed maximum shear strains in the effective stress analysis for the Avondale site throughout the top 11 m of the deposit. The u_e isochrones in Fig. 7.3b correspond to the time of first triggering of liquefaction in the deposit ($t_{tr(CZ)} \approx 7.2$ s), which occurs simultaneously in the two layers of the CZ with the lowest FS_L (Fig. 7.1d), and the time of liquefaction triggering in the deeper triggering zone ($t_{tr(TZ)} \approx 7.8$ s) at 8 m. The triggering of liquefaction occurs first in the critical zone when about half of the energy of the input excitation $(\mathcal{H}_{b,tr(CZ)} = 0.49)$ has been transmitted to the soil-column, whereas the triggering zone at depth liquefies when $\mathcal{H}_{b,tr(TZ)} = 0.61$. Note in Fig. 7.3b that when the deeper triggering zone liquefies, the majority of the critical zone is already at a liquefied state ($u_e \approx \sigma'_{vo}$). The liquefied critical zone (Fig. 7.3c) is characterized by relatively shallow depth ($z_{\gamma(CZ)} = 2.5$ m), large thickness ($h_{\gamma(CZ)} = 3.7$ m), and development of large maximum shear strains ($\gamma_{max(CZ)} > 3\%$, predominantly $4 - 6\%$). Slightly less severe liquefaction effects develop in the higher resistance ($q_{c1Ncs(TZ)} \approx 110$) triggering zone at $z_{\gamma(TZ)} = 8$ m with a total thickness of liquefaction $h_{\gamma(TZ)} = 0.6$ m and $\gamma_{max(TZ)}$ somewhat smaller than $\gamma_{max(CZ)}$.

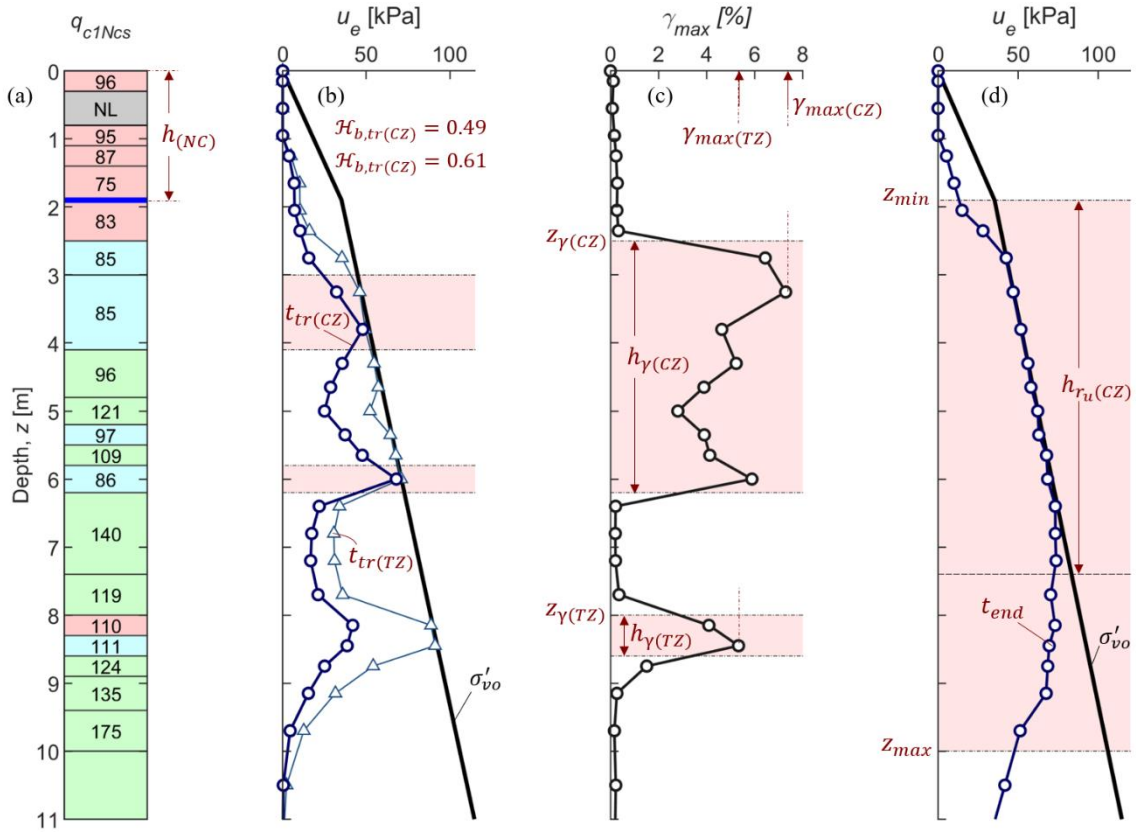

Fig. 7.3 Key response characteristics and parameters for the Avondale YY-site in the effective stress analysis: (a) soil profile; (b) excess pore water pressures at specific time sections, $t_{tr(CZ)} = 7.2$ s and $t_{tr(TZ)} = 7.8$ s; (c) computed maximum shear strains; (d) excess pore water pressures during dissipation ($t_{end} = 31$ s), for the top 11 m of the deposit.

Following the end of the strong shaking, the water flow resulting from the dissipation of the excess pore water pressures causes an additional disturbance of the already liquefied soil in the critical zone and also an increase in the excess pore water pressures of soils which are in contact with the critical zone both below and above it (Fig. 7.3d). The critical liquefied zone is therefore 'expanded' forming a continuous zone of $u_e \approx \sigma'_{vo}$ with a total thickness of $h_{r_u(CZ)} \approx 5.5$ m. Excess pore water pressures with $r_u = u_e/\sigma'_{vo} \geq 0.7$ develop up to a minimum depth of $z_{min} = 1.9$ m from the ground surface, for the considered analysis duration (~400 s). Also, high excess pore water pressures in excess of those at the top of the critical zone ($u_{e(CZ)}$) have been developed up to a depth of $z_{max} = 10$ m. These deeper soils of high excess pore water pressure will supply additional water and sustain the upward inflow of water into the continuous 'liquefied' zone and further towards the ground surface. In effect, the entire deposit below the groundwater table from $z_{max} = 10$ m to $z_{min} = 1.9$ m is vertically connected through the high excess pore water pressures and water flow, and contribute to the severity of liquefaction manifestation at the ground surface. The nominal crust above the groundwater table has a relatively small thickness ($h_{(NC)} = 1.9$ m) and is largely composed of liquefiable materials. For such ground conditions, it is anticipated that the liquefiable crust layer will be subject to seepage-induced liquefaction and

cracking/fissuring under the hydraulic pressures from the upward water (fluidized soil) flow, and therefore, the 'crust' cannot have any mitigating effects on the liquefaction manifestation at the ground surface.

It is important here to recognize the limitations of the effective-stress analysis in accurately simulating specific liquefaction phenomena and soil response characteristics in different phases of the response (e.g. in the post-triggering phase and particularly during the post-liquefaction re-consolidation). As the soil approaches a state of zero effective stress and its phase transforms, from a solid into a fluidized state, key parameters of the reconsolidation process, such as the soil compressibility and hydraulic conductivity can change dramatically and be further exacerbated due to effects of void redistribution, and development of nonuniformities and discontinuities through layers and the deposit as a whole. Such dramatic changes in the post-liquefaction response of the soil (deposit) cannot be rigorously considered in the dynamic effective stress analysis based on the continuum approach. Hence, the above description of the dissipation effects on the deposit and the reported values for the parameters used to quantify the relevant mechanisms are only indicative of what may (and is anticipated to) actually occur during the dissipation process. In fact, the dissipation effects can be much more dramatic as larger amounts of water are expelled from the liquefied soils and at a higher rate than that predicted by the effective stress analysis. With this background in mind, a reduced threshold value of $r_u = 0.7$ has been herein adopted to define z_{min} and $h_{r_u(CZ)}$ (Fig. 7.3d) and to approximately indicate areas that develop high excess pore water pressures during the reconsolidation phase and are likely to undergo seepage-induced liquefaction. Specific criteria for hydraulic fracturing and creation of discontinuities for different crust conditions and deposit responses are beyond the scope of this thesis.

7.3.2 Example response for an NN-site in Hoon Hay

Fig. 7.4 presents the simplified CPT profile (q_{c1Ncs} values and characteristic soil units), V_p profile, and simplified analyses results ($FS_L, LPI,$ and LSN) for an example site in Hoon Hay (southwest Christchurch; CPT_36417) which did not manifest liquefaction in any of the events of the Canterbury earthquake sequence (NN-site). The top 11 m of the soil deposit consist of interbedded liquefiable soils (silty sands, non-plastic or low-plasticity silts) of low tip resistance and non-liquefiable plastic silts. The measured V_p values from the cross-hole test show effects of partial saturation ($V_p < 1500$ m/s) in the deposit from the ground surface up to a depth of about 4.4 m including the shallowest liquefiable layer at 2.7 m depth. Assuming full saturation below the groundwater table, the simplified triggering analyses predict low FS_L, less than 0.5 for the 04Sep10 earthquake and less than 0.4 for the 22Feb11 earthquake, for all liquefiable layers in the deposit. The shallowest of these layers at 2.7 m depth is hence considered as the critical layer (zone) for liquefaction manifestation at the ground surface. The LPI values calculated using the results from the triggering analyses (again without considering the effects of partial saturation on CRR) indicate severe liquefaction manifestation for both earthquakes ($LPI > 15$), whereas somewhat reduced effects (major liquefaction manifestation) are estimated based on LSN ($20 < LSN < 30$). Yet, both indices

heavily over-estimate the liquefaction manifestation at the Hoon Hay site, for both earthquakes, as no liquefaction effects were observed at the site.

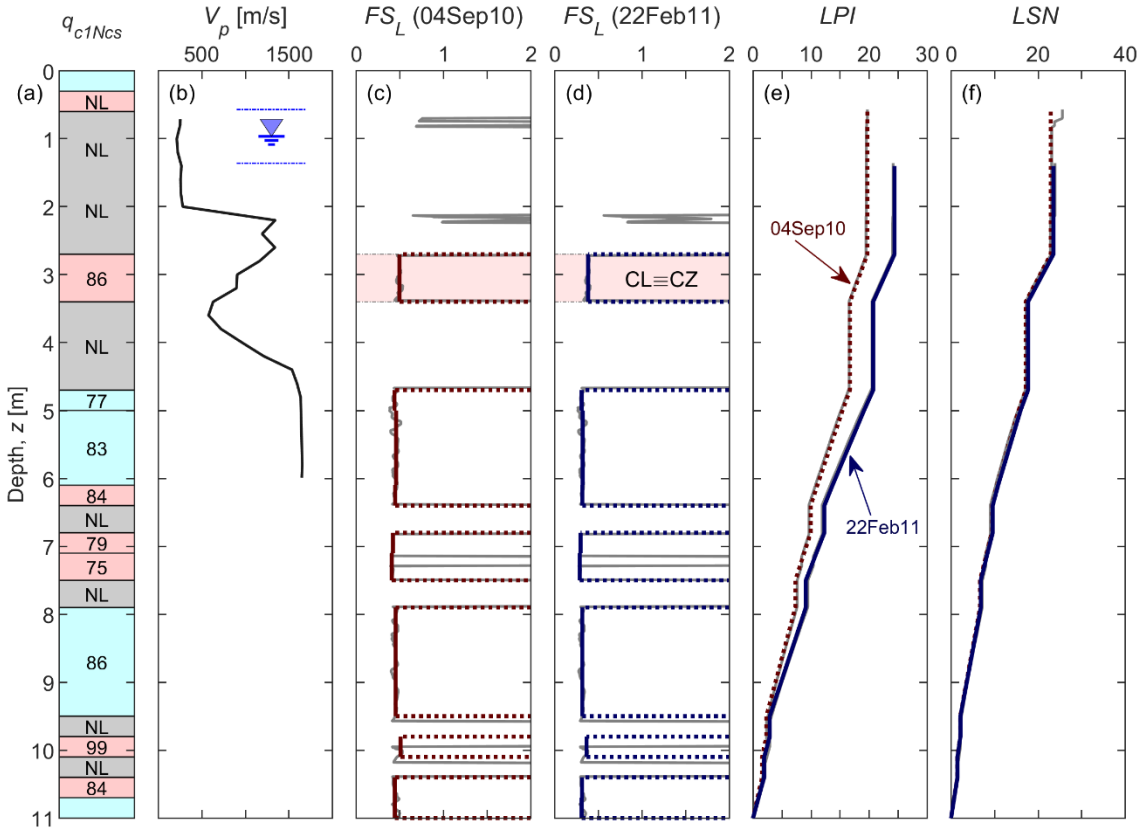

Fig. 7.4 Soil profile characteristics and simplified analysis results for the Hoon Hay NN-site: (a) q_{c1Ncs} values and characteristic soil units illustrated with different colours based on I_c (*for interpretation of the references to colour refer to section 3.4*); (b) V_p profile; (c) FS_L values for the 04Sep10 earthquake; (d) FS_L values for the 22Feb11 earthquake and identified critical layer/zone; (e) LPI; (f) LSN, for the top 11 m of the deposit; *effects of partial saturation ($V_p < 1500\ m/s$) on the CRR of the critical layer have not been considered in the calculation of FS_L and damage indices.*

Fig. 7.5 shows characteristic acceleration and excess pore water pressure time histories obtained from the effective-stress analysis of the Hoon Hay site using an LPCC-based input motion for the 22Feb11 earthquake. In addition, characteristics of the computed response throughout the depth of the deposit in terms of excess pore water pressures, Arias Intensity, and maximum shear strains are illustrated in Fig. 7.6.

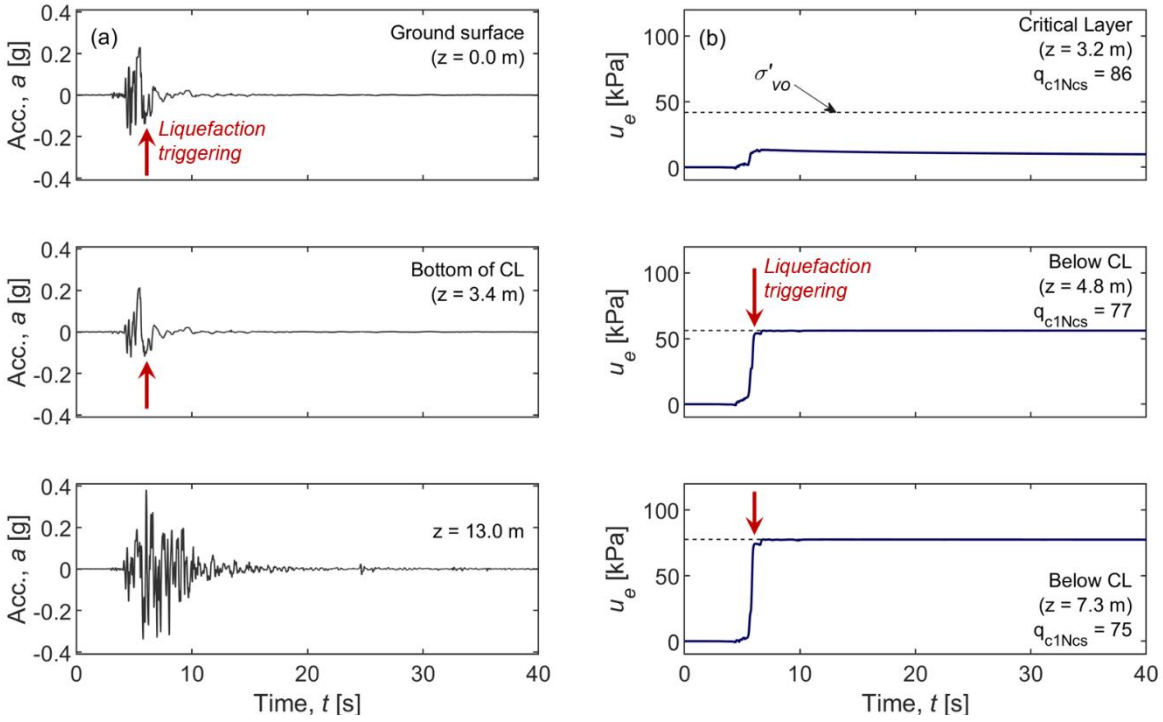

Fig. 7.5 Effective-stress analysis results at selected depths for the Hoon Hay NN-site: (a) acceleration time histories; (b) excess pore water pressure time histories.

Due to the close proximity of the Hoon Hay site to the causative fault of the 22Feb11 earthquake and the shallow depth to the volcanic bedrock, high accelerations reach the shallow part of the deposit at 13 m (Fig. 7.5a). The high seismic demand induces liquefaction first in the two layers with the lowest tip resistance ($q_{c1Ncs(TZ)} = 75 - 77$; as shown in Fig. 7.6b) in the deposit within the first 2-3 seconds of strong shaking, when $\mathcal{H}_{b,tr(TZ)}$ is only 0.21. As illustrated in Fig. 7.5b, the excess pore water pressures in the first two triggering layers increase abruptly from 0 to σ'_{vo} and remain practically at σ'_{vo} for the remaining part of the excitation, a response indicative of the highly contractive behaviour of the soil in these loose layers. Large maximum shear strains ($\gamma_{max(TZ)}$) in excess of 8% develop in the two loosest layers, whereas maximum shear strains associated with triggering of liquefaction develop also in a number of other layers resulting in cumulative thickness of liquefied soil (outside the critical zone) $H_{\gamma(TZ)} = 4.6$ m between $z_{\gamma(TZ)} = 4.7$ m and 11 m. The combination of a significant high-frequency content in the input excitation and the early triggering of liquefaction in loose and relatively thick zones results in a liquefaction-induced 'seismic isolation' effect where, upon triggering of liquefaction in the loose layers at depth, strong de-amplification of the high-frequency shear waves takes place in the triggering zones resulting in reduced seismic demand for the overlying soils. This is clearly illustrated in Fig. 7.6c where the Arias Intensity demand in the critical layer predicted by the effective-stress analysis is seen to be only 16% of that predicted by an equivalent total-stress analysis ($AIR_{(CL)} = 0.16$). This extreme reduction of the seismic demand in the critical layer, in conjunction with partial saturation effects $\left(V_{p(CL)} \approx 900 \text{ m/s}\right)$ on its CRR, which is now modelled in the effective-stress analysis as per Fig. 4.8, effectively prevent occurrence of

liquefaction in the critical layer during shaking. In addition, the presence of thick non-liquefiable layers above the shallowest triggering layer $\left(H_{NL(CZ-TZ)} = 1.3 \text{ m}\right)$ does not allow any seepage effects $(z_{min} = z_{\gamma(TZ)})$ and vertical 'communication' of excess pore water pressures between the triggering zones and the critical layer. Minor excess pore water pressures and shear strains develop in the critical layer ($r_{u(CL)} = 0.3$ and $\gamma_{max(CL)} = 0.3\%$). This effectively results in a non-liquefied (stiff) crust from the ground surface to $z_{min} =$ 4.7 m, the majority of which ($H_{NL(0-z_{min})} = 3.4$ m) is comprised of non-liquefiable soils. Under these conditions, the liquefaction at depth below 4.7 m would be unlikely to manifest at the ground surface for the level of the seismic demand imposed by the 22Feb11 earthquake (i.e. M_w6.2 event with a relatively small number of significant cycles or short duration of strong shaking).

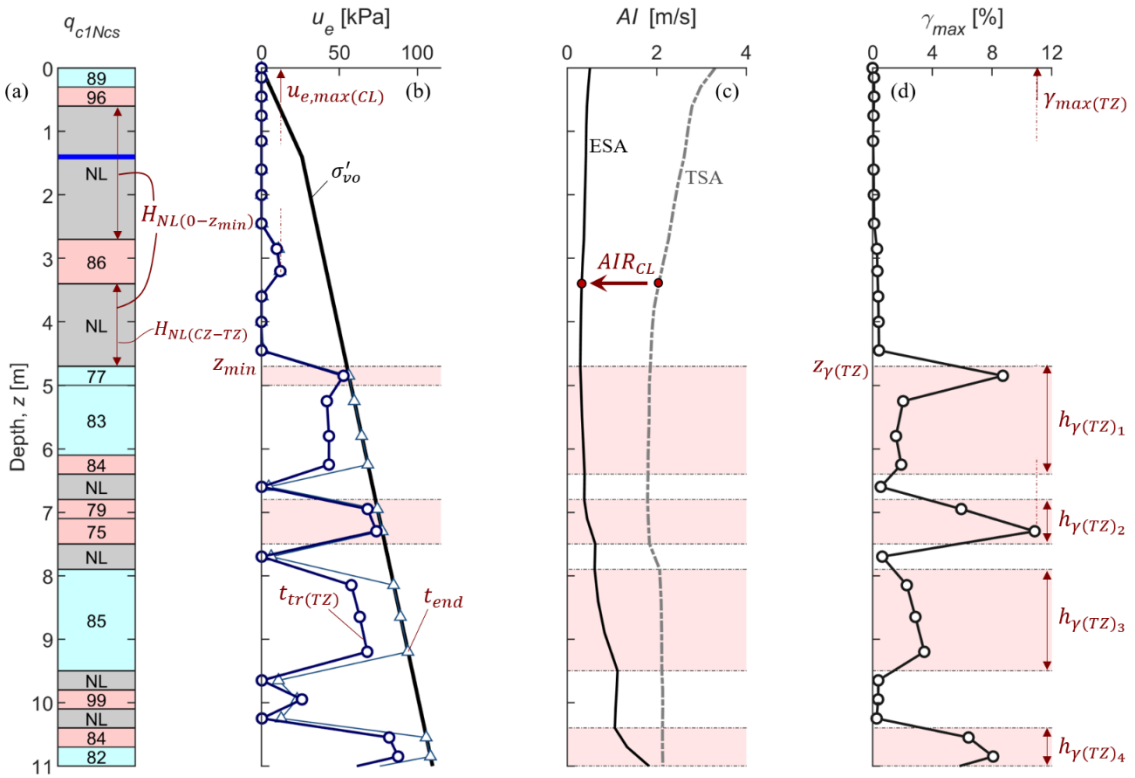

Fig. 7.6 Key response characteristics and parameters for the Hoon Hay NN-site in the effective stress analysis: (a) soil profile; (b) excess pore water pressures at specific time sections, $t_{tr(TZ)} \approx 6$ s and $t_{end} \approx 15$ s (end of shaking); (c) Arias Intensity from the effective-stress analysis (ESA) and an equivalent total stress analysis (TSA); (d) computed maximum shear strains, for the top 11 m of the deposit.

Fig. 7.7 compares side-by-side key characteristics of the responses of the above described YY (Avondale) and NN (Hoon Hay) sites. Both sites are subjected to high input demand, undergo liquefaction and develop large ground deformations with peak horizontal displacements at the ground surface ($D_{cyc,max}$) in the order of 15 to 20 cm, relative to the ground displacement at 11 m depth. Note that this amount of relative horizontal displacements for the demand levels of the 22Feb11 earthquake is generally consistent with observations from vertical array

records at liquefied sites from other historical events (e.g. Pease and O'Rourke 1997, Cubrinovski et al. 2000). A critical difference in the responses of the YY- and NN-sites is the location of liquefaction in the subsurface profile. In the NN-site (Fig. 7.7b), severe liquefaction occurs within weak layers at relatively large depths and results in a substantial reduction in the demand for the critical layer at shallow depth. In the YY-site (7.7a), severe liquefaction occurs in the critical zone at shallow depth. The triggering of liquefaction in the deeper denser layers occurs later in the ground motion and has only minor effect on the demand reaching the critical zone. This difference in the depth of liquefaction occurrence is critical for the manifestation of liquefaction at the ground surface and the impacts on shallowly founded structures and buried utilities (e.g. embedment depths of the potable water and wastewater pipelines in Christchurch are generally less than 3.5 m from the ground surface). Note, however, that the responses of the two sites could have been equally damaging to pile-supported structures with their foundations extended through the liquefied zones, but such structures were not present in the residential areas encompassing the studied sites. In addition to the location of shaking-induced liquefaction in the soil profile, the vertical communication of the developed excess pore water pressures in the case of the YY-deposit which is composed of vertically continuous liquefiable soils, or the absence of it in the case of the interbedded NN-deposit, is another critical factor for the severity of liquefaction manifestation at the ground surface that differentiates between the performances of YY and NN sites.

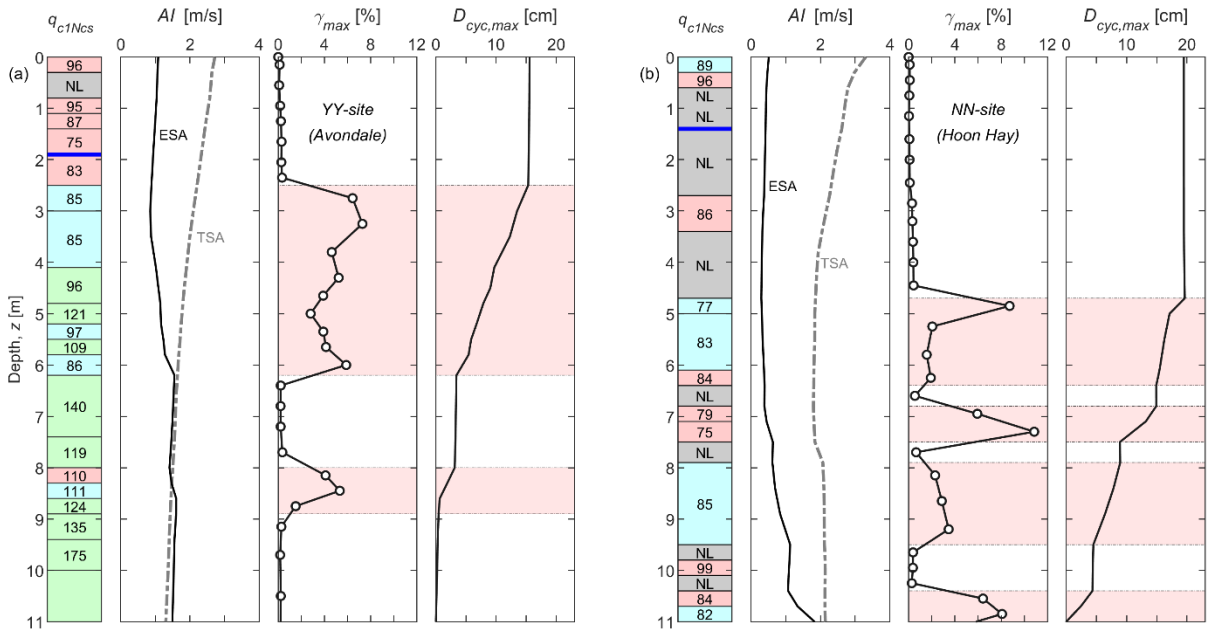

Fig. 7.7 Comparison of Arias Intensity, maximum shear strain, and maximum horizontal displacement (relative to the ground displacement at 11 m) profiles obtained from the effective stress analyses: (a) Avondale YY-site (left); (b) Hoon Hay NN-site (right).

7.3.3 Example responses for two NY-sites

The responses of two NY-sites, i.e. sites that did not manifest liquefaction in the 04Sep10 earthquake but did manifest in the 22Feb11 earthquake, are discussed in this subsection. One site is in Hoon Hay (CPT_57340; at about 1 km distance from the NN-site discussed in the previous section) and manifested minor liquefaction in the 22Feb11 earthquake, whereas the other site is in Shirley suburb (northeast Christchurch; CPT_57366) and manifested severe liquefaction in the 22Feb11 event.

Effective stress analyses results for the Hoon Hay site are shown in Fig. 7.8 in terms of u_e and γ_{max} for the top 11 m of the deposit, for both 04Sep10 and 22Feb11 earthquake simulations. Different types of response are observed in the two simulations.

In the analysis for the 04Sep10 earthquake, liquefaction is first triggered in the low tip resistance ($q_{c1Ncs(TL)} = 74$) silt layer at $z_{\gamma(TZ)} = 4.8$ m depth. Two additional low tip resistance layers at depths from 8.5 m to 9.3 m also liquefied at a later stage of shaking. The liquefied loose layers develop large maximum shear strains ($\gamma_{max(TZ)} \approx 7.5 - 9\%$) and have relatively small cumulative thickness of $H_{\gamma(TZ)} = 1.1$ m. For the 04Sep10 earthquake, no liquefaction triggering is predicted in the critical zone. A thick crust is therefore formed from the ground surface to $z_{min} = z_{\gamma(TZ)} = 4.8$ m with large cumulative thickness of non-liquefiable soil $H_{NL(0-z_{min})} = 2.8$ m and insignificant pore water pressure response developing in the shallow liquefiable soils. The predicted response of the considered NY-site to the 04Sep10 earthquake can explain the absence of liquefaction manifestation for this earthquake.

In the 22Feb11 earthquake simulation, liquefaction is triggered at an early stage of loading simultaneously in the critical zone and in the deeper (triggering) zone (*co-triggering*). The higher demand of this earthquake in the immediate near-source region causes liquefaction of nearly all liquefiable soils in the shallow deposit resulting in cumulative thickness of liquefied soil $H_{\gamma(TZ)} = 3.7$ m below the critical zone and $h_{\gamma(CZ)} = 0.7$ m in the critical zone. A thick non-liquefiable layer of thickness $H_{NL(CZ-TZ)} = 1.9$ m separates the critical zone from the deeper triggering zone, thus preventing the formation of continuous thick liquefied zones through vertical 'communication' of their excess pore water pressures. Seepage effects in the crust above the critical zone are also restricted by the presence of non-liquefiable soils with total thickness $H_{NL(0-z_{min})} = 0.9$ m. The small thickness of the critical zone and the absence of system-response mechanisms that could intensify the severity of liquefaction manifestation at the ground surface can explain the minor liquefaction manifestation observed at this site after the 22Feb11 earthquake.

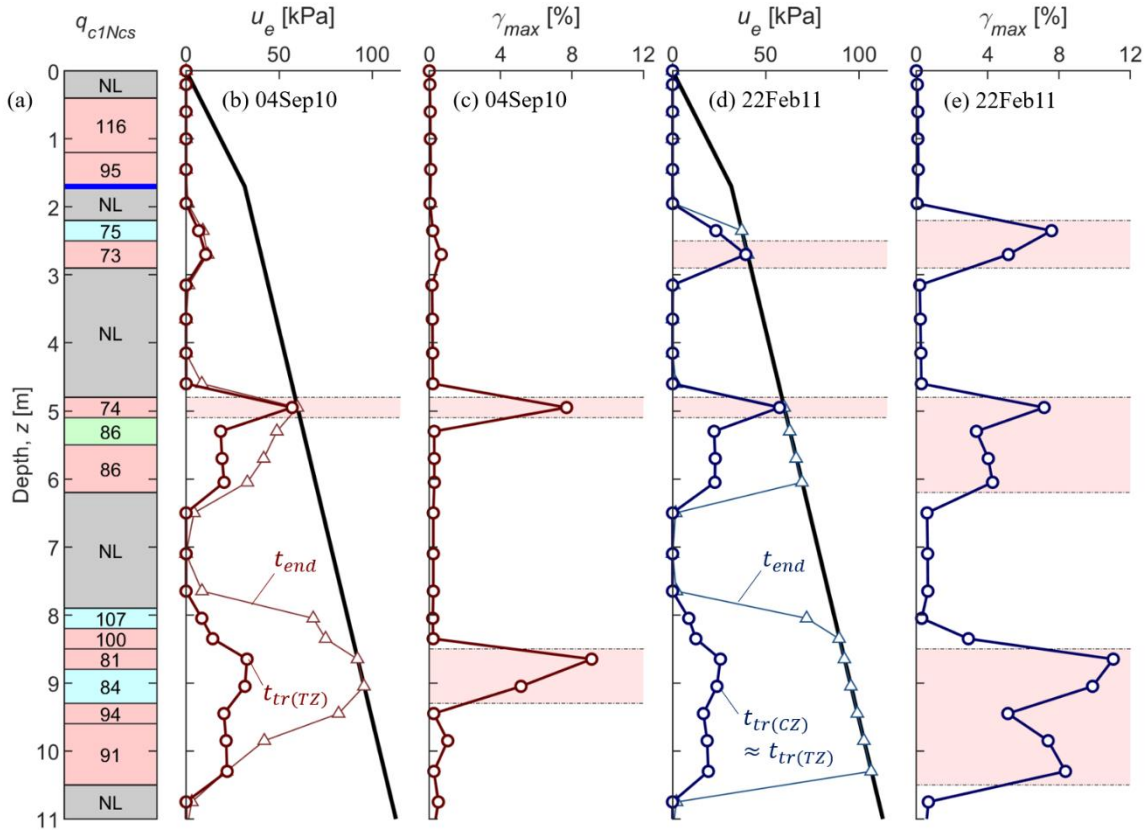

Fig. 7.8 Key response characteristics for the Hoon Hay NY-site (CPT_57340): (a) soil profile; (b) excess pore water pressures at specific time sections, $t_{tr(TZ)}$ and t_{end} (end of shaking) for the 04Sep10 earthquake; (c) computed maximum shear strains for the 04Sep10 earthquake; (d) excess pore water pressures at specific time sections, $t_{tr(TZ)} \approx t_{tr(CZ)}$ and t_{end} (end of shaking) for the 22Feb11 earthquake; (e) computed maximum shear strains for the 22Feb11 earthquake, for the top 11 m of the deposit.

Key characteristics of the response of the Shirley site to the 22Feb11 earthquake are illustrated in Fig. 7.9. This site has a critical zone of relatively low tip resistance layers ($q_{c1Ncs(CZ)} = 84 - 111$) at depths from 3.2 m to 4.6 m. Low tip resistance ($q_{c1Ncs} = 78 - 89$) liquefiable layers are also encountered at greater depths, from 6.7 to 7.5 m from the ground surface. Importantly, the deposit is entirely composed of liquefiable soils below the nominal crust. The effective-stress analysis for the 22Feb11 earthquake predicts triggering of liquefaction first in the layer with the lowest q_{c1Ncs} at 6.7 m depth. The relatively high demand in this earthquake extended the liquefaction front over a triggering zone of thickness $h_{\gamma(TZ)} = 1.5$ m which includes the first triggering layer as well as adjacent layers of low tip resistance. Large maximum shear strains in excess of 4% developed throughout this liquefied zone. The development of liquefaction at depth results in a substantial reduction of the seismic demand for the overlying layers. Consequently, the Arias Intensity reaching the critical zone at 4.5 m depth is only 33% of that corresponding to an equivalent total stress analysis ($AIR_{(CZ)} = 0.33$). As a result of this significant reduction in the demand, the critical zone does not liquefy during the shaking and develops only limited maximum shear strain ($\gamma_{max(CZ)} = 0.3\%$). However, significant excess pore water pressures develop in the critical

zone due to dissipation of excess pore water pressures from the liquefaction in the deeper triggering zone. In fact, following the end of strong shaking, a continuous zone with $u_e \approx \sigma'_{vo}$ is formed from $z_{min} = 3.2$ m to about 8 m depth. This $h_{r_{u(CZ)}} \approx 5$ m thick zone includes both the deeper triggering zone and the shallower critical zone, as well as in-between layers of higher penetration resistance. As large amounts of water seep out of the triggering zone towards the shallower soils, severe liquefaction effects including large shear strains (if earthquake shaking has not been completely ceased during this process), and consequently large re-consolidation volumetric strains may take place also in the shallow soils which were not predicted to liquefy during the strong shaking. The presence of the impervious non-liquefiable layer atop the critical zone can further exacerbate these effects by impeding the dissipation of excess pore water pressures towards the ground surface ('water film' effect) which may prolong the duration of high excess pore water pressures in the $h_{r_{u(CZ)}}$ zone. The large thickness of soils affected by high excess pore water pressures, vertical continuity of liquefaction, and the potentially severe effects induced by seepage and void redistribution can explain the severe liquefaction manifestation observed at the Shirley site after the 22Feb11 earthquake. No triggering of liquefaction was predicted in the 04Sep10 earthquake simulation for this NY-site.

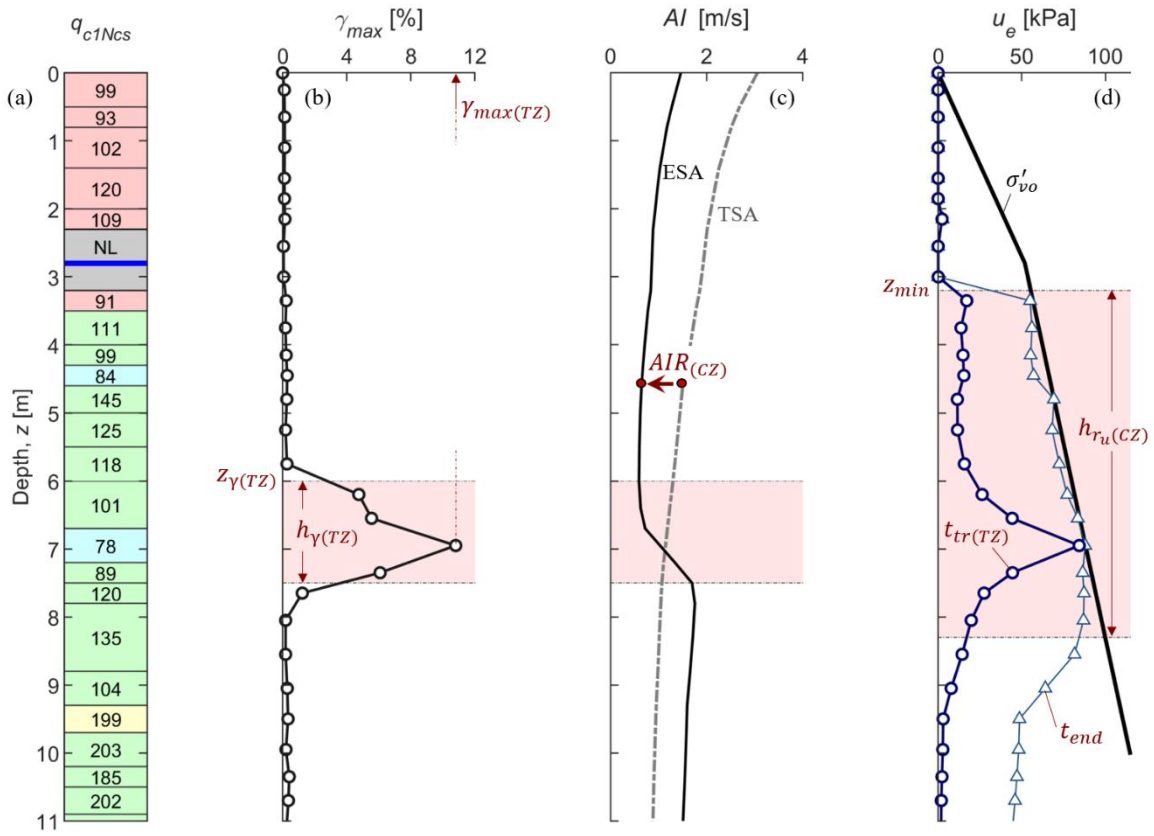

Fig. 7.9 Key response characteristics and parameters for the Shirley NY-site (CPT_57366): (a) soil profile; (b) computed maximum shear strains; (c) Arias Intensity from the effective-stress analysis (ESA) and an equivalent total stress analysis (TSA); (d) excess pore water pressures at specific time sections, $t_{tr(TZ)}$ and t_{end} (end of shaking), for the top 11 m of the deposit.

7.4 Analysis and Quantification of System Response

The above detailed scrutiny of the effective-stress analyses results was applied to all 55 sites. Lessons learned from this exercise were used to develop a procedure that can be consistently used, for all types of deposits and their specific responses, to break down the system response mechanisms and quantify their effects on the evolution and manifestation of liquefaction. The developed procedure for the analysis and quantification of system response is illustrated in the flow chart of Fig. 7.10.

Several steps are involved in the adopted procedure. The first step entails the determination of the critical layer (CL) and critical zone (CZ) in the deposit. To this end, CPT profile characteristics and a simplified triggering analysis are used to identify the layers with the lowest factors of safety and their location within the deposit (depth from the ground surface). Key considerations involved in the selection of critical layers (zones) and illustrative examples have been discussed in Chapter 3. Then, the timing of liquefaction triggering in the critical zone ($\mathcal{H}_{b,tr(CZ)}$) and the timing of first liquefaction triggering outside the critical zone ($\mathcal{H}_{b,tr(TZ)}$) are identified. If liquefaction is first triggered outside the critical zone and the liquefaction effects in the triggering zone(s) are substantially more severe than the effects in the critical zone, e.g. there is either no triggering of liquefaction or 'marginal' liquefaction associated with late triggering ($\mathcal{H}_{b,tr(TZ)} \ll \mathcal{H}_{b,tr(CZ)}$), then the deeper liquefaction of the triggering zones is expected to dominate the system response. In this case (deep liquefaction), the subsequent steps in the analysis are primarily focused on quantifying the mechanisms governed by deep liquefaction. Otherwise, in cases when liquefaction is either triggered first in the critical zone or simultaneously (with small difference in $\mathcal{H}_{b,tr}$) triggered in the critical and triggering zones (shallow liquefaction), the quantification starts from the liquefied critical zone, and then proceeds with the evaluation of potential intensifying and mitigating mechanisms, from below and above it. In either case, all identified mechanisms of system response can be quantified and the distinction between S (for shallow liquefaction) and D (for deep liquefaction) simply provides more logical pathways to interpret and relate the sequence of different mechanisms and their compound effects on the deposit response and liquefaction manifestation at the ground surface.

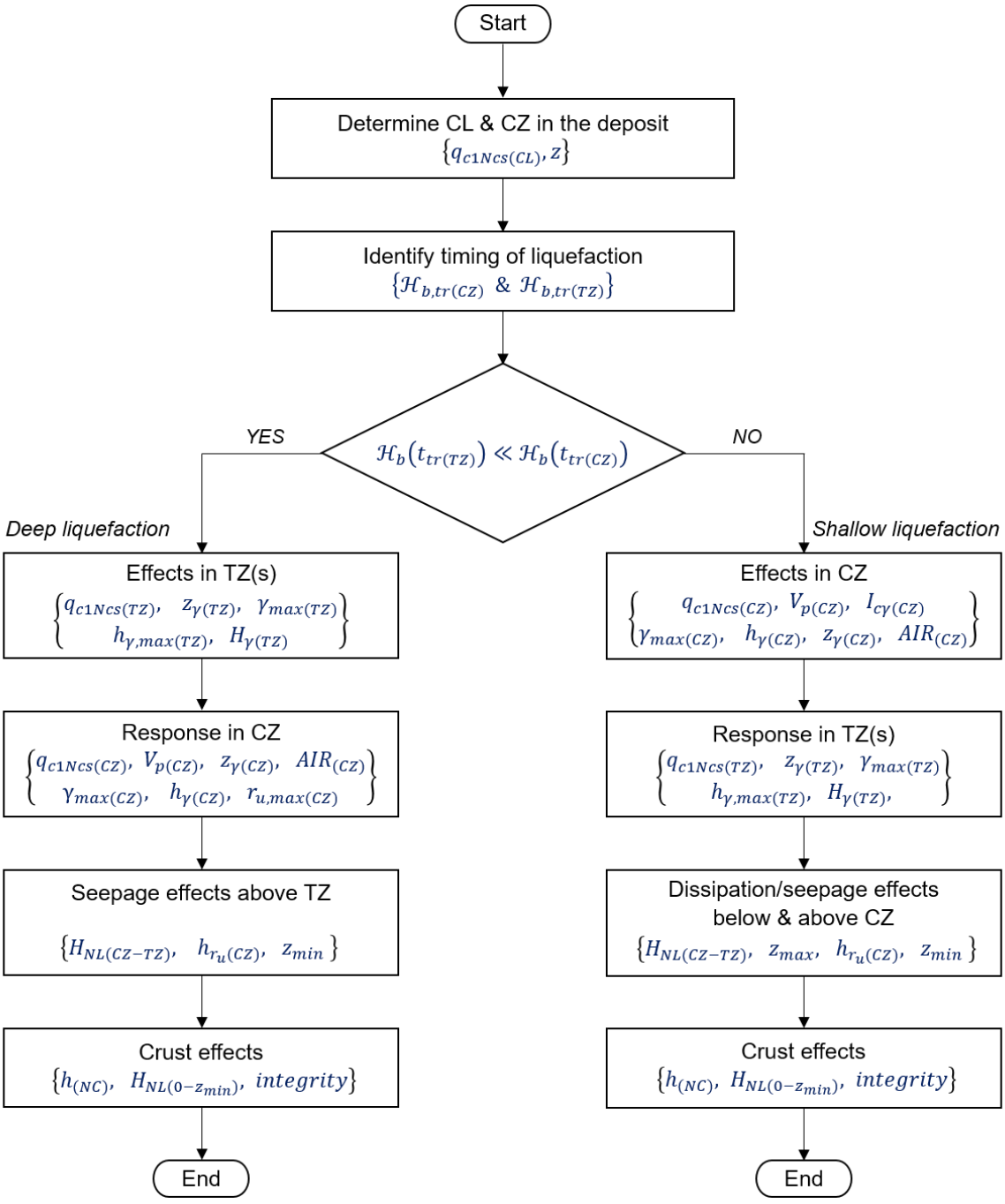

Fig. 7.10 Analysis and quantification of system response: sequence of steps and quantification parameters.

7.5 **Characteristic Types of System Response**

Consistent application of the developed procedure to the effective-stress analyses results for the 55 sites led to the identification of clusters of sites with similar response characteristics (i.e. similar values for the majority of the parameters used in the quantification). The identified clusters were organized into the following main types of system response:

- Shallow liquefaction in vertically 'Continuous' deposit (*SC-response*), where the most severe liquefaction effects occur in the critical zone at shallow depth and the deposit is largely composed of vertically continuous liquefiable soils.
- Deep liquefaction in 'Interbedded' deposit (*DI-response*), where triggering of liquefaction occurs only at a relatively large depth and the deposit consists of interbedded liquefiable and non-liquefiable soils.
- Shallow liquefaction in 'Interbedded' deposit (*SI-response*), where liquefaction may be triggered in multiple zones including the critical zone (co-triggering), but the various liquefied zones are separated by interbedded non-liquefiable soils.
- Deep liquefaction in 'Continuous' deposit (*DC-response*), where the most severe liquefaction effects occur during shaking at relatively large depth and the deposit is composed of vertically continuous liquefiable soils below the nominal crust.
- No Triggering (*NT-response*), where liquefaction triggering does not occur at any depth in the deposit.

The detailed classification of the 55 sites into the above types of system response is given in Table D1 of Appendix D, while a summary of this classification is presented below in Table 7.1, for the 22Feb11 earthquake. The majority of the YY-sites are classified under the SC-response, whereas the DI-response and SI-response types share the majority of the NN-sites. The transient NY-sites are spread across the entire spectrum of system-response types, but the majority of these sites lie under types SC and SI. Note that the classification presented in Tables 7.1 & D1 as well as the response characteristics discussed in the following subsections are based on the analyses cases with the input motion that induces the higher demand in the deposit. While, by and large, the same trends are observed using the analyses cases with the alternative input motion, the exact number of sites under each type of system response and the values for the quantification parameters reported in the following subsections may slightly differ.

Table 7.1 Classification of 55 sites based on manifestation and type of system response.

Liquefaction manifestation	Type of System Response				
	SC	DC	SI	DI	NT
YY (15 sites)	10 (+2) [a]	3	0	0	0
NY (23 sites)	1 (+9)	3	5	2	3
NN (17 sites)	0	(1)	7	8	1

[a] Numbers in parentheses refer to sites with slight deviations from the 'standard response characteristics' of the respective response type, as explained in the relevant subsections.

Typical deposit features and response characteristics associated with each of the identified types of system response are summarized in Figs. 7.11–7.14. The following subsections describe key system response processes and effects involved in each of the five identified types of system response.

7.5.1 SC-Response: Shallow Liquefaction in 'Continuous' Deposit

The following processes are involved in the 'standard' SC-response (Fig. 7.11).

(1) Liquefaction is triggered first in the weakest layers of the shallow critical zone ($q_{c1Ncs(CZ),min} \approx 75-95$). Occasionally, when weak layers ($q_{c1Ncs(TZ)} \approx 100-110$) are present also at larger depth, 'co-triggering' may occur in which case liquefaction triggering occurs concurrently in both the critical zone and a deeper triggering zone at about the same time. In such cases of co-triggering, the triggering occurs relatively late in the ground motion $(\mathcal{H}_{b,tr(TZ)} > 0.6)$.

(2) After the first triggering, liquefaction quickly spreads over the critical zone and large maximum shear strains ($\gamma_{max(CZ)}$) develop in the critical zone during the strong shaking. The large shear strains ($\gamma_{max(CZ)} > 3\%$) reflect the relatively loose soils with low penetration resistance in the critical zone. The depth to the top of the liquefied critical zone ($z_{\gamma(CZ)}$) is shallow and varies from 1.5 to 3.5 m. The thickness of shaking-induced liquefaction in the critical zone ($h_{\gamma(CZ)}$) is typically greater than 2 m. The soil behaviour type in the liquefied critical zone is characterized by $I_{\gamma c(CZ)}$ values between 1.7 and 2.

(3) The triggering zone at depth $z_{\gamma(TZ)} \approx 7-9$ m, when present, has relatively small thickness ($h_{\gamma(TZ)} \approx 0.5-1$ m) and, because of the late triggering and less severe liquefaction effects in this zone, it has only minor effects on the seismic demand in the critical zone ($AIR_{(CZ)} > 0.85$). However, it causes additional disturbance and prolonged fluidization of the critical zone through seepage action and upward flow of large amount of water into the critical zone. Even in the absence of a deeper liquefaction (i.e. triggering zone) excess pore water pressures higher than the initial vertical effective stress at the top of the critical zone develop up to large depths substantially below the critical zone ($z_{max} > 8$ m). These high excess pore water pressures in the deeper soils supply additional water into the critical zone, sustain the upward flow of water towards the ground surface, and prevent downward dissipation of developed excess pore water pressures away from the critical zone.

(4) The soil above the critical zone also loses its effective stress due to an upward flow of water from the critical zone towards the ground surface (seepage-induced liquefaction). High excess pore water pressures develop up to depth $z_{min} \approx 1.5-2$ m and even above the groundwater table. The dissipation effects and the vertically unconstrained flow of water throughout the deposit result in 'expansion' of the liquefied critical zone eventually forming a continuous zone of 'liquefied' soil with thickness of 1 to 2 m greater than the initial thickness of the liquefied soil in the critical zone.

(5) The small thickness of the nominal crust above the groundwater table ($h_{(NC)} \approx 1.5-2$ m) and especially the low thickness of non-liquefiable soils ($H_{NL(0-z_{min})} \lesssim 0.5$ m) are insufficient to mitigate liquefaction manifestation at the ground surface. Instead, the liquefiable soils above the groundwater may also be subject to seepage-induced liquefaction expanding further the total thickness of liquefied soil. Development of cracks, discontinuities, pathways for large volumes of water and soil ejecta, and consequent loss

of crust integrity are anticipated to fully diminish the mitigating effects of such crust characteristics in the field.

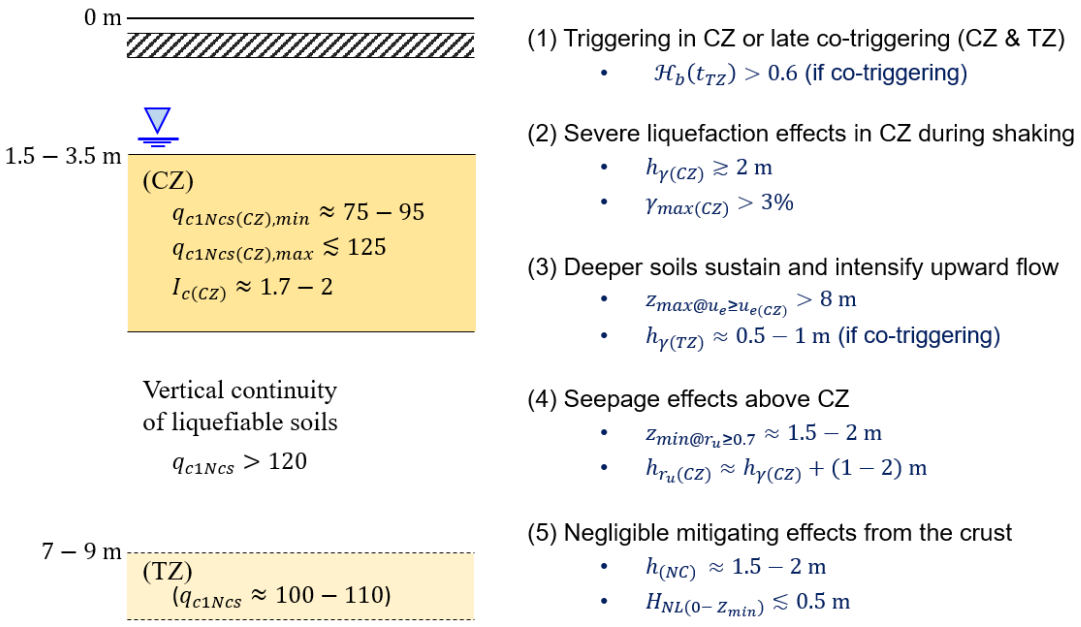

Fig. 7.11 Key deposit features and processes involved in the 'standard' SC-response.

The standard SC-response is typical for the response of 10 YY-sites and 1 NY-site, all of which manifested severe liquefaction in the 22Feb11 earthquake. The above SC-response mechanisms involving vertical communication of excess pore water pressures throughout the deposit and large volumes of water expelled from thick and continuous liquefied zones can explain the severe liquefaction effects observed at the aforementioned sites. As the key feature of the deposits associated with the SC-response is the presence of thick zones of low resistance soils at shallow depth, liquefaction damage indices that combine thickness, depth, and severity of liquefaction in the assessment, such as *LSN* and *LPI*, correctly predict (in most cases) the severe manifestation associated with the SC-response, as illustrated for the example Avondale site in Fig. 7.1.

In addition to the above sites, 2 YY-sites and 9 NY-sites, the majority of which were characterized by moderate liquefaction manifestation in the 22Feb11 earthquake, also follow the main features of the SC-response (i.e. liquefaction of shallow critical zone and vertical communication of excess pore water pressures). However, there are some important differences in the response of these sites including one or more of the following:

- Reduced thickness of liquefaction in the critical zone ($h_{\gamma(CZ)} \approx 1 - 1.7$ m).
- Higher values of I_c in the critical zone ($I_{\gamma c(CZ)} \gtrsim 2.3$), possibly associated with low-plasticity silts. The latter may often be characterized by delayed post-liquefaction

reconsolidation response which can, in turn, reduce pore water movement and ejecta development (Beyazei et al. 2018).

- Low excess pore water pressures below the critical zone ($z_{max} \approx z_{\gamma(CZ)} + h_{\gamma(CZ)}$), hence allowing also for downward dissipation of part of the developed excess pore water pressures from the critical zone.
- Reduced seepage effects above the critical zone ($z_{min} \approx z_{\gamma(CZ)}$) due to a reduced hydraulic gradient.
- Increased mitigation effects from the crust due to higher content of non-liquefiable soils ($H_{NL(0-z_{min})} \approx 1-2$ m).

A reduced thickness of the critical zone and increased thickness of non-liquefiable soils in the crust were the most commonly encountered features in the above sites. These key differences from the characteristics of the standard SC-response can explain the less severe manifestation observed in the majority of these sites, and they also emphasize the importance of considering the combined (and competing) effects from the various intensifying and mitigating mechanisms in the assessment of the severity of liquefaction manifestation.

7.5.2 DI-Response: Deep Liquefaction in 'Interbedded' Deposit

The following key processes and effects are involved in the DI-response (Fig. 7.12).

(1) Liquefaction is triggered outside the critical zone at depth greater than $z_{\gamma(TZ)} > 4.5$ m. The first triggering occurs at an early stage of the excitation ($\mathcal{H}_{b,tr(TZ)} < 0.5$) in the deep layers with the lowest tip resistance ($q_{c1Ncs(TZ),min} \approx 70-80$), slightly lower than that of the shallow critical layer, and then it spreads to neighboring (deep) layers of slightly higher resistance ($q_{c1Ncs(TZ),max} \approx 85-95$). The cumulative thickness of the soil that liquefies in the various triggering zones ($H_{\gamma(TZ)}$) varies from 0.5 to 3 m, but because of the interbedded nature of the deposit thick continuous zones of liquefied soil cannot be formed ($h_{\gamma(TZ),max} \lesssim 1.5$ m).

(2) The liquefaction in the deep triggering zone(s) results in a substantial reduction of accelerations and seismic demand for the overlying soils above $z_{\gamma(TZ)} \approx 4.5$ m. The Arias Intensity demand in the critical zone is typically about 30 to 40% of the respective demand generated in the analysis in which no excess pore water pressures were allowed to develop in the triggering zone.

(3) The reduction in the seismic demand prevents occurrence of liquefaction in the critical layer. The shallow critical layer has equal or slightly higher tip resistance ($q_{c1Ncs(CL)} \approx 75-95$) than the first triggering layer(s) and in about 50% of the cases it is also partially saturated ($V_p \approx 700-1000$ m/s). The maximum response in the critical zone is characterized by relatively small shear strains and low excess pore water pressures of $\gamma_{max(CZ)} \lesssim 0.3\%$ and $r_{u,max(CZ)} < 0.4$.

(4) The high proportion of non-liquefiable soils and interbedded nature of these deposits restrict the development of seepage effects above the triggering zone(s) and towards the

ground surface ($z_{min} \approx z_{\gamma(TZ)}$). This effectively results in a continuous non-liquefied (stiff) crust from the ground surface up to $z_{min} > 4.5$ m, with a high proportion of non-liquefiable soils ($H_{NL(0-z_{min})} \gtrsim 1.5$ m).

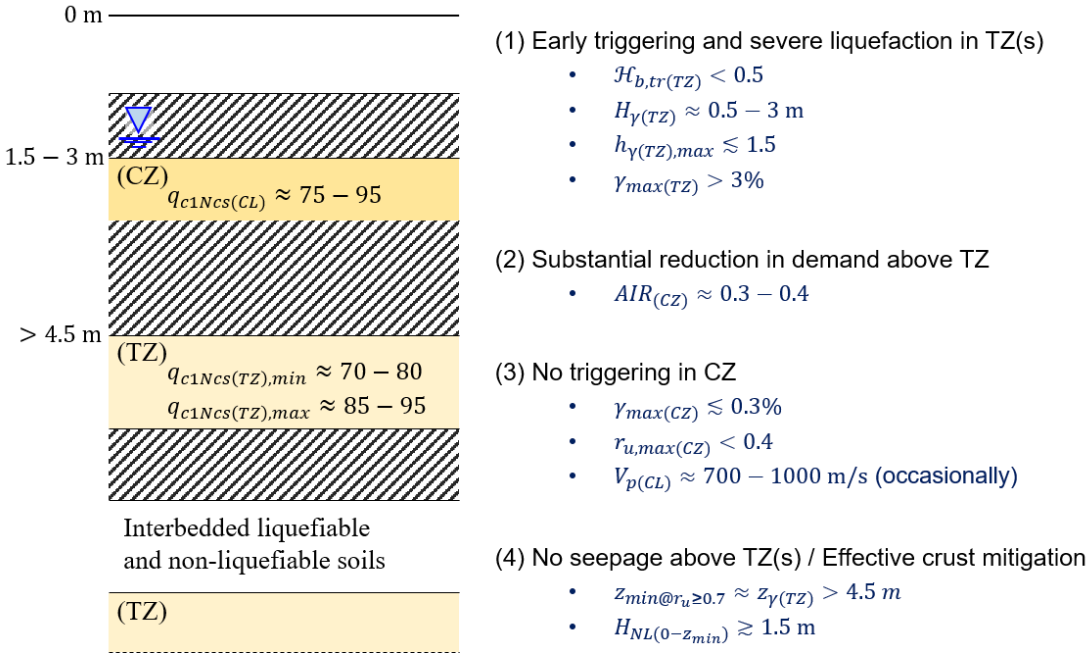

Fig. 7.12 Key deposit features and processes involved in the DI-response.

The above cascading mechanisms of the DI-response work together to effectively mitigate the development of liquefaction and its manifestation at the ground surface. This type of system response was observed in 8 NN-sites (no manifestation) and 2 NY-sites which manifested minor to moderate liquefaction. Note that the mitigating effects arising from the deep liquefaction (reduction in the seismic demand) and the high content of non-liquefiable soils in the deposit (which restrict the vertical communication of excess pore water pressures and supress ejecta movement) are not considered in the simplified method which significantly over-estimates liquefaction manifestation for the DI-response sites, as illustrated for the example Hoon Hay site in Fig. 7.4.

7.5.3 SI-Response: Shallow Liquefaction in 'Interbedded' Deposit

The key processes and effects for the SI-response (Fig. 7.13) are summarized below.

(1) Liquefaction triggering occurs at about the same time (co-triggering) in the critical zone at shallow depth ($z_{\gamma(CZ)} \approx 1.5 - 3.0$ m) and in a deeper triggering layer at $z_{\gamma(TZ)} \approx 4 - 6$ m. The q_{c1Ncs} values for the critical layer and the first triggering layer outside the critical zone are practically identical, typically in the range from 75 to 85, and 75 to 90

respectively. The (co-)triggering occurs relatively early in the ground motion ($\mathcal{H}_{b,tr(TZ)} \approx \mathcal{H}_{b,tr(CZ)} < 0.5$).

(2) The deep liquefaction is characterized by large shear strains ($\gamma_{max(TZ)} > 3$) and cumulative thickness of $H_{\gamma(TZ)} \approx 1-3$ m. The occurrence of liquefaction at depth (at $\mathcal{H}_{b,tr(CZ)} < 0.5$) reduces the Arias Intensity demand in the critical layer to about 35 to 50% of that corresponding to an equivalent total-stress analysis (without excess pore water pressure generation).

(3) The liquefaction in the critical zone is characterized by smaller maximum shear strains than those in the deeper triggering zone(s) ($\gamma_{max(CZ)} \lesssim \gamma_{max(TZ)}$) and relatively small thickness ($h_{\gamma(CZ)} \lesssim 1.2$ m). The I_c values in the critical zone are most often associated with non-plastic or low-plasticity silt type of behaviour ($I_{c\gamma(CZ)} \gtrsim 2.1$).

(4) There is no vertical 'communication' of excess pore water pressures between the critical zone and the deeper triggering zone(s), as non-liquefiable soils with thickness $H_{NL(CZ-TZ)}$ greater than 1 m separate the critical zone from the deeper liquefied zone(s).

(5) Non-liquefiable soils in the crust above the critical zone with thickness ($H_{NL(0-z_{min})}$) typically greater than 1 m impede seepage effects and development of excess pore water pressures above the critical zone ($z_{min} \approx z_{\gamma(CZ)}$).

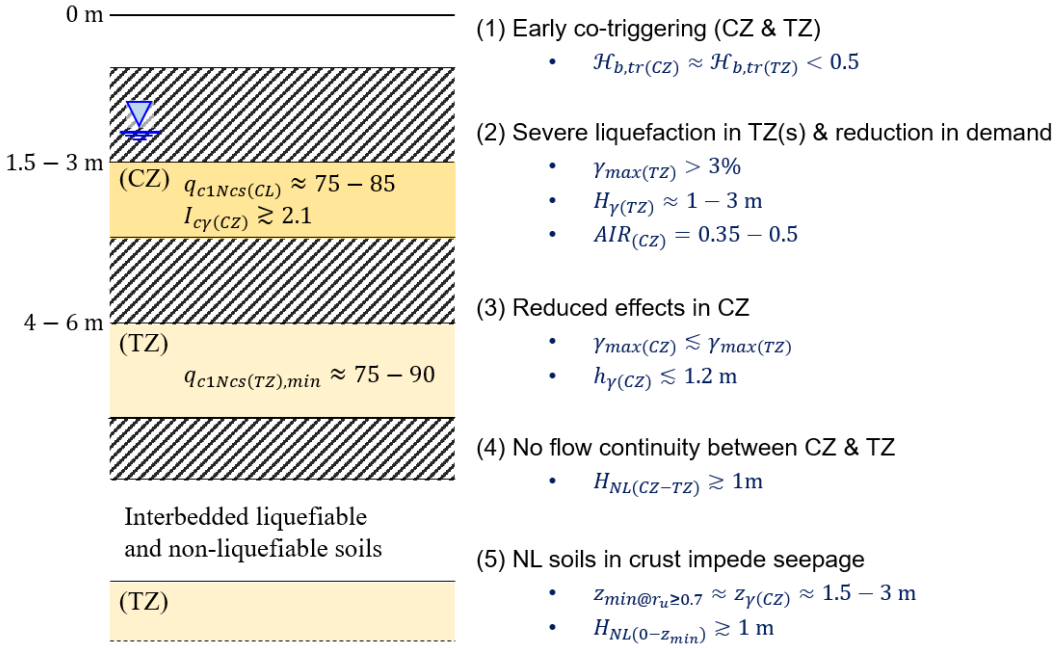

Fig. 7.13 Key deposit features and processes involved in the SI-response.

The above mechanisms were encountered in 7 NN-sites (no manifestation) and 5 NY-sites which manifested only minor volumes of ejected material in the 22Feb11 earthquake. The none-to-minor liquefaction manifestation associated with the SI-response can be explained by: (a) the reduced liquefaction effects in the critical zone (i.e. relatively small strains, small

thickness of liquefaction, and possibly delayed reconsolidation response due to increased plasticity), (b) the interbedded nature of the deposits which impedes the formation of continuous liquefied zones and isolates the critical zone from the deeper liquefied layers, and (c) the high content of non-liquefiable soils in the crust above the critical zone which improves the crust integrity during the shaking and post liquefaction. Assessment of the severity of liquefaction manifestation using current state-of-practice damage indices, such as LSN and LPI, ignores important mitigating mechanisms of the SI-response, and hence it over-estimates liquefaction manifestation for sites exhibiting this type of response.

7.5.4 DC-Response: Deep Liquefaction in 'Continuous' Deposit

The following key processes and effects are involved in the DC-response (Fig. 7.14).

(1) Liquefaction is triggered in a relatively deep layer of low tip resistance ($q_{c1Ncs(TL)} \approx 80-90$) when $\mathcal{H}_{b,tr(TZ)} < 0.6$. A continuous triggering zone with large maximum shear strains ($\gamma_{max(TZ)} > 3$) and thickness ($h_{\gamma(TZ)} \gtrsim 1.5$ m) is developed around the triggering layer. The depth to the top of the triggering zone ($z_{\gamma(TZ)}$) varies from 5 to 8 m from the ground surface.

(2) The deep liquefaction reduces the seismic demand for all soils above the triggering zone. The Arias Intensity demand above the triggering zone is reduced to 30% – 60% of that that would have occurred had no excess pore pressures been developed at depth.

(3) There is (either) no triggering of liquefaction (or, in some cases, triggering with minor consequences, i.e. relatively small shear strains and thickness of liquefied soils) at shallow depth during shaking.

(4) Significant seepage action and upward flow of water from the triggering zone results in seepage-induced liquefaction of the critical zone at shallow depth ($r_{u,max(CZ)} \gtrsim 0.9$) and development of a thick ($h_{r_u(CZ)} \gtrsim 4.5$ m) and continuous 'liquefied or nearly liquefied' zone with $u_e \approx \sigma'_{vo}$ up to $z_{min} = 2-3$ m. Void redistribution and upward flow of water can cause significant disturbance in the upper soils of this thick zone which were initially not predicted to liquefy during shaking.

(5) The proportion of non-liquefiable soils in the crust ($H_{NL(0-z_{min})}$) vary significantly among the sites that exhibited this type of response. However, even in the extreme case where $H_{NL(0-z_{min})} \approx z_{min}$, it does not appear to be sufficient to effectively suppress the liquefaction manifestation of the underlying liquefied zone.

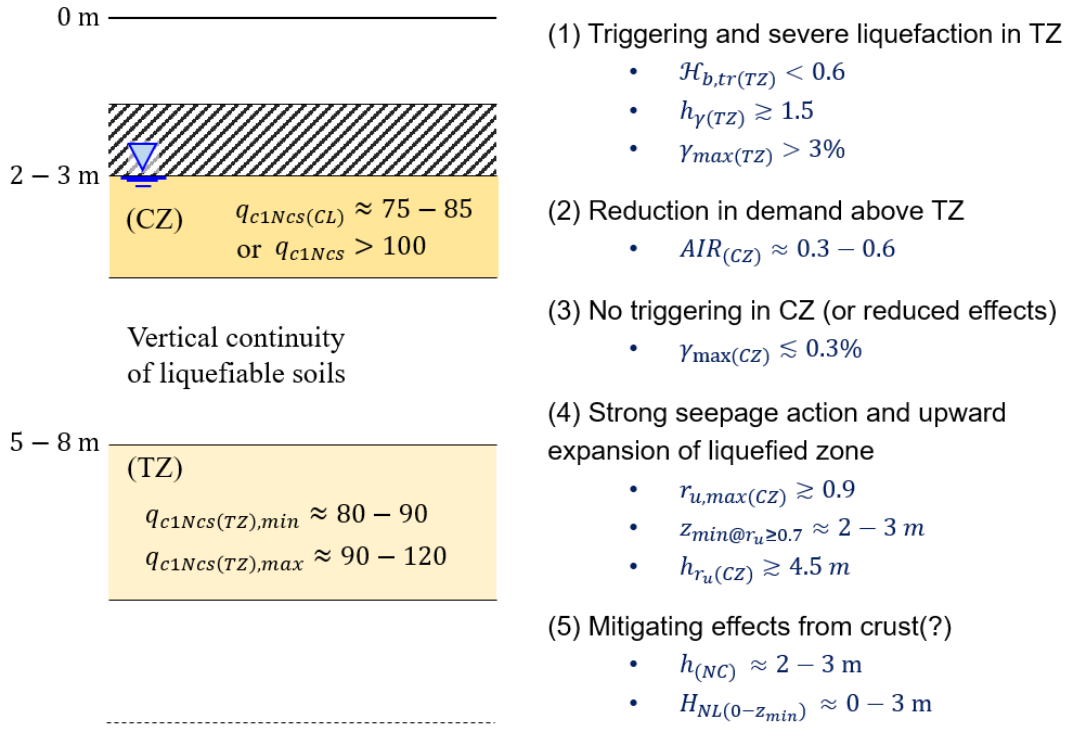

Fig. 7.14 Key deposit features and processes involved in the DC-response.

The above processes and effects are typical for the computed response of 3 YY-sites and 3 NY-sites, all of which were associated with severe liquefaction manifestation in the 22Feb11 earthquake. 1 NN-site was also characterized by deep triggering of liquefaction and vertical continuity of liquefiable soils, but the liquefaction effects in the triggering layer and, consequently, the associated seepage effects were significantly less severe for this site (e.g. $h_{\gamma(TZ)} = 0.4$ m, and $r_{u,max} < 0.4$ above the triggering zone). In such a case, the relatively small amount of excess water from the thin triggering layer is expected to be dissipated throughout the deposit without causing high excess pore water pressures and considerable disturbance to the overlying soils or liquefaction manifestation.

The mechanisms associated with the DC-response highlight the important influence of the material composition and overall permeability (flow continuity) of the deposit on the severity of liquefaction manifestation. The simplified method ignores important seepage mechanisms that contribute to the spread and severity of liquefaction and its manifestation, and therefore, in the absence of thick and shallow critical zones of low resistance soils, it tends to under-estimate the severity of liquefaction manifestation for sites with the above characteristics.

7.5.5 NT-Response: No Triggering of Liquefaction

The remaining 4 sites in which triggering of liquefaction was not predicted at any depth in the deposit ($\gamma_{max} < 1\%$) are sites of uniform clean sands with high penetration resistance, predominantly in the range between $q_{c1N} = 130$ and 170. One of these sites did not manifest

liquefaction (NN-site), whereas the other 3 NY-sites were characterized by minor (2 sites) to moderate liquefaction manifestation (1 site). 2 out of the latter have a thin layer of lower penetration resistance ($q_{c1N} \approx 105$) at about 4 m depth. While liquefaction triggering is not predicted in the analyses, excess pore water pressures slowly build up in the deposit and cause upward hydraulic gradients and flow of pore water towards the ground surface. It is therefore not unlikely that the unconstrained upward flow of water in such uniform sand deposits can develop locally hydraulic gradients high enough to buoy up soil particles from the near-surface soil and eject them at the ground surface in the form of minor manifestation.

7.6 Assessing the Severity of Liquefaction Manifestation

The above analysis and system-level interpretation of the responses of the 55 sites provide reasonable explanations for the strong variation in their performance (liquefaction manifestation) and the overall poor quality of the predictions by the simplified procedures, which ignore important system-response effects in the assessment. Table 7.2 summarizes the performance of the simplified analyses (quality of predictions based on LSN) for the identified types of system response. As previously discussed, there is a significant and systematic bias in the predictions of the existing simplified procedures with over-estimation of liquefaction manifestation for nearly all sites with interbedded deposits (SI-response and DI-response) and under-estimation of liquefaction manifestation for sites with 'continuous' deposits in which liquefaction is triggered at a relatively large depth and the shallower soils have relatively high liquefaction resistance (DC-response).

Table 7.2 Summary of predictions by simplified analyses classified based on the identified types of system response.

	Type of System Response				
LSN–based prediction [a]	SC (22 [b])	DC (7)	SI (12)	DI (10)	NT (4)
Good agreement	**77%**	29%	0%	10%	**75%**
Under-estimation	9%	**57%**	0%	0%	0%
Over-estimation	14%	14%	**100%**	**90%**	25%

[a] agreement between predictions and observations

[b] number of sites classified under each type of system response

Existing procedures for the assessment of liquefaction-induced damage and severity of surface manifestation focus on the evaluation of three important factors (e.g. Iwasaki et al. 1978, Ishihara 1985, Maurer et al. 2014, van Ballegooy et al. 2014): (1) the thickness of the liquefied soil, (2) the severity of liquefaction, and (3) the depth of the liquefied soil from the ground surface. It is important to note that even when using the results from the effective-stress analyses to evaluate these three factors, the existing procedures cannot explain the vastly different manifestations of liquefaction observed among the 55 sites. Fig. 7.15 shows

the normalized (frequency) histograms of LSN values computed using results from both simplified analyses (LSN; Fig. 7.15a) and effective-stress analyses (LSN_{ESA}; Fig. 7.15b) for the 22Feb11 earthquake. In both approaches, the computed maximum shear strains from the analyses are used to estimate post-liquefaction reconsolidation volumetric strains based on the Ishihara and Yoshimine (1992) chart (Yoshimine et al. 2006, Idriss and Boulanger 2008) and using the Tatsuoka et al. (1990) relationship to infer relative density from q_{c1Ncs}. Note that, because the effective-stress analysis inherently accounts for the effects of pore water pressure generation and liquefaction on the seismic demand, the extent of liquefaction and magnitude of maximum shear strains computed by the effective-stress analyses and, consequently, the reconsolidation volumetric strains and LSN_{ESA} values are significantly lower than the LSN values predicted by the simplified method. Hence, the LSN_{ESA} values reported in Fig. 7.16b for the effective-stress analyses should not be interpreted using the standard LSN thresholds for differentiating between different levels of damage and liquefaction manifestation. Yet, Fig. 7.16b clearly illustrates the poor performance of LSN and LSN_{ESA} for liquefaction assessment of the 55 sites as indicated by the significant portion of overlapping predictions associated with vastly different liquefaction manifestation, from none to severe. This implies that 'correcting' the simplified procedures for the effects of liquefaction on the seismic demand and effects of partial saturation on liquefaction resistance alone (effects which are considered in the effective-stress analyses and reflected in the computed shear strains) would not be sufficient to provide a substantial improvement in the simplified assessment, as other important interactions, system response mechanisms and effects would still be missing.

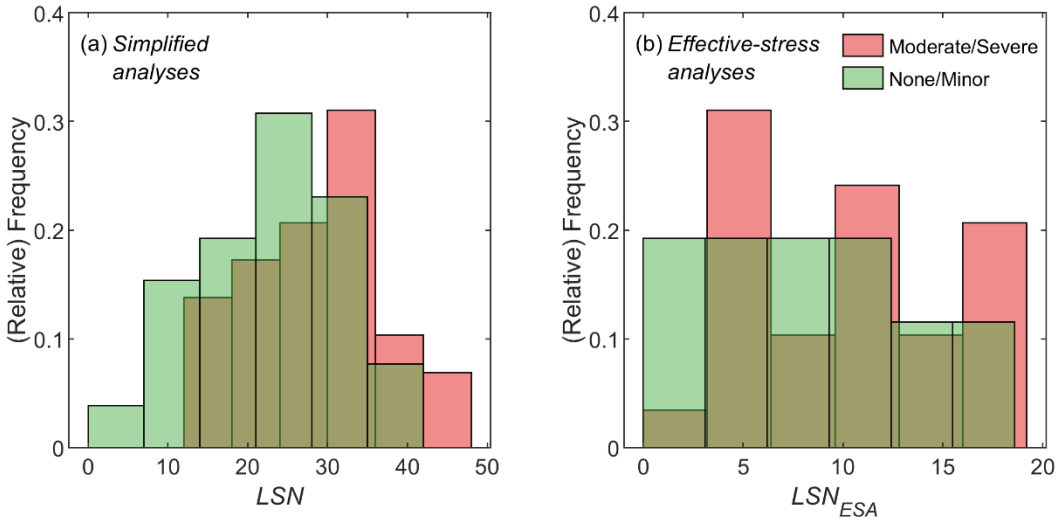

Fig. 7.15 Histograms summarizing the distribution of LSN and LSN_{ESA} values and associated liquefaction manifestation for the 55 sites based on: (a) simplified analyses; (b) effective-stress analyses.

Insights from the system-response interpretation presented in this chapter can be used to improve current frameworks for the assessment of liquefaction manifestation and associated damage. A preliminary framework was designed and tested in this study using the effective-stress analysis results for the 55 sites to examine whether incorporating key system response

effects has indeed the potential to improve liquefaction damage assessment. Key objectives in mind when developing this preliminary framework were: (a) to account for (most of) the key factors and system response mechanisms that appear to be influencing liquefaction manifestation, and (b) to maintain simplicity in the evaluation. On this basis, a modified Liquefaction Severity Number (LSN_{SR}) incorporating system response effects was defined. The evaluation of LSN_{SR} involves the following procedure and parameters:

- First, the various zones in the deposit where liquefaction has been triggered during shaking are identified. In this context, a liquefied zone is defined as a continuous zone of soils with $\gamma_{max} \geq 1\%$. Among the various liquefied zones in the deposit, a critical liquefied zone is defined as the liquefied zone that is most likely to manifest liquefaction at the ground surface. Fig. 7.16 illustrates the identification of the liquefied zones for two example sites based on the results (computed maximum shear strains) from effective-stress analyses. The critical liquefied zone is denoted as '*zone 1*', whereas the remaining liquefied zones below zone 1 are numbered sequentially (i.e. *zone 2*, *zone 3*, etc.).
- The post-liquefaction reconsolidation settlement of each liquefied zone ($S_{v1D(i)}$), obtained by integration of the post-liquefaction volumetric reconsolidation strains over depth of liquefaction, is used to quantify the consequences of liquefaction within each zone, as illustrated in Fig. 7.16. $S_{v1D(i)}$ accounts for the combined influence of thickness and severity of liquefaction and incorporates the effect of soil density on the liquefaction response. Besides, $S_{v1D(i)}$ is directly related to the volume of water expelled by the liquefied soil and, hence, it reflects its potential for ejecta manifestation.
- A 'minimum depth of influence' ($z_{min(i)}$) is assigned to each liquefied zone (Fig. 7.16). $z_{min(i)}$ is defined as the shallowest depth above the liquefied *zone* i where significant excess pore water pressures develop ($r_{u,max} \geq 0.7$) during or post- shaking. $z_{min(i)}$ cannot be less than the depth to the bottom of *zone* $i-1$ or, in case no shallower zone exists, it cannot be less than the depth of the surface crust ($h_{(NC)}$). $z_{min(i)}$ reflects several important factors including the depth to the liquefied zone, the extent of seepage effects and seepage-induced liquefaction above the liquefied zone, and the depth of the surface crust while accounting for effects of liquefaction on the crust thickness and integrity.
- The cumulative thickness of non-liquefiable soils between each liquefied zone (*zone* i) and the critical liquefied zone (*zone* 1), denoted as $H_{NL(1-i)}$ (Fig. 7.16), is used as a mitigating factor to reduce the contribution from liquefaction in deeper zones that are overlaid by non-liquefiable soils. In addition, the cumulative thickness of non-liquefiable soils in the crust above the critical liquefied zone ($H_{NL(0-1)}$) is also considered separately.

The above parameters are combined according to the following equation to calculate LSN_{SR}:

$$LSN_{SR} = S_{v1D(1)} \cdot \frac{1}{\sqrt{z_{min(1)}}} + \sum_{i=2}^{n} S_{v1D(i)} \cdot \frac{1}{\sqrt{z_{\min(i)}}} \cdot \exp\left(-H_{NL(1-i)}\right) \qquad (7\text{-}1)$$

where n indicates the total number of continuous liquefied zones in the deposit.

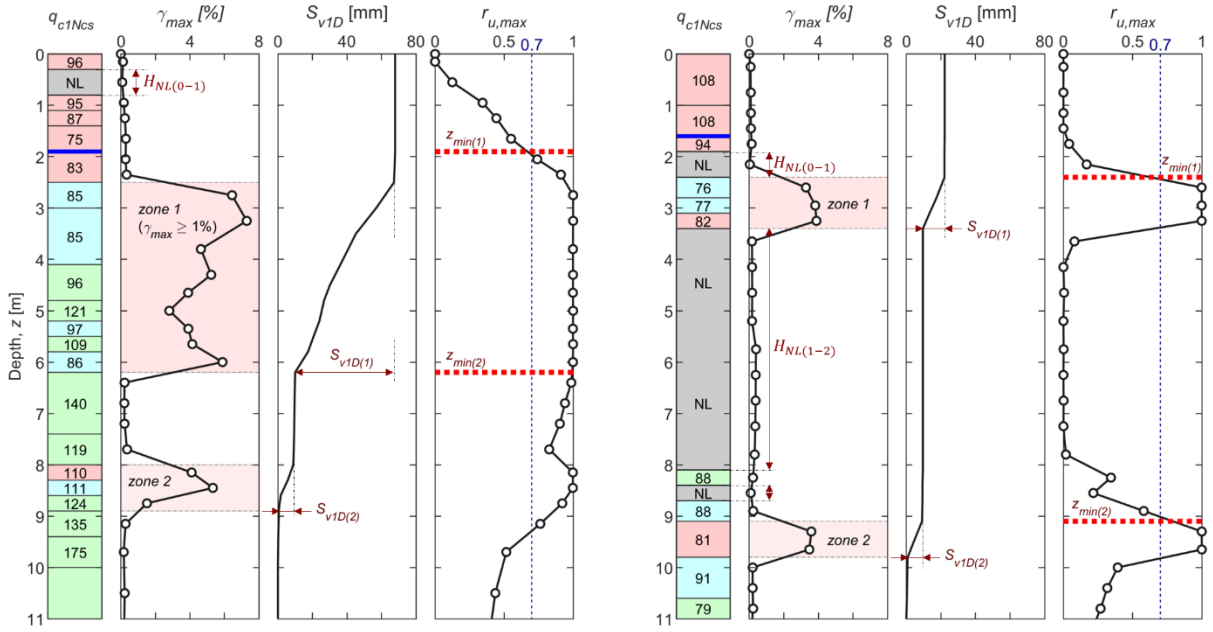

Fig. 7.16 Determination of parameters used in the evaluation of LSN_{SR}.

. There are two key differences between the system-response-based index LSN_{SR} and the original LSN definition:

(1) In LSN, the consequences of liquefaction in each individual layer are weighted by a factor that is function of the depth of the layer from the ground surface ($1/z$). On the other hand, LSN_{SR} considers the individual layers within each continuous zone of liquefied soil as a unit and 'lumps' the consequences of liquefaction across the zone into the minimum depth of influence ($z_{min(i)}$) for the zone. Furthermore, $z_{min(i)}$ accounts for possible expansion of the liquefied zone and seepage-induced effects during dissipation.

(2) LSN ignores mitigating effects from the presence of non-liquefiable soils in the deposit. On the other hand, LSN_{SR} uses an additional factor that reduces the contribution from deeper zones (below the critical liquefied zone) depending on the thickness of interbedded non-liquefiable soils between each zone and the critical liquefied zone (*zone* 1).

Both modifications to the original definition of LSN intend to place more emphasis on the great importance of vertical 'communication' of excess pore water pressures and water flow within and between the liquefiable layers and zones of the deposit, as suggested by the preceding analyses and interpretation.

In Fig. 7.17, LSN_{SR} values calculated from the effective stress analyses results for the 55 sites are plotted against $H_{NL(0-1)}$, where $H_{NL(0-1)}$ is the thickness of the crust comprised of non-liquefiable soils. It can be seen from this figure that the modified LSN_{SR} incorporating system response effects, achieves a very good separation between the sites that manifested moderate-to-severe liquefaction and the sites that either did not manifest liquefaction or manifested minor liquefaction in the 22Feb11 earthquake. More specifically, there is a good agreement

between predictions and observations (clear separation in the chart) for 85% of the cases. Liquefaction manifestation is underestimated for 20% of the sites that manifested moderate or severe liquefaction (solid symbols below the dividing line of the chart), and it is over-estimated for only 8% of the sites that did not manifest liquefaction or had only minor liquefaction manifestation (open symbols above the dividing line). Importantly, there is a substantial improvement in the predictions using $LSN_{SR} - H_{NL(0-1)}$ compared to those based on the original definition of LSN (Fig. 7.15).

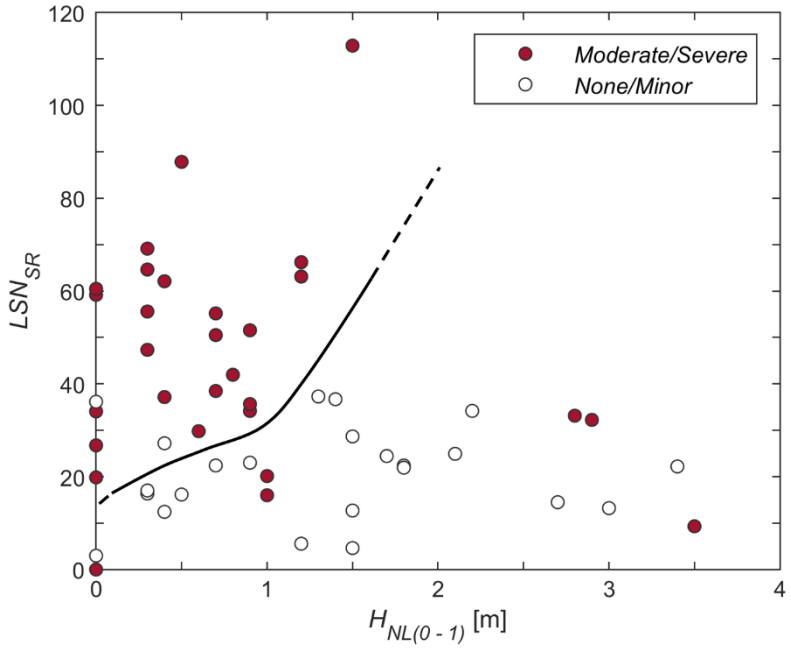

Fig. 7.17 Relationship between LSN_{SR} and $H_{NL(0-1)}$ for sites that manifested moderate to severe liquefaction (filled symbols) and sites that did not manifest liquefaction or manifested only minor liquefaction (open symbols) in the 22Feb11 earthquake.

The current implementation of the $LSN_{SR} - H_{NL(0-1)}$ framework for assessing the severity of liquefaction manifestation relies on results from effective-stress analyses for the evaluation of the maximum shear strains throughout the deposit (used in determining the various liquefied zones and $S_{v1D(i)}$) and seepage-induced excess pore water pressures (used in determining $z_{min(i)}$). The above can be sensitive to, among other factors, the constitutive model used in the analysis and its calibration, the adopted permeability values, analysis duration and numerical damping. In this study, the magnitude of maximum shear strains was also found to be sensitive to the input motion used for the 22Feb11 earthquake. All the above factors affect LSN_{SR} and the location of the dividing line in the $LSN_{SR} - H_{NL(0-1)}$ chart making it difficult for a generic use in forward assessments. Nevertheless, the above framework has clearly illustrated that appropriate consideration of system response effects can substantially enhance liquefaction assessment. Further work is required to establish a complete and robust framework that could be used more widely, and which will be also incorporated within the simplified liquefaction evaluation procedures.

7.7 Summary

A comprehensive scrutiny of the effective-stress analyses results for the 55 Christchurch sites has been presented in this chapter. Detailed analyses results at selected sites demonstrated the ability of the adopted CPT-based effective-stress analysis to capture key aspects of the response of liquefiable soils and deposits as it develops through time, including pore water pressure development, soil liquefaction and resulting deformations (shear strains) during the dynamic shaking, and post-shaking dissipation of excess pore water pressures. Importantly, system-response mechanisms involving cross-interactions amongst different soil layers in the dynamic response and through pore water pressure redistribution and water flow were also rigorously simulated in the analyses, and found to often govern the ground response and liquefaction performance. On the other hand, specific post-liquefaction field processes involving, among others, severe disturbance and fluidization of liquefied soils under seepage action, hydraulic fracturing, formation of cracks (discontinuities) and sand boils, and their effects on the response and liquefaction manifestation either cannot be rigorously modelled or are ignored in the effective-stress analysis based on the continuum approach. It is important to emphasize that the effective stress analysis captures the development and evolution of soil liquefaction throughout the deposit in a most rigorous way. In addition, the results from such analyses provide quantifiers and response measures that are indicative of the severity of liquefaction manifestation, which is associated with phenomena (mentioned above) that are beyond the direct scope of the effective stress analysis. This clear recognition of a response domain where the effective stress analysis provides the most robust and rigorous methodology for analysis of soil liquefaction and response features for which it provides only indirect measures or indicators of liquefaction effects is critically important for an appropriate use of the effective stress analysis.

With the above in mind, a set of response measures (parameters) and associated criteria were used to quantify the onset of independent system response mechanisms and effects of interaction between different mechanisms. This allowed for rigorous analysis and quantification of the system response effects on the seismic performance of the studied sites. On this basis, five characteristic types of system responses were identified for the 55 sites and their specific response features including representative values for the above response measures were summarized in Figs. 7.11 to 7.14.

The vertical continuity (or discontinuity) of critical zones and liquefiable soils in the deposit was identified as a key factor for the activation of certain system response mechanisms that can either intensify (in the case of deposits with vertically continuous liquefiable soils) or mitigate (in the case of interbedded deposits) the development of liquefaction and its consequences throughout the deposit including surface liquefaction manifestation.

Mechanisms that intensify liquefaction manifestation involve: (i) shaking-induced liquefaction of thick and vertically continuous zones of relatively low resistance soils, as such zones are expected to strongly interact, develop large deformations, and cause strong and damaging discharge of excess pore water pressures and soil ejecta during dissipation; and (ii)

vertically unconstrained water flow through and between liquefiable layers (zones) and seepage action resulting in additional disturbance to that caused by the ground shaking, both contributing to either further fluidization of already liquefied soils or seepage-induced liquefaction and hydraulic fracturing of initially stable soils. Such intensifying mechanisms are primarily encountered in deposits comprising vertically continuous liquefiable soils which allow vertical 'communication' of excess pore water pressures and water flow through and between layers. Provided the existence of a zone of relatively low resistance soils within the top 5 to 8 m and with sufficiently high level of loading to liquefy these soils, such 'continuous' liquefiable deposits can manifest severe liquefaction effects at the ground surface (YY-sites and part of NY-sites).

Mechanisms that mitigate liquefaction manifestation involve: (i) reduction in the seismic demand for shallow critical layers due to deeper liquefaction; (ii) isolation or vertical confinement of layers that liquefy or develop high excess pore water pressures by overlying and underlying relatively thick non-liquefiable layers resulting in either reduced or complete loss of water flow between liquefiable layers; (iii) partial saturation of shallow soils and consequent increase in their liquefaction resistance; (iv) reduced hydraulic gradients in upper soils due to delayed post-liquefaction reconsolidation response of underlying low-plasticity silts; and (v) at-depth suppression of ejecta movement from thick crust of non-liquefiable soils. Such mitigating mechanisms are mostly encountered in deposits with interbedded liquefiable and non-liquefiable soils. For the levels of seismic demand considered in this study, such deposits show a limited liquefaction manifestation potential, from no manifestation to minor manifestation (NN-sites and part of NY-sites).

Current simplified liquefaction evaluation procedures ignore system response effects. Hence, they systematically over-estimate liquefaction manifestation for sites with interbedded deposits, while they tend to either predict correctly or under-estimate liquefaction manifestation for sites with vertically continuous liquefiable soils (Table 7.2). Preliminary developments of this study toward an improved framework for liquefaction damage (manifestation) assessment show that appropriate consideration of system response effects can substantially improve predictions. Future work will explore various alternatives or refine the presented preliminary framework, and eventually incorporate it in the simplified liquefaction evaluation procedures.

8 SUMMARY AND CONCLUSIONS

Seismic effective-stress analysis was used to thoroughly investigate the liquefaction performance of 55 well-documented case-history sites from Christchurch. At each site, the liquefaction performance during four major events of the 2010-2011 Canterbury earthquake sequence was documented based on detailed field inspections which covered not only the specific sites of interest, but also their adjacent properties and wider neighbouring areas. The performance of the 55 sites varied significantly, from no liquefaction manifestation at the ground surface (in any of the major events) to very severe liquefaction manifestation in multiple events. For the majority of the 55 sites, the simplified liquefaction evaluation procedures could not explain these dramatic differences in the manifestation. The present study focused on the two most damaging events of the earthquake sequence, i.e. the 04Sep10 M_w7.1 and 22Feb11 M_w6.2 earthquakes, and aimed to explain the above inconsistencies between simplified method predictions and field observations for the 55 sites through a rigorous interpretation of their responses using results from effective-stress analyses.

Comprehensive geotechnical and geophysical investigations (primarily CPT and high-resolution crosshole V_p data) at each of the 55 sites were initially examined to identify similarities and differences in soil profile characteristics between sites with different seismic performance (liquefaction manifestation). Then, a CPT-based effective-stress analysis procedure was developed to analyse the seismic response of the 55 Christchurch sites in a consistent but also practical manner that would allow for rigorous comparisons with the predictions obtained from simplified procedures. Input motions for the analyses were derived based on selected recordings from the specific events of interest and with appropriate modifications to address some of the challenges associated with the spatial variability of ground motion in the near-source region. The quality of the simulations using the developed effects stress analysis procedure and derived input motions was evaluated through rigorous comparisons with available seismic recordings at 13 strong motion station sites throughout Christchurch. Finally, effective stress analyses results from the 55 sites were scrutinized to elucidate the system response of Christchurch deposits, identify and quantify relevant interaction mechanisms, and examine their combined influence on the liquefaction manifestation.

Overall, this study has set a paradigm for rigorous forensic assessments of ground response including comparative analyses and consistent treatment (from model calibration and definition of input motions to evaluation and interpretation of results) of a large number of (case-history) sites, and it has demonstrated how such a comprehensive and unbiased approach can provide valuable insights into various aspects of ground response and seismic performance and, eventually, inform and advance current engineering practices.

In the following sections, the most important findings and contributions on three specific topics addressed in this research are summarized. Limitations of the study and future research needs are also discussed.

8.1 CPT-based Effective Stress Analysis Procedure

As part of this research, a 1D CPT-based effective stress analysis procedure was developed and implemented for the analyses of the 55 Christchurch sites. Key objective in mind when developing this procedure was to bridge the gap between the simplified liquefaction evaluation procedures used in engineering practice and advanced dynamic effective-stress analyses whose application in practice can often be highly demanding on the user. In this context, the proposed CPT-based procedure provides a simplified (in use and calibration) but advanced (in simulation capabilities) computational tool for liquefaction assessment of free-field soil columns which (a) can be fully automated in a programming environment and (b) requires no additional input compared to simplified CPT-based liquefaction evaluation procedures. In this way, 1D effective-stress analysis can be routinely applied for quick, yet more robust estimations of liquefaction hazards, in a similar fashion to the simplified procedures.

Key elements in the proposed procedure can be summarized as follows:

(1) As a first step, a simplified, discretized soil profile is determined from the nearly continuous CPT data. A practical algorithm that automates this process has been presented in Fig. 4.2. Apart from the obvious necessity of a discretized soil profile for use in finite element and finite difference numerical analyses, this profile 'simplification' allows for rigorous geotechnical scrutiny of the overall deposit characteristics and identification of critical layers in the deposit. Based on their inferred behaviour characteristics, the soil layers resulting from this process are classified as either liquefiable or non-liquefiable.

(2) Modelling of the liquefiable soil layers focuses on the simulation of their (cyclic) liquefaction resistance, while using representative values for elastic and plastic stress-strain parameters for sand. A set of liquefaction resistance curves (LRCs) were derived over relevant $q_{c1Ncs} - \sigma'_{vo}$ conditions by directly following the simplified liquefaction triggering procedure of Boulanger and Idriss (2014). These target curves were then used to calibrate an elastic-plastic constitutive model (S-D Model) capable of reproducing the

target behavior over all densities and confining stresses of interest, with a single set of values for model parameters. The calibration methodology was extended to allow for incorporation of partial saturation effects on LRC based on V_p measurements from the field. A complete set of S-D Model parameters calibrated based on the Boulanger and Idriss (2014) liquefaction triggering curves is provided in Table 4.1.

(3) Modelling of the non-liquefiable soil layers targets their cyclic stress-strain response, typically defined in terms of modulus reduction and damping ratio curves. Reasonably accurate and concurrent modelling of target modulus reduction and damping ratio curves over the expected range of shear strains is the key requirement in this case.

(4) With respect to the seismic input for forward application of the method, it is recommended to select an ensemble of ground motions for the earthquake scenario of interest using the generalized conditional intensity measure (GCIM) approach (Bradley 2010, 2012), or an equivalent method, considering a suitable set of intensity measures (IMs) relevant to liquefaction problems, including not only amplitude-related IMs, but also duration- and energy-related measures, as they are also important for liquefaction problems. For problems of forensic assessment, recommendations for the definition of input motion are provided in the following section.

(5) In the final step, numerical model (i.e. element size, boundary conditions, initial stress state of the soil) and analysis parameters (i.e. computational time increment, integration scheme, numerical damping) are defined. Here, basic rules of a good numerical analysis need to be followed, always taking into consideration the characteristics of the given soil profile and its anticipated behaviour.

Detailed analyses results at selected Christchurch sites demonstrated the ability of the proposed effective-stress analysis procedure to capture key aspects of the response of liquefiable soils and deposits in realistic chronological sequence, including pore water pressure development, triggering of soil liquefaction and resulting deformations (shear strains) during the dynamic shaking, and post-shaking dissipation of excess pore water pressures. Importantly, system-response mechanisms involving cross-interactions amongst different soil layers in the dynamic response and through pore water pressure redistribution and water flow were also simulated and rigorously considered in the analyses. The acceleration response and surface ground motions were also reasonably well captured (given appropriate definition of input motion) by the effective stress analyses, as illustrated through a comprehensive validation study of 13 strong motion station sites in Christchurch.

Limitations of the procedure itself but also of the constitutive model and numerical analysis framework have to be recognized. The simplified CPT-based calibration adopted in the proposed procedure cannot be compared in rigor and consequent accuracy of the predicted response with a detailed model calibration based on laboratory tests on site-specific soils. Also, specific post-liquefaction field processes involving, among others, severe fluidization of liquefied soils under seepage action, hydraulic fracturing, formation of cracks

(discontinuities) and sand boils, and their effects on the response and ground deformations are beyond the capacity of continuum-based approaches to be rigorously modelled.

8.2 Definition of Input Motions for Forensic Seismic Analyses

The strong spatial variation of ground motion in the near-source region of an earthquake imposes significant challenges in the derivation of representative input motions for forensic ground response analysis, based on the available recordings of the event at strong motion station sites. Addressing such challenges was necessary to realistically simulate the seismic demand caused by the 04Sep10 and 22Feb11 earthquakes across Christchurch, at the various target sites, for the purposes of liquefaction assessment. A series of steps and considerations were used in this study and are proposed to more rigorously approach the problem of the determination of input motions for forensic ground response analysis in the near-source region.

(1) Step 1 involves the selection of appropriate reference (strong motion station) site and reference recorded motion. In this process, consideration is given to: (a) the appropriateness of the candidate reference site for deconvolution (i.e. negligible nonlinearity in the response and shallow thickness of soft soil deposits); (b) potential differences between hanging-wall and footwall motions, in case the considered sites (target site and reference site) are located on opposite sides of the fault; (c) the deeper geological structure below the reference site and the target site (e.g. basin depth) and associated possible ray paths of seismic waves; (d) extended-source effects and their impact on the azimuthal variation in radiated seismic energy and ground-motion characteristics; and, (e) the proximity of the target site to the reference site, which generally increases the likelihood of similarities in the above characteristics and reduces bias introduced by the subsequent scaling.

(2) Step 2 involves deconvolution of the selected reference motion at the reference site using equivalent-linear analysis. Key requirement from this analysis is that the maximum shear strains throughout the soil profile do not exceed a threshold strain (e.g. $\gamma_{max} \lesssim 0.5\% - 1\%$) beyond which the equivalent-linear approximation of the nonlinear soil behaviour is no longer credible.

(3) Step 3 involves the scaling of the deconvolved motion to account for path effects arising from differences in the source-to-site distance between the reference site and the target site. Amplitude scaling factors can be derived using Eqs. 5-3 or 5-4. The use of scaling factors that significantly deviate from unity should generally be avoided as large bias in the energy content of ground motion can be introduced in such cases (Fig. 5.10). To overcome this issue, an alternative ‘amplitude-duration’ scaling method that provides consistent distance-scaling of amplitude, energy content, and duration was developed as part of this study (Appendix B). The amplitude-duration scaling method allows for

frequency-dependent scaling of amplitudes and changes in strong motion duration. It was shown to provide substantial improvements in the prediction for a case of large difference in the source-to-site distance between the reference and target sites (Appendix B).

Comparative evaluation of the performance of alternative reference input motions in the simulations of ground response at the strong motion station sites of Christchurch showed clearly that proper selection and scaling of within-event records, in accordance with the above criteria and methods, are essential for a good prediction of the ground motion at target sites. However, for some areas (sites), the derivation of realistic input motions can be challenging mainly due to absence of representative (compatible with the target sites) within-event records. In such situations of significant uncertainty in the input motion, it is considered important to examine the sensitivity of the response to variations in the reference motion and scaling factor.

8.3 System Response of Liquefiable Deposits

The comprehensive study on the performance of the 55 case-history sites has provided important insights into the system response of liquefiable deposits and the effects of relevant interaction mechanisms on the development of liquefaction and its surface manifestation.

Initial scrutiny of the soil profile characteristics of the 55 sites identified some key differences between sites that manifested liquefaction in both considered earthquakes (YY-sites) and sites that did not manifestation liquefaction in either event (NN-sites). In particular, YY-sites are generally characterized by vertically continuous liquefiable soils in the top 10 m. They are typically composed of a shallow silty sand or sandy silt layer in the top 2 to 3 m overlying a vertically continuous 7 to 8 m thick sand or fine sand layer up to 10 m depth. Partial saturation, when present at soils below the groundwater table, is typically confined within the top 0.5 to 1 m from the water table. The vertical continuity of liquefiable soils in the deposit, shallow water table at about 2 m depth, and absence or minor thickness of non-liquefiable soils in the crust are key features of the YY-sites. Conversely, the NN sites are highly stratified deposits comprising interbedded liquefiable and non-liquefiable soils. A crust of non-liquefiable soil, shallow water table at about 1 to 2 m depth, partial saturation of plastic and non-plastic silt layers up to a depth of about 4 m below the groundwater table, horizontal ‘grid’ of non-liquefiable layers, and vertical discontinuity of liquefiable soils are key features of the NN-sites. It is important to note that in terms of the characteristics of their critical layers (depth from the ground surface and penetration resistance), YY-sites and NN-sites have essentially no difference.

Subsequent in-depth investigation of the effective stress analyses results showed that, in fact, the vertical continuity (or discontinuity) of liquefiable soils is a key factor for the occurrence of certain system response mechanisms that can either intensify or mitigate the development

of liquefaction and its consequences throughout the deposit including surface liquefaction manifestation.

Mechanisms that intensify liquefaction manifestation involve: (i) shaking-induced liquefaction of relatively thick and vertically continuous zones of soils with low penetration (liquefaction) resistance, as such zones are expected to strongly interact, develop large deformations, and generate strong and damaging discharge of excess pore water pressures during dissipation; and (ii) vertically unconstrained water flow through and between liquefiable layers (zones) with seepage action resulting in additional disturbance and further fluidization of already liquefied soils, and also seepage-induced liquefaction or hydraulic fracturing of initially stable soils near the ground surface (at and above the water table). Such intensifying mechanisms are primarily encountered in deposits comprising vertically continuous liquefiable soils which allow vertical 'communication' of excess pore water pressures and water flow through and between layers. Provided the existence of a zone of relatively low resistance soils within the top 5 to 8 m and with sufficiently high level of loading to liquefy these soils, such 'continuous' liquefiable deposits can manifest severe liquefaction effects at the ground surface (YY-sites and part of NY-sites).

Mechanisms that mitigate liquefaction manifestation involve: (i) reduction in the seismic demand for shallow critical layers due to deeper liquefaction; (ii) isolation or vertical confinement of layers that liquefy or develop high excess pore water pressures by capping and underlying non-liquefiable layers; (iii) partial saturation of shallow soils and consequent increase in their liquefaction resistance; (iv) reduced hydraulic gradients in upper soils due to delayed post-liquefaction reconsolidation response of underlying low-plasticity silts; and (v) at-depth suppression of ejecta movement from thick crust of non-liquefiable soils. Such mitigating mechanisms are mostly encountered in deposits with interbedded liquefiable and non-liquefiable soils. For the levels of seismic demand considered in this study, such deposits show a limited liquefaction manifestation potential, from no manifestation to minor manifestation (NN-sites and part of NY-sites).

Results from the comprehensive series of effective stress analyses were used to identify a set of response measures (parameters) and associated criteria that allow to quantify the onset of independent mechanisms and effects of interaction between different mechanisms. This in turn provides basis for quantification of the system response effects on the seismic performance of liquefiable deposits. Specific processes and response features for five characteristic types of system responses identified by this rigorous quantification were summarized in Figs. 7.11 to 7.14.

The system-level interpretation of the responses of the 55 sites provided reasonable explanations for the strong variation in their performance (liquefaction manifestation) and the overall poor quality of the predictions by the simplified procedures, which ignore important system-response effects in the assessment. More specifically, the simplified procedures systematically over-estimate liquefaction manifestation for sites with interbedded deposits, while they tend to predict correctly for the majority of the cases or sometimes under-estimate

liquefaction manifestation, for sites with vertically continuous liquefiable soils (Table 7.2). Significant improvements in the assessment of the severity of liquefaction manifestation are possible when system response effects are appropriately considered, as illustrated by the promising predictions of a preliminary framework ($LSN_{SR} - H_{NL(0-1)}$) that incorporates such effects.

In conclusion, the scrutiny presented in this study highlights the governing influence of system response effects on liquefaction manifestation and emphasizes the need to incorporate such considerations in the liquefaction assessment.

REFERENCES

Abrahamson, C., Shi, H.-J., M., and Yang, B., 2016. *Ground-Motion Prediction Equations for Arias Intensity Consistent with the NGA-West2 Ground-Motion Models, PEER Report No. 2016/05,* University of California Berkeley, Berkeley, CA.

Abrahamson, N. A., Silva, W. J., and Kamai, R., 2014. Summary of the ASK14 ground motion relation for active crustal regions, *Earthquake Spectra* **30** (3), 1025–1055.

Afshari, K., and Stewart, J. P., 2016. Physically parameterized prediction equations for significant duration in active crustal regions, *Earthquake Spectra* **32** (4), 2057–2081.

Ambraseys, N., and Sarma, S., 1969. Liquefaction of soils induced by earthquakes, *Bulletin of the Seismological Society of America* **59** (2), 651–664.

Arias, A. 1970. Measure of earthquake intensity, in *Seismic Design for Nuclear Power Plants* (R. J. Hansen, ed.), MIT Press, Cambridge, MA, 438–483.

Arulanandan, K., Seed, H. B., Yogachandran, C., Muraleetharan, K., and Seed, R. B., 1993. Centrifuge study on volume changes and dynamic stability of earth dams, *Journal of Geotechnical Engineering* **119** (11), 1717–1731.

Baki, M. A. L. et al., 2020. *Personal communication.*

Balakrishnan, A., and Kutter, B. L., 1999. Settlement, sliding, and liquefaction remediation of layered soil, *Journal of Geotechnical Engineering* **125** (11), 968–978.

Bayless, J., and Abrahamson, N. A., 2019. Summary of the BA18 ground-motion model for Fourier amplitude spectra for crustal earthquakes in California, *Bulleting of the Seismological Society of America* **109** (5), 2088–2105.

Beavan, J., Motagh, M., Fielding, E. J., Donnelly, N., and Collett, D., 2012. Fault slip models of the 2010-2011 Canterbury, New Zealand, earthquakes from geodetic data and observations of postseismic ground deformation, *New Zealand Journal of Geology and Geophysics* **55** (3), 207–221.

Been, K., and Jefferies, M. G., 1985. A state parameter for sands. *Geotechnique* **35** (2), 99–112.

Benjamin and Associates, 1988. *A Criterion for Determining Exceedance of the Operating Basis Earthquake, EPRI Report NP-5930,* Electrical Power Research Institute, Palo Alto, CA.

Beyzaei, C. Z., Bray, J. D., Cubrinovski, M., Riemer, M., and Stringer, M., 2018. Laboratory-based characterization of shallow silty soils in southwest Christchurch, *Soil Dynamics and Earthquake Engineering* **110**, 93–109.

Biot, M. A., 1956. Theory of propagation of elastic waves in a fluid saturated porous solid, part I–low frequency range; part II–high frequency range. *Journal of Acoustical Society of America* **28** (1), 168–191.

Bommer, J. J., and Acevedo, A. B., 2004. The use of real earthquake accelerograms as input to dynamic analysis, *Journal of Earthquake Engineering* **8** (S1), 43-91.

Bommer, J. J., Stafford, P. J., and Alarcon, J. E., 2009. Empirical equations for the prediction of the significant, bracketed, and uniform duration of earthquake ground motion, *Bulleting of the Seismological Society of America* **99** (6), 3217–3233.

Bonilla, L. F., Archuleta, R. J., and Lavallee, D., 2005. Hysteretic and dilatant behavior of cohesionless soils and their effects on nonlinear site response: field data observations and modeling, *Bulleting of the Seismological Society of America* **95** (6), 2373–2395.

Boore, D. M., 2003a. Simulation of ground motion using the stochastic method, *Pure and Applied Geophysics* **160**, 635–676.

Boore, D. M., 2003b. Phase derivatives and simulation of strong ground motions, *Bulletin of the Seismological Society of America* **93** (3), 1132–1143.

Boore, D. M., and Thompson, E. M., 2014. Path durations for use in the stochastic-method simulation of ground motions, *Bulletin of the Seismological Society of America* **104** (5), 2541–2552.

Boore, D. M., and Thompson, E. M., 2015. Revisions to some parameters used in stochastic-method simulations of ground motion, *Bulletin of the Seismological Society of America* **105** (2A), 1029–1041.

Boore, D. M., Gibbs, J. F., Joyner, W. B., Tinsley, J. C., and Ponti, D. J., 2003. Estimated ground motion from the 1994 Northridge, California, earthquake at the site Interstate 10 and La Cienega Boulevard bridge collapse, West Los Angeles, California, *Bulletin of the Seismological Society of America* **93** (6), 2737–2751.

Bora, S. S., Cotton, F., and Scherbaum, F., 2019. NGA-West2 empirical Fourier and duration models to generate adjustable response spectra, *Earthquake Spectra* **35** (1), 61–93.

Bouckovalas, G. D., Tsiapas, Y. Z, Theocharis, A. I., and Chaloulos, Y. K., 2016. Ground response at liquefied sites: seismic isolation or amplification?, *Soil Dynamics and Earthquake Engineering* **91**, 329–339.

Boulanger, R. W., and DeJong, J. T., 2018. Inverse filtering procedure to correct cone penetration data for thin-layer and transition effects, in *Proceedings, 4th International Symposium on Cone Penetration Testing*, 21–22 June, 2018, Delft, The Netherlands.

Boulanger, R. W., and Idriss, I. M., 2014. *CPT and SPT Based Liquefaction Triggering Procedures, Rep. No. UCD/CGM-14/01*, Center for Geotechnical Modeling, Department of Civil and Environmental Engineering, University of California, Davis, CA.

Boulanger, R. W., and Truman, S. P., 1996. Void redistribution in sand under post-earthquake loading, *Canadian Geotechnical Journal* **33**, 829–834.

Boulanger, R. W., Kamai, R., and Ziotopoulou, K., 2014. Liquefaction induced strength loss and deformation: simulation and design, *Bulletin of Earthquake Engineering* **12**, 1107–1128.

Boulanger, R. W., Khosravi, M., Cox, B. R., and DeJong, J. T., 2018. Liquefaction evaluation for an interbedded soil deposit: St. Teresa's school, Christchurch, New Zealand, in *Proceedings, International Conference on Geotechnical and Earthquake Engineering*, 20–21 October, 2018, Chongqing, China.

Bradley, B. A., 2010. A generalized conditional intensity measure approach and holistic ground-motion selection, *Earthquake Engineering and Structural Dynamics* **39** (12), 1321–1342.

Bradley, B. A., 2012a. A ground motion selection algorithm based on the generalized conditional intensity measure approach, *Soil Dynamics and Earthquake Engineering* **40** (1), 48–61.

Bradley, B. A., 2012b, Strong ground motion characteristics observed in the 4 September 2010 Darfield, New Zealand earthquake, *Soil Dynamics and Earthquake Engineering* **42**, 32–46.

Bradley, B. A., 2013. A New Zealand-specific pseudospectral acceleration ground-motion prediction equation for active shallow crustal earthquakes based on foreign models, *Bulletin of the Seismological Society of America* **103** (3), 1801–1822.

Bradley, B. A., 2014. Site-specific and spatially-distributed ground-motion intensity estimation in the 2010-2011 Canterbury earthquakes, *Soil Dynamics and Earthquake Engineering* **61-62**, 83–91.

Bradley, B. A., 2015. Systematic ground motion observations in the Canterbury earthquakes and region-specific non-ergodic empirical ground motion modeling, *Earthquake Spectra* **31** (3), 1735–1761.

Bradley, B. A., 2019. On-going challenges in physics-based ground motion prediction and insights from the 2010-2011 Canterbury and 2016 Kaikoura, New Zealand earthquakes, *Soil Dynamics and Earthquake Engineering* **124**, 354–364.

Bradley, B. A., 2020. https://sites.google.com/site/brendonabradley/software/ground-motion-selection-gcim (last accessed 13 June 2020).

Bradley, B. A., and Baker, J. W., 2015. Ground motion directionality in the 2010-2011 Canterbury earthquakes, *Earthquake Engineering and Structural Dynamics* **44**, 371–384.

Bradley, B. A., and Cubrinovski, M., 2011. Near-source strong ground motions observed in the 22 February 2011 Christchurch earthquake, *Seismological Research Letters* **82** (6), 853–865.

Bradley, B. A., Cubrinovski, M., Dhakal, R. P., and MacRae, G. A., 2009. Intensity measures for the seismic response of pile foundations, *Soil Dynamics and Earthquake Engineering* **29**, 1046–1058.

Bradley, B. A., Quigley, M. C., Van Dissen, R. J., and Litchfield, N. J., 2014. Ground motion and seismic source aspects of the Canterbury earthquake sequence, *Earthquake Spectra* **30** (1), 1–15.

Bray, J. D., and Luque, R., 2017. Seismic performance of a building affected by moderate liquefaction during the Christchurch earthquake, *Soil Dynamics and Earthquake Engineering* **102**, 99–111.

Bray, J. D., and Macedo, J., 2017. 6th Ishihara lecture: simplified procedure for estimating liquefaction-induced building settlement, *Soil Dynamics and Earthquake Engineering* **102**, 215–231.

Bray, J. D., and Sancio, R. B., 2006. Assessment of the liquefaction susceptibility of fine grained soils, *Journal of Geotechnical and Geoenvironmental Engineering* **132** (9), 1165–1177.

Bray, J. D., Cubrinovski, M., Zupan, J. D., and Taylor, M. L., 2014. Liquefaction effects on buildings in the central business district of Christchurch, *Earthquake Spectra* **30** (1), 85–109.

Brown, L. J., and Weeber, J. H., 1992. *Geology of the Christchurch urban area*, Institute of Geological and Nuclear Sciences, Lower Hutt, New Zealand, GNS Science.

Bullock, Z., Karimi, Z., Dashti, S., Porter, K., Liel, A. B., and Franke, K. W., 2019. A physics-informed semi-empirical probabilistic model for the settlement of shallow-founded structures on liquefiable ground, *Geotechnique* **69** (5), 406–419.

Burger, R. W., Somerville, P. G., Barker, J. S., Herrmann, R. B., and Helmberger, D. V., 1987. The effect of crustal structure on strong ground motion attenuation relations in eastern North America, *Bulletin of the Seismological Society of America* **77** (2), 420–439.

Campbell, K. W., and Bozorgnia, Y., 2014. NGA-West2 ground motion model for the average horizontal components of PGA, PGV, and 5% damped linear acceleration response spectra, *Earthquake Spectra* **30** (3), 1087–1115.

Castro, G., 1975. Liquefaction and cyclic mobility of saturated sands, *Journal of Geotechnical Engineering Division*, ASCE **101** (GT6), 551–569.

Ching, J., Wang, J-S., Hsein Juang, C., and Ku, C-S., 2015. Cone penetration test (CPT)-based stratigraphic profiling using the wavelet transform modulus maxima method, *Canadian Geotechnical Journal* **52** (1), 1993–2007.

Chiou, B. S. J., and Youngs, R. R., 2014. Update of the Chiou and Youngs NGA model for the average horizontal component of peak ground motion and response spectra, *Earthquake Spectra* **30** (3), 1117–1153.

Cox, B. R., McLaughlin, K. A., van Ballegooy, S., Cubrinovski, M., Boulanger, R., and Wotherspoon, L., 2017. In-situ investigation of false-positive liquefaction sites in Christchurch, New Zealand: St. Teresa's school case history, in *Proceedings, PBD-III Earthquake Geotechnical Engineering,* 16–19 July, 2017, Vancouver, Canada.

Cox, B. R., Stolte, A. C., Stokoe, K. H., and Wotherspoon, L. M., 2019. A direct-push crosshole (DPCH) test method for the in situ evaluation of high-resolution P- and S-wave velocities. *Geotechnical Testing Journal* **42** (5), 1101–1132.

Cubrinovski, M., 2019. Some important considerations in the engineering assessment of soil liquefaction, in *Proceedings, 2019 ANZ Conference*, 1–3 April, 2019, Perth, Australia.

Cubrinovski, M., and Ishihara, K., 1998a. Modelling of sand behaviour based on state concept, *Soils and Foundations* **38** (3), 115–127.

Cubrinovski, M., and Ishihara, K., 1998b. State concept and modified elastoplasticity for sand modelling, *Soils and Foundations* **38** (4), 213–225.

Cubrinovski, M., and McCahon, I., 2011. *Foundations on Deep Alluvial Soils, Technical Report Prepared for Canterbury Earthquakes Royal Commission,* University of Canterbury, Christchurch.

Cubrinovski, M., and Robinson, K., 2016. Lateral spreading: evidence and interpretation from the 2010-2011 Christchurch earthquakes, *Soil Dynamics and Earthquake Engineering* **91**, 187–201.

Cubrinovski, M., Bradley, B., Wotherspoon, L., Green, R., Bray, J., Wood, C., Pender, M., Allen, J., Bradshaw, A., Rix, G., Taylor, M., Robinson, K., Henderson, D., Giorgini, S., Ma, K., Winkley, A., Zupan, J., O'Rourke, T., DePascale, G., and Wells, D., 2011. Geotechnical aspects of the 22 February 2011 Christchurch earthquake, *Bulletin of the New Zealand Society for Earthquake Engineering* **44** (4), 205–226.

Cubrinovski, M., Green, R. A., Allen, J., Ashford, S., Bowman, E., Bradley, B., Cox, B., Hutchinson, T., Kavazanjian, E., Orense, R., Pender, M., Quigley, M., and Wotherspoon, L., 2010. Geotechnical reconnaissance of the 2010 Darfield (Canterbury) earthquake, *Bulletin of the New Zealand Society for Earthquake Engineering* **43** (4), 243–320.

Cubrinovski, M., Ishihara, K., and Furukawazono, K., 2000. Analysis of two case histories of liquefaction of reclaimed deposits, Paper No. 1618, in *Proceedings, 12th World Conference on Earthquake Engineering*, 30 January – 4 February, 2000, Auckland, New Zealand.

Cubrinovski, M., Ishihara, K., and Tanizawa, F., 1996. Numerical simulation of the Kobe Port island liquefaction, Paper No. 330, in *Proceedings, 11th World Conference on Earthquake Engineering*, 23–28 June, 1996, Acapulco, Mexico.

Cubrinovski, M., Ntritsos, N., Dhakal, R., and Rhodes, A., 2019a. Key aspects in the engineering assessment of soil liquefaction, in *Earthquake Geotechnical Engineering for Protection and Development of Environment and Constructions* (Silvestri & Moraci eds.), Associazione Geotecnica Italiana, Rome, 189–208.

Cubrinovski, M., Rhodes, A., Ntritsos, N., and van Ballegooy, S., 2019b. System response of liquefiable deposits, *Soil Dynamics and Earthquake Engineering* **124**, 212–229.

Cubrinovski, M., Robinson, K., Taylor, M., Hughes, M., and Orense, R. 2012. Lateral spreading and its impacts in urban areas in the 2010-2011 Christchurch earthquakes, *New Zealand Journal of Geology and Geophysics* **55** (3), 255–269.

Cubrinovski, M., Uzuoka, R., Sugita, H., Tokimatsu, K., Sato, M., Ishihara, K., Tsukamoto, Y., and Kamata, T. 2008. Prediction of pile response to lateral spreading by 3-D soil-water coupled dynamic analysis: Shaking in the direction of ground flow, *Soil Dynamics and Earthquake Engineering* **28** (1), 421–435.

Cubrinovski, M., Winkley, A., Haskell, J., Palermo, A., Wotherspoon, L., Robinson, K., Bradley, B., Brabhaharan, P., and Hughes, M., 2014. Spreading-induced damage to short-span bridges in Christchurch, New Zealand, *Earthquake Spectra* **30** (1), 57–83.

Darendeli, M. B., 2001. Development of a new family of normalized modulus reduction curves and material damping curves, Ph.D. Thesis, University of Texas, Austin.

Dashti, S., and Karimi, Z., 2017. Ground motion intensity measures to evaluate I: the liquefaction hazard in the vicinity of shallow-founded structures, *Earthquake Spectra* **33** (1), 241–276.

Dashti, S., Bray, J. D., Pestana, J. M., Riemer, M., and Wilson, D., 2010. Mechanisms of seismically induced settlement of buildings with shallow foundations on liquefiable soil, *Journal of Geotechnical and Geoenvironmental Engineering* **136** (1), 151–164.

Dobry, R., 1989. Some basic aspects of soil liquefaction during earthquakes, in *Earthquake Hazards and the Design of Constructed Facilities in the Eastern United States, Annals of the New York Academy of Science* (K. H. Jacob, and C. J. Turkstra, eds.), New York, NY, 558, 172–182.

Dobry, R., and Abdoun, T., 2015. 3rd Ishihara Lecture: An investigation into why liquefaction charts work: A necessary step toward integrating the states of art and practice, *Soil Dynamics and Earthquake Engineering* **68**, 40–56.

Dobry, R., and Liu, L., 1992. Centrifuge modeling of soil liquefaction, in *Proceedings, 10th World Conference on Earthquake Engineering*, 19–24 July, 1992, Madrid, Spain, 6801–6809.

Douglas, J., 2007. Inferred ground motions on Guadeloupe during the 2004 Les Saintes earthquake, *Bulletin of the Seismological Society of America* **5**, 363–376.

Dziewonski, A. M., and Hales, A. L., 1972. Numerical analysis of dispersed seismic waves, in *Methods in Computational Physics Vol. 11 Seismology: Surface Waves and Earth Oscillations* (B. A. Bolt, ed.), Academic Press, New York, NY, 39–85.

Elgamal, A. W., Dobry, R., and Adalier, K., 1989. Study of effects of clay layers on liquefaction of sand deposits using small-scale models, in *Proceedings, 2nd US-Japan Workshop on Liquefaction, Large Ground Deformation and Their Effects on Lifelines*, 26–29 September, 1989, NCEER, SUNY-Buffalo, Buffalo, NY, 233–245.

Elwood, K. J., Comerio, M., Cubrinovski, M., Davis, C., Johnston, D., O'Rourke, T. D., and Pampanin, S. (eds.), 2014. Special issue on the 2010-2011 Canterbury earthquake sequence, *Earthquake Spectra* **30** (1), 1–613.

Fiegel, G. L., and Kutter, B. L., 1994. Liquefaction mechanism of layered soils, *Journal of Geotechnical Engineering* **120** (4), 737–755.

Field, E. H., Jordan, T. H., and Cornell, C. A., 2003. OpenSHA: a developing community-modeling environment for seismic hazard analysis, *Seismological Research Letters* **74** (1), 406–419.

Gingery, J. R., Elgamal, A., and Bray, J. D., 2015. Response spectra at liquefaction sites during shallow crustal earthquakes, *Earthquake Spectra* **31** (4), 2325–2349.

Graves, R. W., and Pitarka, A., 2010. Broadband ground-motion simulation using a hybrid approach, *Bulletin of the Seismological Society of America* **100** (5A), 2095–2123.

Green, R. A., Cubrinovski, M., Cox, B., Wood, C., Wotherspoon, L., Bradley, B., and Maurer, B., 2014. Select liquefaction case histories from the 2010-2011 Canterbury earthquake sequence, *Earthquake Spectra* **30** (1), 131–153.

Grozic, J. L. H., Robertson, P. K., and Morgenstern, N. R., 2000. Cyclic liquefaction of loose gassy sand, *Canadian Geotechnical Journal* **37** (4), 843–856.

Hashash, Y. M. A., Musgrove, M. I., Harmon, J. A., Groholski, D. R., Phillips, C. A. and Park, D., 2016. *DEEPSOIL 6.1, User Manual*, University of Illinois at Urbana-Champaign, IL.

Hossain, A. M., Andrus, R. D., and Camp, W. M., III., 2013. Correcting liquefaction resistance of unsaturated soil using wave velocity, *Journal of Geotechnical and Geoenvironmental Engineering* **139** (2), 277–287.

Housner, G. W., 1952. Spectrum intensities of strong-motion earthquakes, in *Proceedings, Symposium on Earthquakes and Blast Effects on Structures*, June, 1952, Los Angeles, CA.

Housner, G. W., 1958. The mechanism of sandblows, *Bulletin of the Seismological Society of America* **48**, 155–161.

Iai, S., Morita, T., Kameoka, T., Matsunaga, Y., and Abiko., K., 1995. Response of a dense sand deposit during 1993 Kushiro-oki earthquake, *Soils and Foundations* **35** (1), 115–131.

Idriss, I. M., and Boulanger, R. W., 2008. *Soil Liquefaction during Earthquakes*, Monograph MNO-12, Earthquake Engineering Research Institute, Oakland, CA, 261 pp.

Ishihara, K., 1985. Stability of natural deposits during earthquakes, in *Proceedings, 11th International Conference on Soil Mechanics and Foundation Engineering*, 12–16 August, 1985, San Francisco, CA.

Ishihara, K., 1993. Liquefaction and flow failure during earthquakes, *33rd Rankine Lecture, Geotechnique* **43** (3), 351–451.

Ishihara, K., 1996. *Soil Behaviour in Earthquake Geotechnics*, Oxford Engineering Science Series, No. 46, 340 pp.

Ishihara, K., and Yoshimine, M., 1992. Evaluation of settlements in sand deposits following liquefaction during earthquakes, *Soils and Foundations* **32** (1), 173–188.

Iwasaki, T., Tatsuoka, F., Tokida, K., and Yasuda, S., 1978. A practical method for assessing soil liquefaction potential based on case studies at various sites in Japan, in *Proceedings, 2nd International Conference on Microzonation*, National Science Foundation, Washington, D.C., 1978.

Kaklamanos, J., and Bradley, B. A., 2018. Challenges in predicting seismic site response with 1D analyses: conclusions from 114 KiK-net seismometer arrays, *Bulletin of the Seismological Society of America* **108** (5A), 2816–2838.

Kamata, T., Tsukamoto, Y., and Ishihara, K., 2009. Undrained shear strength of partially saturated sand in triaxial tests, *Bulletin of the New Zealand Society for Earthquake Engineering* **42** (1), 57–62.

Karimi, Z., and Dashti, S., 2017. Ground motion intensity measures to evaluate II: the performance of shallow-founded structures on liquefiable ground, *Earthquake Spectra* **33** (1), 277–298.

Katsanos, E. I., Sextos, A. G., and Manolis, G. D., 2010. Selection of earthquake ground motion records: A state-of-the-art review from a structural engineering perspective, *Soil Dynamics and Earthquake Engineering* **30**, 157–169.

Kayen, R. E., and Mitchell, J. K., 1997. Assessment of liquefaction potential during earthquakes by Arias intensity, *Journal of Geotechnical and Geoenvironmental Engineering* **123** (12), 1162–1174.

Kokusho, T., 1999. Water film in liquefied sand and its effect on lateral spread, *Journal of Geotechnical Engineering* **125** (10), 817–826.

Kokusho, T., 2000. Mechanism for water film generation and lateral flow in liquefied sand layer, *Soils and Foundations* **40** (5), 99–111.

Kokusho, T., 2014. Seismic base-isolation mechanism in liquefied sand in terms of energy, *Soil Dynamics and Earthquake Engineering* **63**, 92–97.

Kokusho, T., and Kojima, T., 2002. Mechanism for postliquefaction water film generation in layered sand, *Journal of Geotechnical Engineering* **128** (2), 129–137.

Kottke, A. R., and Rathje, E. M., 2009. *Technical Manual for Strata*, *PEER Report No. 2008/10*, University of California Berkeley, Berkeley, CA.

Kramer, S. L., and Mitchell, R. A., 2006. Ground motion intensity measures for liquefaction hazard evaluation, *Earthquake Spectra* **22** (2), 413–438.

Kramer, S. L., Hartvigsen, A. J., Sideras, S. S., and Ozener, P. T., 2011. Site response modeling in liquefiable soil deposits, in *Proceedings, 4th International IASPEI/IAEE Symposium on the Effects of Surface Geology on Seismic Motion*, 23–26 August, 2011, University of California Santa Barbara, CA.

Kramer, S. L., Sideras, S. S., and Greenfield, M. W., 2016. The timing of liquefaction and its utility in liquefaction hazard evaluation, *Soil Dynamics and Earthquake Engineering* **91**, 133–146.

Kuhlemeyer, R. L., and Lysmer, J., 1973. Finite element method accuracy for wave propagation problems, *Journal of Soil Mechanics and Foundation Division* **99** (SM5), 421–427.

Kulasingam, R., Malvick, E. J., Boulanger, R. W., and Kutter, B. L., 2004. Strength loss and localization at silt interlayers in slopes of liquefied sand, *Journal of Geotechnical and Geoenvironmental Engineering* **130** (11), 1192–1202.

Kwak, D. Y., Stewart, J. P., Brandenberg, S. J., and Mikami, A., 2016. Characterization of seismic levee fragility using field performance data, *Earthquake Spectra* **32** (1), 193–215.

Lee, R. L., Bradley, B. A., and McGann, C. R., 2017a. 3D models of Quaternary-aged sedimentary successions within the Cantebury, New Zealand region, *New Zealand Journal of Geology and Geophysics* **60** (4), 320–340.

Lee, R. L., Bradley, B. A., Ghisetti, F. C., and Thompson, E. M., 2017b. Development of a 3D velocity model of the Canterbury, New Zealand region for broadband ground-motion simulation, *Bulletin of the Seismological Society of America* **107** (5), 2131–2150.

Liu, H., and Qiao, T., 1984. Liquefaction potential of saturated sand deposits underlying foundation of structure, in *Proceedings, 8th World Conference on Earthquake Engineering*, 21–28 July, 1984, San Francisco, CA.

Liu, J. M., Wang, T., Wu, S. R., and Gao, M. T., 2016. New empirical relationships between Arias intensity and peak ground acceleration, *Bulletin of the Seismological Society of America* **106** (5), 2168–2176.

Luco, N., and Bazzurro, P., 2007. Does the amplitude scaling of ground motion records result in biased nonlinear structural drift responses?, *Earthquake Engineering and Structural Dynamics* **36**, 1813–1835.

Lysmer, J., and Kuhlemeyer, R. L., 1969. Finite dynamic model for infinite media, *Journal of Engineering Mechanics* **95** (EM4), 859–877.

Macedo, J., Abrahamson, N., and Bray, J. D., 2019. Arias intensity conditional scaling ground-motion models for subduction zones, *Bulletin of the Seismological Society of America* **109** (4), 1343–1357.

Mai, P. M., 2009. Ground motion: complexity and scaling in the near field of earthquake ruptures, in *Encyclopedia of Complexity and Systems Science* (W. H. K. Lee & R. Meyers, eds.), Springer, NY, 4435–4474.

Malvick, E. J., Kutter, B. L., and Boulanger, R. W., 2004. Postshaking shear strain localization in a centrifuge model of a saturated sand slope, *Journal of Geotechnical and Geoenvironmental Engineering* **134** (2), 164–174.

Markham, C. S., Bray, J. D., Cubrinovski, M., and Riemer, M. F., 2018. Liquefaction resistance and steady-state characterization of shallow soils within the Christchurch Central Business District, *Journal of Geotechnical and Geoenvironmental Engineering* **144** (6), https://doi.org/10.1061/(ASCE)GT.1943-5606.0001823.

Markham, C. S., Bray, J. D., Macedo, J., and Luque, R., 2016. Evaluating nonlinear effective stress site response analyses using records from the Canterbury earthquake sequence, *Soil Dynamics and Earthquake Engineering* **82**, 84–98.

Masing, G. 1926. Eigenspannungen and verfertigung beim messing, in *Proceedings, 2nd International Congress on Applied Mechanics*, Zurich.

Maugeri, M., Simonelli, A. L., Ferraro, A., Grasso, S., and Penna, A., 2011. Recorded ground motion and site effects evaluation for the April 6, 2009 L'Aquila earthquake, *Bulletin of Earthquake Engineering* **9**, 157–179.

Maurer, B. W., Green, R. A., Cubrinovski, M., and Bradley, B. A., 2014. Evaluation of the liquefaction potential index for assessing liquefaction hazard in Christchurch, New Zealand, *Journal of Geotechnical and Geoenvironmental Engineering* **140** (7).

McGann, C. R., Bradley, B. A., Taylor, M. L., Wotherspoon, L. M., and Cubrinovski, M., 2015. Development of an empirical correlation for predicting shear wave velocity for Christchurch soils from cone penetration test data, *Soil Dynamics and Earthquake Engineering* **75**, 66–75.

Moss, R. E., Seed, R. B., Kayen, R. E., Stewart, J. P., Der Kiureghian, A., and Cetin, K. O., 2006. CPT-based probabilistic and deterministic assessment of in situ seismic soil liquefaction potential, *Journal of Geotechnical and Geoenvironmental Engineering* **132** (8), 1032–1051.

Motazedian, D., and Atkinson, G. M., 2005. Stochastic finite-fault modeling based on dynamic corner frequency, *Bulletin of the Seismological Society of America* **95** (3), 995–1010.

Nakazawa, H., Ishihara, K., Tsukamoto, Y., and Kamata, T., 2004. Case studies on evaluation of liquefaction resistance of imperfectly saturated soil deposits, in *Proceedings, International Conference on Cyclic Behaviour of Soils and Liquefaction Phenomena*, 31 March – 2 April, 2004, Bochum, Germany.

New Zealand Geotechnical Database (NZGD), 2020. New Zealand Geotechnical Database, available at http://www. nzgd.org.nz (last accessed 4 April 2020).

Novikova, E. I., and Trifunac, M. D., 1994. Duration of strong ground motion in terms of earthquake magnitude, epicentral distance, site conditions and site geometry, *Earthquake Engineering and Structural Dynamics* **23** (9), 1023–1043.

Ntritsos, N., and Cubrinovski, M., 2020a. A CPT-based effective stress analysis procedure for liquefaction assessment, *Soil Dynamics and Earthquake Engineering* **131**, (available online).

Ntritsos, N., and Cubrinovski, M., 2020b. Input motions for effective stress analyses of sites affected by the 2010 Darfield and 2011 Christchurch earthquakes, *Earthquake Spectra* (submitted).

Ntritsos, N., Cubrinovski, M., and Bradley, B. A., 2019. Effective stress analysis of Christchurch strong motion station sites, in *Earthquake Geotechnical Engineering for Protection and Development of Environment and Constructions* (Silvestri & Moraci ed.), Associazione Geotecnica Italiana, Rome, 4144–4153.

Ntritsos, N., Cubrinovski, M., and Bradley, B. A., 2020. On the use of within-event recorded ground motions in forensic analysis of sites in the near-source region, *Earthquake Spectra* (submitted).

O'Rourke, T. D., Jeon, S.-S., Torpak, S., Cubrinovski, M., Hughes, M., van Ballegooy, S., and Bouziou, D., 2014. Earthquake response of underground pipeline networks in Christchurch, NZ, *Earthquake Spectra* **30** (1), 183–204.

Ohsaki, Y., 1979. On the significance of phase content in earthquake ground motions, *Earthquake Engineering and Structural Dynamics* **7**, 427–439.

Okamura, M., and Soga, Y., 2006. Effects of pore fluid compressibility on liquefaction resistance of partially saturated sand, *Soils and Foundations* **46** (5), 695–700.

Okamura, M., Ishihara, K., and Tamura, K., 2006. Degree of saturation and liquefaction resistances of sand improved with sand compaction pile, *Journal of Geotechnical and Geoenvironmental Engineering* **132** (2), 258–264.

Ou, G. B., and Herrmann, R. B., 1990. A statistical model for ground motion produced by earthquakes at local and regional distances, *Bulletin of the Seismological Society of America* **80** (6A), 1397–1417.

Pease, J. W., and O'Rourke, T. D., 1997. Seismic response of liquefaction sites, *Journal of Geotechnical and Geoenvironmental Engineering*, **123** (1), 37–45.

Pradel, D., Smith, P. M., Stewart, P. J., and Raad, G., 2005. Case history of landslide movement during the Northridge earthquake, *Journal of Geotechnical and Geoenvironmental Engineering*, **131** (11), 1360–1369.

Rathje, E. M., Abrahamson, N. A., and Bray, J. D., 1998. Simplified frequency content estimates of earthquake ground motions, *Journal of Geotechnical and Geoenvironmental Engineering* **124** (2), 150–159.

Reynolds, O., 1885. On the dilatancy of media composed of rigid particles in contact, with experimental illustrations, *Philosophical Magazine, Series 5* **20** (127), 469–481.

Rhodes, A., 2017. Liquefaction evaluation in stratified soils, M.E. Thesis, University of Canterbury, Christchurch.

Ripperger, J., Mai, P. M., and Ampuero, J.-P., 2008. Variability of near-field ground motion from dynamic earthquake rupture simulations, *Bulleting of the Seismological Society of America* **98** (3), 1207–1228.

Robertson, P. K., 2016. Cone penetration test (CPT)-based soil behaviour type (SBT) classification system – an update, *Canadian Geotechnical Journal* **53** (12), 1910–1927.

Robertson, P. K., and Cabal, K. L., 2015. *Guide to Cone Penetration Testing*, 6th edition, Greg Drilling & Testing, Inc., Signal Hill, CA, 133 pp.

Robertson, P. K., and Wride, C. K., 1998. Evaluating cyclic liquefaction potential using the cone penetration test, *Canadian Geotechnical Journal* **35** (3), 442–459.

Roesset, J. M., Huerta, C. I., and Stokoe, K. H. II, 1995. Effect of magnitude and type of damping on soil amplification, Paper No. 10.25, in *Proceedings, 3rd International Conference on Recent Advances in Geotechnical Earthquake Engineering and Soil Dynamics*, 2–7 April, 1995, St. Louis, MO.

Roscoe, K. H., and Poorooshasb, H. B., 1963. A fundamental principle of similarity in model tests for earth pressure problems, in *Proceedings, 2nd Asian Conference on Soil Mechanics*, **1**, 134–140.

Russell, J., and van Ballegooy, S., 2015. *Canterbury Earthquake Sequence: Increased Liquefaction Vulnerability Assessment Methodology, Tonkin+Taylor Report prepared for the Earthquake Commission.*

Schofield, A., and Wroth, P., 1968. *Critical State Soil Mechanics*, McGraw-Hill, New York, NY, 310 pp.

Scott, R. F., and Zuckerman, K. A., 1973. Sandblows and liquefaction, in *The Great Alaska Earthquake of 1964*, Committee on the Alaska Earthquake, Division of Earth Sciences, National Research Council, National Academy of Sciences, Washington, D. C., 179–189.

Seed, H. B., 1979. Soil liquefaction and cyclic mobility evaluation of level ground during earthquakes, *Journal of the Geotechnical Engineering Division* **105** (GT2), 201–255.

Seed, H. B., 1987. Design problems in soil liquefaction, *Journal of the Geotechnical Engineering Division* **113** (8), 827–845.

Seed, H. B., and Idriss, I. M., 1971. Simplified procedure for evaluating soil liquefaction potential, *Journal of Soil Mechanics and Foundations Division* **97** (SM9), 1249–1273.

Seed, H. B., Tokimatsu, K., Harder, L. F., and Chung, R. M., 1985. Influence of SPT procedure in soil liquefaction resistance evaluations, *Journal of Geotechnical Engineering*, **111** (12), 1425–1445.

Seed, R. B., Cetin, K. O., Moss, R. E. S., Kammerer, A. M., Wu, J., Pestana, J. M., Riemer, M. F., Sancio, R. B., Bray, J. D., Kayen, R. E., and Faris, A. 2003. Recent advances in soil liquefaction engineering: a unified and consistent framework, in *Proceedings, 26th Annual ASCE Los Angeles Geotechnical Spring Seminar*, 30 April, 2003, Long Beach, CA.

Seid-Karbasi, M., and Byrne, P. M., 2007. Seismic liquefaction, lateral spreading, and flow slides: a numerical investigation into void redistribution, *Canadian Geotechnical Journal*, **44** (7), 873–890.

Sento, N., Kazama, M., Uzuoka, R., Ohmura, H., and Ishimaru, M., 2004. Possibility of postliquefaction flow failure due to seepage, *Journal of the Geotechnical and Geoenvironmental Engineering*, **130** (7), 707–716.

Sherif, M. A., Ishibasi, I., and Tsuchiya, C., 1977. Saturation effects on initial soil liquefaction, *Journal of the Geotechnical Engineering Division*, **103** (GT8), 914–917.

Silva, W. J., 1988. *Soil Response to Earthquake Ground Motion*, *EPRI Report No. NP-5747*, Electric Power Research Institue, Palo Alto, CA.

Smyrou, E., Tasiopoulou, P., Bal, I. E., and Gazetas, G., 2011. Ground motions versus geotechnical and structural damage in the February 2011 Christchurch earthquake, *Seismological Research Letters* **82** (6), 882–892.

Standards New Zealand, 2004. Structural design actions, Part 5: Earthquake actions – New Zealand, NZS 1170.5:2004, Standards New Zealand, Wellington, 87 pp.

Stoffa, P. L., Buhl, P., and Bryan, G. M., 1974. The application of homomorphic deconvolution to shallow-water marine seismology. I. Models, *Geophysics* **39**, 401–416.

Stringer, M., Taylor, M. L., and Cubrinovski, M., 2015. *Advanced Soil Sampling of Silty Sands in Christchurch, Rep. No. 2015-06, University of Canterbury*, Christchurch.

Taisei Corporation, 1997. *DIANA-J3: Finite Element Program for Effective Stress Analysis of Two-phase Soil Medium, Internal report* (in Japanese).

Tarbali, K., and Bradley, B. A., 2015. Ground motion selection for scenario ruptures using the generalized conditional intensity measure (GCIM) method, *Earthquake Engineering and Structural Dynamics* **44**, 1601–1621.

Tarbali, K., and Bradley, B. A., 2016. The effect of causal parameter bounds in PSHA-based ground motion selection algorithm, *Earthquake Engineering and Structural Dynamics* **45** (1), 1515–1535.

Tarbali, K., Bradley, B. A., and Baker, J. W., 2018. Consideration and propagation of ground motion selection epistemic uncertainties to seismic performance metrics, *Earthquake Spectra* **34** (2), 587–610.

Tasiopoulou, P., Smyrou, E., Bal, I. E., Gazetas, G., and Vintzileou, E., 2011. *Geotechnical and Structural Field Observations from Christchurch, Research Report,* National Technical University of Athens, Athens.

Tatsuoka, F., Zhou, S., Sato, T., and Shibuya, S., 1990. *Method for Evaluating Liquefaction Potential and its Application, Report on Seismic hazards in the Soil Deposits in Urban Areas,* Ministry of Education of Japan (in Japanese).

Taylor, M. L., 2015. The geotechnical characterization of Christchurch sands for advanced soil modelling, Ph.D. Thesis, University of Canterbury, Christchurch.

Teague, D. P., Cox, B. R., Bradley, B. A., and Wotherspoon, L. M., 2018. Development of deep shear wave velocity profiles with estimates of uncertainty in the complex interbedded geology of Christchurch, New Zealand, *Earthquake Spectra* **34** (2), 639–672.

Thrainsson, H., and Kiremidjian, A. S., 2002. Simulation of digital earthquake accelerograms using the inverse discrete Fourier transform, *Earthquake Engineering and Structural Dynamics* **31**, 2023–2048.

Tokimatsu, K., Taya, Y., and Zhang, J. M., 2001. Effects of pore water redistribution on post-liquefaction deformation of sands, in *Proceedings, 15th International Conference on Soil Mechanics and Geotechnical Engineering*, 27–31 August, 2001, Istanbul, Turkey.

Trifunac, M. D., and Brady, A. G., 1975. A study on the duration of strong earthquake ground motion, *Bulletin of the Seismological Society of America* **65** (3), 581–626.

Tsaparli, V., Kontoe, S., Taborda, D. M. G., and Potts, D. M., 2020. A case study of liquefaction: demonstrating the application of an advanced model and understanding the pitfalls of the simplified procedure, *Geotechnique* **70** (6), 538–558.

Tsukamoto, Y., Ishihara, K., Nakazawa, H., Kamada, K., and Huang, Y., 2002. Resistance of partly saturated sand to liquefaction with reference to longitudinal and shear wave velocities, *Soils and Foundations* **42** (6), 93–104.

Tsukamoto, Y., Kawabe, S., Matsumoto, J., and Hagiwara, S., 2014. Cyclic resistance of two unsaturated silty sands against soil liquefaction, *Soils and Foundations* **54** (6), 1094–1103.

Vaid, Y. P., and Eliadorani, A., 1998. Instability and liquefaction of granular soils under undrained and partially drained states, *Canadian Geotechnical Journal* **35** (6), 1053–1062.

van Ballegooy, S., Cox, S. C., Thurlow, C., Rutter, H. K., Reynolds, T., Harrington, G., Fraser, J., and Smith, T., 2014a. *Median Water Table Elevation in Christchurch and Surrounding Area after the 4 September 2010 Darfield Earthquake, Version 2, GNS Science Report 2014/18*, Lower Hutt, New Zealand.

van Ballegooy, S., Malan, P., Lacrosse, V., Jacka, M. E., Cubrinovski, M., Bray, J. D., O'Rourke, T. D., Crawford, S. A., and Cowan, H., 2014b. Assessment of liquefaction-induced land damage for residential Christchurch, *Earthquake Spectra* **30** (1), 31–55.

Verdugo, R., 1992. Characterization of sandy soils and its application to seismic response analysis, Ph.D. Thesis, University of Tokyo, Tokyo.

Wang, Y., Huang, K., and Cao, Z., 2013. Probabilistic identification of underground soil stratification using cone penetration tests, *Canadian Geotechnical Journal* **50** (1), 766–776.

Whitman, R. V., 1985. On liquefaction, in *Proceedings, 11th International Conference on Soil Mechanics and Foundation Engineering*, A. A. Balkema, San Francisco, CA, 1923–1926.

Wood, C. M., Cox, B. R., Wotherspoon, L. M., and Green, R. A., 2011. Dynamic site characterization of Christchurch strong motion stations. *Bulletin of the New Zealand Society for Earthquake Engineering* **44** (4), 195–204.

Worden, B. C., Thompson, E. M., Baker, J. W., Bradley, B. A., Luco, N., and Wald, D. J., 2018. Spatial and spectral interpolation of ground-motion intensity measure observations, *Bulletin of the Seismological Society of America* **108** (2), 866–875.

Wotherspoon, L. M., Orense, R., Bradley, B. A., Cox, B. R., Wood, C. M., and Green, R. A., 2015a. *Geotechnical Characterization of Christchurch Strong Motion Stations, Version 3.0, Earthquake Commission Report, Project No. 12/269*, University of Auckland, Auckland.

Wotherspoon, L. M., Orense, R., Green, R. A., Bradley, B. A., Cox, B. R., and Wood, C. M., 2015b. Assessment of liquefaction evaluation procedures and severity index frameworks at Christchurch strong motion stations, *Soil Dynamics and Earthquake Engineering* **79**, 335–346.

Yang, J., Savidis, S., and Roemer, M., 2004. Evaluating liquefaction potential of partially saturated sand, *Journal of Geotechnical and Geoenvironmental Engineering* **130** (9), 975–979.

Yang, Z., and Elgamal, A. W., 2002. Influence of permeability on liquefaction-induced shear deformation, *Journal of Engineering Mechanics* **128** (7), 720–729.

Yee, E., Stewart, J. P., and Tokimatsu, K., 2013. Elastic and large-strain nonlinear seismic site response from analysis of vertical array recordings, *Journal of Geotechnical and Geoenvironmental Engineering* **139** (10), 1789–1801.

Yenier, E., and Atkinson, G. M., 2014. Equivalent point-source modeling of moderate-to-large magnitude earthquakes and associated ground-motion saturation effects, *Bulletin of the Seismological Society of America* **104** (3), 1458–1478.

Yoshimi, Y., and Kuwabara, F., 1973. Effect of subsurface liquefaction on the strength of surface soil, *Soils and Foundations* **13** (2), 67–81.

Yoshimi, Y., Tanaka, K., and Tokimatsu, K., 1989. Liquefaction resistance of a partially saturated sand. *Soils and Foundations* **29** (3), 157–162.

Yoshimine, M., Nishizaki, H., Amano, K., and Hosono, Y., 2006. Flow deformation of liquefied sand under constant shear load and its application to analysis of flow slide in infinite slope, *Soil Dynamics and Earthquake Engineering* **26** (1), 253–264.

Yost, K. M., Cox, B. R., Wotherspoon, L., Boulanger, R. W., van Ballegooy, S., and Cubrinovski, M., 2019. In-situ investigation of false-positive liquefaction sites in Christchurch, New Zealand: Palinurus road case history, in *Proceedings, Geo-Congress*, 24–27 March, 2019, Philadelphia, PA.

Youd, T. L., and Carter, B. L., 2005. Influence of soil softening and liquefaction on spectral acceleration, *Journal of Geotechnical and Geoenvironmental Engineering* **131**, 811–825.

Youd, T. L., Idriss, I. M., Andrus, R. D., Arango, I., Castro, G., Christian, J. T., … Stokoe, K. H. II, 2001. Liquefaction resistance of soils: Summary report from the 1996 NCEER and 1998 NCEER/NSF workshops on evaluation of liquefaction resistance of soils, *Journal of Geotechnical and Geoenvironmental Engineering* **127** (20), 817–833.

Zerva, A., 2009. *Spatial Variation of Seismic Ground Motions: Modeling and Engineering Applications*, CRC Press, Taylor & Francis Group, Boca Raton, FL, 486 pp.

APPENDIX A: Results from Simplified Liquefaction Analysis of 55 Sites using the Boulanger and Idriss (2014) Triggering Procedure

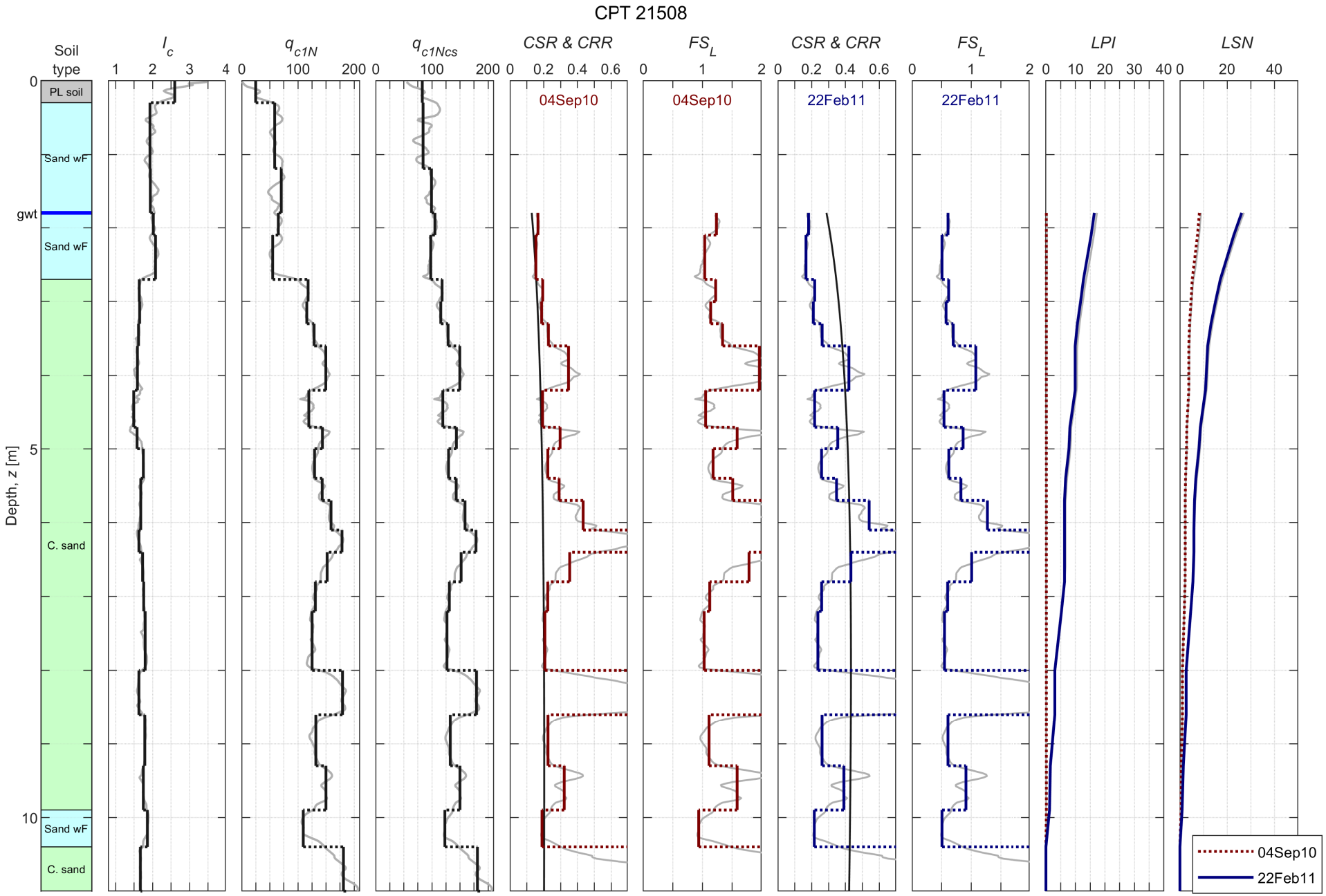
CPT 21508
Soil type
I_c
q_{c1N}
q_{c1Ncs}
CSR & CRR
FS_L
CSR & CRR
FS_L
LPI
LSN
04Sep10
04Sep10
22Feb11
22Feb11
PL soil
Sand wF
gwt
Sand wF
C. sand
Sand wF
C. sand
Depth, z [m]
0
5
10
1 2 3 4
0 100 200
0 100 200
0 0.2 0.4 0.6
0 1 2
0 0.2 0.4 0.6
0 1 2
0 10 20 30 40
0 20 40
04Sep10
22Feb11

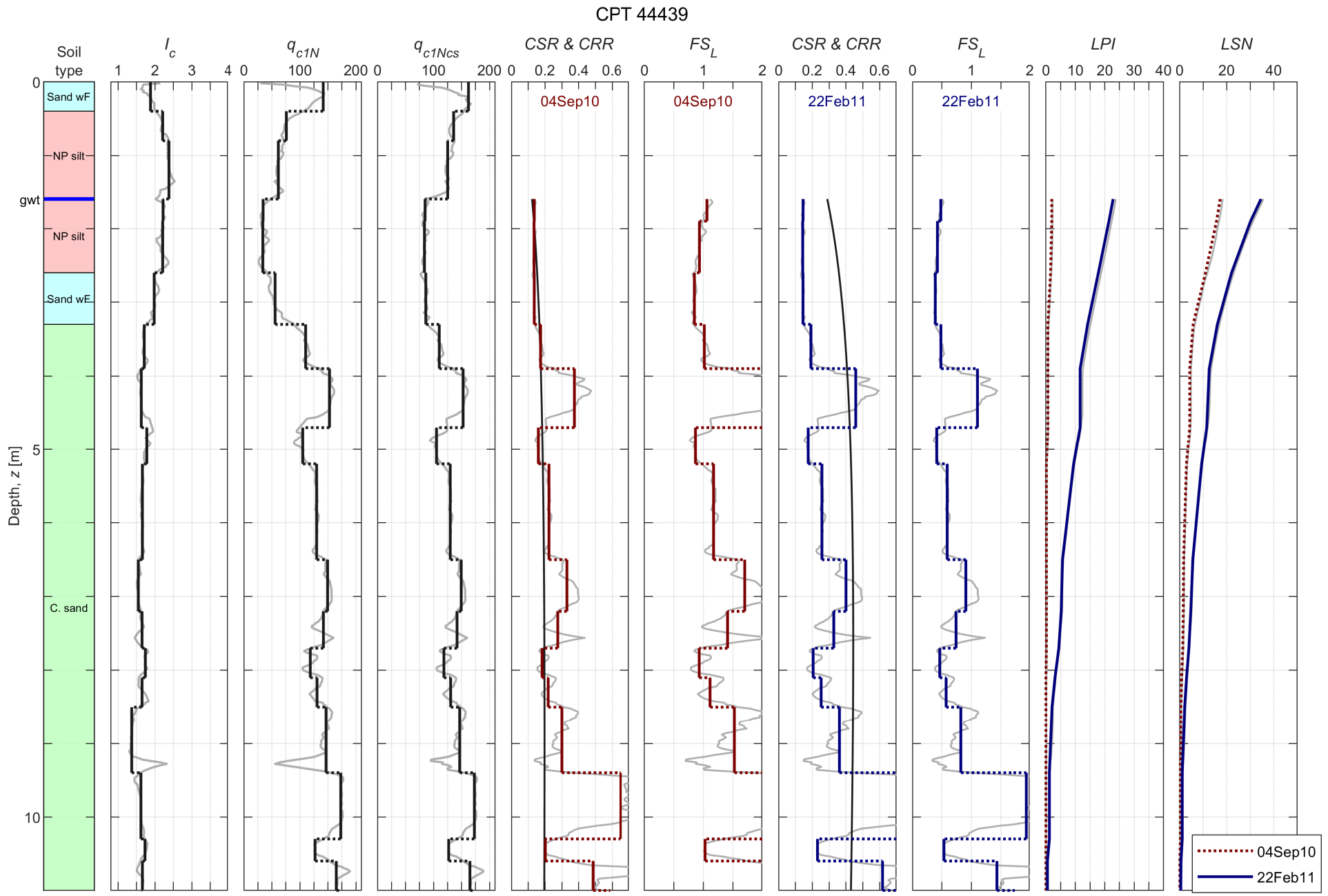
CPT 44439
Soil type
I_c
q_{c1N}
q_{c1Ncs}
CSR & CRR
FS_L
CSR & CRR
FS_L
LPI
LSN
Sand wF
NP silt
gwt
NP silt
Sand wF
C. sand
Depth, z [m]
04Sep10
04Sep10
22Feb11
22Feb11
04Sep10
22Feb11

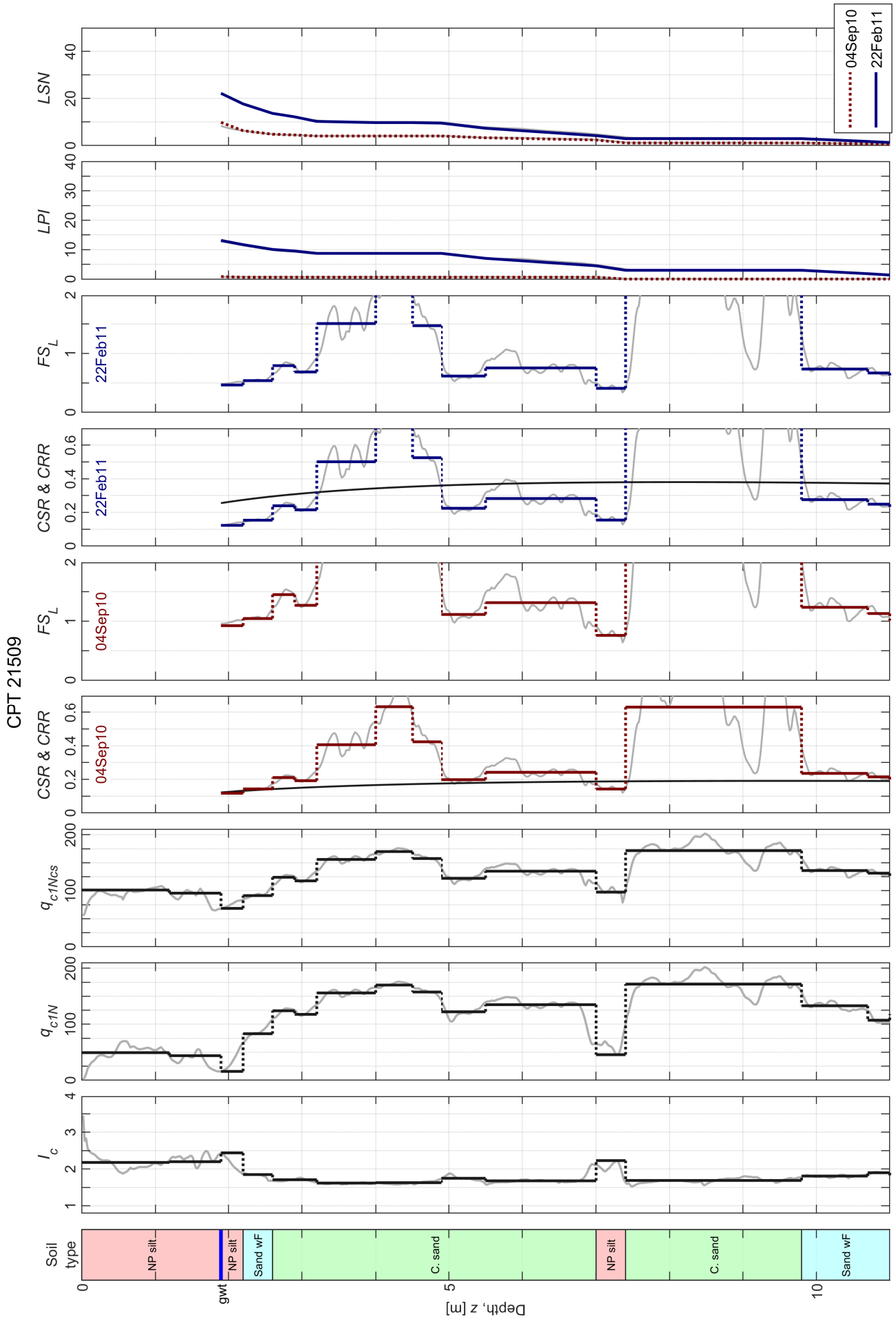
CPT 21509
Soil type
NP silt
NP silt
Sand wF
C. sand
NP silt
C. sand
Sand wF
gwt
0
5
10
Depth, z [m]
I_c
q_{c1N}
q_{c1Ncs}
CSR & CRR
04Sep10
FS_L
04Sep10
CSR & CRR
22Feb11
FS_L
22Feb11
LPI
LSN
04Sep10
22Feb11

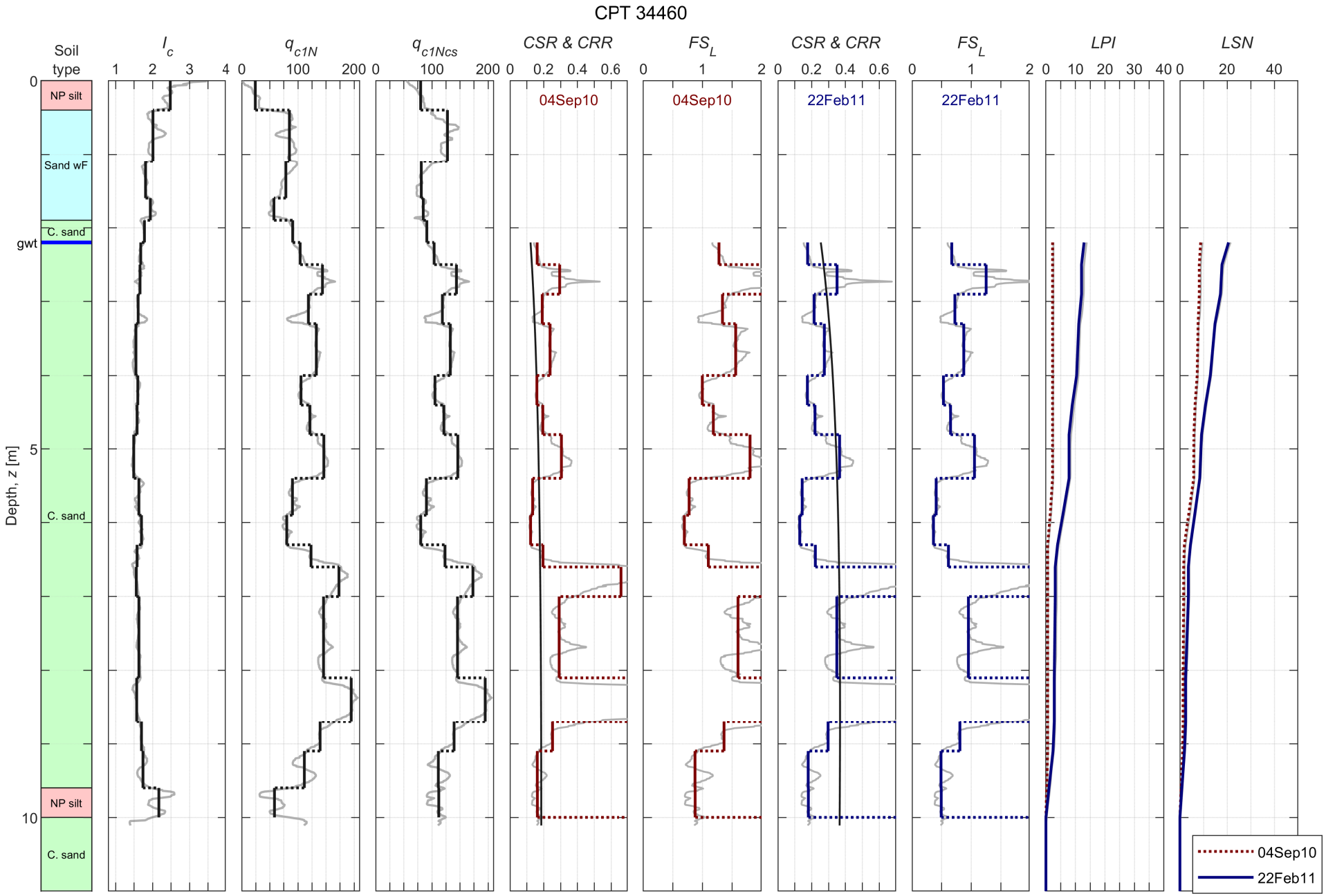
CPT 34460
Soil type
I_c
q_{c1N}
q_{c1Ncs}
CSR & CRR
FS_L
CSR & CRR
FS_L
LPI
LSN
04Sep10
04Sep10
22Feb11
22Feb11
NP silt
Sand wF
C. sand
gwt
C. sand
NP silt
C. sand
Depth, z [m]
0
5
10
1 2 3 4
0 100 200
0 100 200
0 0.2 0.4 0.6
0 1 2
0 0.2 0.4 0.6
0 1 2
0 10 20 30 40
0 20 40
04Sep10
22Feb11

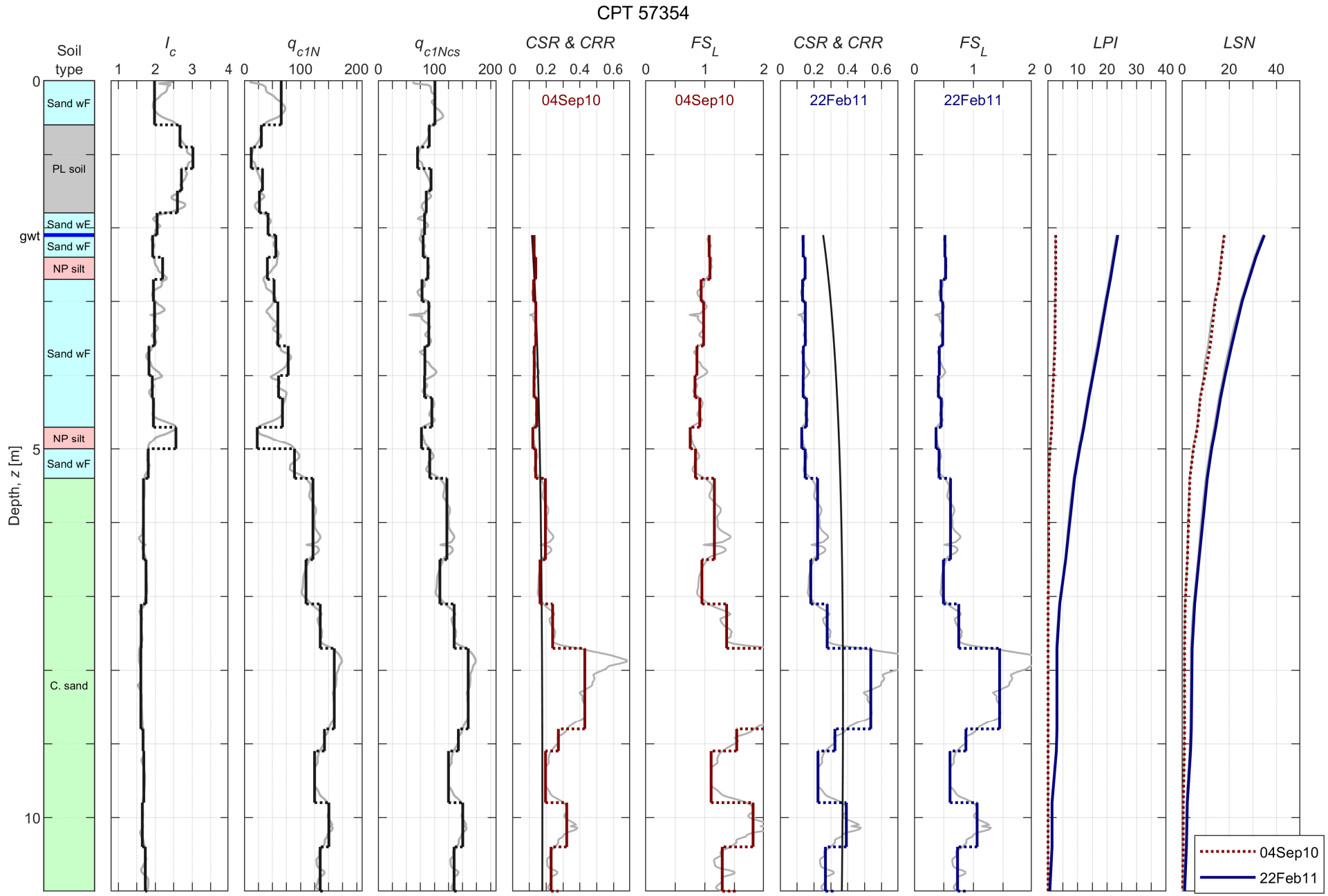
CPT 57354
Soil type
I_c
q_{c1N}
q_{c1Ncs}
CSR & CRR
FS_L
CSR & CRR
FS_L
LPI
LSN
Depth, z [m]
gwt
Sand wF
PL soil
Sand wE
Sand wF
NP silt
Sand wF
NP silt
Sand wF
C. sand
04Sep10
04Sep10
22Feb11
22Feb11
04Sep10
22Feb11

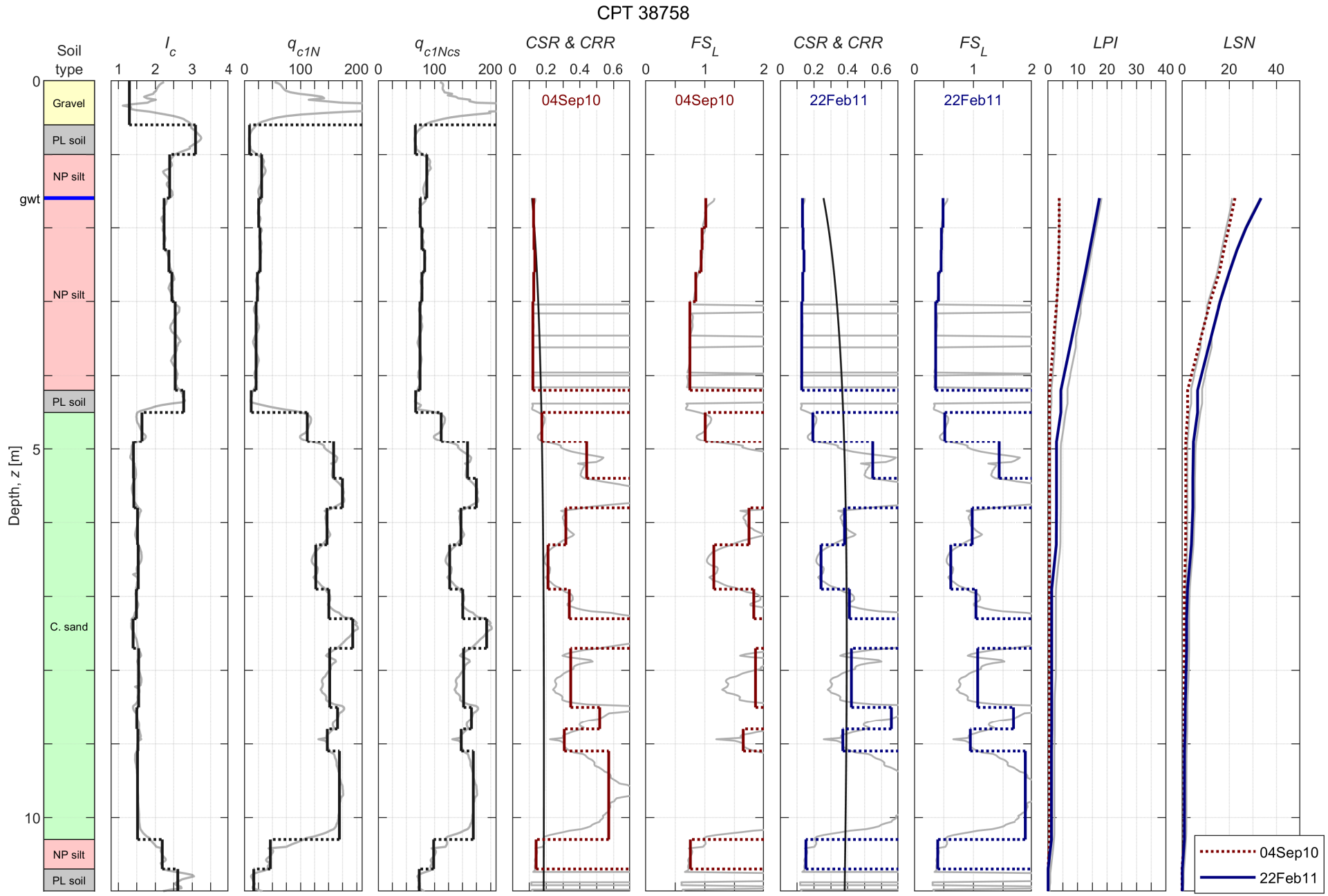
CPT 38758
Soil type
I_c
q_{c1N}
q_{c1Ncs}
CSR & CRR
FS_L
CSR & CRR
FS_L
LPI
LSN
04Sep10
04Sep10
22Feb11
22Feb11
Gravel
PL soil
NP silt
gwt
NP silt
PL soil
C. sand
NP silt
PL soil
Depth, z [m]
0
5
10
1 2 3 4
0 100 200
0 100 200
0 0.2 0.4 0.6
0 1 2
0 0.2 0.4 0.6
0 1 2
0 10 20 30 40
0 20 40
04Sep10
22Feb11

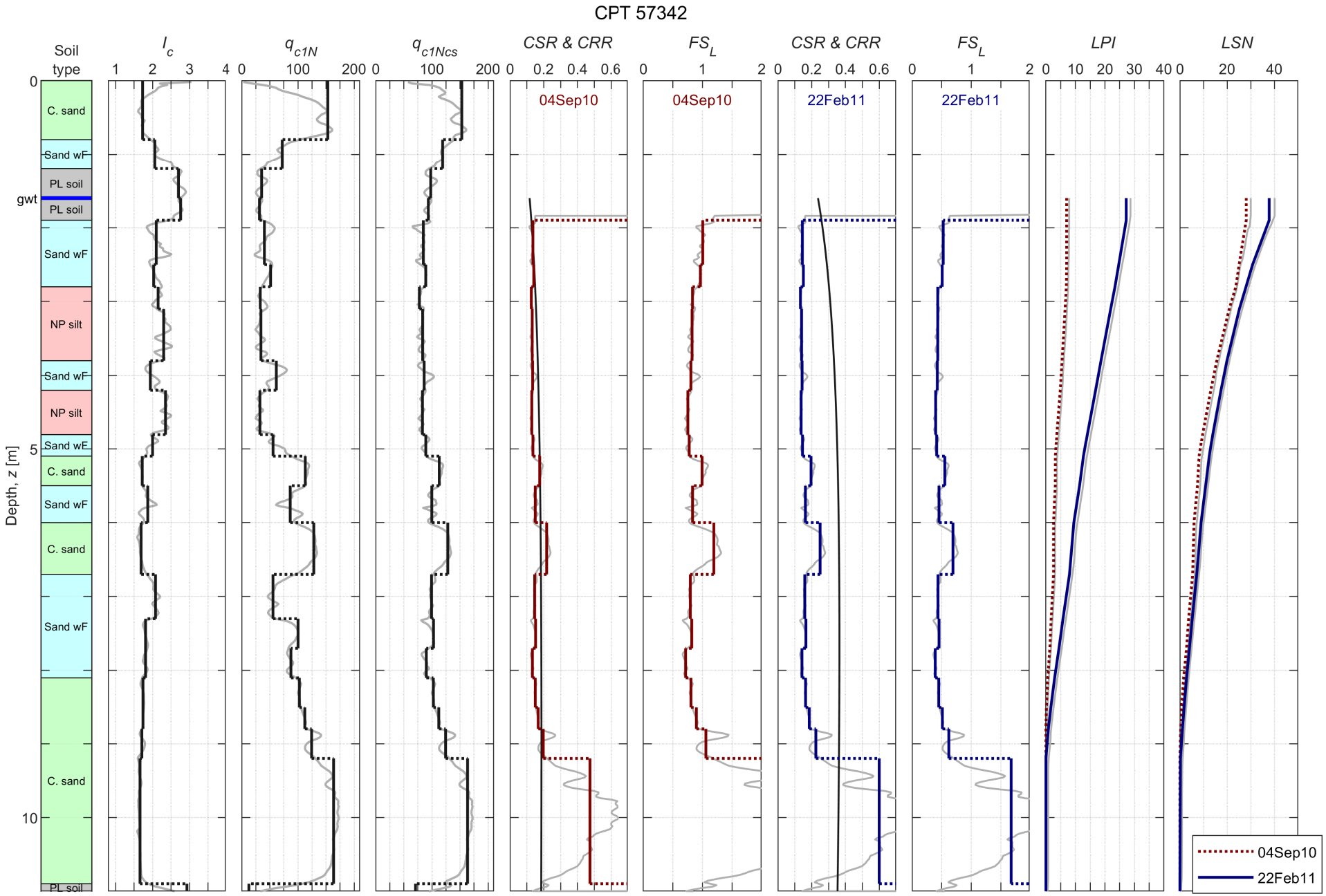
CPT 57342
Soil type
I_c
q_{c1N}
q_{c1Ncs}
CSR & CRR
FS_L
CSR & CRR
FS_L
LPI
LSN
04Sep10
04Sep10
22Feb11
22Feb11
Depth, z [m]
gwt
C. sand
Sand wF
PL soil
PL soil
Sand wF
NP silt
Sand wF
NP silt
Sand wE
C. sand
Sand wF
C. sand
Sand wF
C. sand
PL soil
04Sep10
22Feb11

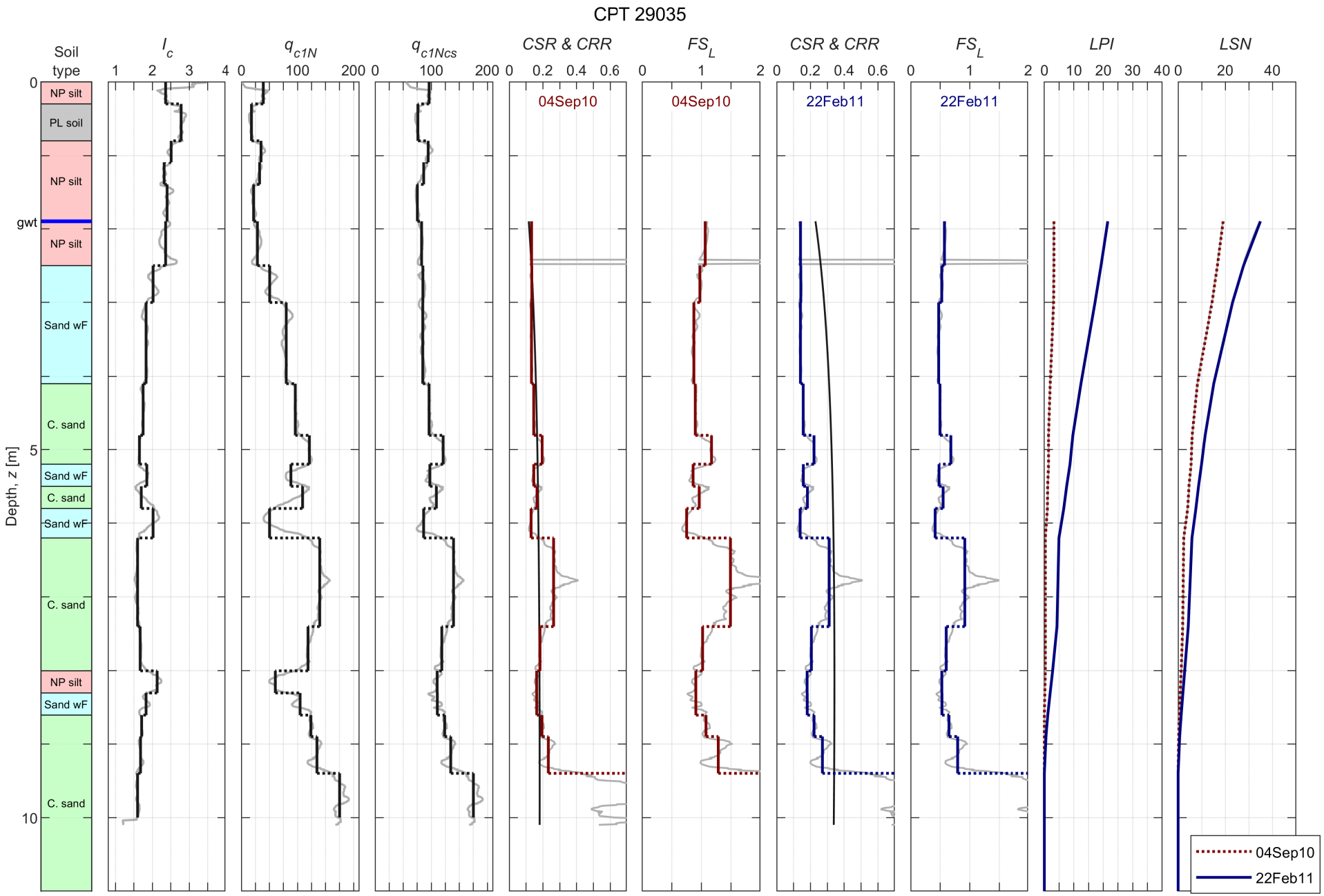
CPT 29035
Soil type
I_c
q_{c1N}
q_{c1Ncs}
CSR & CRR
FS_L
CSR & CRR
FS_L
LPI
LSN
04Sep10
04Sep10
22Feb11
22Feb11
NP silt
PL soil
NP silt
gwt
NP silt
Sand wF
C. sand
Sand wF
C. sand
Sand wF
C. sand
NP silt
Sand wF
C. sand
Depth, z [m]
04Sep10
22Feb11

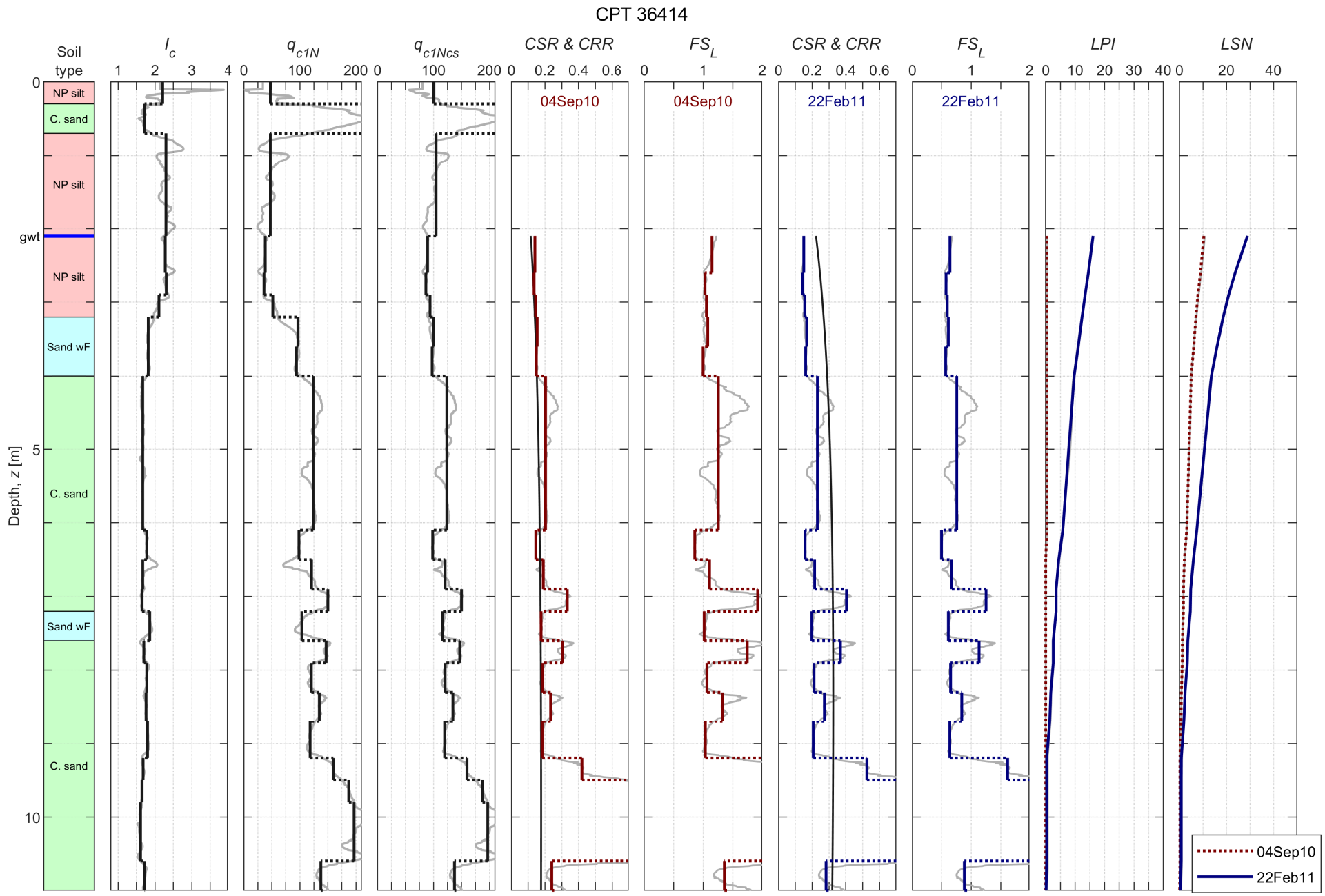
CPT 36414
Soil type
I_c
q_{c1N}
q_{c1Ncs}
CSR & CRR
FS_L
CSR & CRR
FS_L
LPI
LSN
04Sep10
04Sep10
22Feb11
22Feb11
NP silt
C. sand
NP silt
gwt
NP silt
Sand wF
C. sand
Sand wF
C. sand
Depth, z [m]
0
5
10
1 2 3 4
0 100 200
0 100 200
0 0.2 0.4 0.6
0 1 2
0 0.2 0.4 0.6
0 1 2
0 10 20 30 40
0 20 40
04Sep10
22Feb11

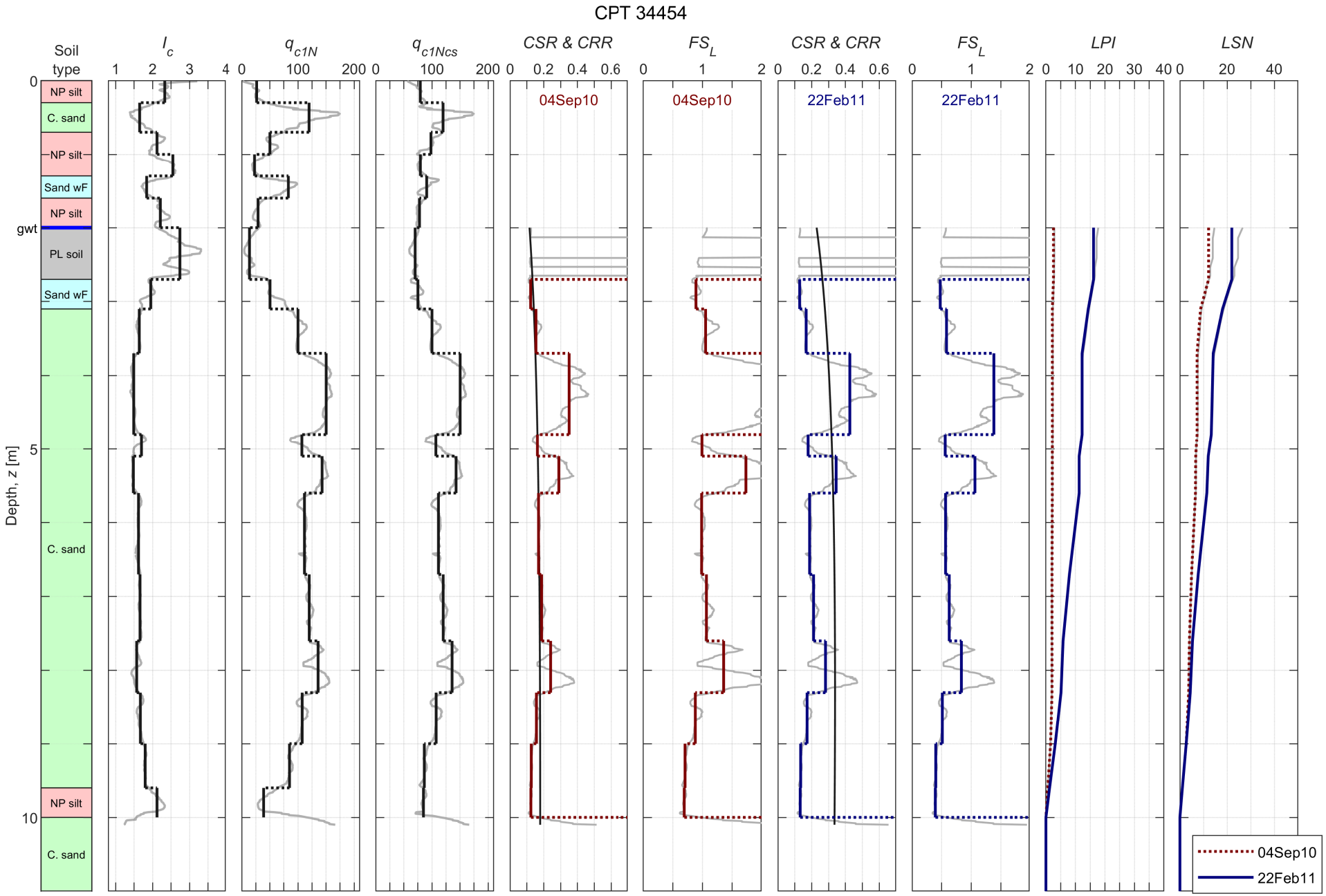
CPT 34454
Soil type
I_c
q_{c1N}
q_{c1Ncs}
CSR & CRR
FS_L
CSR & CRR
FS_L
LPI
LSN
04Sep10
04Sep10
22Feb11
22Feb11
NP silt
C. sand
NP silt
Sand wF
NP silt
gwt
PL soil
Sand wF
C. sand
NP silt
C. sand
Depth, z [m]
0
5
10
1 2 3 4
0 100 200
0 100 200
0 0.2 0.4 0.6
0 1 2
0 0.2 0.4 0.6
0 1 2
0 10 20 30 40
0 20 40
04Sep10
22Feb11

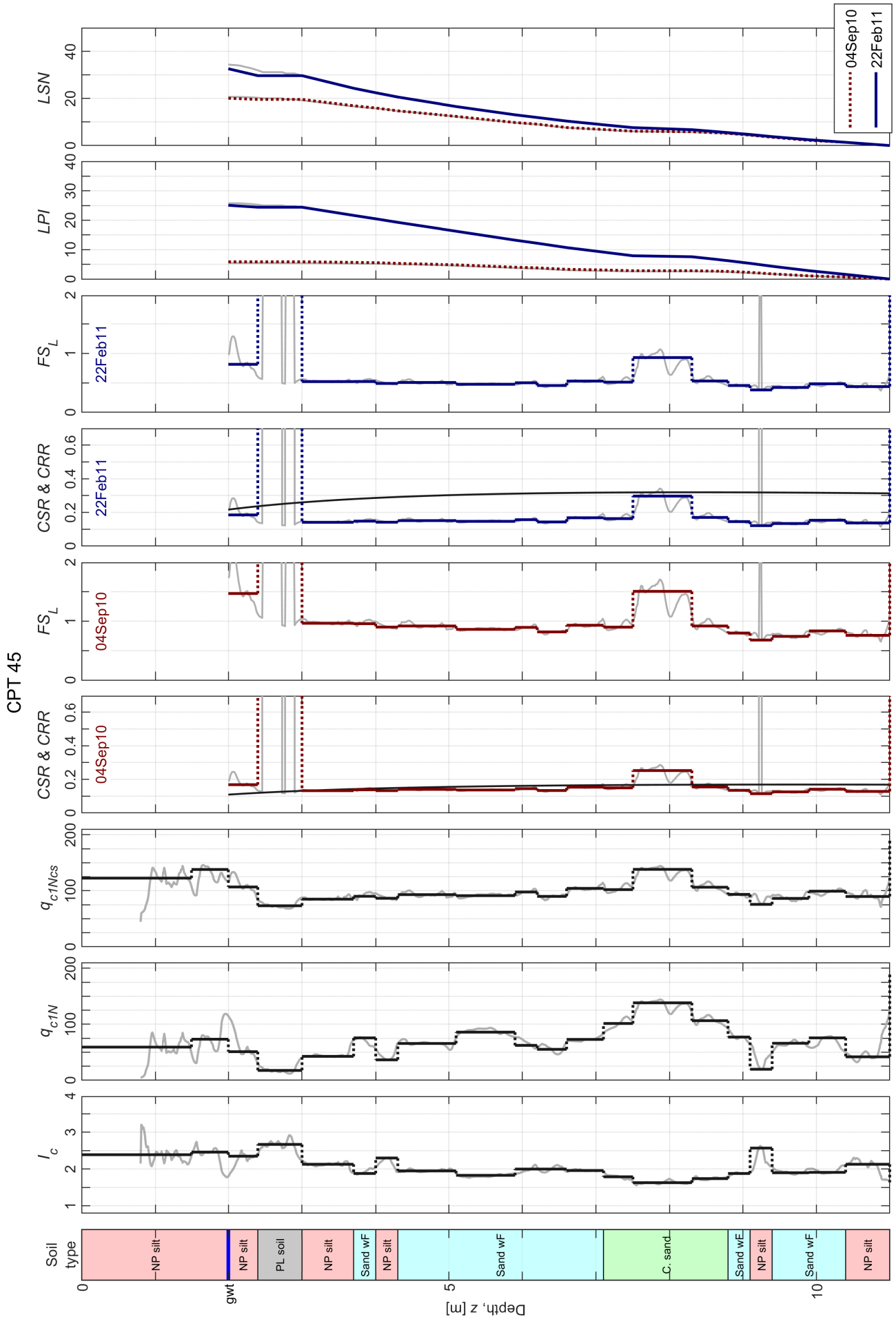
CPT 45
Soil type
NP silt
NP silt
PL soil
NP silt
Sand wF
NP silt
Sand wF
C. sand
Sand wF
NP silt
Sand wF
NP silt
gwt
Depth, z [m]
0
5
10
I_c
q_{c1N}
q_{c1Ncs}
CSR & CRR
04Sep10
FS_L
04Sep10
CSR & CRR
22Feb11
FS_L
22Feb11
LPI
LSN
04Sep10
22Feb11

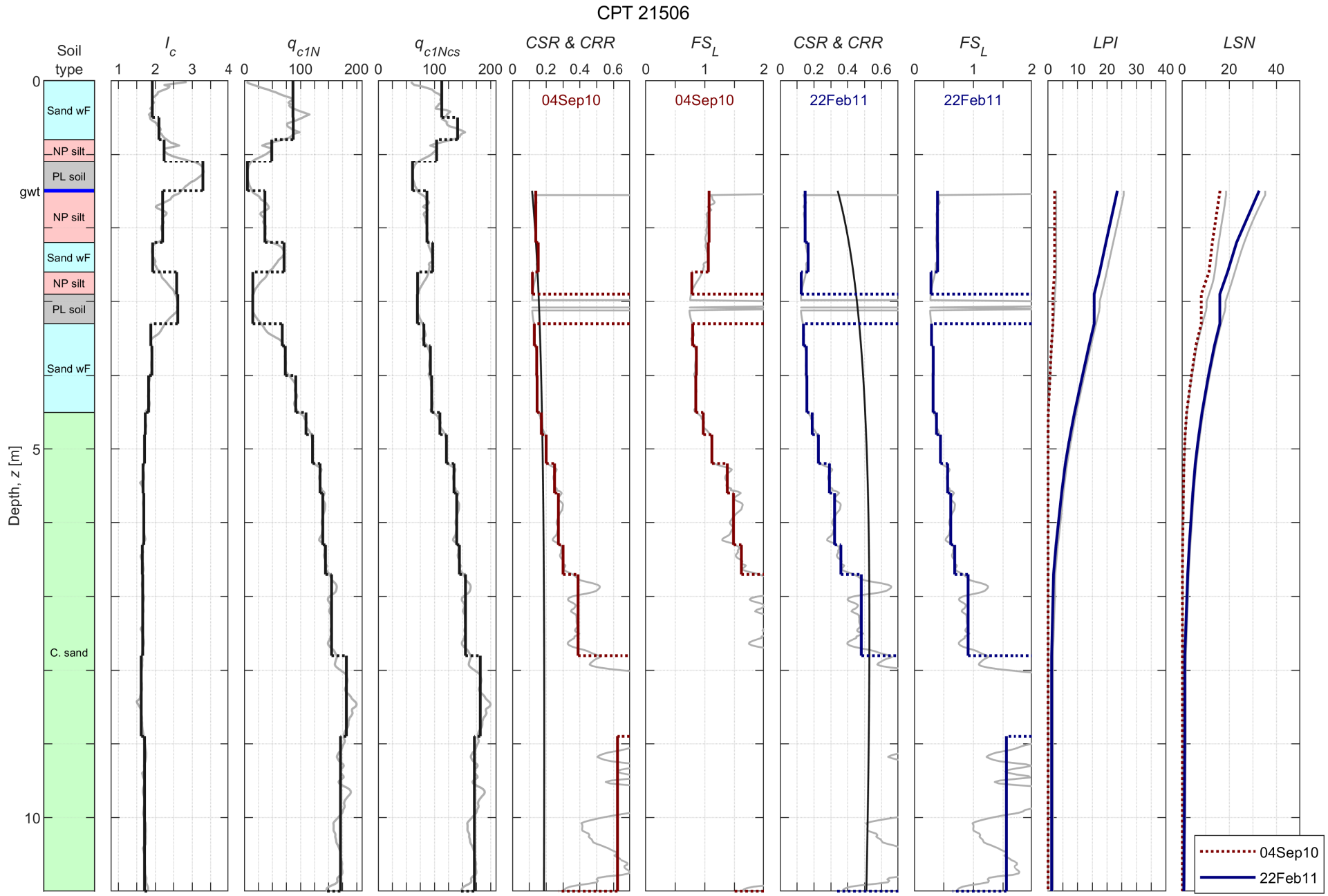
CPT 21506
Soil type
I_c
q_{c1N}
q_{c1Ncs}
CSR & CRR
FS_L
CSR & CRR
FS_L
LPI
LSN
Sand wF
NP silt
PL soil
gwt
NP silt
Sand wF
NP silt
PL soil
Sand wF
C. sand
Depth, z [m]
04Sep10
04Sep10
22Feb11
22Feb11
04Sep10
22Feb11

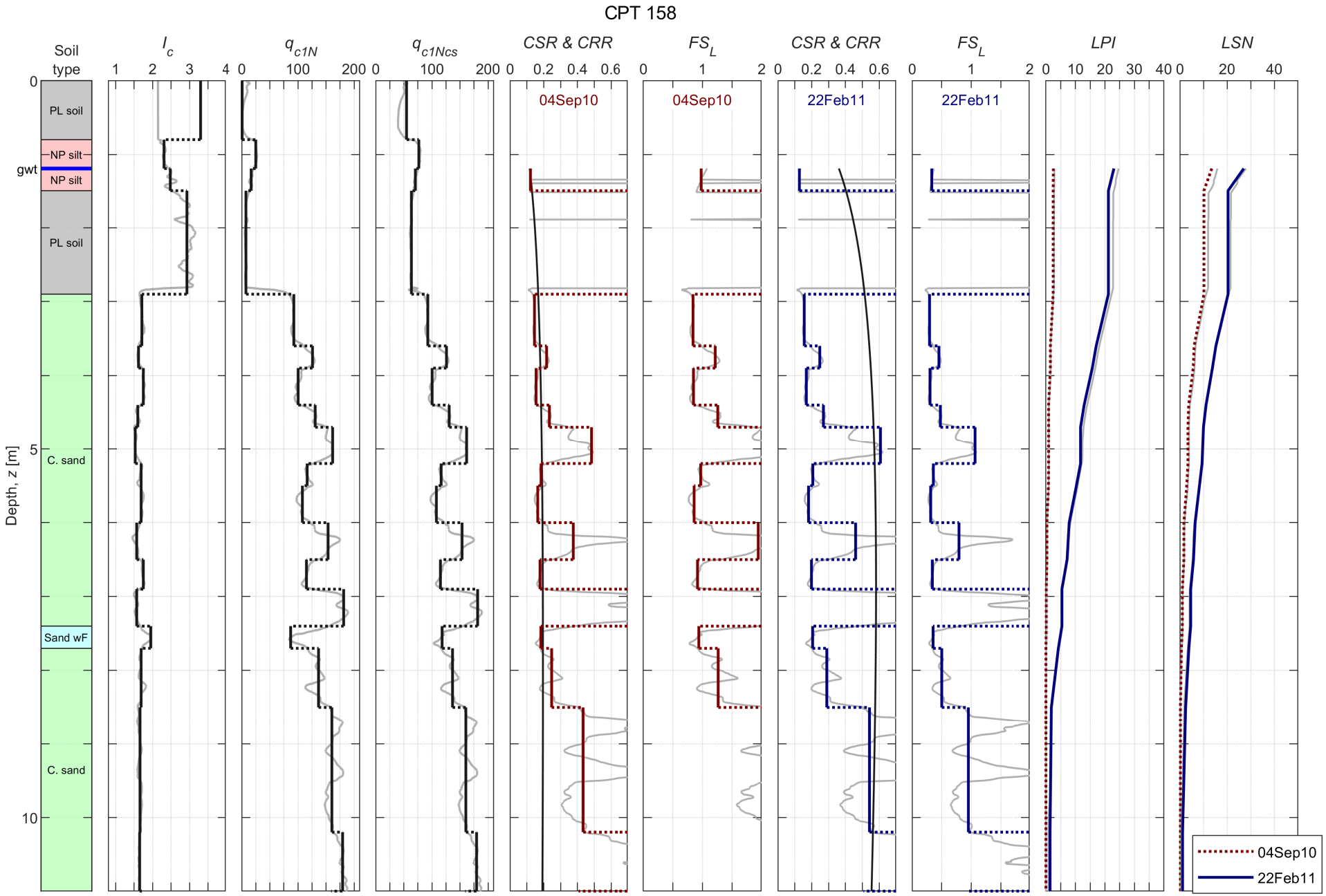
CPT 158
Soil type
I_c
q_{c1N}
q_{c1Ncs}
CSR & CRR
FS_L
CSR & CRR
FS_L
LPI
LSN
04Sep10
04Sep10
22Feb11
22Feb11
PL soil
NP silt
gwt
NP silt
PL soil
C. sand
Sand wF
C. sand
Depth, z [m]
0
5
10
1 2 3 4
0 100 200
0 100 200
0 0.2 0.4 0.6
0 1 2
0 0.2 0.4 0.6
0 1 2
0 10 20 30 40
0 20 40
04Sep10
22Feb11

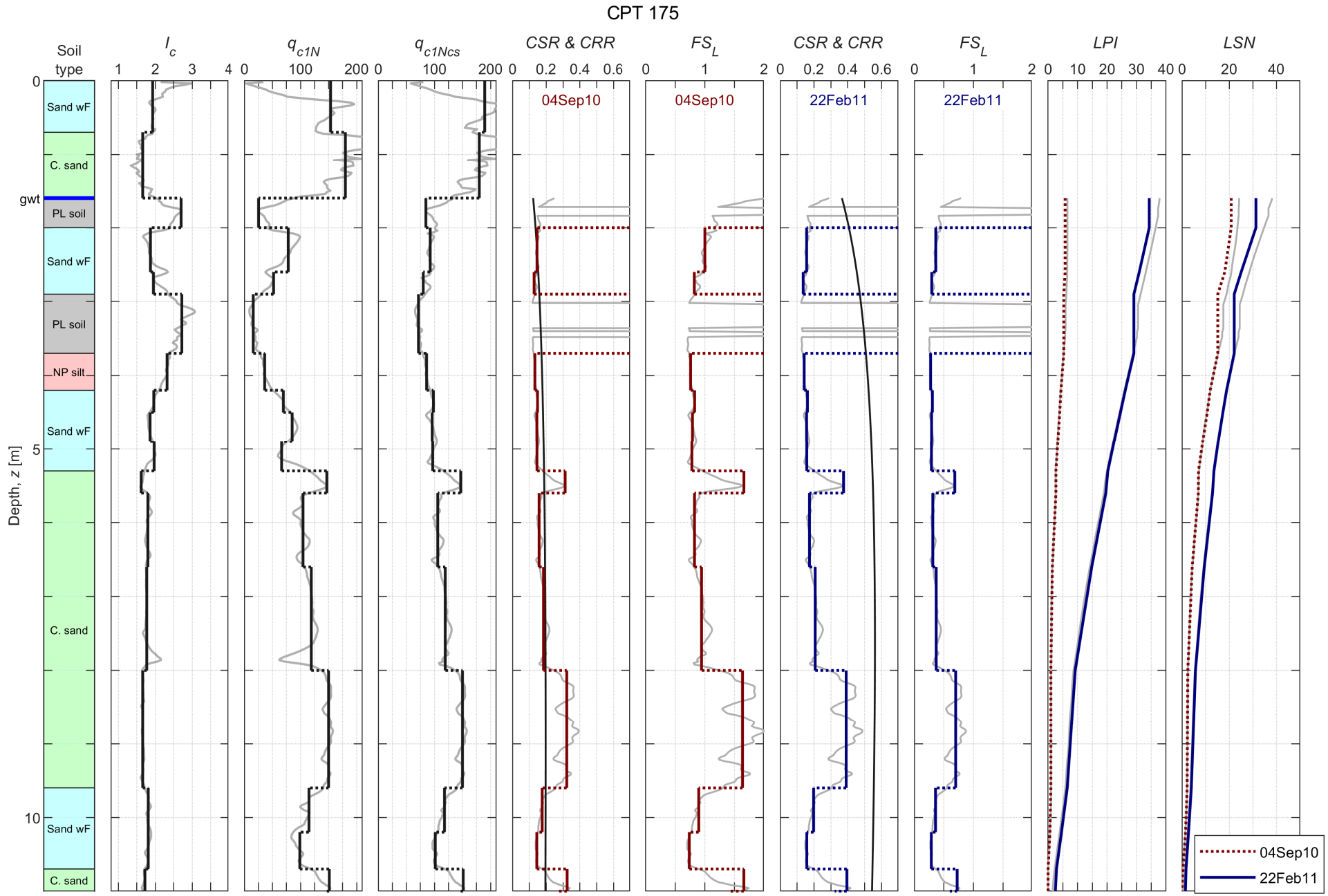
CPT 175
Soil type
I_c
q_{c1N}
q_{c1Ncs}
CSR & CRR
FS_L
CSR & CRR
FS_L
LPI
LSN
04Sep10
04Sep10
22Feb11
22Feb11
Depth, z [m]
gwt
Sand wF
C. sand
PL soil
Sand wF
PL soil
NP silt
Sand wF
C. sand
Sand wF
C. sand
04Sep10
22Feb11

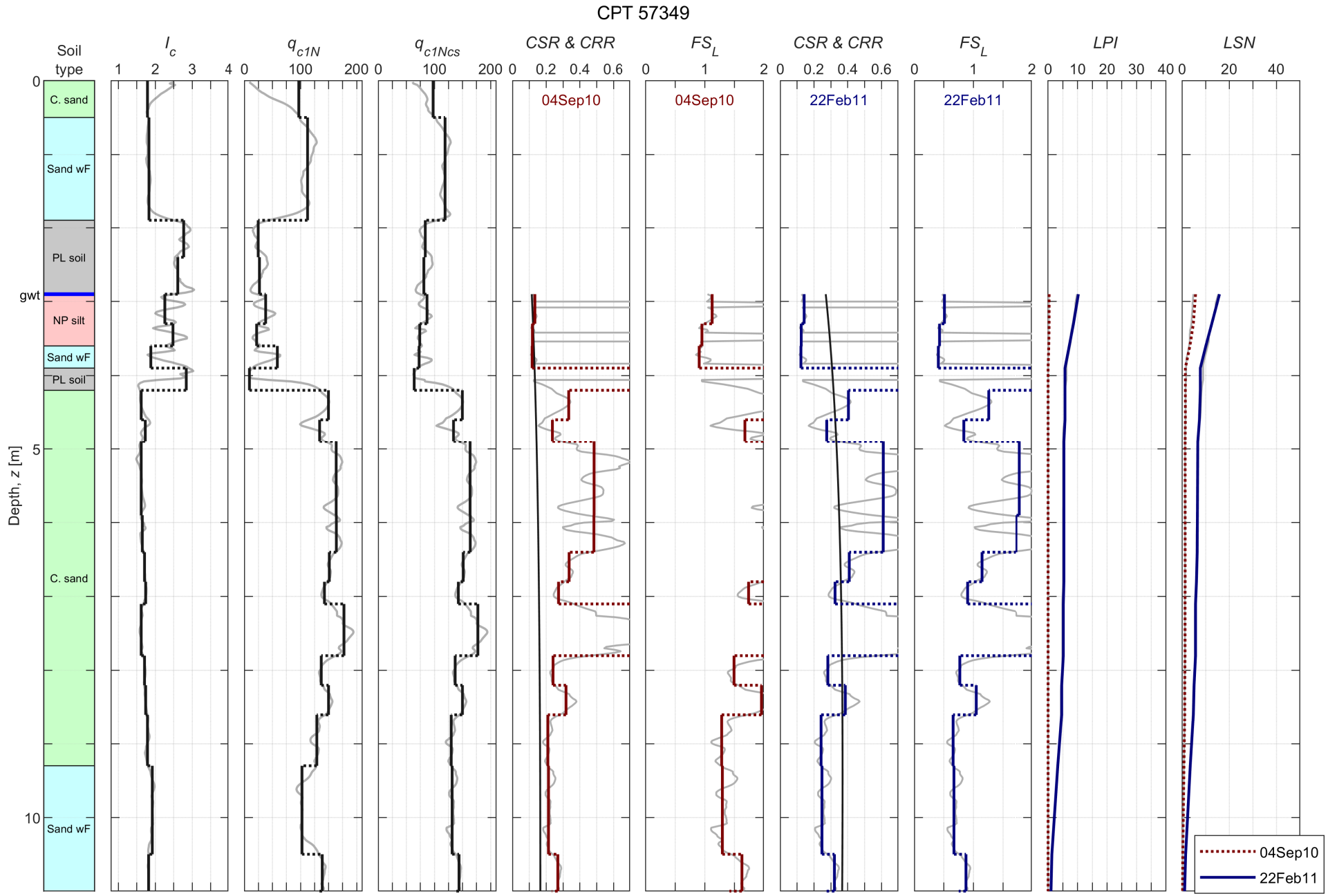
CPT 57349
Soil type
I_c
q_{c1N}
q_{c1Ncs}
CSR & CRR
FS_L
CSR & CRR
FS_L
LPI
LSN
C. sand
Sand wF
PL soil
gwt
NP silt
Sand wF
PL soil
C. sand
Sand wF
Depth, z [m]
04Sep10
04Sep10
22Feb11
22Feb11
04Sep10
22Feb11

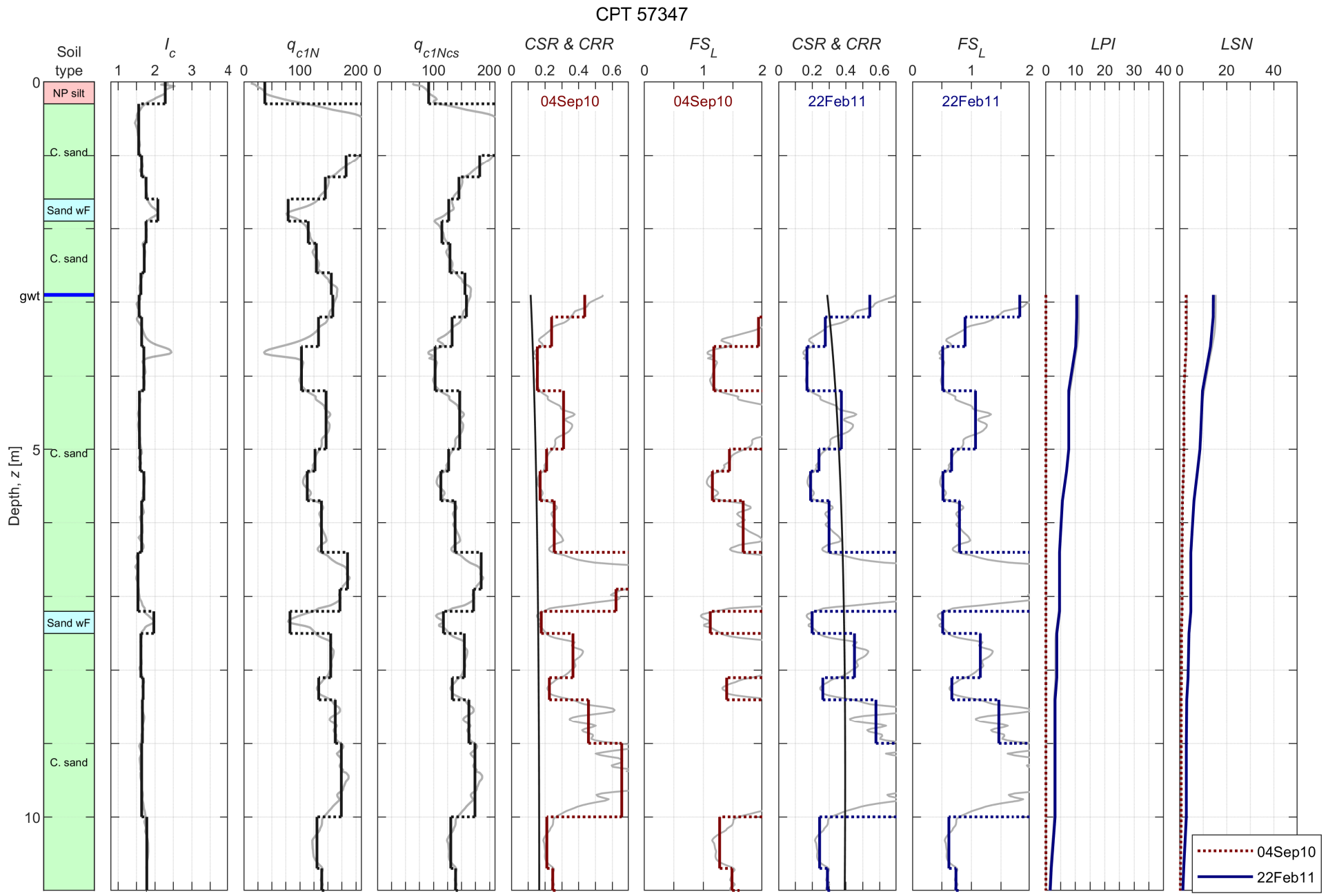
CPT 57347
Soil type
I_c
q_{c1N}
q_{c1Ncs}
CSR & CRR
FS_L
CSR & CRR
FS_L
LPI
LSN
04Sep10
04Sep10
22Feb11
22Feb11
NP silt
C. sand
Sand wF
C. sand
gwt
C. sand
Sand wF
C. sand
Depth, z [m]
0
5
10
1 2 3 4
0 100 200
0 100 200
0 0.2 0.4 0.6
0 1 2
0 0.2 0.4 0.6
0 1 2
0 10 20 30 40
0 20 40
04Sep10
22Feb11

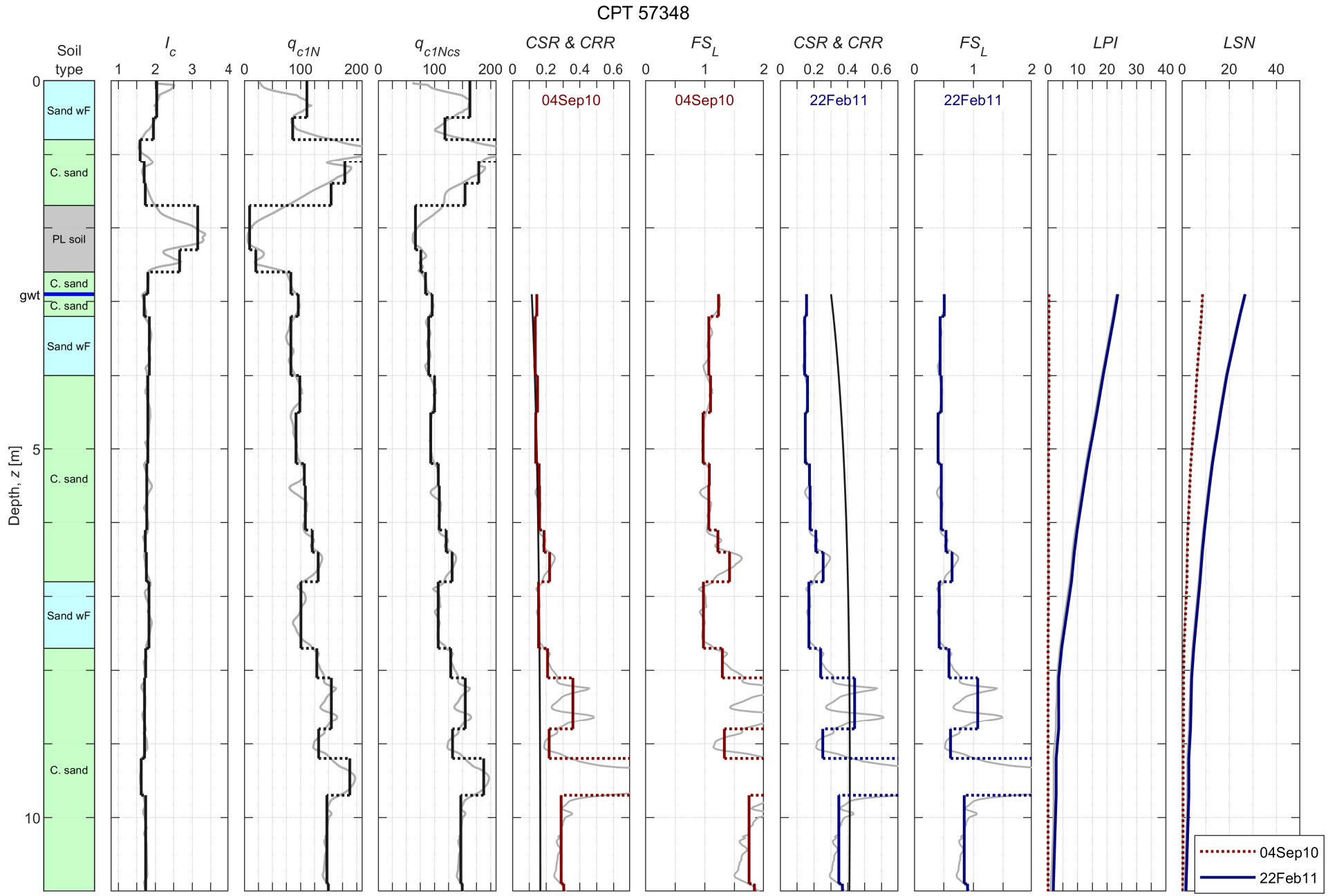
CPT 57348
Soil type
I_c
q_{c1N}
q_{c1Ncs}
CSR & CRR
FS_L
CSR & CRR
FS_L
LPI
LSN
Sand wF
C. sand
PL soil
C. sand
gwt
C. sand
Sand wF
C. sand
Sand wF
C. sand
Depth, z [m]
04Sep10
04Sep10
22Feb11
22Feb11
04Sep10
22Feb11

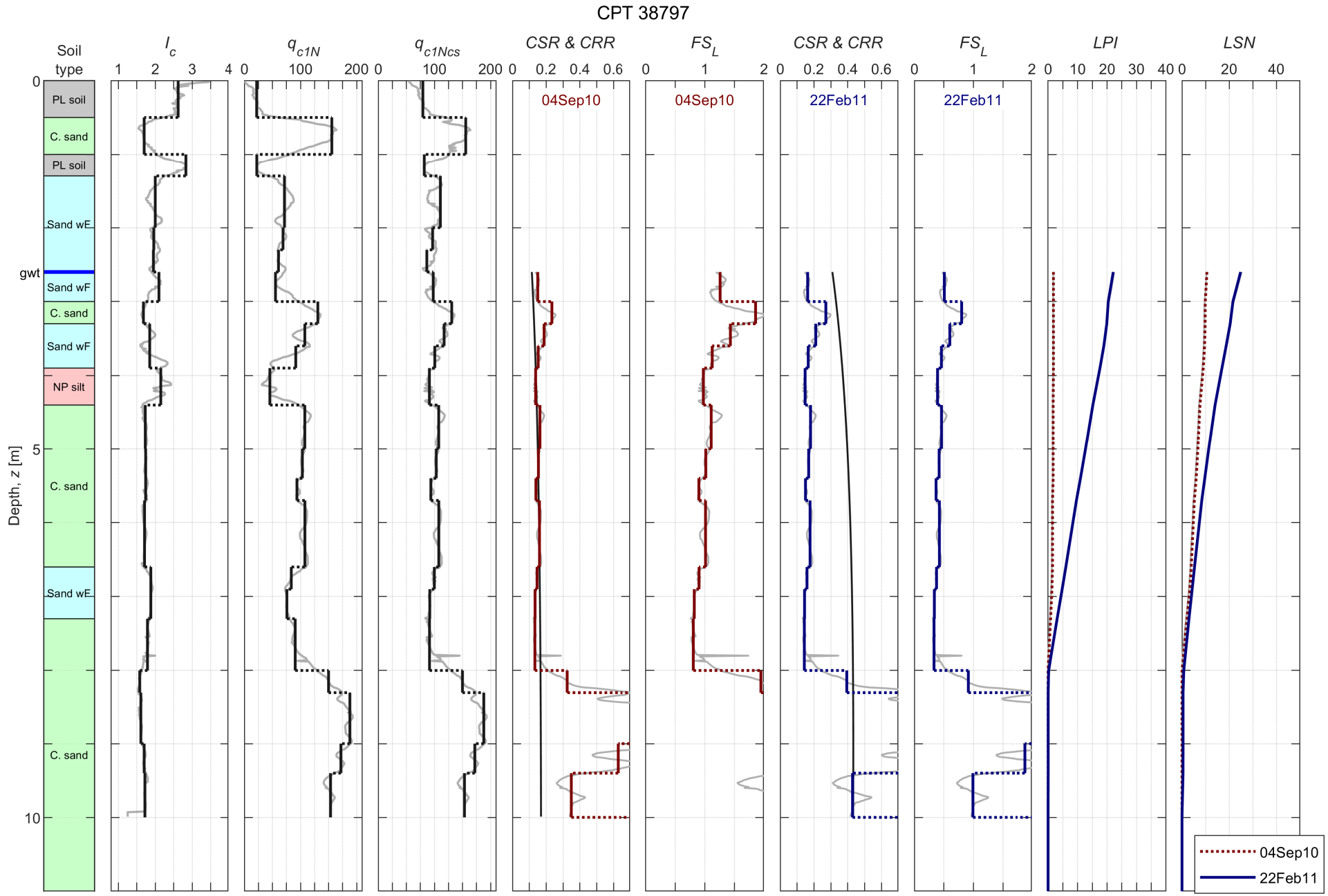
CPT 38797
Soil type
I_c
q_{c1N}
q_{c1Ncs}
CSR & CRR
FS_L
CSR & CRR
FS_L
LPI
LSN
04Sep10
04Sep10
22Feb11
22Feb11
PL soil
C. sand
PL soil
Sand wF
gwt
Sand wF
C. sand
Sand wF
NP silt
C. sand
Sand wF
C. sand
Depth, z [m]
0
5
10
1 2 3 4
0 100 200
0 100 200
0 0.2 0.4 0.6
0 1 2
0 0.2 0.4 0.6
0 1 2
0 10 20 30 40
0 20 40
04Sep10
22Feb11

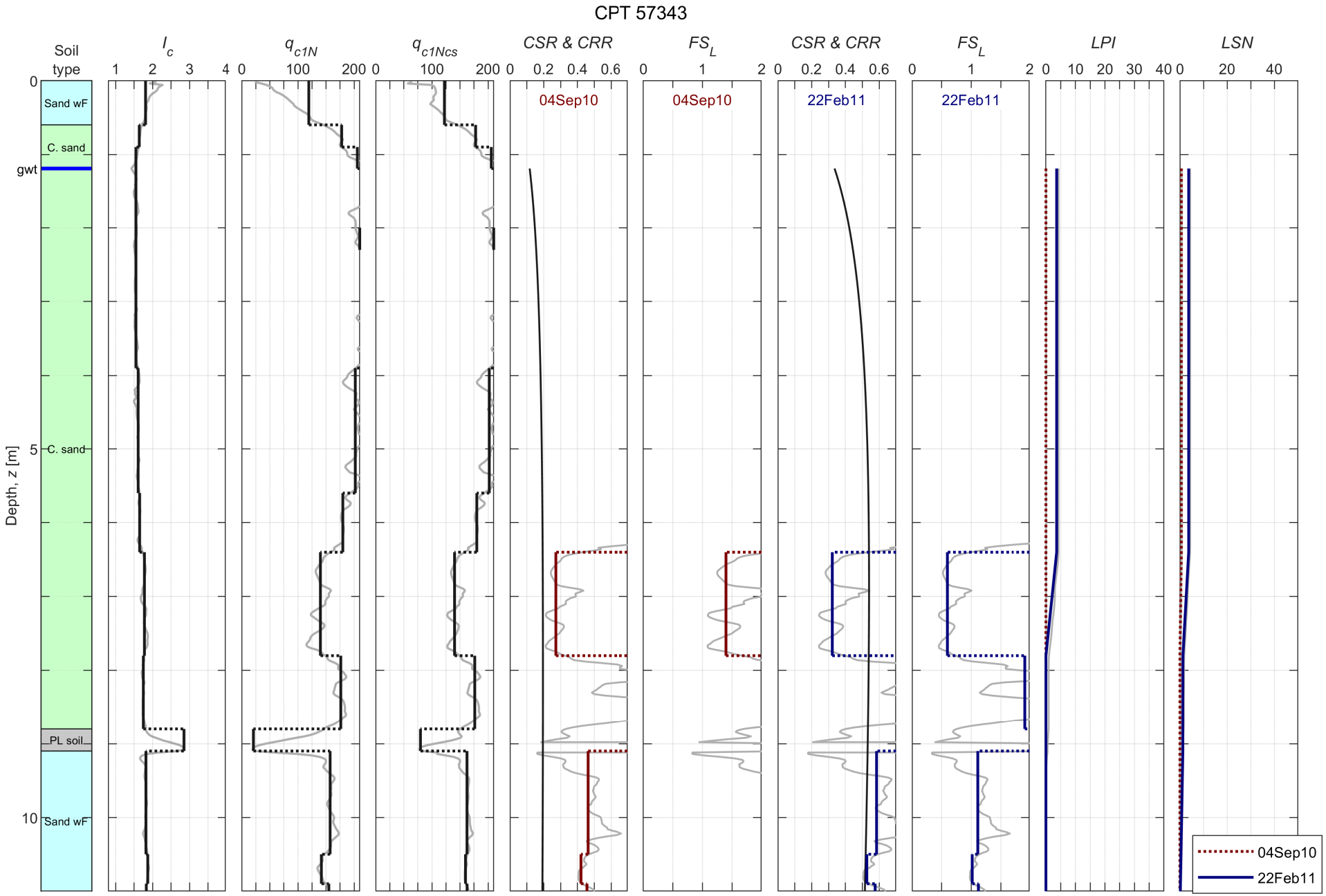
CPT 57343
Soil type
I_c
q_{c1N}
q_{c1Ncs}
CSR & CRR
FS_L
CSR & CRR
FS_L
LPI
LSN
Sand wF
C. sand
gwt
C. sand
PL soil
Sand wF
Depth, z [m]
04Sep10
04Sep10
22Feb11
22Feb11
04Sep10
22Feb11

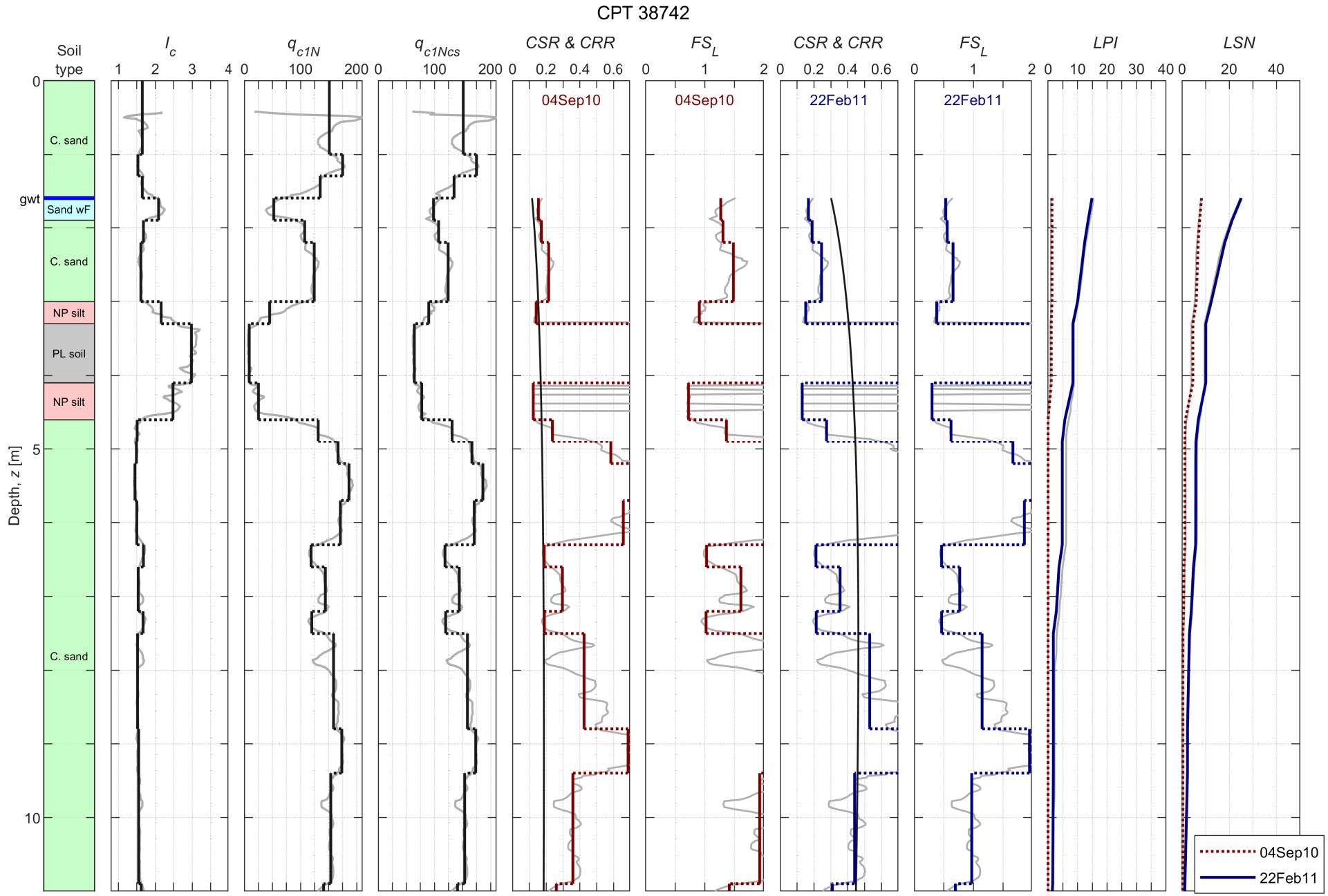
CPT 38742
Soil type
I_c
q_{c1N}
q_{c1Ncs}
CSR & CRR
FS_L
CSR & CRR
FS_L
LPI
LSN
04Sep10
04Sep10
22Feb11
22Feb11
C. sand
gwt
Sand wF
C. sand
NP silt
PL soil
NP silt
C. sand
Depth, z [m]
0
5
10
1 2 3 4
0 100 200
0 100 200
0 0.2 0.4 0.6
0 1 2
0 0.2 0.4 0.6
0 1 2
0 10 20 30 40
0 20 40
04Sep10
22Feb11

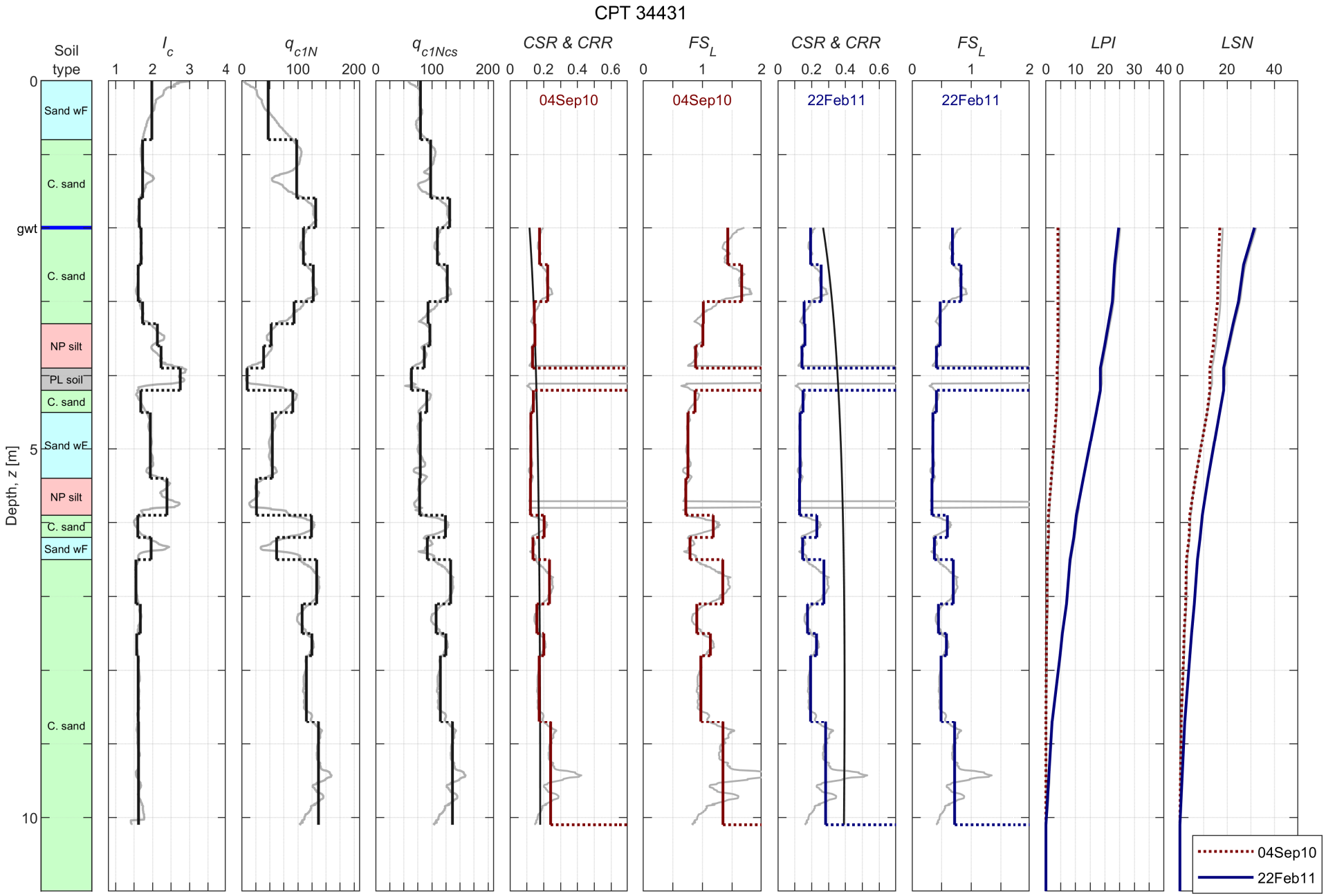
CPT 34431
Soil type
I_c
q_{c1N}
q_{c1Ncs}
CSR & CRR
FS_L
CSR & CRR
FS_L
LPI
LSN
04Sep10
04Sep10
22Feb11
22Feb11
Sand wF
C. sand
gwt
C. sand
NP silt
PL soil
C. sand
Sand wF
NP silt
C. sand
Sand wF
C. sand
Depth, z [m]
0
5
10
04Sep10
22Feb11

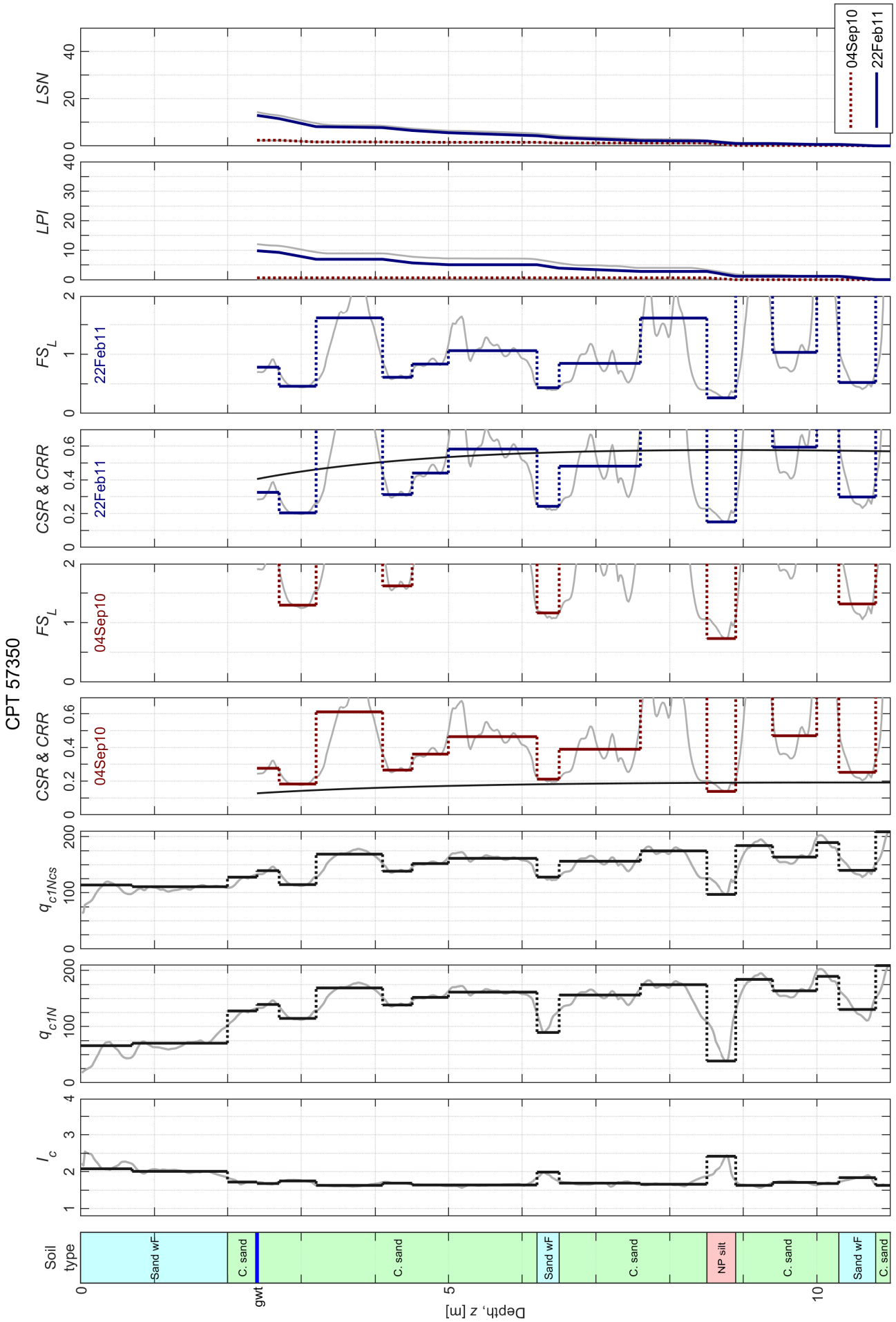
CPT 57350
Soil type
Sand wF
C. sand
C. sand
Sand wF
C. sand
NP silt
C. sand
Sand wF
C. sand
gwt
0
5
10
Depth, z [m]
I_c
q_{c1N}
q_{c1Ncs}
CSR & CRR
04Sep10
FS_L
04Sep10
CSR & CRR
22Feb11
FS_L
22Feb11
LPI
LSN
04Sep10
22Feb11

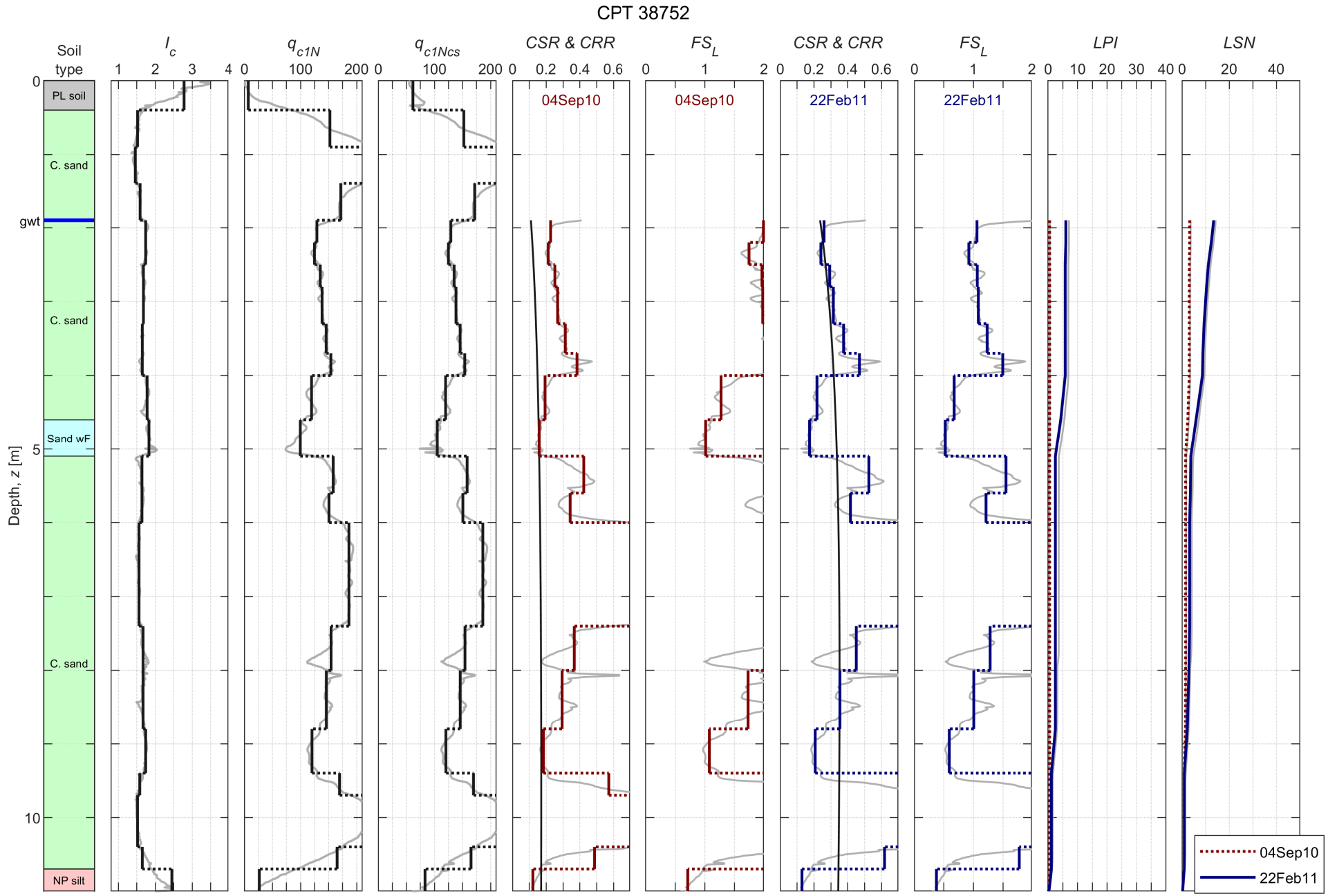
CPT 38752
Soil type
I_c
q_{c1N}
q_{c1Ncs}
CSR & CRR
FS_L
CSR & CRR
FS_L
LPI
LSN
04Sep10
04Sep10
22Feb11
22Feb11
PL soil
C. sand
gwt
C. sand
Sand wF
C. sand
NP silt
Depth, z [m]
0
5
10
1 2 3 4
0 100 200
0 100 200
0 0.2 0.4 0.6
0 1 2
0 0.2 0.4 0.6
0 1 2
0 10 20 30 40
0 20 40
04Sep10
22Feb11

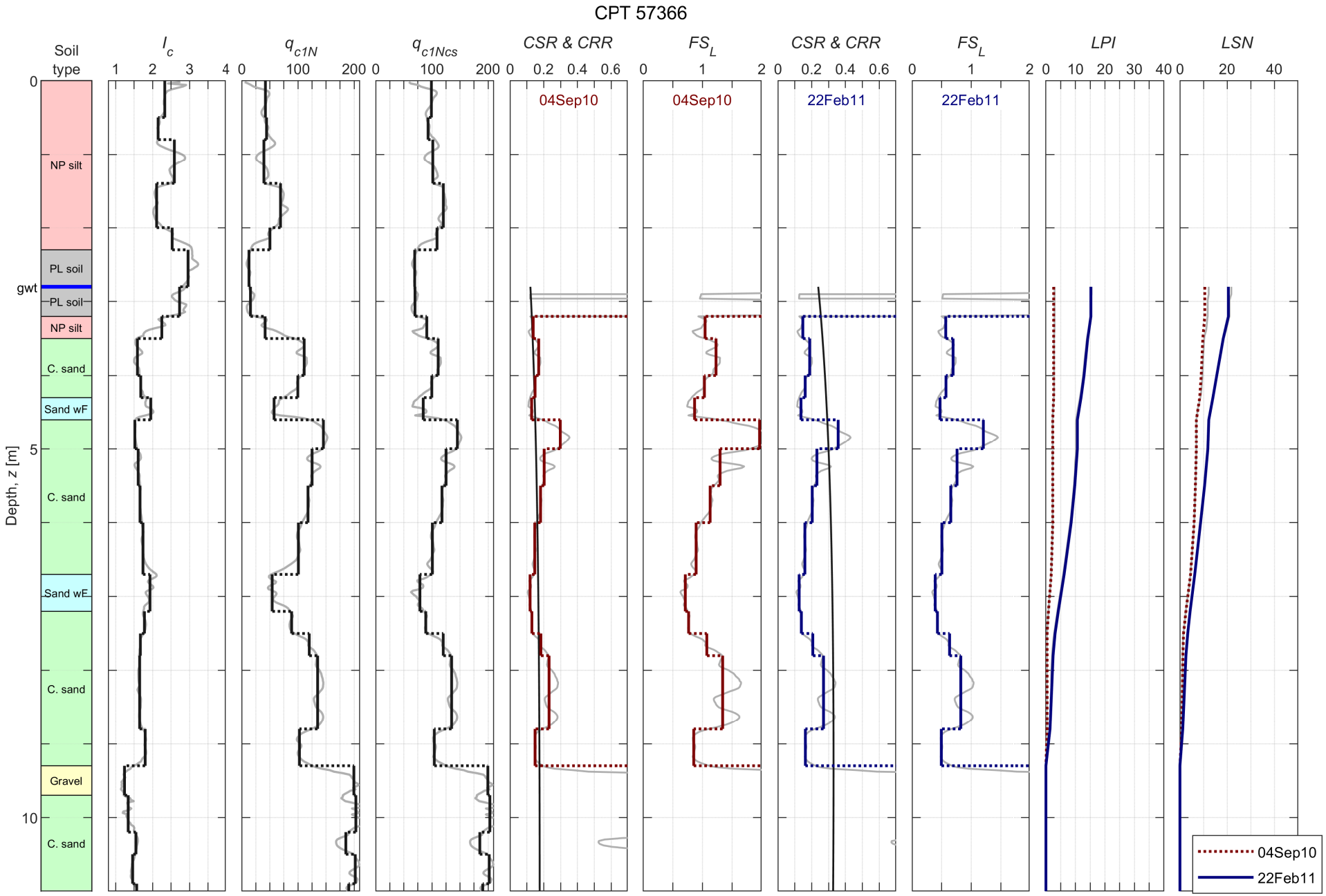
CPT 57366
Soil type
I_c
q_{c1N}
q_{c1Ncs}
CSR & CRR
FS_L
CSR & CRR
FS_L
LPI
LSN
04Sep10
04Sep10
22Feb11
22Feb11
NP silt
PL soil
gwt
PL soil
NP silt
C. sand
Sand wF
C. sand
Sand wF
C. sand
Gravel
C. sand
Depth, z [m]
04Sep10
22Feb11

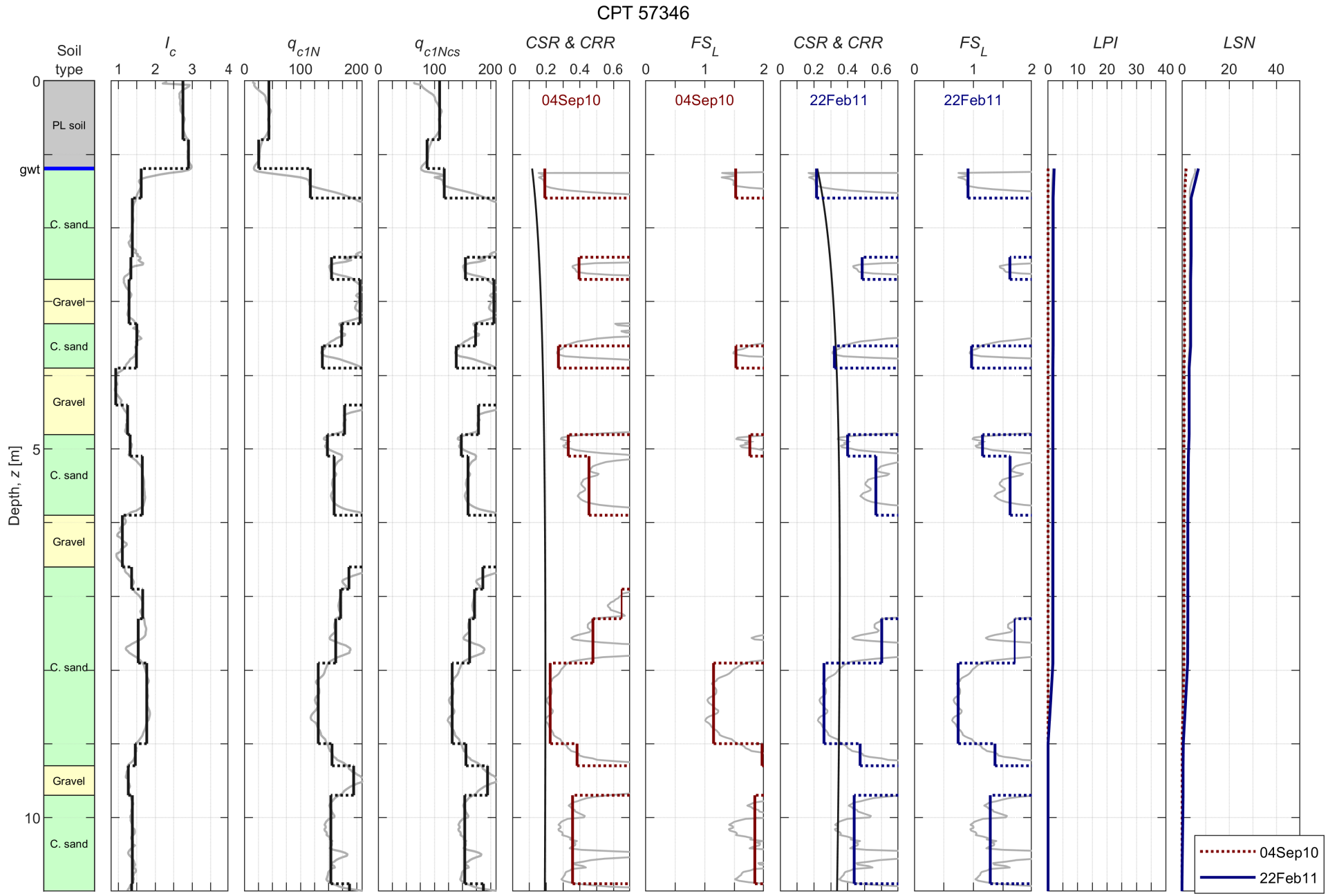
CPT 57346
Soil type
I_c
q_{c1N}
q_{c1Ncs}
CSR & CRR
FS_L
CSR & CRR
FS_L
LPI
LSN
04Sep10
04Sep10
22Feb11
22Feb11
PL soil
gwt
C. sand
Gravel
C. sand
Gravel
C. sand
Gravel
C. sand
Depth, z [m]
04Sep10
22Feb11

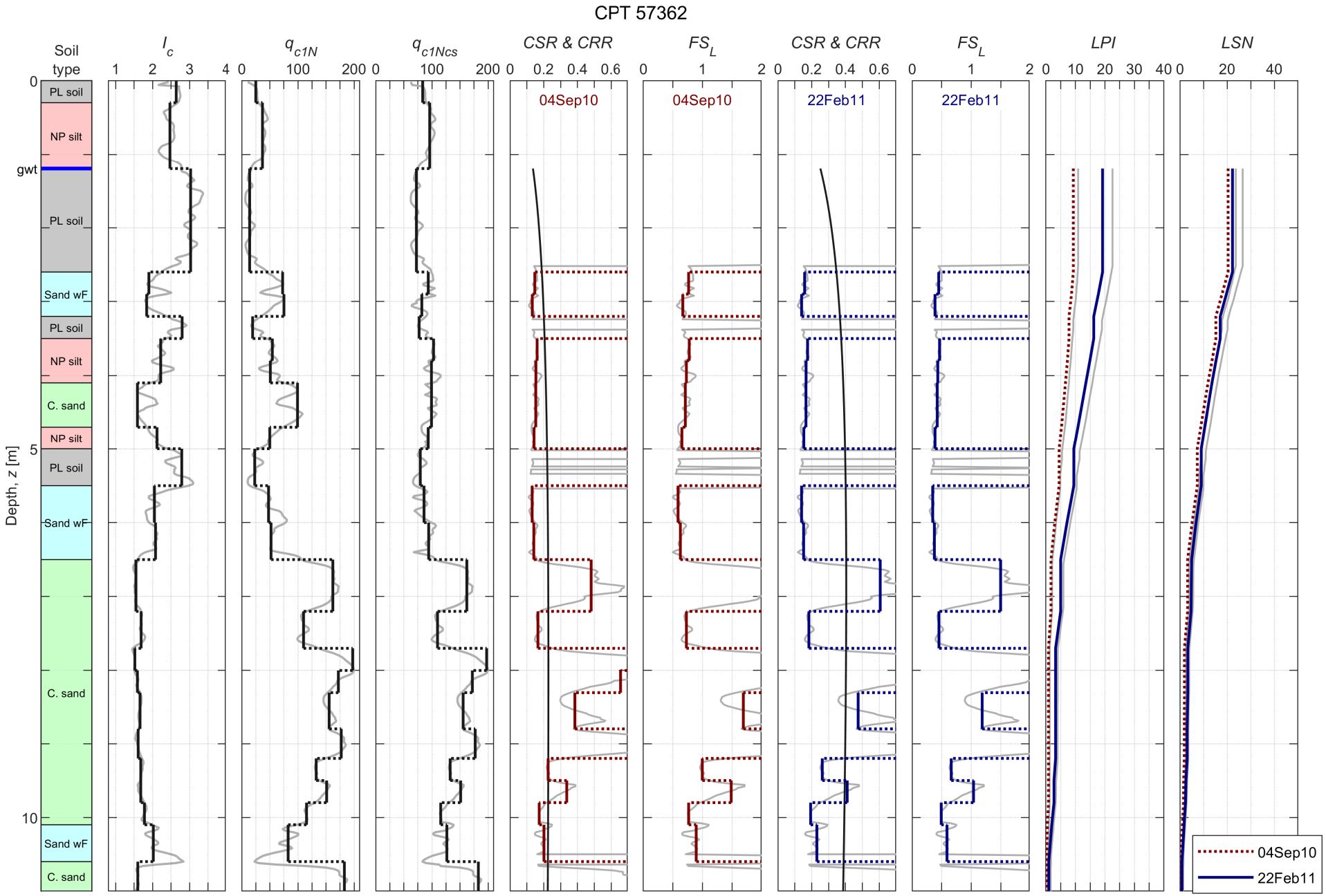
CPT 57362
Soil type
I_c
q_{c1N}
q_{c1Ncs}
CSR & CRR
FS_L
CSR & CRR
FS_L
LPI
LSN
04Sep10
04Sep10
22Feb11
22Feb11
PL soil
NP silt
gwt
PL soil
Sand wF
PL soil
NP silt
C. sand
NP silt
PL soil
Sand wF
C. sand
Sand wF
C. sand
Depth, z [m]
0
5
10
04Sep10
22Feb11

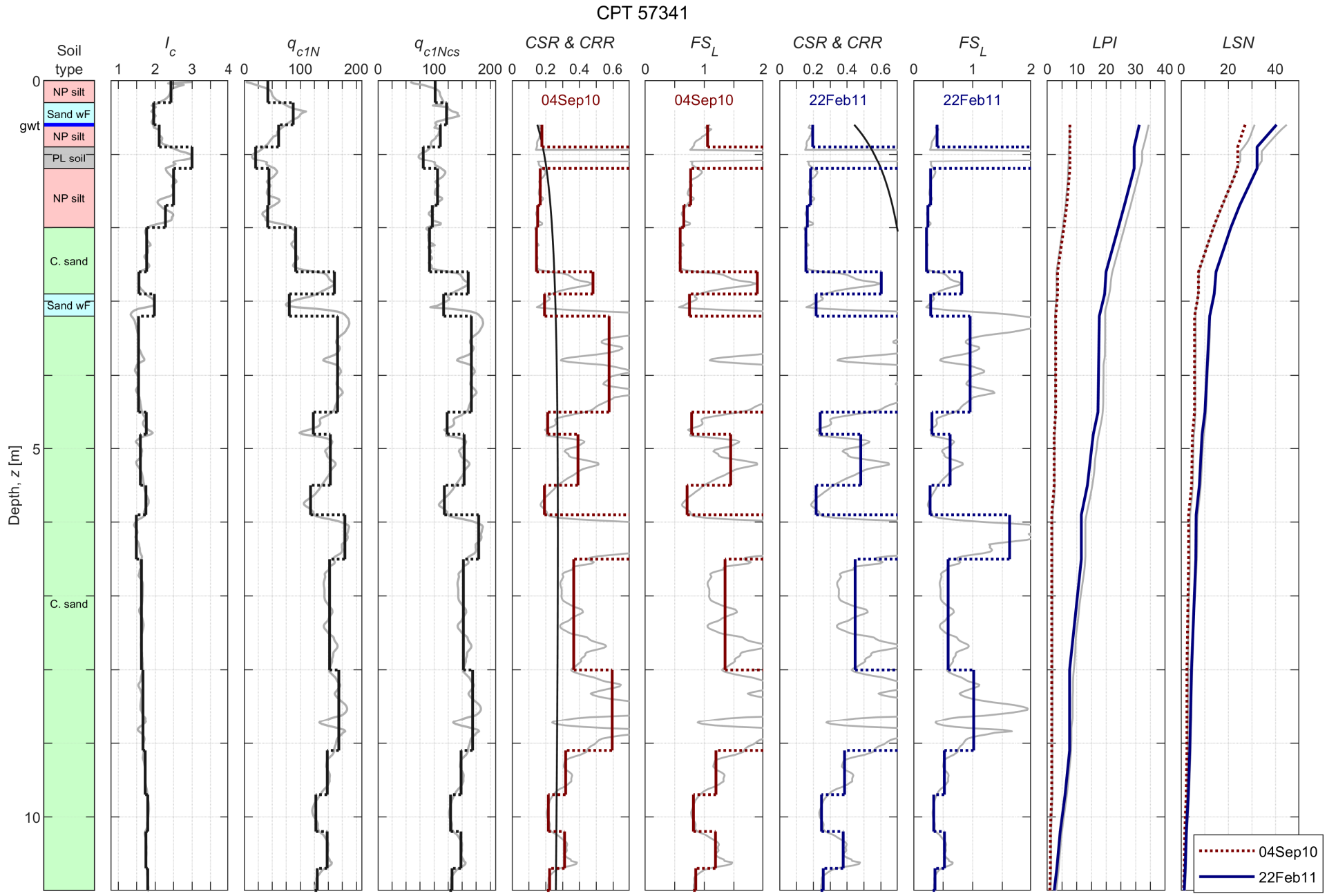
CPT 57341
Soil type
I_c
q_{c1N}
q_{c1Ncs}
CSR & CRR
FS_L
CSR & CRR
FS_L
LPI
LSN
NP silt
Sand wF
gwt
NP silt
PL soil
NP silt
C. sand
Sand wF
C. sand
Depth, z [m]
04Sep10
04Sep10
22Feb11
22Feb11
04Sep10
22Feb11

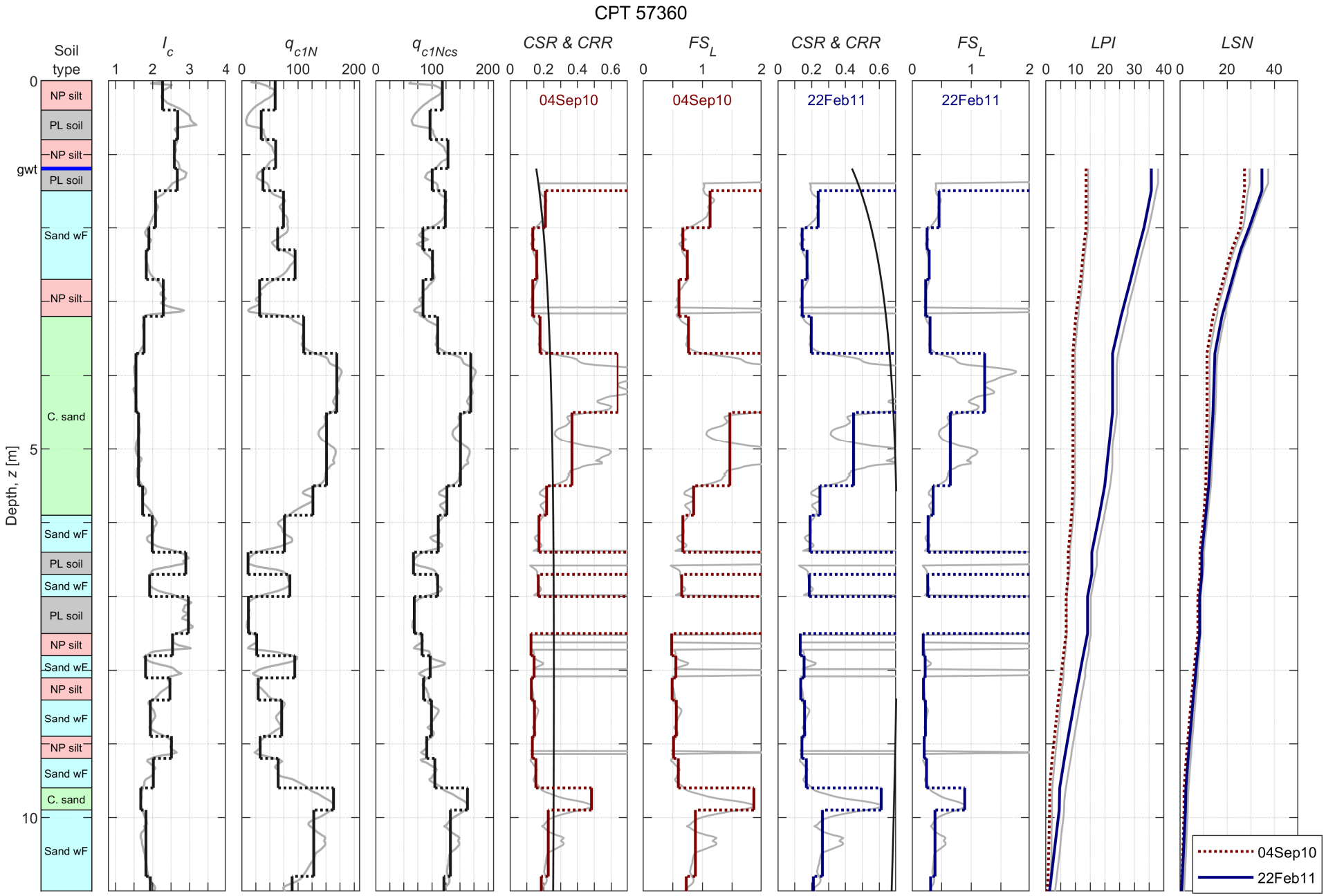
CPT 57360
Soil type
I_c
q_{c1N}
q_{c1Ncs}
CSR & CRR
FS_L
CSR & CRR
FS_L
LPI
LSN
04Sep10
04Sep10
22Feb11
22Feb11
NP silt
PL soil
NP silt
gwt
PL soil
Sand wF
NP silt
C. sand
Sand wF
PL soil
Sand wF
PL soil
NP silt
Sand wF
NP silt
Sand wF
NP silt
Sand wF
C. sand
Sand wF
Depth, z [m]
0
5
10
1 2 3 4
0 100 200
0 100 200
0 0.2 0.4 0.6
0 1 2
0 0.2 0.4 0.6
0 1 2
0 10 20 30 40
0 20 40
04Sep10
22Feb11

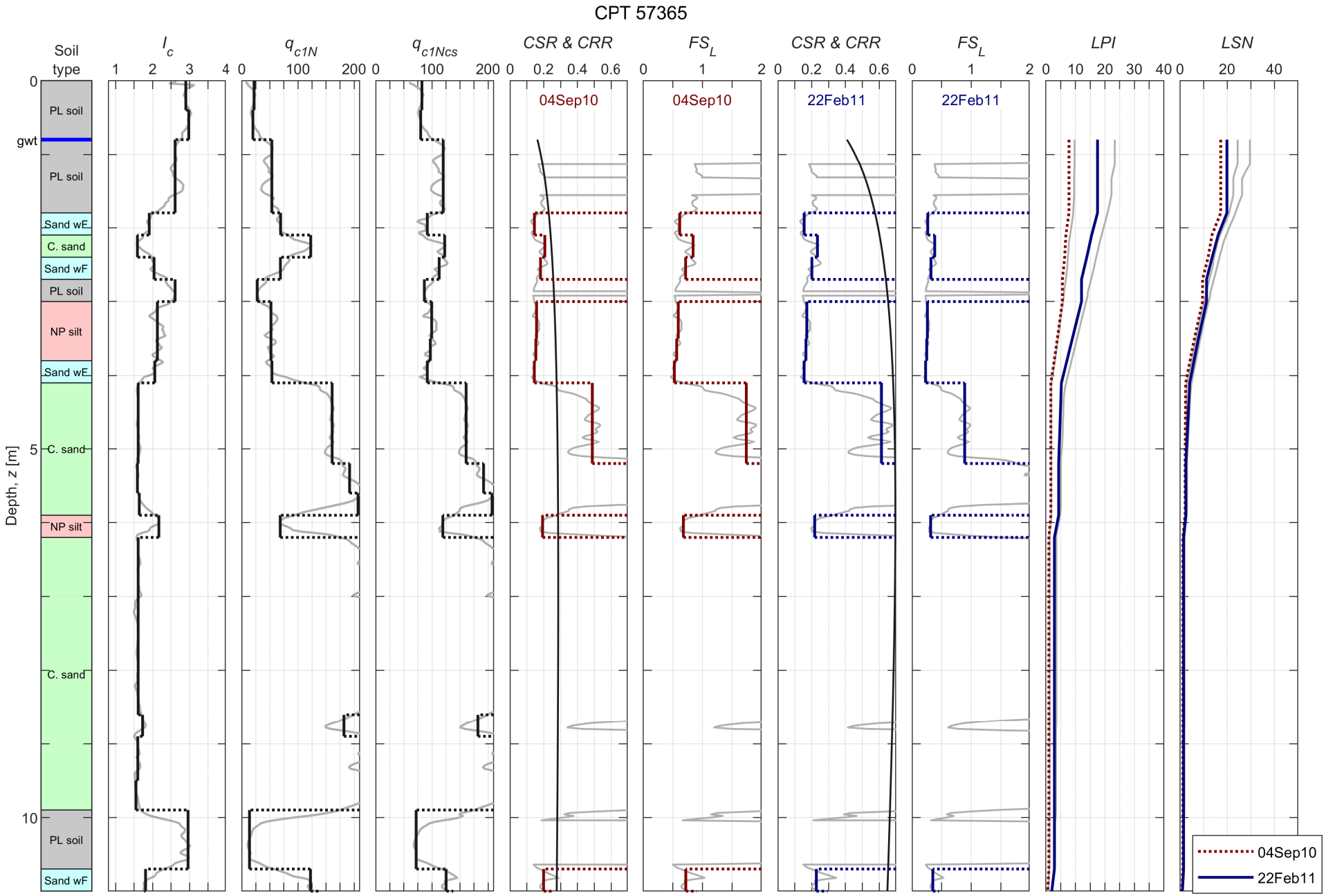
CPT 57365
Soil type
I_c
q_{c1N}
q_{c1Ncs}
CSR & CRR
FS_L
CSR & CRR
FS_L
LPI
LSN
04Sep10
04Sep10
22Feb11
22Feb11
PL soil
gwt
PL soil
Sand wE
C. sand
Sand wF
PL soil
NP silt
Sand wE
C. sand
NP silt
C. sand
PL soil
Sand wF
Depth, z [m]
04Sep10
22Feb11

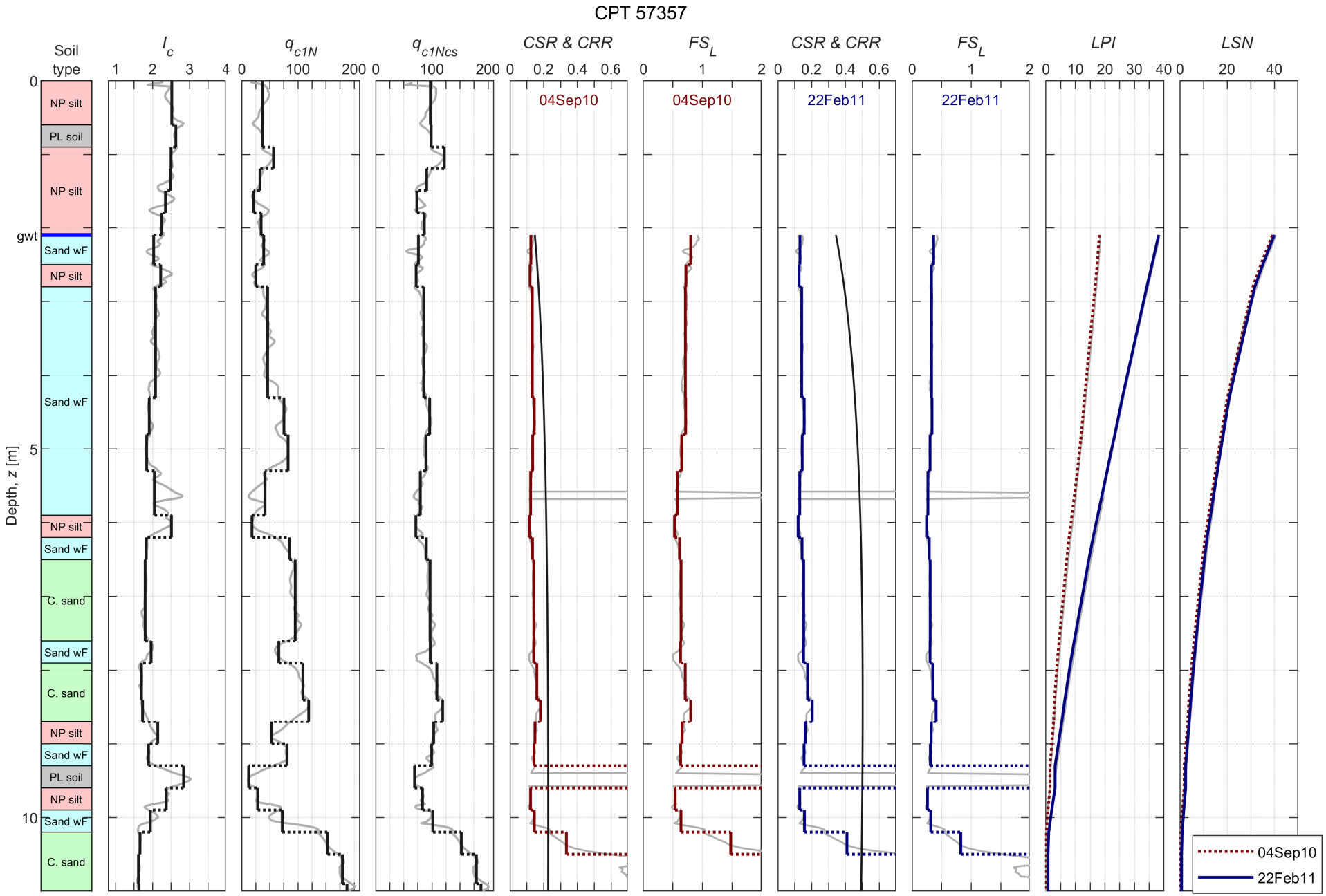
CPT 57357
Soil type
I_c
q_{c1N}
q_{c1Ncs}
CSR & CRR
FS_L
CSR & CRR
FS_L
LPI
LSN
04Sep10
04Sep10
22Feb11
22Feb11
NP silt
PL soil
NP silt
gwt
Sand wF
NP silt
Sand wF
C. sand
Sand wF
C. sand
NP silt
Sand wF
PL soil
NP silt
Sand wF
C. sand
Depth, z [m]
04Sep10
22Feb11

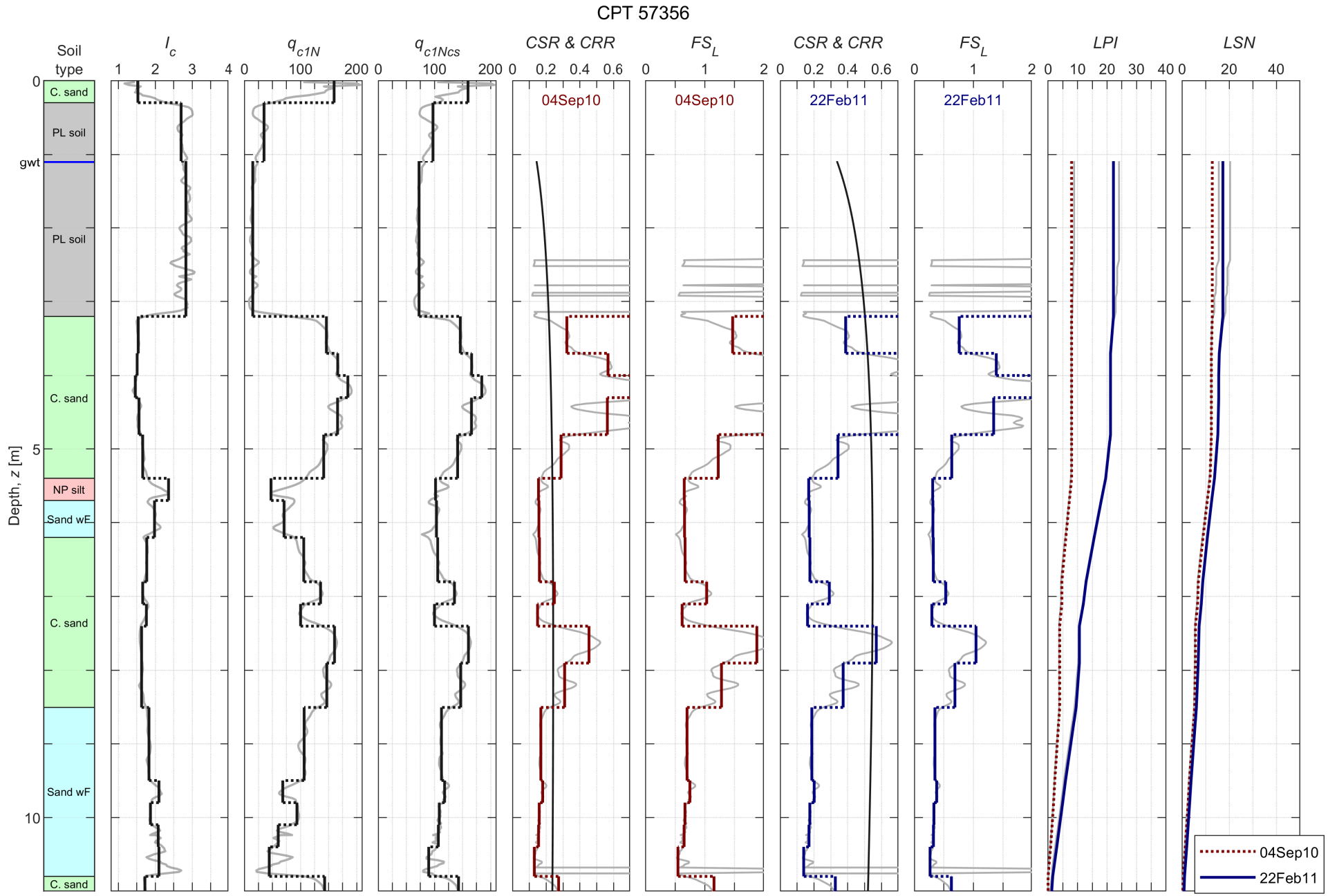
CPT 57356
Soil type
I_c
q_{c1N}
q_{c1Ncs}
CSR & CRR
FS_L
CSR & CRR
FS_L
LPI
LSN
04Sep10
04Sep10
22Feb11
22Feb11
C. sand
PL soil
gwt
PL soil
C. sand
NP silt
Sand wE
C. sand
Sand wF
C. sand
Depth, z [m]
0
5
10
1 2 3 4
0 100 200
0 100 200
0 0.2 0.4 0.6
0 1 2
0 0.2 0.4 0.6
0 1 2
0 10 20 30 40
0 20 40
04Sep10
22Feb11

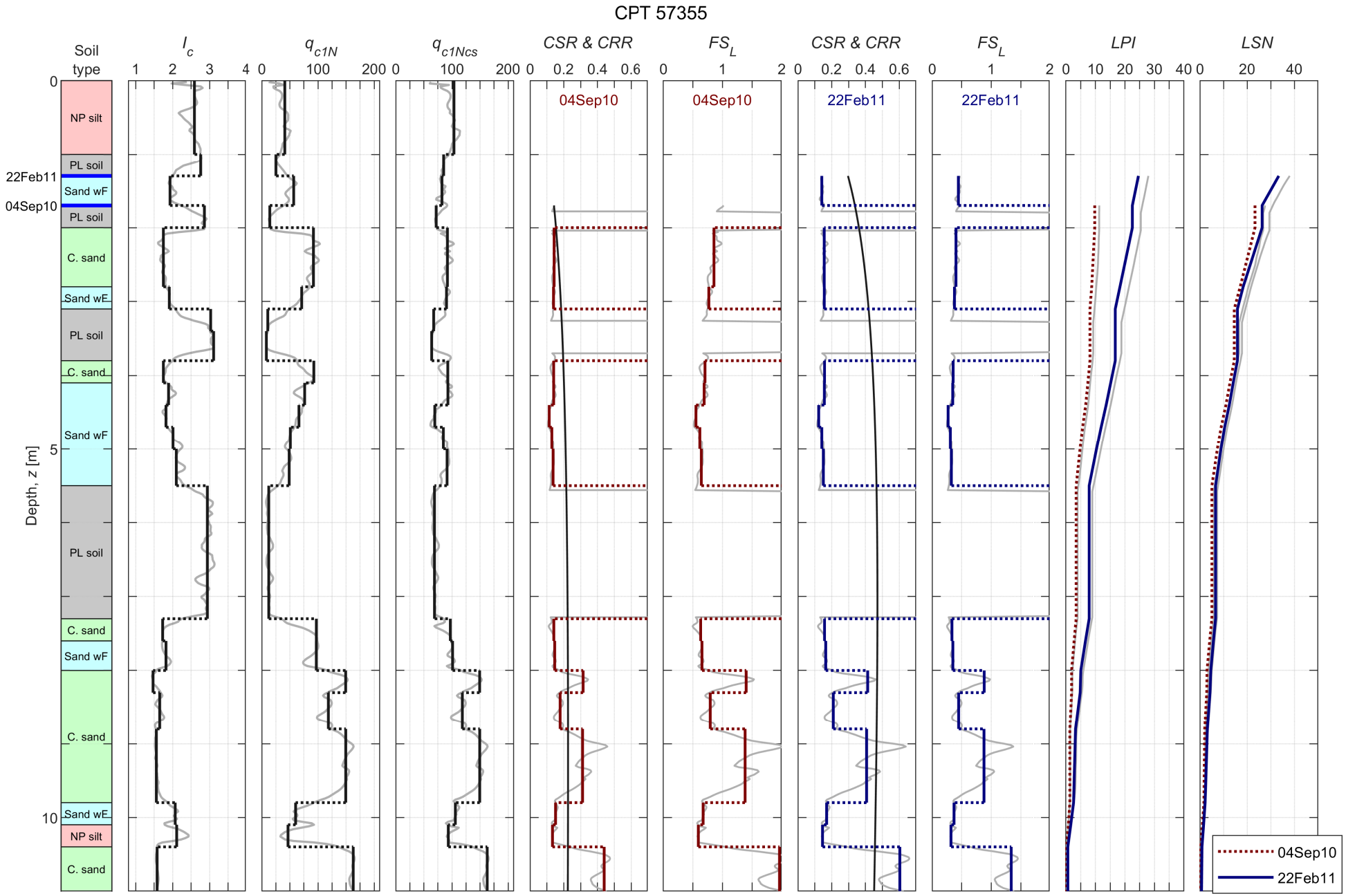
CPT 57355
Soil type
I_c
q_{c1N}
q_{c1Ncs}
CSR & CRR
FS_L
CSR & CRR
FS_L
LPI
LSN
04Sep10
04Sep10
22Feb11
22Feb11
NP silt
PL soil
Sand wF
PL soil
C. sand
Sand wF
PL soil
C. sand
Sand wF
PL soil
C. sand
Sand wF
C. sand
Sand wE
NP silt
C. sand
22Feb11
04Sep10
Depth, z [m]
0
5
10
1 2 3 4
0 100 200
0 100 200
0 0.2 0.4 0.6
0 1 2
0 0.2 0.4 0.6
0 1 2
0 10 20 30 40
0 20 40
04Sep10
22Feb11

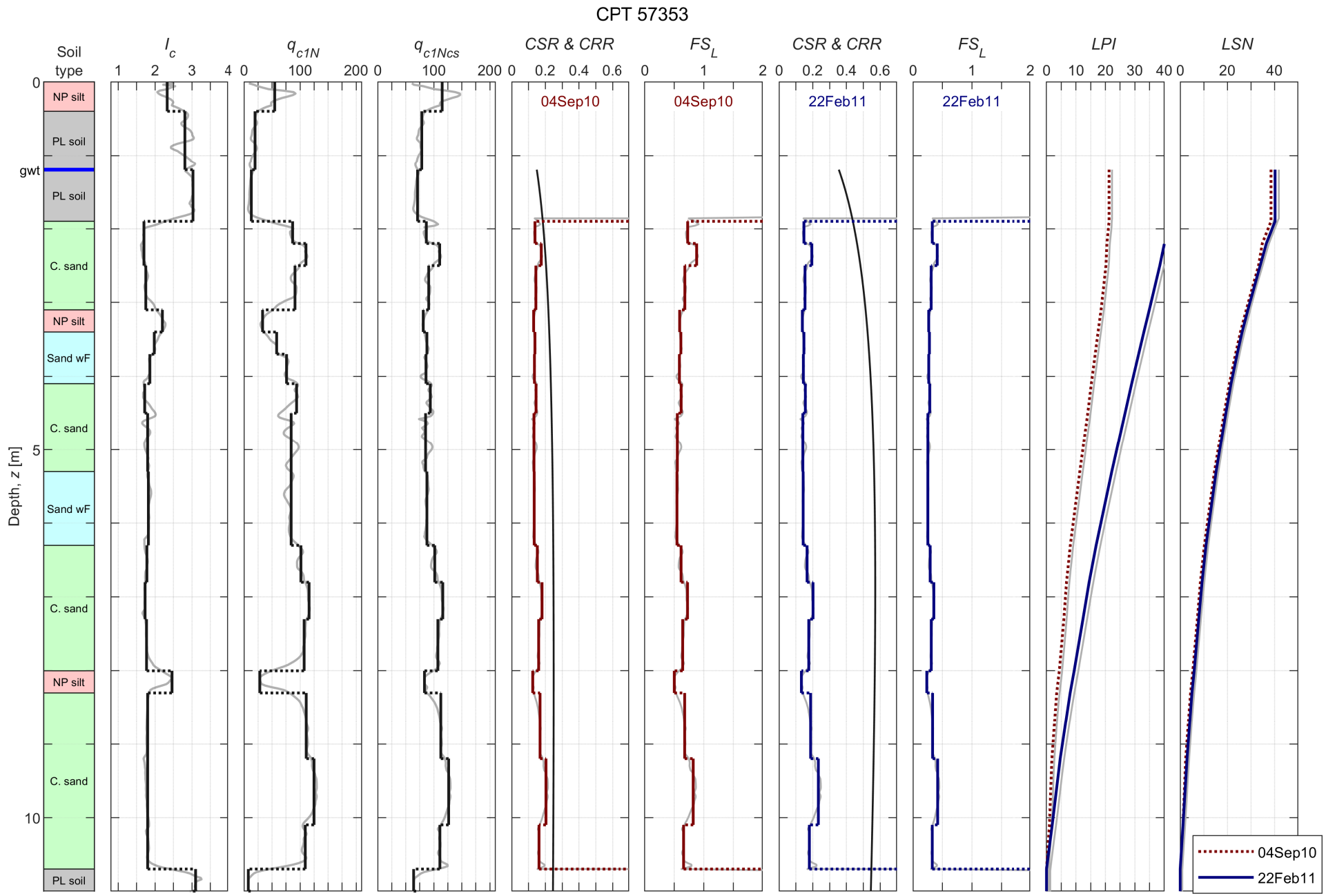
CPT 57353
Soil type
I_c
q_{c1N}
q_{c1Ncs}
CSR & CRR
FS_L
CSR & CRR
FS_L
LPI
LSN
NP silt
PL soil
gwt
PL soil
C. sand
NP silt
Sand wF
C. sand
Sand wF
C. sand
NP silt
C. sand
PL soil
Depth, z [m]
04Sep10
04Sep10
22Feb11
22Feb11
04Sep10
22Feb11

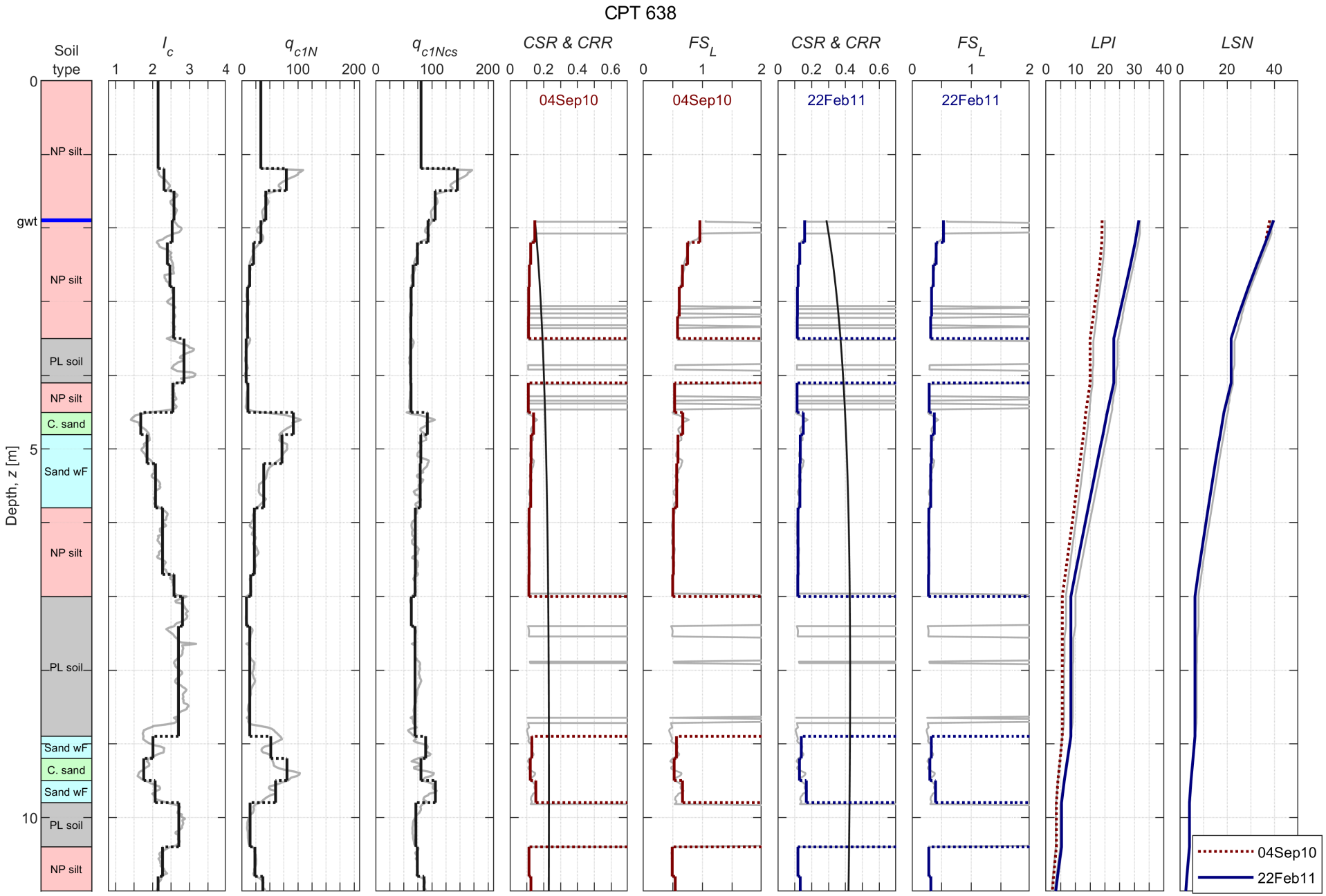
CPT 638
Soil type
I_c
q_{c1N}
q_{c1Ncs}
CSR & CRR
FS_L
CSR & CRR
FS_L
LPI
LSN
04Sep10
04Sep10
22Feb11
22Feb11
Depth, z [m]
gwt
NP silt
NP silt
PL soil
NP silt
C. sand
Sand wF
NP silt
PL soil
Sand wF
C. sand
Sand wF
PL soil
NP silt
04Sep10
22Feb11

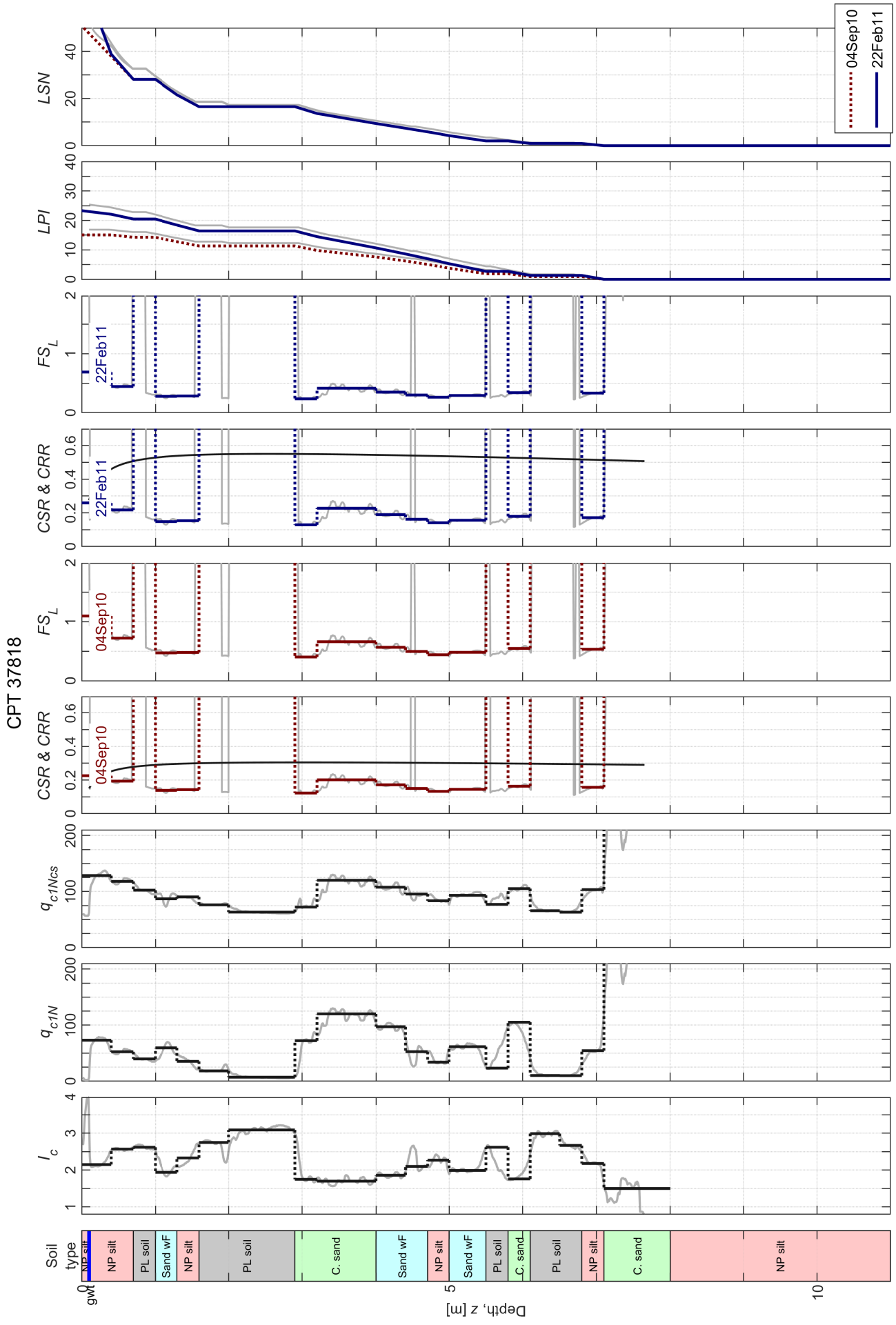
CPT 37818
Soil type
NP silt
PL soil
Sand wF
C. sand
I_c
q_{c1N}
q_{c1Ncs}
CSR & CRR
FS_L
LPI
LSN
04Sep10
22Feb11
gwt
Depth, z [m]
0
5
10

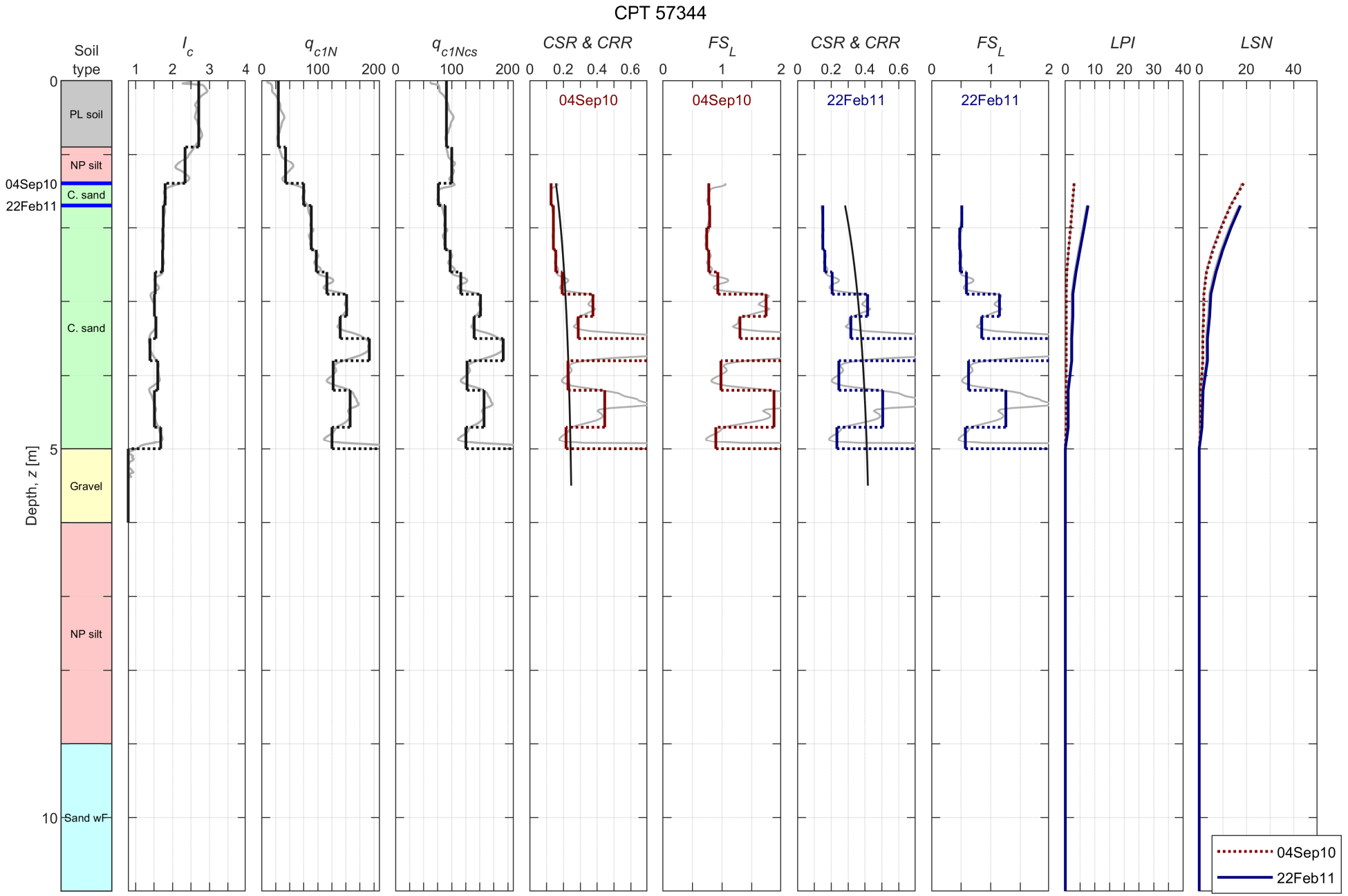
CPT 57344
Soil type
I_c
q_{c1N}
q_{c1Ncs}
CSR & CRR
FS_L
CSR & CRR
FS_L
LPI
LSN
PL soil
NP silt
C. sand
C. sand
Gravel
NP silt
Sand wF
04Sep10
22Feb11
Depth, z [m]
04Sep10
22Feb11
04Sep10
22Feb11

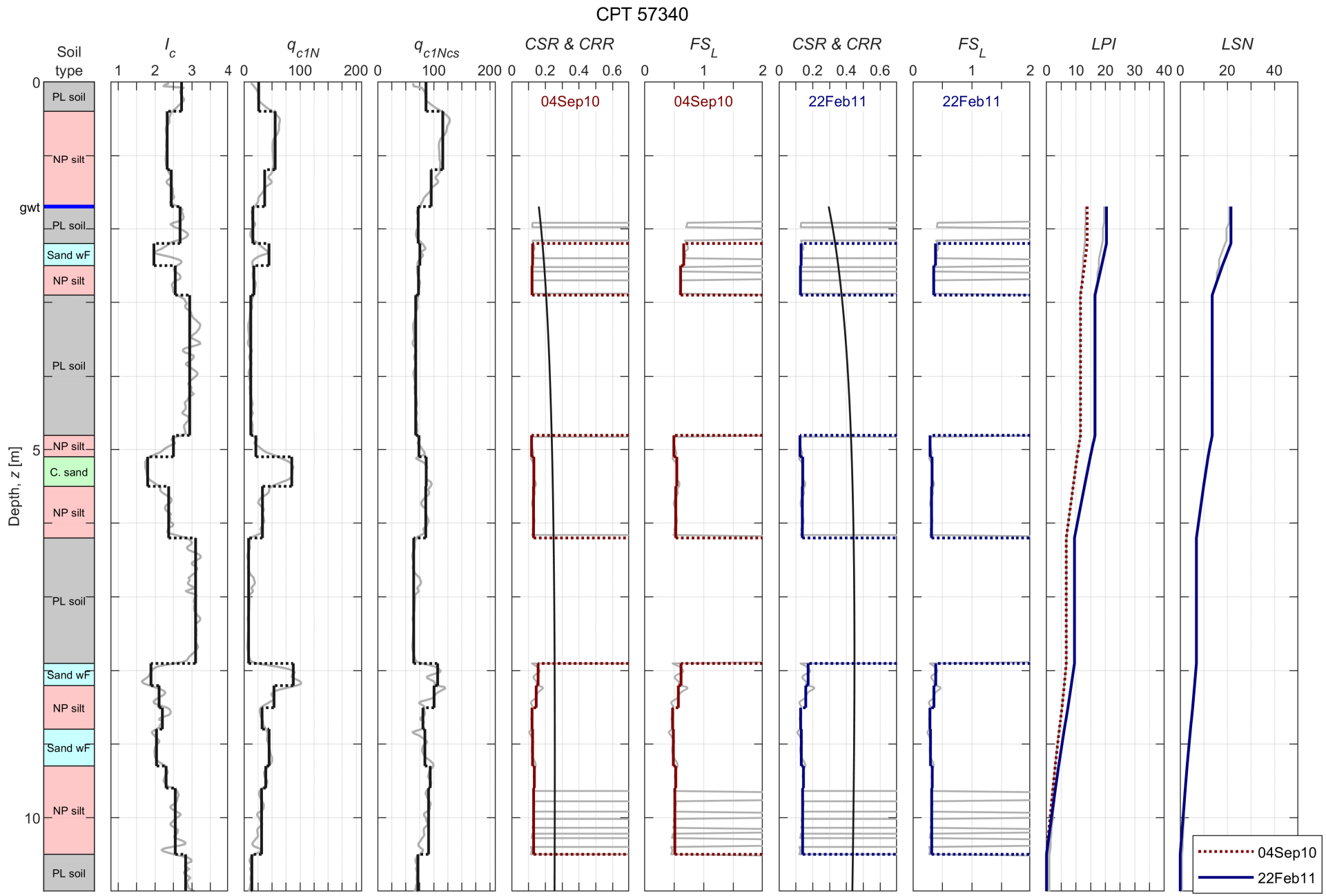
CPT 57340
Soil type
I_c
q_{c1N}
q_{c1Ncs}
CSR & CRR
FS_L
CSR & CRR
FS_L
LPI
LSN
04Sep10
04Sep10
22Feb11
22Feb11
PL soil
NP silt
gwt
PL soil
Sand wF
NP silt
PL soil
NP silt
C. sand
NP silt
PL soil
Sand wF
NP silt
Sand wF
NP silt
PL soil
Depth, z [m]
0
5
10
1 2 3 4
0 100 200
0 100 200
0 0.2 0.4 0.6
0 1 2
0 0.2 0.4 0.6
0 1 2
0 10 20 30 40
0 20 40
04Sep10
22Feb11

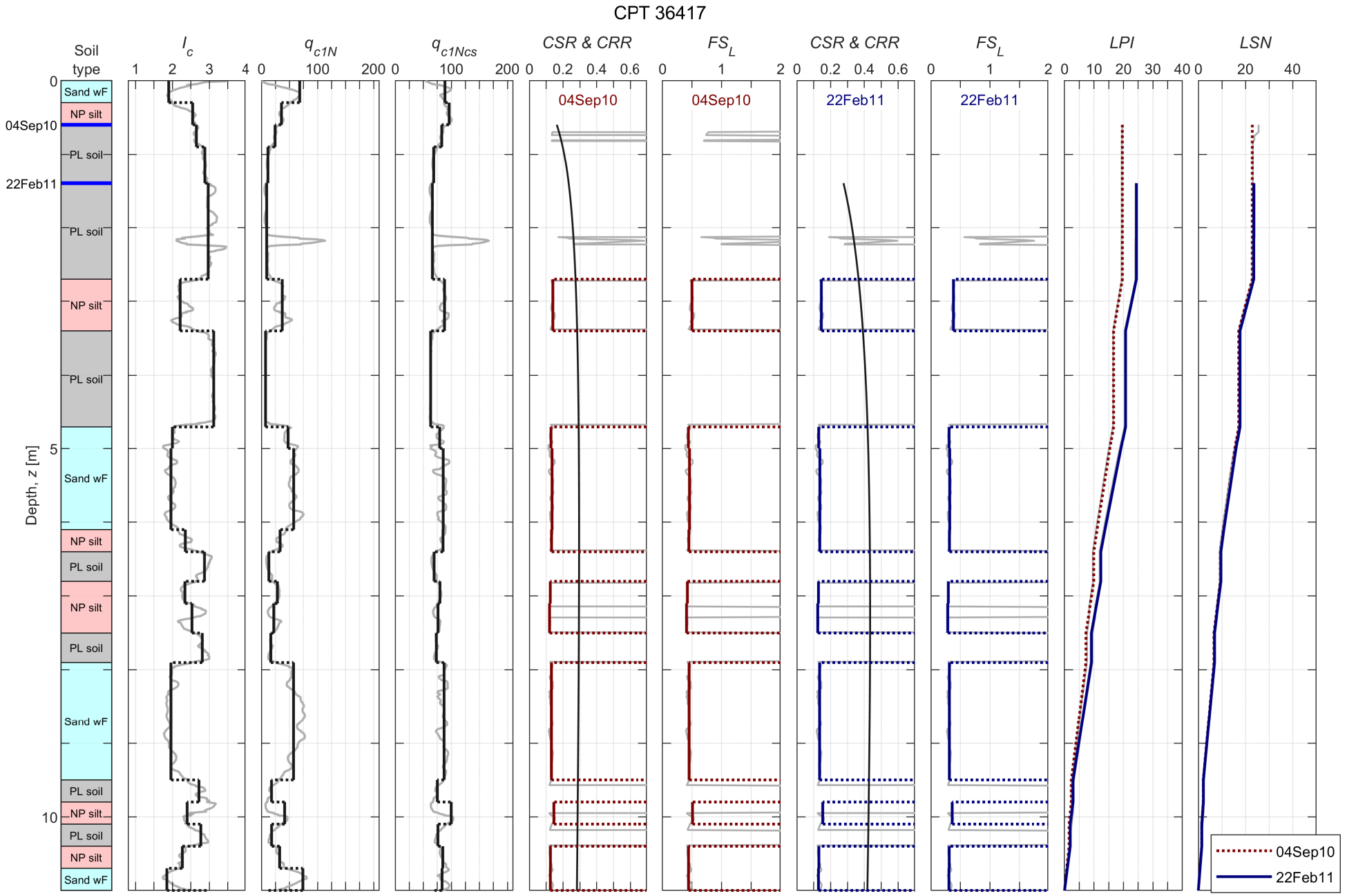
CPT 36417
Soil type
I_c
q_{c1N}
q_{c1Ncs}
CSR & CRR
FS_L
CSR & CRR
FS_L
LPI
LSN
Depth, z [m]
Sand wF
NP silt
PL soil
04Sep10
22Feb11
04Sep10
22Feb11
04Sep10
22Feb11

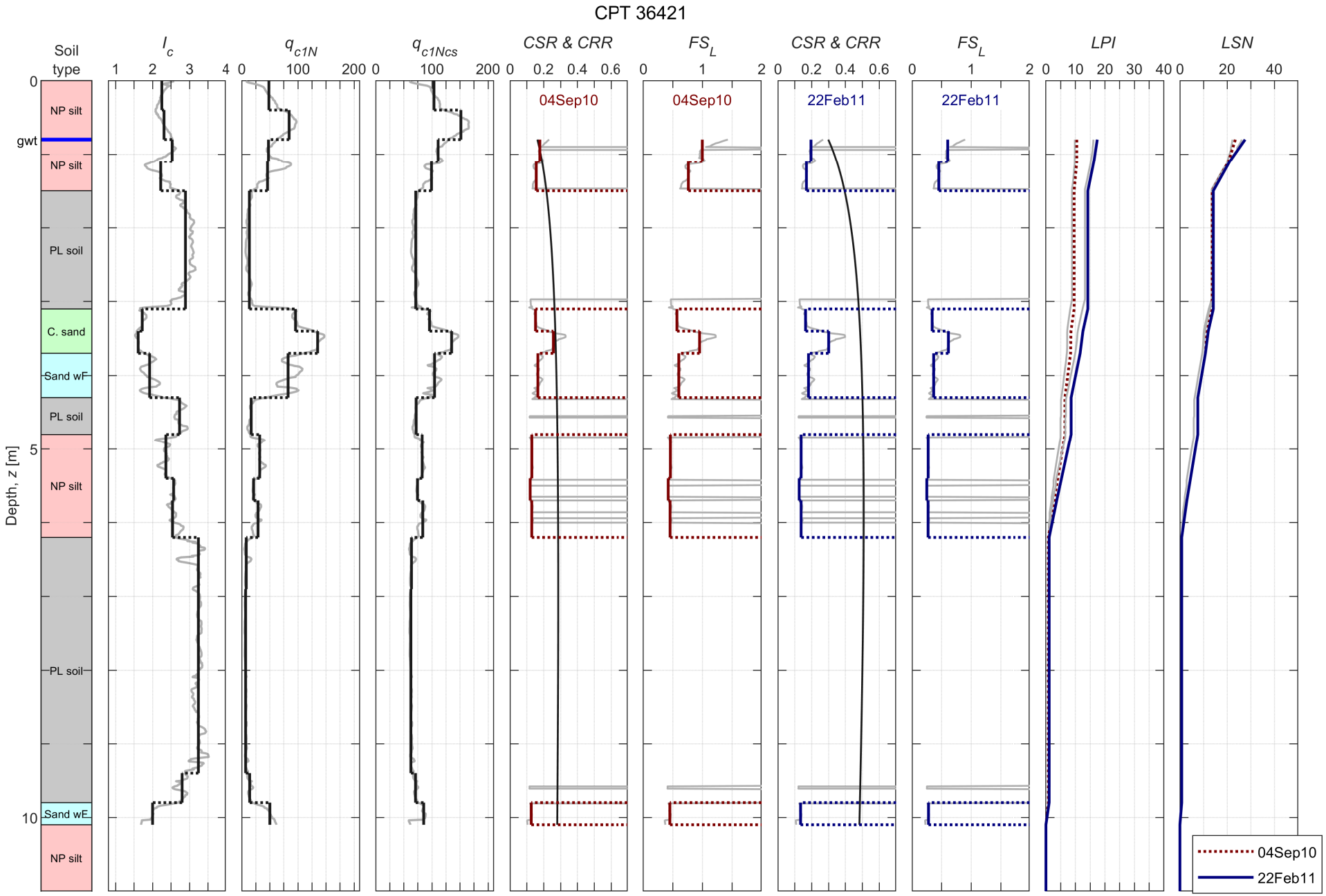
CPT 36421
Soil type
I_c
q_{c1N}
q_{c1Ncs}
CSR & CRR
FS_L
CSR & CRR
FS_L
LPI
LSN
04Sep10
04Sep10
22Feb11
22Feb11
NP silt
gwt
NP silt
PL soil
C. sand
Sand wF
PL soil
NP silt
PL soil
Sand wE
NP silt
Depth, z [m]
0
5
10
1 2 3 4
0 100 200
0 100 200
0 0.2 0.4 0.6
0 1 2
0 0.2 0.4 0.6
0 1 2
0 10 20 30 40
0 20 40
04Sep10
22Feb11

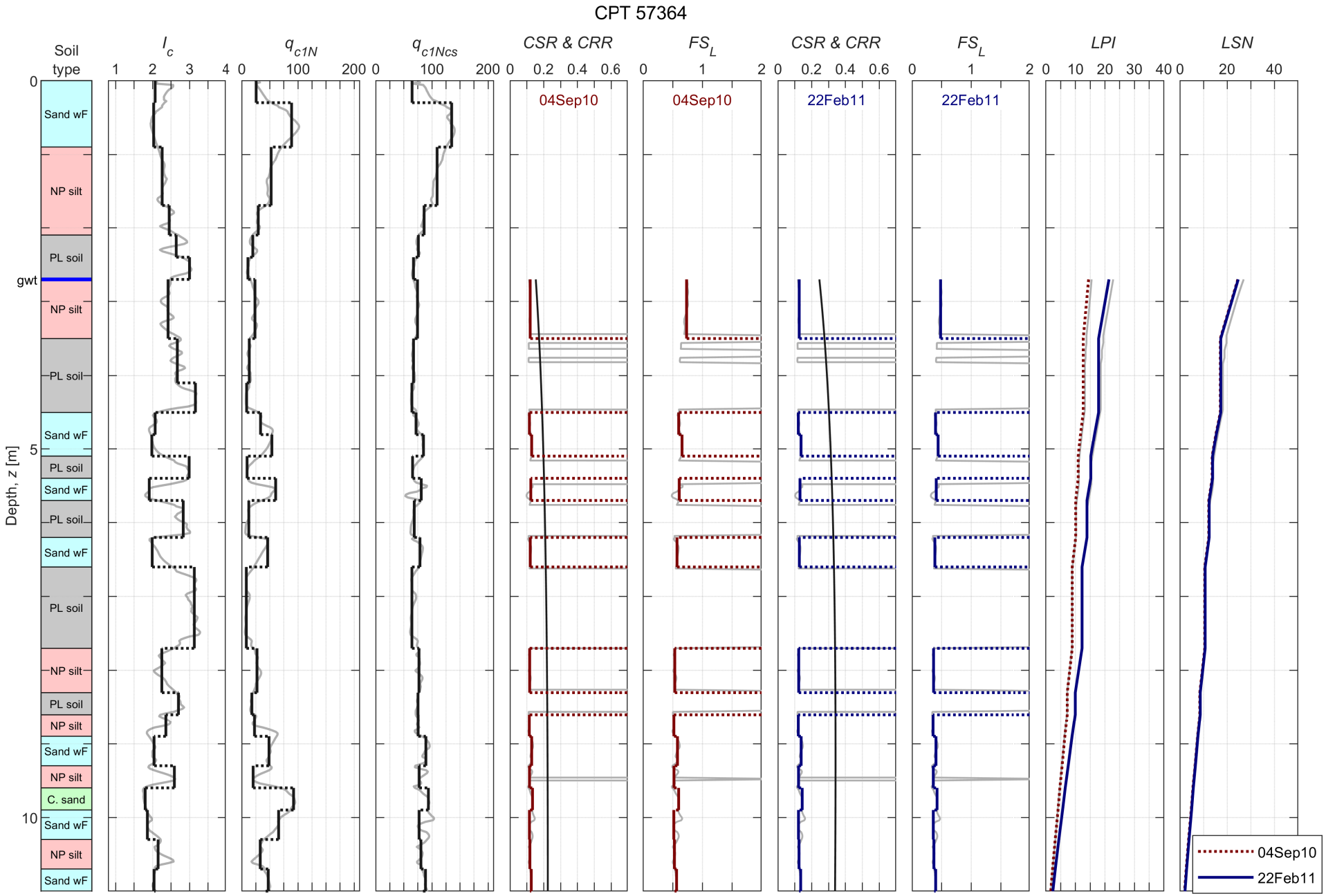
CPT 57364
Soil type
I_c
q_{c1N}
q_{c1Ncs}
CSR & CRR
FS_L
CSR & CRR
FS_L
LPI
LSN
04Sep10
04Sep10
22Feb11
22Feb11
Depth, z [m]
gwt
Sand wF
NP silt
PL soil
Sand wF
PL soil
Sand wF
PL soil
Sand wF
PL soil
NP silt
PL soil
NP silt
Sand wF
NP silt
C. sand
Sand wF
NP silt
Sand wF
04Sep10
22Feb11

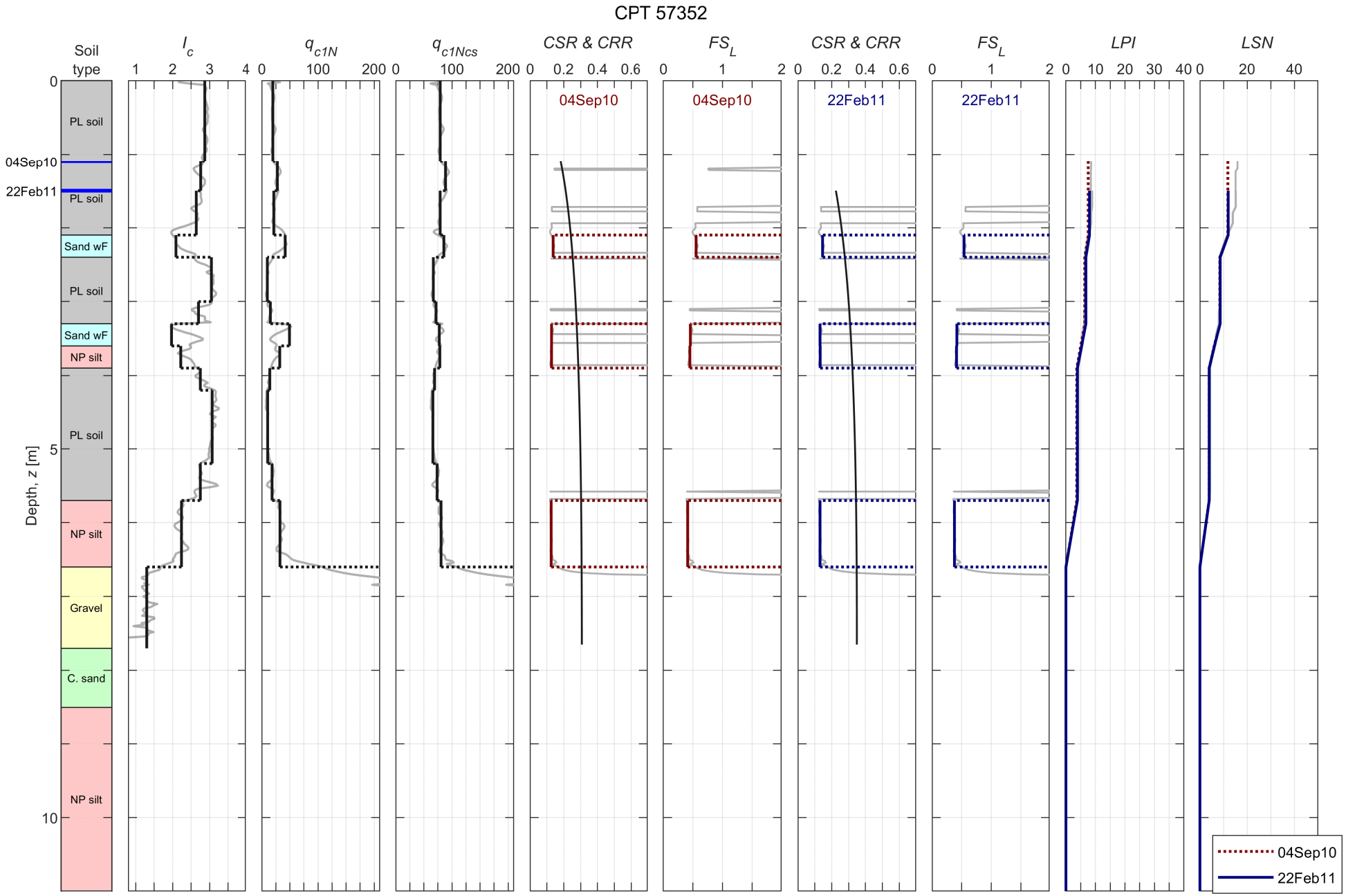
CPT 57352
Soil type
I_c
q_{c1N}
q_{c1Ncs}
CSR & CRR
FS_L
CSR & CRR
FS_L
LPI
LSN
04Sep10
22Feb11
PL soil
Sand wF
PL soil
Sand wF
NP silt
PL soil
NP silt
Gravel
C. sand
NP silt
Depth, z [m]
0
5
10
1 2 3 4
0 100 200
0 100 200
0 0.2 0.4 0.6
0 1 2
0 0.2 0.4 0.6
0 1 2
0 10 20 30 40
0 20 40
04Sep10
22Feb11

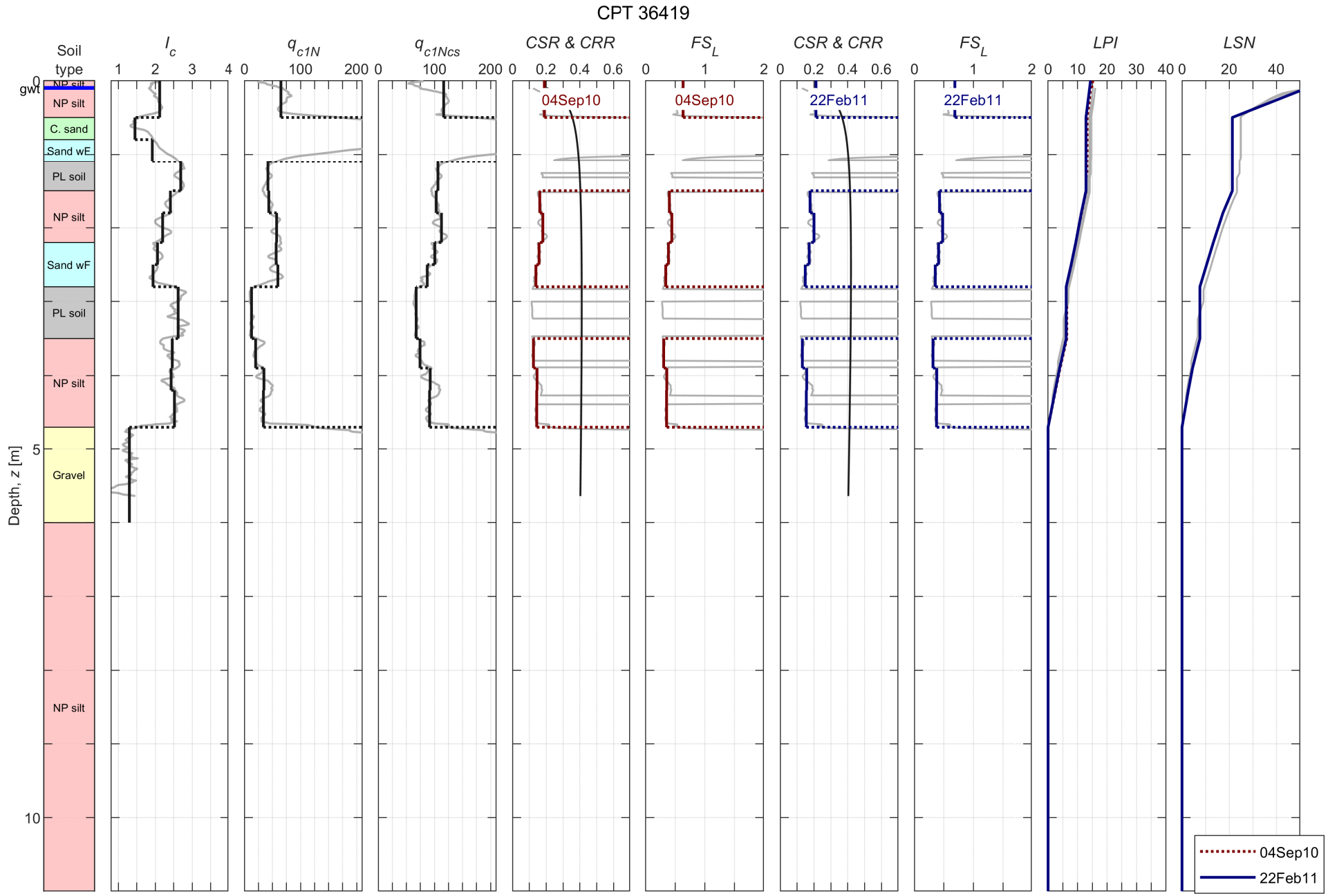
CPT 36419
Soil type
I_c
q_{c1N}
q_{c1Ncs}
CSR & CRR
FS_L
CSR & CRR
FS_L
LPI
LSN
gwt
NP silt
C. sand
Sand wE
PL soil
NP silt
Sand wF
PL soil
NP silt
Gravel
NP silt
Depth, z [m]
04Sep10
04Sep10
22Feb11
22Feb11
04Sep10
22Feb11

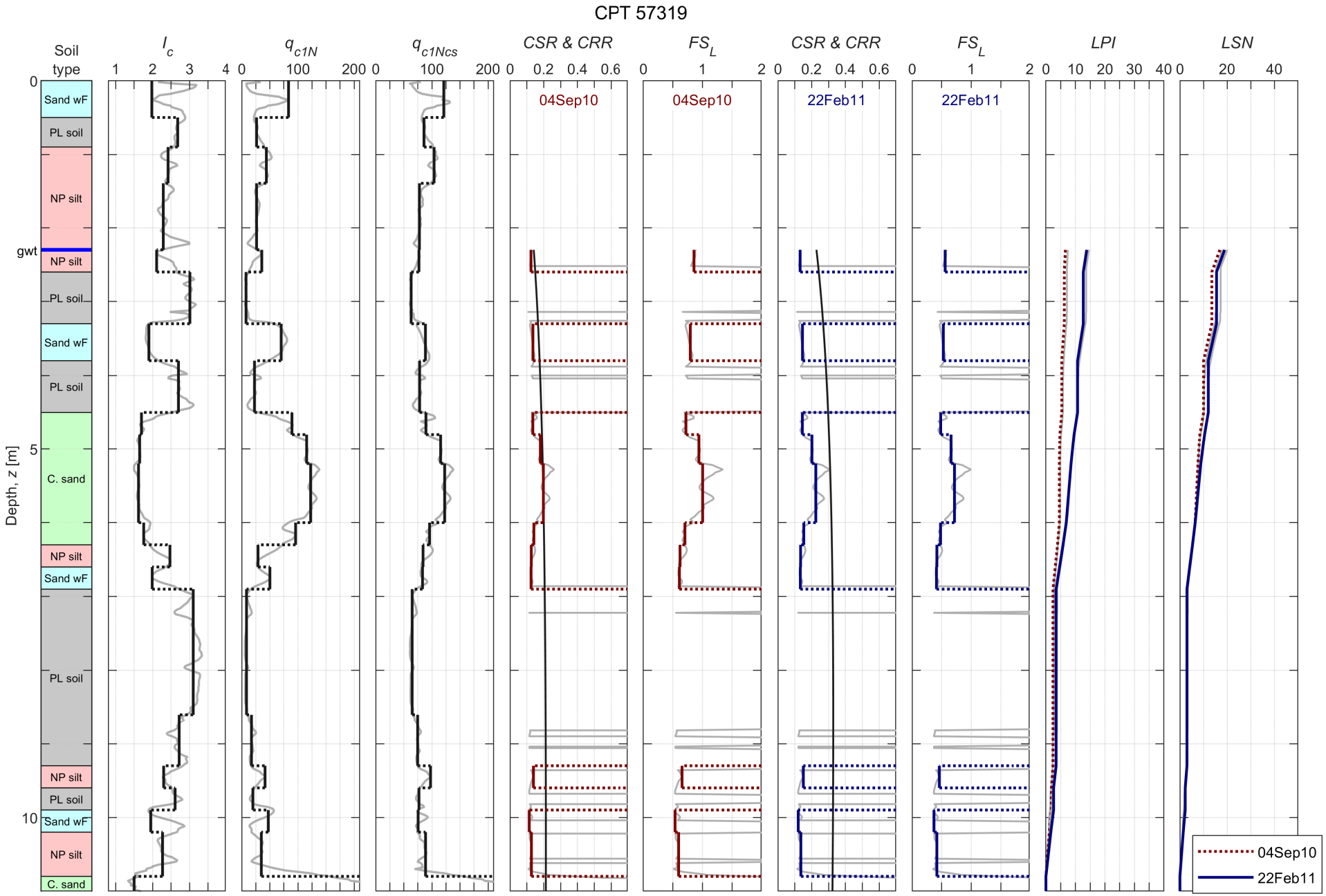
CPT 57319
Soil type
I_c
q_{c1N}
q_{c1Ncs}
CSR & CRR
FS_L
CSR & CRR
FS_L
LPI
LSN
04Sep10
04Sep10
22Feb11
22Feb11
Depth, z [m]
gwt
Sand wF
PL soil
NP silt
NP silt
PL soil
Sand wF
PL soil
C. sand
NP silt
Sand wF
PL soil
NP silt
PL soil
Sand wF
NP silt
C. sand
04Sep10
22Feb11

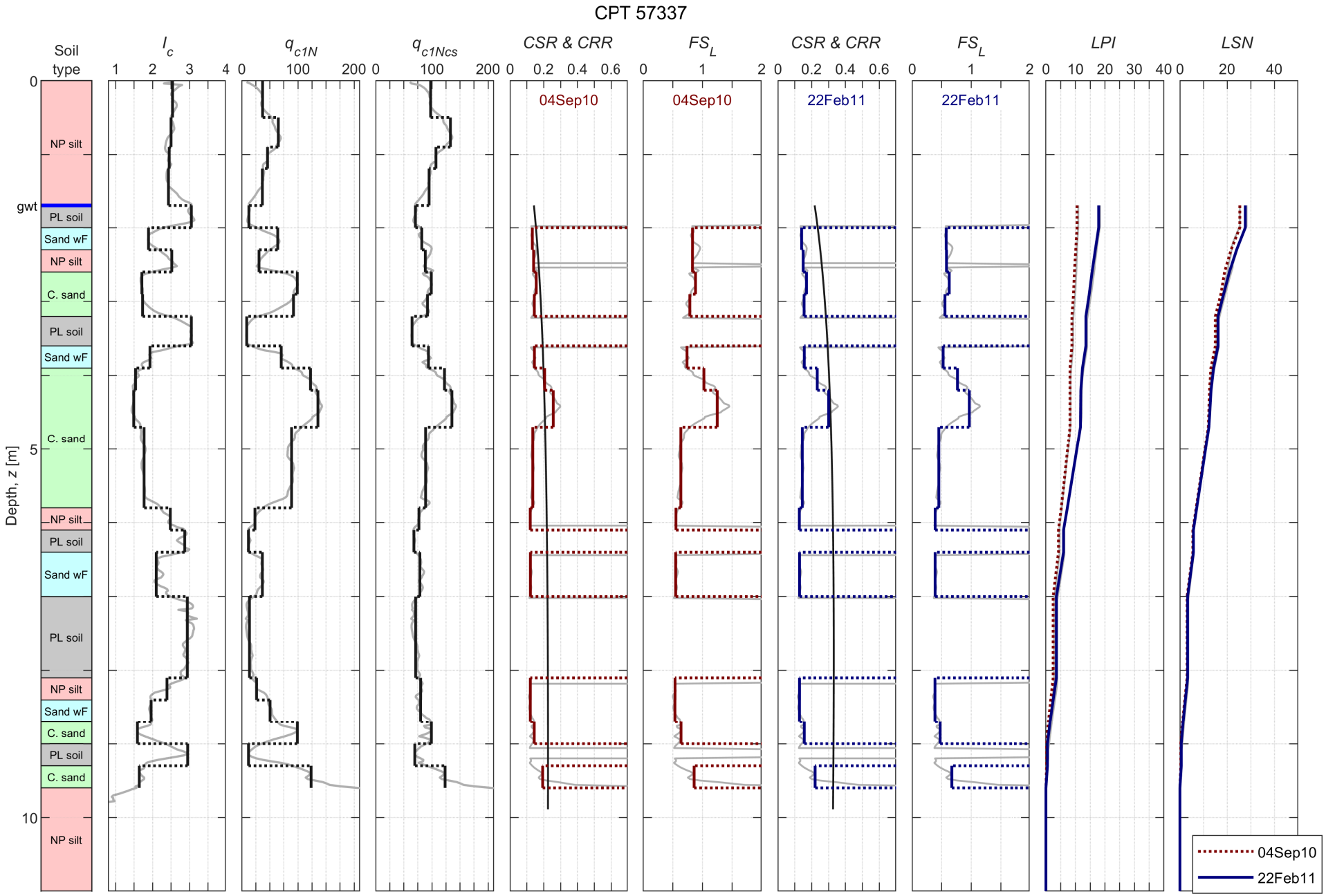
CPT 57337
Soil type
I_c
q_{c1N}
q_{c1Ncs}
CSR & CRR
FS_L
CSR & CRR
FS_L
LPI
LSN
04Sep10
04Sep10
22Feb11
22Feb11
Depth, z [m]
gwt
NP silt
PL soil
Sand wF
NP silt
C. sand
PL soil
Sand wF
C. sand
NP silt
PL soil
Sand wF
PL soil
NP silt
Sand wF
C. sand
PL soil
C. sand
NP silt
04Sep10
22Feb11

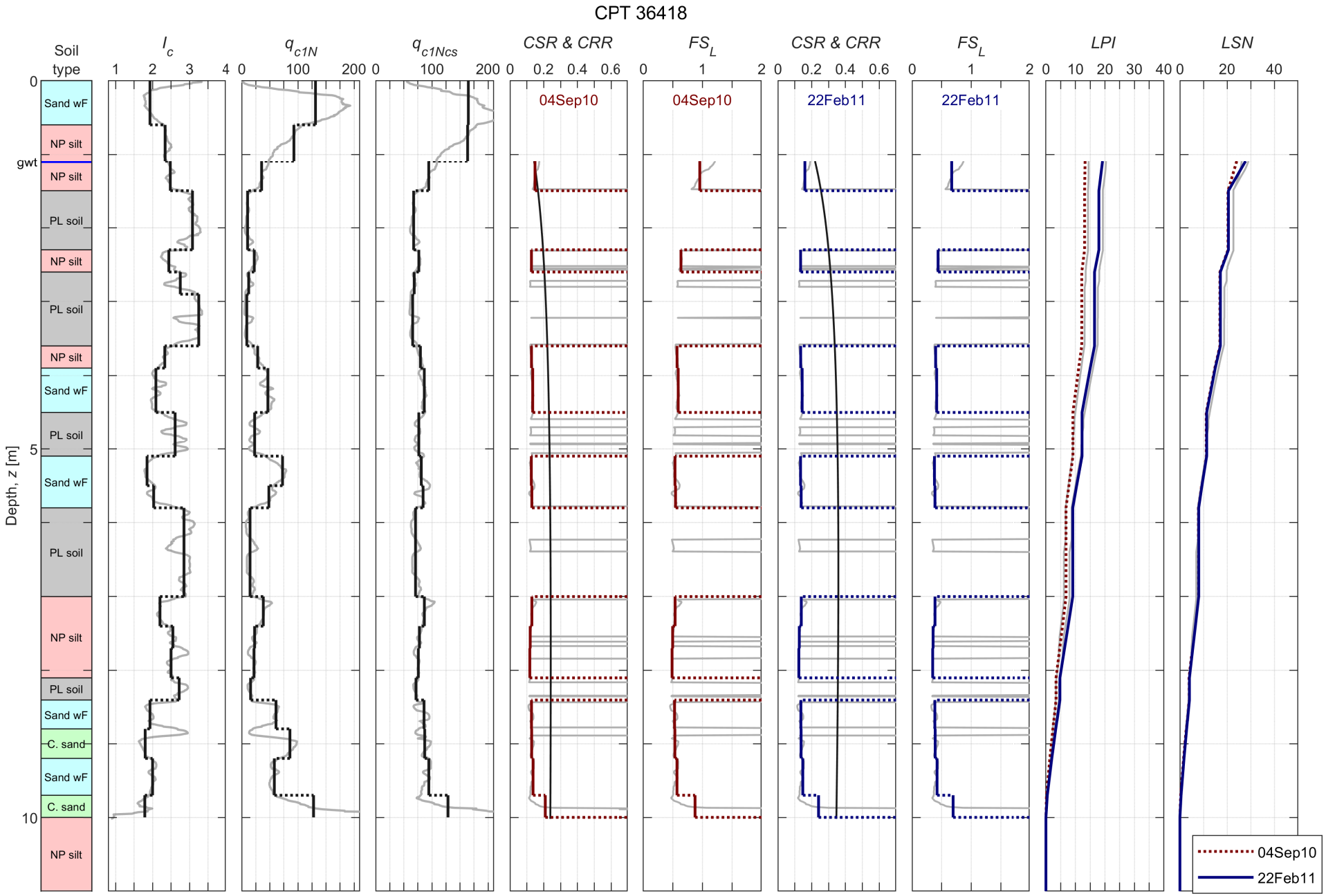
CPT 36418
Soil type
I_c
q_{c1N}
q_{c1Ncs}
CSR & CRR
FS_L
CSR & CRR
FS_L
LPI
LSN
04Sep10
04Sep10
22Feb11
22Feb11
Depth, z [m]
gwt
Sand wF
NP silt
NP silt
PL soil
NP silt
PL soil
NP silt
Sand wF
PL soil
Sand wF
PL soil
NP silt
PL soil
Sand wF
C. sand
Sand wF
C. sand
NP silt
04Sep10
22Feb11

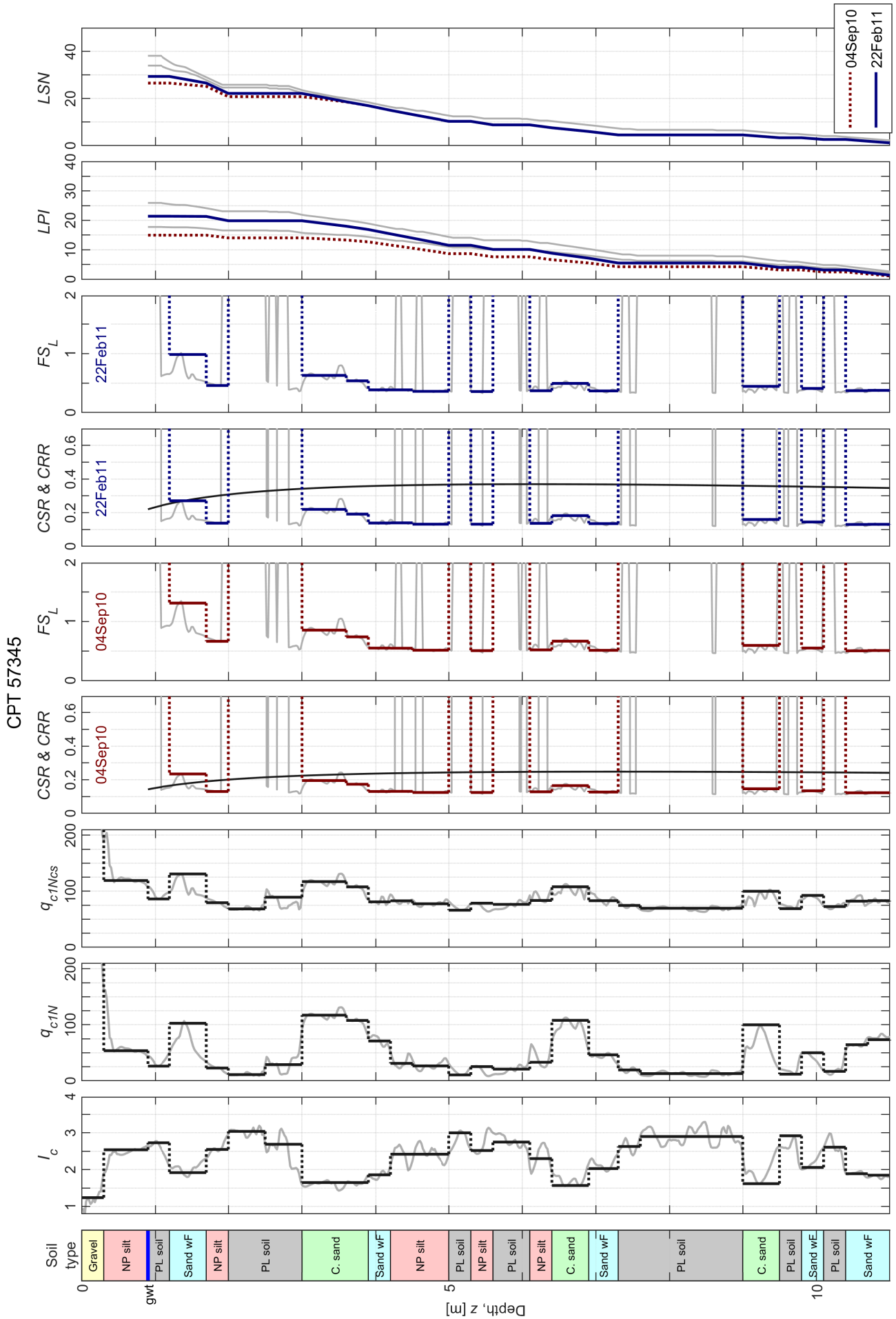
CPT 57345
Soil type
Gravel
NP silt
PL soil
Sand wF
NP silt
PL soil
C. sand
Sand wF
NP silt
PL soil
NP silt
PL soil
NP silt
C. sand
Sand wF
PL soil
C. sand
PL soil
Sand wF
PL soil
Sand wF
gwt
Depth, z [m]
I_c
q_{c1N}
q_{c1Ncs}
CSR & CRR
04Sep10
FS_L
04Sep10
CSR & CRR
22Feb11
FS_L
22Feb11
LPI
LSN
04Sep10
22Feb11

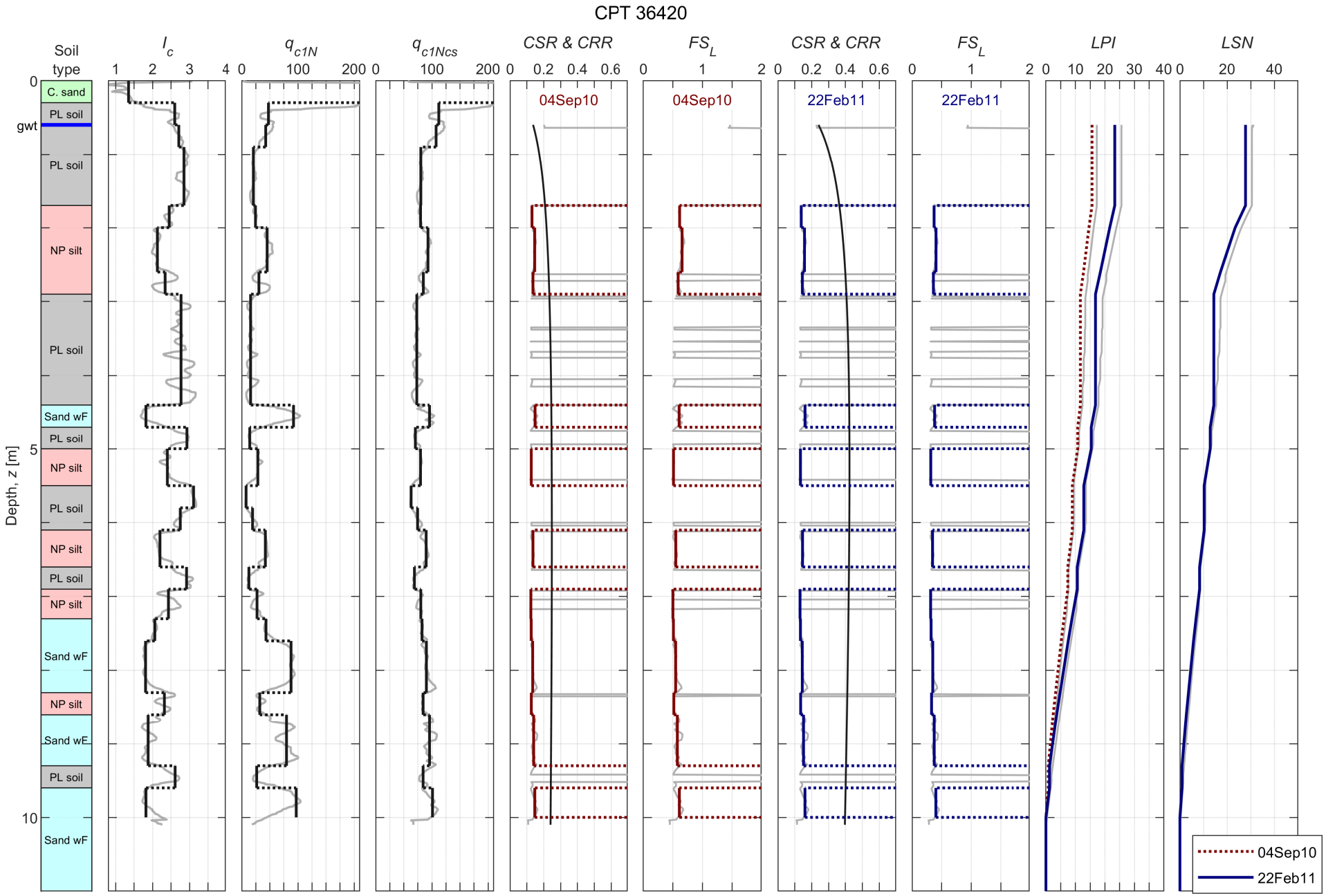
CPT 36420
Soil type
I_c
q_{c1N}
q_{c1Ncs}
CSR & CRR
FS_L
CSR & CRR
FS_L
LPI
LSN
04Sep10
04Sep10
22Feb11
22Feb11
C. sand
PL soil
gwt
PL soil
NP silt
PL soil
Sand wF
PL soil
NP silt
PL soil
NP silt
PL soil
NP silt
Sand wF
NP silt
Sand wF
PL soil
Sand wF
Depth, z [m]
0
5
10
1 2 3 4
0 100 200
0 100 200
0 0.2 0.4 0.6
0 1 2
0 0.2 0.4 0.6
0 1 2
0 10 20 30 40
0 20 40
04Sep10
22Feb11

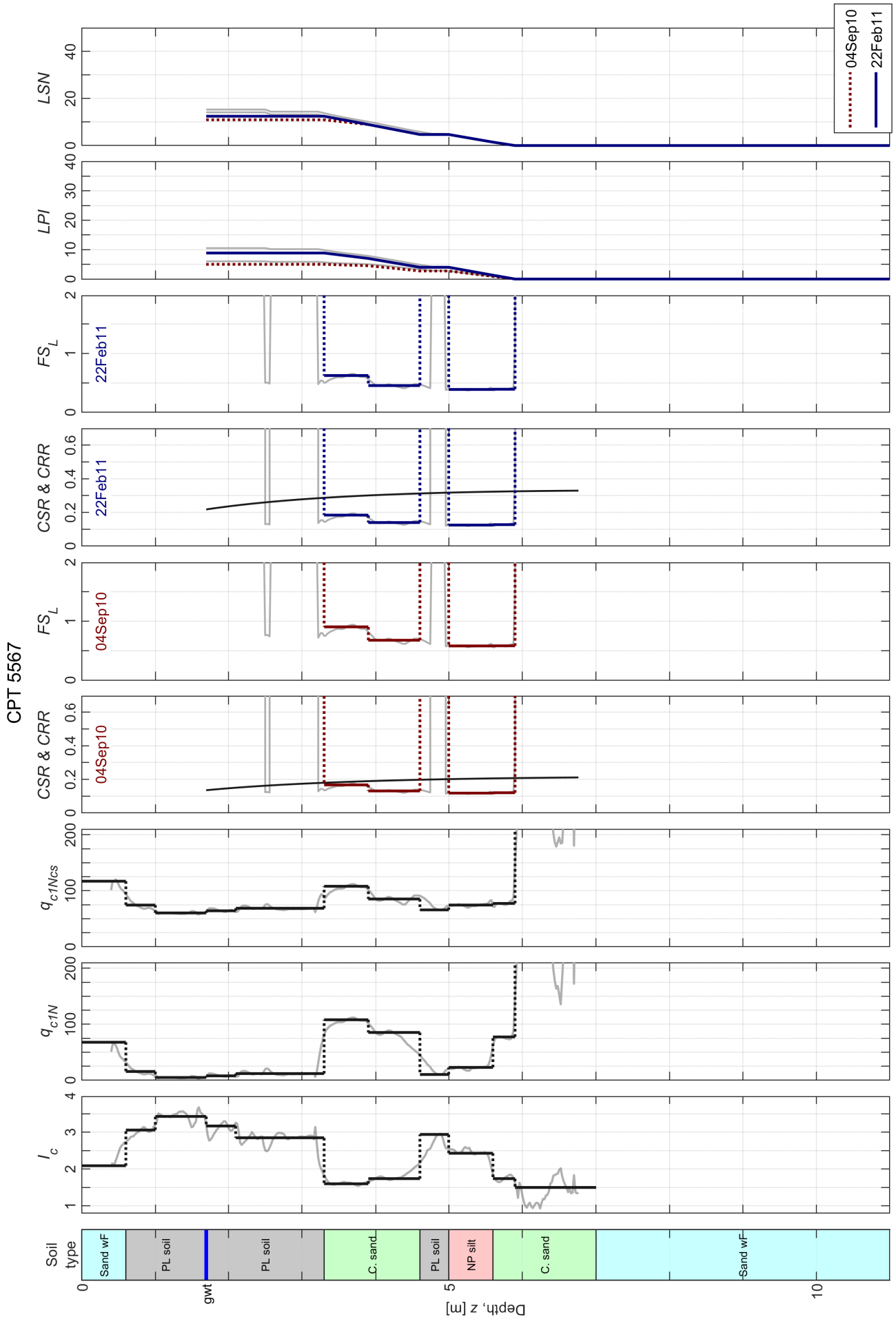
CPT 5567
Soil type
Sand wF
PL soil
PL soil
C. sand
PL soil
NP silt
C. sand
Sand wF
gwt
Depth, z [m]
I_c
q_{c1N}
q_{c1Ncs}
CSR & CRR
04Sep10
FS_L
04Sep10
CSR & CRR
22Feb11
FS_L
22Feb11
LPI
LSN
04Sep10
22Feb11

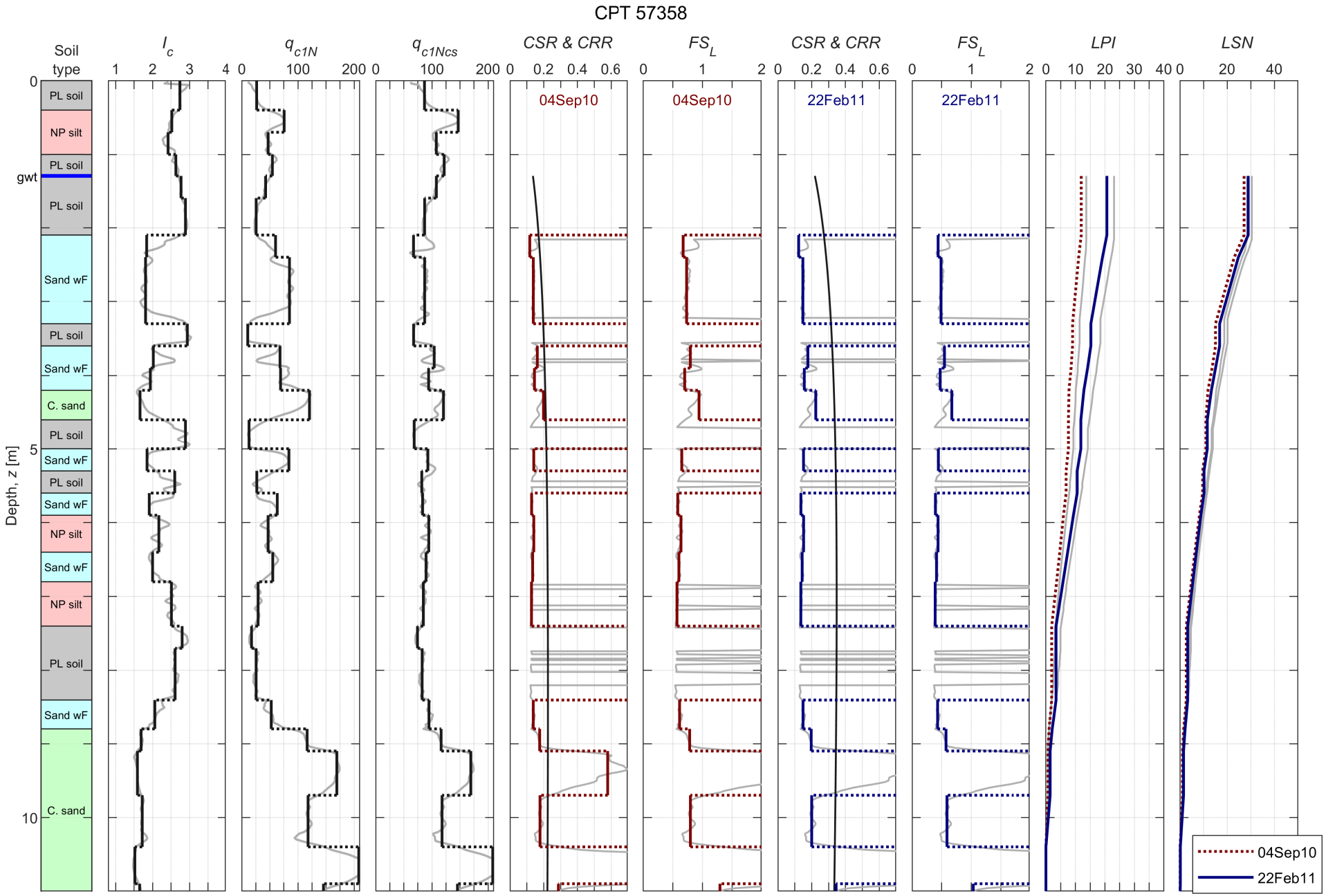
CPT 57358
Soil type
I_c
q_{c1N}
q_{c1Ncs}
CSR & CRR
FS_L
CSR & CRR
FS_L
LPI
LSN
04Sep10
04Sep10
22Feb11
22Feb11
PL soil
NP silt
PL soil
gwt
PL soil
Sand wF
PL soil
Sand wF
C. sand
PL soil
Sand wF
PL soil
Sand wF
NP silt
Sand wF
NP silt
PL soil
Sand wF
C. sand
Depth, z [m]
0
5
10
1 2 3 4
0 100 200
0 100 200
0 0.2 0.4 0.6
0 1 2
0 0.2 0.4 0.6
0 1 2
0 10 20 30 40
0 20 40
04Sep10
22Feb11

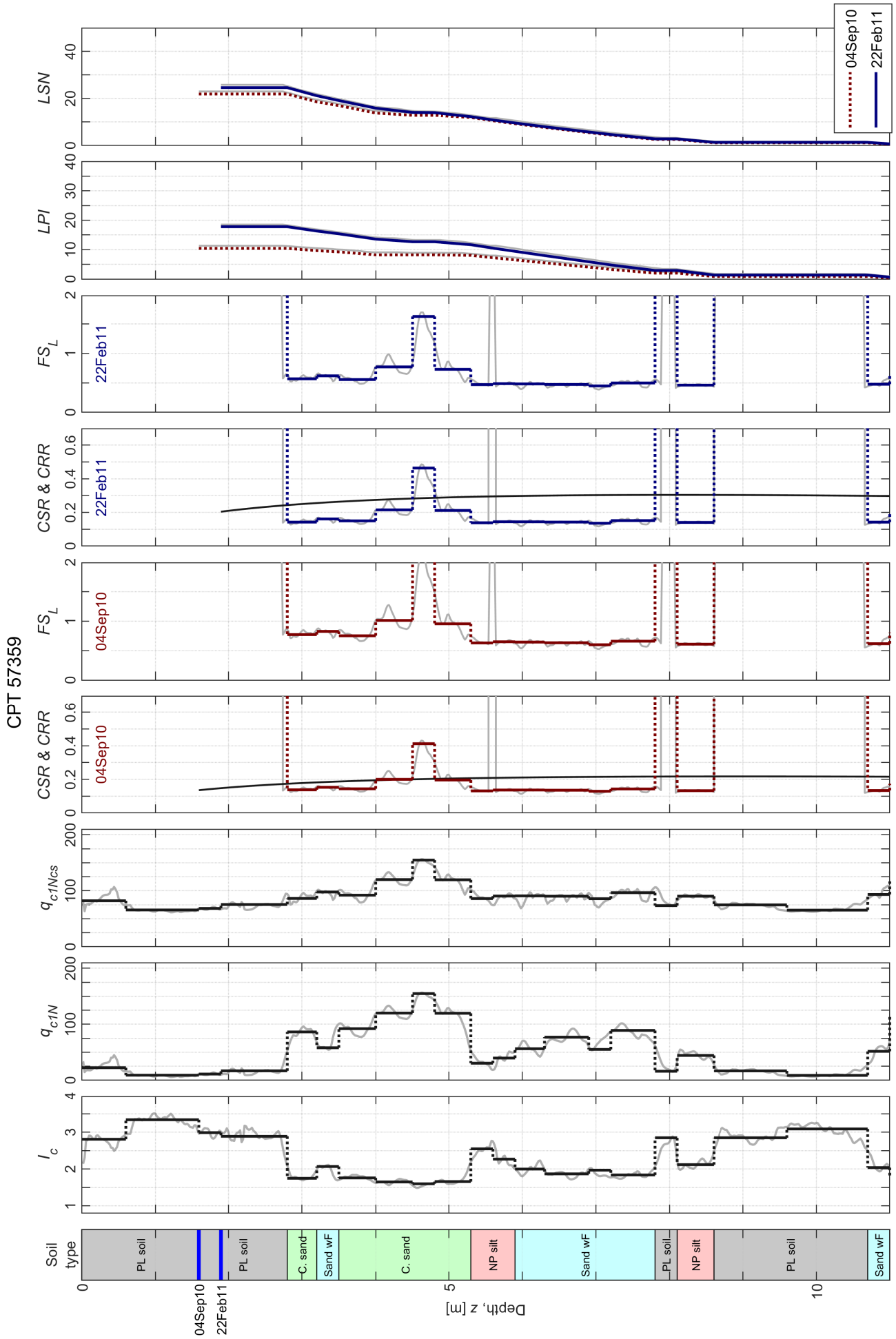
CPT 57359
Soil type
PL soil
C. sand
Sand wF
NP silt
I_c
q_{c1N}
q_{c1Ncs}
CSR & CRR
FS_L
04Sep10
22Feb11
LPI
LSN
Depth, z [m]
0
5
10

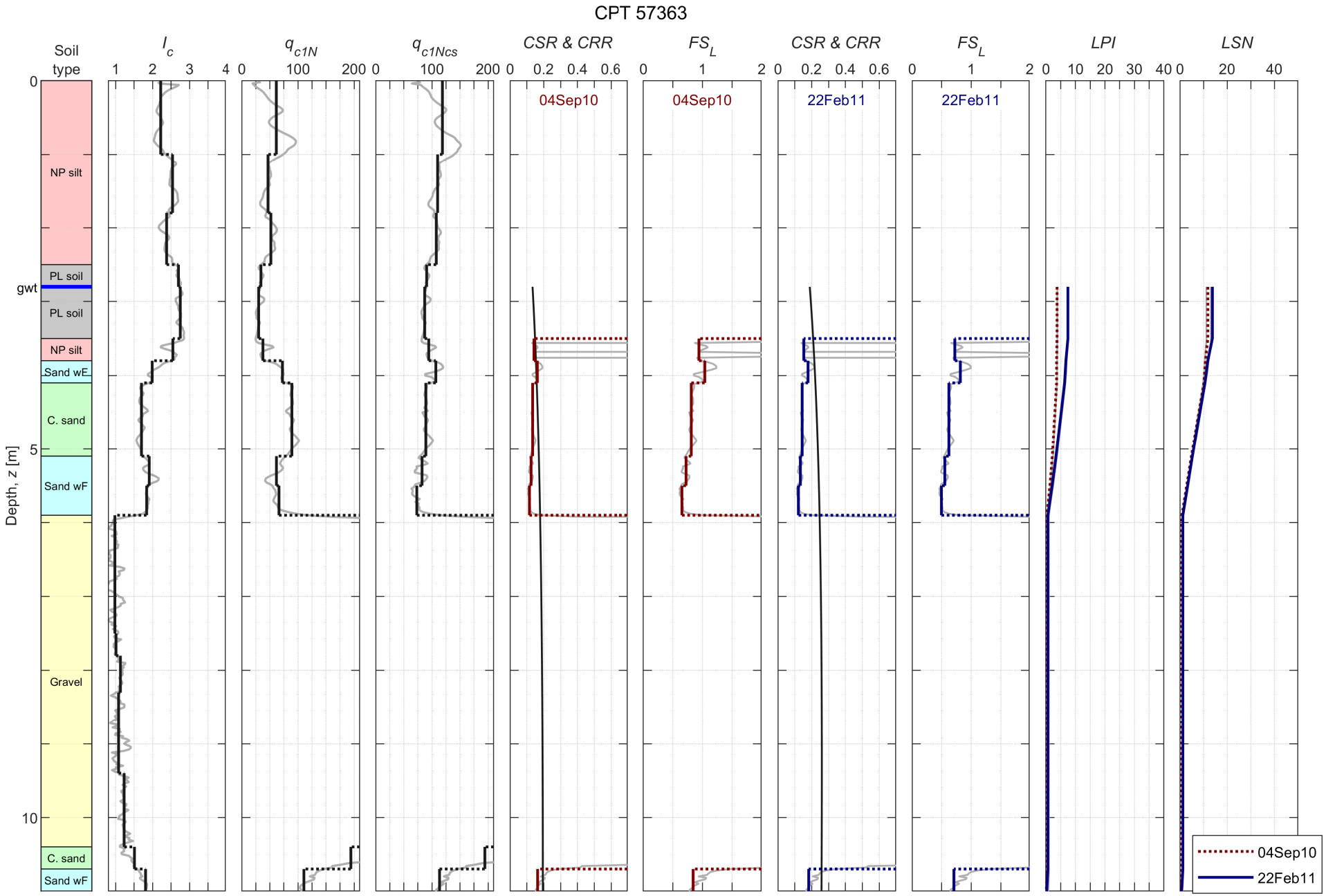
CPT 57363
Soil type
I_c
q_{c1N}
q_{c1Ncs}
CSR & CRR
FS_L
CSR & CRR
FS_L
LPI
LSN
04Sep10
04Sep10
22Feb11
22Feb11
NP silt
PL soil
gwt
PL soil
NP silt
Sand wE
C. sand
Sand wF
Gravel
C. sand
Sand wF
Depth, z [m]
0
5
10
1 2 3 4
0 100 200
0 100 200
0 0.2 0.4 0.6
0 1 2
0 0.2 0.4 0.6
0 1 2
0 10 20 30 40
0 20 40
04Sep10
22Feb11

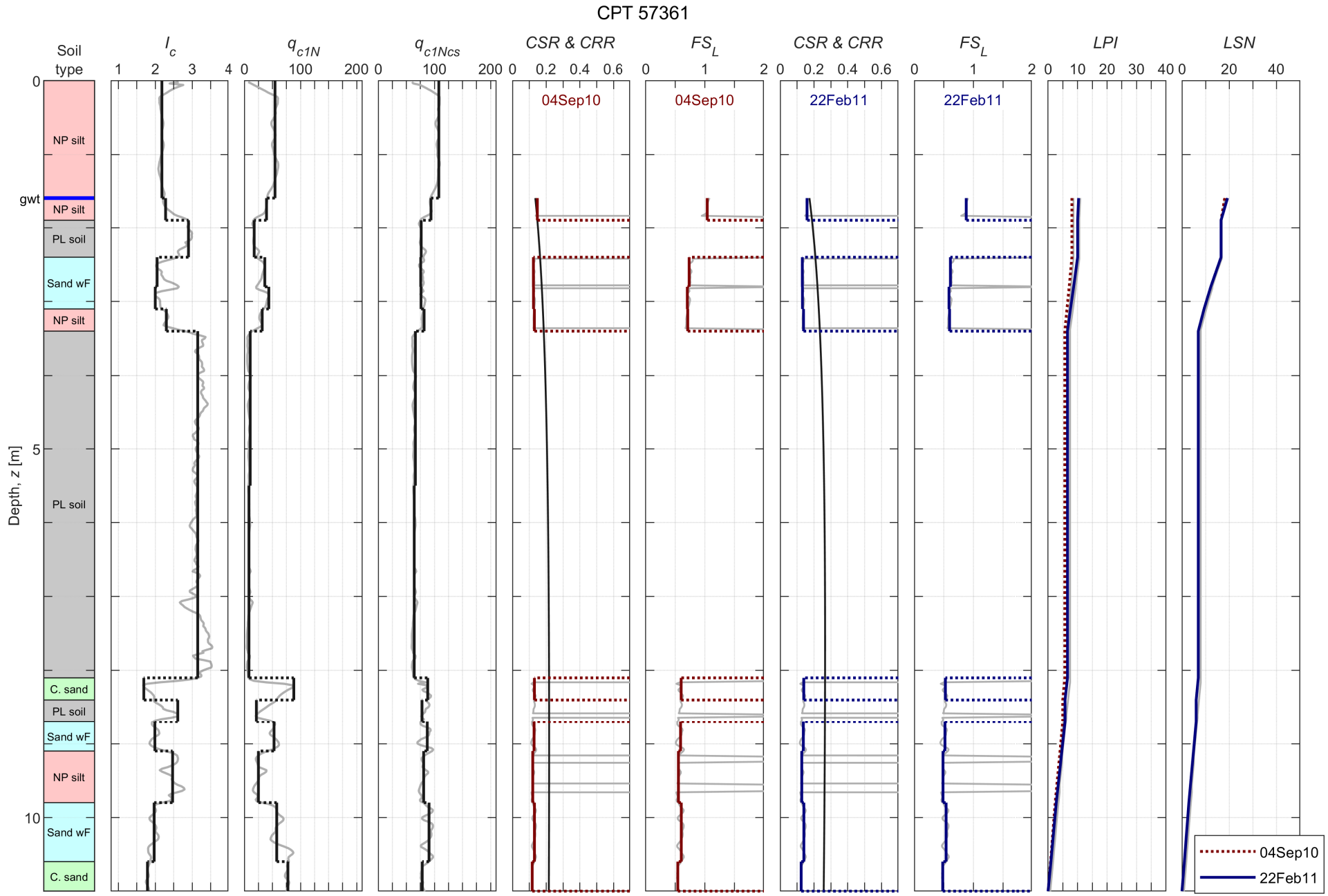
CPT 57361
Soil type
I_c
q_{c1N}
q_{c1Ncs}
CSR & CRR
FS_L
CSR & CRR
FS_L
LPI
LSN
04Sep10
04Sep10
22Feb11
22Feb11
Depth, z [m]
gwt
NP silt
NP silt
PL soil
Sand wF
NP silt
PL soil
C. sand
PL soil
Sand wF
NP silt
Sand wF
C. sand
04Sep10
22Feb11

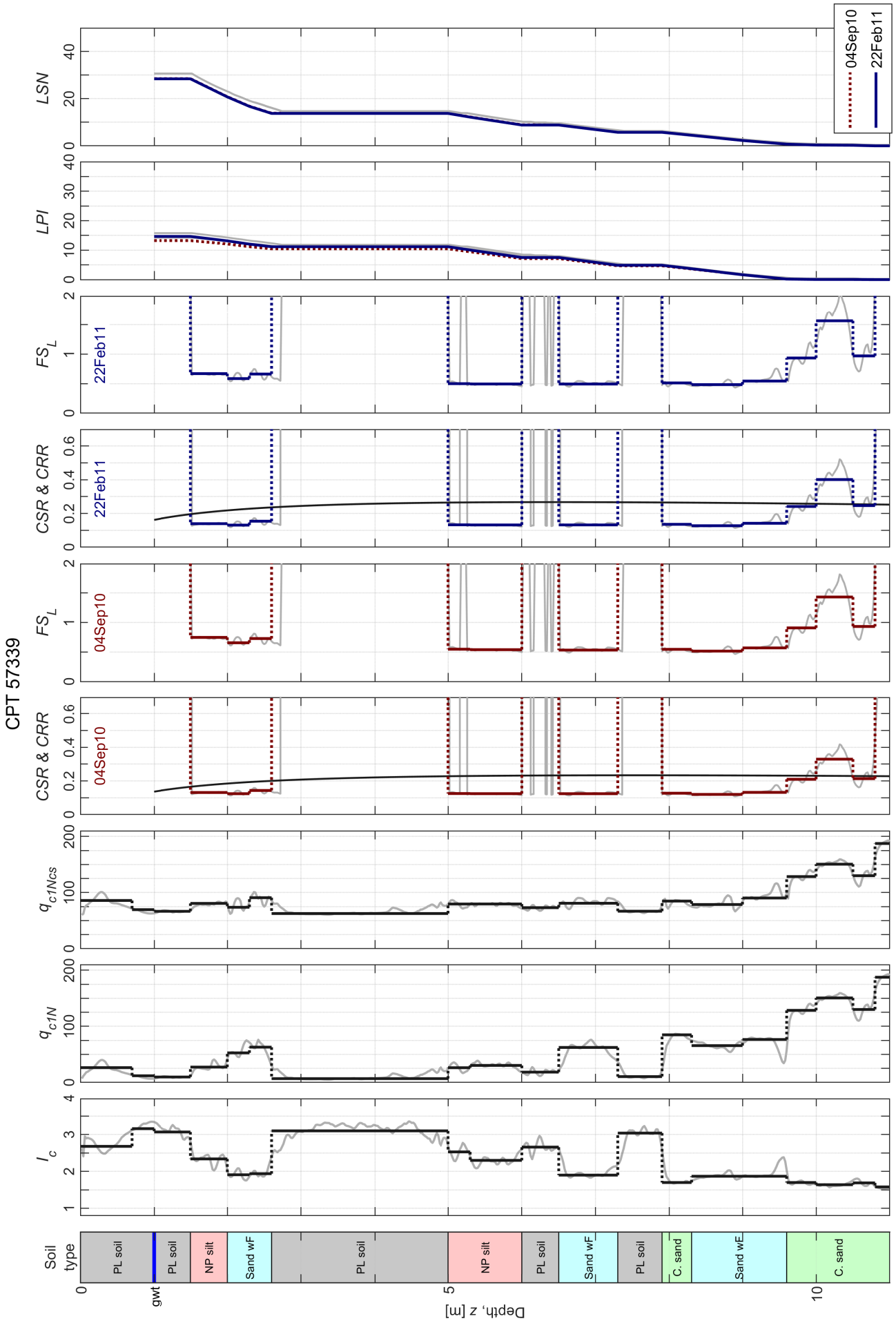
CPT 57339
Soil type
PL soil
PL soil
NP silt
Sand wF
PL soil
NP silt
PL soil
Sand wF
PL soil
C. sand
Sand wF
C. sand
gwt
Depth, z [m]
0
5
10
I_c
q_{c1N}
q_{c1Ncs}
CSR & CRR
04Sep10
FS_L
04Sep10
CSR & CRR
22Feb11
FS_L
22Feb11
LPI
LSN
04Sep10
22Feb11

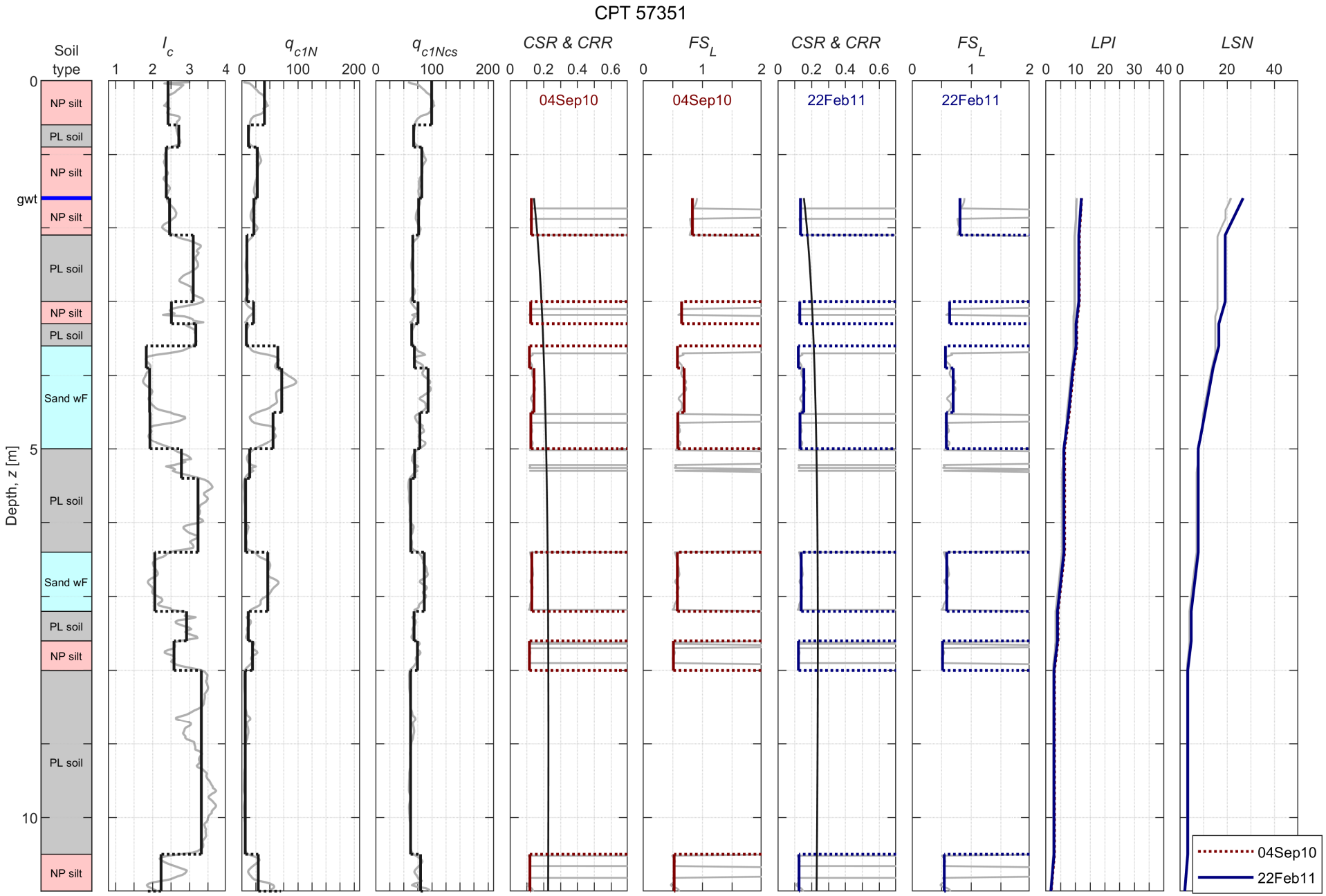
CPT 57351
Soil type
I_c
q_{c1N}
q_{c1Ncs}
CSR & CRR
FS_L
CSR & CRR
FS_L
LPI
LSN
04Sep10
04Sep10
22Feb11
22Feb11
NP silt
PL soil
NP silt
gwt
NP silt
PL soil
NP silt
PL soil
Sand wF
PL soil
Sand wF
PL soil
NP silt
PL soil
NP silt
Depth, z [m]
04Sep10
22Feb11

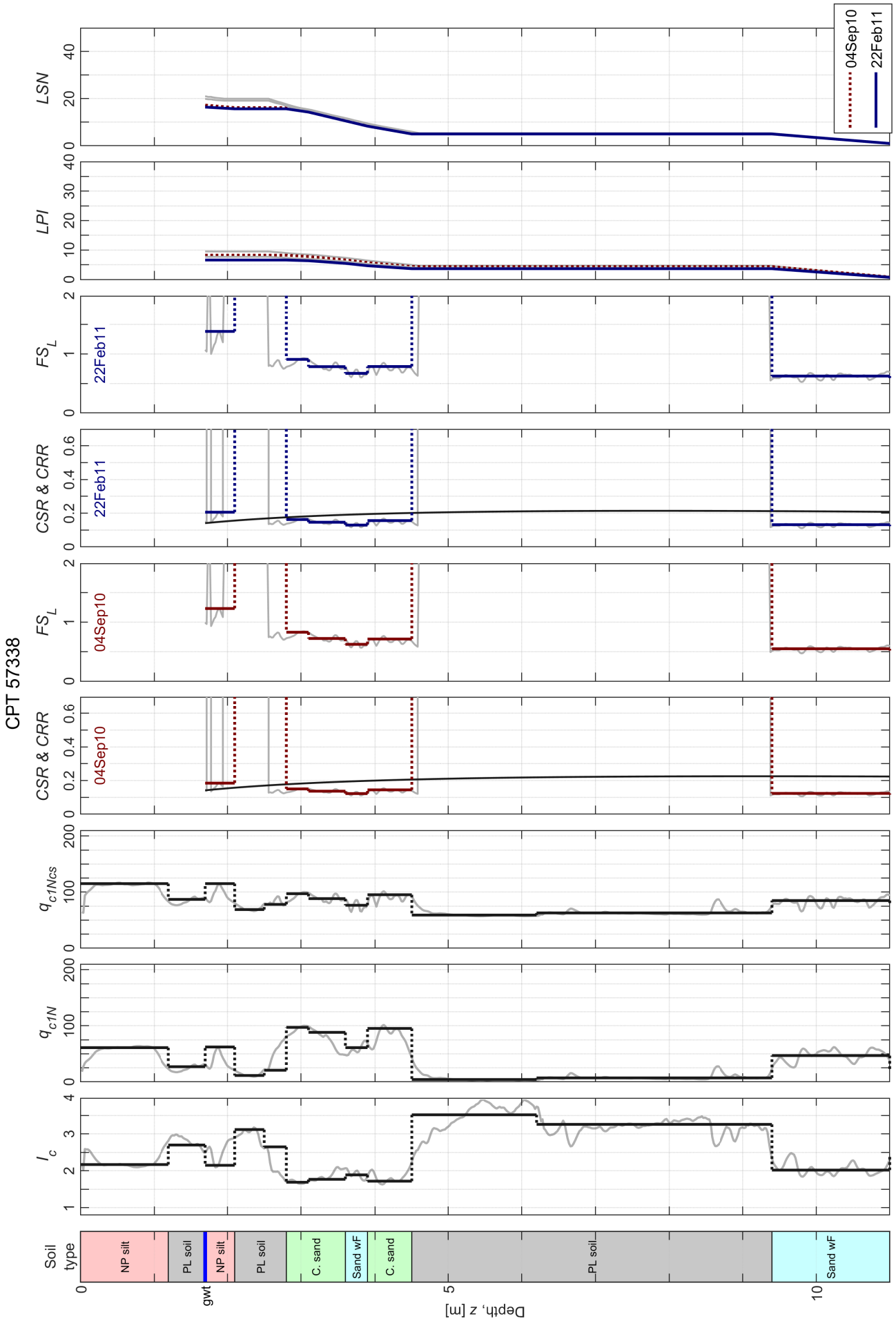
CPT 57338
Depth, z [m]
Soil type
NP silt
PL soil
NP silt
PL soil
C. sand
Sand wF
C. sand
PL soil
Sand wF
gwt
I_c
q_{c1N}
q_{c1Ncs}
CSR & CRR
04Sep10
FS_L
04Sep10
CSR & CRR
22Feb11
FS_L
22Feb11
LPI
LSN
04Sep10
22Feb11

APPENDIX B: Amplitude-Duration Scaling

B.1 Introduction

As discussed in the main body of this thesis, the scaling of reference motions using amplitude scaling factors that significantly deviate from unity can introduce significant bias in the energy content of the obtained input motions (Fig. 5.10) and, consequently, result in biased estimates of the seismic response of nonlinear systems. The reason behind this bias of the amplitude-only scaling approach lies in the fact that, in this method, potentially large changes in the response spectral amplitudes of ground motion can occur without analogous changes in its duration, as observed in actual earthquake ground motions. To overcome this issue, a new scaling method which is intended to provide a consistent scaling of amplitude, duration, and energy content with distance was developed as part of this study. In this method, the scaling is performed in the frequency domain, with amplitude changes applied to the Fourier amplitude spectra, and duration handled by modifications of the Fourier phase spectra. A schematic illustration of key elements in the proposed method is presented in Fig. B.1.

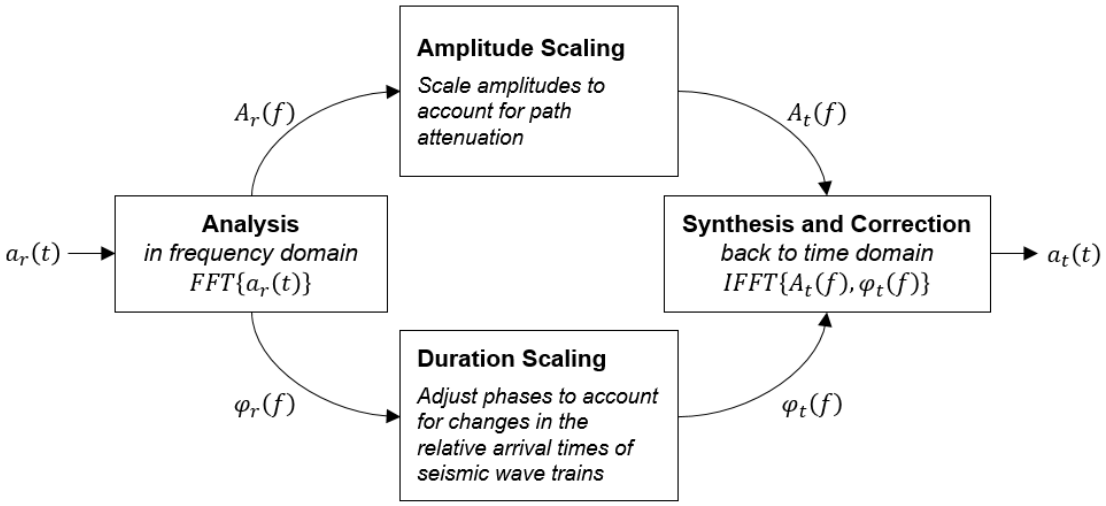

Fig. B.1 Key elements in the amplitude–duration scaling method.

The first step in the method involves the transformation of the time series of the reference ground motion $y_r(t)$ into the frequency domain:

$$Y_r(f) = \int_{-\infty}^{+\infty} y_r(t)\,\exp(\mathrm{i}2\pi f t)\,dt = A_r(f)\cdot\exp[\mathrm{i}\phi_r(f)] \tag{B-1}$$

where $Y_r(f)$ is the complex Fourier Transform of $y_r(t)$, and $A_r(f)$, $\phi_r(f)$ are the amplitude and phase angle of $Y_r(f)$, respectively.

B.2 **Amplitude Scaling**

Scaling of the Fourier amplitudes can be performed on the basis of simple theoretical functions that represent the path contribution to the spectral amplitudes $P(R,f)$ accounting for geometrical spreading and anelastic (including scattering) effects (e.g. Boore 2003a):

$$P(R,f) = G(R)\cdot\exp\left[\frac{-\pi f R}{Q(f)\beta}\right] \tag{B-2}$$

where $Q(f)$ is the regional quality factor, β is the seismic velocity in the vicinity of the source, and $G(R)$ is the geometrical spreading function, which, in the general case, is given by a log-multilinear model as:

$$G(R) = \begin{cases} R^{b_1} & R \le R_1 \\ {R_1}^{b_1}(R/R_1)^{b_2} & R_1 \le R \le R_2 \\ \vdots & \\ {R_1}^{b_1}(R_2/R_1)^{b_2}\cdots(R/R_n)^{b_n} & R_n \le R \end{cases} \tag{B-3}$$

Yenier and Atkinson (2014) fitted the observed near-source ground motion amplitudes from the 22Feb11 earthquake using these simple functions for the path effect with parameters $b_1 = -1.2$, $b_2 = -0.5$, $R_1 = 30$ km, $\beta = 3.5$ km/s, and using an 'effective distance' measure given as $R = \left(R_{rup}^2 + h^2\right)^{0.5}$, where R_{rup} is the closest distance to the fault, and h is a pseudo-depth term, equal to 5.2 km, that accounts for near-source saturation. Their obtained values of quality factors were herein fitted by the model $Q(f) = \max(35, 150f^{0.9})$. With the above data, frequency-dependent amplitude scaling factors $ASF(f)$ can be computed for any given pair of reference and target sites for the 22Feb11 earthquake as:

$$ASF(f) = \frac{P(R_{rup,t},f)}{P(R_{rup,r},f)} = \frac{G(R_{rup,t})}{G(R_{rup,r})}\cdot\exp\left[\frac{-\pi f(R_{rup,t}-R_{rup,r})}{Q(f)\beta}\right] \tag{B-4}$$

where $R_{rup,r}$ and $R_{rup,t}$ are the rupture distances for the reference site and the target site, respectively. Note that, because the total energy of a signal in the time and frequency domains is equivalent, scaling of Fourier amplitudes in the frequency domain is theoretically fully consistent with the scaling of Arias intensity.

It is worth mentioning that as an alternative to the simple model described above, and, particularly, in the absence of event- and region-specific calibration parameters, amplitude scaling factors can be similarly determined from empirical models for the attenuation of Fourier amplitudes (e.g. Bayless and Abrahamson 2019, Bora et al. 2019).

B.2.1 Directionality

An added benefit from the use of the Fourier transform in amplitude-duration scaling is that it also provides a way to account for potential differences in the directionality of ground motion between the reference site and the target site. Near-source ground motions often exhibit strong polarity, while complex fault ruptures can additionally induce considerable variability in the maximum direction orientation from site-to-site (e.g. Bradley and Baker 2015). Also, soil nonlinearity and development of excess pore water pressures in liquefiable soils are known to be largely controlled by the maximum component of motion (e.g. Cubrinovski et al. 1996), therefore, unless a bi-directional ground-response analysis is carried out, the evaluation of the target-site response should ideally consider the maximum shaking intensity direction.

Let $c(f)$ denote the ratio of the Fourier amplitudes of the maximum component at the target site to the amplitudes of its orthogonal component. This can be computed from the recorded motion at the same site, if the target site is an SMS site, or inferred from the nearest recordings. Assuming that directionality is not affected by the site response (i.e. the same bedrock-to-surface transfer function applies in all directions), $c(f)$ may also describe the directionality of the ground motion at the bedrock level. The Fourier amplitudes of the bedrock ground motion at the maximum direction can be computed from Eq. B-5:

$$A_{t,max}(f) = ASF(f) \cdot A_{r,eff}(f) \cdot c(f) \cdot \{2/[c(f)^2 + 1]\}^{0.5} \quad \text{(B-5)}$$

where $ASF(f)$ is given by Eq. A-4, and $A_{r,eff}(f)$ denotes the orientation-independent Fourier amplitudes of the deconvolved motion at the reference site given by $A_{r,eff}(f) = \left\{0.5\left[A_{r,1}(f)^2 + A_{r,2}(f)^2\right]\right\}^{0.5}$, in which $A_{r,1}(f)$ and $A_{r,2}(f)$ are the Fourier amplitudes of two orthogonal horizontal components.

B.3 **Duration Scaling**

Changes in ground motion duration can be accommodated by an appropriate adjustment of the phase spectrum. To identify the means to achieve this, it is first important to elaborate on some of the key properties of the phase content of earthquake ground motions (e.g. Ohsaki 1979, Thrainsson and Kiremidjian 2002, Boore 2003b).

Consider the acceleration time-series shown in Fig. B.2a, which corresponds to the deconvolved motion at CACS from the 04Sep10 earthquake (Bradley 2012). A notable feature of the observed ground motions from the 04Sep10 earthquake is the large amplitude of

long-period motion resulting from a combination of forward directivity effects and basin-generated surface waves, evident in Fig. B.2a from the strong long-period cycles following the peak response. An insightful representation of the phase characteristics of ground motion can be obtained by taking the phase derivatives with respect to frequency (Stoffa et al. 1974, Boore, 2003b):

$$t_{gr} = \frac{d\phi}{d\omega} = [\Re(Y)\Re(Z) + \Im(Y)\Im(Z)]/A^2 \tag{B-6}$$

where ω denotes angular frequency, Z is the Fourier transform of $z(t) = t \cdot y(t)$, and $\Re(X)$ and $\Im(X)$ are the real and imaginary parts of the complex variable X, respectively. $d\phi/d\omega$ has units of time and is often termed 'group delay' (t_{gr}) or 'envelope delay' (t_e) for reasons that will be made clear in the following. Fig. B.2b shows a scatter plot of t_{gr} versus frequency, including a continuous line representing the moving median of the data across frequencies. At high frequencies, the phase derivatives appear to be distributed in time following a normal-like distribution with the median roughly coinciding in time with the occurrence of the peak acceleration in the original ground motion (Fig. B.2a). As frequency decreases, the median t_{gr} shifts toward later times in accordance with the later arrivals of low frequency waves in the original motion, and the dispersion about the median increases. At very low frequencies, both the median and the dispersion about the median decrease.

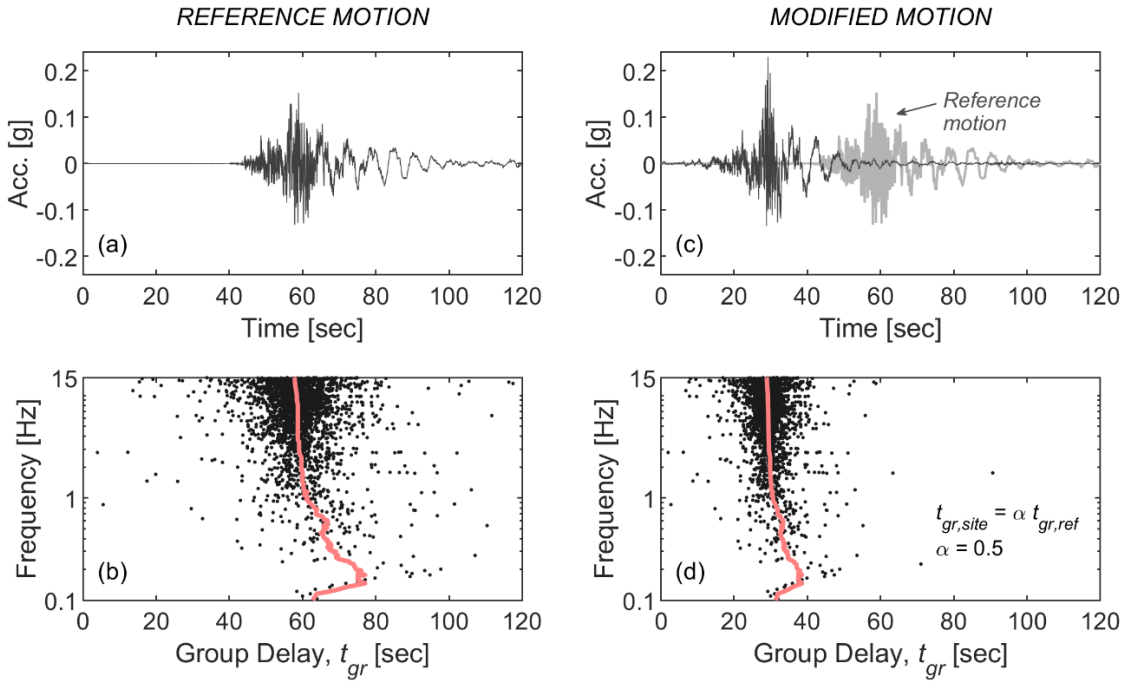

Fig. B.2 (a) Acceleration time-series, and (b) frequency versus group delays for the reference motion; (c) acceleration time-series, and (d) frequency versus group delays for a modified motion obtained by scaling the group delays of the reference motion with a constant factor $a = 0.5$; *the continuous lines in (b) and (d) represent the moving medians of the data across frequencies.*

The above observations allude to a close relationship between the non-stationary characteristics of the original ground motion and the time-frequency distribution of phase derivatives. In fact, it can be easily proven that the phase derivatives correspond to the arrival times of the maximum energy (or peak amplitude) of a narrow-band group of harmonic waves in the vicinity of the evaluated frequency (e.g. Dziewonski and Hales, 1972), hence the term 'group delays' used in seismology literature. The observed time-frequency distribution of t_{gr} can be explained by differences in the propagation velocities between body waves (dominating the high-frequency components of motion) and surface waves (dominant in the low-frequency range), and by the fact that surface waves are dispersive (i.e. their propagation velocity varies with frequency and mode of propagation). The observed dispersion at high frequencies is mainly a result of scattering effects of short-wavelength body waves, whereas the nearly absent dispersion at the very low frequencies is because at these low frequencies only the fundamental mode of surface-wave propagation is possible, hence dispersion is minimized (Novikova and Trifunac 1994).

Changes in ground motion duration can be introduced by modifying the group delays. Fig. B.2d shows the distribution of group delays obtained by multiplication of the group delays of Fig. B.2b with a scalar factor $a = 0.5$. With this operation, the median t_{gr} has been shifted towards earlier arrival times, the difference in the median t_{gr} between high-frequencies and low-frequencies has been reduced, and the dispersion about the median at each frequency has also been reduced. These are changes that would have expected to occur at a site located closer to the causative fault, if the observed t_{gr} distribution was simply a result of the different propagation velocities of different wave groups. A key assumption here is that the phase delay caused by the rupture process is constant or varies only slowly with frequency. A modified ground motion y_m can now be obtained by combining the Fourier amplitude of the reference motion A_r with the phase spectrum ϕ_m obtained from integration of the modified group delays via an inverse Fourier transform:

$$y_m(t) = \int_{-\infty}^{+\infty} A_r(f)\exp[\mathrm{i}\phi_m(f)]\exp(-\mathrm{i}2\pi f t)\, df \tag{B-7}$$

The synthesized ground motion y_m (Fig. B.2b) has higher peak response and shorter strong motion duration compared with the original motion. Note that the original (reference) and the modified ground motions have identical Fourier amplitude spectra and energy content, however, in the modified motion, the total energy is distributed over a shorter time window resulting in higher peak responses. Thus, by modifying the phase derivatives and hence the duration of ground motion, consistent distance-scaling of response spectral amplitudes and energy content can be achieved.

Fig. B.3 compares the interquartile range of t_{gr} computed within several separate frequency bands and for varying a factors applied to the group delays of Fig. B.2b, with an empirical frequency-dependent model for path duration obtained from regression analyses of band-pass filtered ground motions within the same frequency bands (Novikova and Trifunac 1994). The interquartile ranges represent the difference between late and early wave arrival times within

each frequency band, and hence have a direct correlation with the ground motion duration. The similarity between the two plots suggest that the application of a scalar factor a to the group delays of the reference motion can capture well the frequency- and distance- dependent trends in path duration.

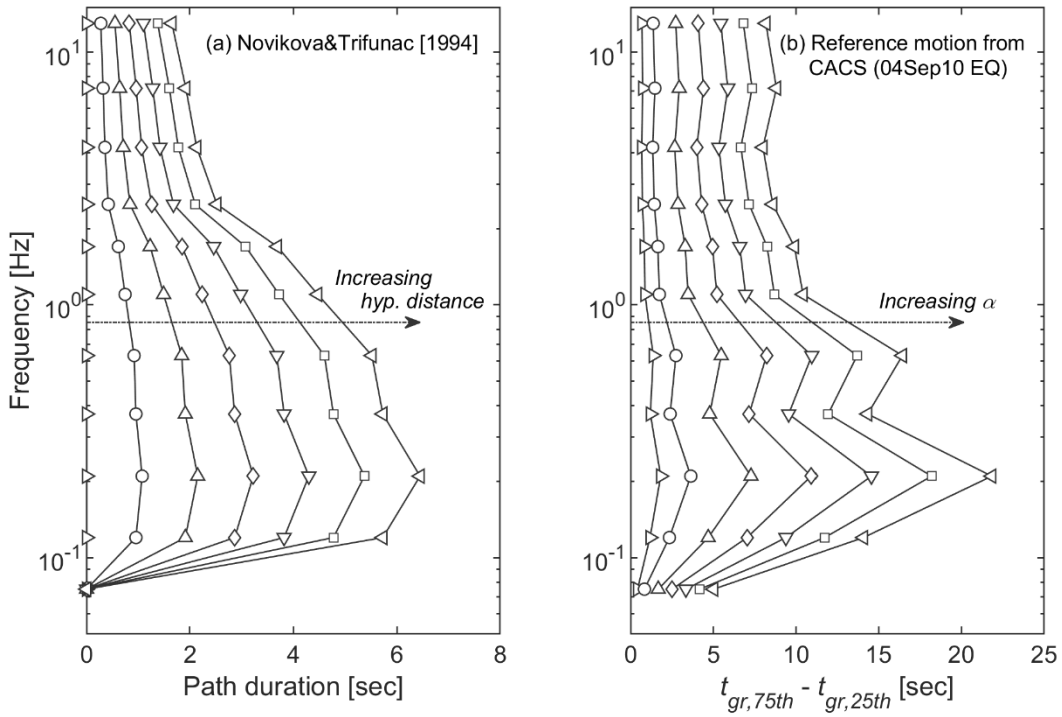

Fig. B.3 Comparison between: (a) the path duration defined at separate narrow frequency bands as a function of hypocentral distance, based on the model by Novikova and Trifunac (1994); and, (b) the interquartile range of group delays computed at the same frequency bands for various a factors applied to the group delays of Fig. B.2b.

Further work is required to establish robust models for the variation of phase derivatives with source-to-site distance, as done with the Fourier amplitudes. Existing empirical models for the phase differences (e.g. Thrainsson and Kiremidjian 2002) and strong motion duration can provide useful insights in that regard. At present, the scaling factor a may be determined such that the synthesized ground motion from the combination of the scaled amplitude and phase spectra complies with a target strong motion duration or response spectral amplitude.

B.4 **Synthesis and Correction**

The synthesized (scaled) motions obtained from the inverse Fourier transform using modified amplitude and phase spectra were often found to contain unphysical vibrations before the expected start of the scaled motion ($\sim at_1$ roughly, where t_1 is the time of the first non-zero acceleration value of the unscaled acceleration time-series) and baseline errors. Such spurious effects are introduced by the changes in the phase spectrum and may be due to errors in the

numerical integration of the phase derivatives or incompatibility between the modified Fourier amplitude and phase spectra. A 'correction' procedure was implemented to remove these effects from the scaled motion by: (1) imposing zero acceleration amplitude before the expected start ($< at_1$) and after the expected end of the scaled motion ($> at_2$, where t_2 is the time of the last non-zero acceleration value of the unscaled acceleration time-series) and applying a half-cosine taper for the transition from the zero pads to the motion; (2) scaling the spectral amplitudes of the modulated motion to the target amplitude spectrum (using a smooth transfer function) to compensate for possible energy losses resulting from the modulation; and (3) applying a low-cut causal Butterworth filter of 0.05 Hz for baseline correction.

Fig. B.4 illustrates acceleration, velocity, and displacement time histories for the unscaled reference CACS motion from the Darfield earthquake, the uncorrected duration-scaled motion using $ASF = 1$ and $a = 0.5$, and the corrected duration-scaled motion obtained from the above correction procedure. Superimposed on the acceleration plots of this figure are Husid plots illustrating the temporal evolution of Arias Intensity for each motion. The time intervals corresponding to the $D_{5-75\%}$ and $D_{5-95\%}$ definitions of significant duration are also marked in the acceleration plots. Note that, in this case where $ASF = 1$, the unscaled motion and the duration-scaled motion have nearly identical Arias Intensity (according to Parseval's theorem, the total energy of a signal in the time domain and frequency domain is equivalent), however, in the duration-scaled motion the total energy is distributed over a shorter time window resulting in higher peak responses.

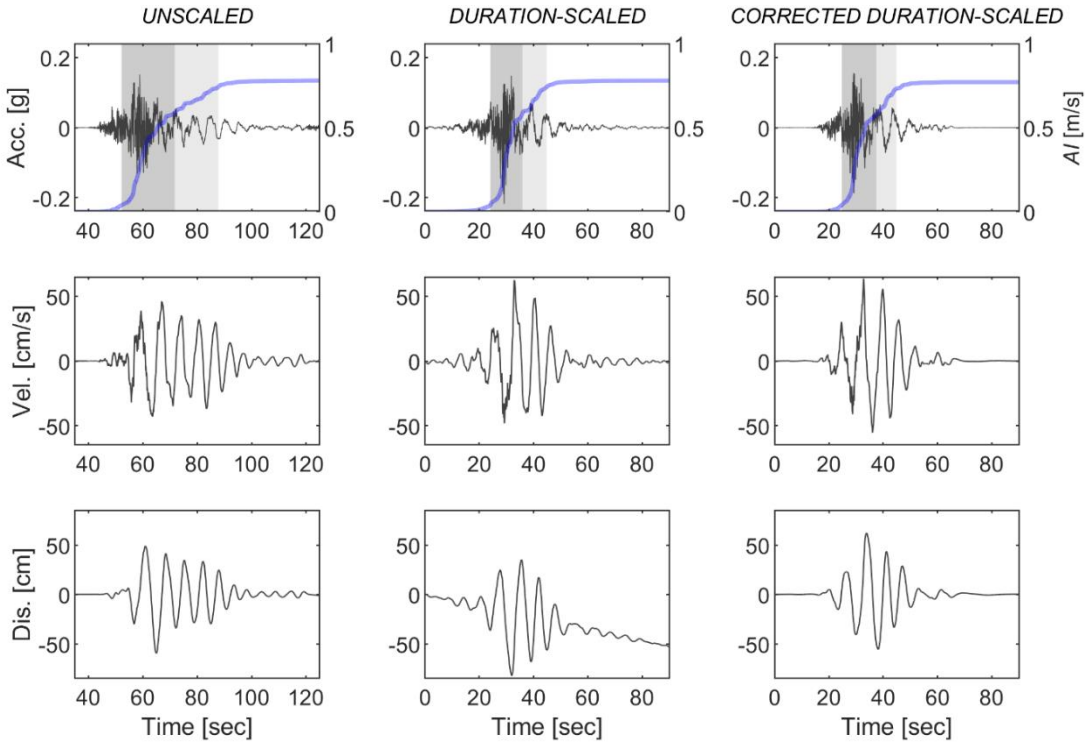

Fig. B.4 Acceleration and Husid plot (top row), velocity (middle row), and displacement (bottom row): unscaled motion (left); uncorrected duration-scaled motion (middle); corrected duration-scaled motion (right); the shadings in the acceleration plots correspond to the time intervals for the $D_{5-75\%}$ (dark shading) and $D_{5-95\%}$ (light shading) definitions of significant duration.

B.5 Example Application (Validation)

This section discusses the application of the proposed amplitude-duration scaling to reference motions from the 22Feb11 earthquake. The specific purpose is to derive appropriate input motions for effective-stress analysis at the CMHS SMS site (Fig. 5.1a), which is a site at very close proximity to the causative fault ($R_{rup} = 1.4$ km). To this end, reference motions from the CACS ($R_{rup} = 12.8$ km) and SMTC ($R_{rup} = 10.8$ km) reference SMS sites were deconvolved by the local site-response and scaled using both the amplitude-only scaling method and the proposed amplitude-duration scaling method. The obtained equivalent-outcrop RG motions were used for 1D effective-stress analysis at the CMHS site in accordance with the procedure described in the main body text. The performances of the two different scaling methods and associated input motions are herein evaluated by comparing the simulated surface motions to the observed ground motion at CMHS, in terms of acceleration and velocity waveforms, 5% damped pseudo-acceleration response spectra, and temporal accumulation of Arias Intensity. In both cases, comparisons of the surface motions are made in the direction of the recorded maximum Arias Intensity at the CMHS site.

In the application of the amplitude-only scaling method, amplitude scaling factors were calculated using the B13 model for the distance-scaling of spectral accelerations yielding values equal to 3.49 for the CACS motion and 2.95 for the SMTC motion. For these large values of the scaling factor, the overprediction of the Arias Intensity can be in the order of 40% and greater, according to Fig. 5.10. Fig. B.5 presents comparisons between the observed and simulated surface ground motions at CMHS using the amplitude-only scaling method with the above scaling factors. There are two key observations that can be made with respect to this figure. First, as expected, the simulations with the amplitude-only approach result in significant overprediction of the cumulative Arias Intensity and strong motion duration with strong acceleration and velocity cycles in the simulated waveforms evident beyond the end of the strong shaking of the observed ground motion. Second, both simulations severely overpredict the spectral amplitudes at long periods ($T > 2$ s). This second effect is likely the result of differences between the reference sites and CMHS in the basin depth and the response of the deeper soils below the RG layer, as can be inferred from Fig. 5.8.

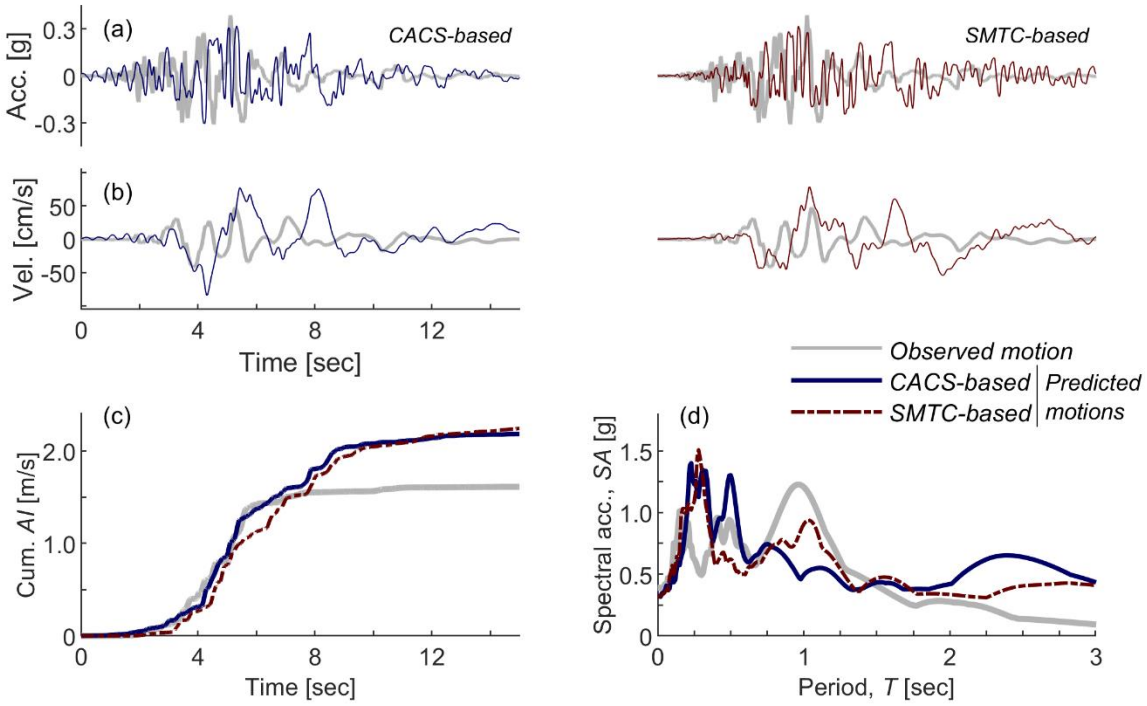

Fig. B.5 Comparisons between observed and simulated surface ground motions at CMHS (22Feb11 earthquake) using *amplitude-only* scaling: (a) acceleration time-series; (b) velocity time-series; (c) temporal evolution of AI; and, (d) pseudo-acceleration response spectra.

In the application of the amplitude-duration scaling method, target Fourier amplitudes for CMHS were determined using Eqs. B-4 and B-5 with the parameters provided in the relevant sections, accounting for both amplitude attenuation and directionality effects. Target Fourier phase angles and group delays were derived from the group delays of the maximum direction reference RG motions using an α factor of 0.48 for CACS and 0.65 for SMTC. These factors were determined such that the relation between the respective significant durations of the target and reference RG motions follows the distance-scaling of duration suggested by Boore and Thompson (2014). Fig. B.6 compares the surface motions obtained using the proposed amplitude-duration scaling method to the observed surface motion at CMHS. In both simulations, there is a clear improvement of the predictions manifested in nearly all examined aspects of ground motion, including the acceleration waveforms, response spectra, temporal accumulation of AI, and strong motion durations. Yet, the long-period motion and peak ground velocities are still significantly overpredicted, as basin amplification effects are still present in the amplitude-duration scaled motions.

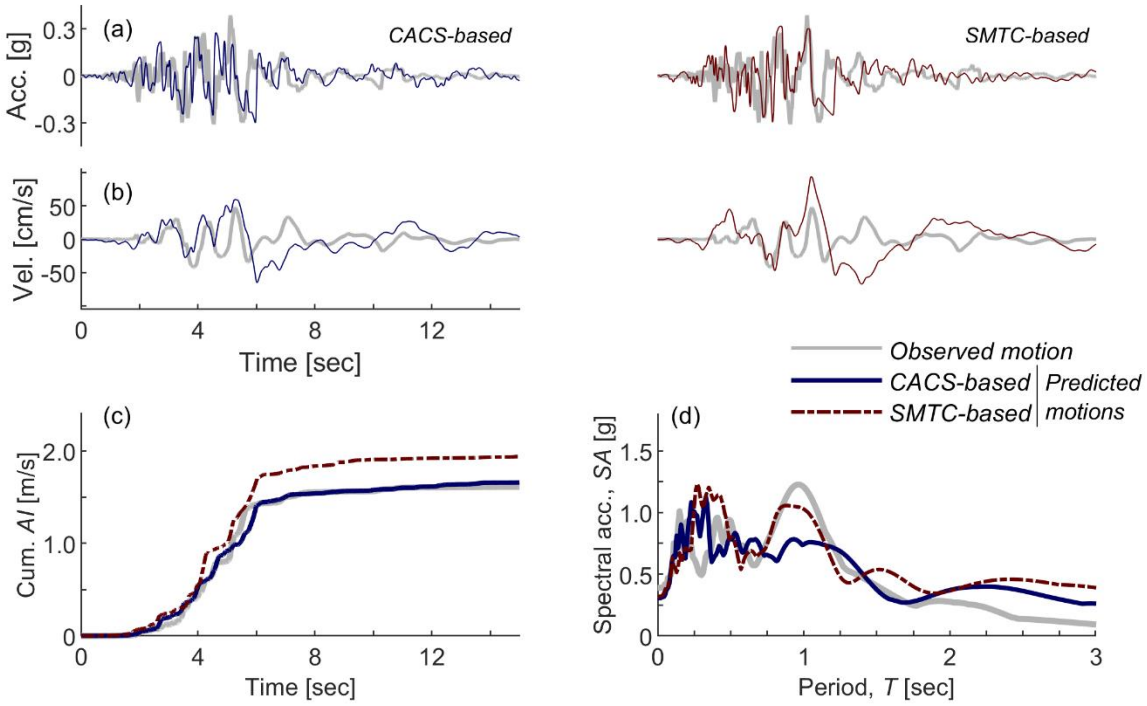

Fig. B.6 Comparisons between observed and simulated surface ground motions at CMHS (22Feb11 earthquake) using *amplitude–duration* scaling: (a) acceleration time-series; (b) velocity time-series; (c) temporal evolution of *AI*; and, (d) pseudo-acceleration response spectra.

By allowing for concurrent scaling of both amplitude and duration of ground motion, amplitude-duration scaling can achieve physically consistent scaling of response spectral amplitudes, duration, and energy content with distance. Thus, the method offers significant advantages over the conventional amplitude-only scaling especially in cases of relatively large difference in the source-to-site distance between the reference site and the target site. Yet, because this scaling method may considerably distort the original motion, it should be applied with great care and the reasonableness of any amplitude-duration scaled motion should be evaluated carefully.

APPENDIX C: Supplementary Results from the Analyses of the SMS Sites

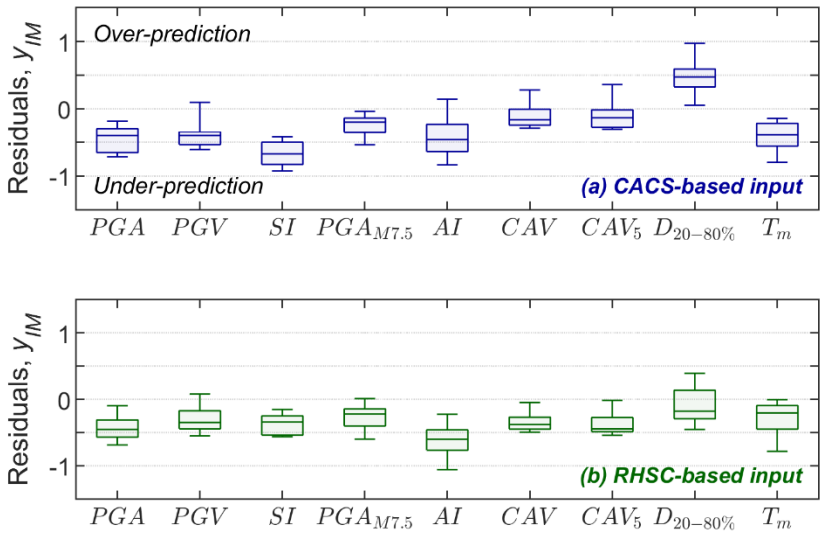

Fig. C.1 Box-and-whisker plots illustrating the distribution of the considered *IM* residuals for the 04Sep10 earthquake simulations using the B13 model for the relative distance-scaling of the reference motions: (a) CACS-based simulations; and (b) RHSC-based simulations.

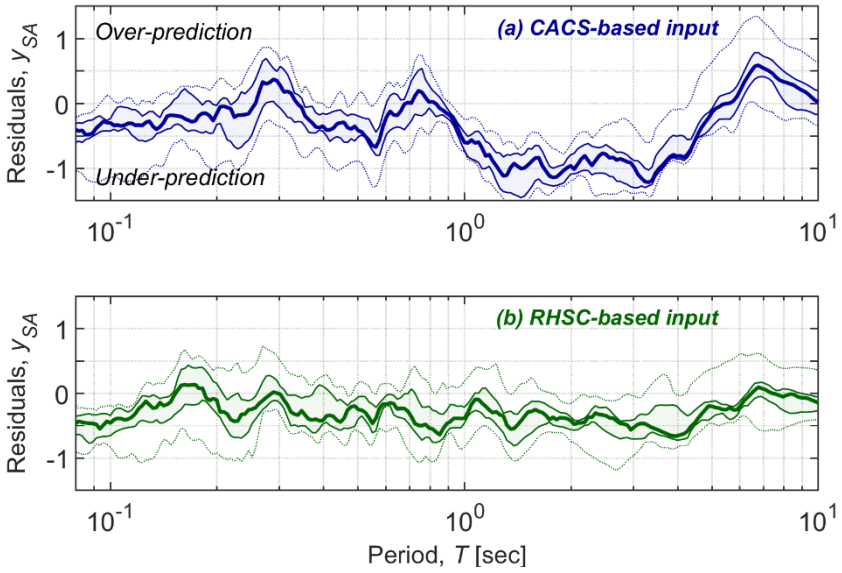

Fig. C.2 Box-and-whisker plots illustrating the distribution of the considered *IM* residuals for the 04Sep10 earthquake simulations using the B13 model for the relative distance-scaling of the reference motions: (a) CACS-based simulations; and (b) RHSC-based simulations.

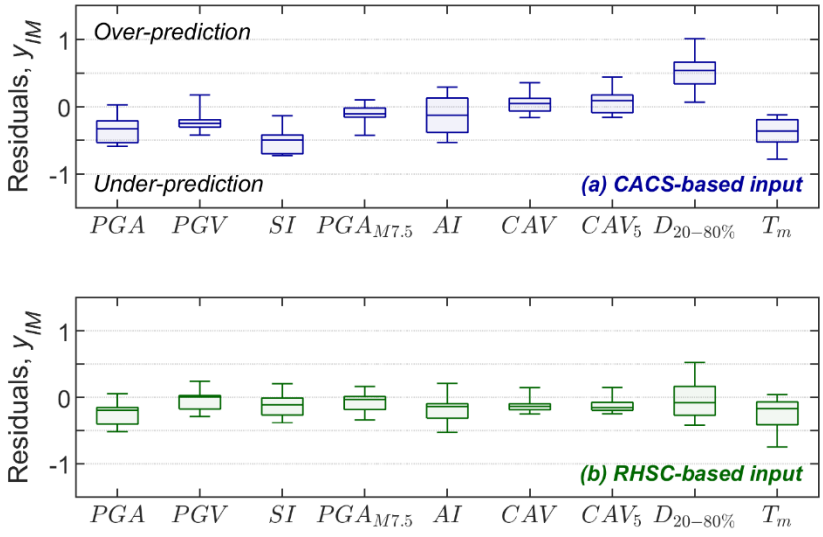

Fig. C.3 Box-and-whisker plots illustrating the distribution of the considered *IM* residuals for the 04Sep10 earthquake simulations using the default YA14 ($h = 20.6$ km) model for the relative distance-scaling of the reference motions: (a) CACS-based simulations; and (b) RHSC-based simulations.

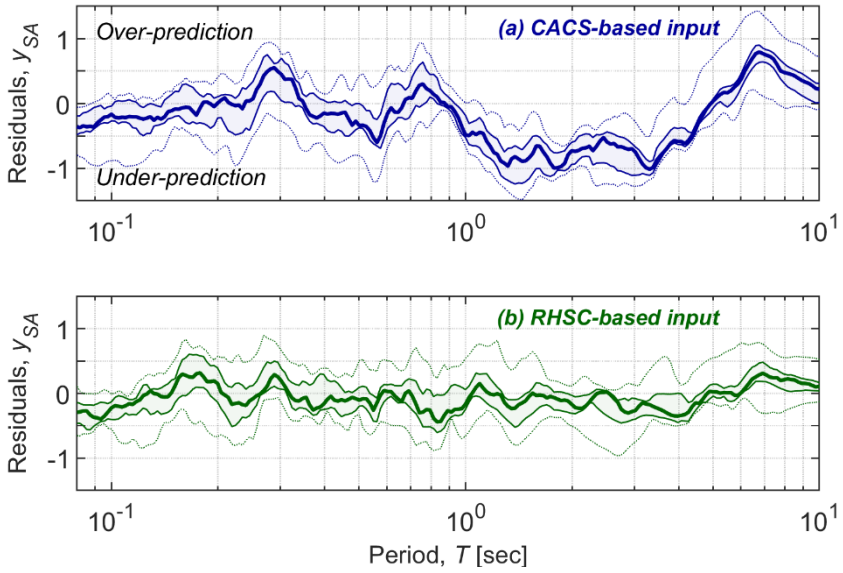

Fig. C.4 Distribution of the spectral acceleration residuals for the 04Sep10 earthquake simulations as a function of vibration period using the default YA14 ($h = 20.6$ km) model for the relative distance-scaling of the reference motions: (a) CACS-based simulations; and (b) RHSC-based simulations; *thick lines represent the median of the distribution, shaded regions indicate the interquartile range, and dotted lines show the total (minimum to maximum of all residuals) range.*

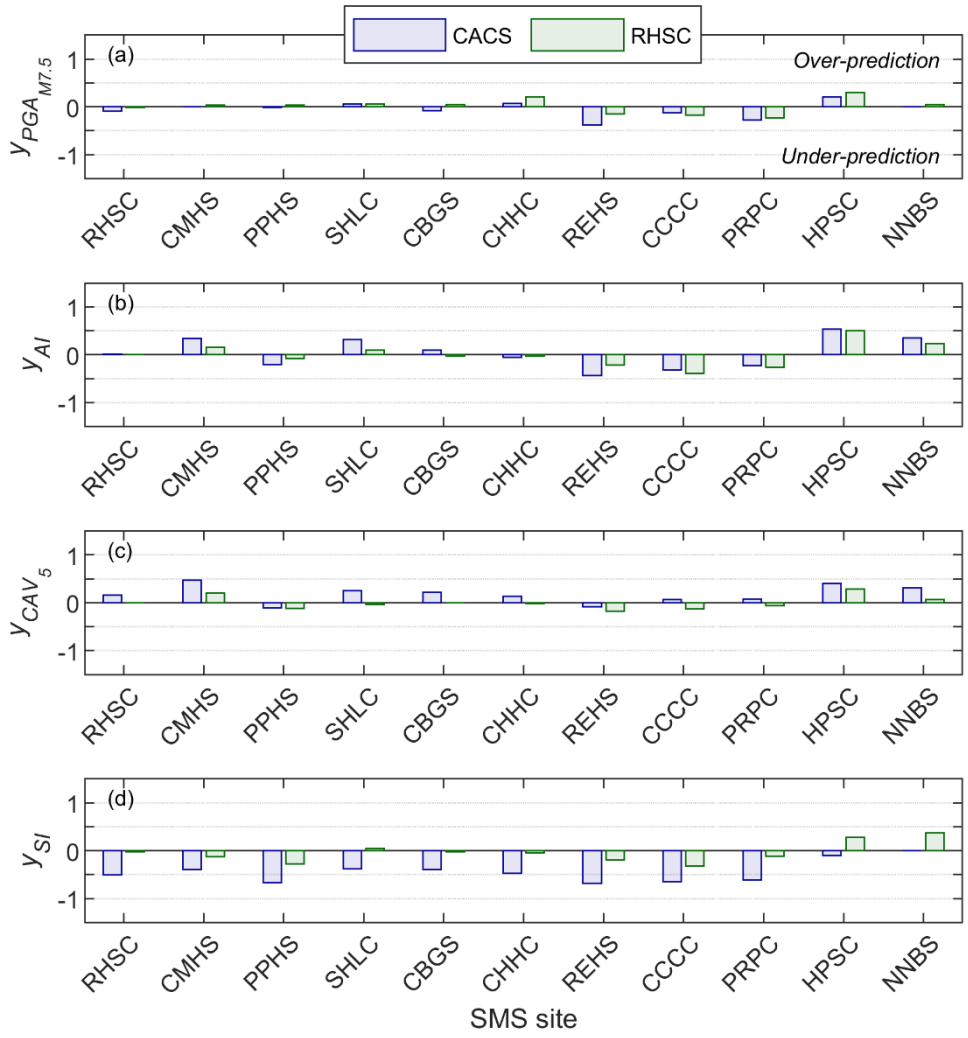

Fig. C.5 Prediction residuals from the 04Sep10 earthquake simulations, using the YA14 ($h = 33.3$ km) distance-scaling model, on a site-by-site basis for: (a) $PGA_{M7.5}$; (b) AI; (c) CAV_5; and (d) SI.

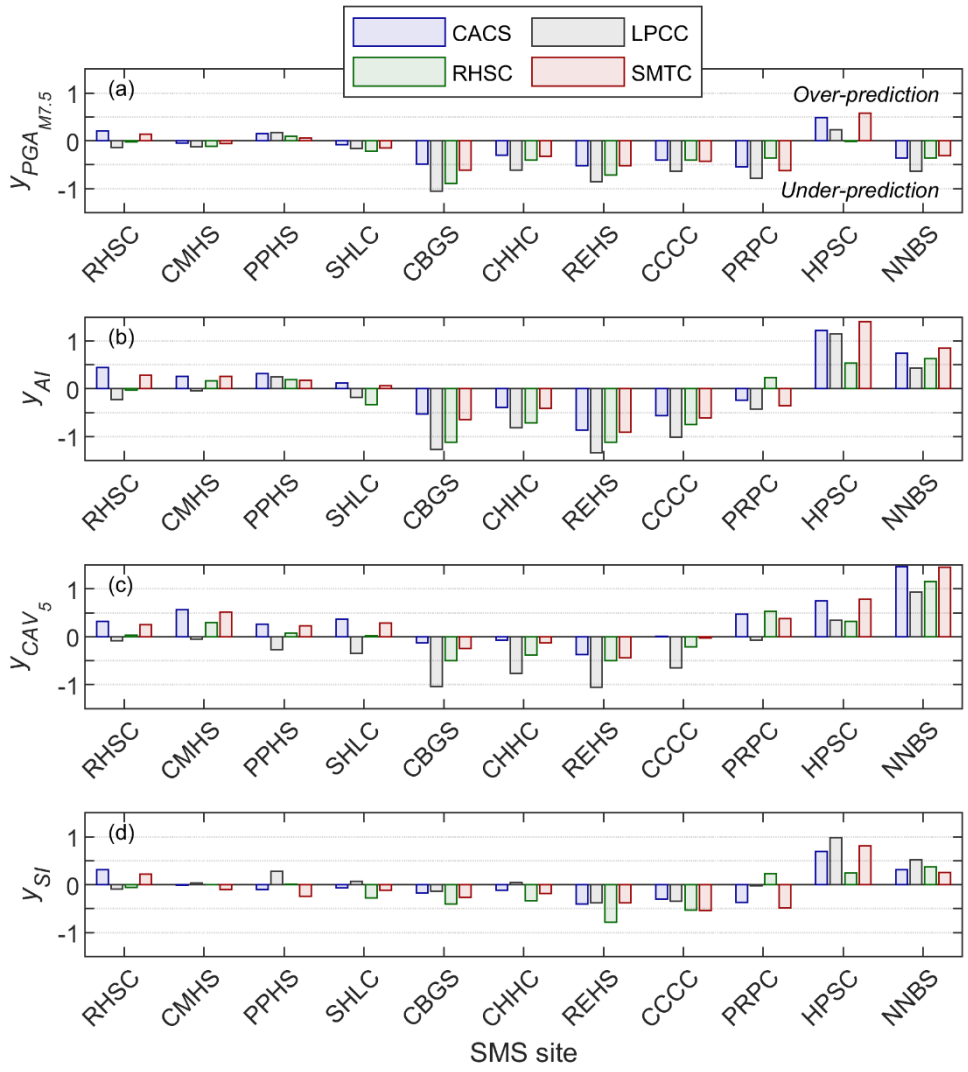

Fig. C.6 Prediction residuals from all the 22Feb11 earthquake simulations on a site-by-site basis for: (a) $PGA_{M7.5}$; (b) AI; (c) CAV_5; and (d) SI.

APPENDIX D: Results from Effective Stress Analysis of 55 Sites for the 22Feb11 Earthquake

Table D.1 Response-based classification of 55 sites for the 22Feb11 earthquake, as per Section 7.5.

NZGD ID[i]	Suburb	Liquefaction manifestation			Response-based classification
		04Sep10	22Feb11	Classification	
21508	Avonside	Severe	Severe	YY	SC
44439	Avondale	Severe	Severe	YY	SC
21509	Avondale	Moderate	Severe	YY	SC
34460	Avondale	Severe	Severe	YY	DC
57354	Avondale	None	Severe	NY	(SC)
38758	Avondale	None	Moderate	NY	(SC)
57342	Avondale	None	Severe	NY	(SC)
29035	Avondale	Severe	Severe	YY	SC
36414	Avondale	Moderate	Severe	YY	SC
34454	Avondale	Moderate	Severe	YY	DC
45	Avondale	Minor	Severe	YY	SC
21506	Bexley	Minor	Severe	YY	SC
158	Bexley	Minor	Minor	YY	(SC)
175	Bexley	Severe	Severe	YY	SC
57349	Aranui	Moderate	Moderate	YY	(SC)
57347	Aranui	None	Minor	NY	NT
57348	Aranui	None	Moderate	NY	(SC)
38797	Aranui	Minor	Severe	YY	SC
57343	North New Brighton	None	None	NN	NT
38742	North New Brighton	None	Moderate	NY	(SC)
34431	North New Brighton	None	Severe	NY	SC
57350	North New Brighton	None	None	NN	(DC)
38752	Parklands	None	Moderate	NY	NT
57366	Shirley	None	Severe	NY	DC
57346	Shirley	None	Minor	NY	NT
57362	Shirley	None	Minor	NY	SI

[i] CPT identification code in New Zealand Geotechnical Database (NZGD 2020).

Table D.1 Response-based classification of 55 sites for the 22Feb11 earthquake, as per Section 7.5 (Continued)

NZGD ID	Suburb	Liquefaction manifestation			Response-based classification
		04Sep10	22Feb11	Classification	
57341	Woolston	None	Severe	NY	(SC)
57360	Woolston	None	Moderate	NY	(SC)
57365	Hillsborough	None	None	NN	SI
57357	Waltham	None	Severe	NY	DC
57356	Waltham	None	Severe	NY	DC
57355	Sydenham	None	Minor	NY	DI
57353	St Martins	None	Severe	NY	(SC)
638	Somerfield	None	Minor	NY	SI
37818	Spreydon	None	Minor	NY	SI
57344	Hoon Hay	Minor	Severe	YY	SC
57340	Hoon Hay	None	Minor	NY	SI
36417	Hoon Hay	None	None	NN	DI
36421	Hoon Hay	None	None	NN	DI
57364	Hoon Hay	None	Moderate	NY	DI
57352	Halswell	None	None	NN	SI
36419	Halswell	None	None	NN	SI
57319	Riccarton	None	None	NN	DI
57337	Riccarton	None	None	NN	DI
36418	Riccarton	None	None	NN	DI
57345	Riccarton	None	None	NN	SI
36420	Riccarton	None	None	NN	SI
5567	Fendalton	None	None	NN	DI
57358	St Albans	None	Minor	NY	SI
57359	Papanui	Moderate	Severe	YY	DC
57363	Merivale	None	Moderate	NY	(SC)
57361	Papanui	None	None	NN	SI
57339	Papanui	None	None	NN	DI
57351	Papanui	None	None	NN	DI
57338	Papanui	None	None	NN	SI

CPT 21508

LPCC-based input

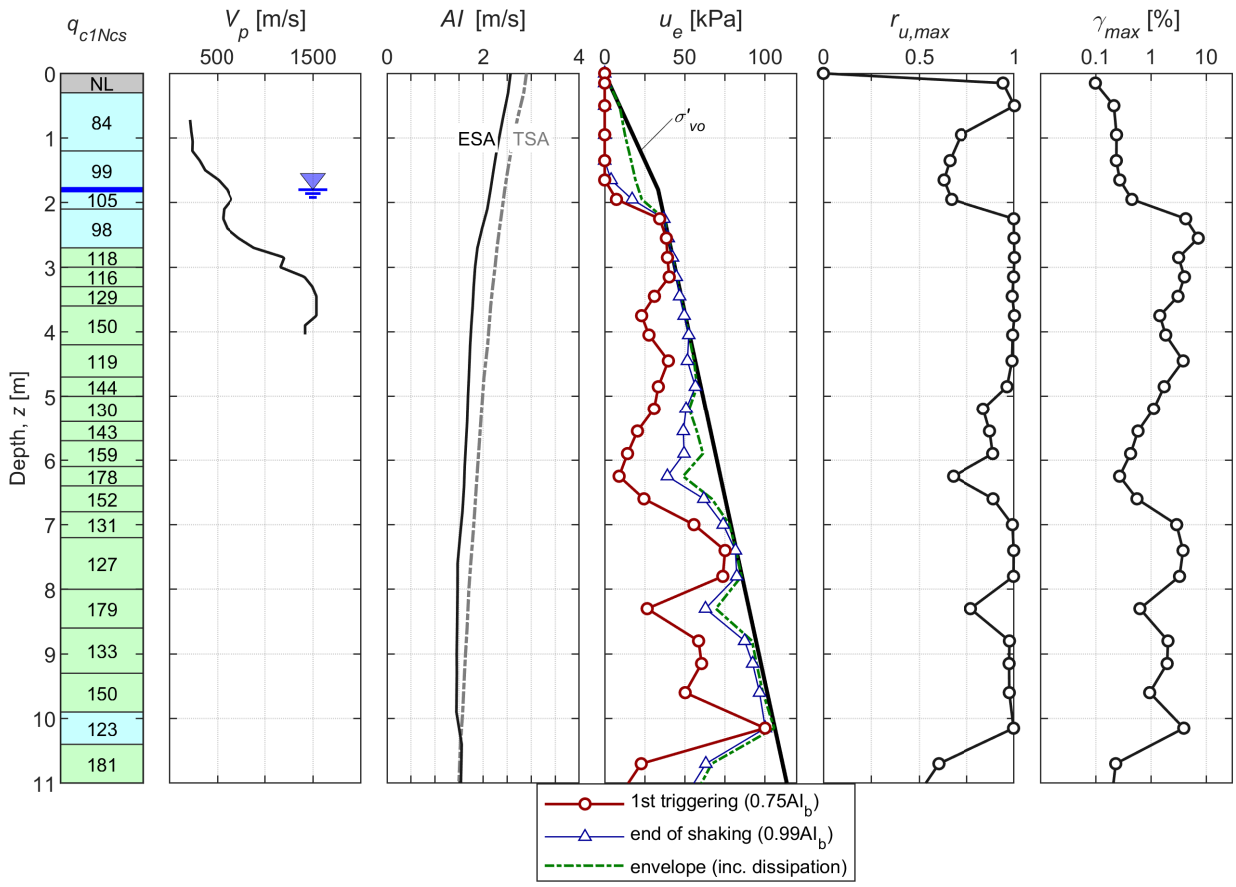

RHSC-based input

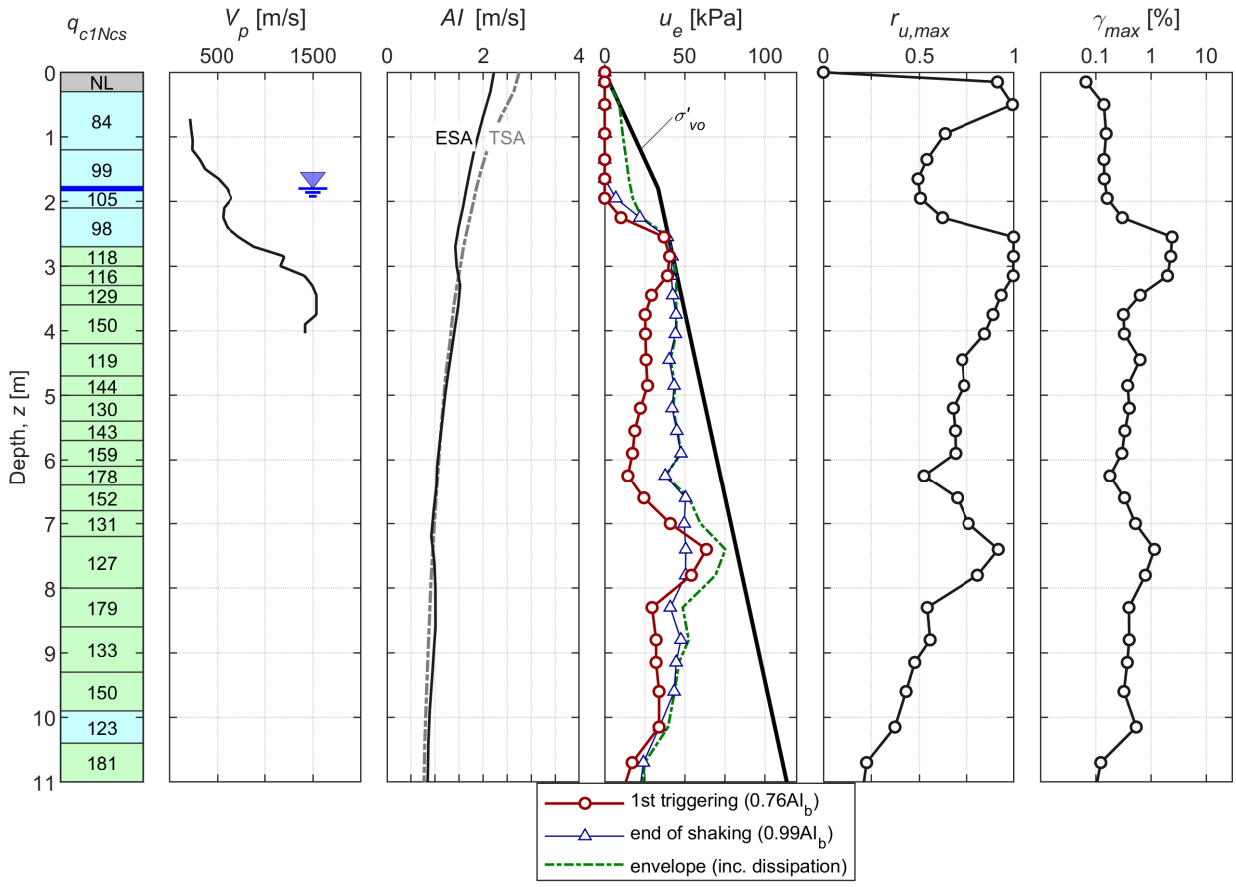

CPT 44439

LPCC-based input

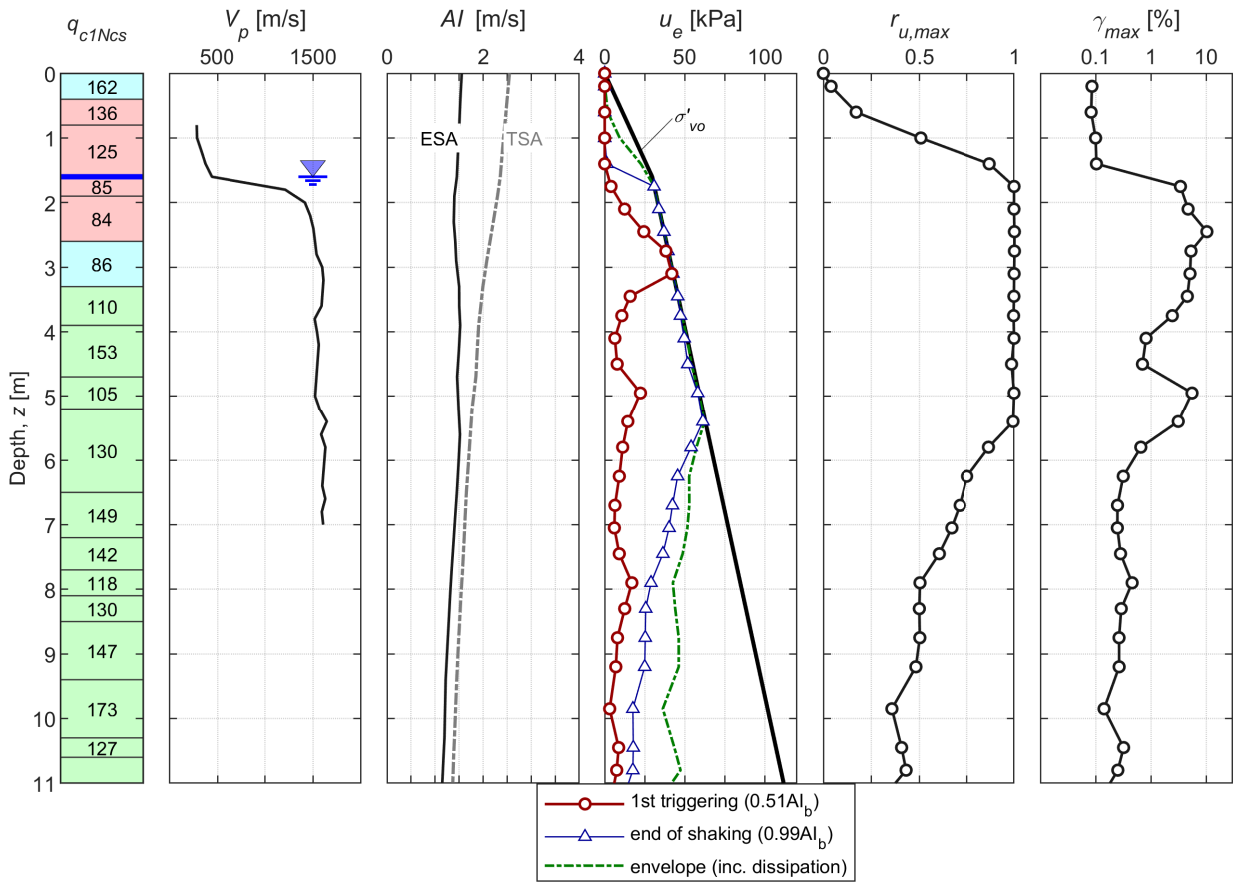

RHSC-based input

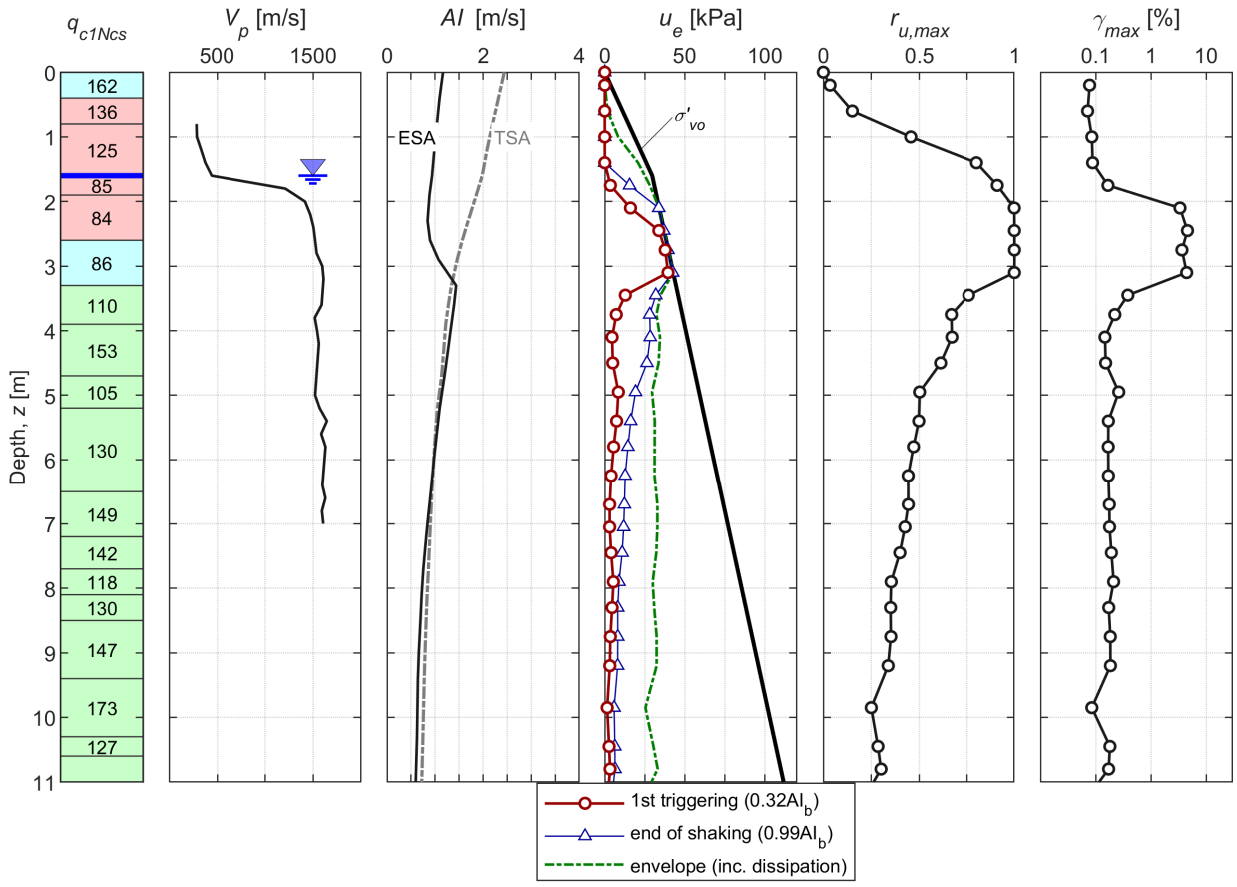

CPT 21509

LPCC-based input

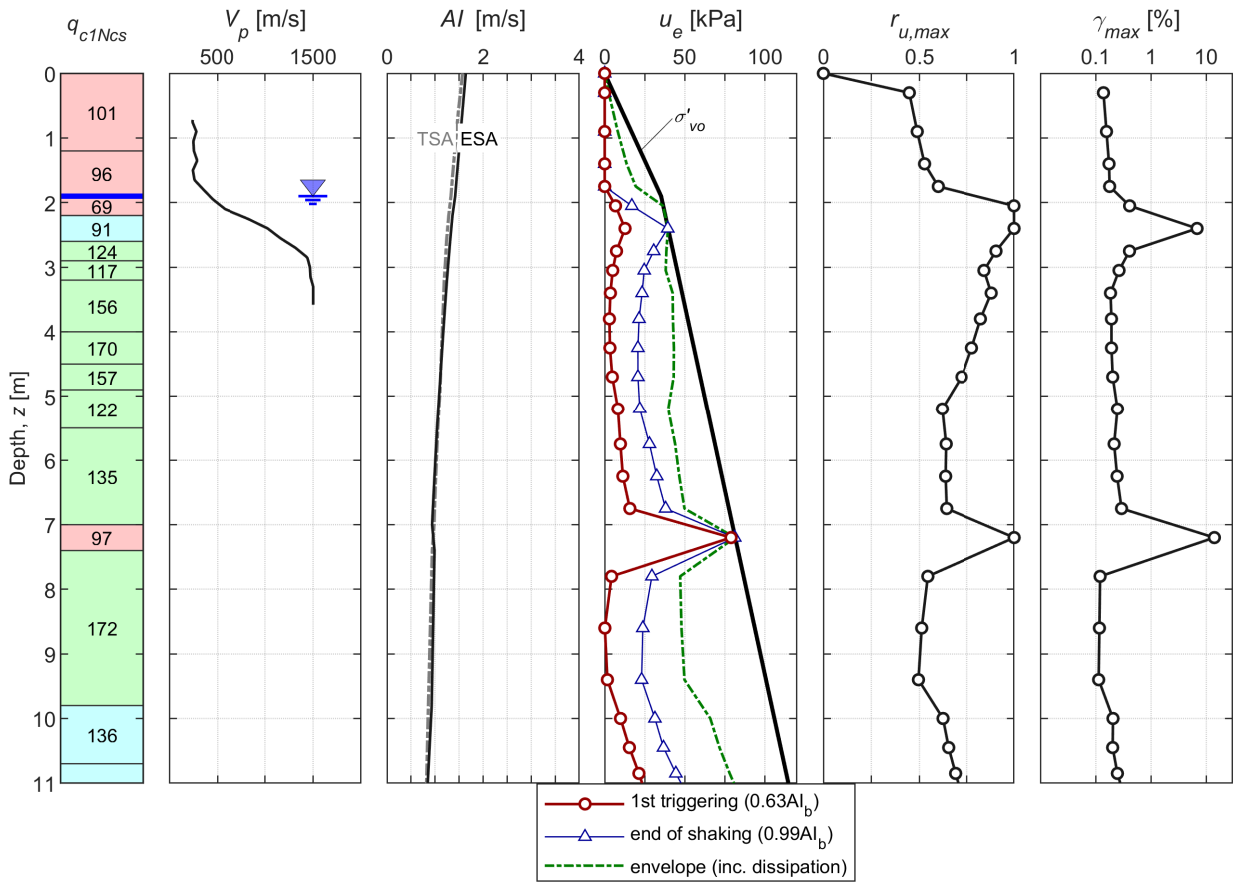

RHSC-based input

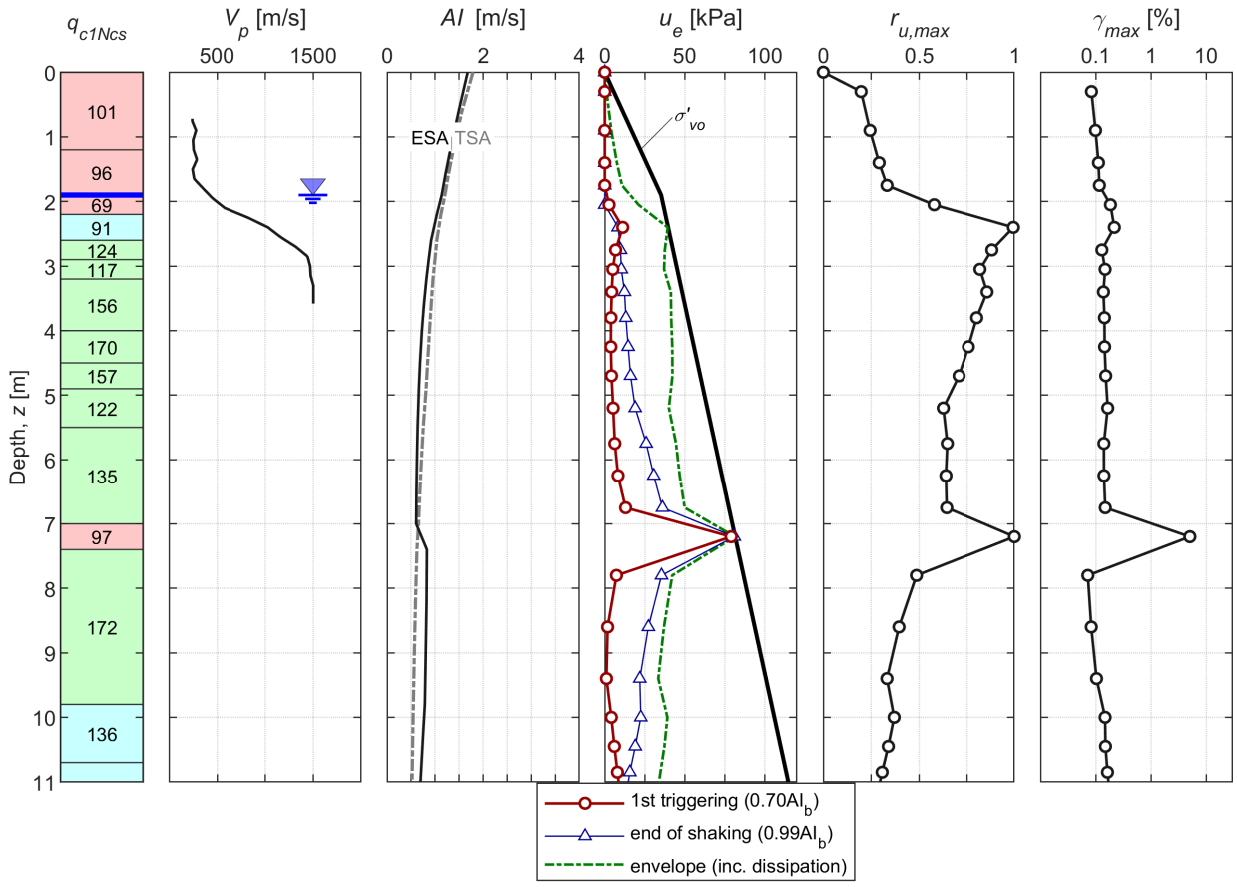

CPT 34460

LPCC-based input

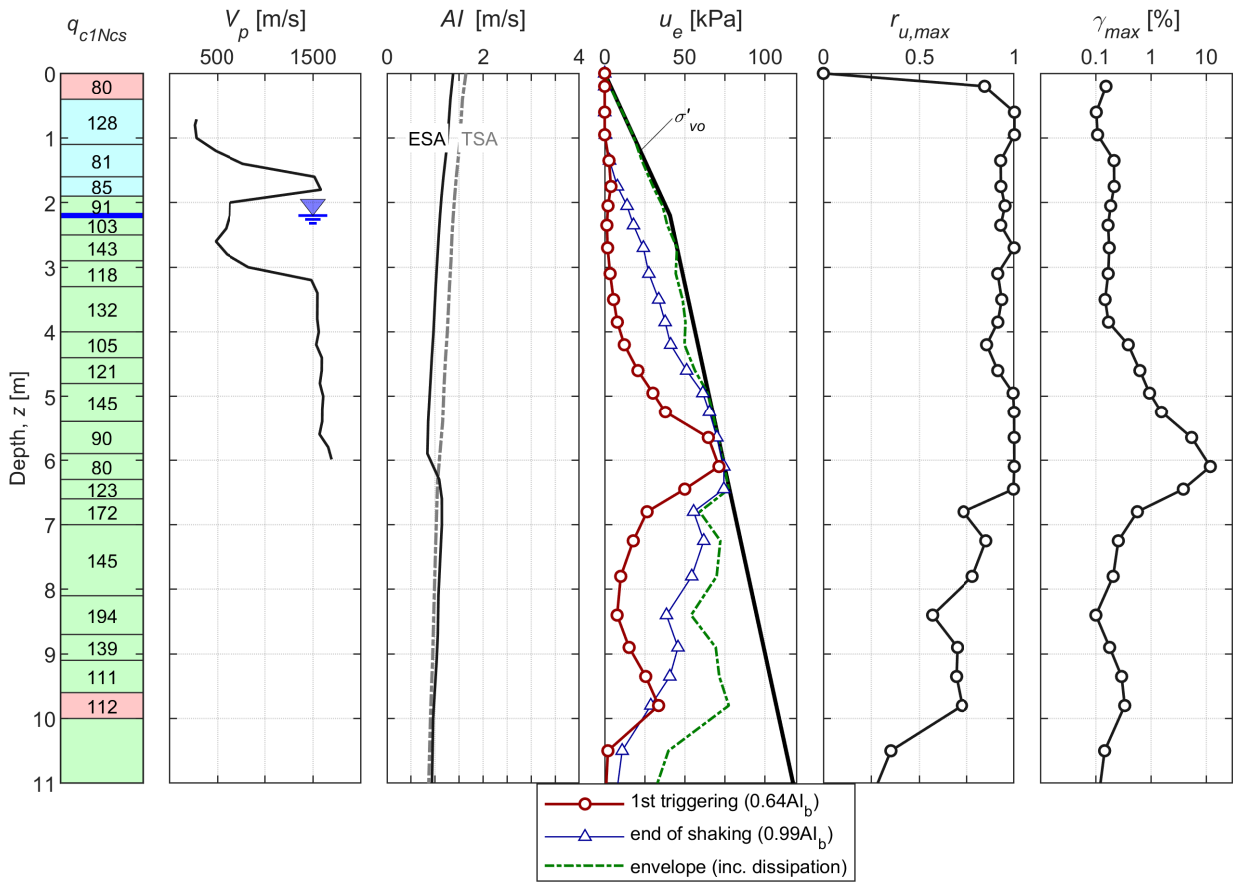

RHSC-based input

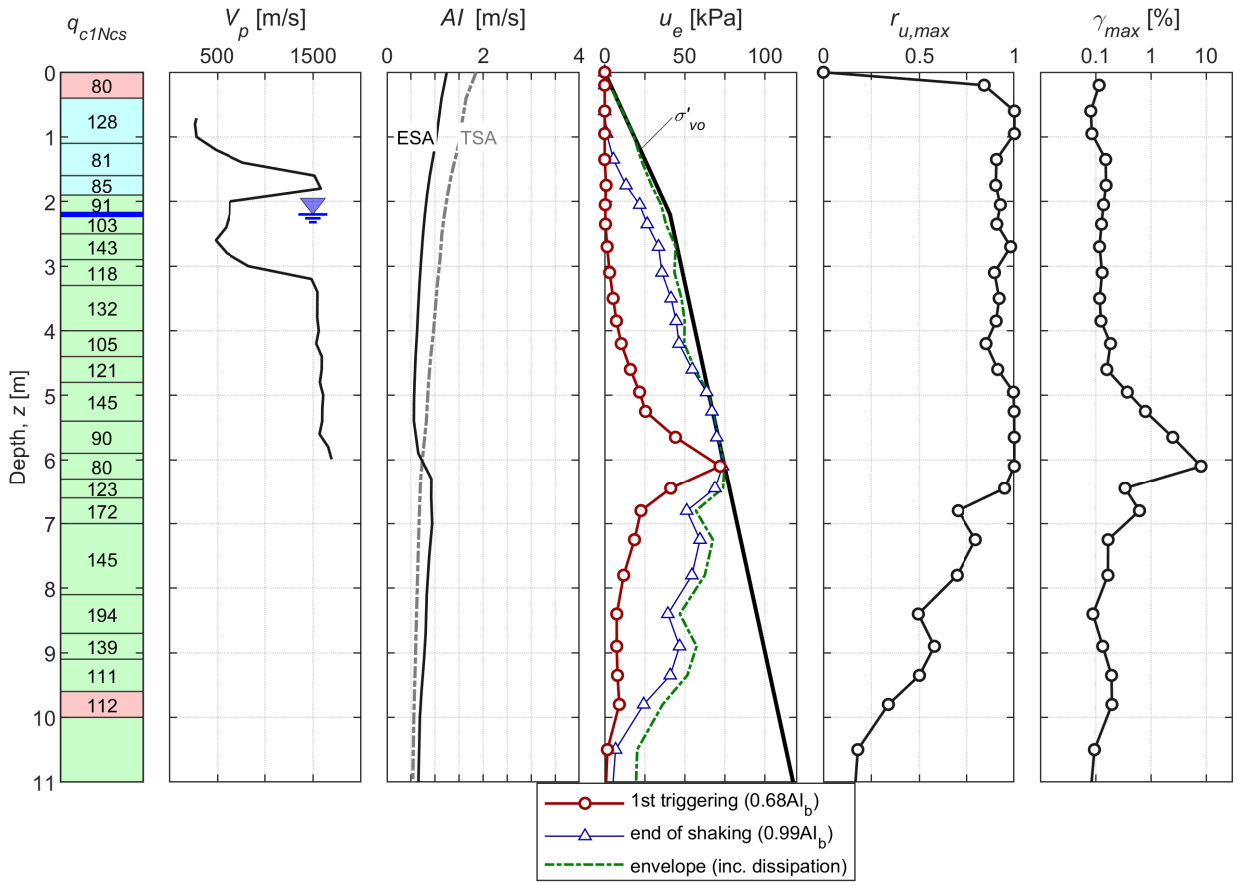

CPT 57354

LPCC-based input

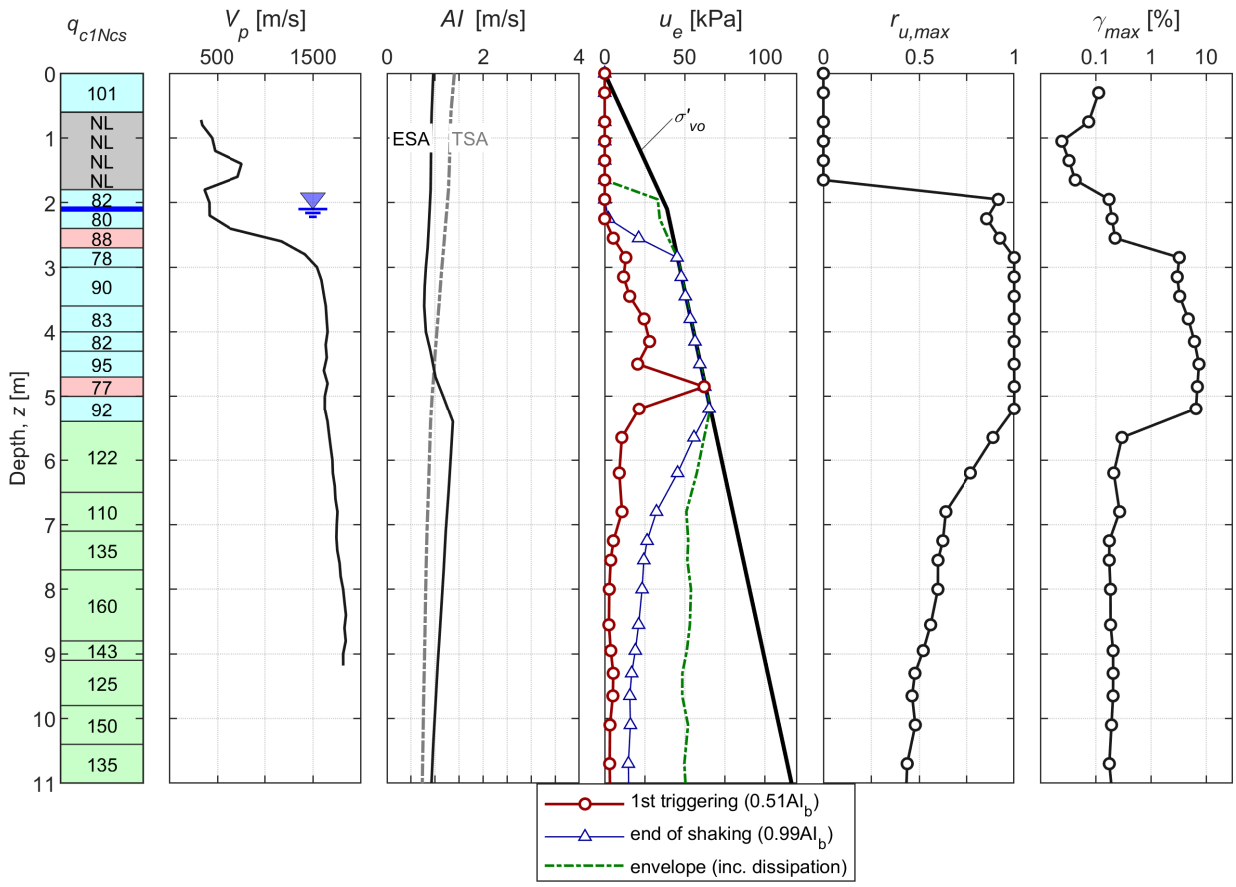

RHSC-based input

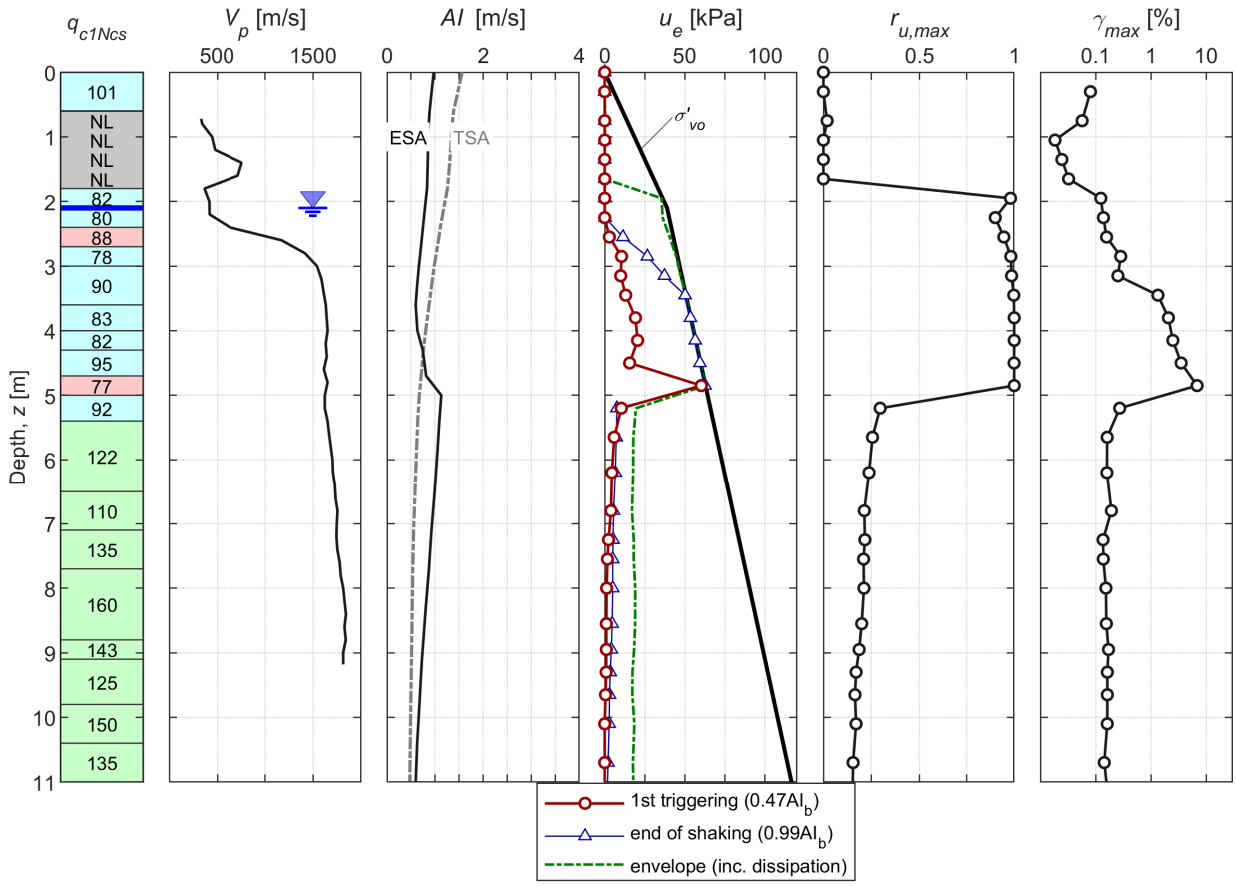

CPT 38758

LPCC-based input

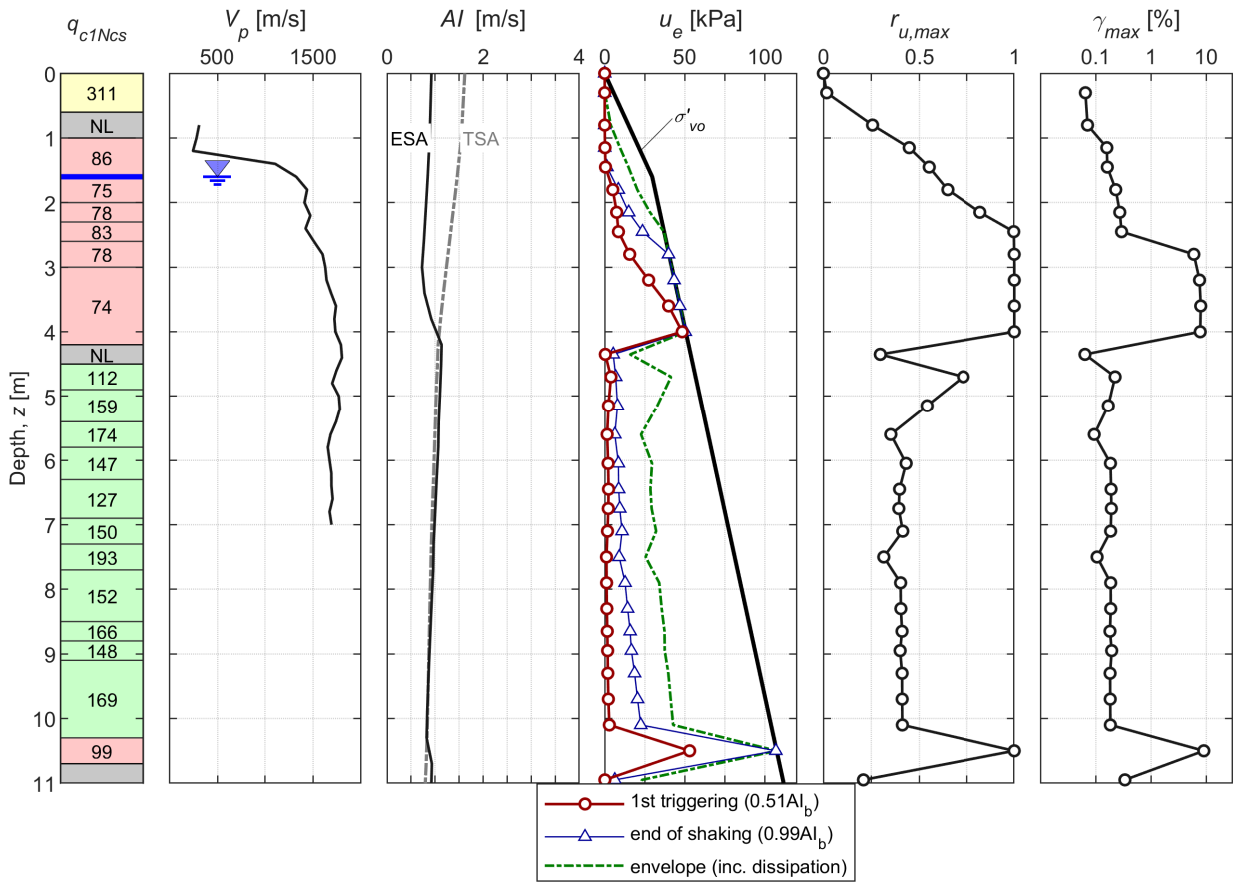

RHSC-based input

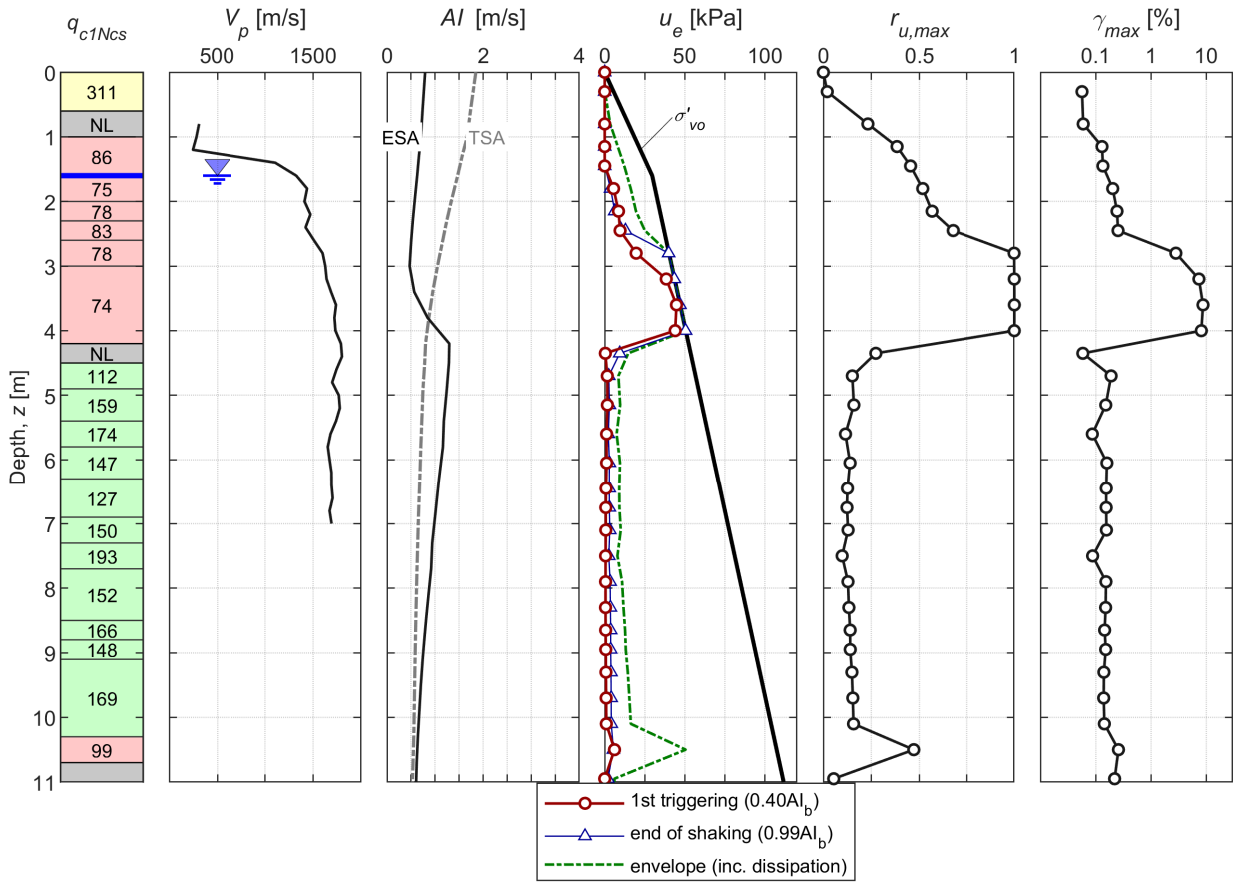

CPT 57342

LPCC-based input

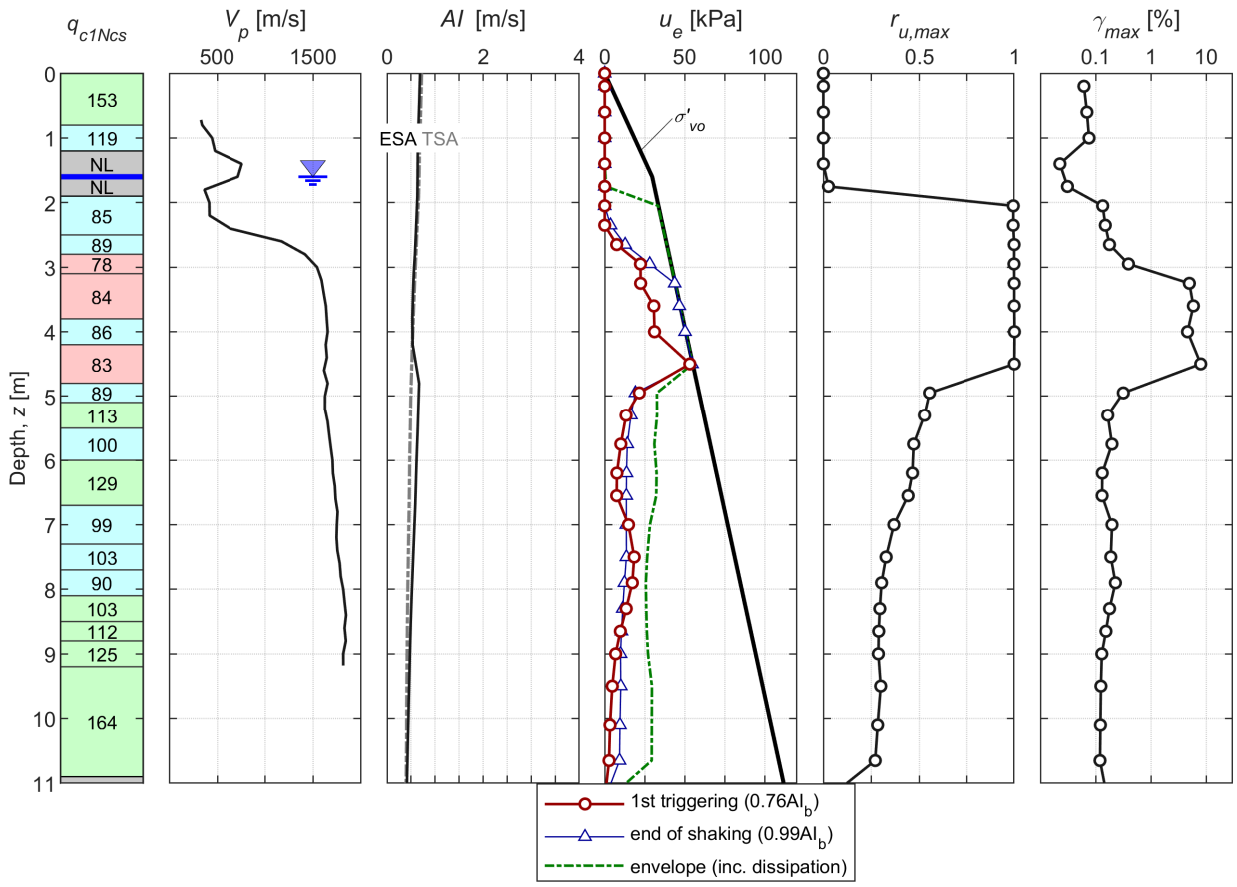

RHSC-based input

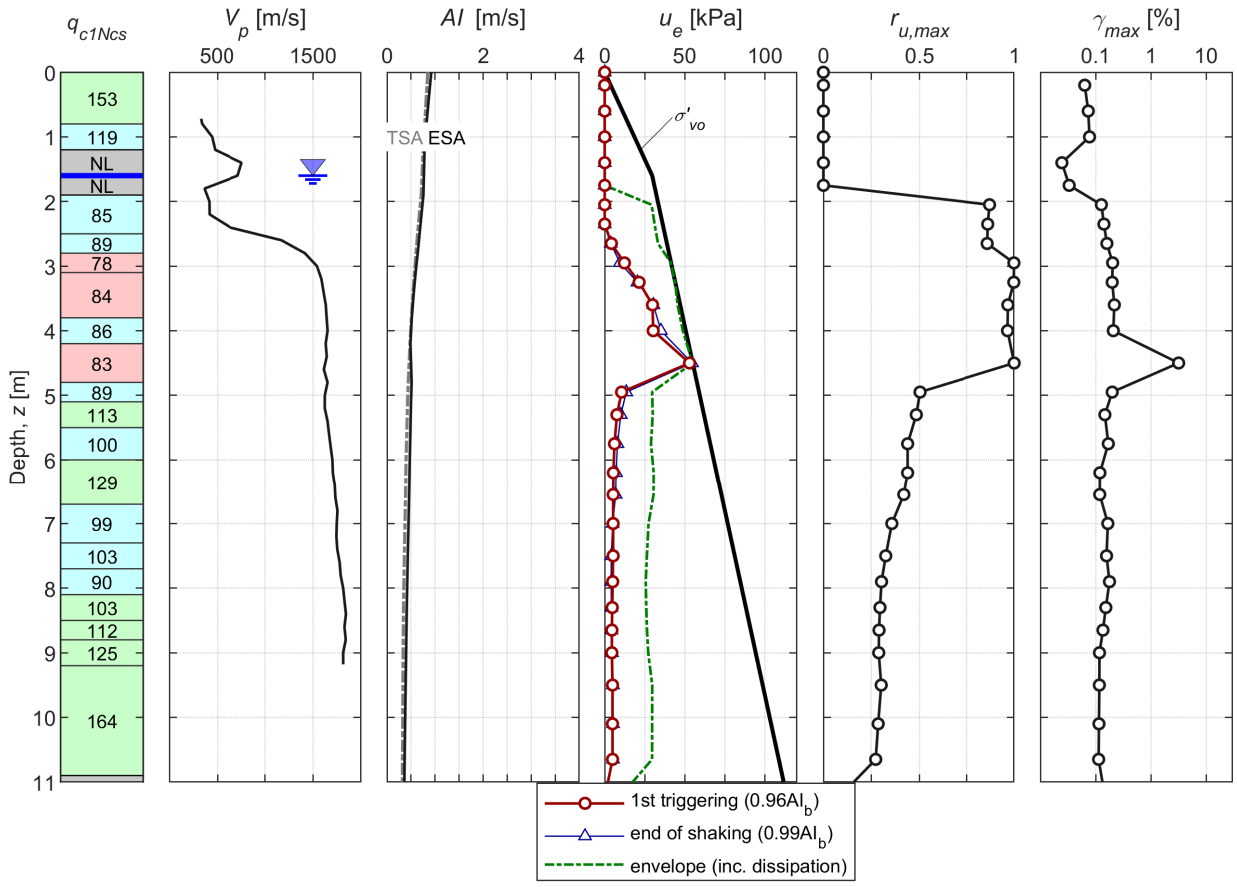

CPT 29035

LPCC-based input

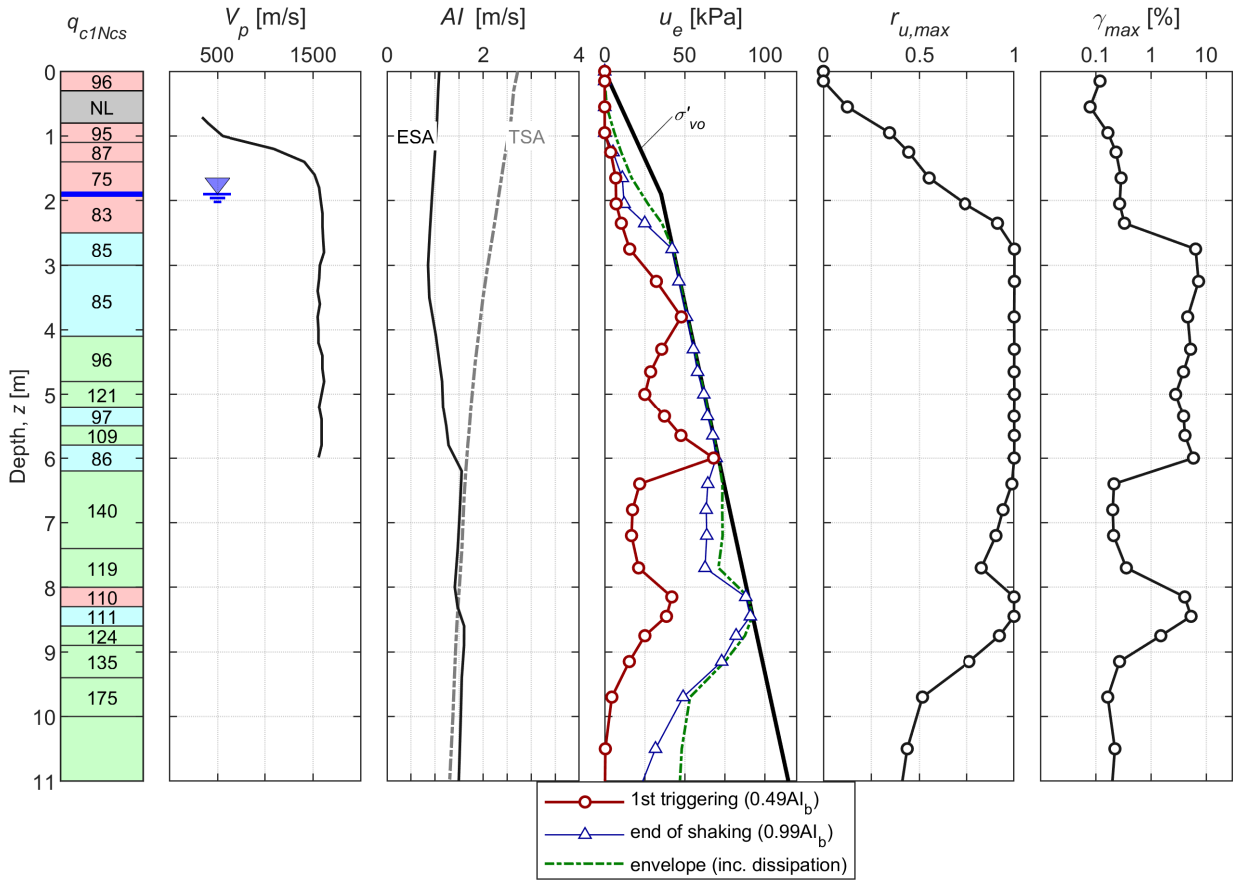

RHSC-based input

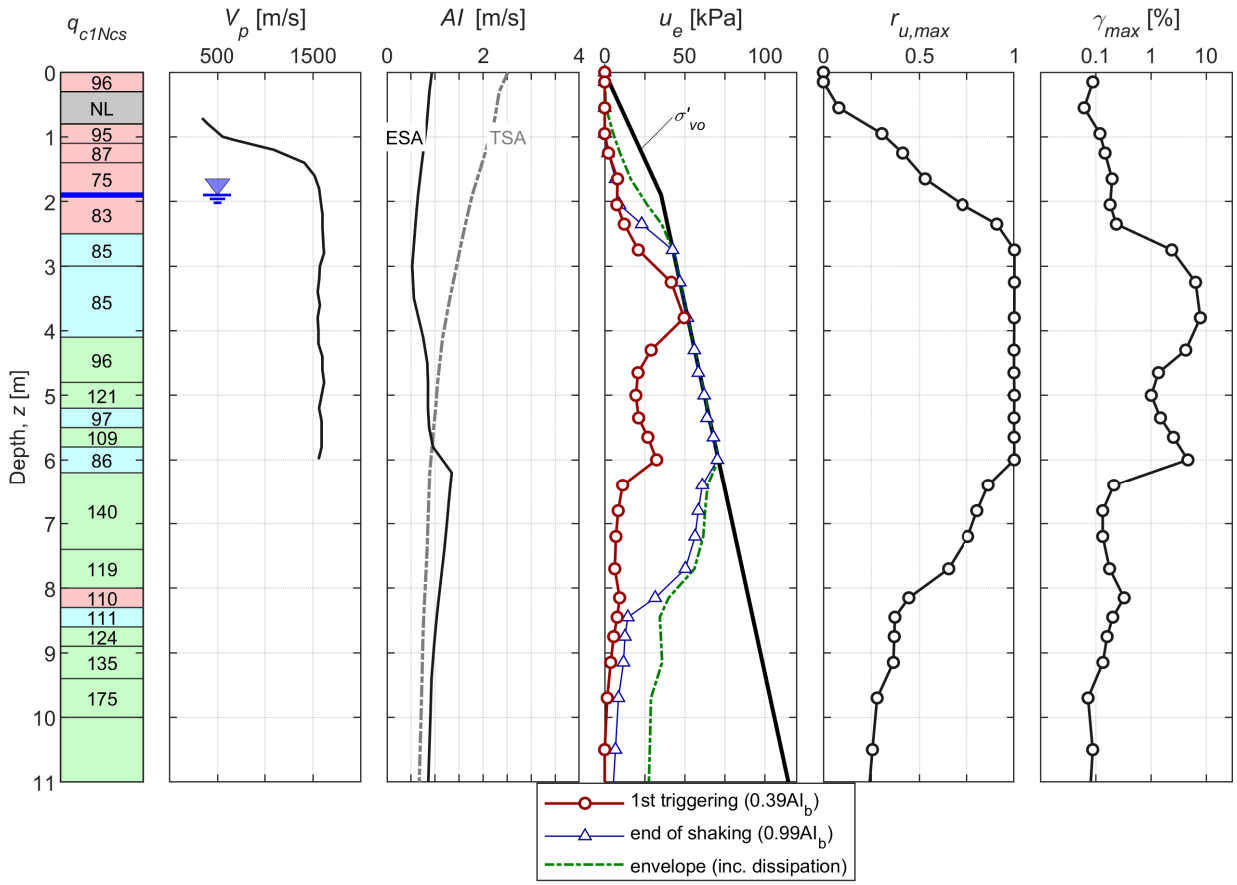

CPT 36414

LPCC-based input

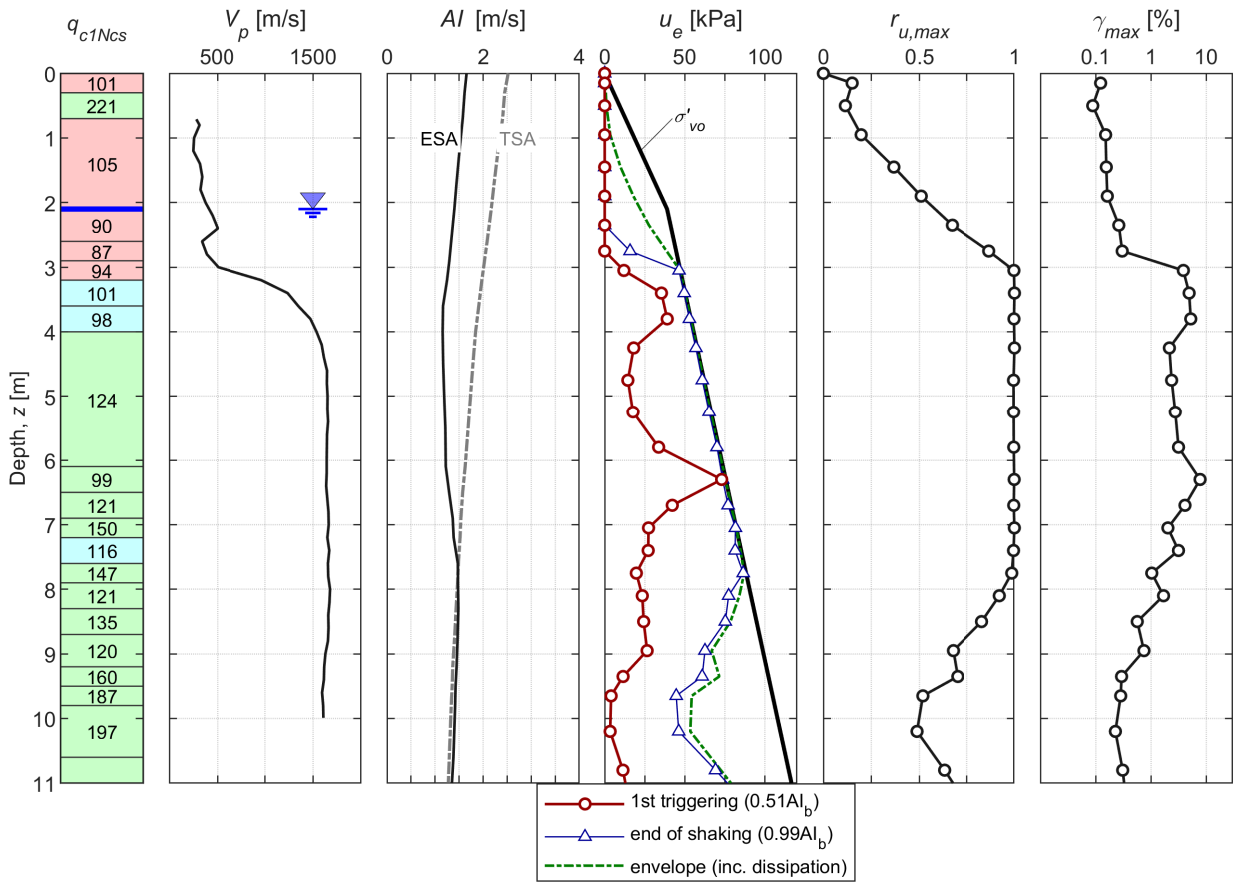

RHSC-based input

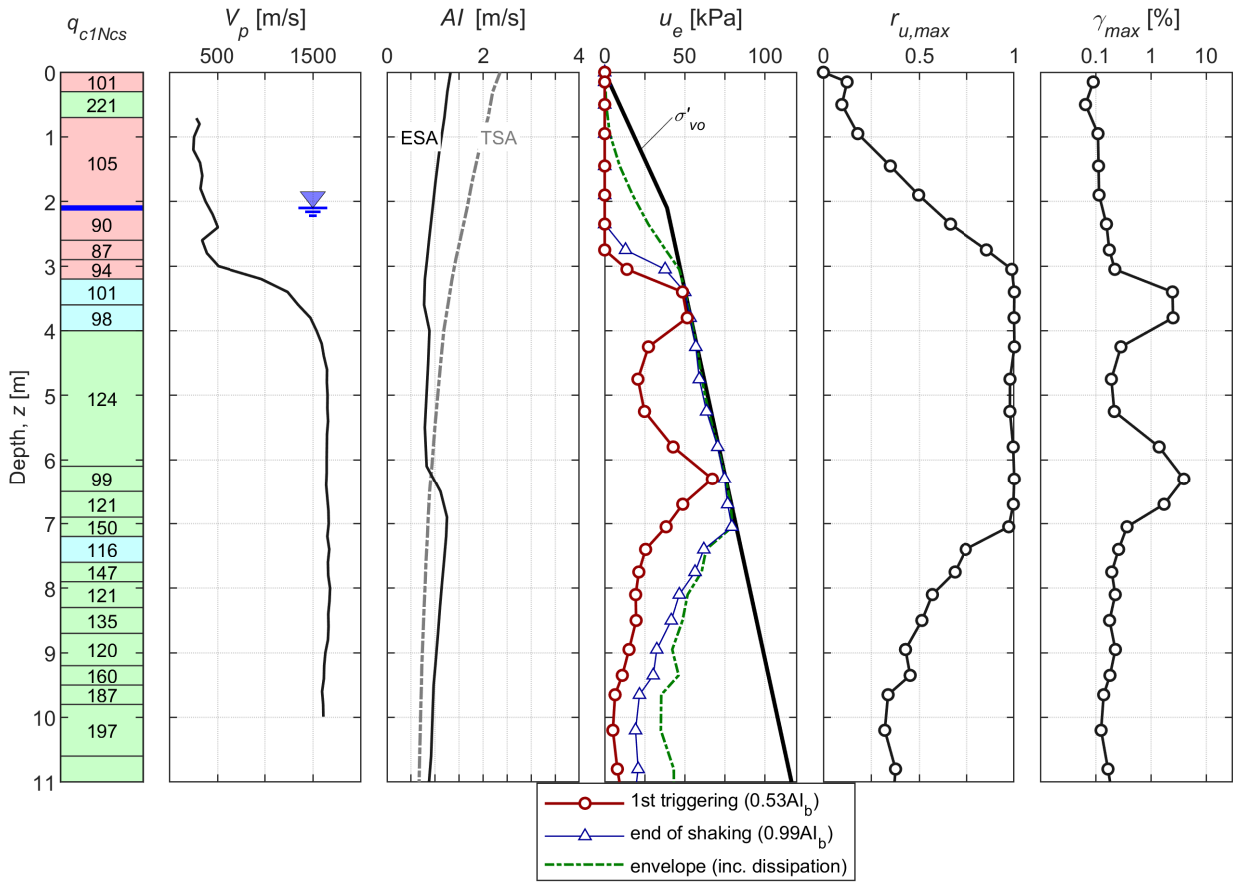

CPT 34454

LPCC-based input

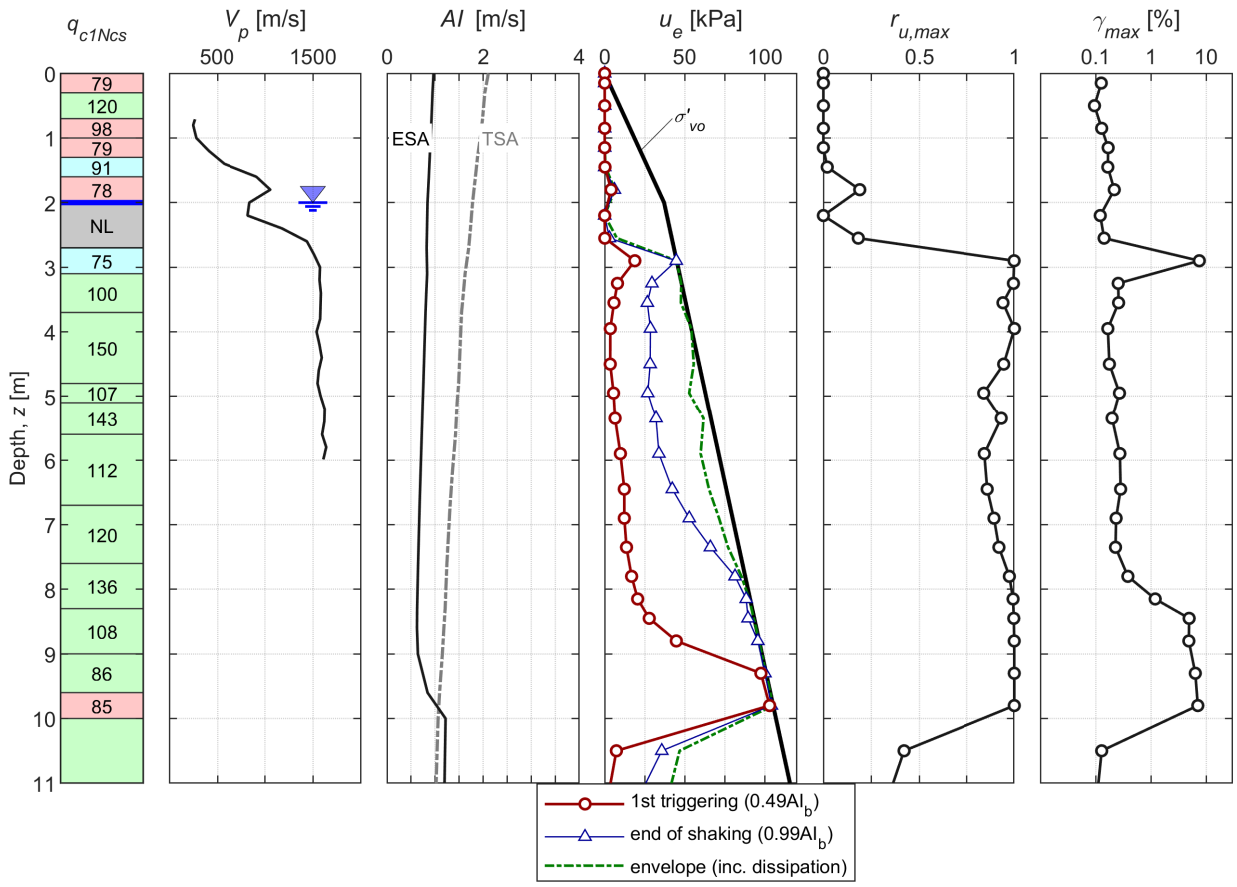

RHSC-based input

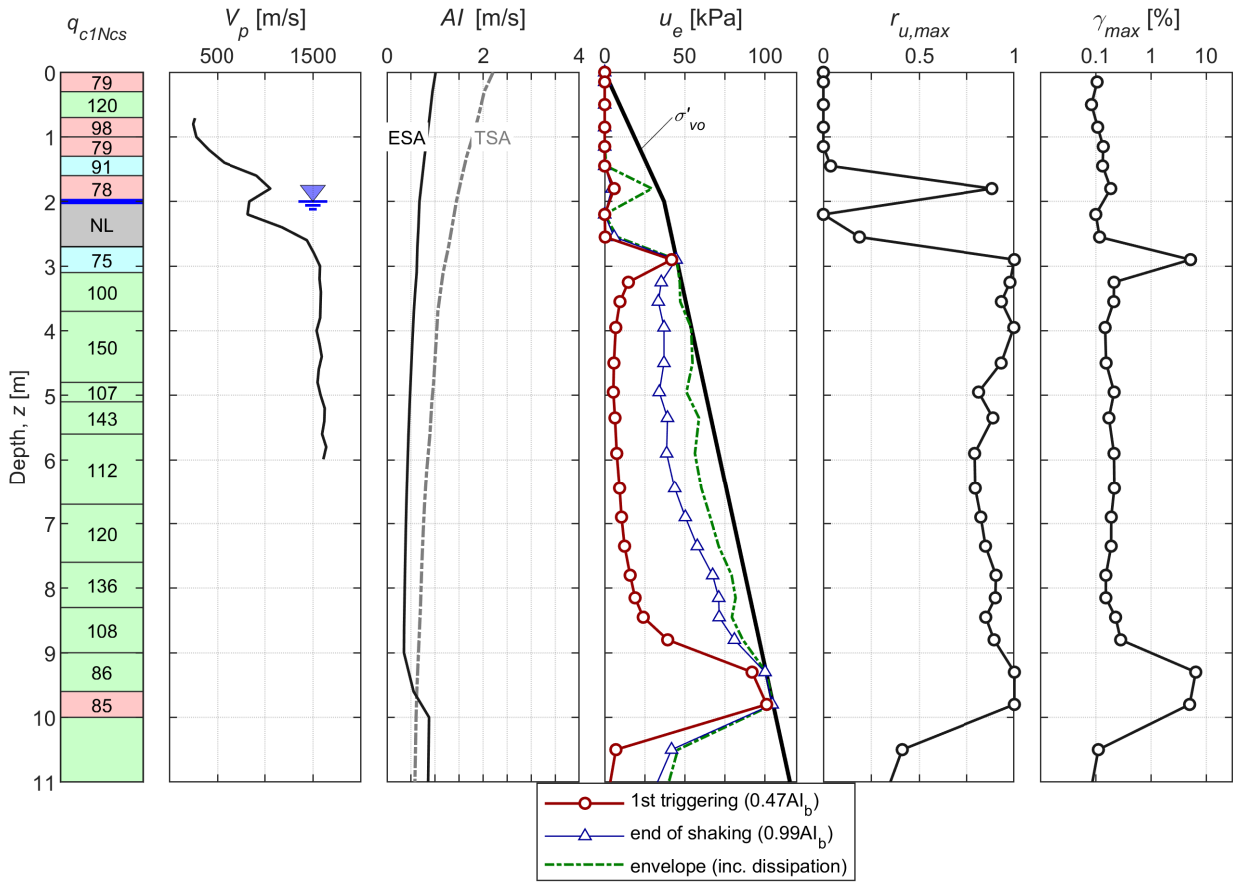

CPT 45

LPCC-based input

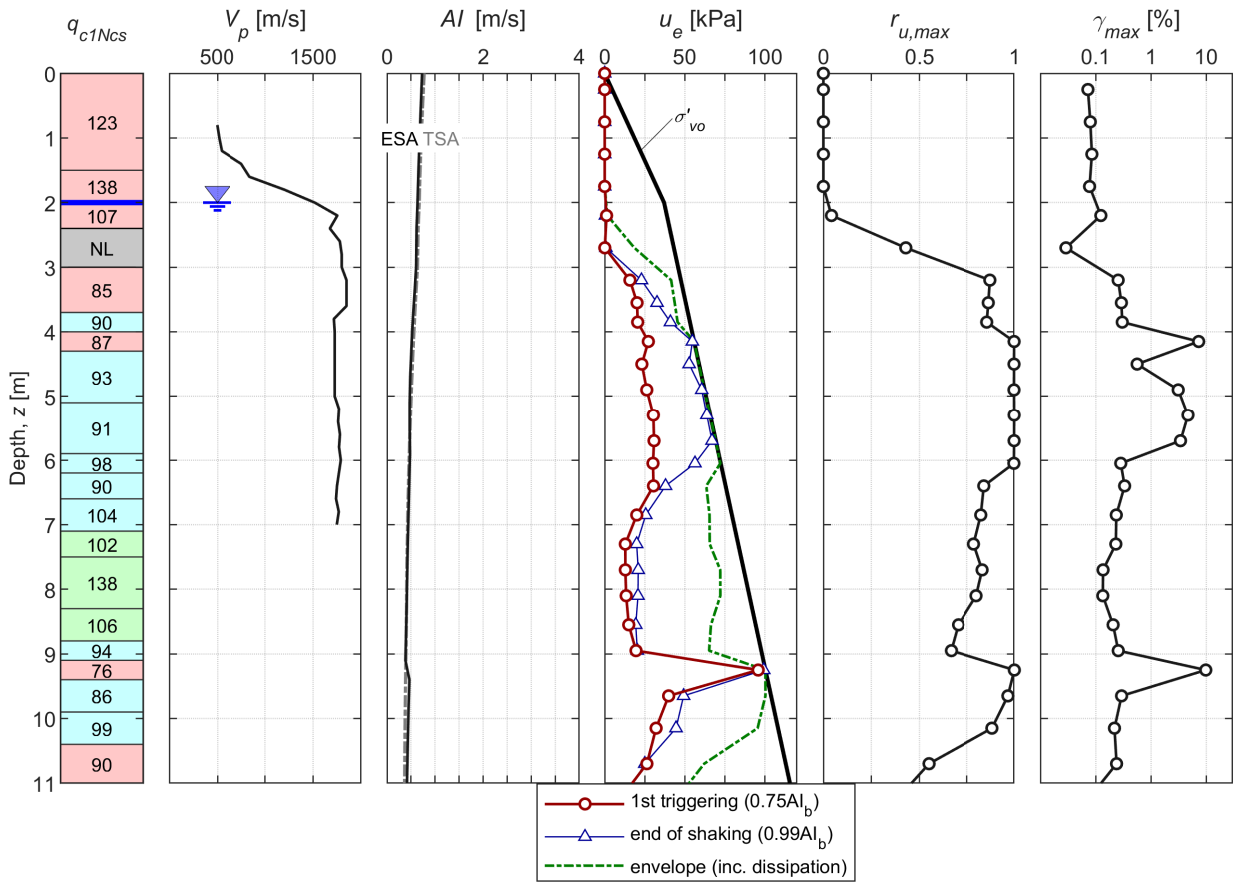

RHSC-based input

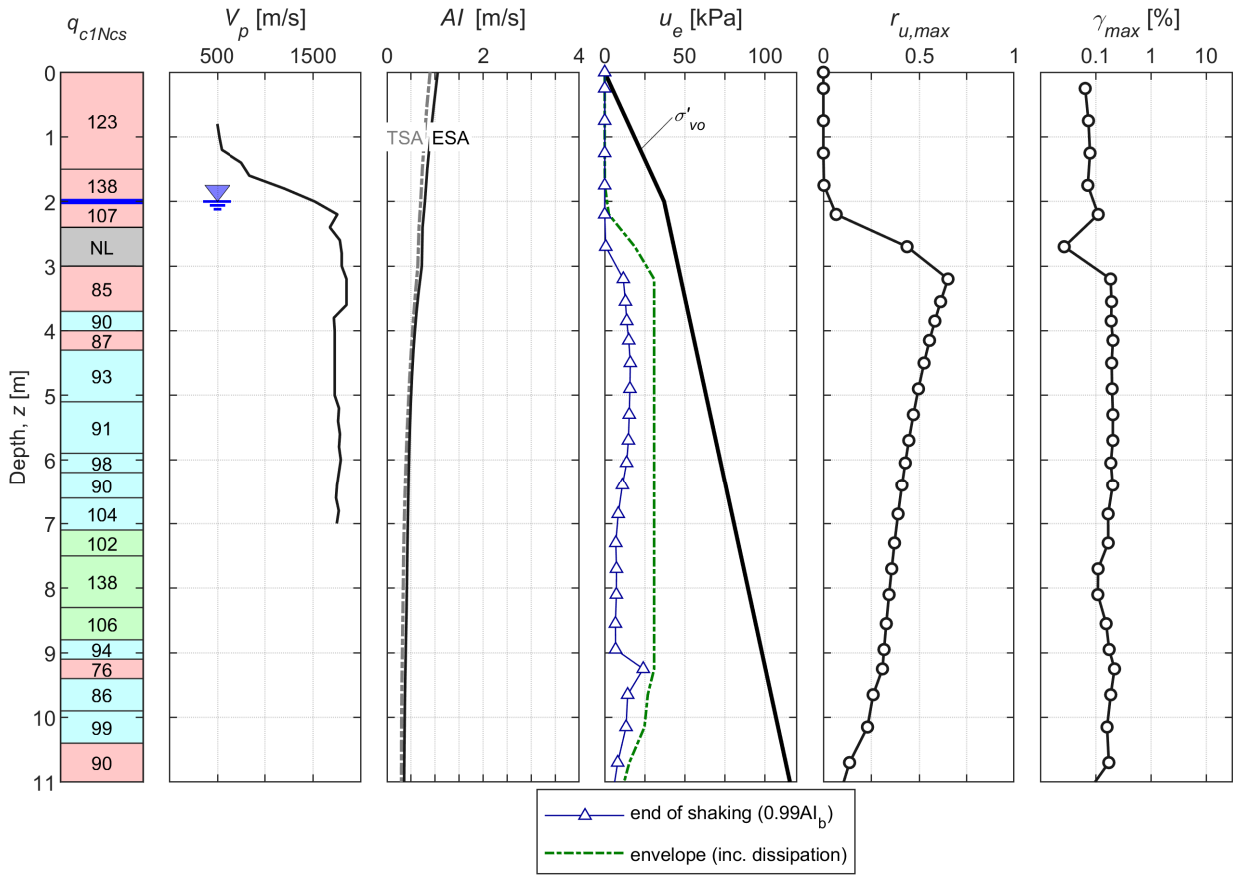

CPT 21506

LPCC-based input

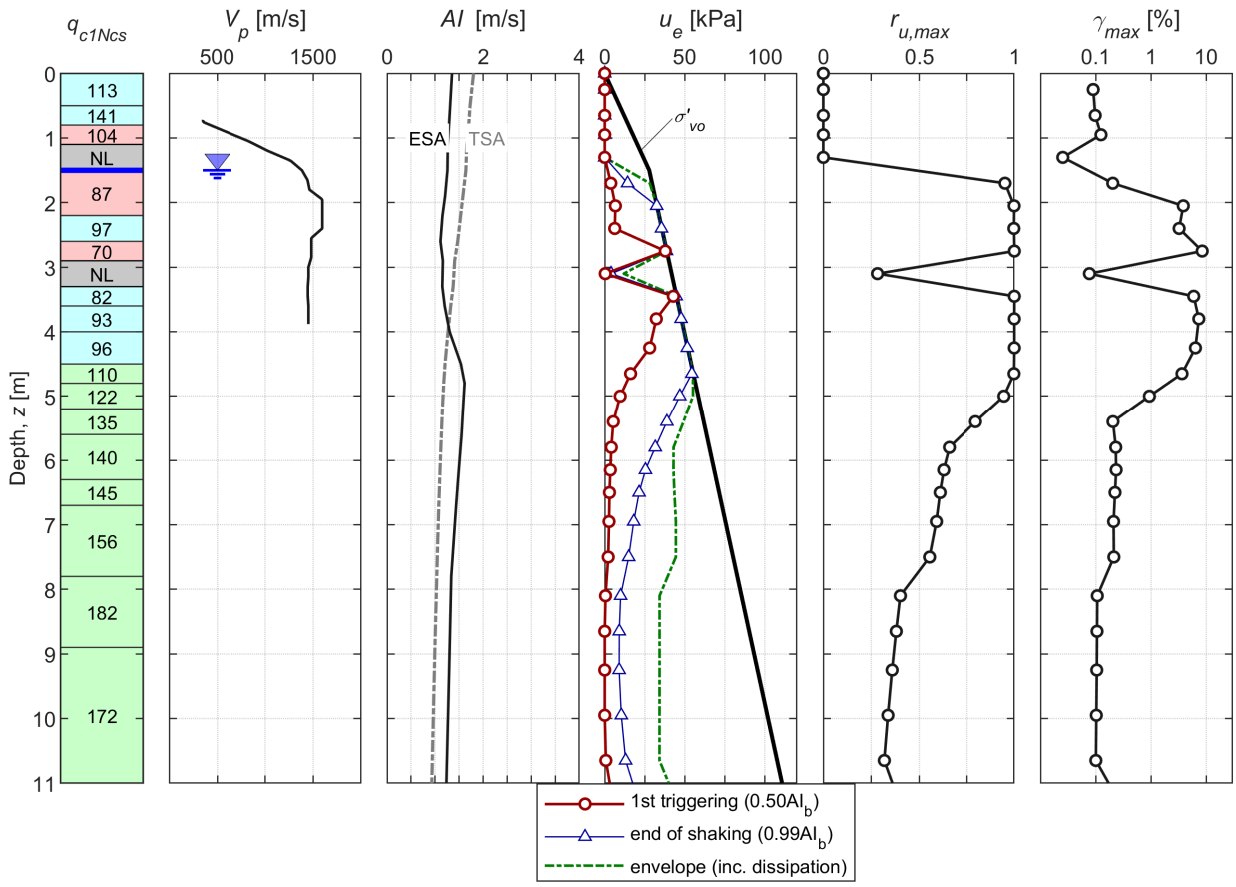

RHSC-based input

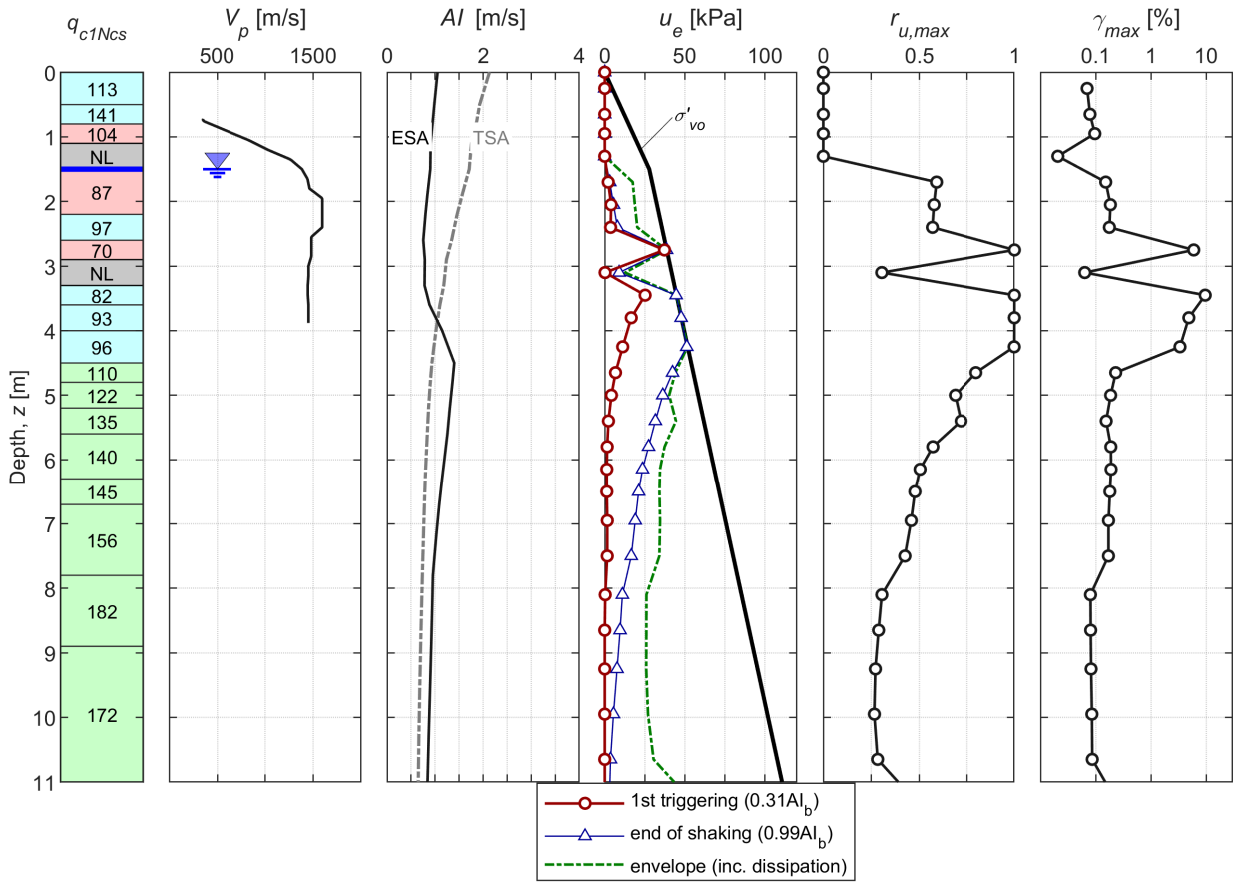

CPT 158

LPCC-based input

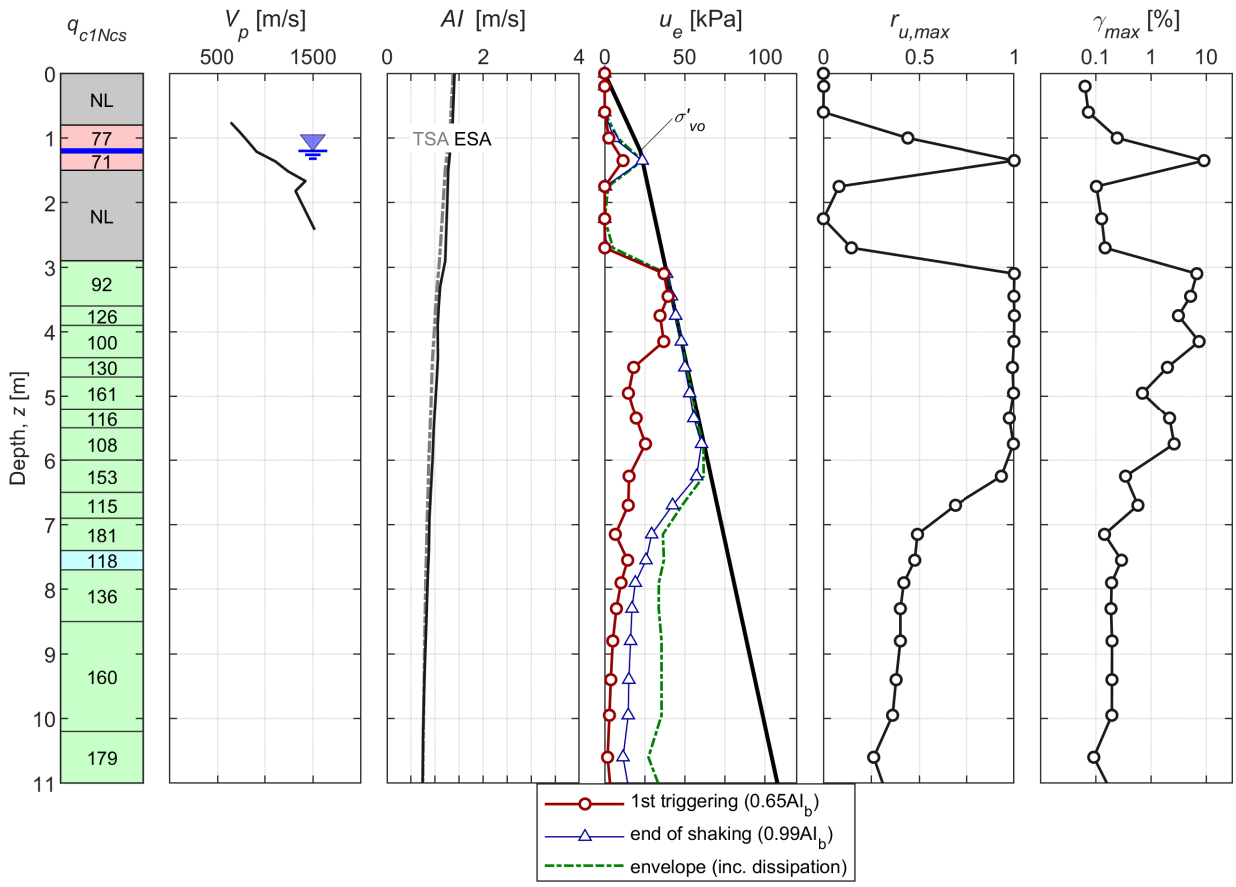

RHSC-based input

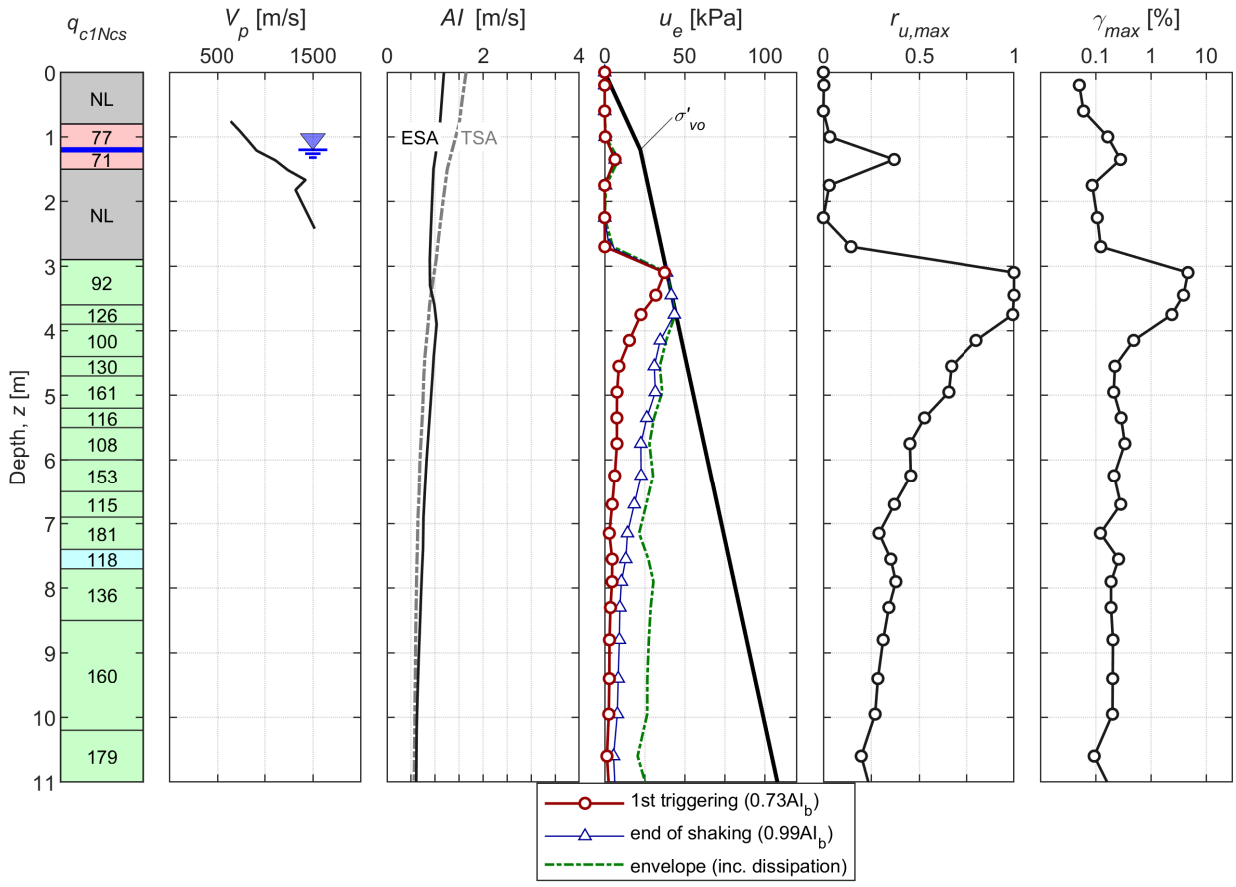

CPT 175

LPCC-based input

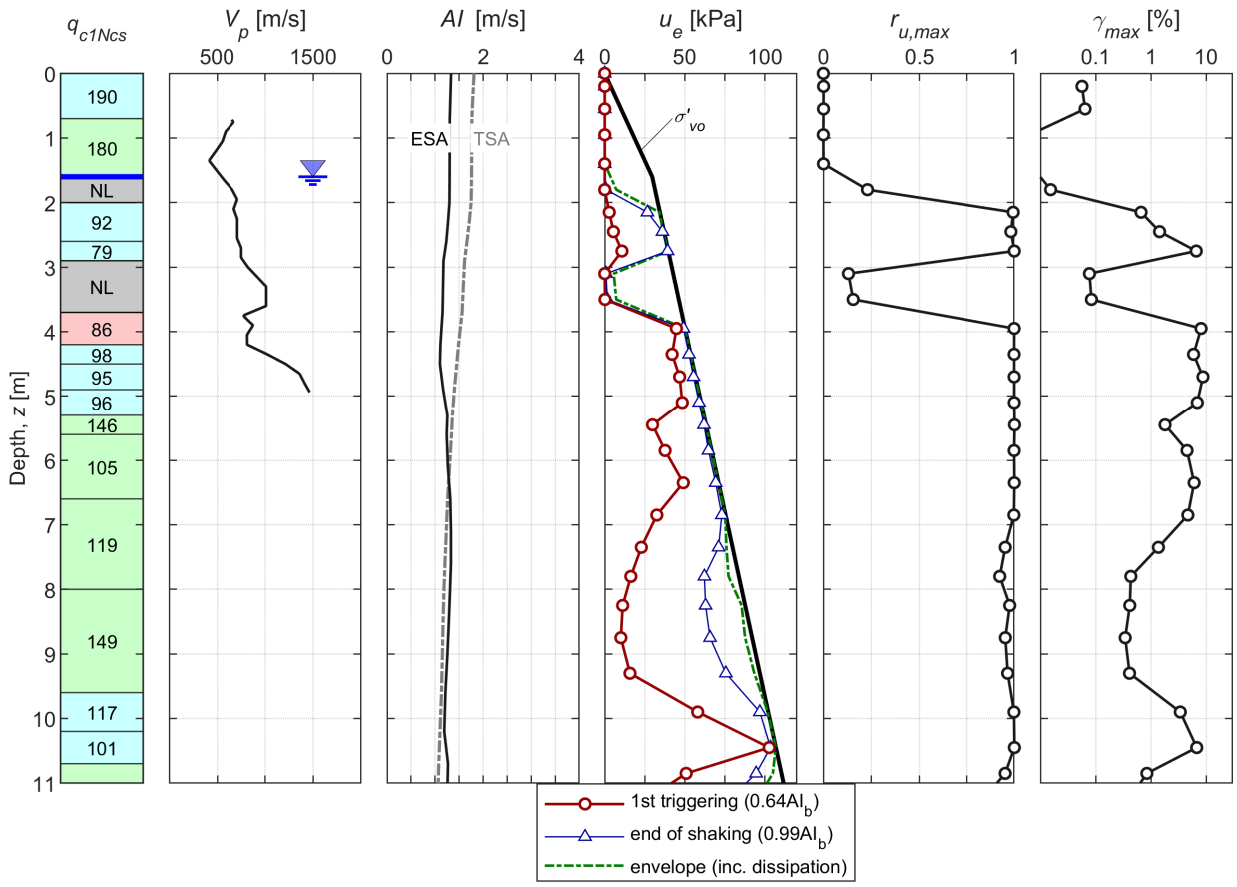

RHSC-based input

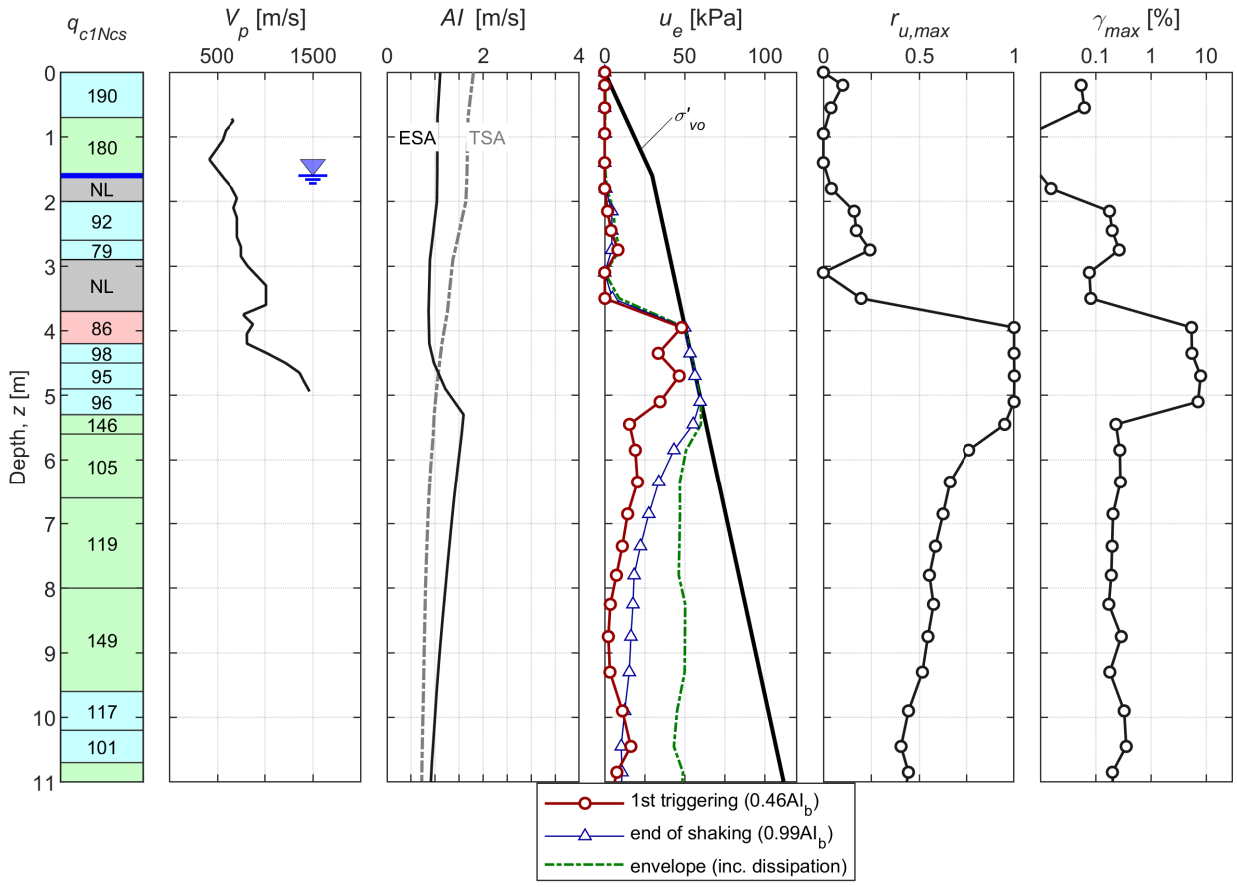

CPT 57349

LPCC-based input

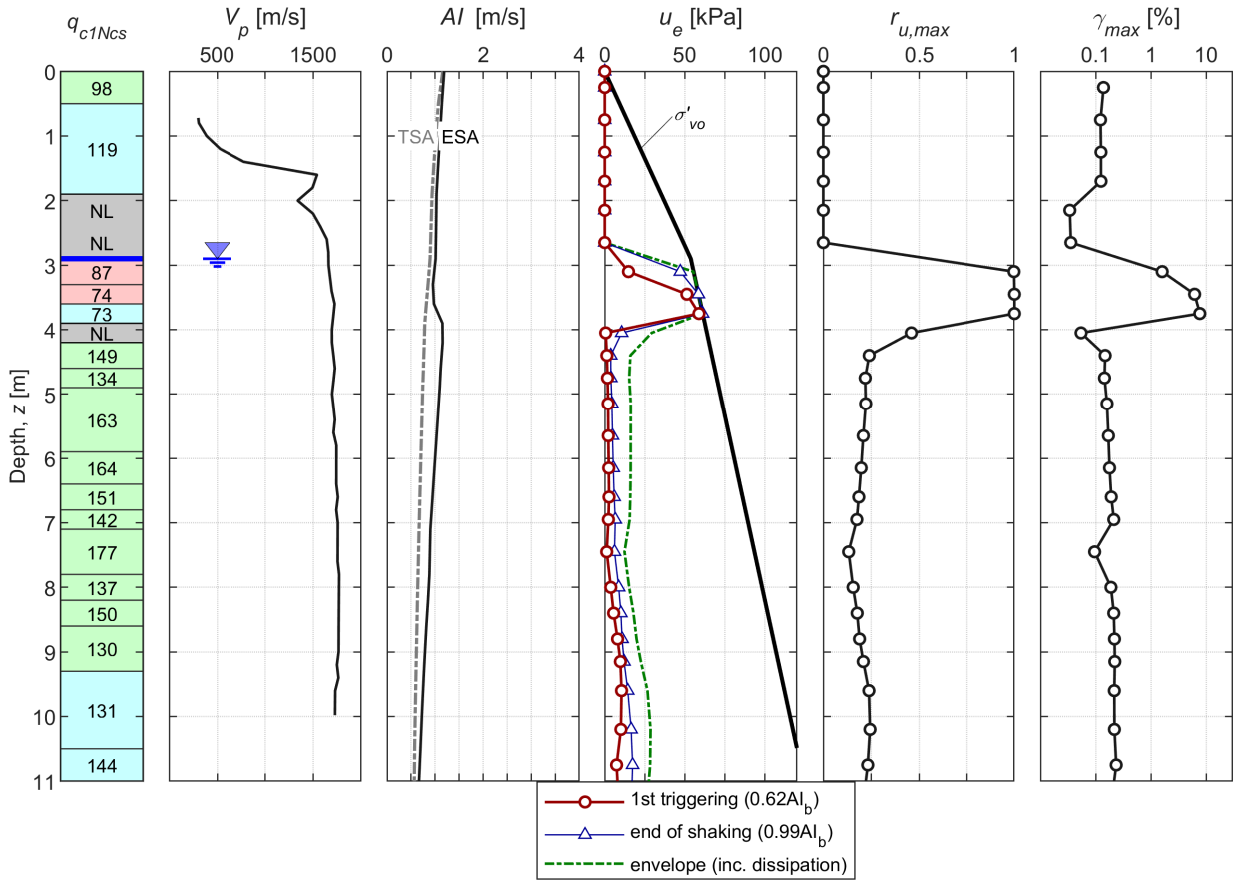

RHSC-based input

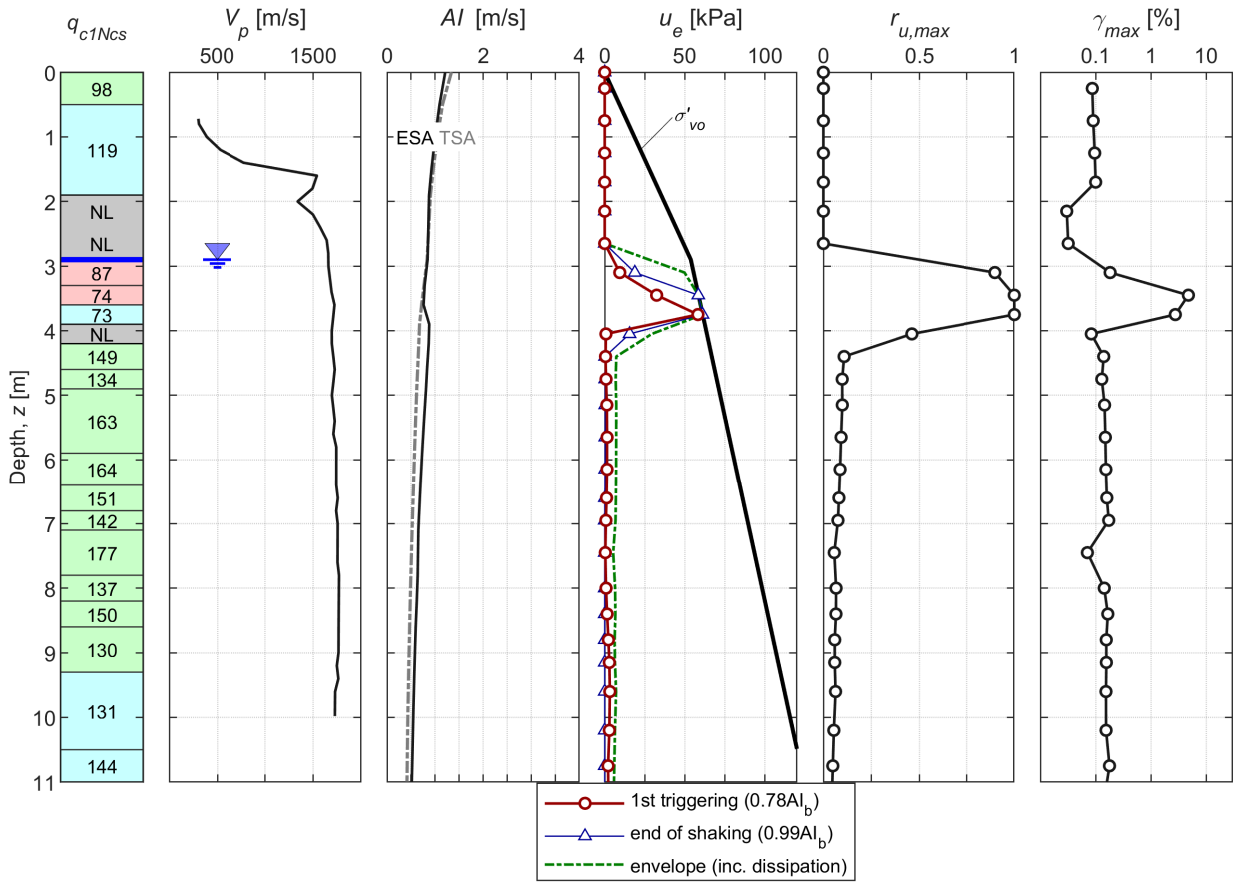

CPT 57347

LPCC-based input

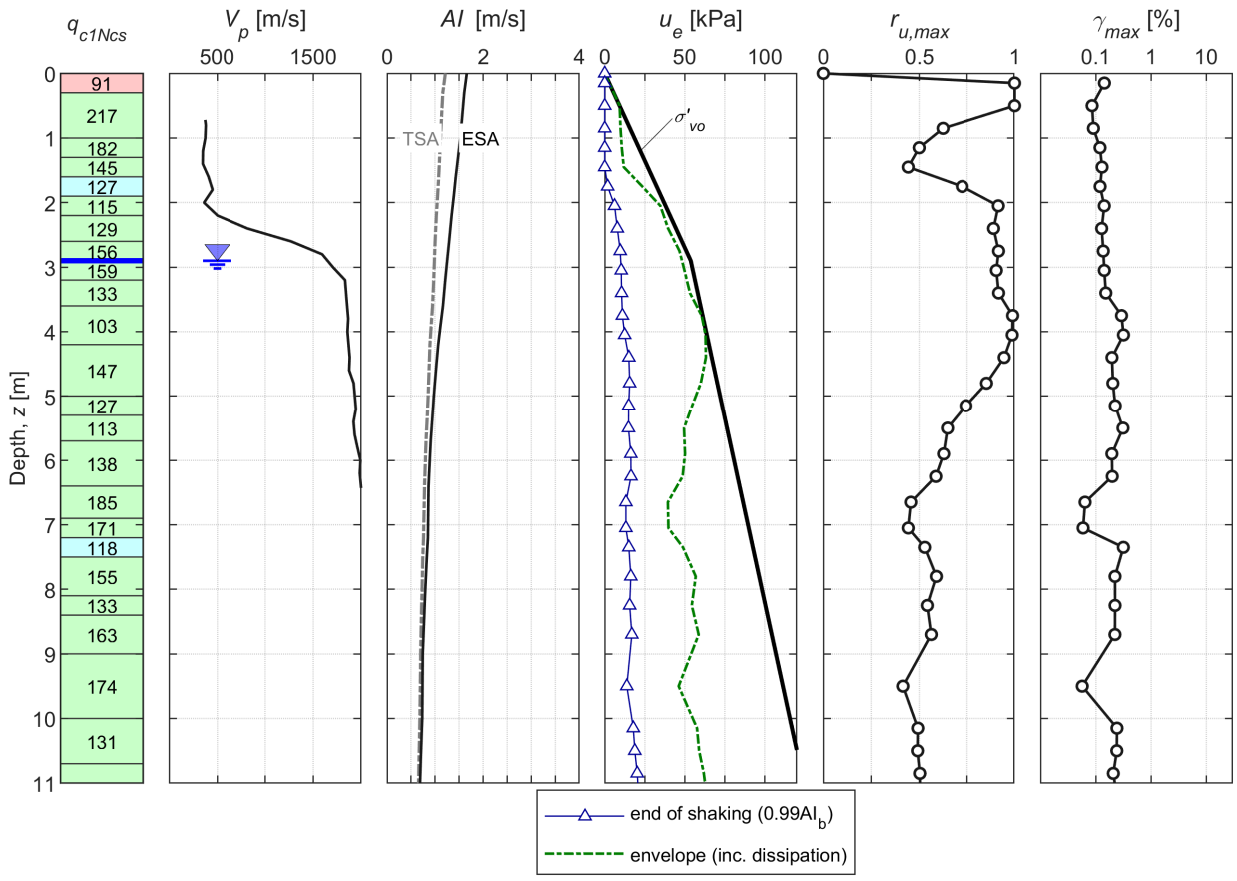

RHSC-based input

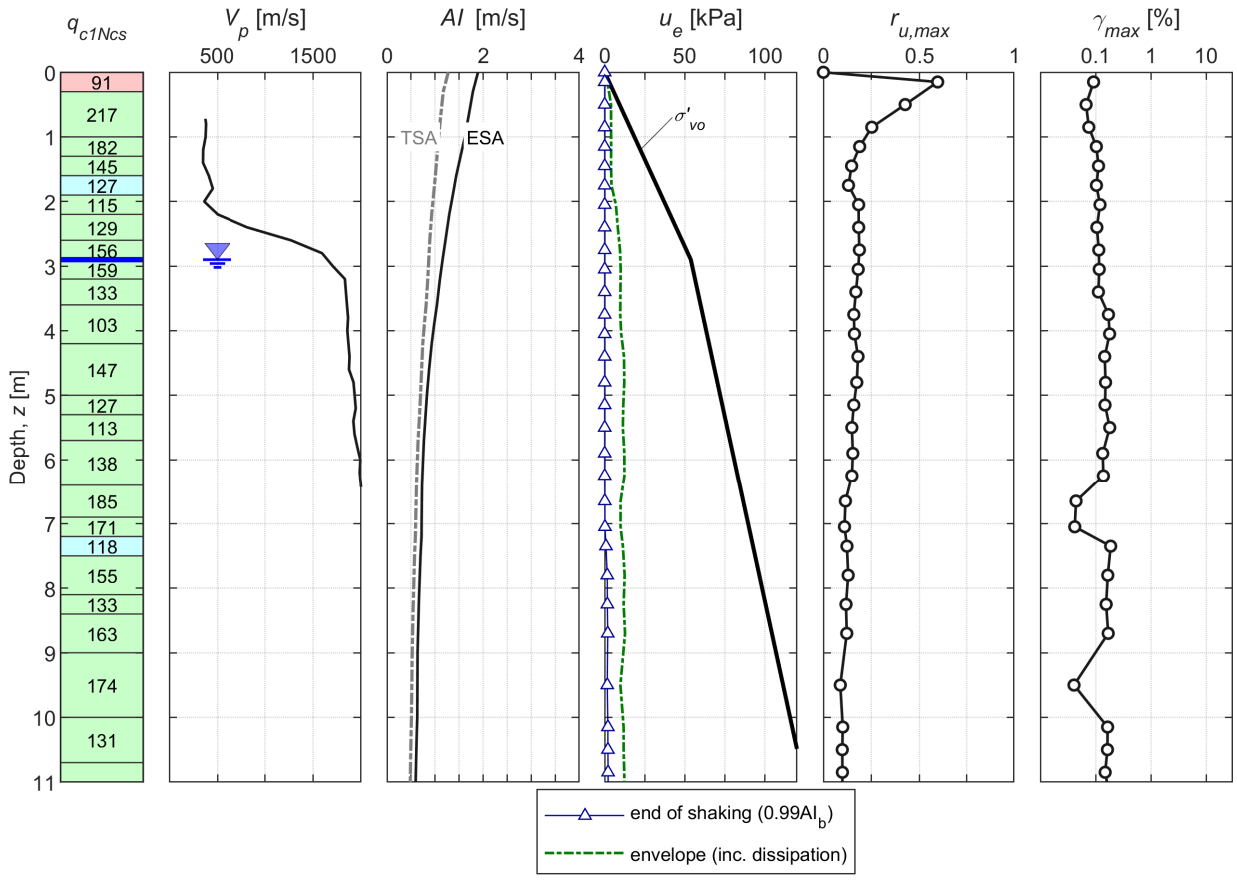

CPT 57348

LPCC-based input

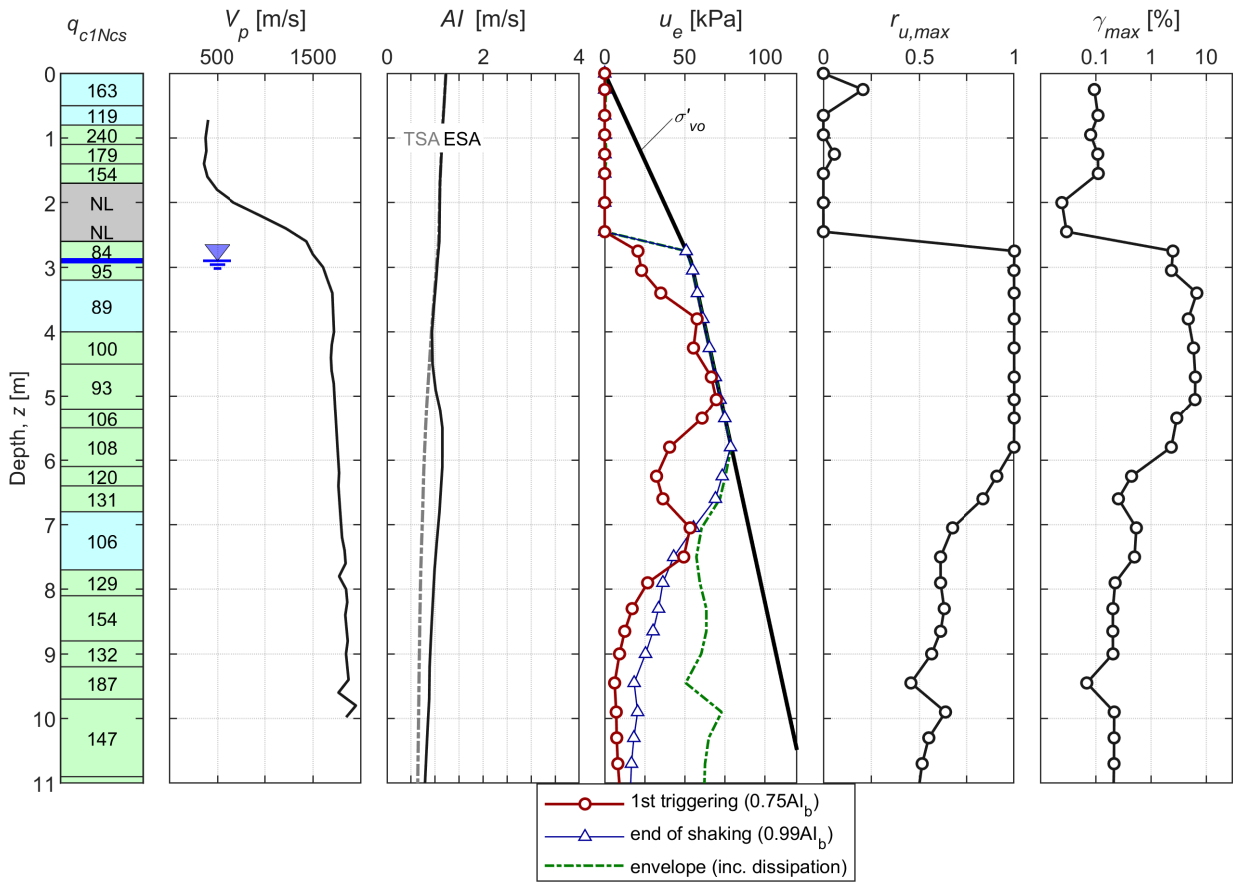

RHSC-based input

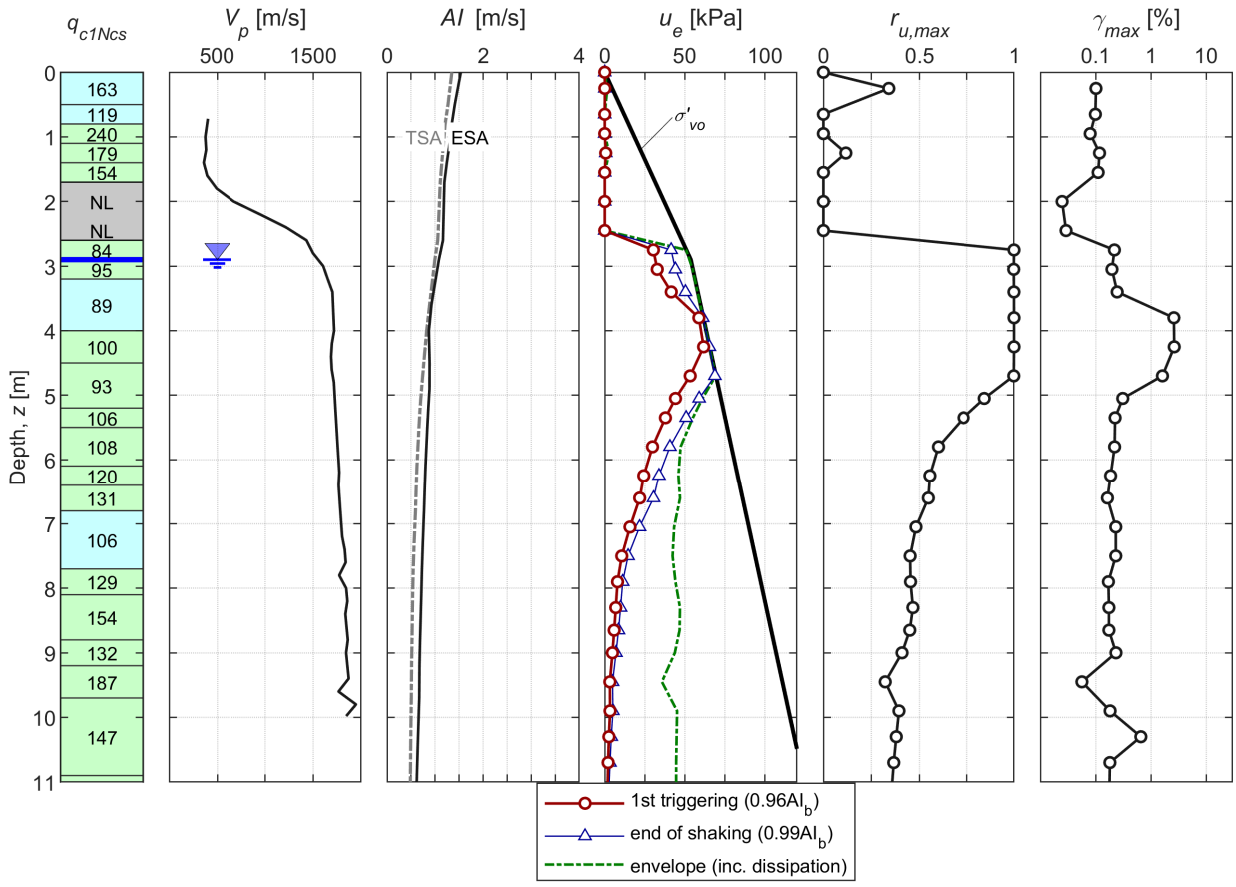

CPT 38797

LPCC-based input

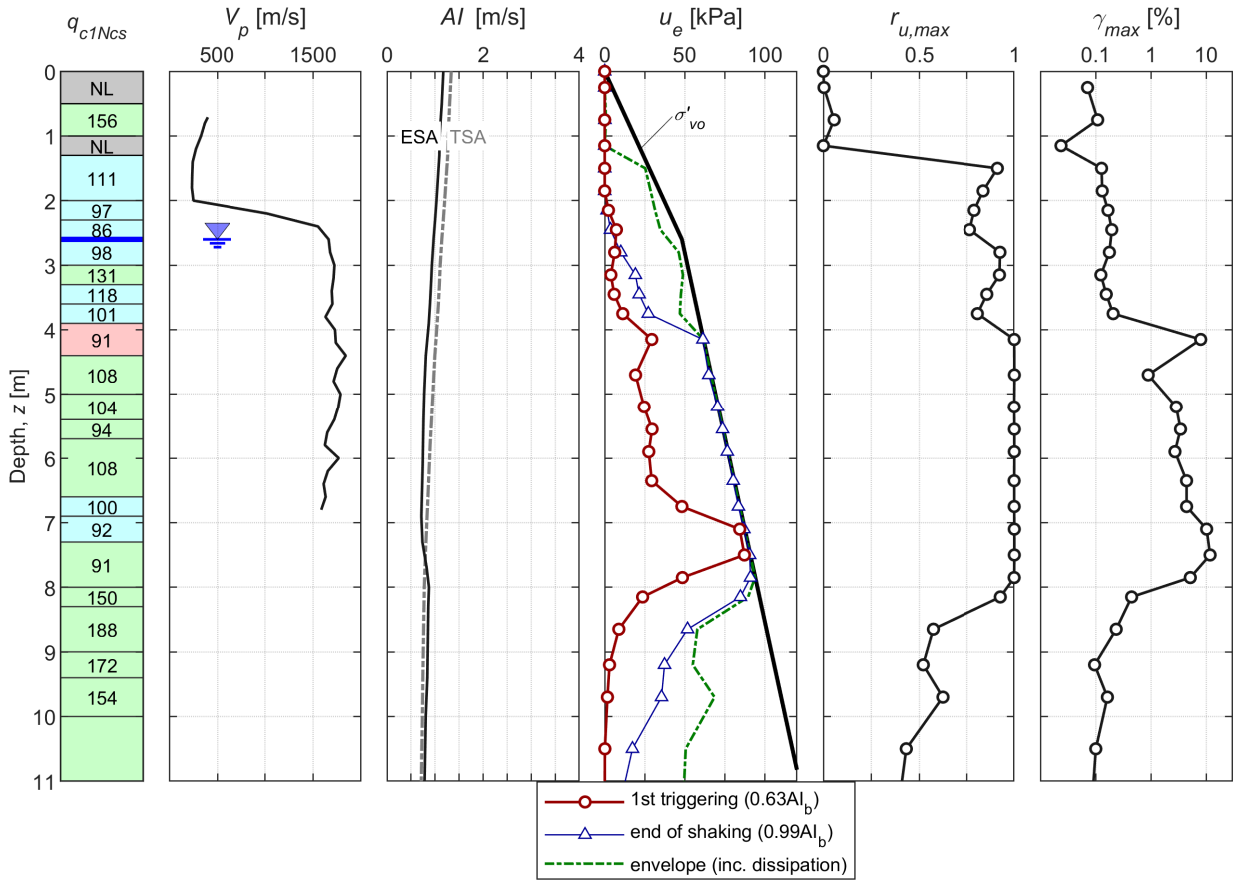

RHSC-based input

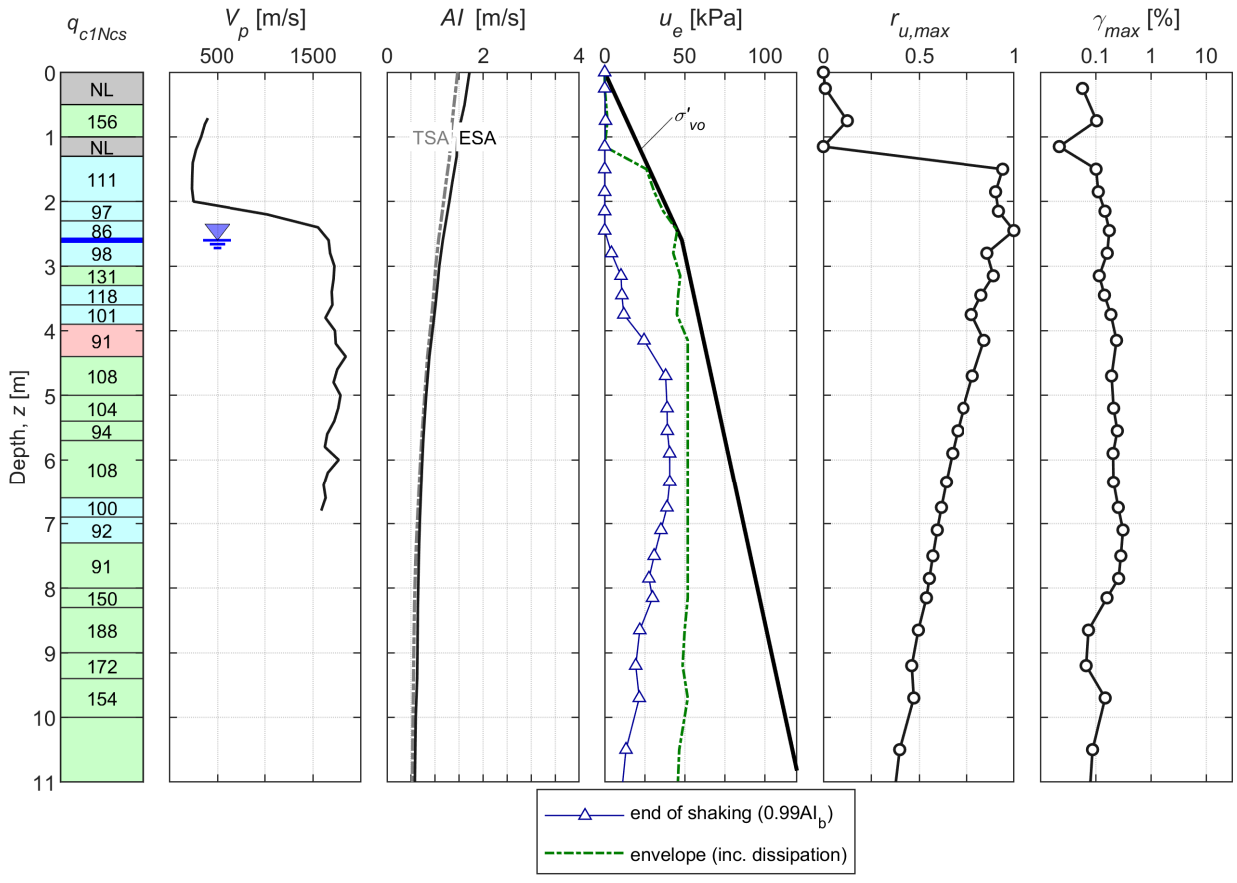

CPT 57343

LPCC-based input

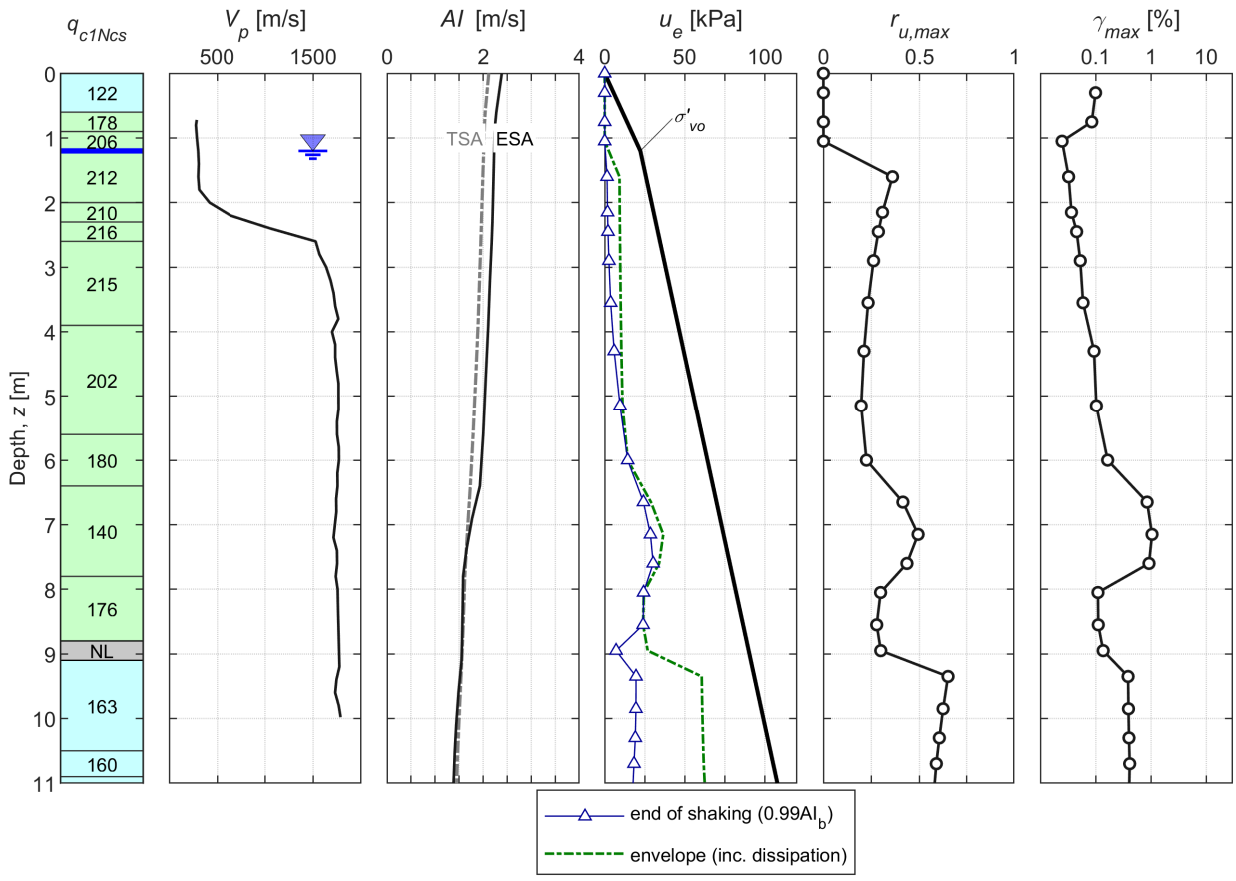

RHSC-based input

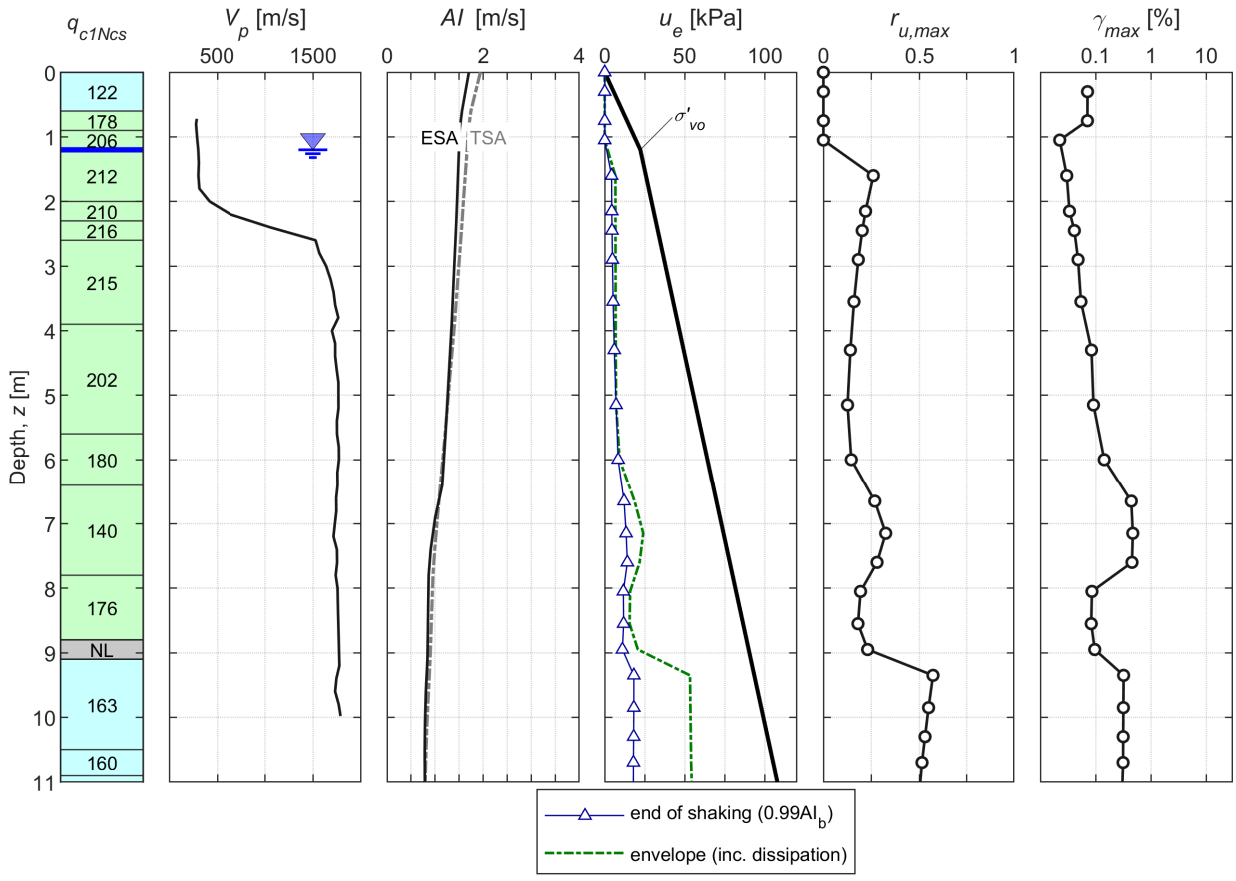

CPT 38742

LPCC-based input

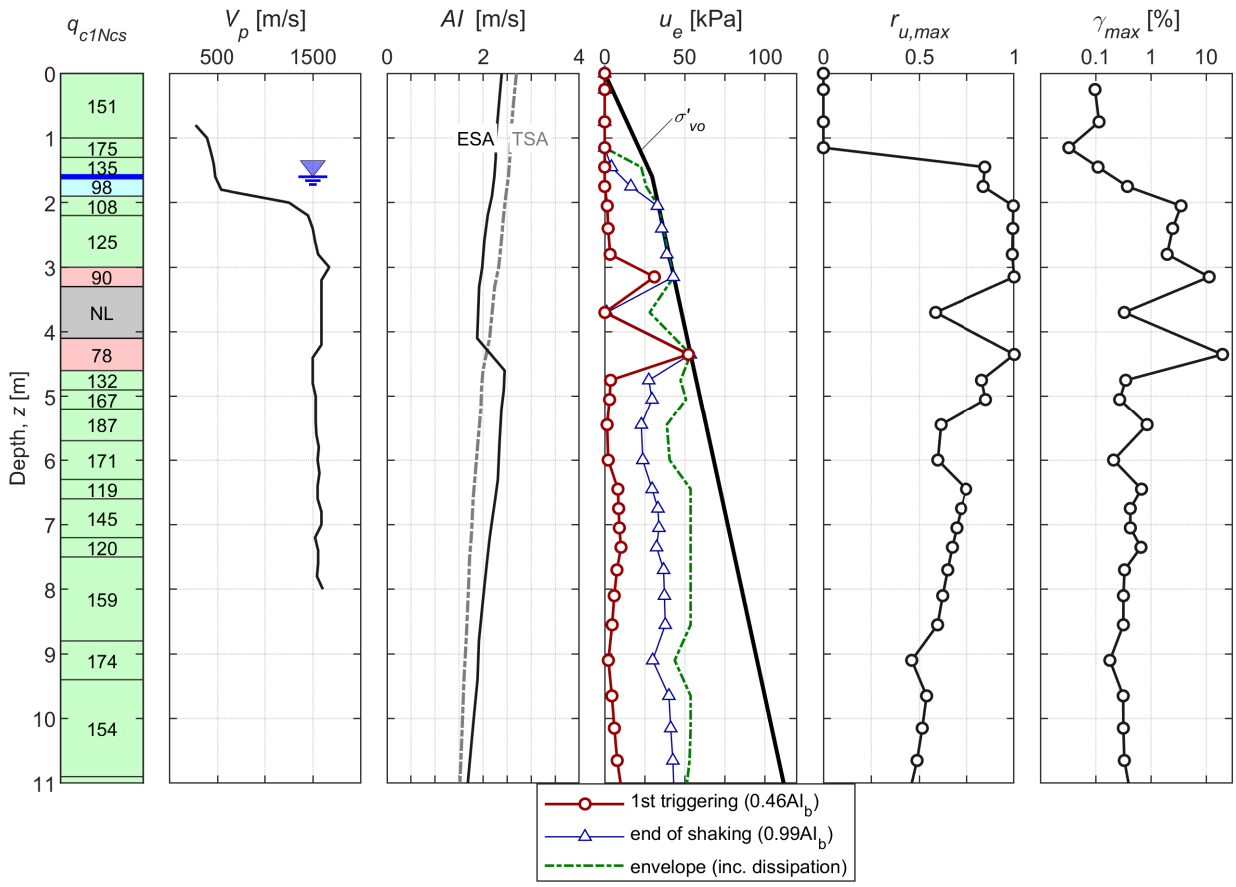

RHSC-based input

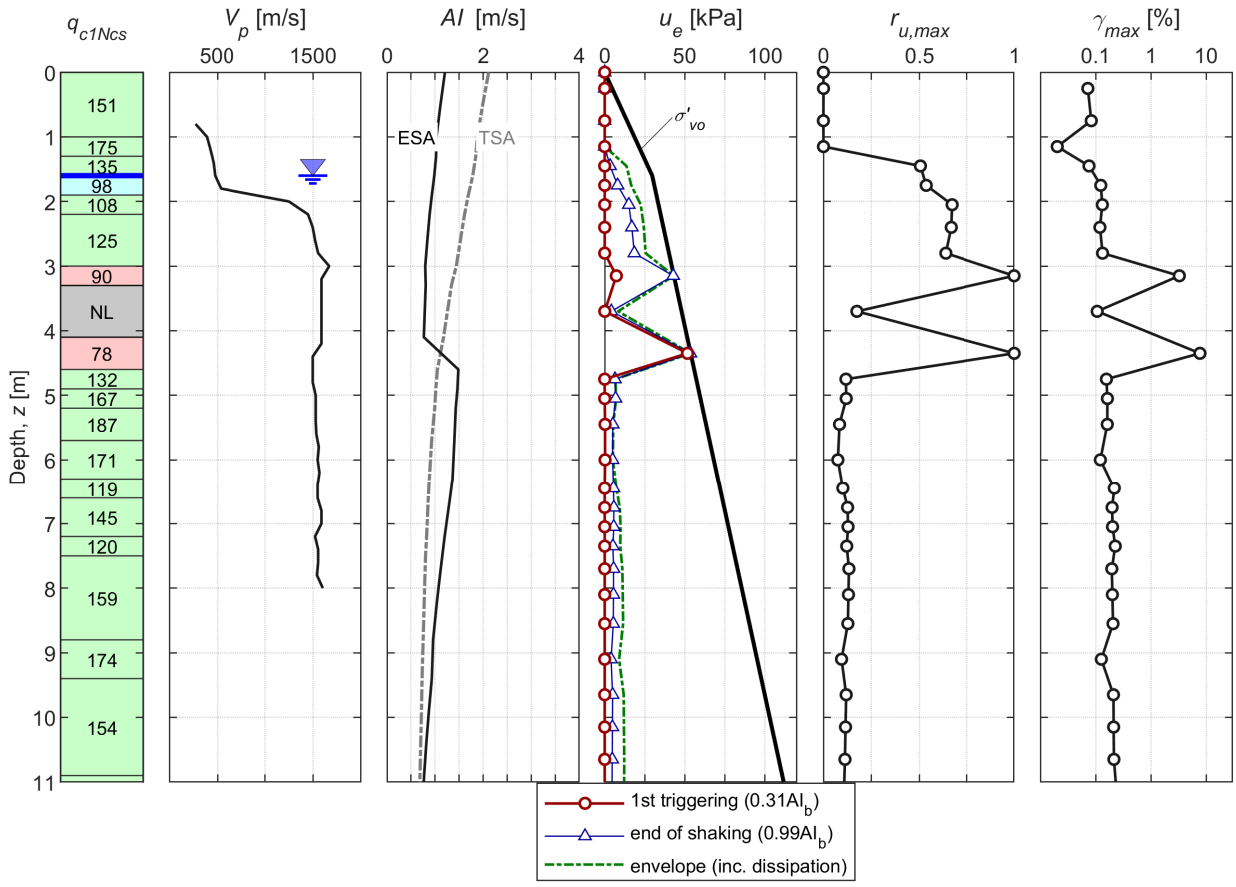

CPT 34431

LPCC-based input

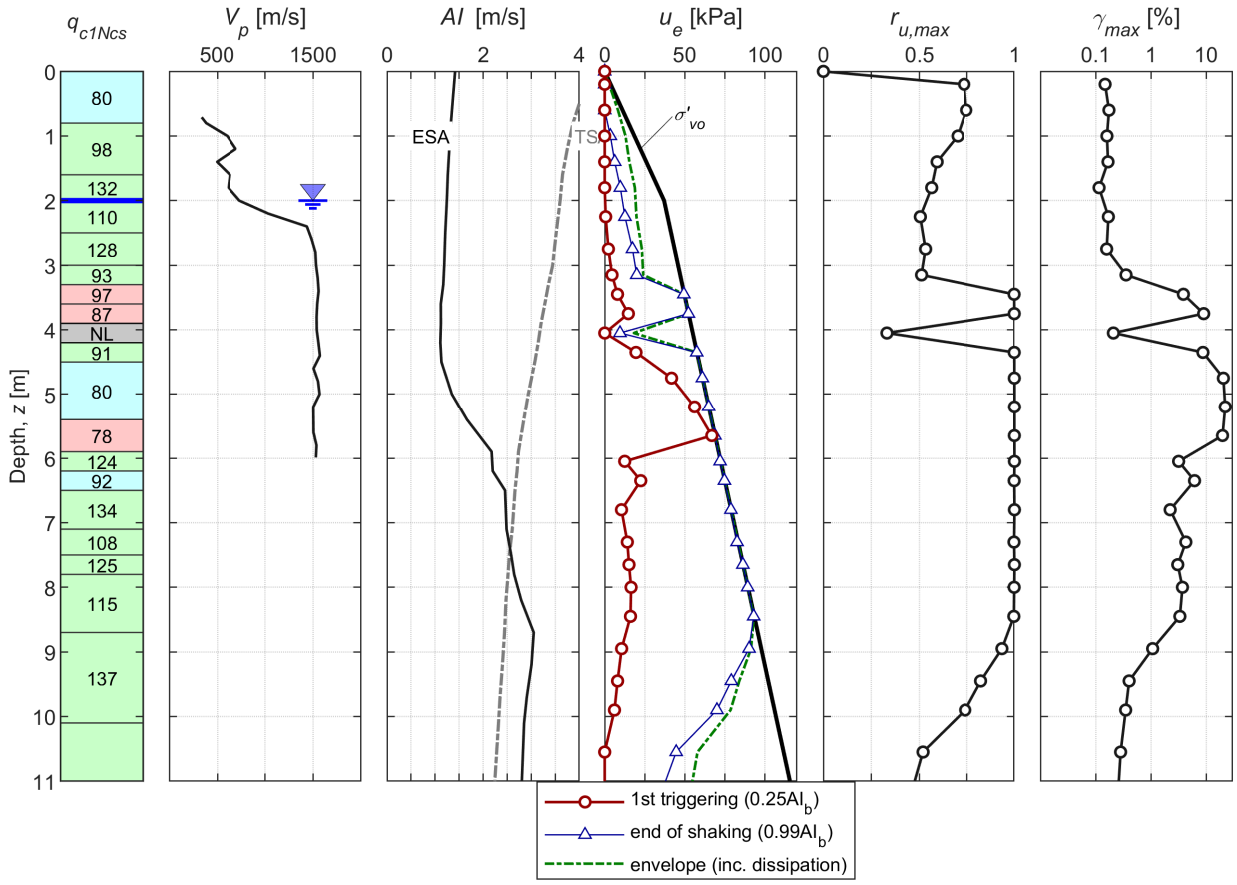

RHSC-based input

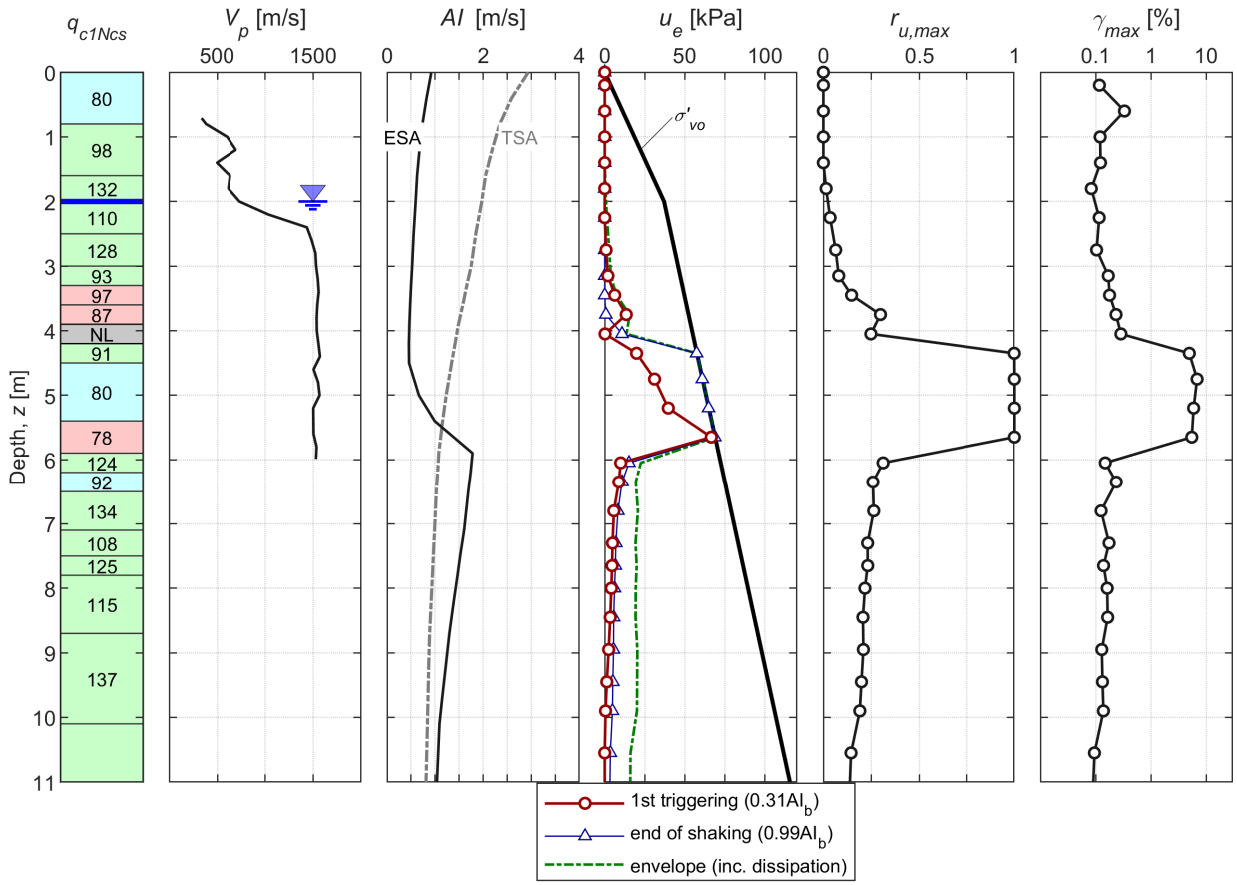

CPT 57350

LPCC-based input

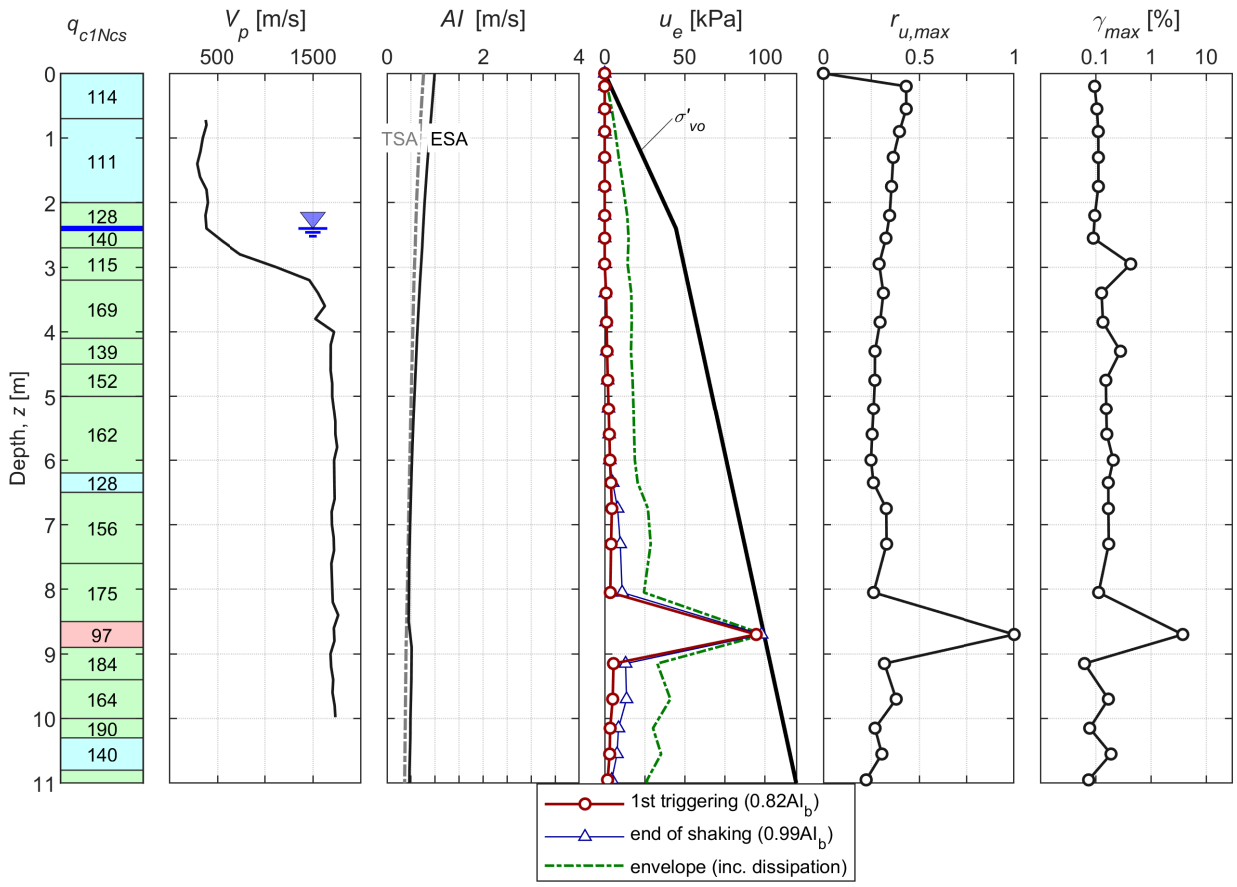

RHSC-based input

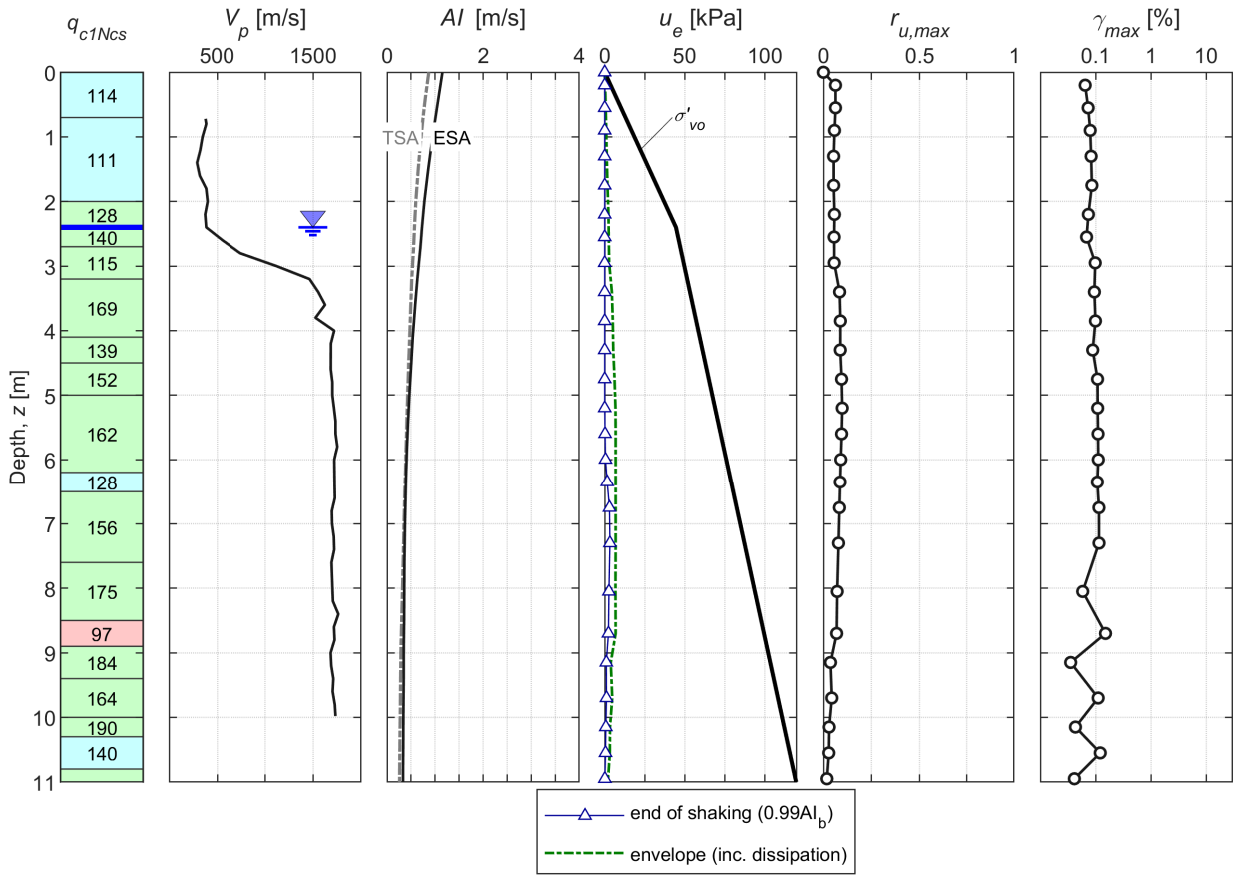

CPT 38752

LPCC-based input

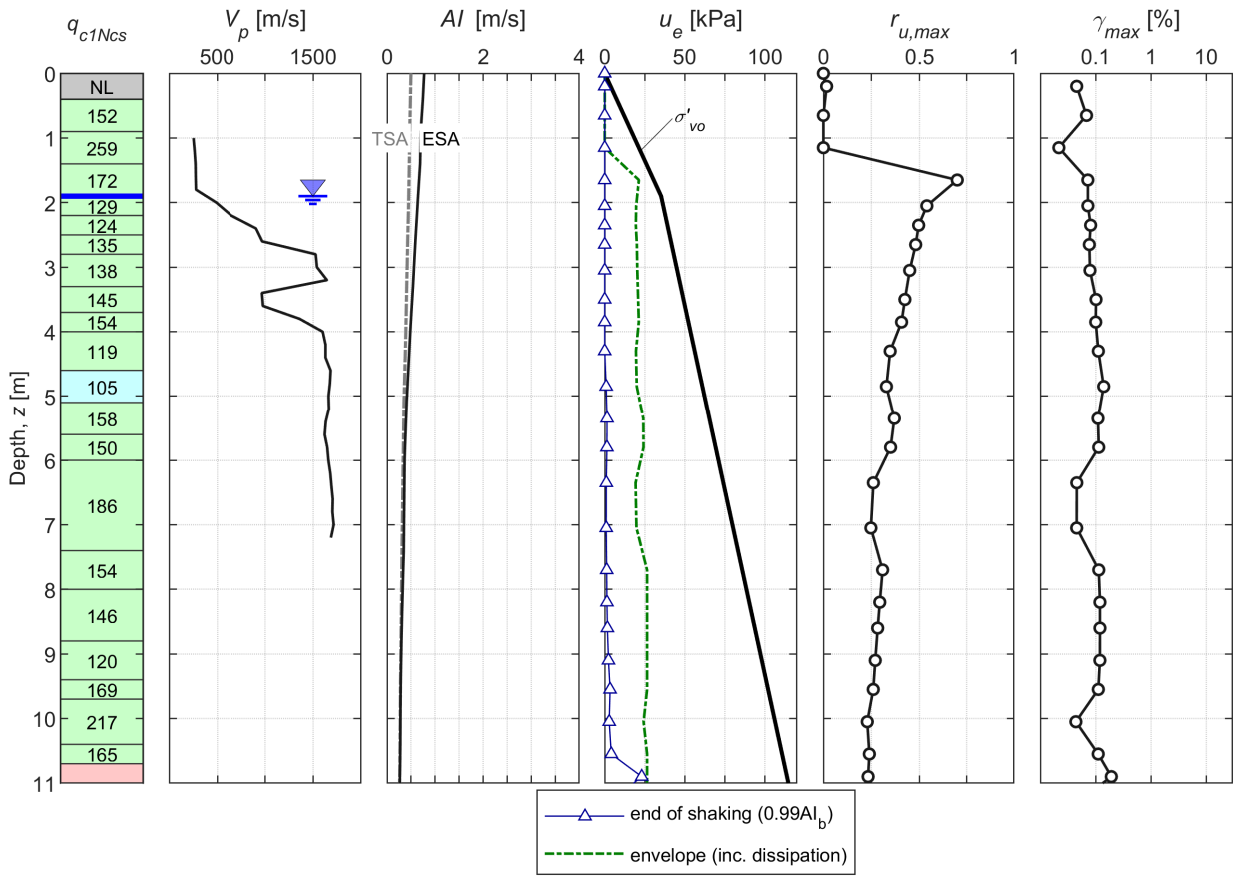

RHSC-based input

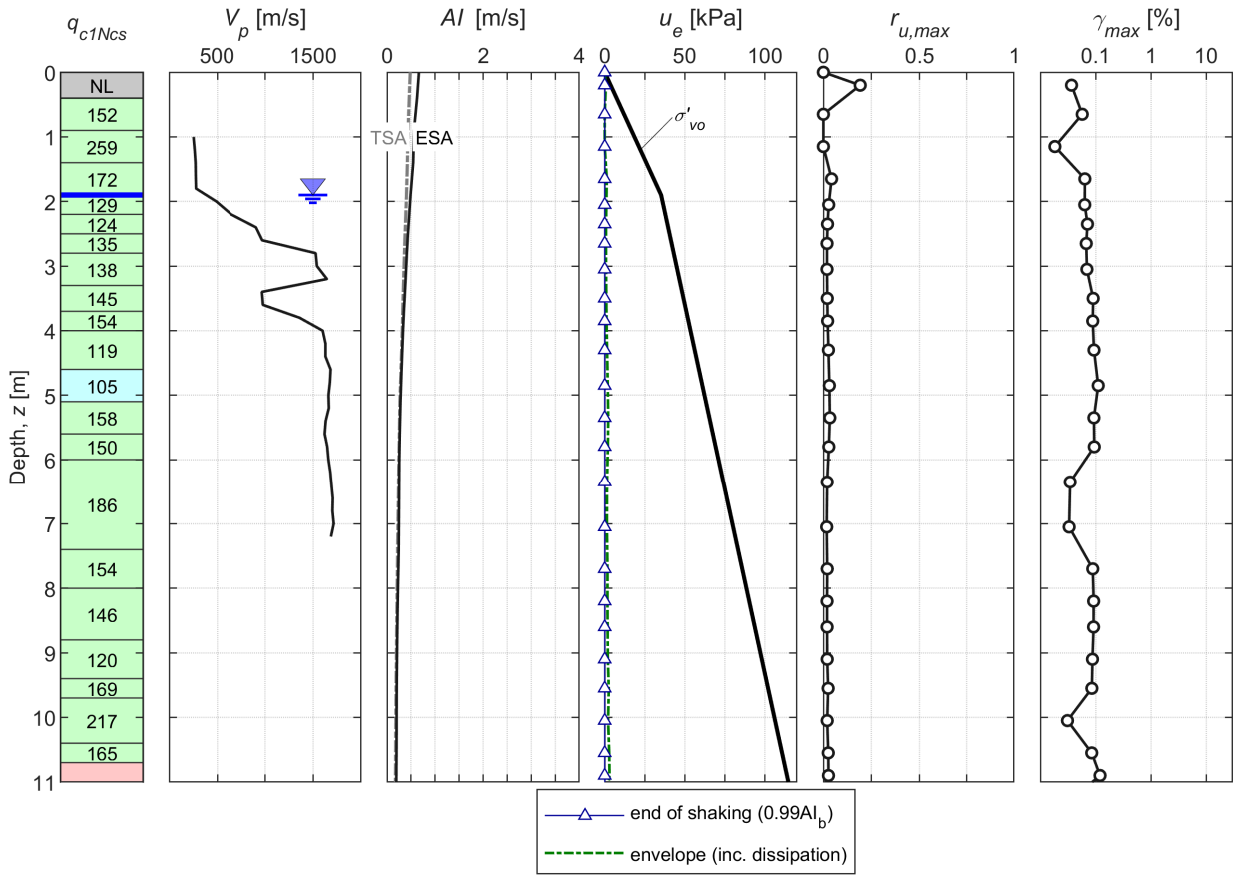

CPT 57366

SMTC-based input

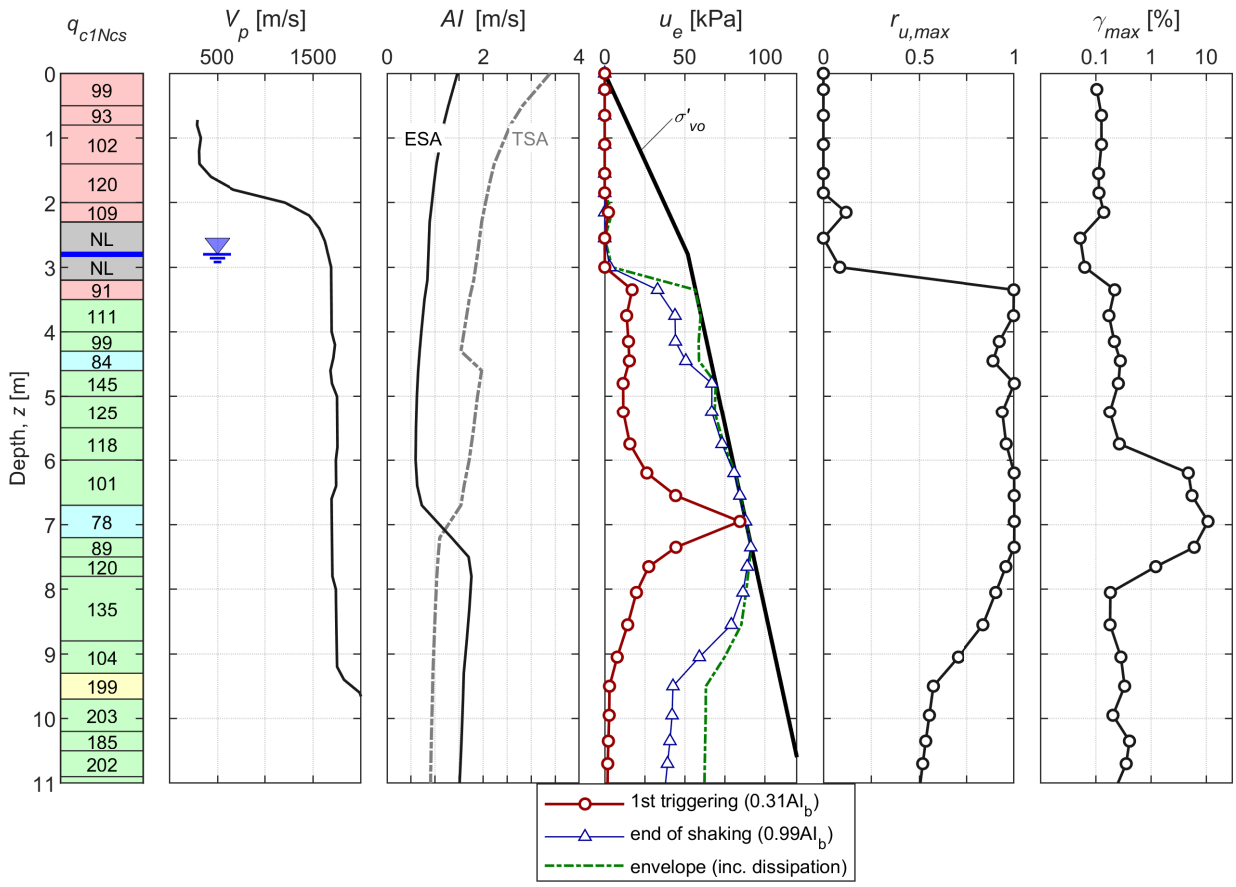

RHSC-based input

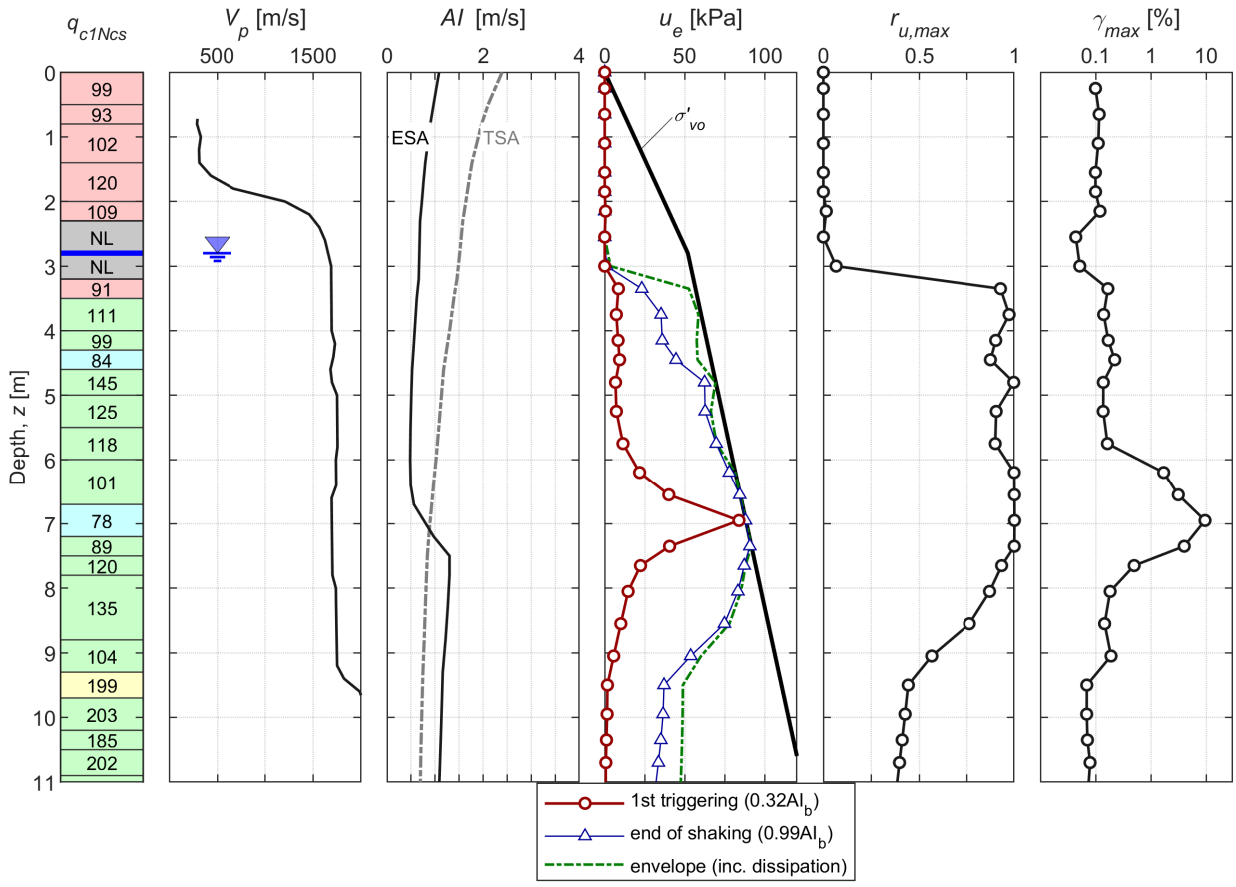

CPT 57346

SMTC-based input

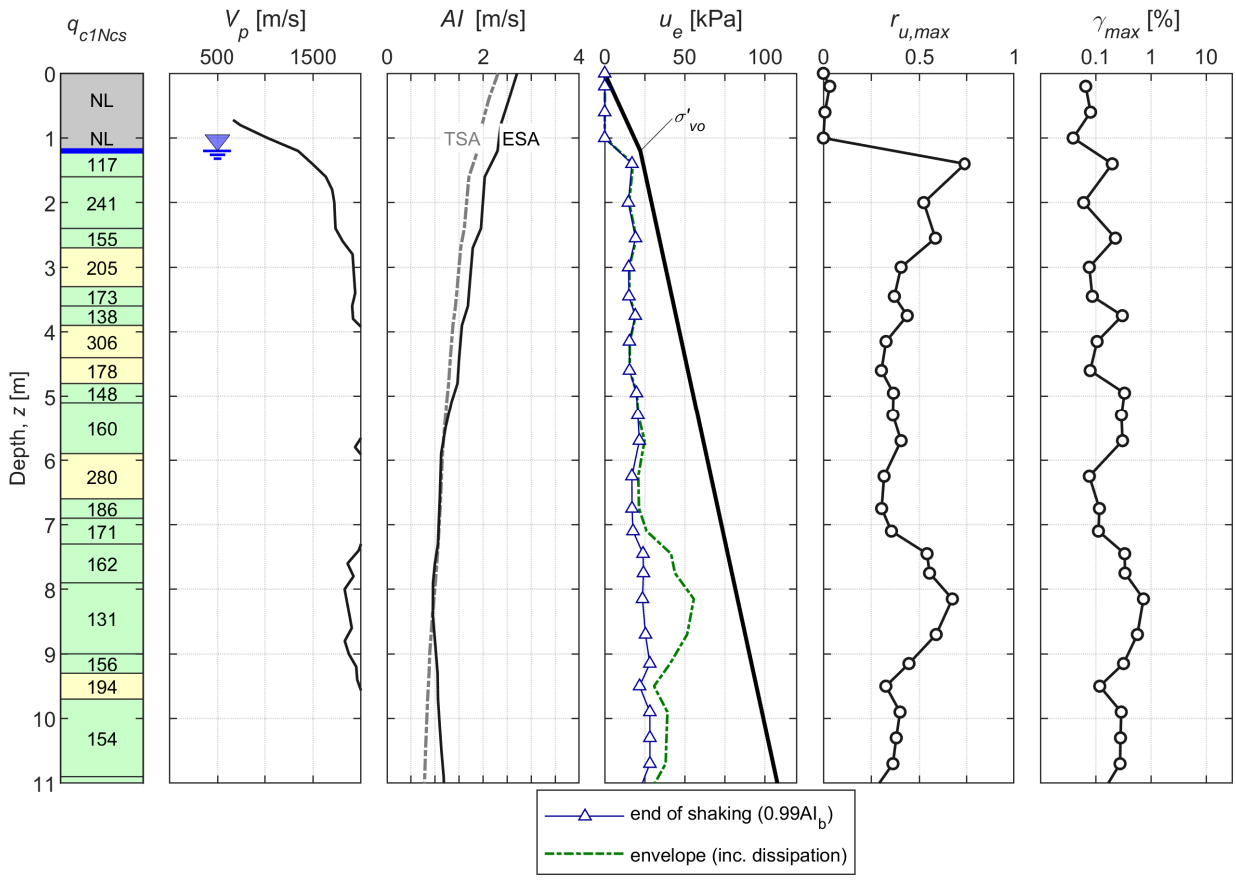

RHSC-based input

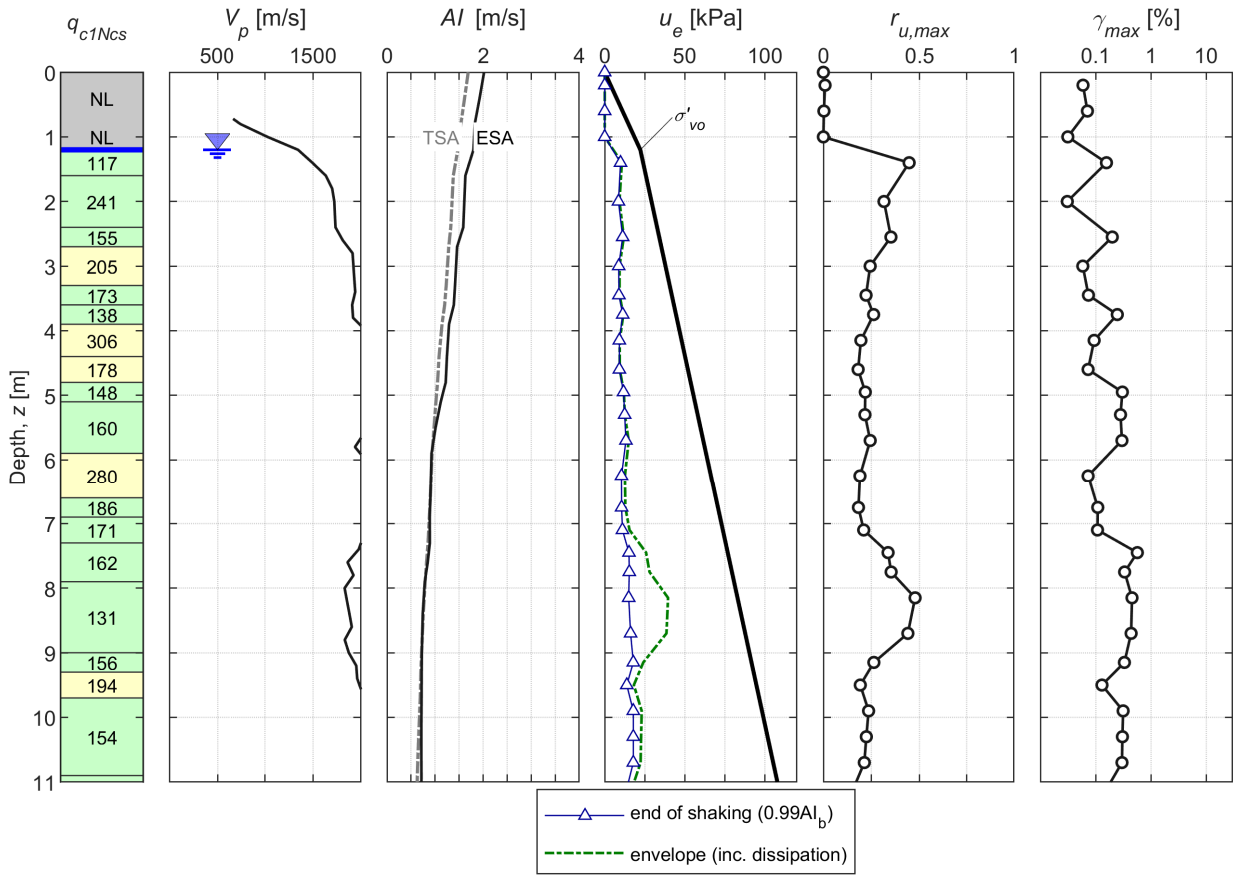

CPT 57362

SMTC-based input

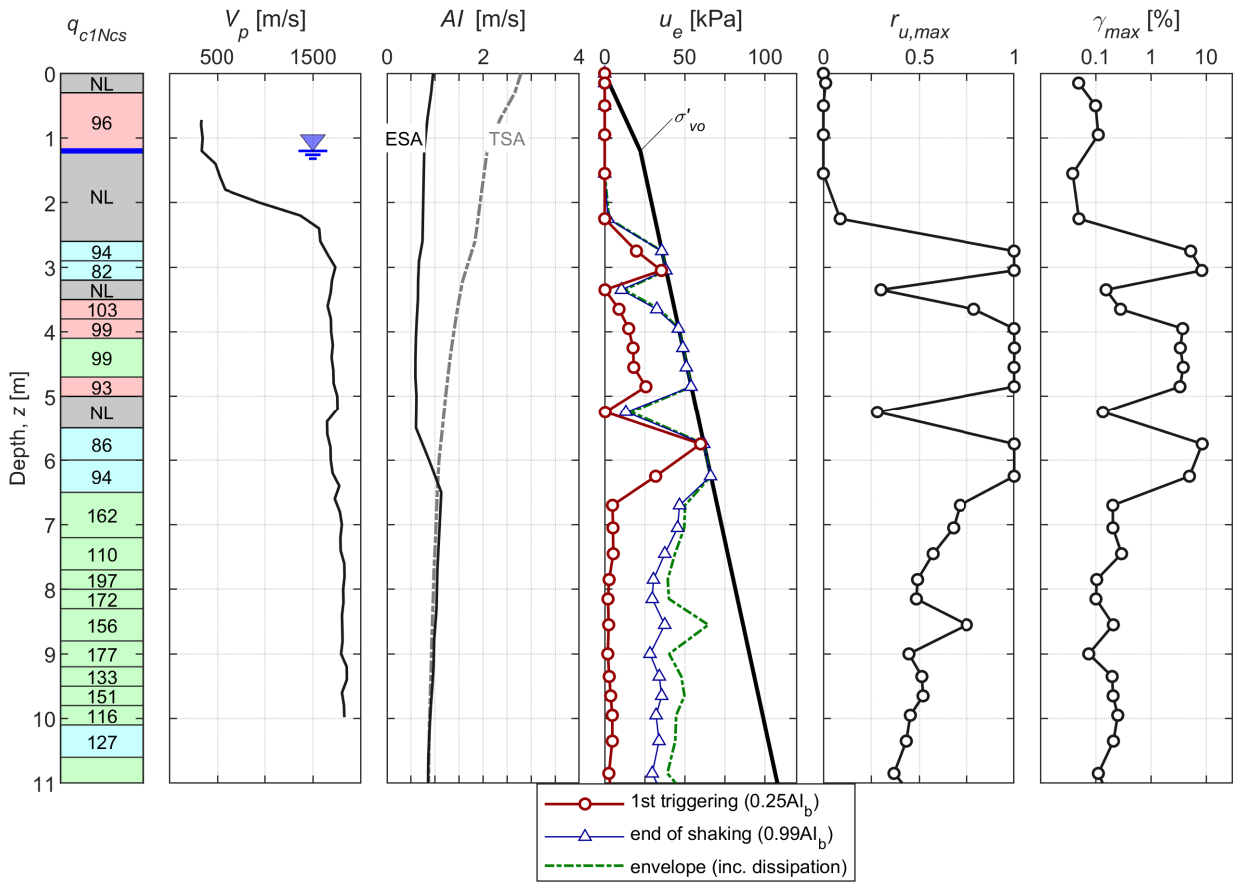

RHSC-based input

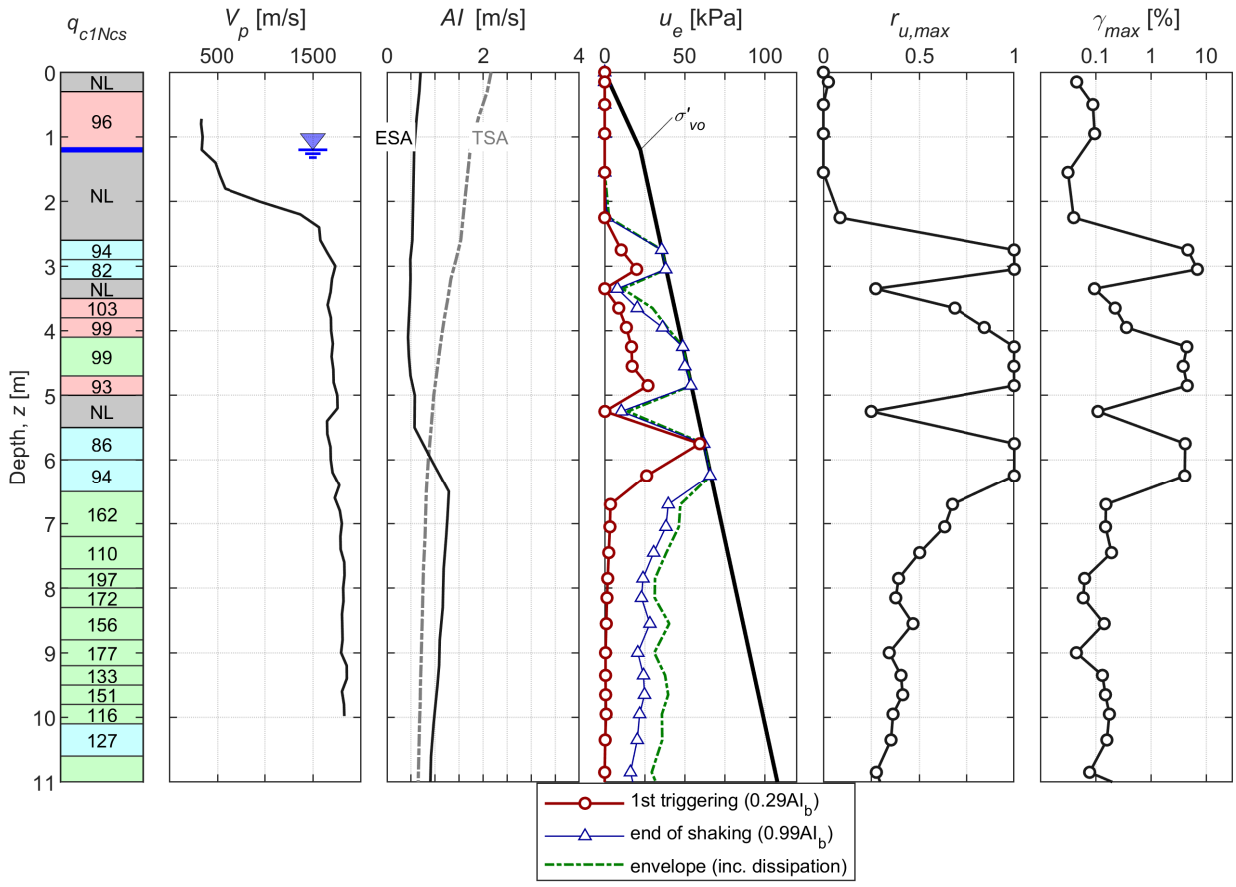

CPT 57341

LPCC-based input

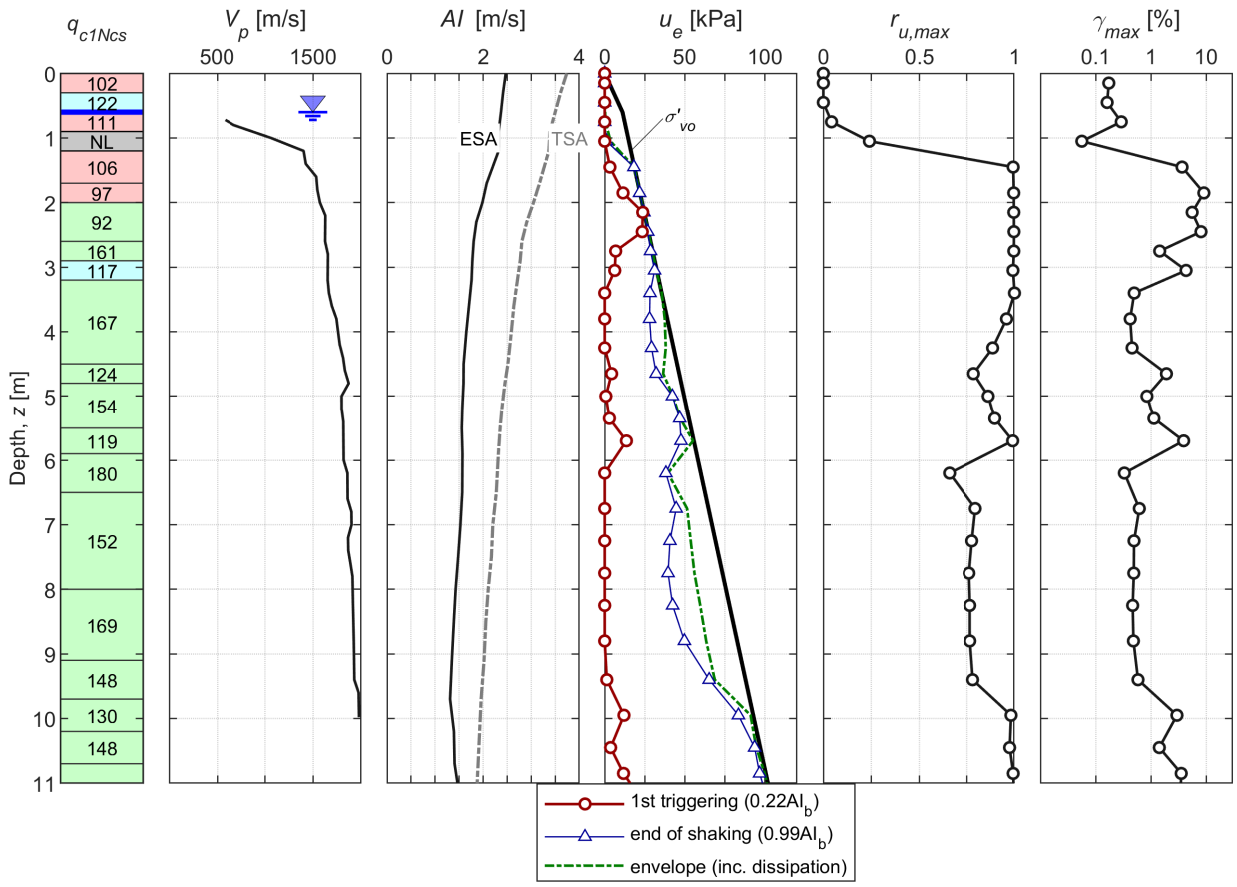

RHSC-based input

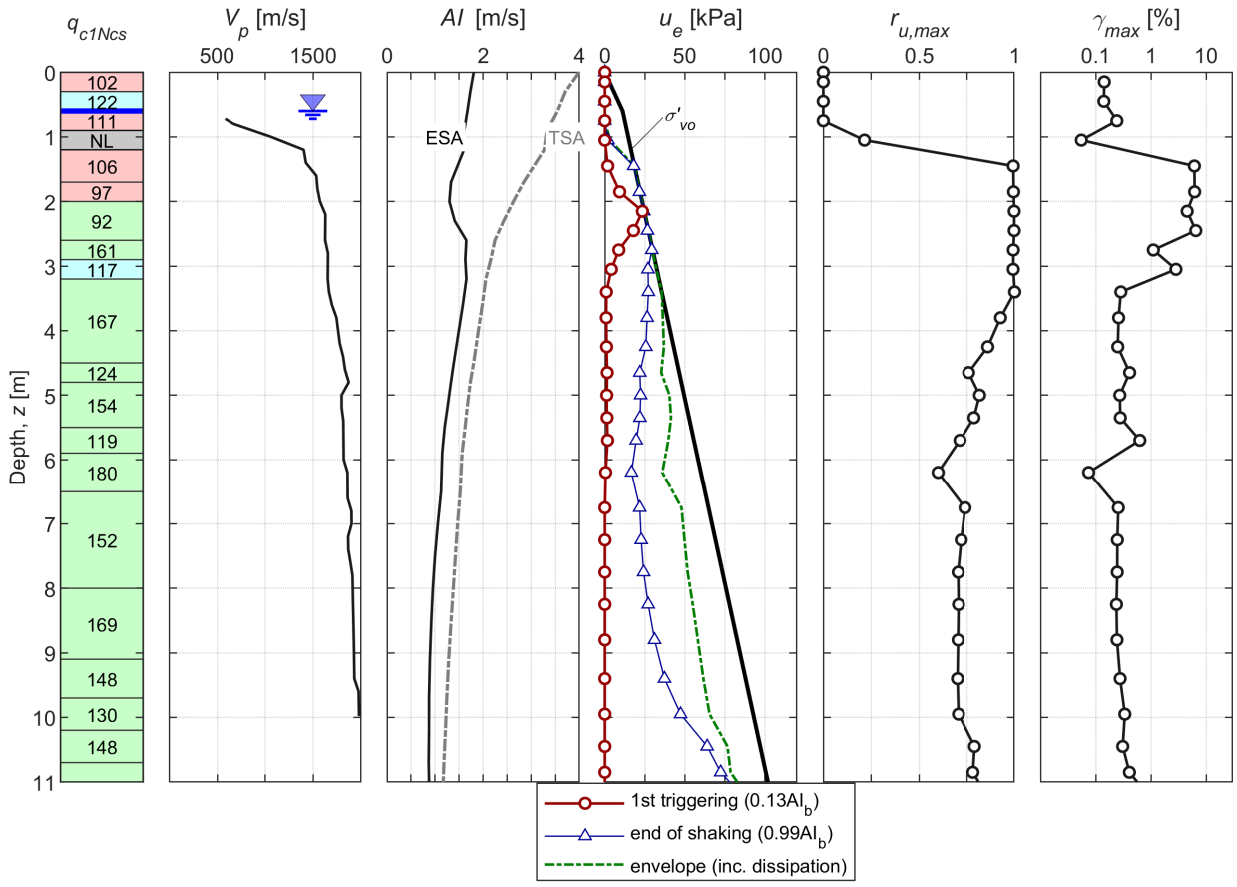

CPT 57360

LPCC-based input

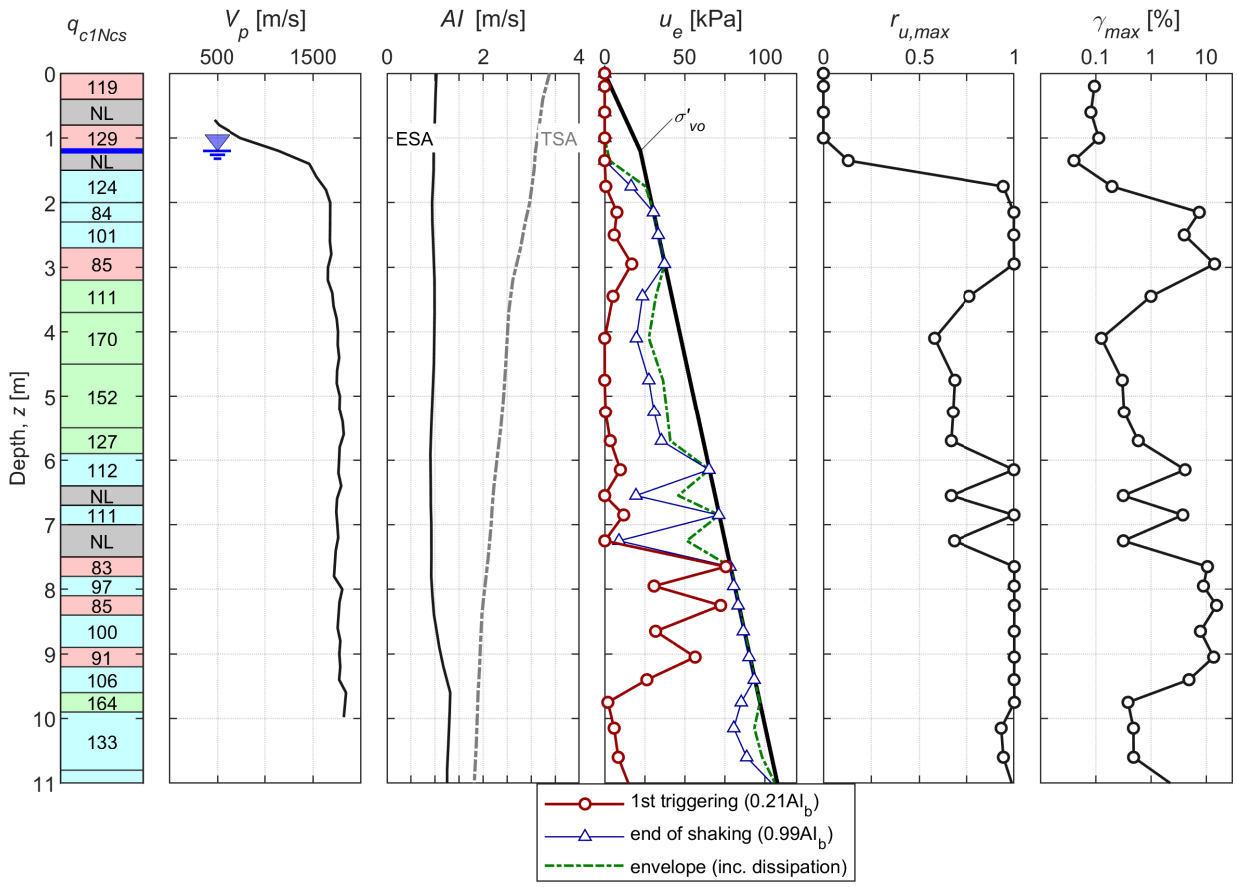

RHSC-based input

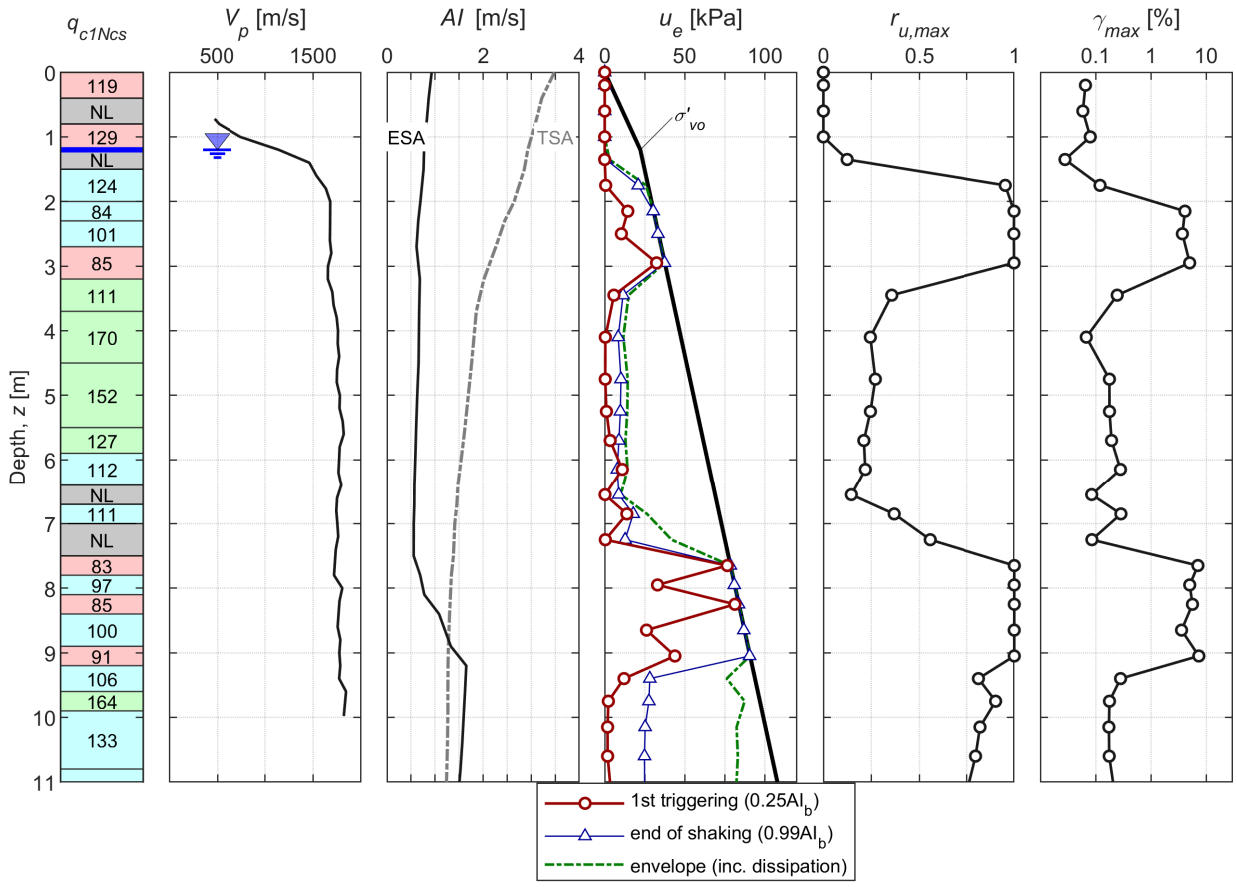

CPT 57365

LPCC-based input

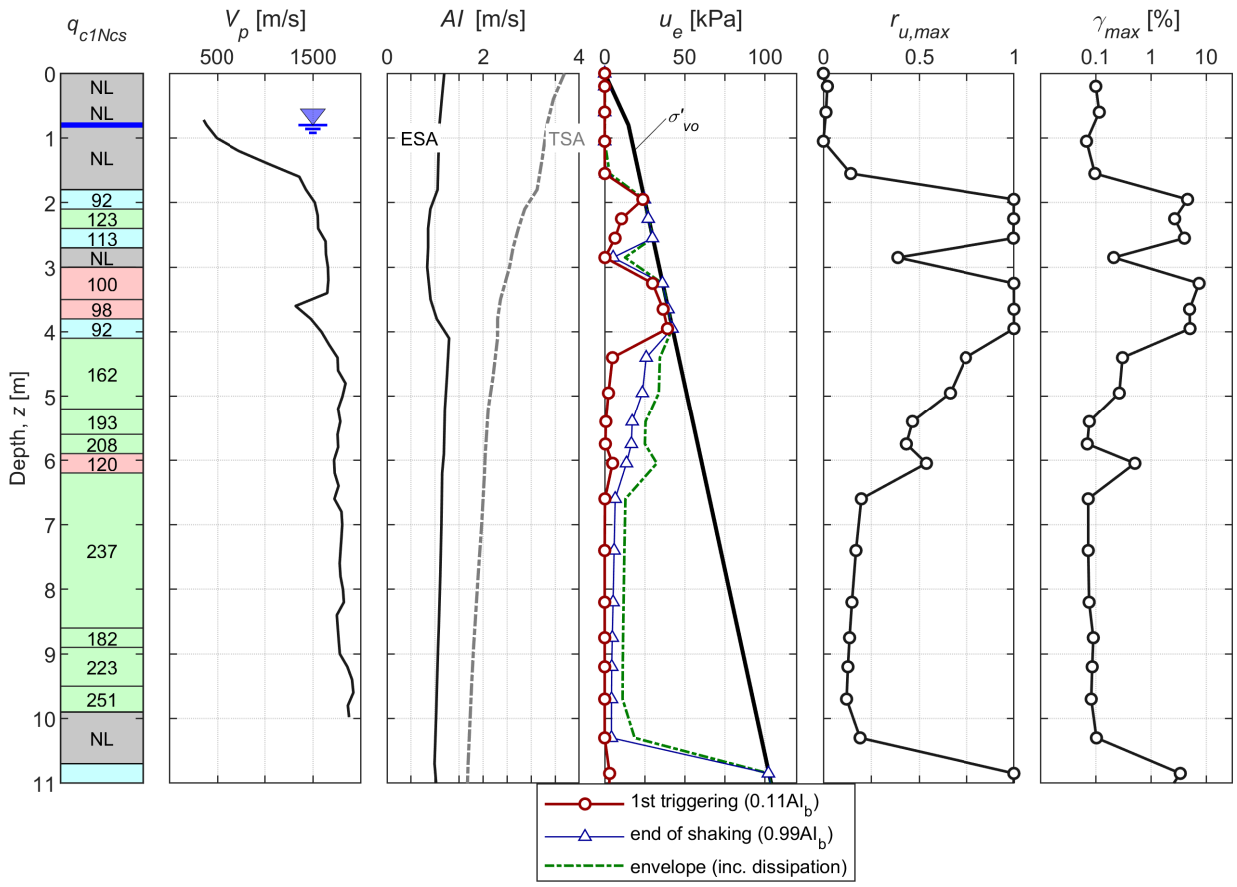

RHSC-based input

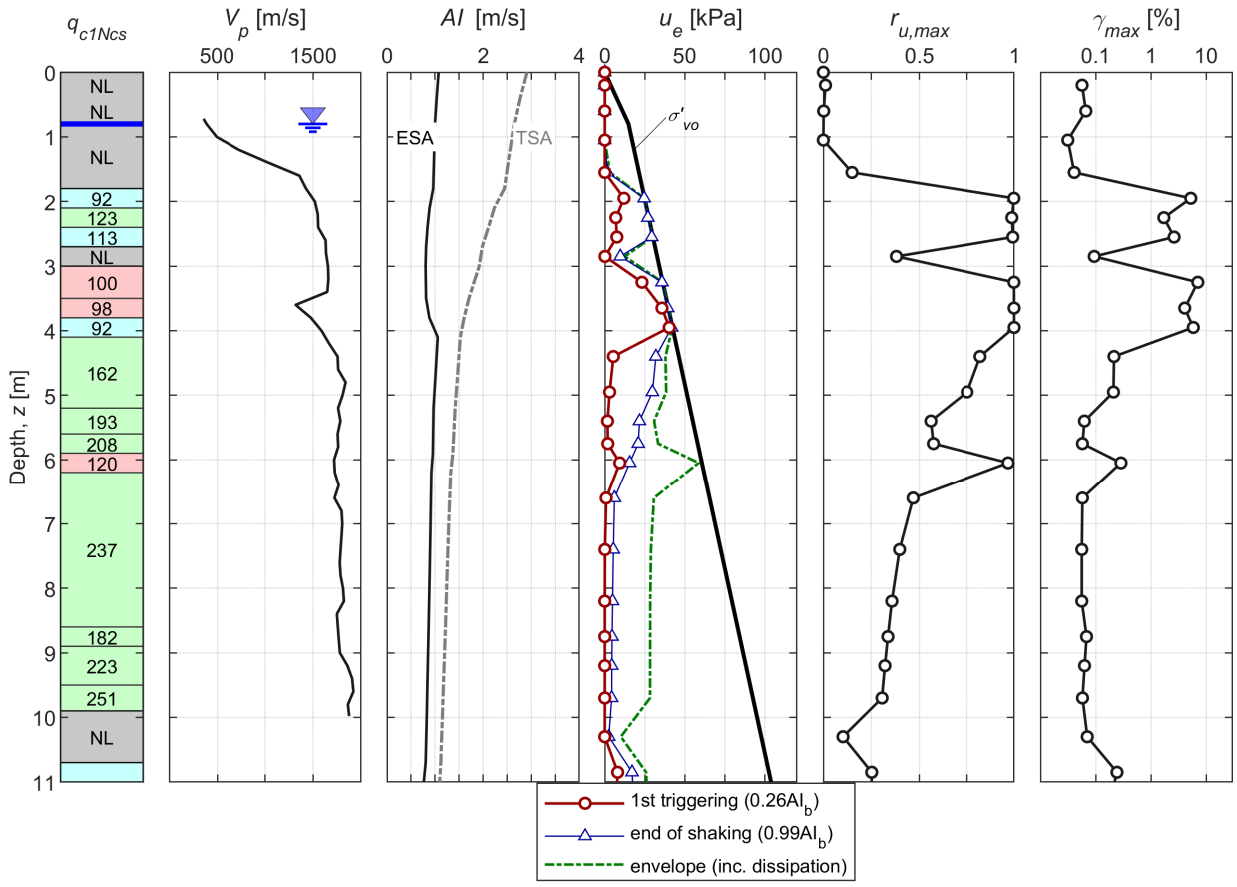

CPT 57357

LPCC-based input

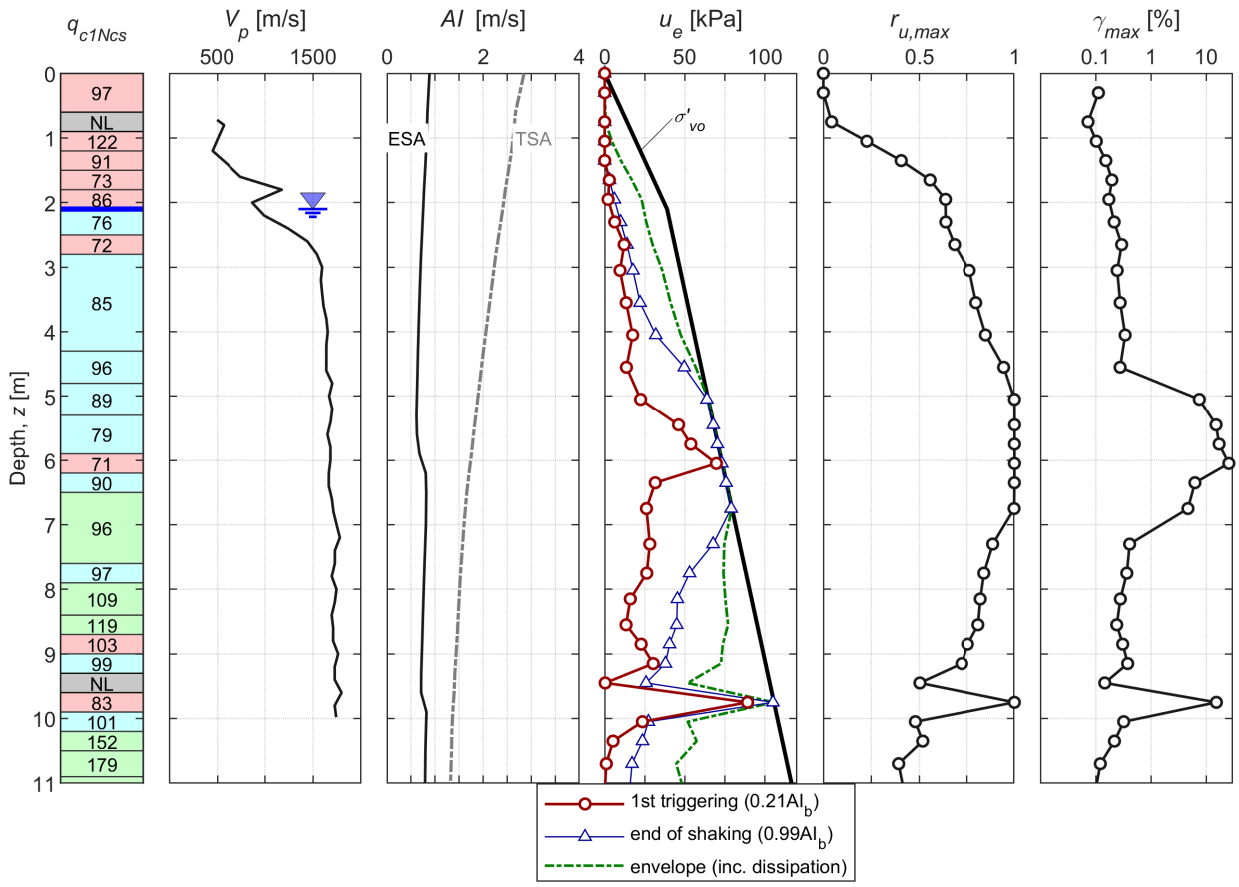

RHSC-based input

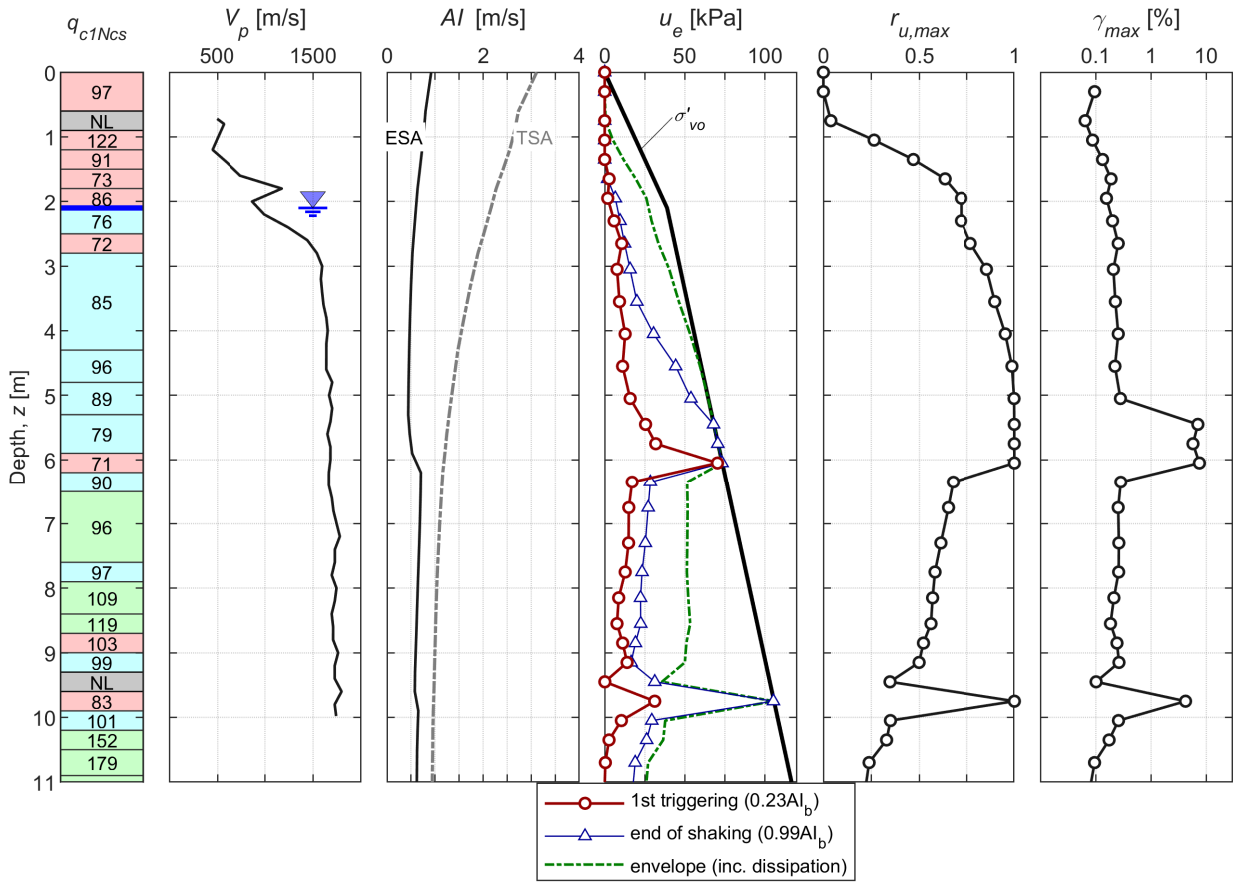

CPT 57356

LPCC-based input

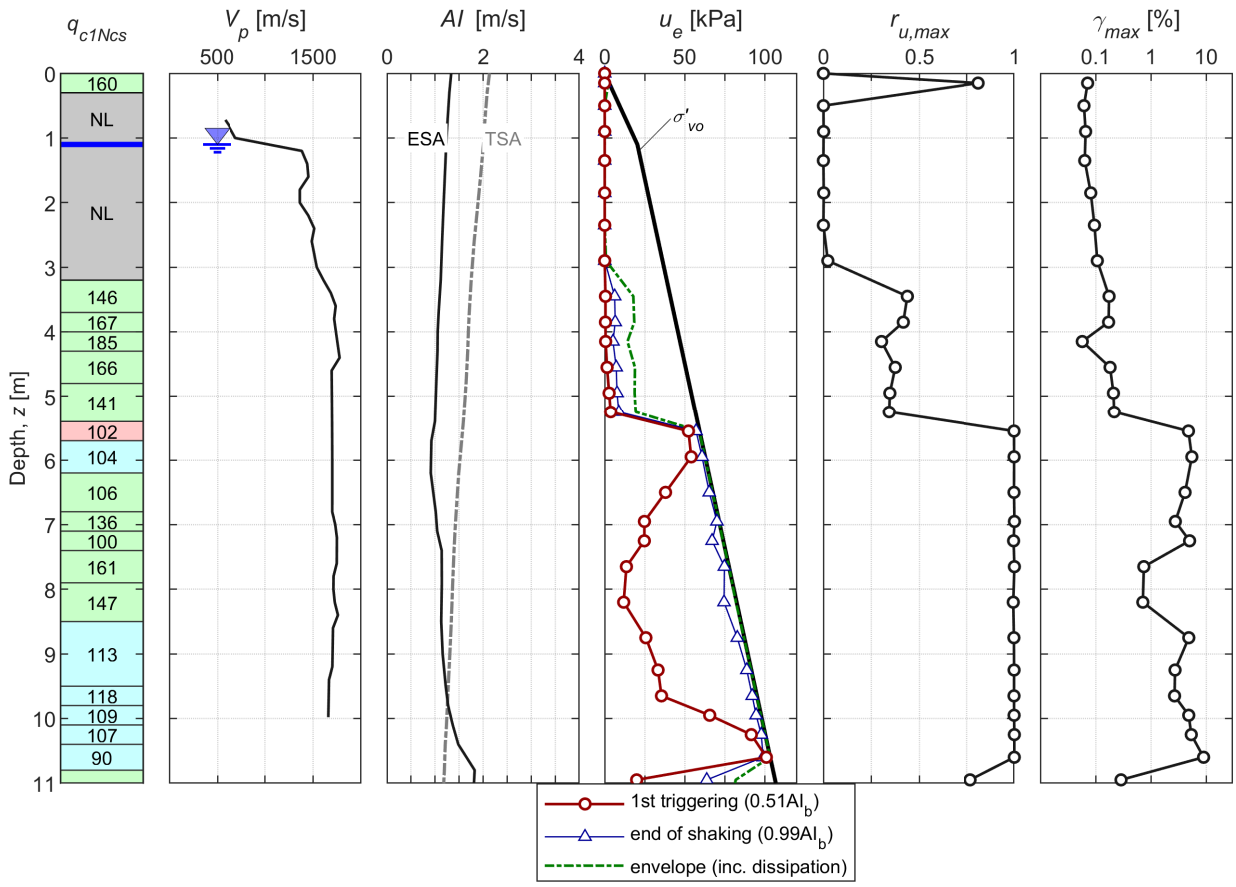

RHSC-based input

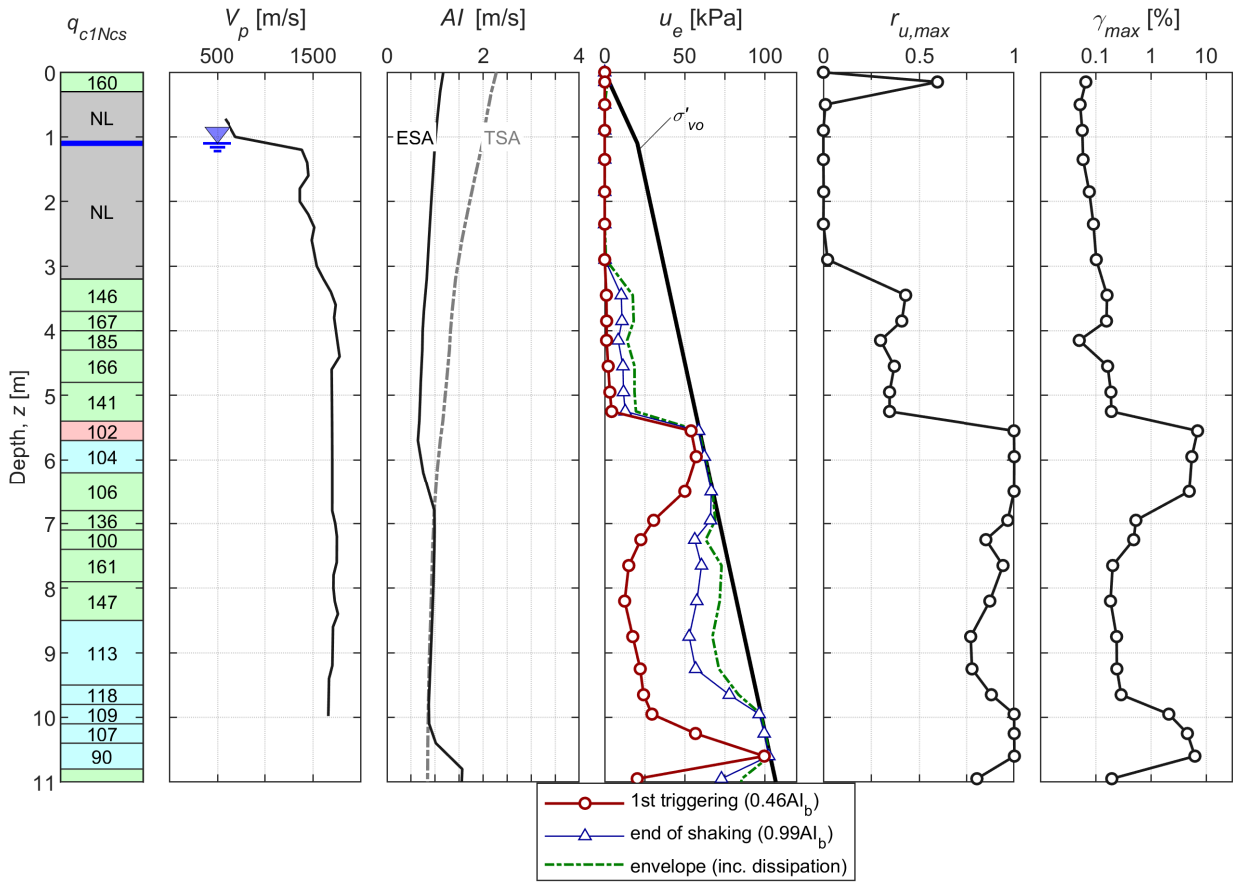

CPT 57355

LPCC-based input

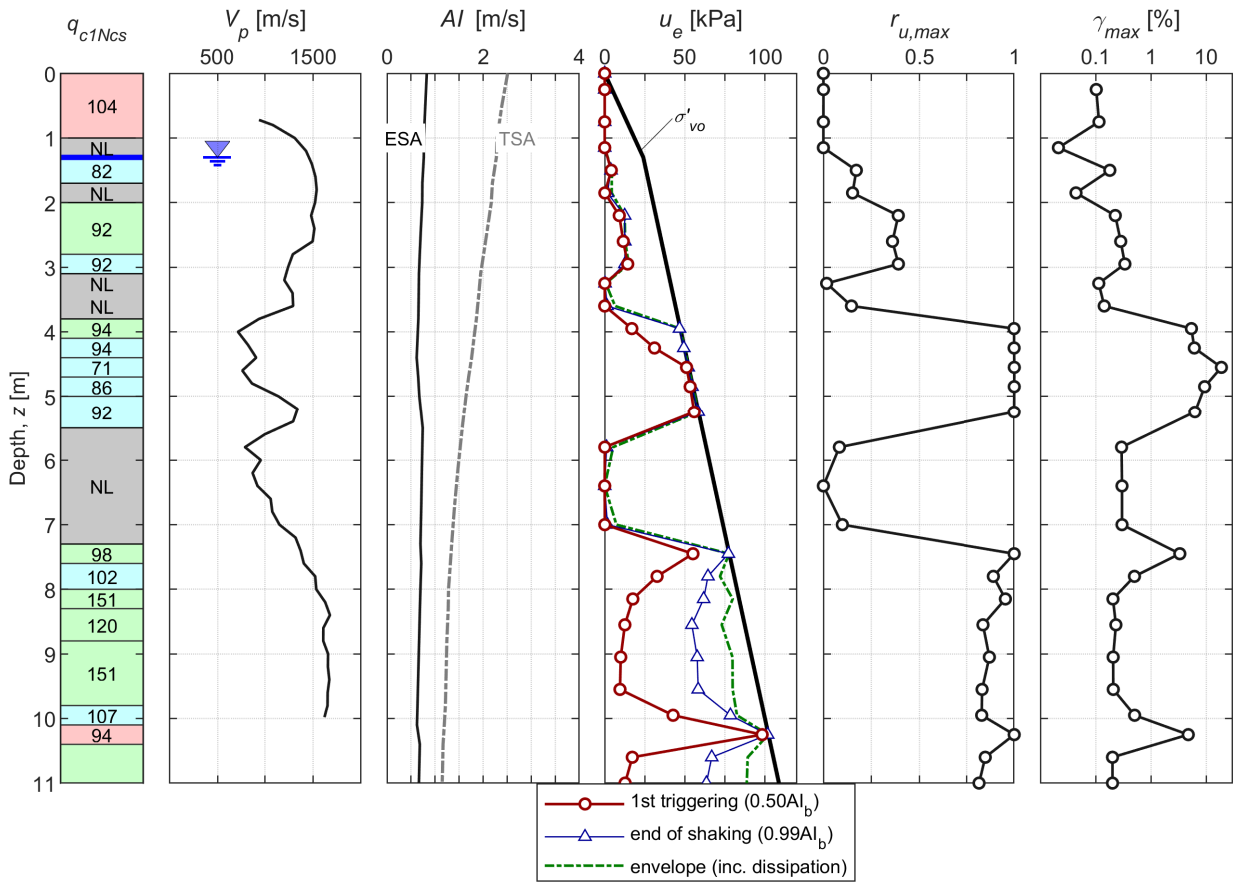

RHSC-based input

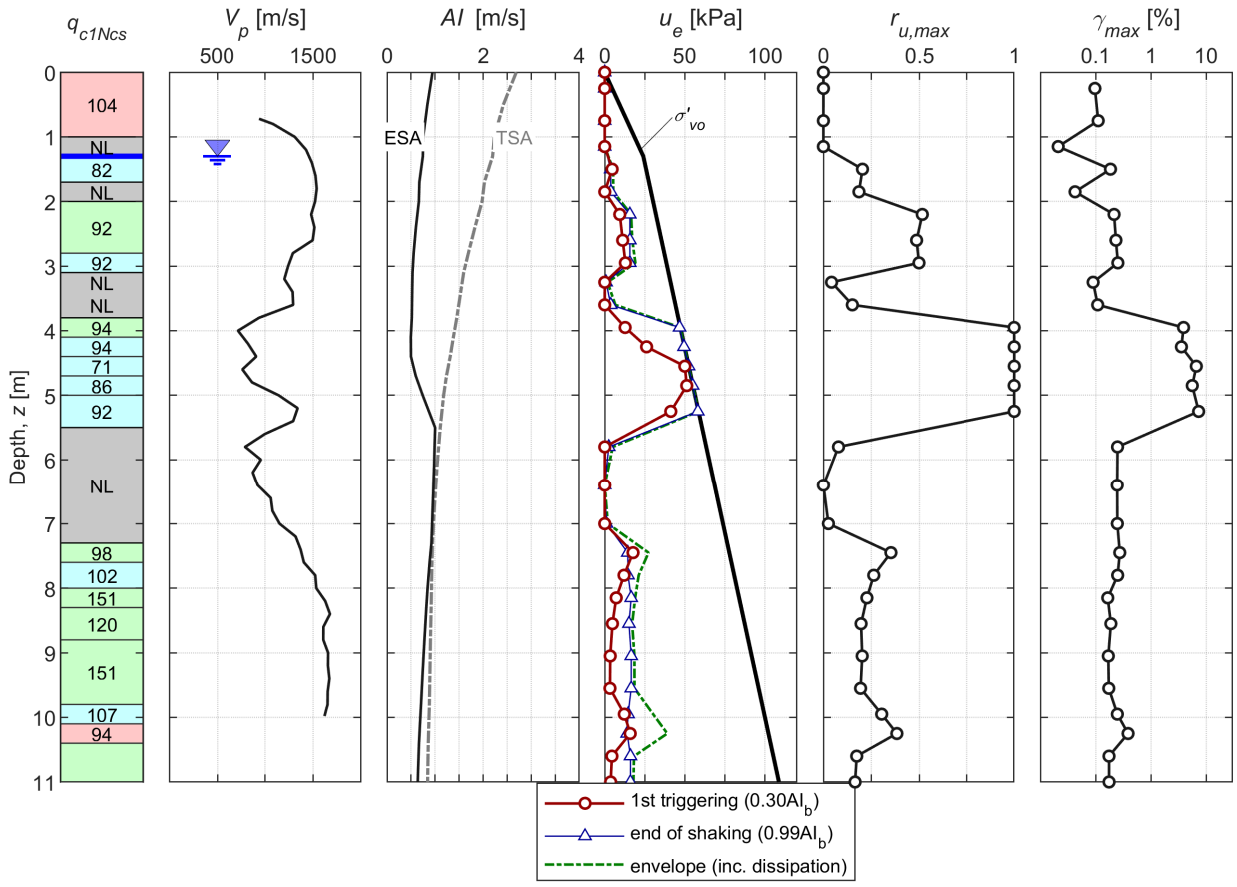

CPT 57353

LPCC-based input

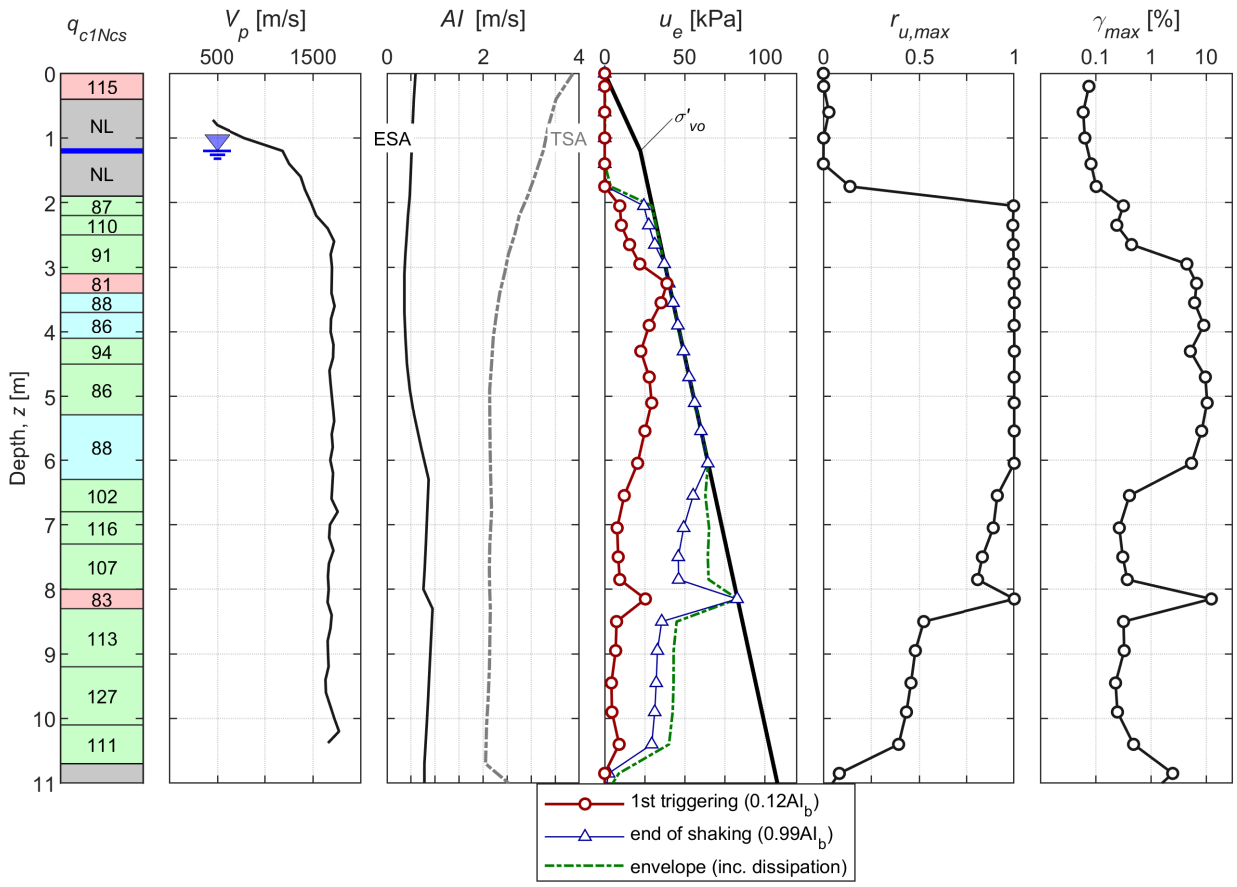

RHSC-based input

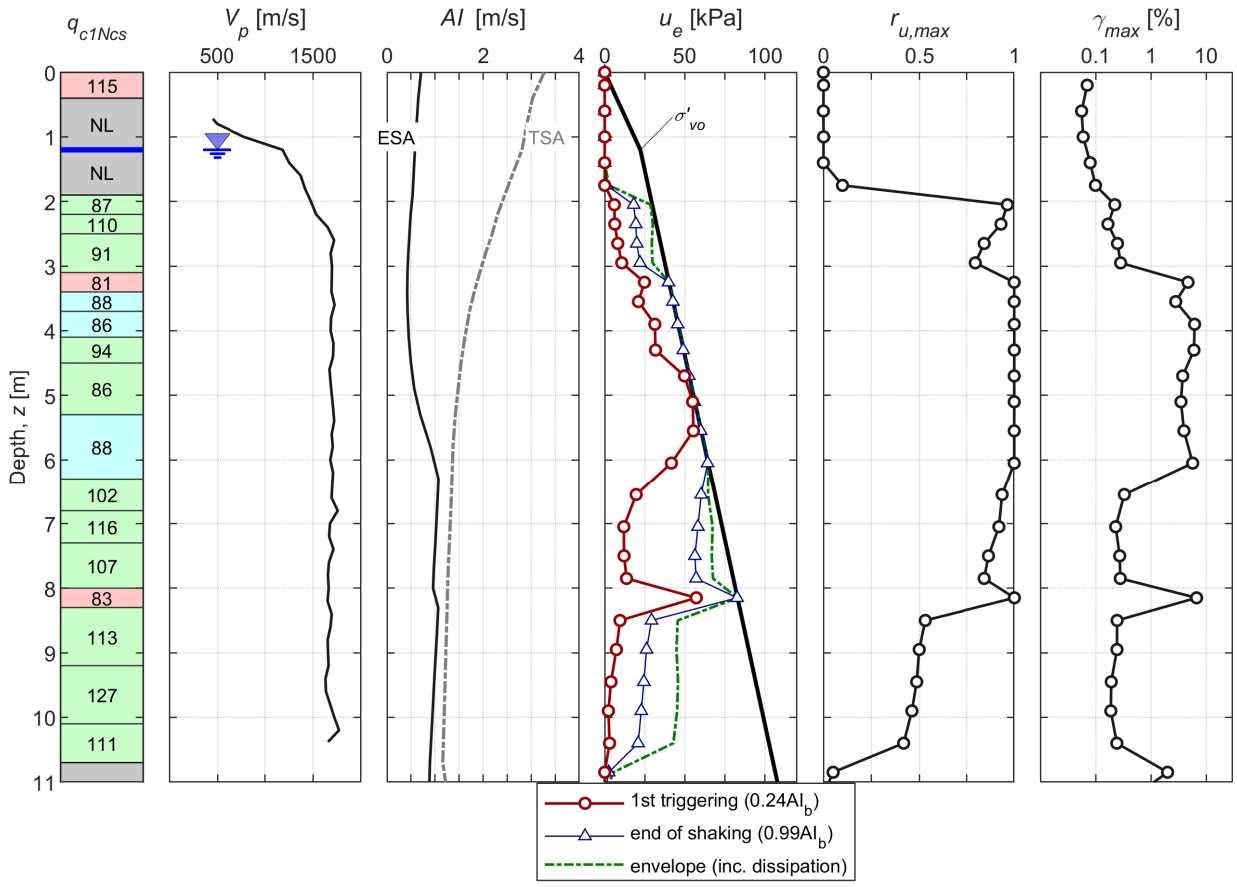

CPT 638

LPCC-based input

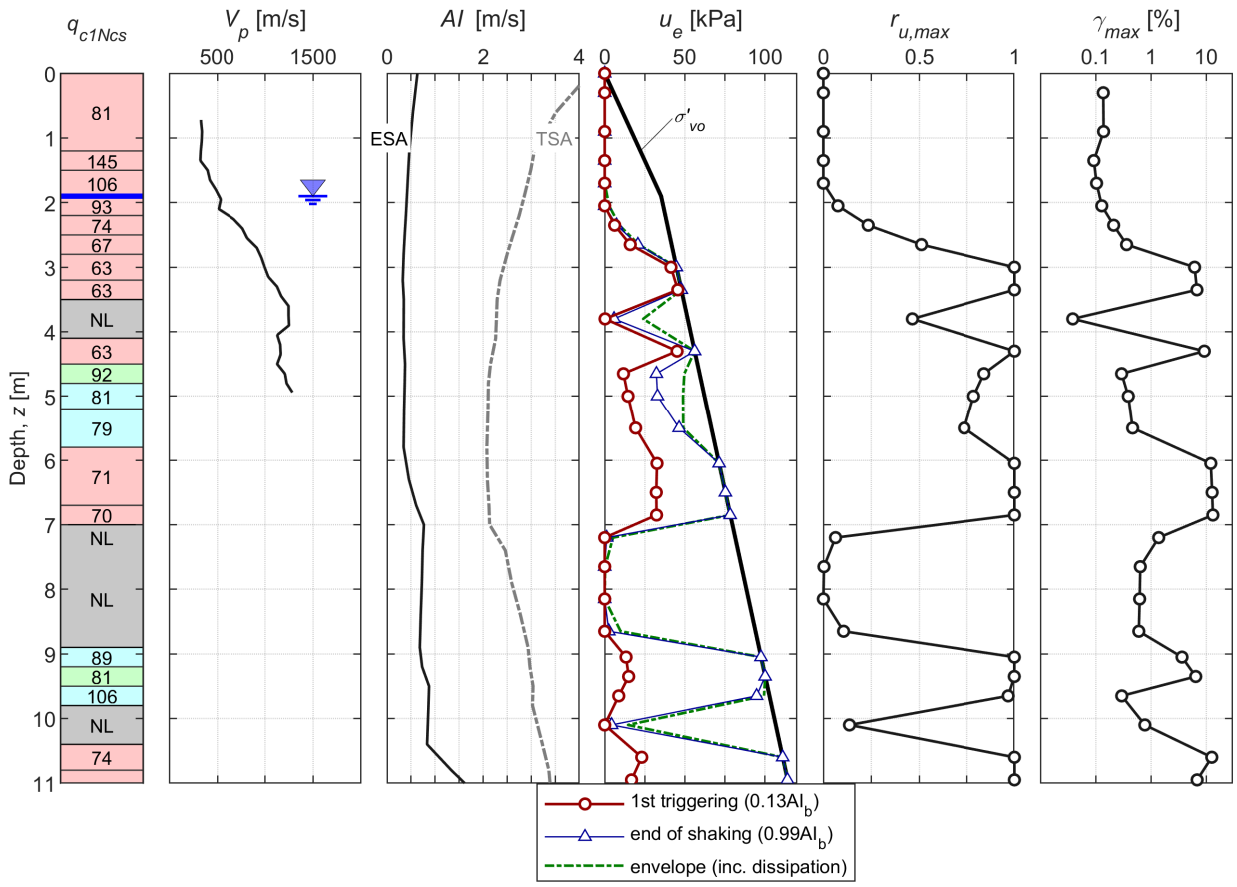

RHSC-based input

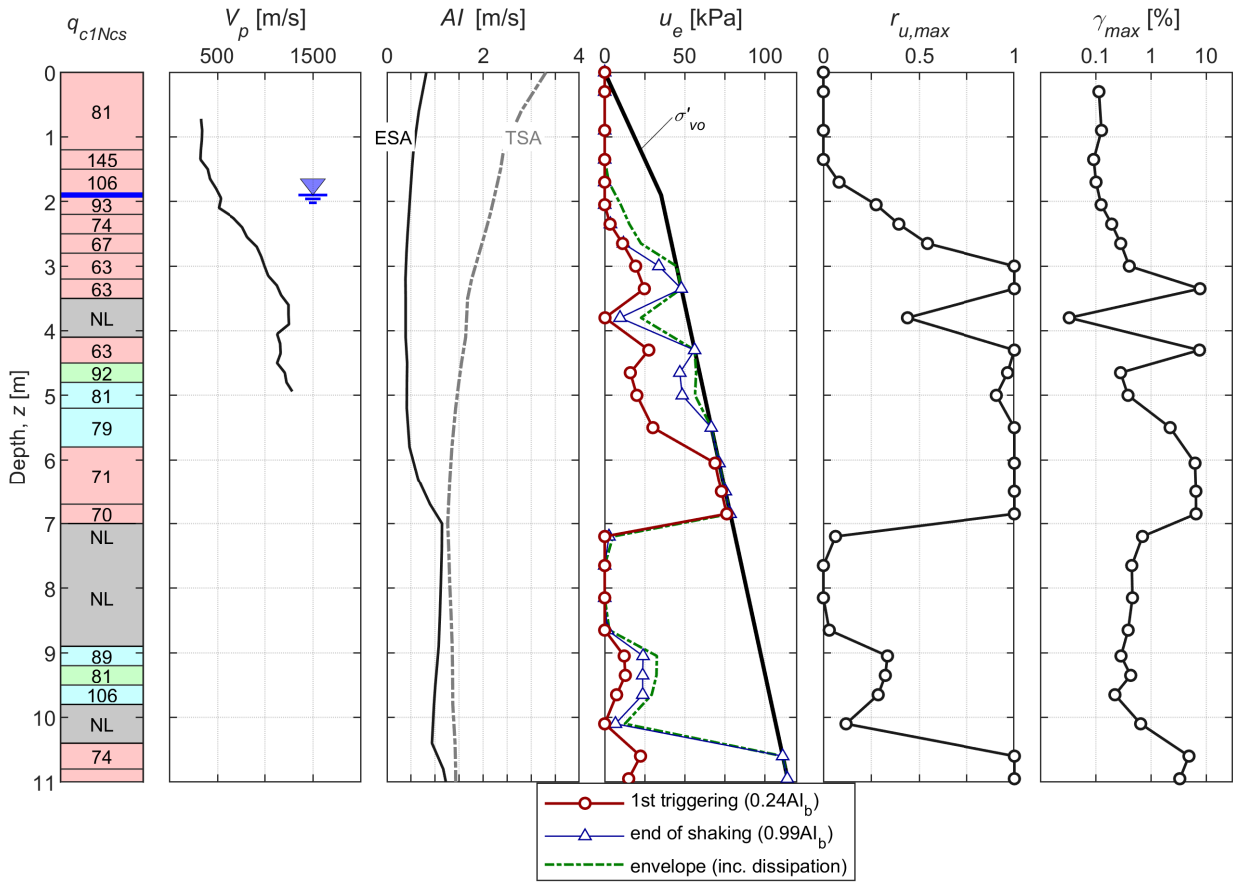

CPT 37818

LPCC-based input

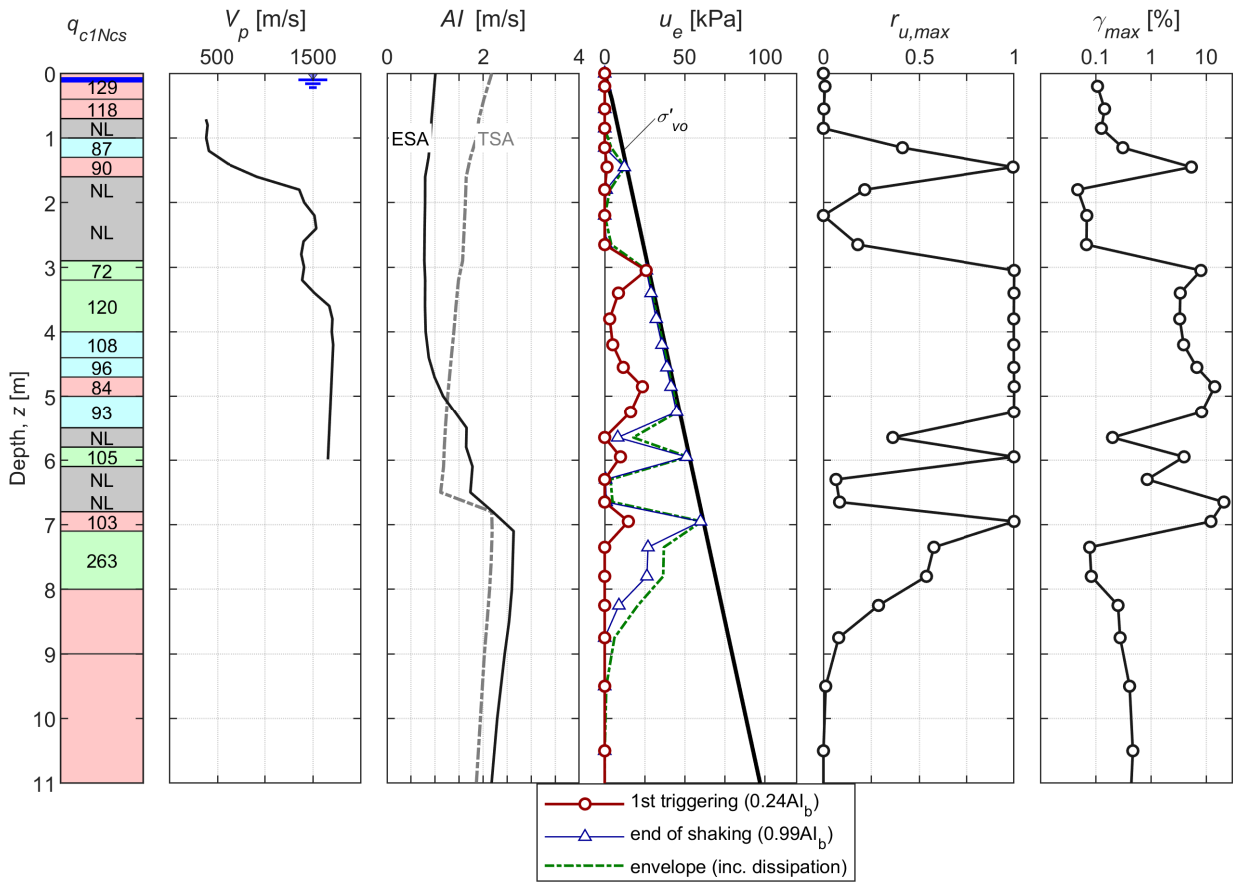

RHSC-based input

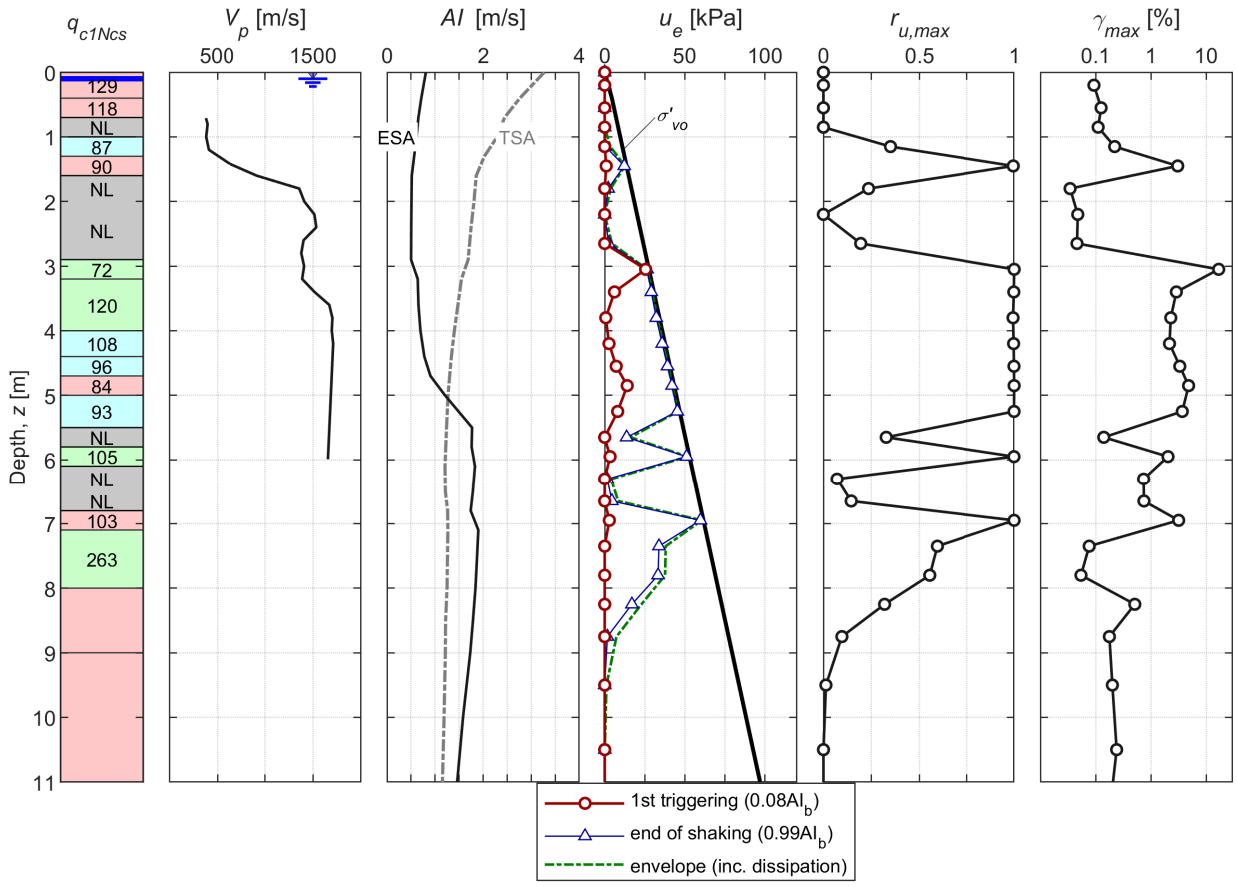

CPT 57344

LPCC-based input

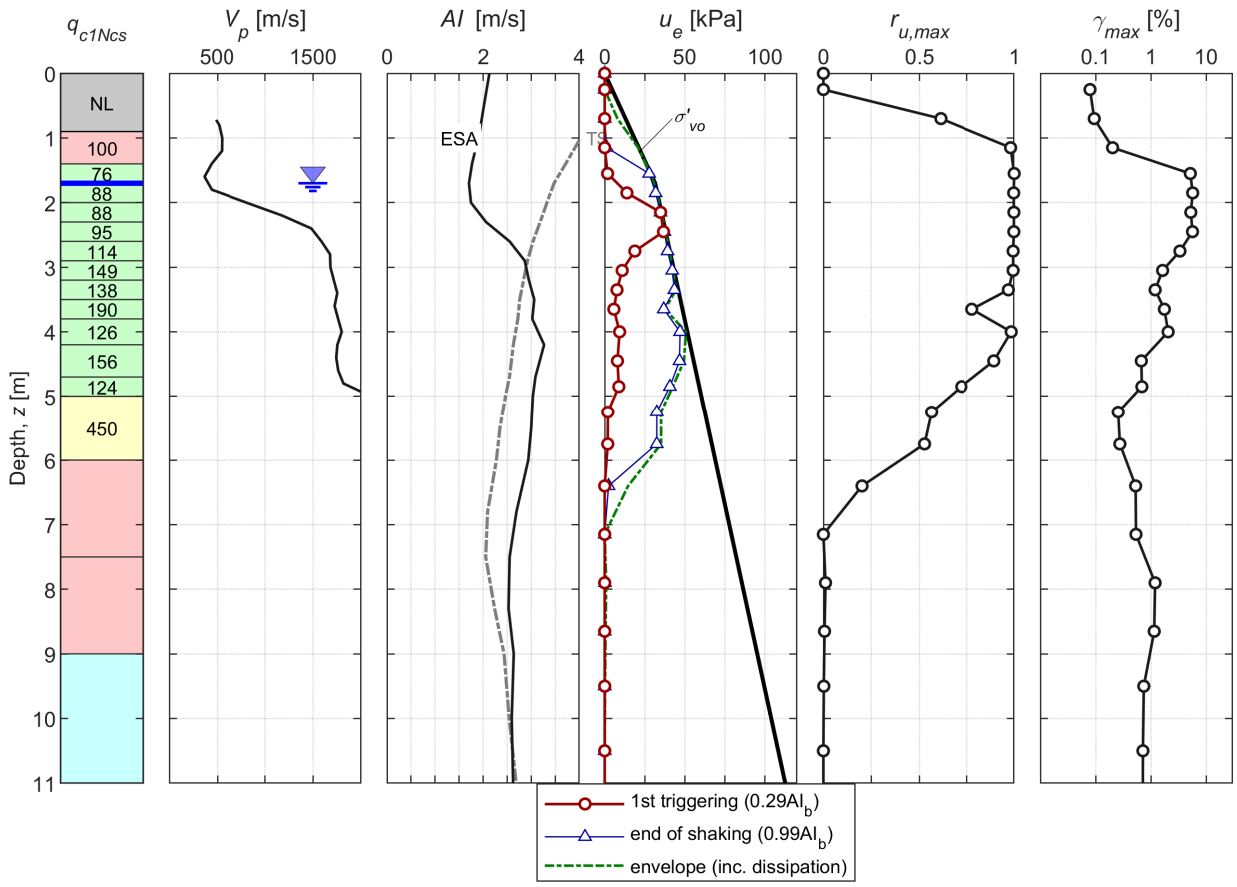

RHSC-based input

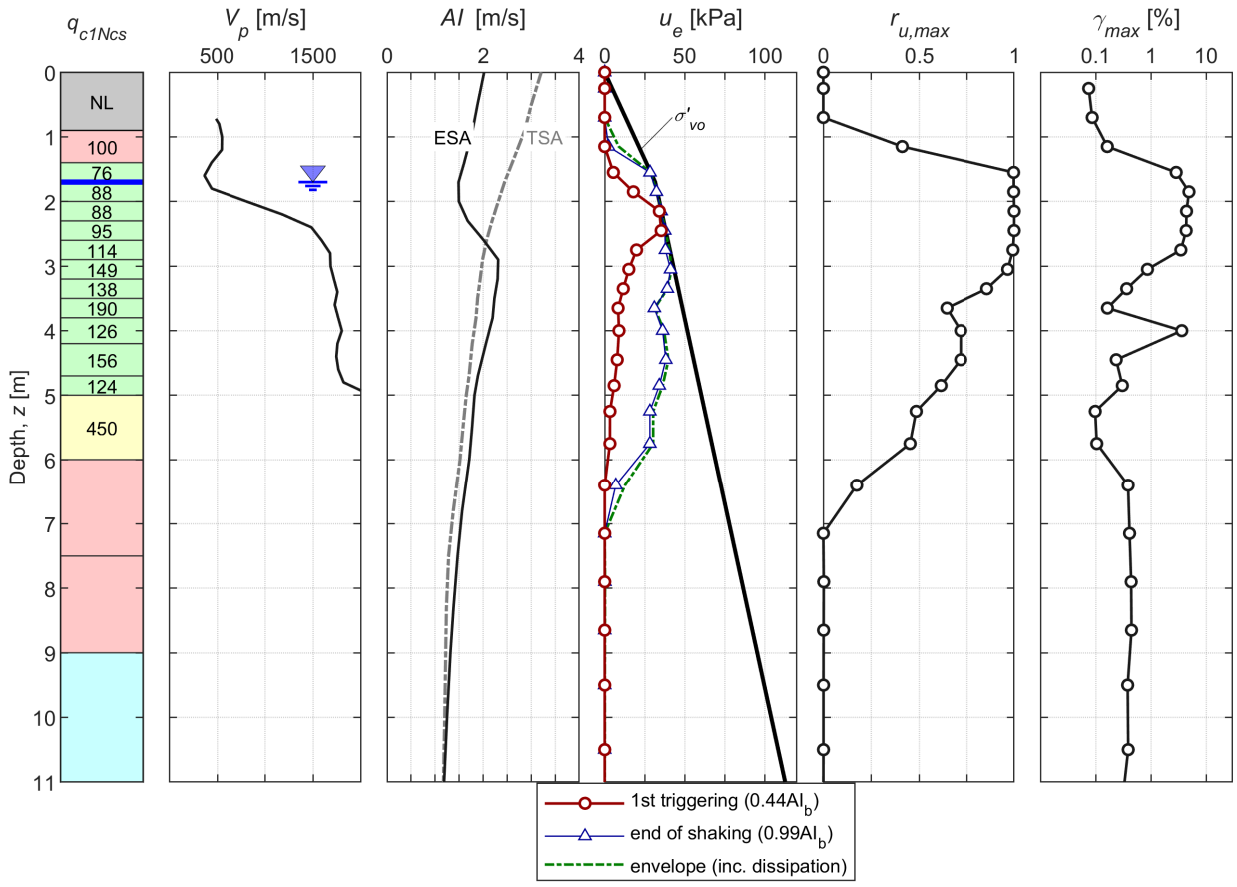

CPT 57340

LPCC-based input

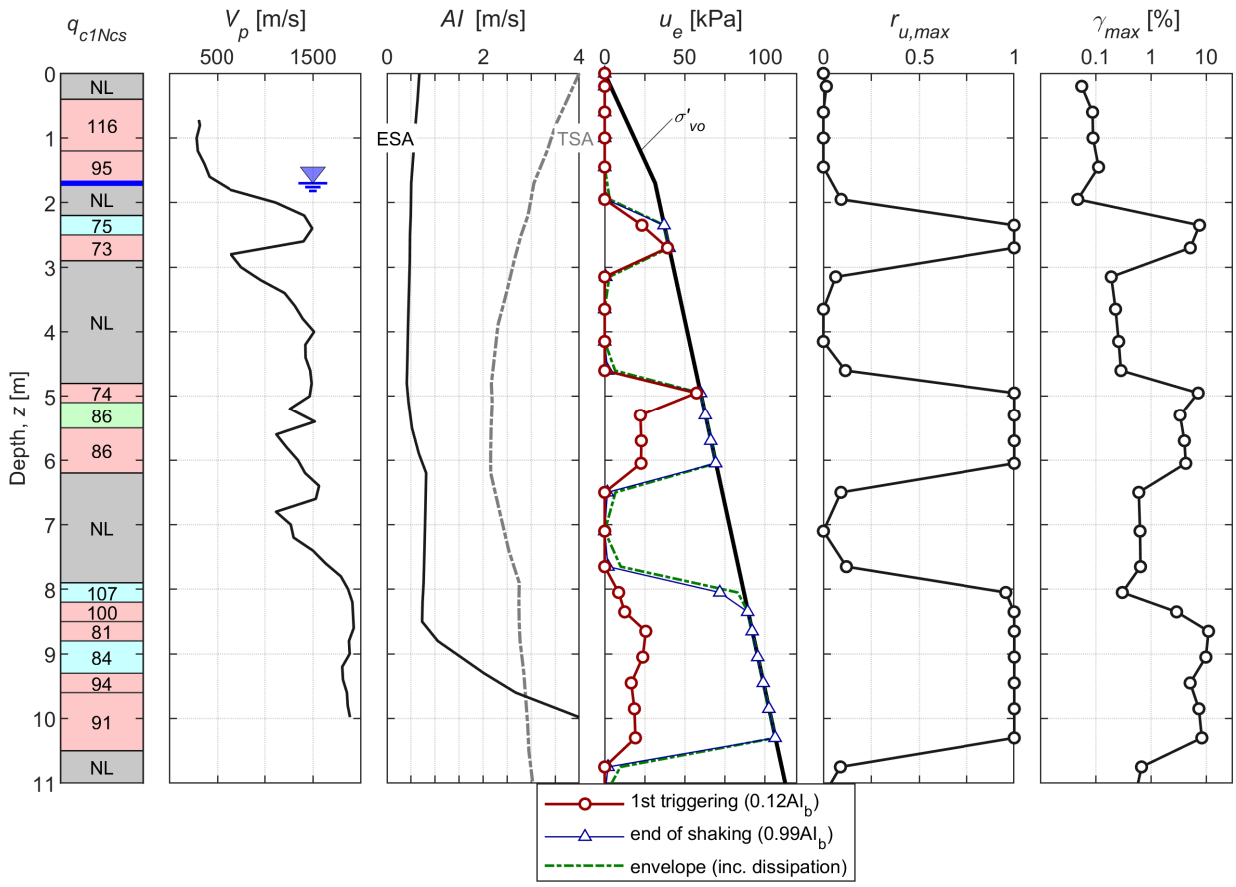

RHSC-based input

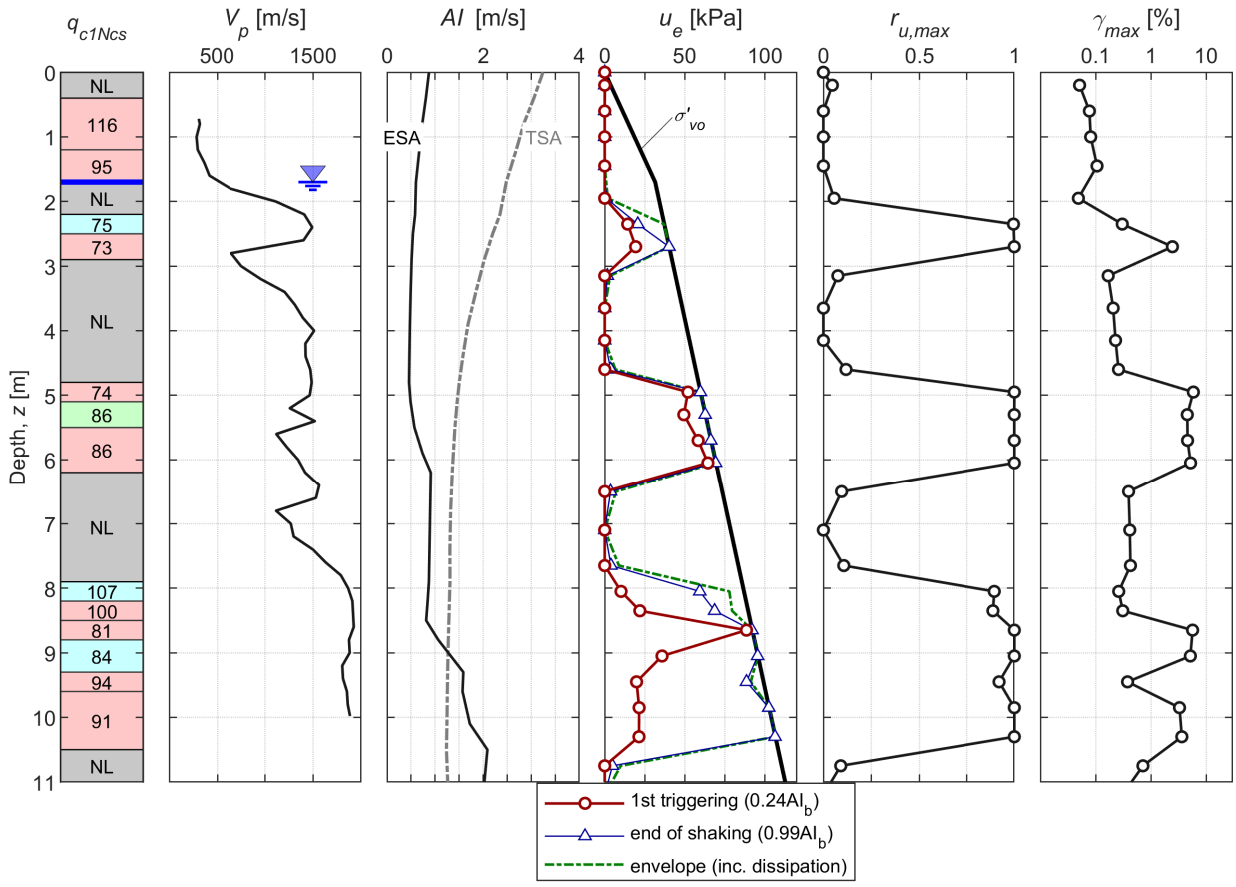

CPT 36417

LPCC-based input

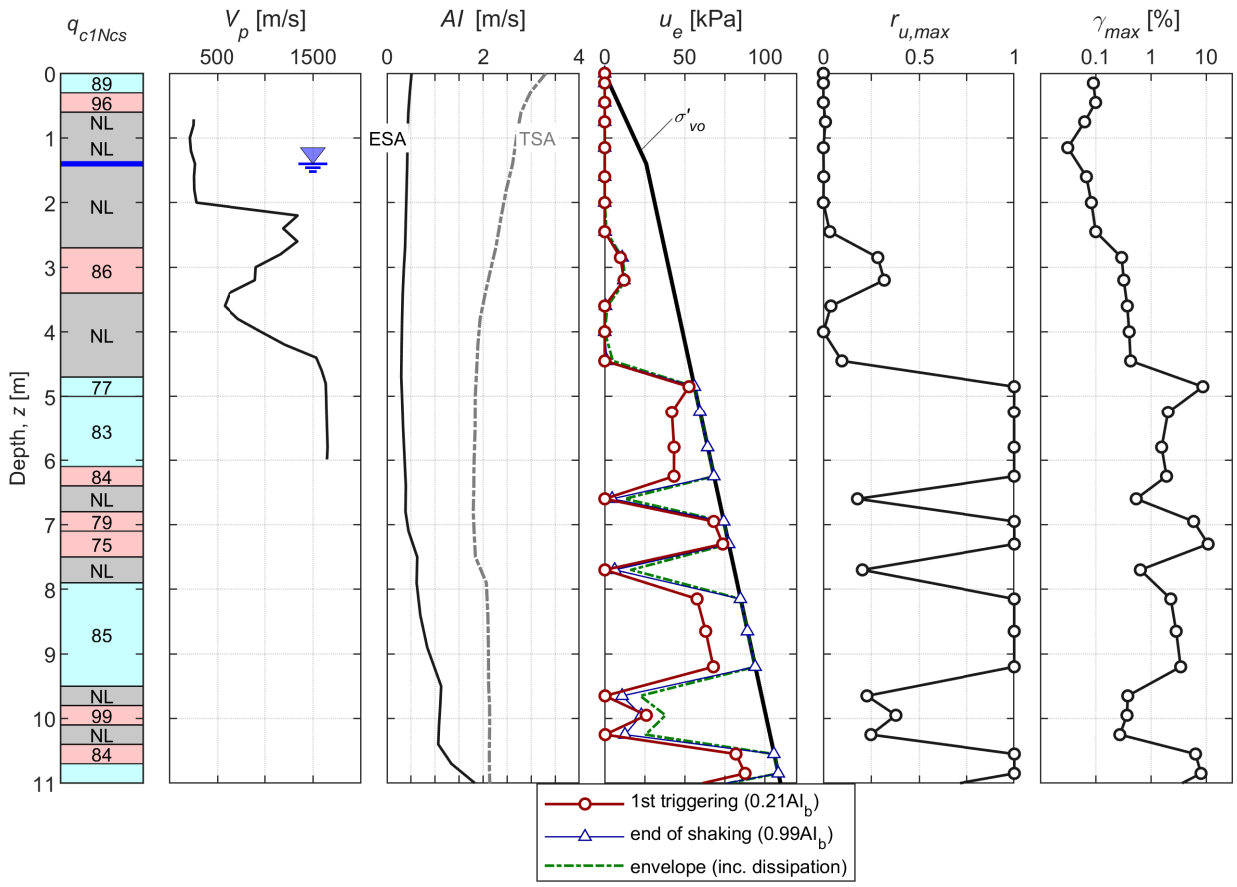

RHSC-based input

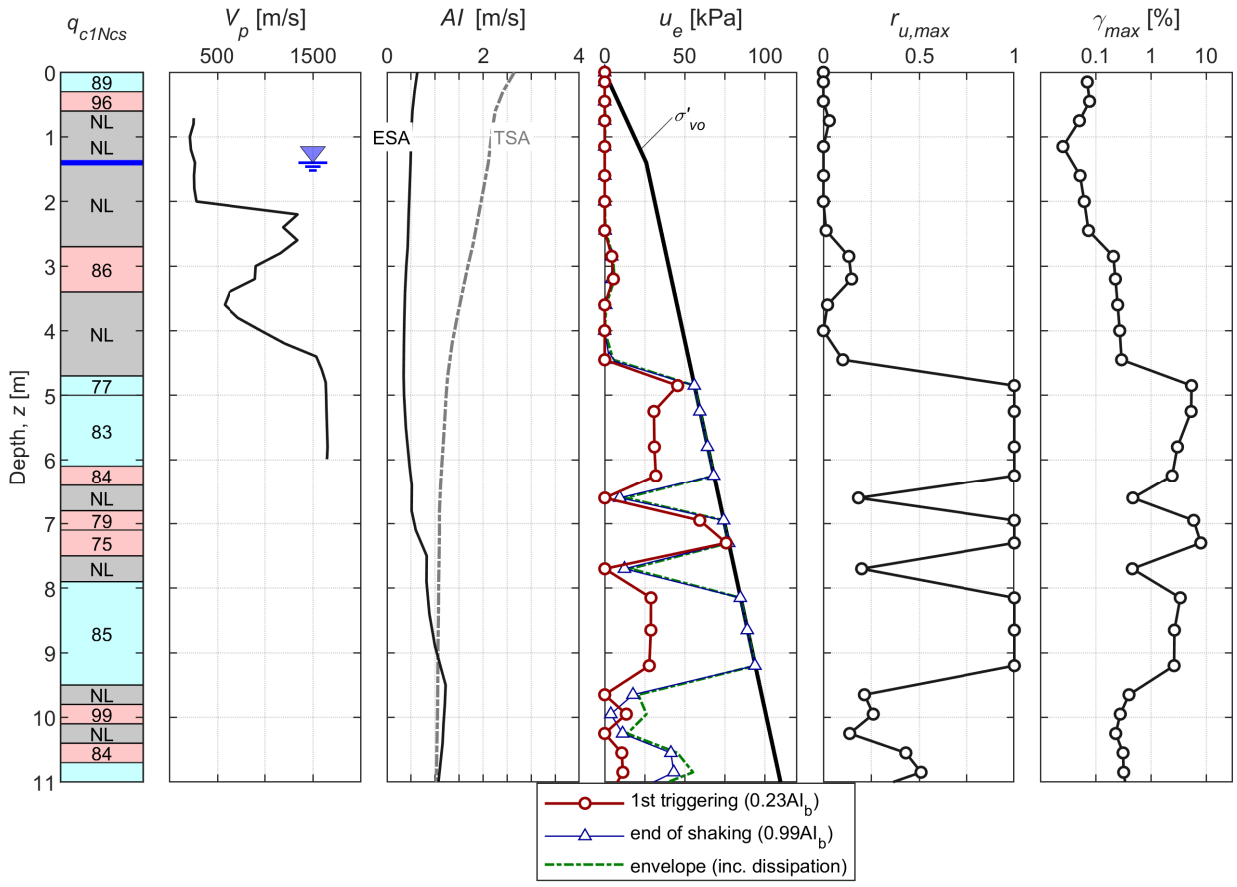

CPT 36421

LPCC-based input

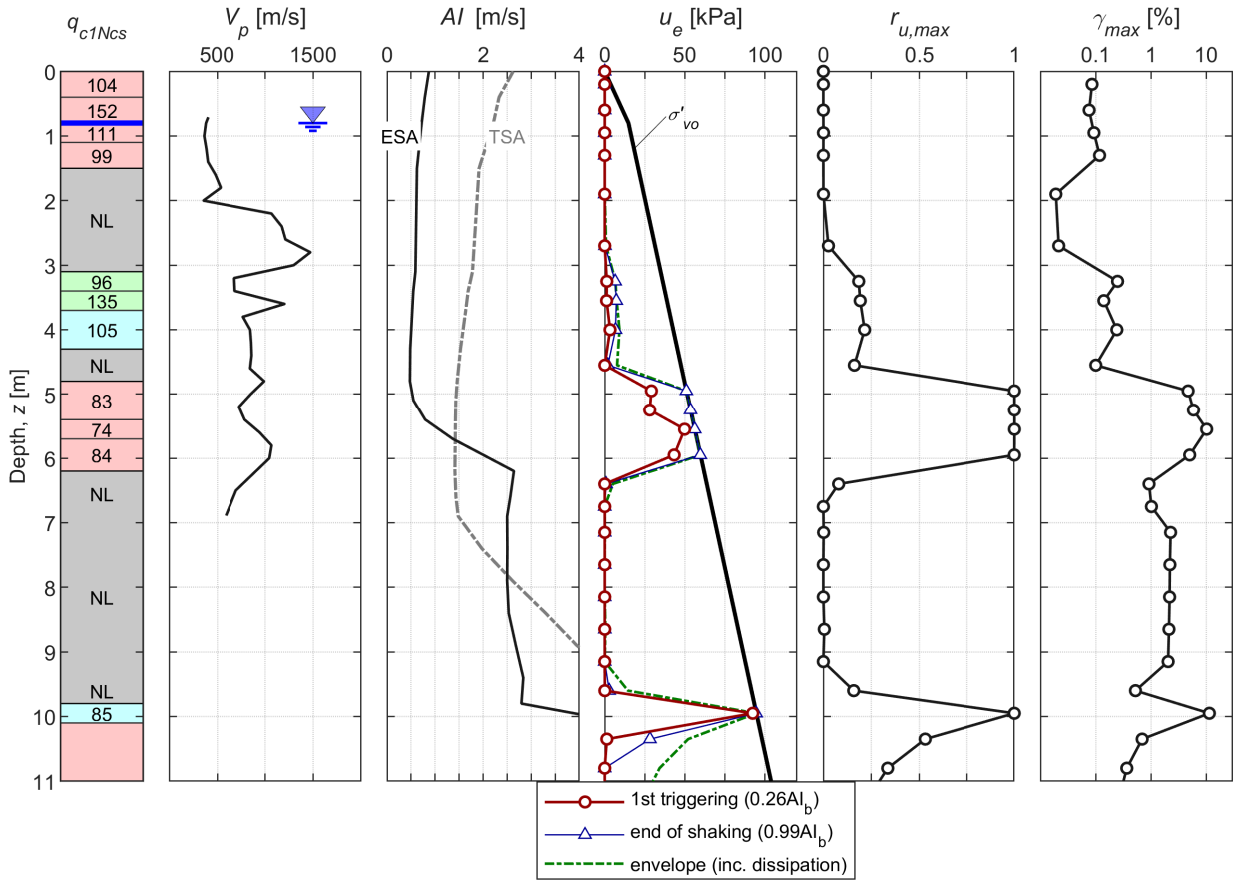

RHSC-based input

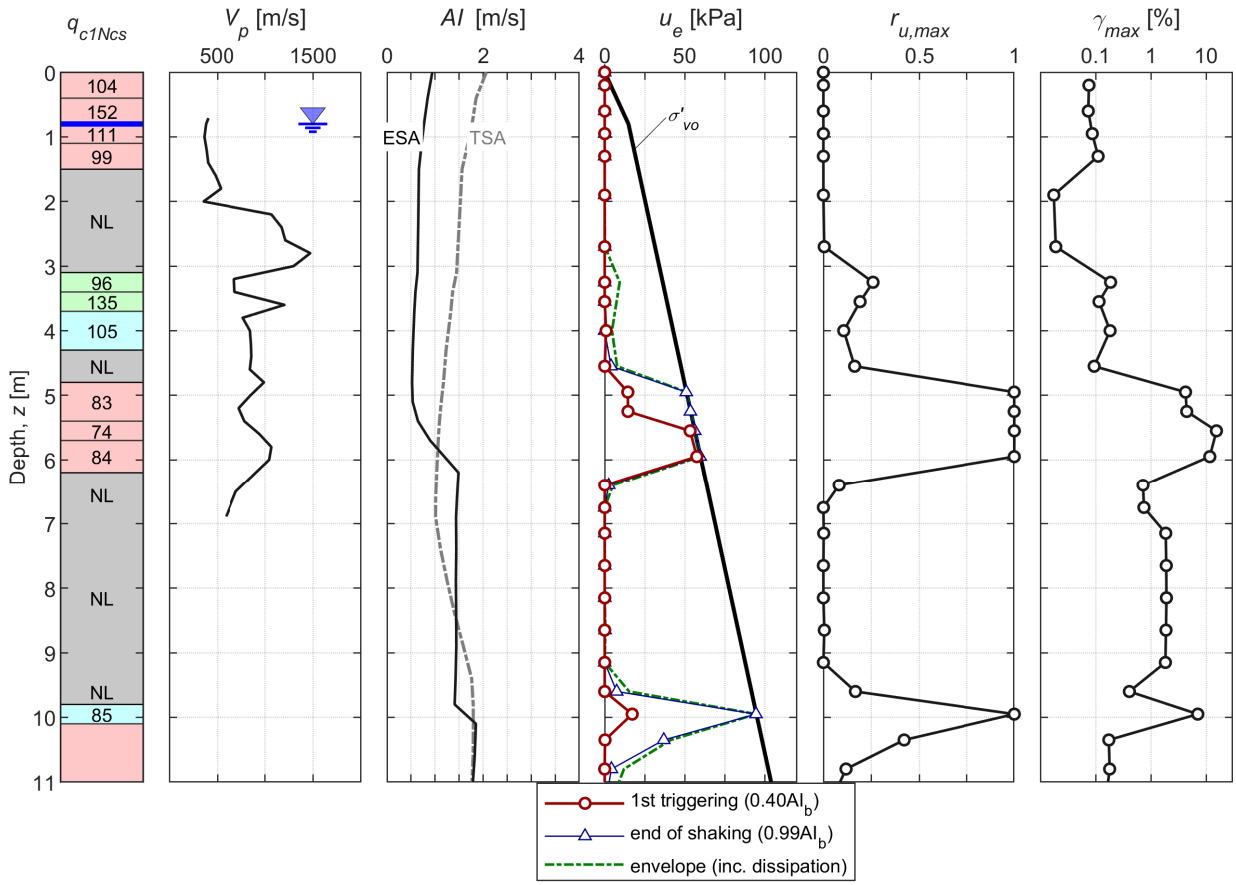

CPT 57364

LPCC-based input

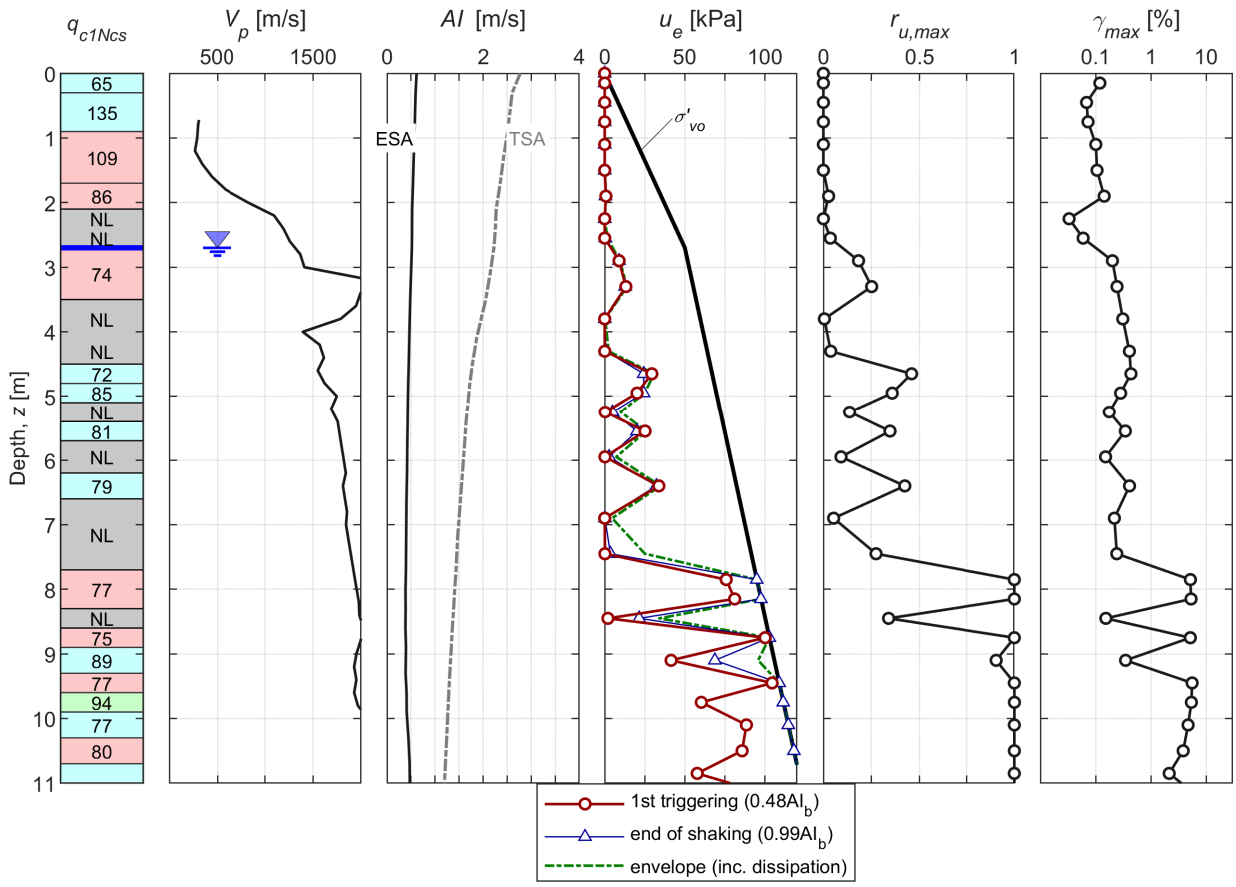

RHSC-based input

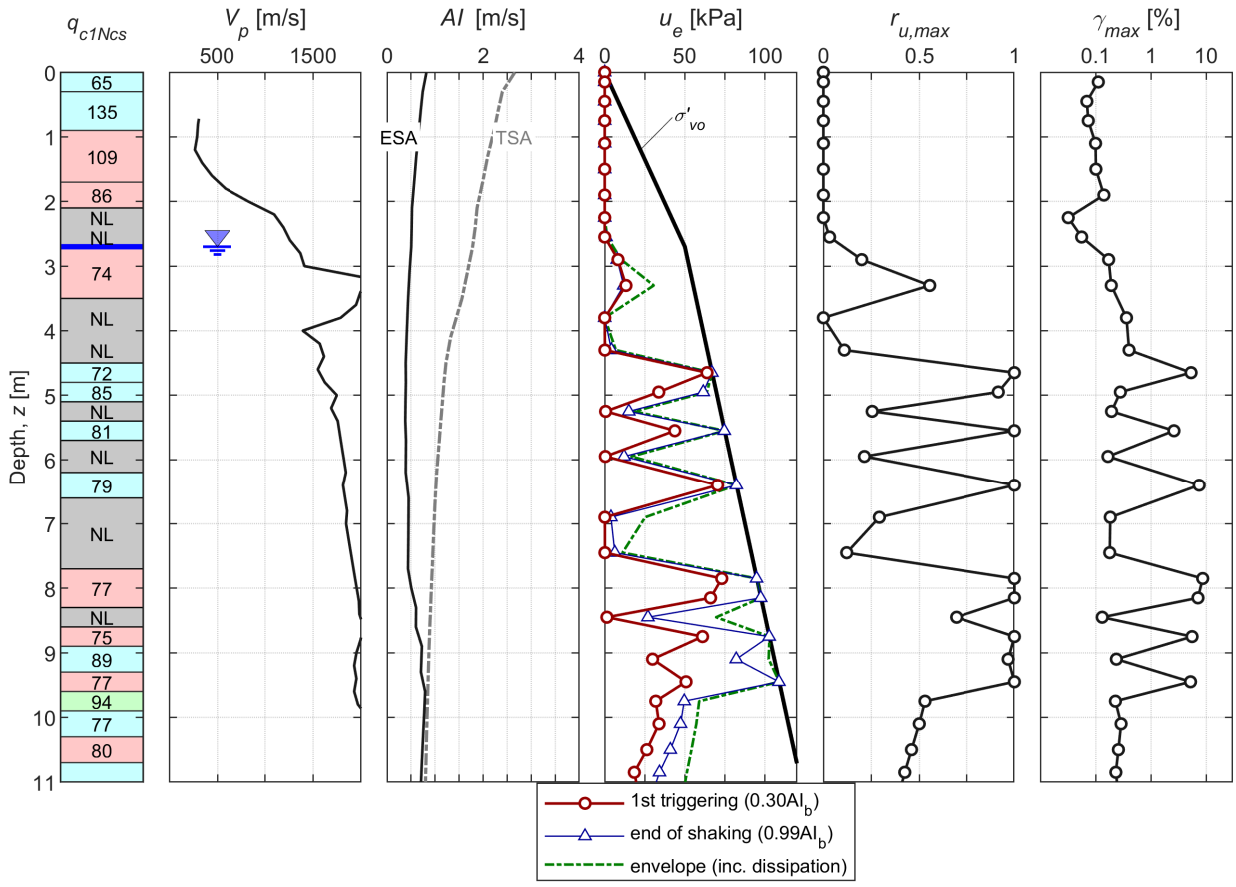

CPT 57352

LPCC-based input

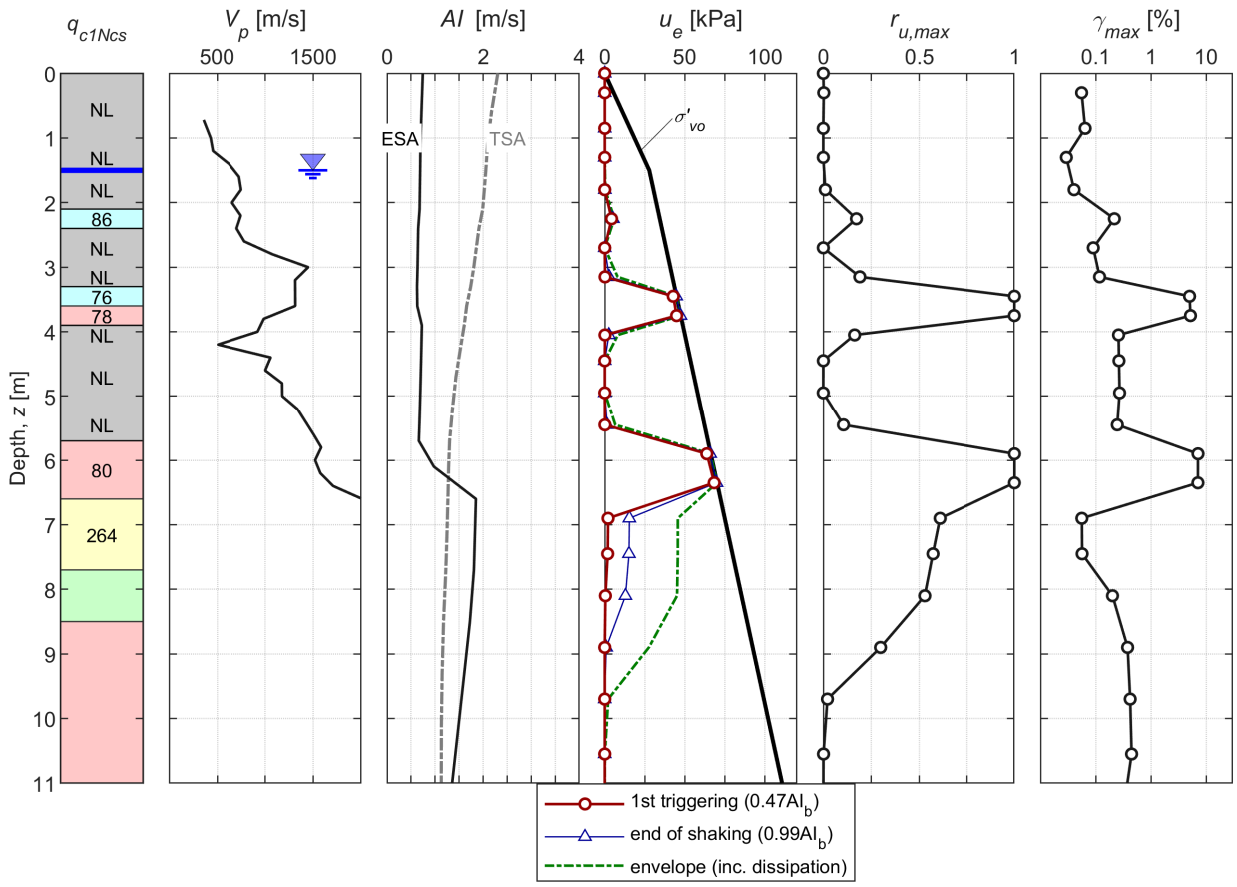

RHSC-based input

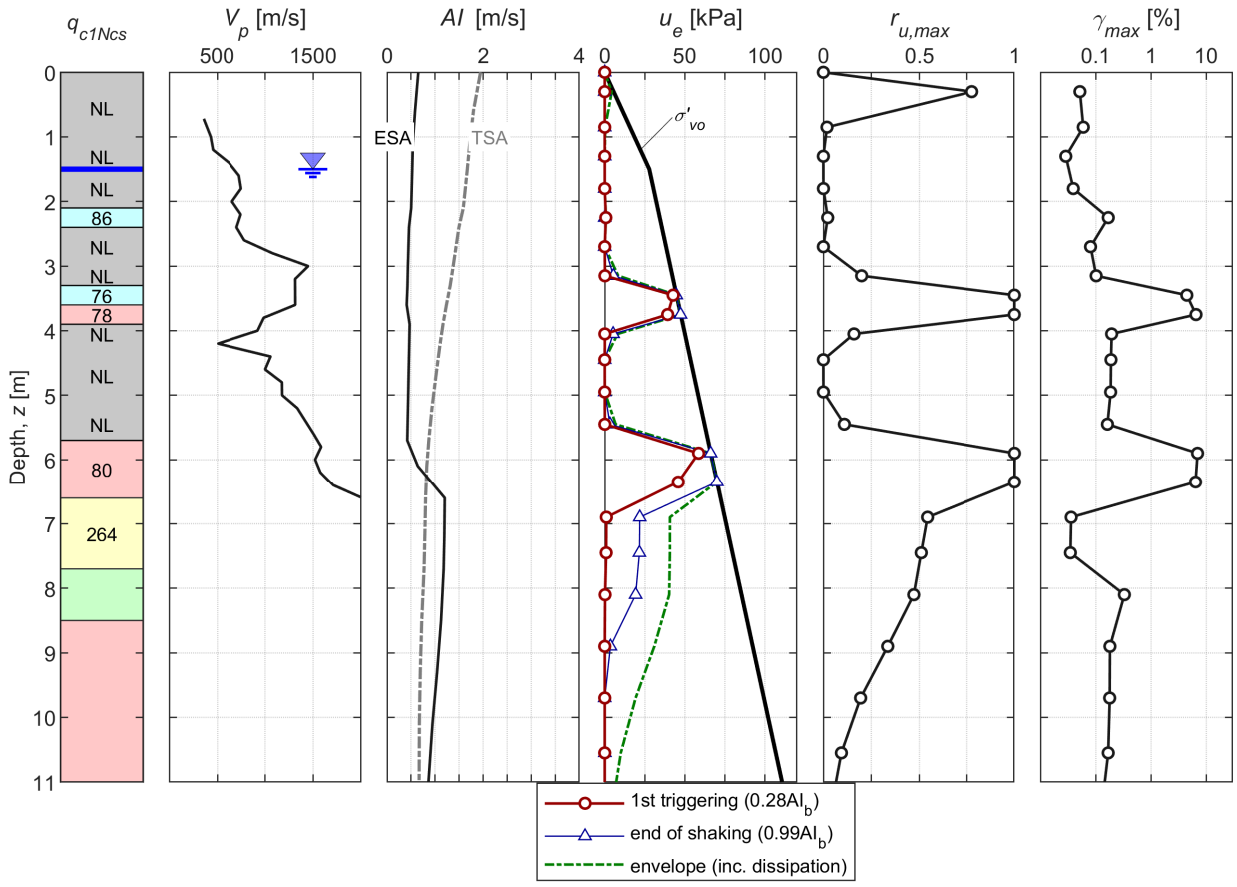

CPT 36419

LPCC-based input

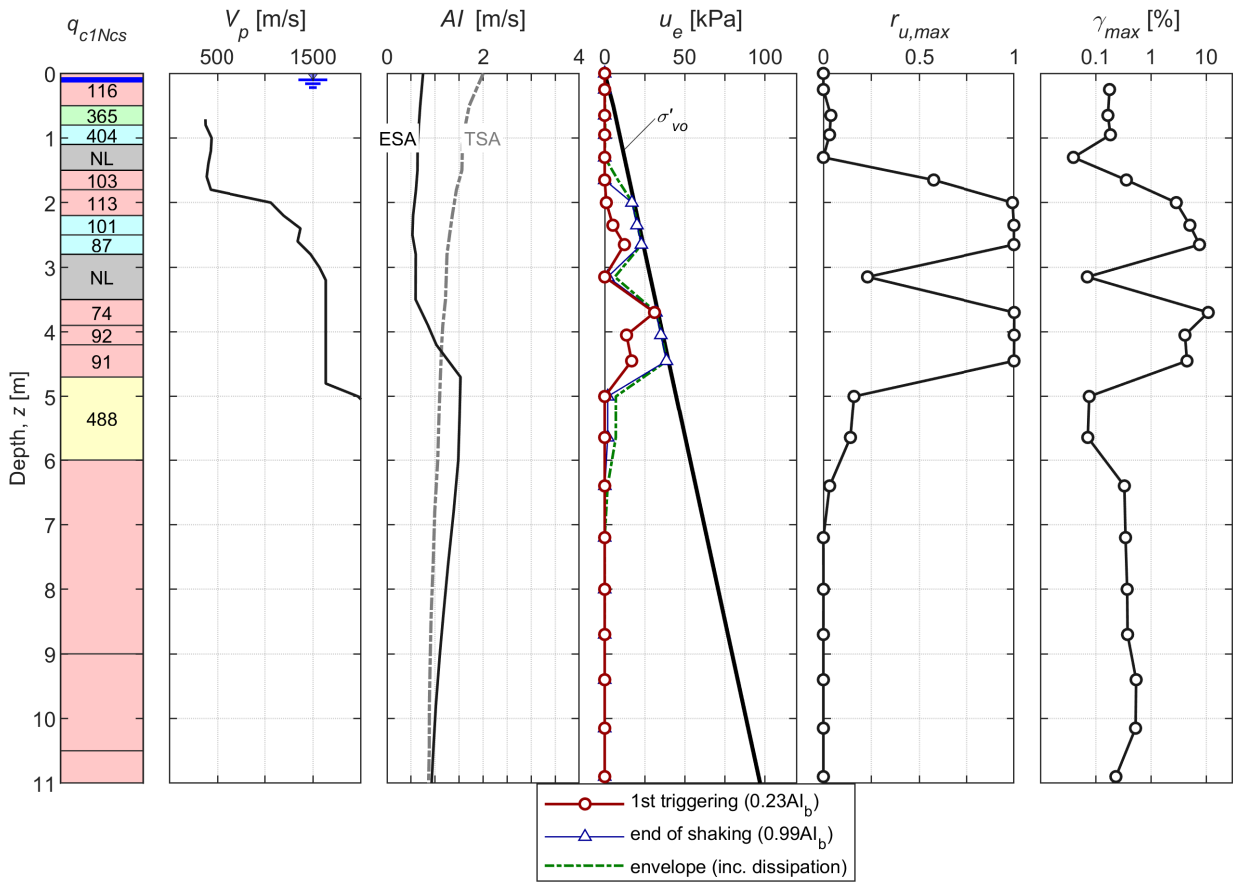

RHSC-based input

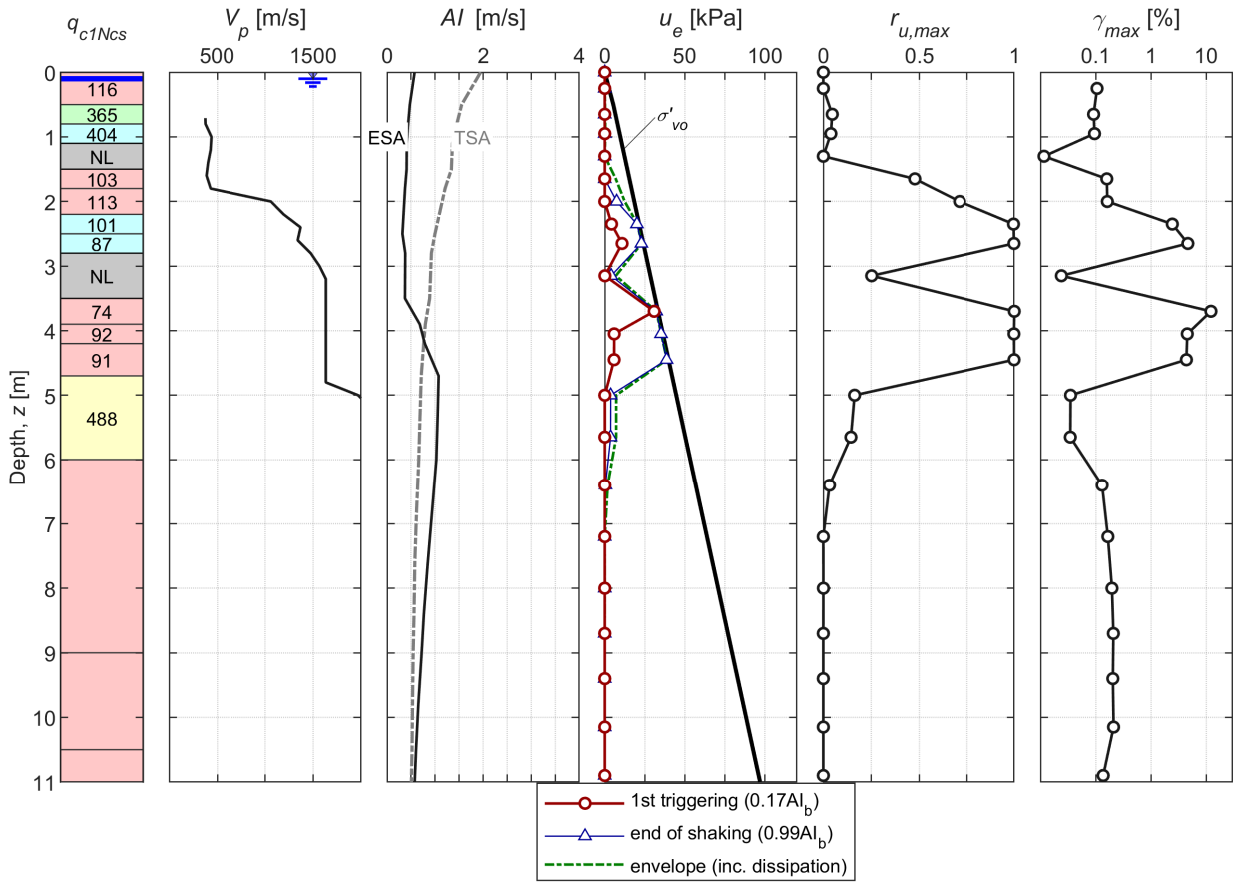

CPT 57319

CACS-based input

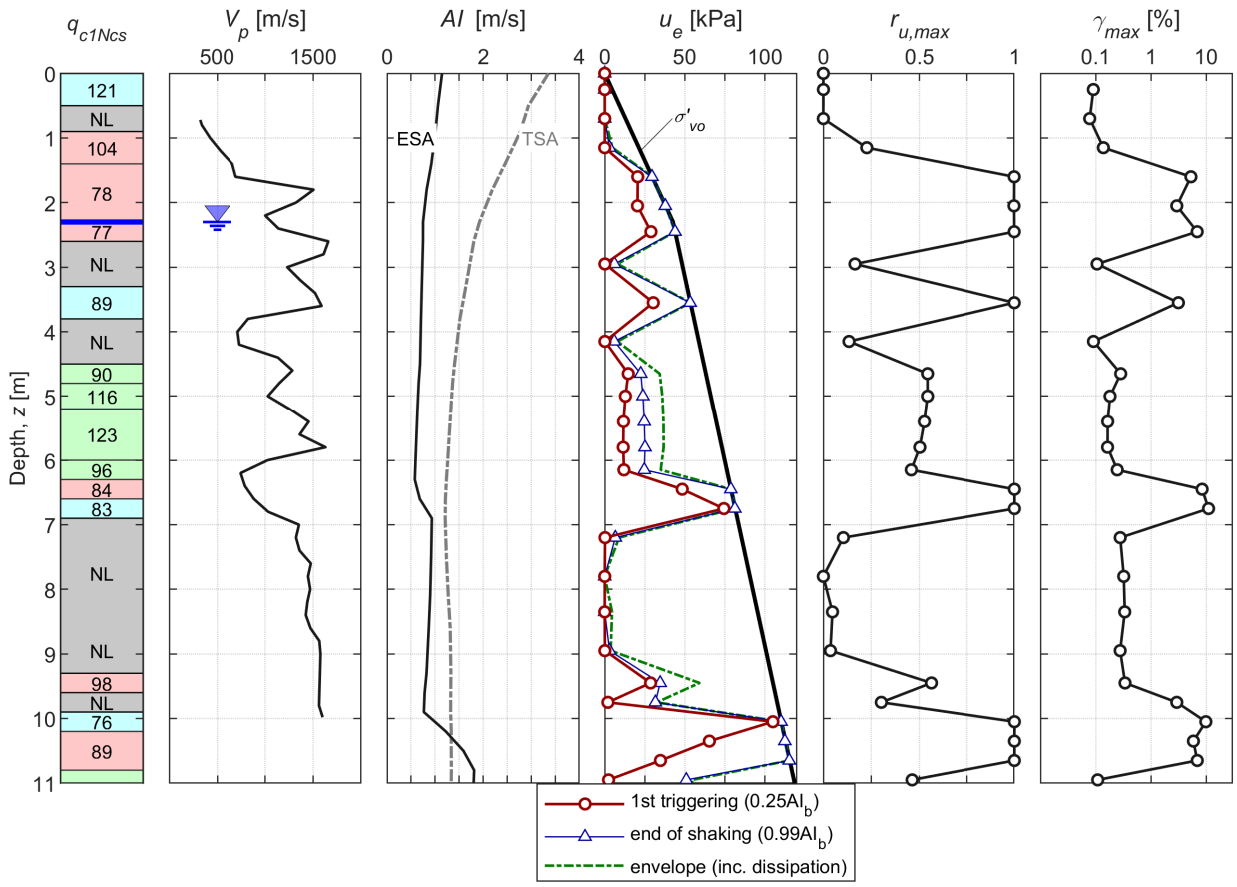

RHSC-based input

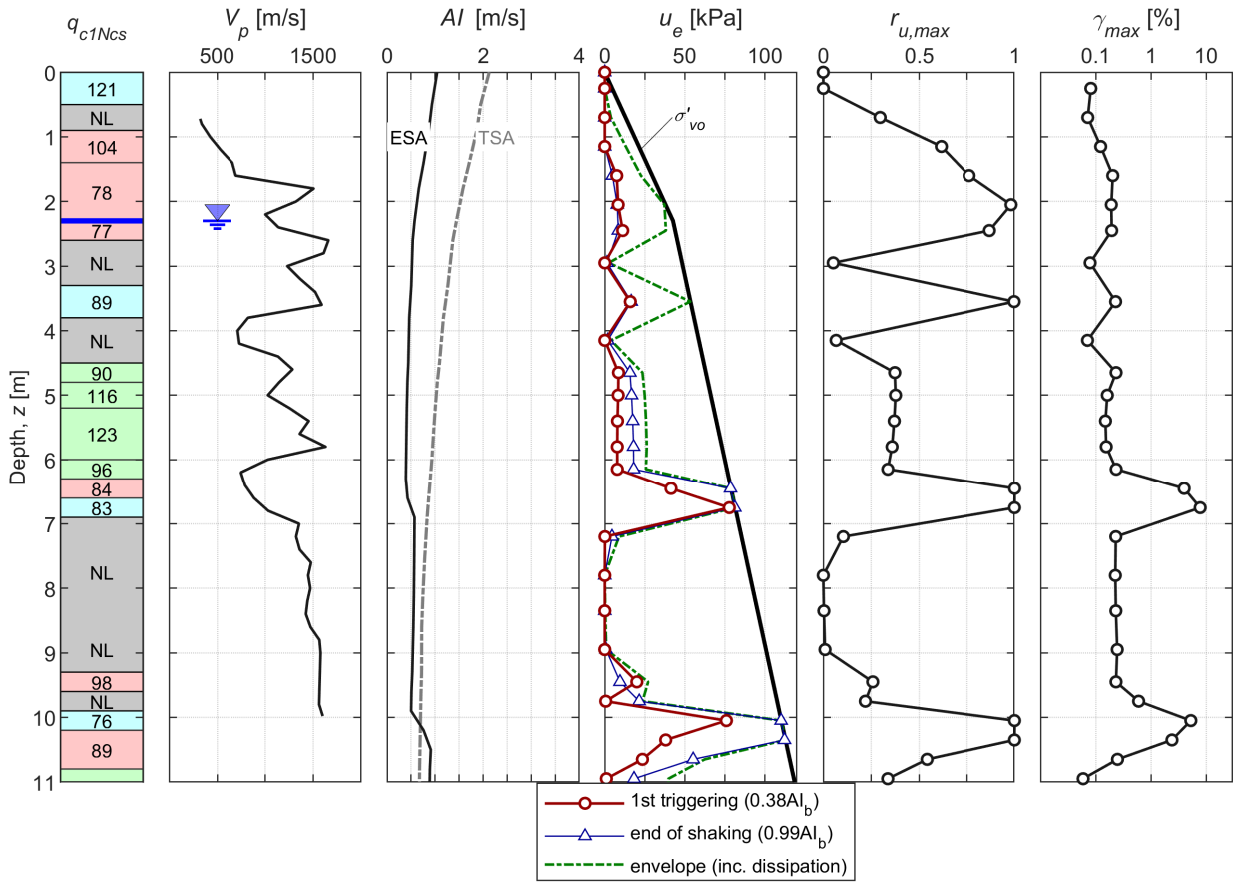

CPT 57337

CACS-based input

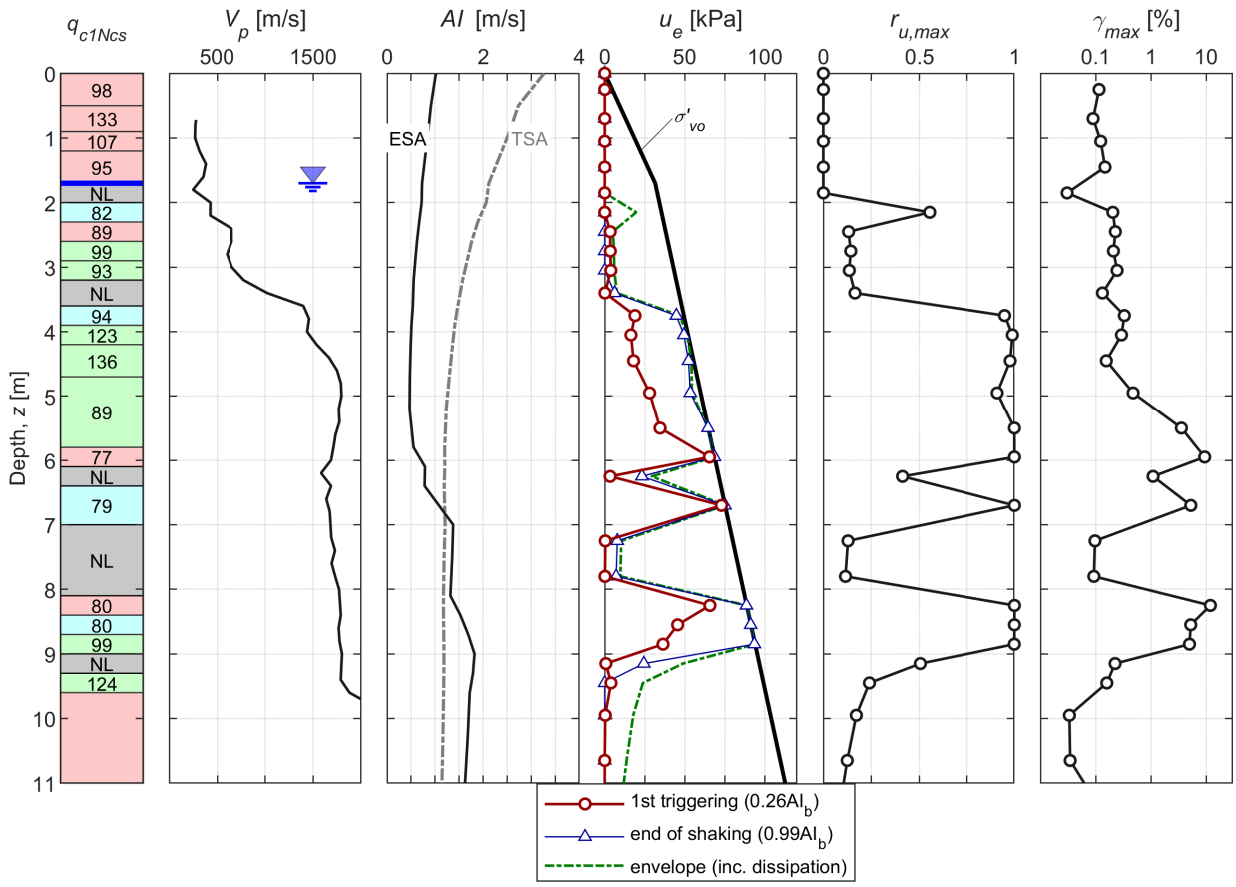

RHSC-based input

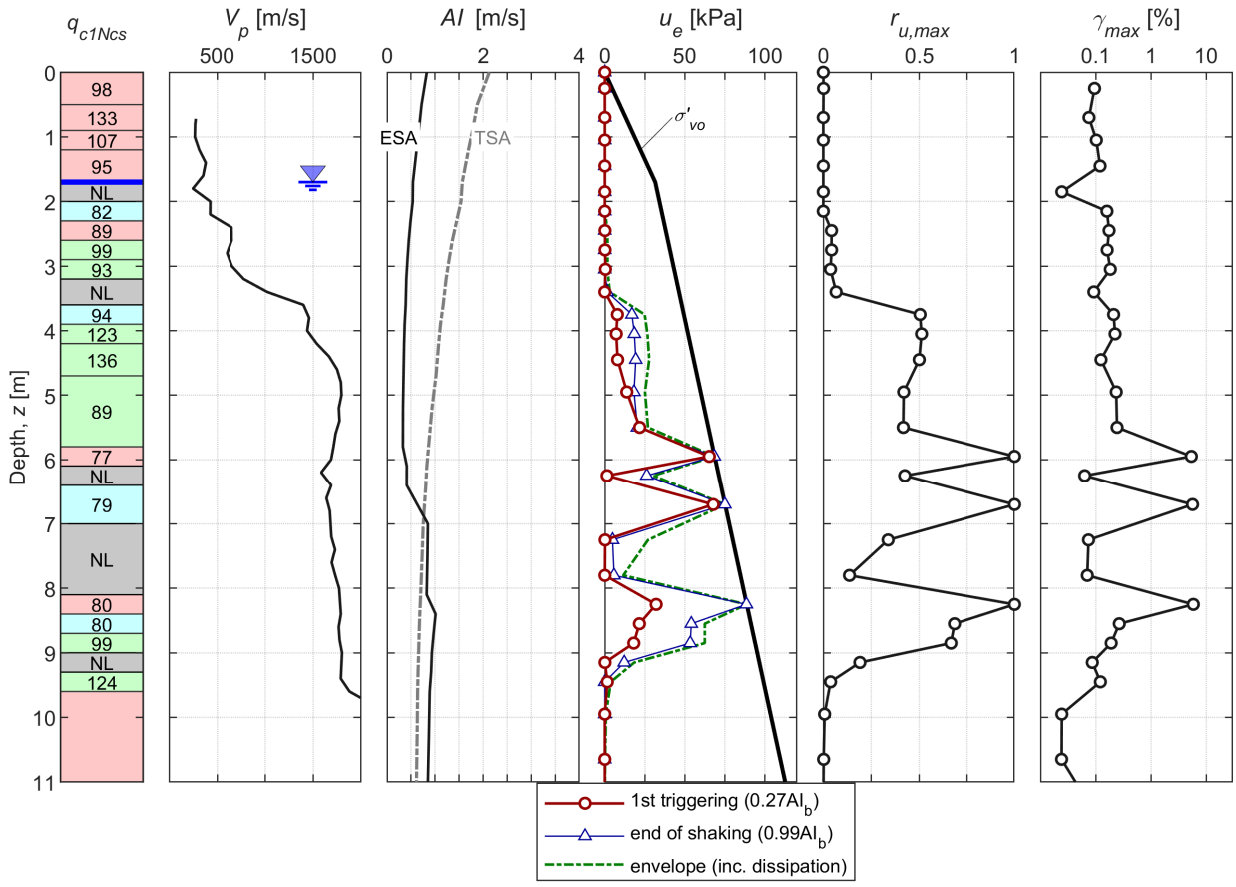

CPT 36418

CACS-based input

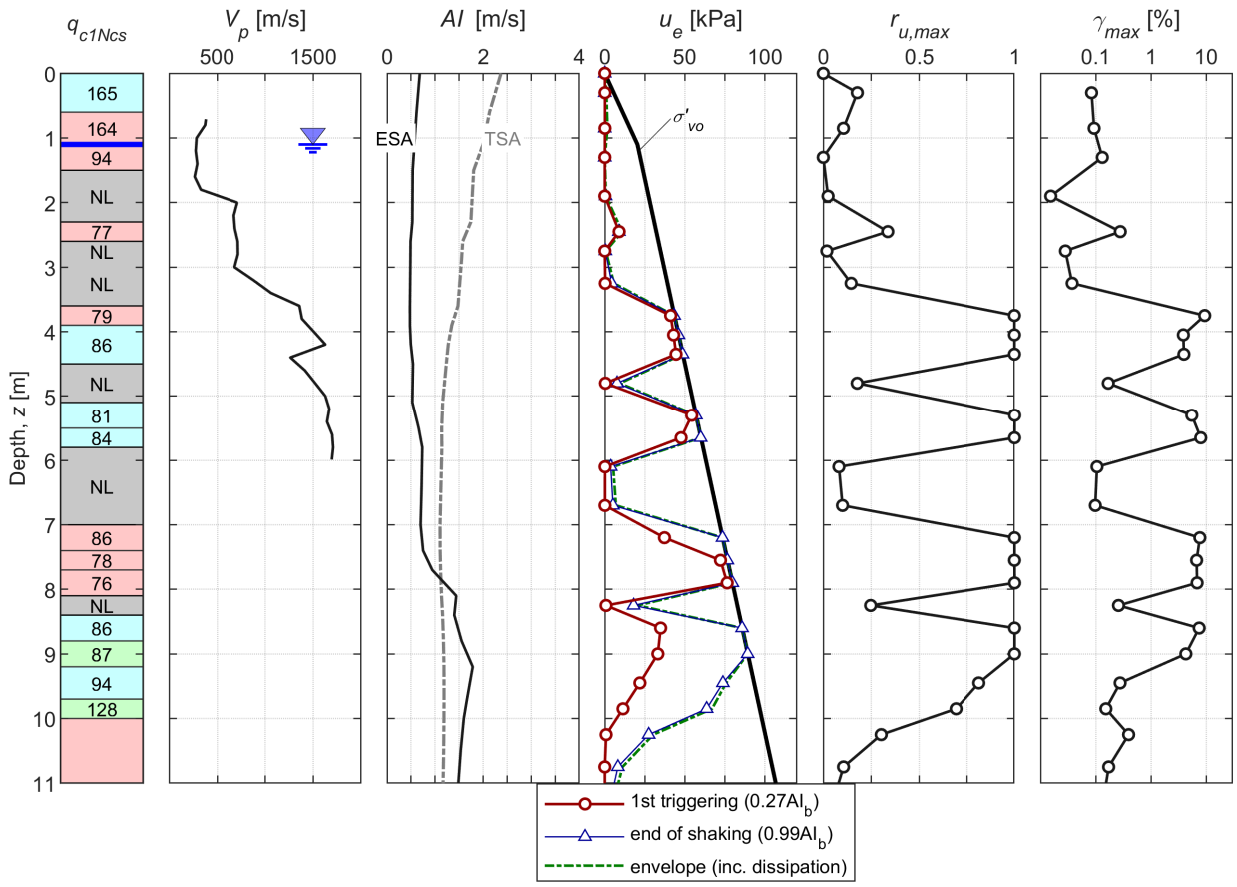

RHSC-based input

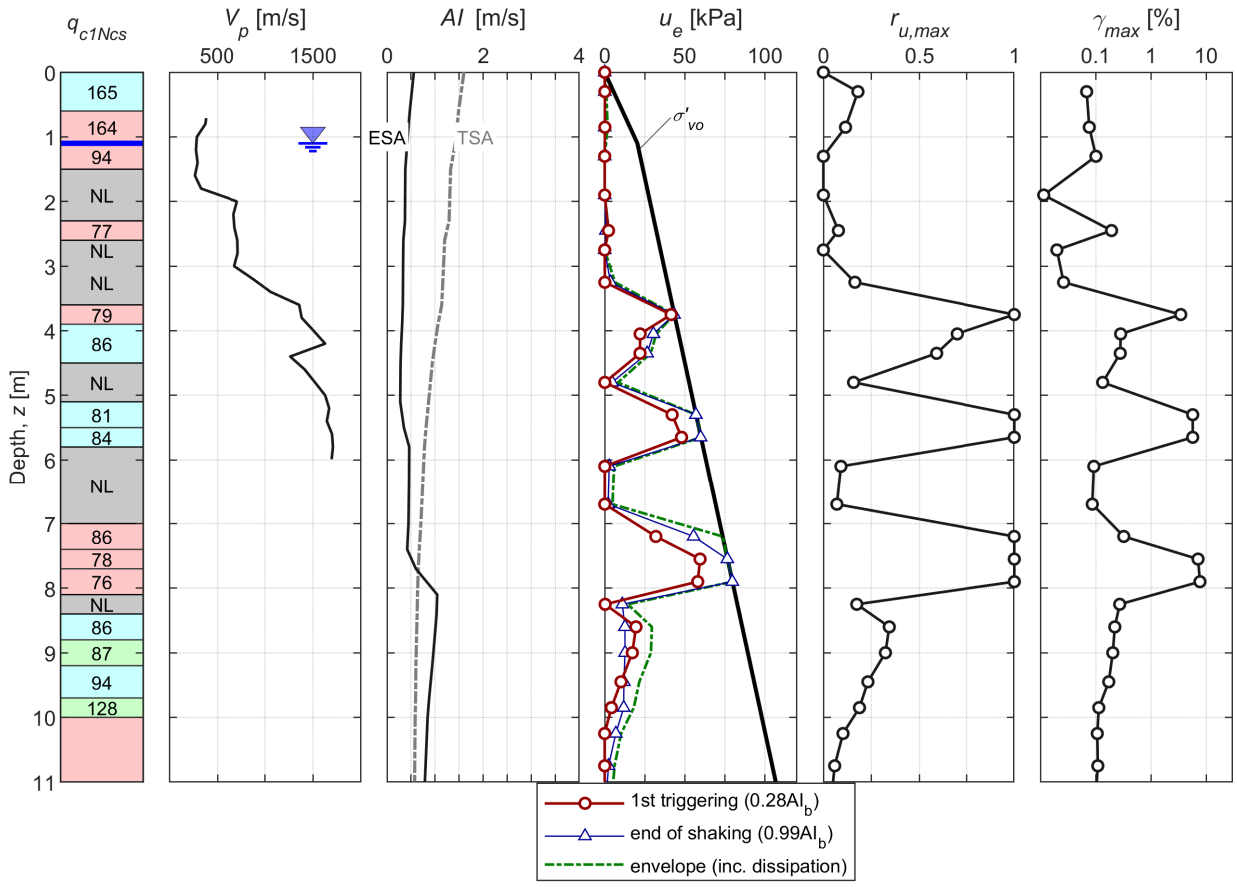

CPT 57345

CACS-based input

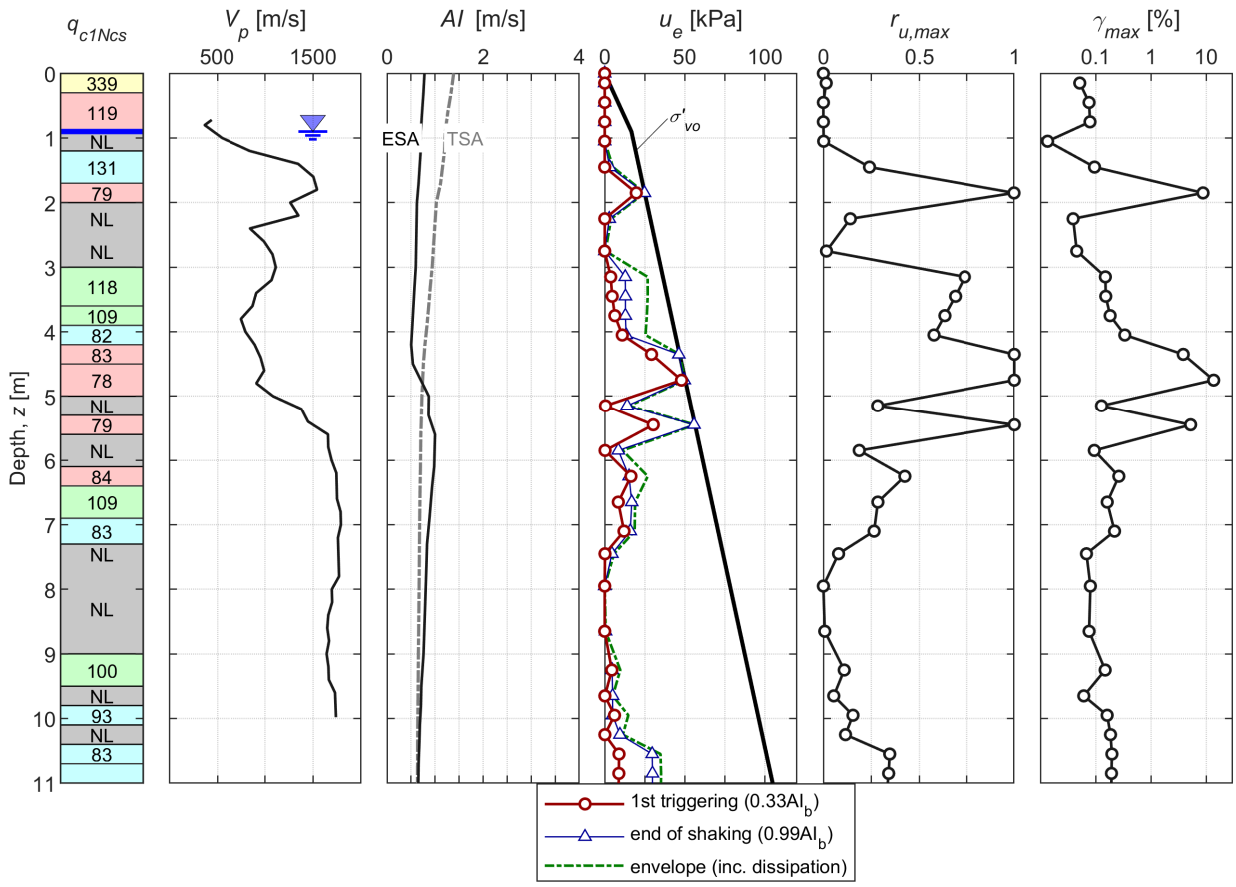

RHSC-based input

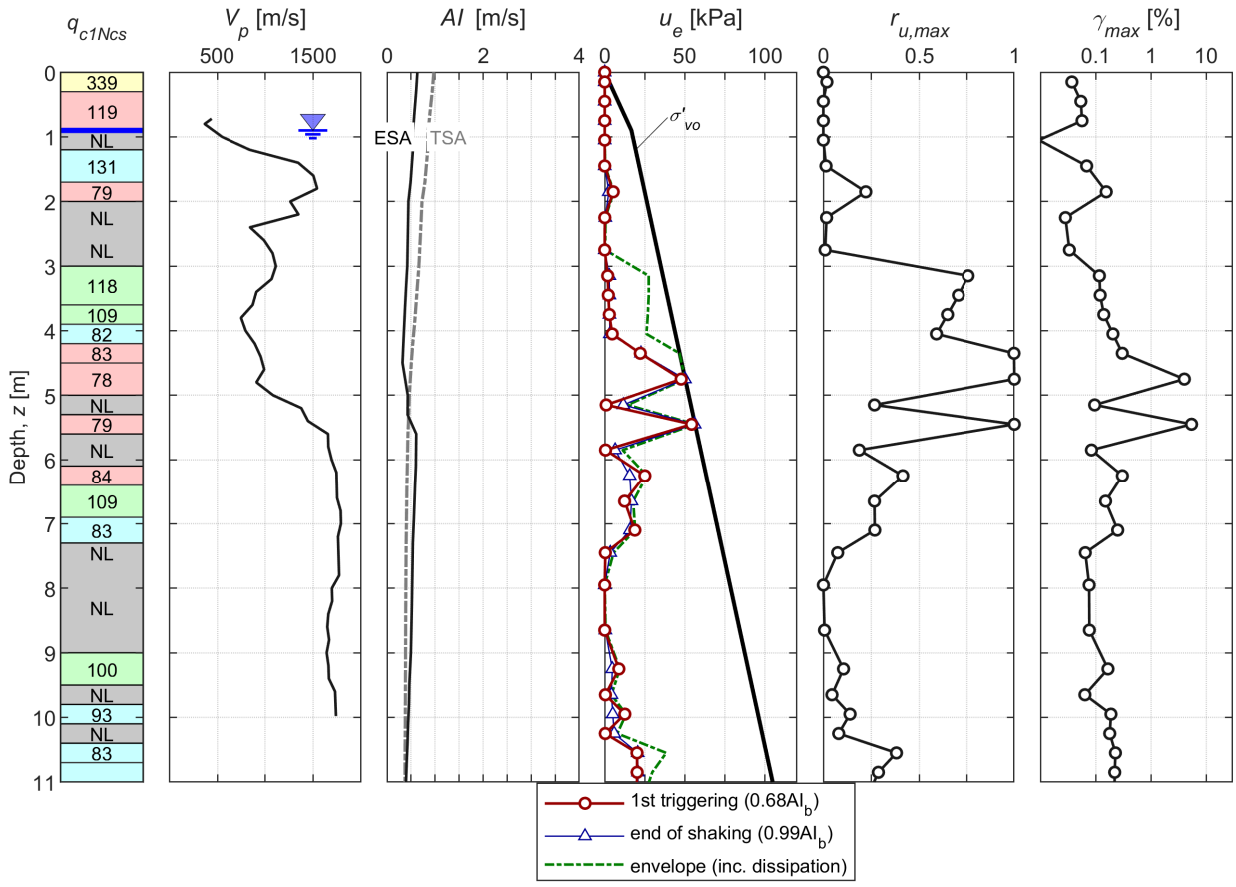

CPT 36420

CACS-based input

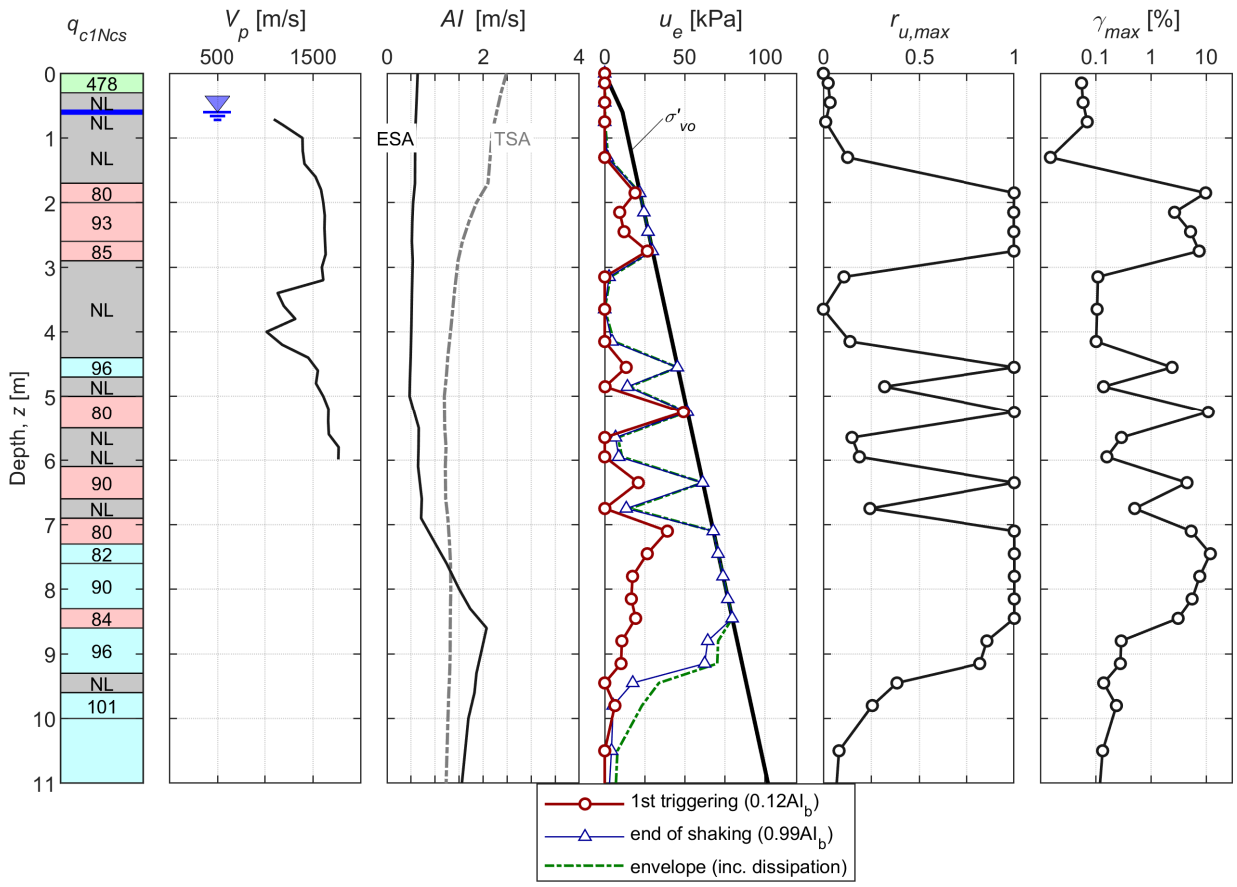

RHSC-based input

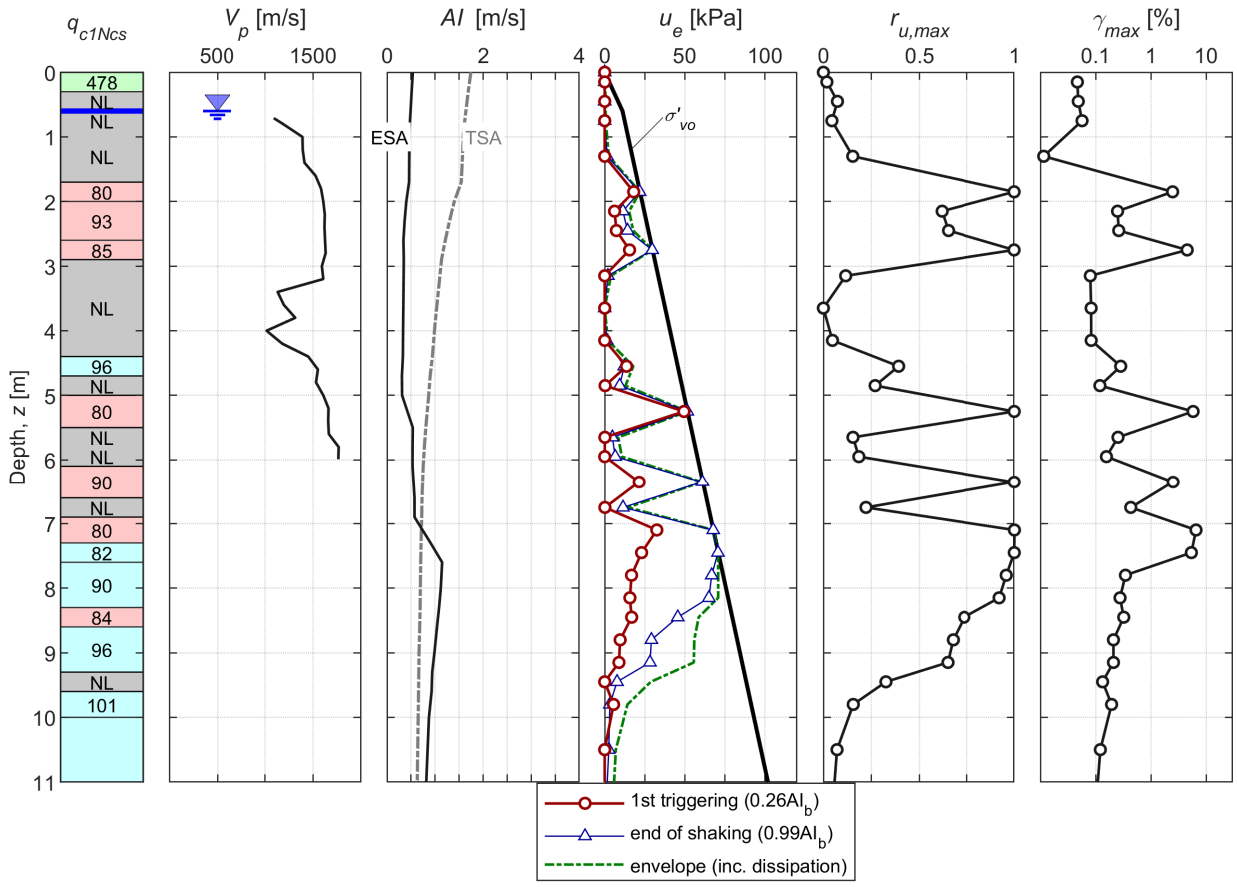

CPT 5567

CACS-based input

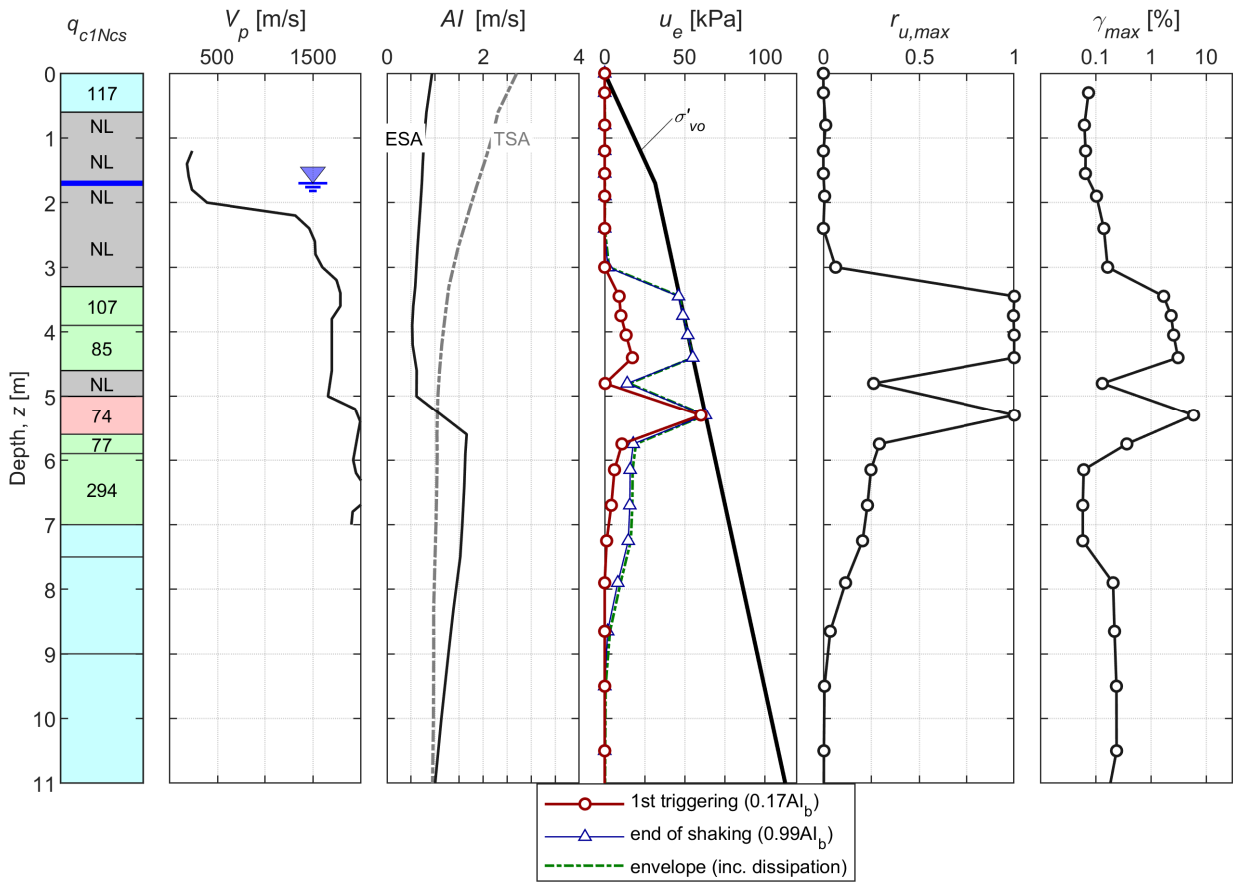

RHSC-based input

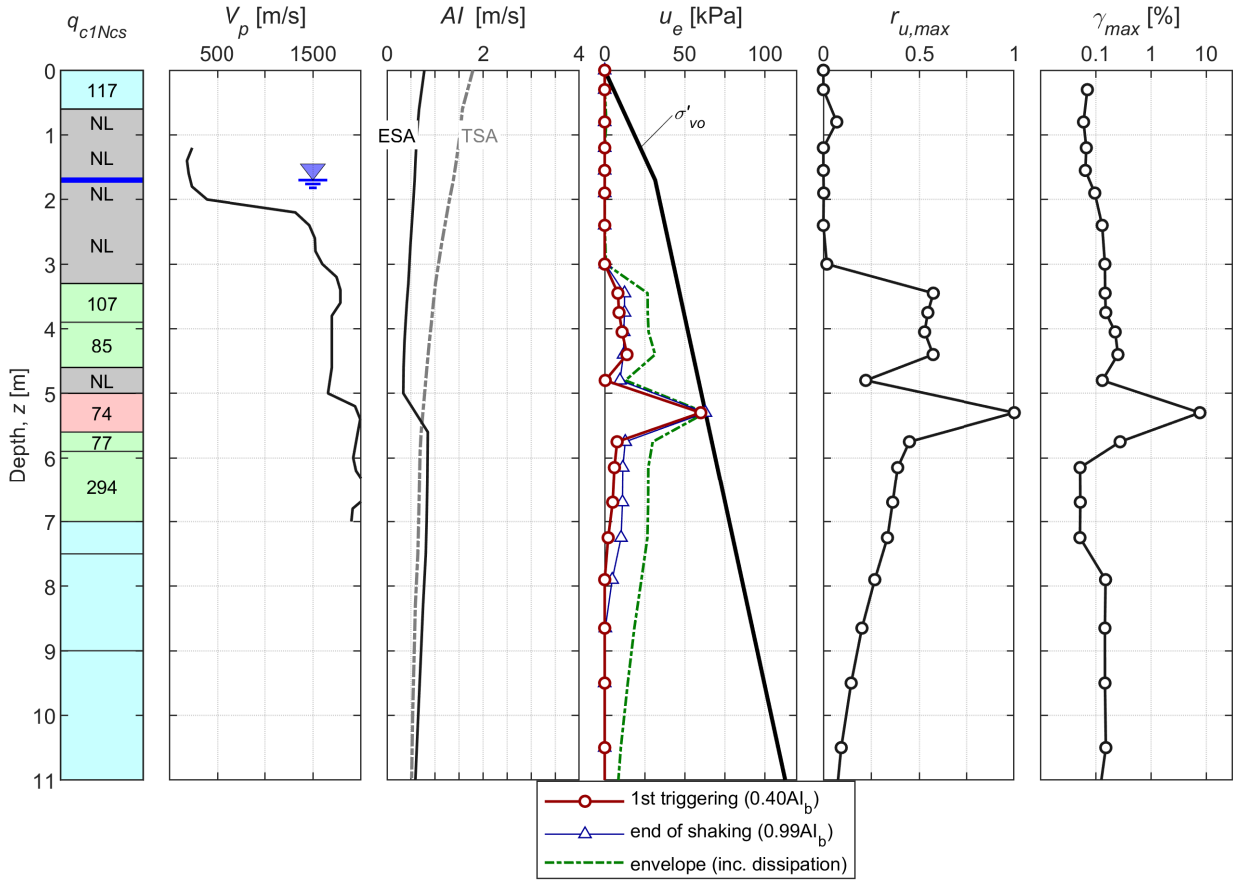

CPT 57358

SMTC-based input

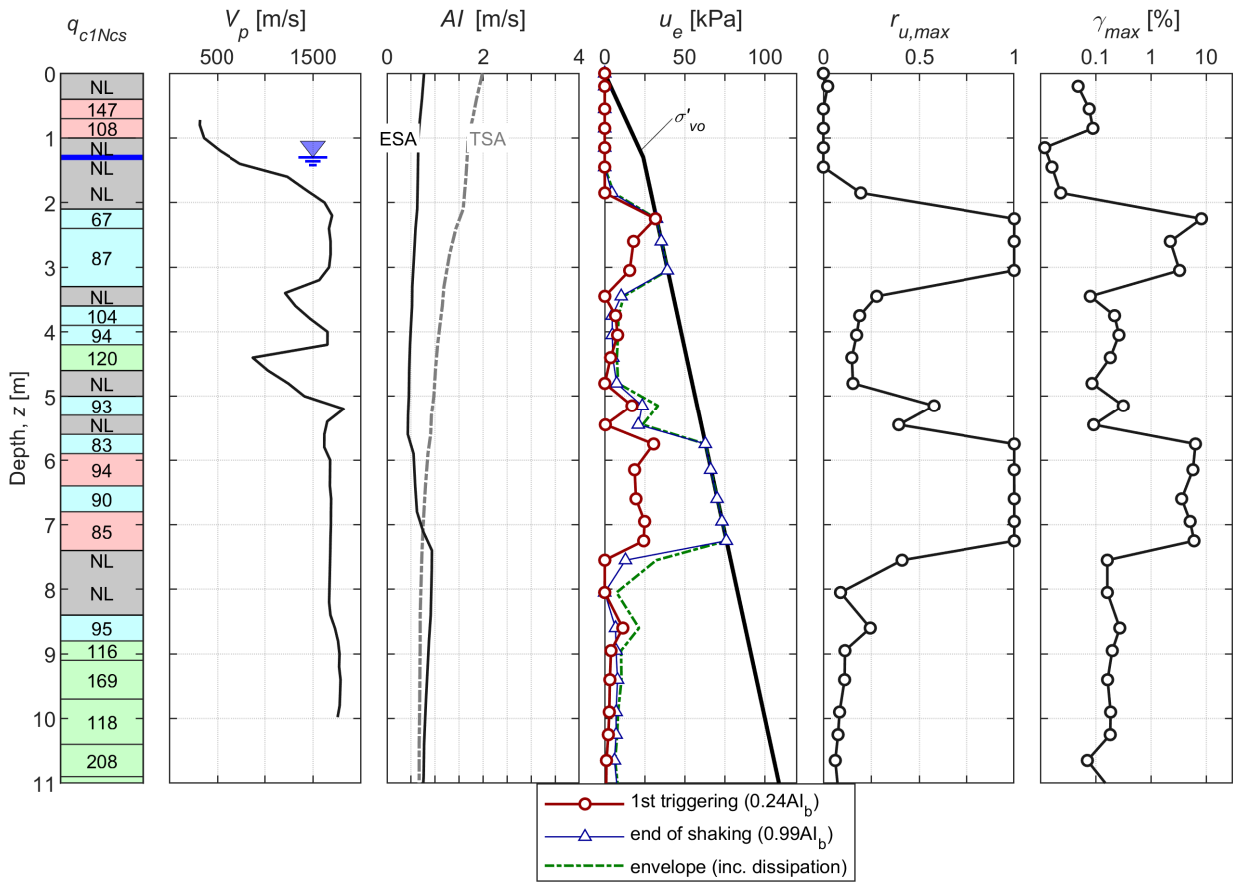

RHSC-based input

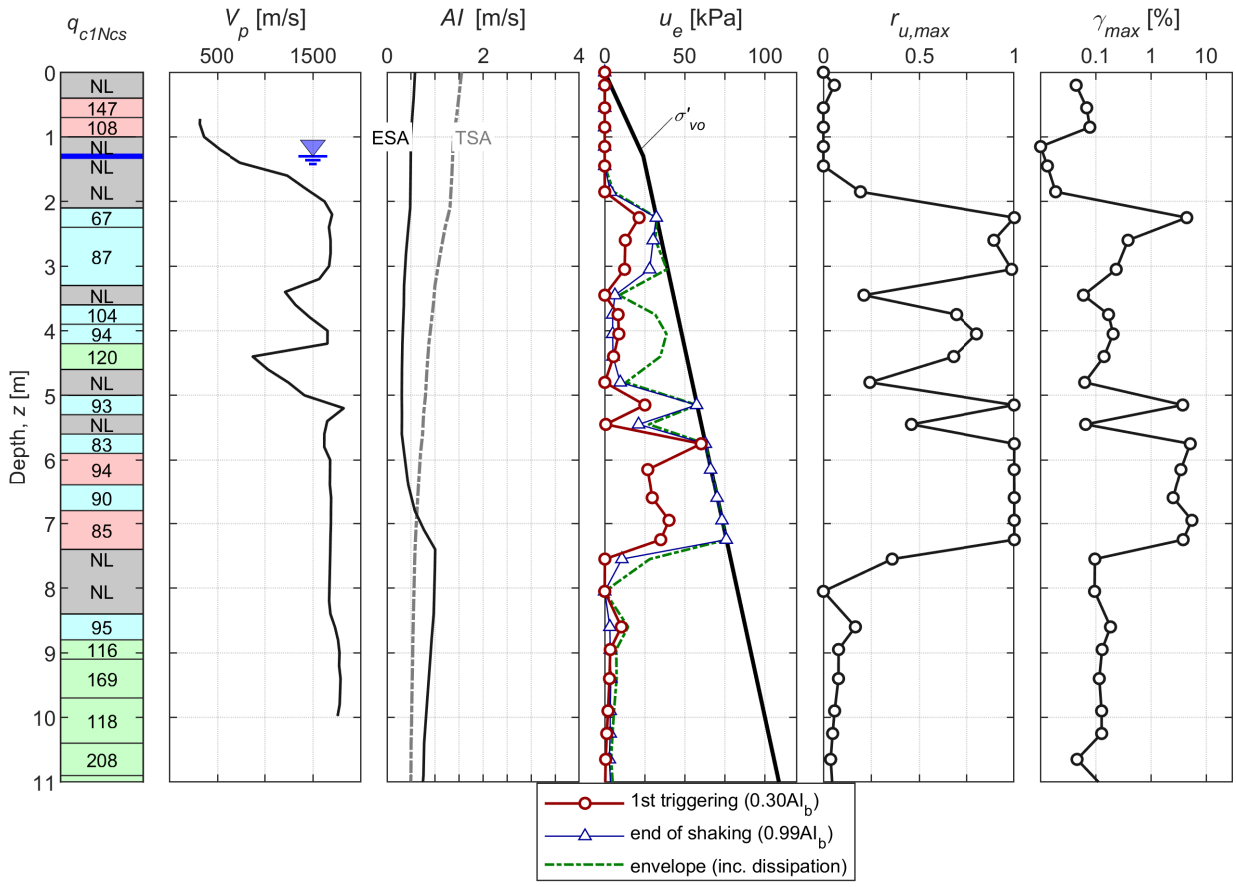

CPT 57359

SMTC-based input

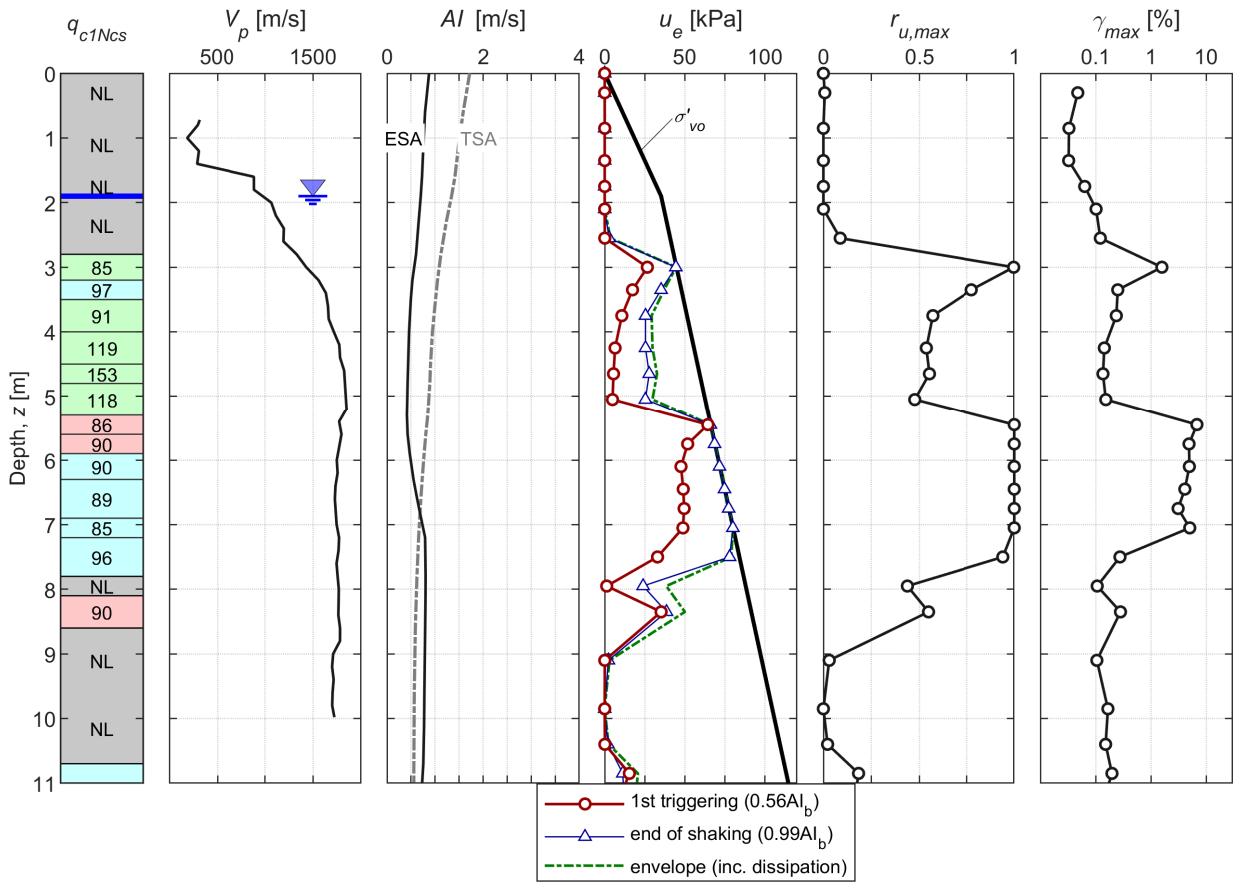

RHSC-based input

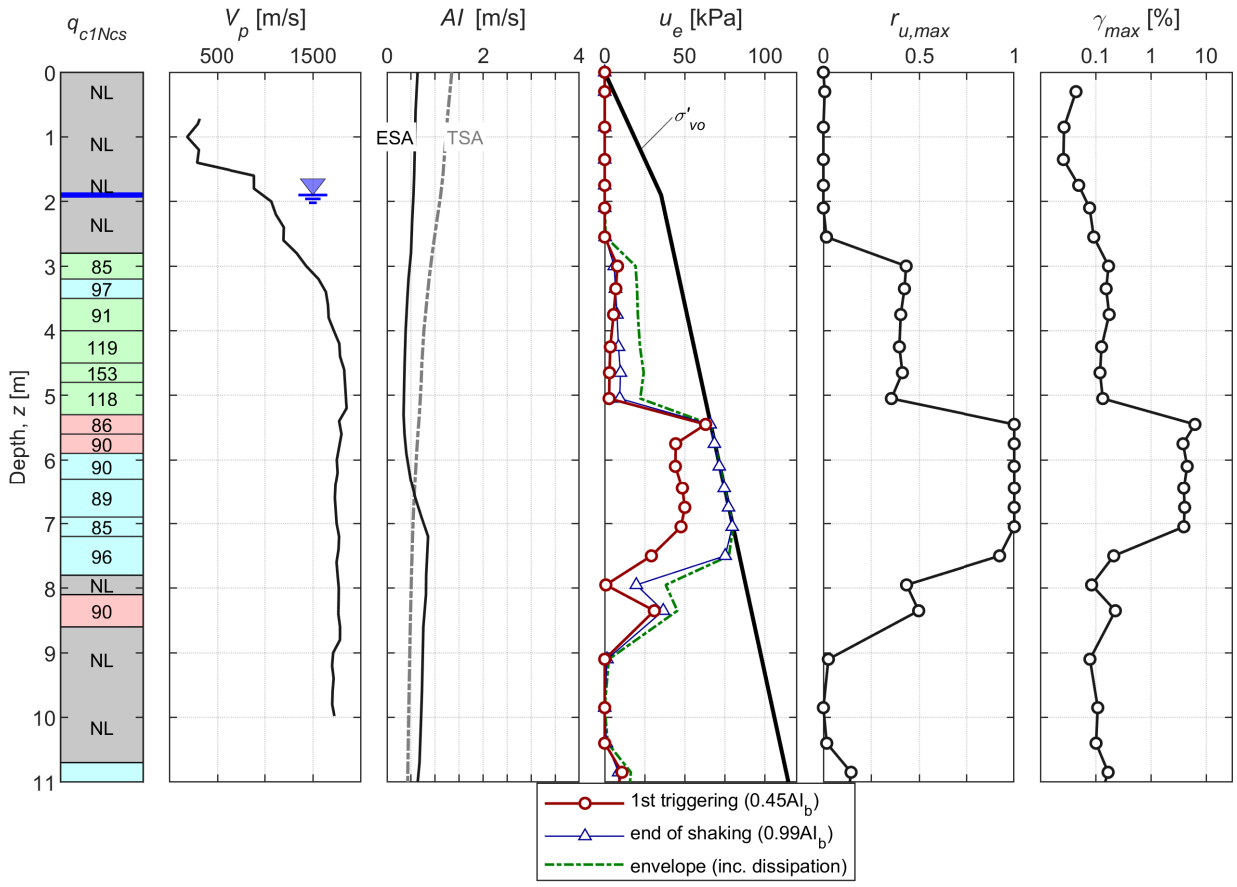

CPT 57363

SMTC-based input

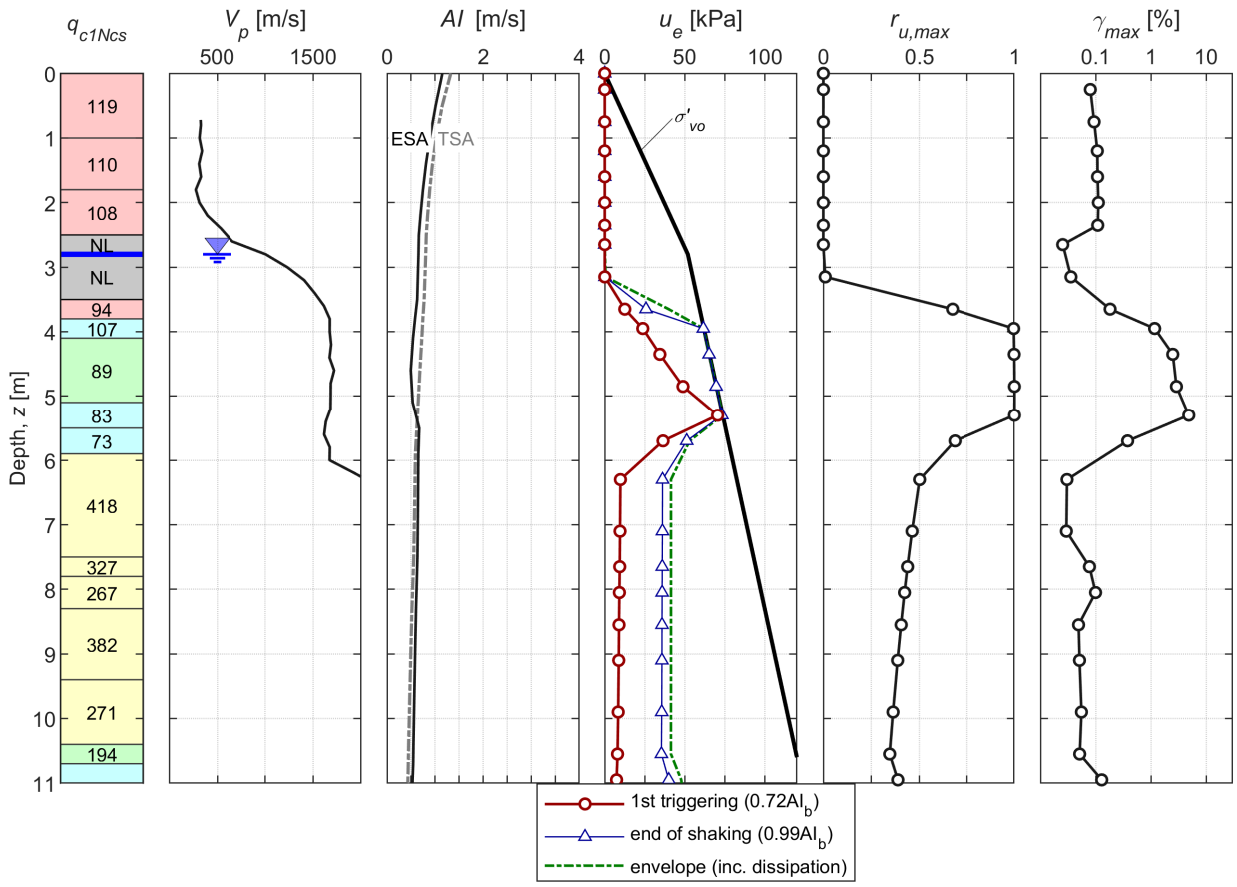

RHSC-based input

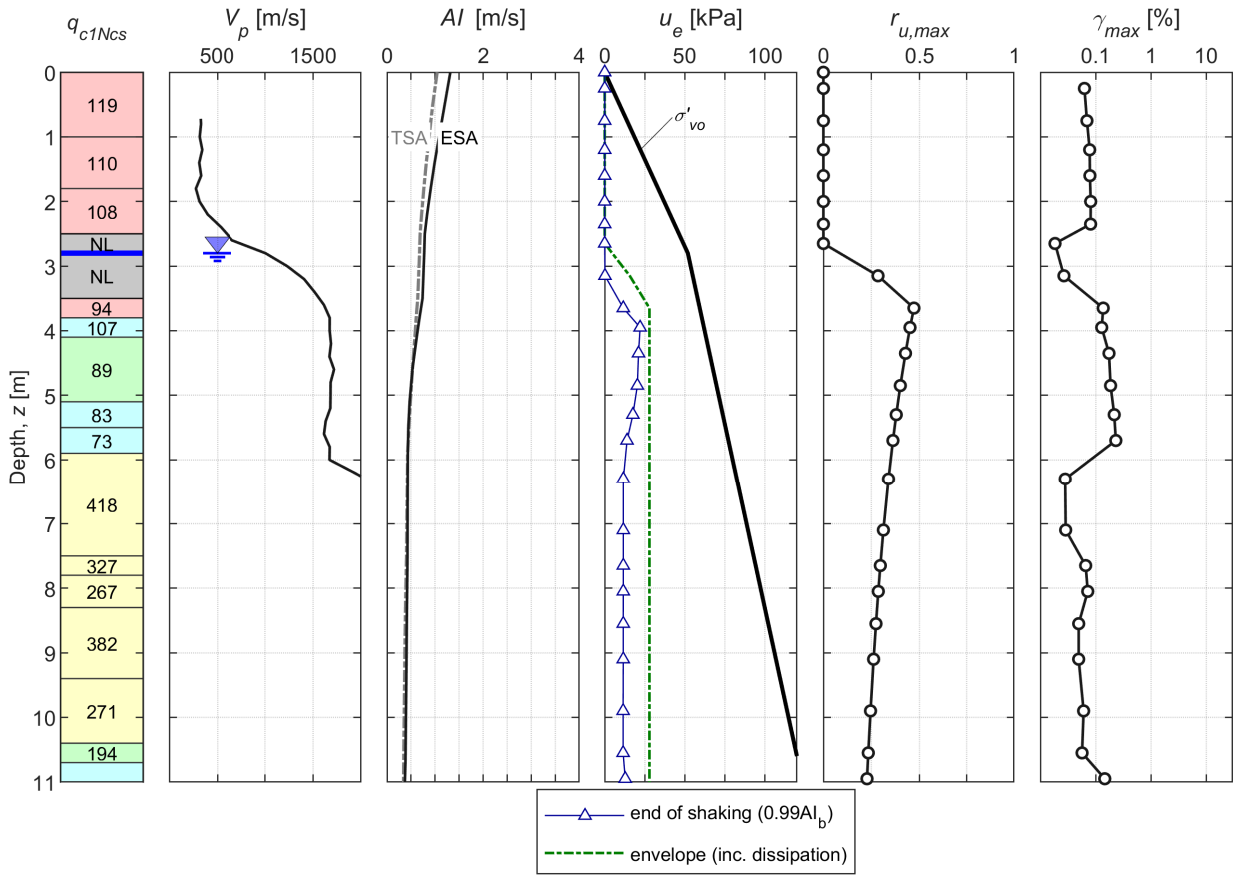

CPT 57361

SMTC-based input

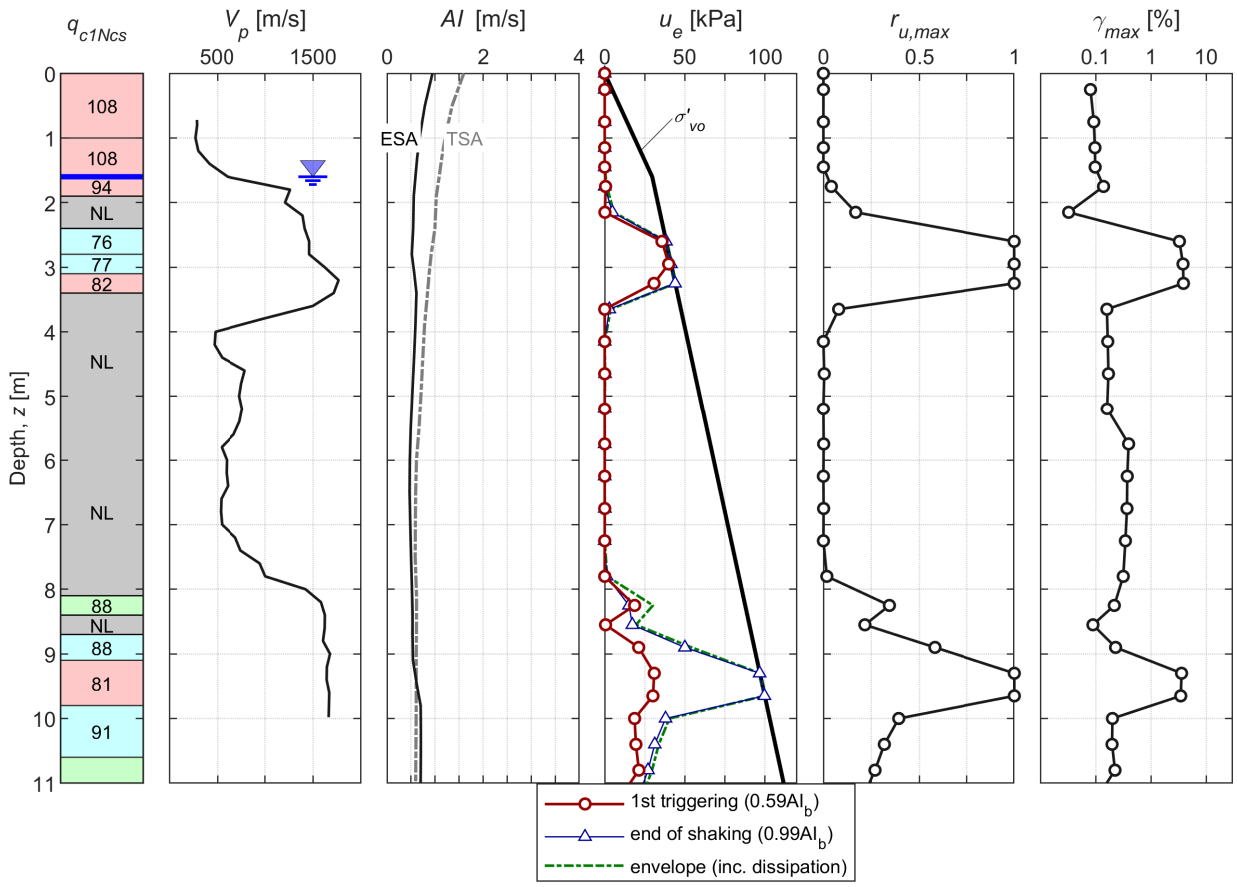

RHSC-based input

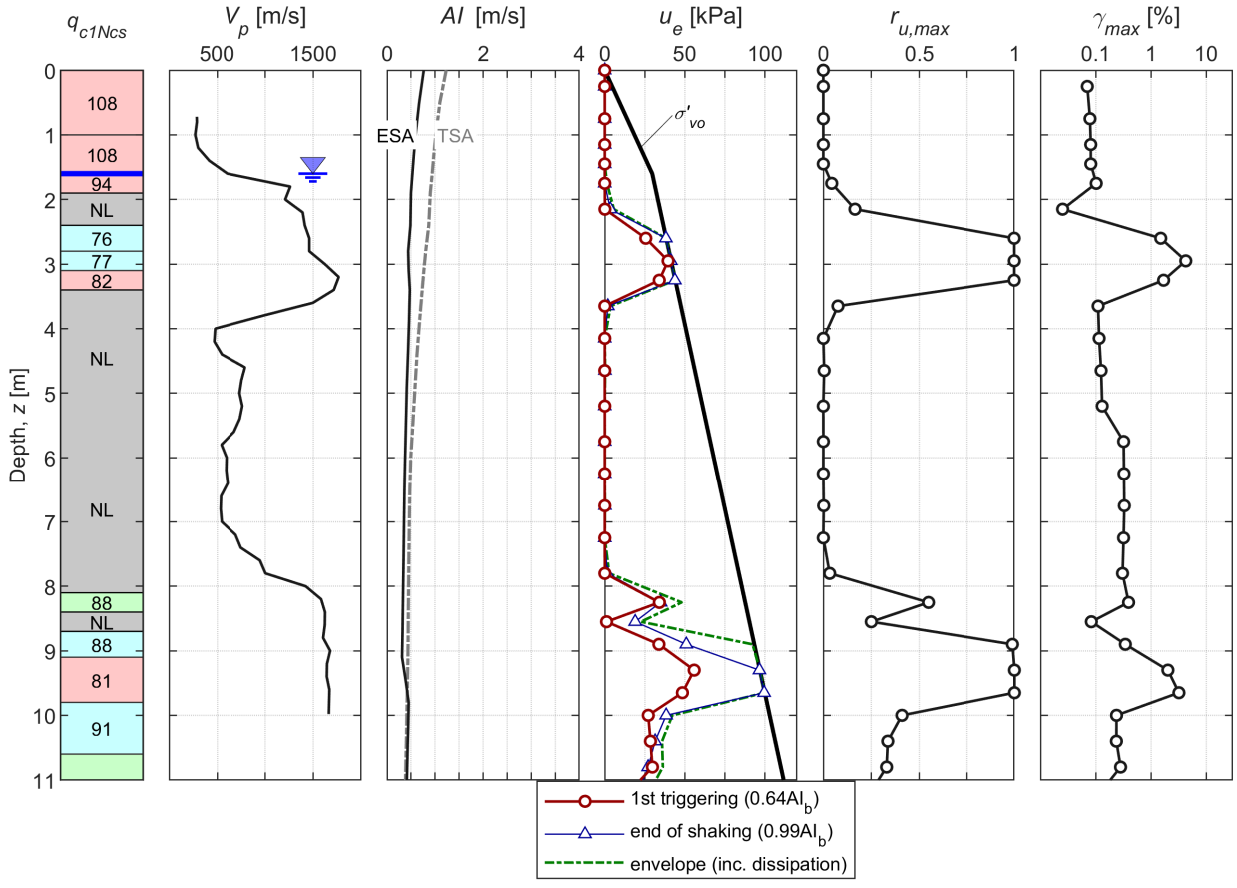

CPT 57339

SMTC-based input

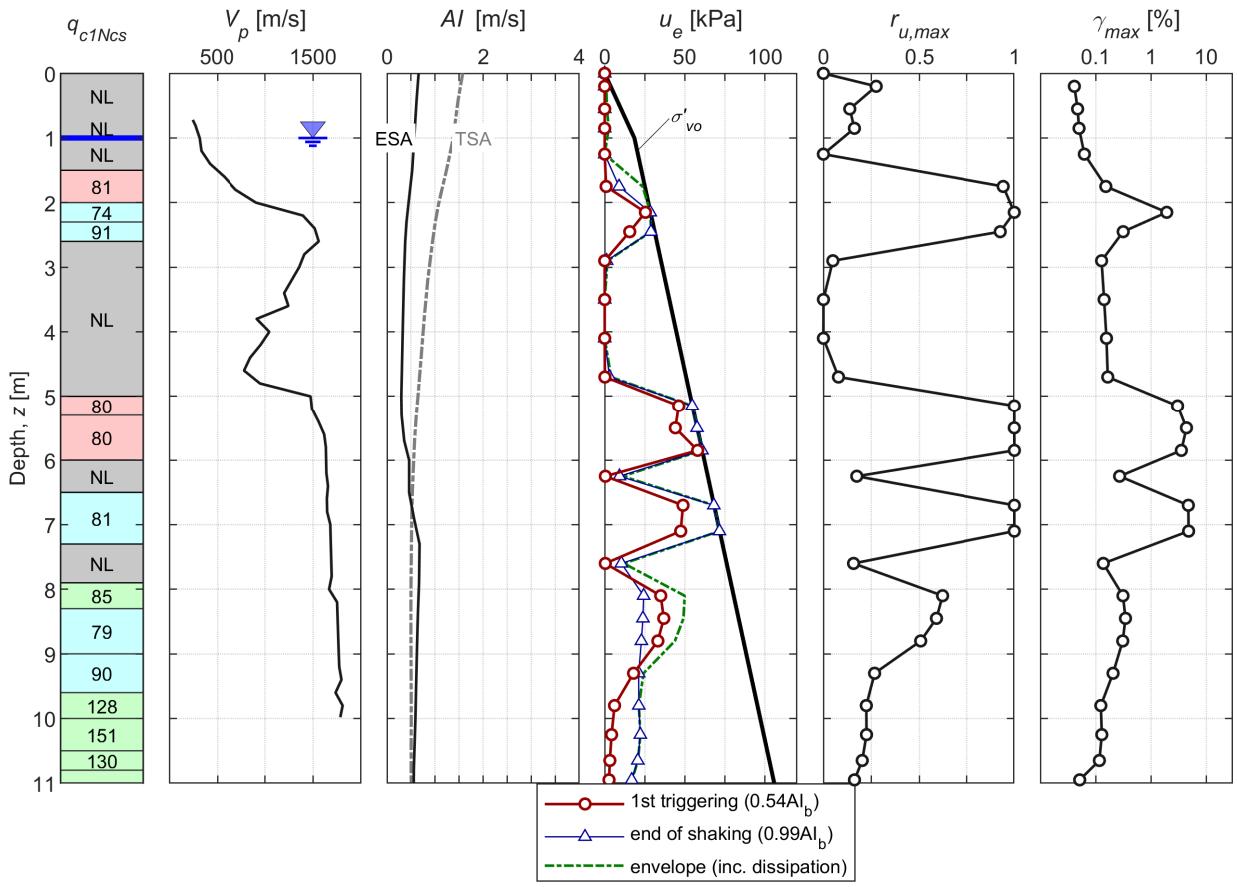

RHSC-based input

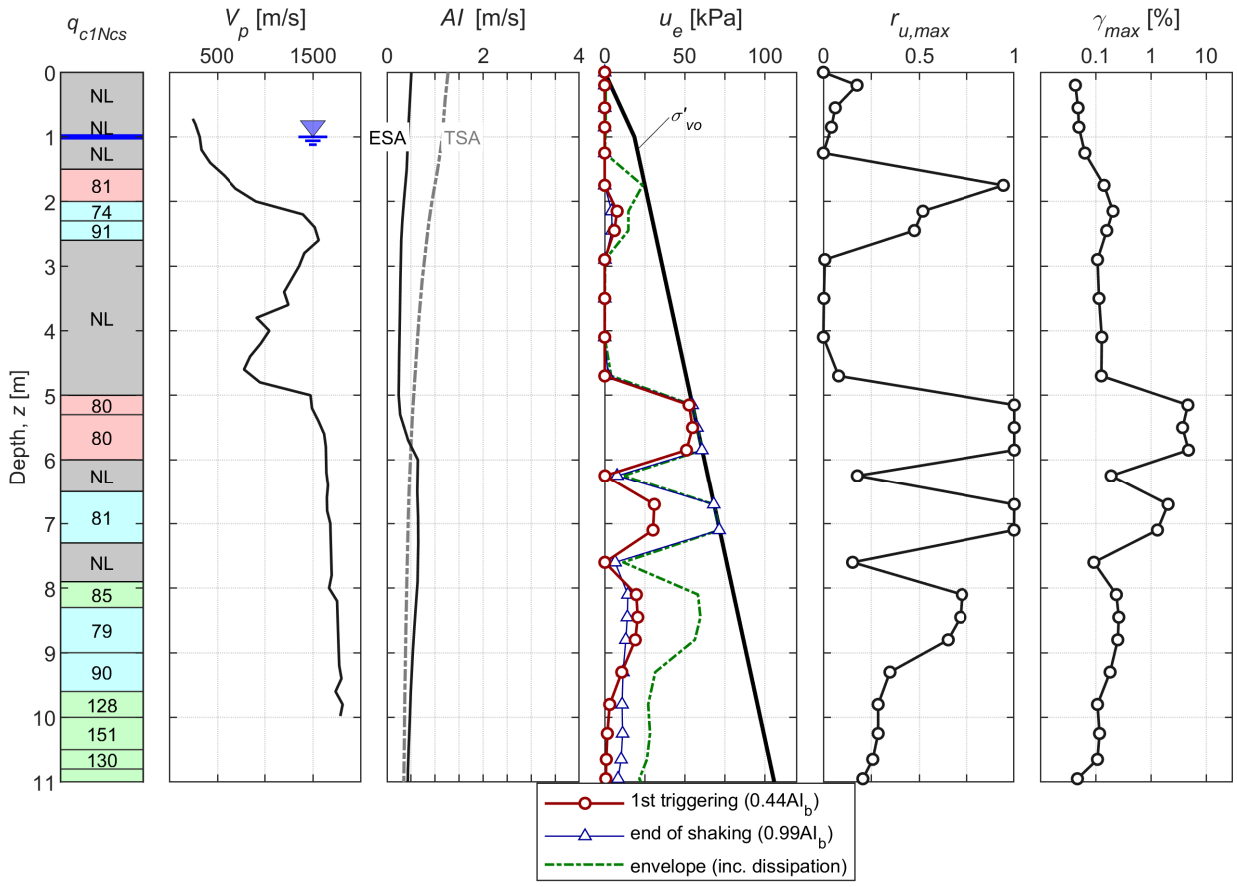

CPT 57351

SMTC-based input

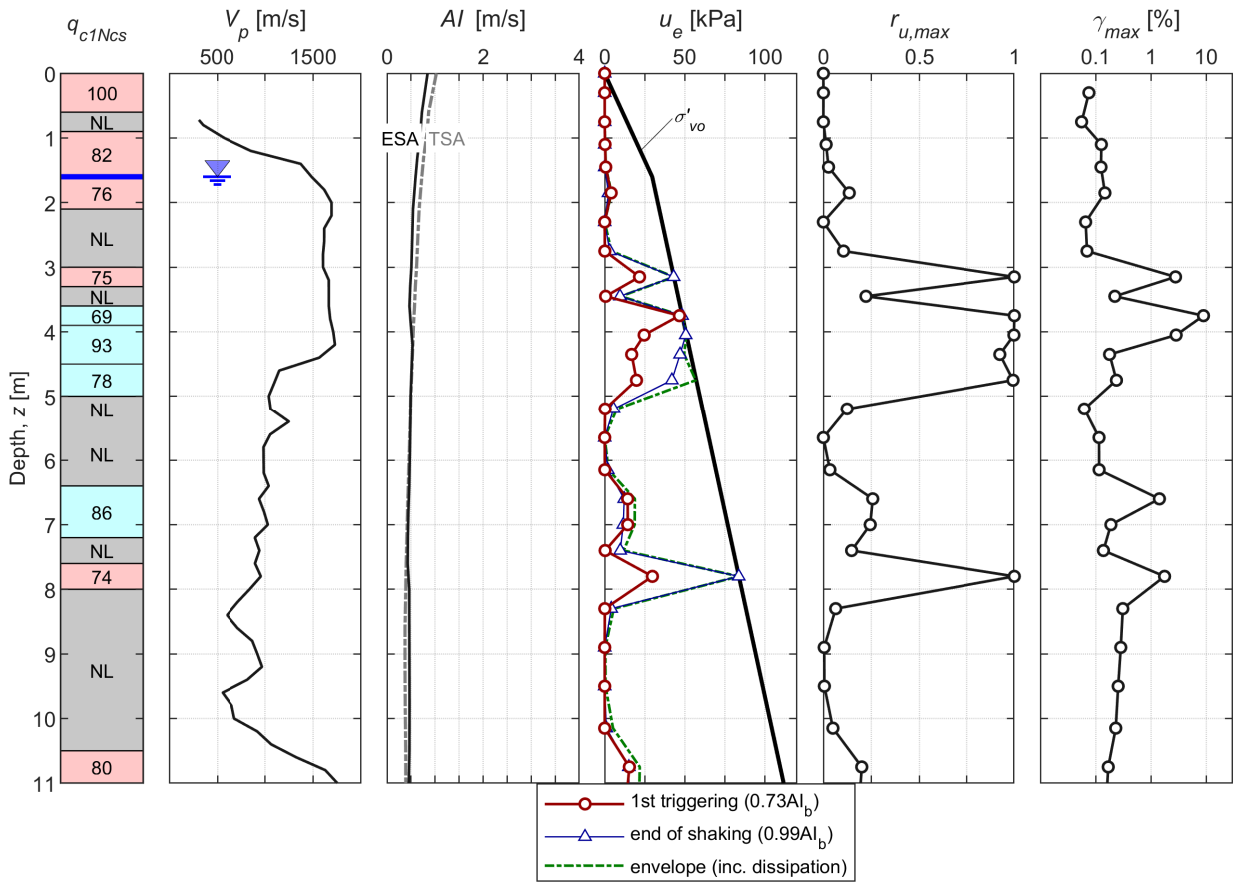

RHSC-based input

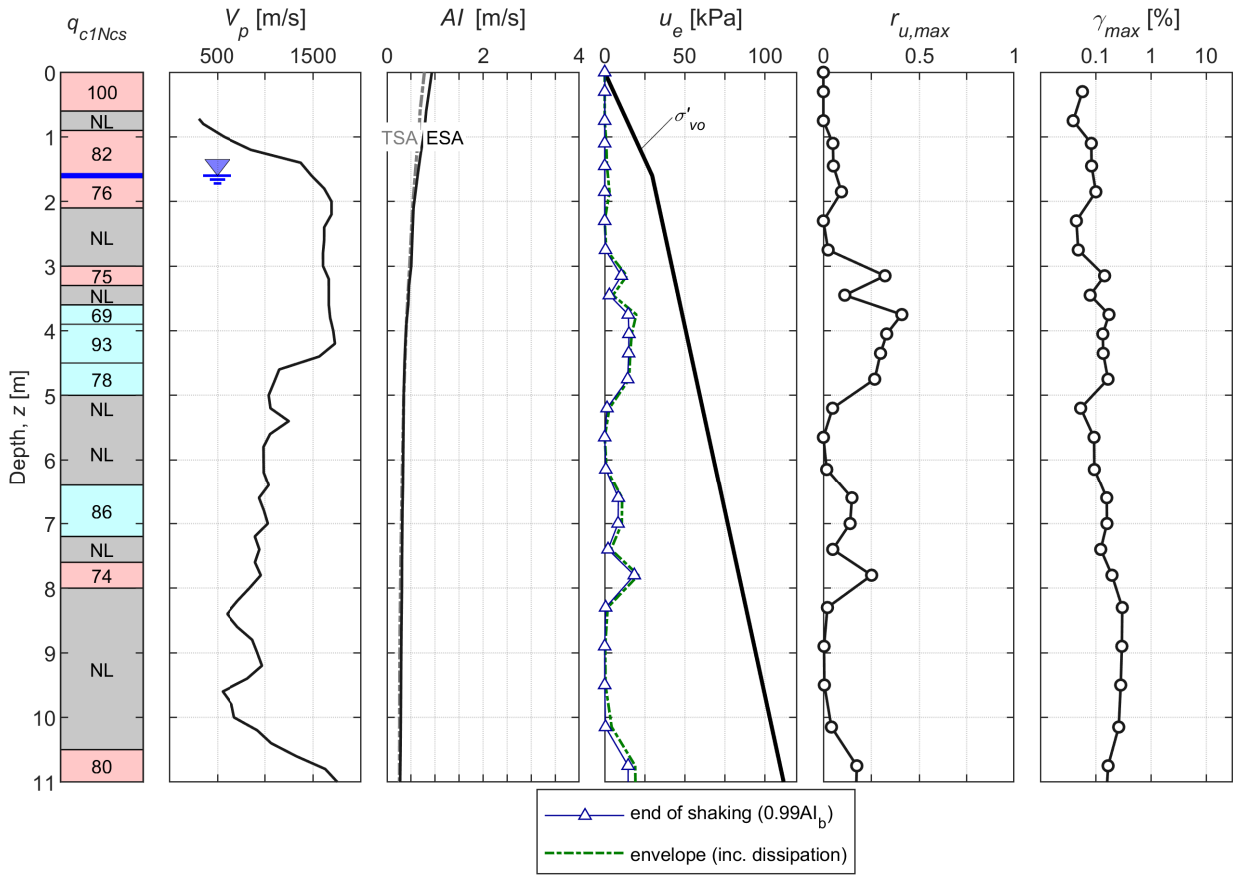

CPT 57338

SMTC-based input

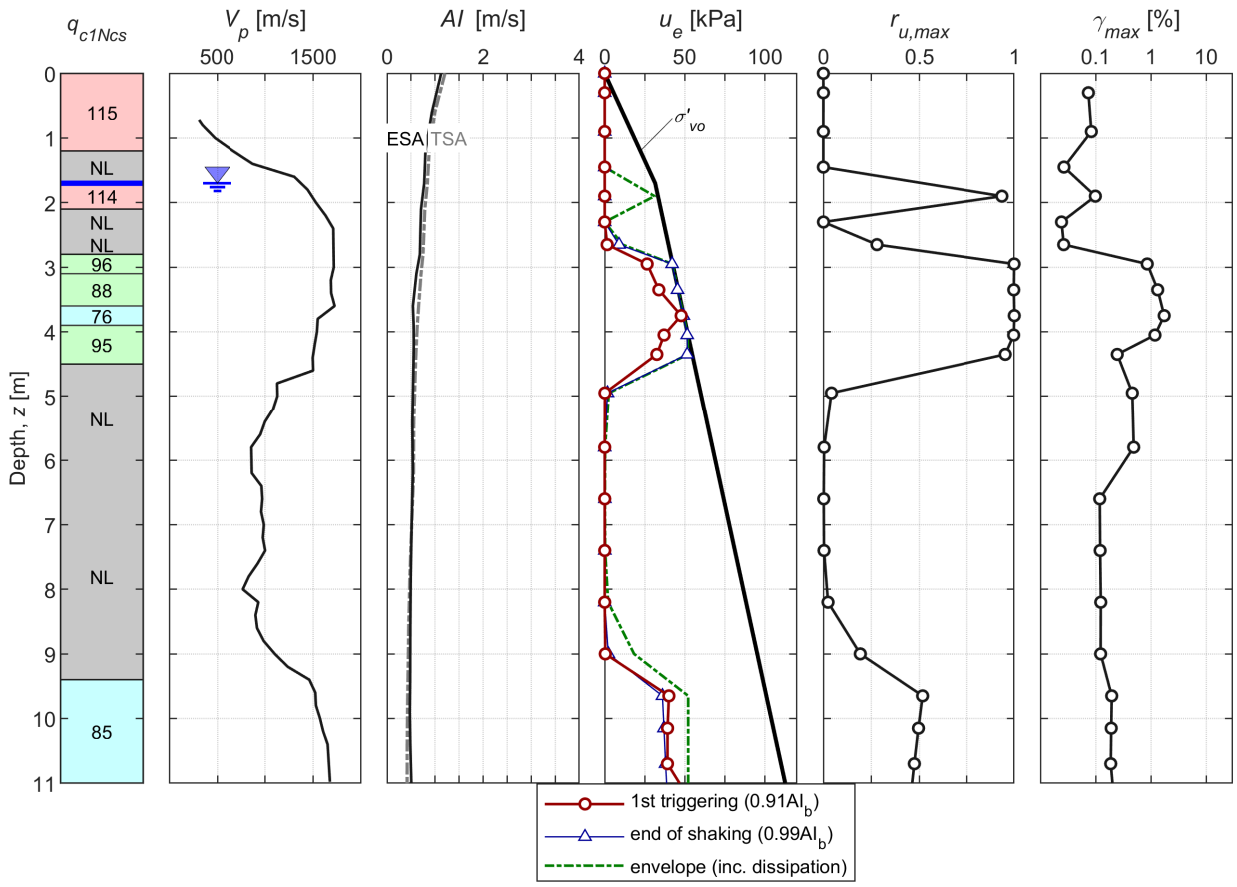

RHSC-based input